

THIS WEEK

EDITORIALS

TECHNOLOGY The digital lab is here, so what now for notebooks? **p.410**

WORLD VIEW The cultural baggage that holds back science in China **p.411**

RESISTANCE Australian bluetongue skink tackles invasive toads **p.413**



Access all areas

To create a sustainable, open research literature, governments need to find the finances to make it viable — and recognize that adding value to diversifying research outputs has its own costs.

The past week has seen several twists and turns along the road towards a truly open research literature. But the underlying questions have hardly been touched on: who needs whom to add what value to what literature, and who is willing to pay for it?

Consider first a ridiculous distraction: the US Research Works Act. Proposed late last year in the House of Representatives, this seeks to stop US federal funders from mandating that research papers be made freely available. The current policy of the US National Institutes of Health — a policy supported and assisted by *Nature* and its publishers — is that authors' final versions of papers should be deposited in the freely accessible PubMed Central database within a year of publication. That policy would be prohibited by the Research Works Act. The proposal has provoked an outcry, stimulating several publishers to state their opposition (including, last week, ours; see go.nature.com/myil4g).

Why is this a ridiculous distraction? Because it tries to reverse a slow but strong political tide that is in favour of access, and because even its supporters believe that it has no chance of passing.

Next, consider the more serious and necessary debate about online theft of copyrighted content. In 2002, *Nature's* publishers resolved that the authors of original research papers should retain copyright while giving our journals an exclusive licence to publish, but there remain justified concerns in science publishing and more generally that unlicensed online distribution threatens the viability of producers of valued content.

Two draft measures introduced to Congress last year — the PROTECT Intellectual Property Act and the Stop Online Piracy Act — intended to counteract such threats, but triggered huge opposition because of the threat of collateral damage to Internet activity. This climaxed last week with a day-long blackout of Wikipedia and hostile statements by several publishers including *Nature's* (see go.nature.com/ktt yax). Both proposals have been put on hold, and the piracy act will be redrafted.

Despite these skirmishes, the vision of an open research literature has both scientific merit and strong international political support. But there are still substantive issues regarding the future of the primary research literature, which are unlikely to be resolved for years.

ADDING VALUE

No one disagrees that a publisher of review articles deserves to charge for access to them. After all, the publisher's staff have contributed value in various ways: identifying the author and the article's aim, assessing and editing the draft, selecting peer reviewers, working with the author to build on their advice, developing illustrations, rendering the article into print and online forms, maintaining it online and including links, citation statistics and other enhancements.

A publisher of research papers also does all of these things, except that authors voluntarily submit the article, the editors undertake careful assessment of scientific significance, and the refereeing stage involves much deliberation, occasional debate and revisions that

significantly enhance the robustness and scientific impact of the paper.

The publishers and editors of *Nature* and its related journals remain committed to sustaining and developing these components of added value. For example, we organize researcher meetings to review our acceptance and technical standards in fast-moving fields, we upgrade the online search and other facilities surrounding our papers, and we are investing in improved presentation of online data and illustrations. As for the business model, anyone who wishes to preserve these modes

“The vision of an open research literature has both scientific merit and strong political support.”

of added value should favour a publishing evolution with a mixed economy of author-pays open access and subscriptions, with some journals, such as *Nature Communications*, allowing both options (see go.nature.com/slwr3t).

But the literature itself is changing. It no longer consists of only static papers that document a research insight. In the future,

online research literature will, in an ideal world at least, be a seamless amalgam of papers linked to relevant data, stand-alone data and software, 'grey literature' (policy or application reports outside scientific journals) and tools for visualization, analysis, sharing, annotation and providing credit.

And 'publishers' will increasingly include organizations or individuals who are not established journal publishers, but who host and provide access and other added value to this online edifice. Some may be research funders, such as the National Institutes of Health in its hosting of various databases; some may be research institutions, such as the European Bioinformatics Institute. Others may be private companies, including suppliers of tools such as the reference manager Mendeley and Digital Science, sister company to Nature Publishing Group.

This literature will need to be readable and computable not only by people but also by machines, which will, in turn, require publishers to develop new standards.

In short, the literature is becoming ever more multifaceted, and intermediaries will be needed to supply added value and usability. It is hard to imagine such a primary literature and all of those seeking to add genuine value to it thriving when its key results are behind subscription firewalls. But a vision for open access in which all results — text, data, grey literature and so on — are immediately available in their published versions requires the costs of that added value to be paid for.

None of this will occur until the tide in its favour becomes unstoppable. The only way that can happen is for governments to recognize the complexities of this terrain, and the damage that can be done to the providers of added value and to research itself as a result of poorly considered prohibitions or compulsions. Above all, they need to find the money to make the vision viable. Only then will the open research literature truly come to fruition, and only then will those wishing to provide added value be able to invest confidently in doing so. ■

S. DUBREY

Fertile union

Scientists and politicians are working together to bring new reproductive techniques to Britain.

Too often, scientists and policy-makers talk past one another and ‘science-based’ policy-making is anything but. But sometimes, they get it right, and when they do, they deserve praise.

One such case is last week’s announcement that Britain intends to develop *in vitro* fertilization (IVF) techniques that could cut the number of children born with devastating genetic conditions such as muscular dystrophy. Not only are scientists, lawmakers and ethicists speaking the same language, they are also synchronizing their efforts to make Britain the first country to test the techniques in humans, taking it light years ahead of other nations (see page 419).

Uniquely among IVF procedures, the new techniques involve embryos that combine genetic material from three people. The prospect of a child with three genetic parents has inevitably raised concern among some commentators, and among politicians worried about what those commentators will say.

The diseases targeted by these techniques are passed to children by mothers through faulty mitochondria in their eggs. The techniques therefore remove the genetic material from the nucleus of the faulty egg and insert it into a healthy egg that has been stripped of its own nucleus. This is where the third ‘parent’ comes in: a different woman must supply the healthy egg. A child born from IVF using one of the modified eggs will therefore carry the genes of three people: nuclear DNA from both parents and mitochondrial DNA from the donor.

Concerns over the science, safety and ethics of the procedures prompted the British government to ban them in 2008, in an amendment to the Human Fertilisation and Embryology Act, which governs fertility treatments and research. But the law also anticipated scientific advances in these technologies and set out a streamlined mechanism to legalize the procedures if a future government saw fit. Since then, one of the techniques has been used to produce two healthy rhesus monkeys and the other has been tested successfully in defective human eggs fertilized *in vitro*.

Britain has now decided that the time is right to revisit its legislative

ban. A scientific review released in April 2011 by the Human Fertilisation and Embryology Authority (HFEA) — the agency that would regulate the procedures — found no scientific evidence that the techniques are unsafe, but did recommend additional studies that would be needed before clinical trials could begin. Many of those studies are now under way or soon will be. The Wellcome Trust, Britain’s biggest biomedical charity, announced last week that it would pay for some of them.

Legislators and regulators are not standing idle while the scientists work away. Simultaneously, and in anticipation of positive scientific findings, the HFEA announced a public consultation on the techniques. The consultation is the first step towards legalizing clinical

“Elected officials do seem to be giving the issue a fair and informed hearing.”

trials. Under the 2008 change to the fertility act, the government can write an amendment to legalize the procedures that would require only brief discussion before being voted on by Parliament.

Any number of issues could yet derail the trials. Additional research could raise safety problems or find the process too inefficient.

The public, perhaps swayed by ‘three-parent baby’ headlines, could resist. And the Nuffield Council on Bioethics in London, which has just started an independent review of the techniques, could identify more ethics qualms. Allowing changes to the mitochondria of an embryo, for instance, could increase the chances that changes to nuclear DNA will be allowed in order to treat other conditions, such as cystic fibrosis. In exploring that path, we eventually come to designer babies, with non-medical tinkering to develop certain traits.

Critics may say that the UK government could have addressed these issues more quickly by legalizing the procedures and then leaving regulators to decide when the science was sufficient. But elected officials do seem to be giving the issue a fair and informed hearing, and are placing science at its centre.

The situation is very different in other countries. A government review of embryo research in Australia last year recommended against changing the law to legalize clinical use of the procedures. And in the United States, regulators consider the techniques to be a form of gene therapy, controlled by the Food and Drug Administration, which seems in no hurry to consider their clinical use.

About one in 200 women passes a mitochondrial disease on to her children. In Britain, those children have a chance of a better future because scientists and politicians, for once, are seeing eye to eye. ■

Notes on screen

Computer tablets are changing the way that scientists record their experiments.

In its introductory handbook for physics students, the Cavendish Laboratory at the University of Cambridge, UK, says that lab notes “need not be particularly tidy, but they should be understandable by the writer or somebody else at a later date”. Written in 2008, the guidance adds: “Your notebook must be A4 in size and hard-bound. A suitable book can be bought from the laboratory technician.”

So far, no doubt, so familiar — but technology is marching on, and commuters are starting to abandon dog-eared paperbacks for e-books. For how much longer will the lab book prevail in its current form? And how many more notebooks will the Cavendish technicians sell?

Reports of the death of the standard lab book — in use for hundreds of years — are, of course, as premature as they are exaggerated. And *Nature* has been here before — in a feature in 2005, we reported that electronic notebooks were poised to become increasingly popular among researchers (see *Nature* 436, 20–21; 2005). The News Feature

on page 430 of this issue, which takes a look at the rise of the digital lab, shows that we were right.

“Paper has nothing to offer me,” says Michelle James, an Alzheimer’s disease researcher at Stanford University in California who is profiled in the feature, and who has moved her scientific notes to her iPad. James is far from alone — a generation of bench scientists is ditching paper and taking advantage of computer tablets and software that allow people to share protocols and swap notes. (If it cheers the old guard, who even now are vowing never to abandon their trusty notebooks and pencils, the digital-savvy researchers must place their fancy kit in plastic bags to protect it from spills.)

There is more to this than the migration of content from print to web. Just as newspapers have been able to exploit the Internet to reach readers and build communities in ways that they could not have imagined when they first started placing their copy online, so powerful processors and the digitization of data could let researchers analyse their results much earlier in the scientific process than is common now.

Such an approach is not completely new, but digitization makes it easier. The Cavendish introductory notes say: “Ideally you should plot graphs as you go along, not after completing the experiment, though in practice this is not always possible.” It is now. ■

➔ NATURE.COM
To comment online,
click on Editorials at:
go.nature.com/xhbnqv

RESEARCH HIGHLIGHTS

Selections from the
scientific literature

IMMUNOLOGY

Culprits in diabetic heart risk

People with type 1 diabetes have an above-average risk of developing heart disease, or atherosclerosis, and two related groups of inflammatory immune cells may be to blame.

Immune cells called monocytes and macrophages — which develop from bone marrow — from mice and humans with diabetes express unusually high levels of the enzyme ACSL1. This modifies fat molecules that then trigger inflammation, according to Karin Bornfeldt at the University of Washington in Seattle and her team. Diabetic mice that received transplanted bone-marrow cells lacking ACSL1 developed fewer and smaller blood-vessel lesions characteristic of atherosclerosis than did diabetic mice transplanted with normal cells.

Blocking this enzyme could prevent the accelerated atherosclerosis common in patients with diabetes, the authors suggest.

Proc. Natl Acad. Sci. USA
<http://dx.doi.org/10.1073/pnas.1111600109> (2012)

MATERIALS

Circuit, heal thyself

A crack in an electrical circuit no longer needs to be permanent, thanks to the

development of circuits that can 'heal' themselves. The incorporation of tiny capsules of liquid metal allows electrical circuits to recover almost all of their function after being broken.

Nancy Sottos, Scott White and their colleagues at the University of Illinois at Urbana-Champaign created capsules of gallium and indium (**pictured**) and placed them either directly onto gold circuits or into an insulating layer above the wires. If a crack breaks the circuit and ruptures the capsules, the liquid metal is released, filling in the crack.

After damage, the researchers' circuit recovered 99% of its conductance in less than 1 millisecond. However, the team's method may not be immediately applicable because the demonstration circuit is significantly larger than most current micro-electronics.
Adv. Mater. 24, 398–401 (2012)

CANCER

Tumour cells lend a hand

Cells that provide tumours with support may also defend against the cancer's spread,

so chemotherapies that target these cells could inadvertently fuel metastasis.

Pericytes are cells that provide structural support to blood vessels, including those that feed tumours. Raghu Kalluri at Harvard Medical School in Boston, Massachusetts, and his group found that patients with invasive breast cancer tended to fare poorly if they had few pericytes covering the blood vessels in their tumours. Selectively killing pericytes in tumour-bearing mice slowed tumour growth but increased metastasis and



S. BOBACK

ANIMAL BEHAVIOUR

Snakes strangle with feeling

As boa constrictors tighten their bodies around their prey, the snakes sense the dying animal's heart rate to determine how much pressure to apply and when to stop squeezing.

Scott Boback and his colleagues at Dickinson College in Carlisle, Pennsylvania, implanted simulated hearts into warm, dead rats and presented them to 16 snakes. In the presence of a heartbeat, the boas constricted for nearly twice as long and with more than

double the pressure than in the absence of a heartbeat. When the heart stopped midway through constriction, the snakes released their prey.

The researchers speculate that the ability to detect a heartbeat co-evolved with constriction (pictured) to help snakes identify when death occurs and minimize energy expenditure.

Biol. Lett. <http://dx.doi.org/10.1098/rsbl.2011.1105> (2012)



the expression of a cancer-promoting gene called *Met*.

Two chemotherapies that target pericytes — imatinib and sunitinib — produced similar effects in mice, but their effects on metastasis were suppressed when a *Met* inhibitor was given simultaneously. The authors suggest that pericyte loss makes tumour blood vessels leaky, which may set in motion events that promote metastasis. *Cancer Cell* 21, 66–81 (2012)

PHYSICS

One molecule, one photon

To harness quantum technology for applications such as computing and cryptography, researchers must develop materials that can emit single photons in response to electrical signals. However, existing approaches require an ultracold environment.

Maximilian Nothaft at the University of Stuttgart in Germany and his colleagues tested phosphorescent iridium-based organic molecules as the active layer in a light-emitting diode (LED) at room temperature. They showed that the molecules could emit photons in response to electrical and laser stimulation. The distribution of the emitted photons suggests that each was emitted by a single molecule.

The authors say that their method should allow for further study of photon-emission mechanisms in organic LEDs. *Nature Commun.* <http://dx.doi.org/10.1038/ncomms1637> (2012)

CELL BIOLOGY

Manganese fights deadly toxin

A toxin produced by certain deadly strains of pathogenic bacteria can be stopped in its tracks by the element manganese.

Shiga toxin — generated by *Shigella* bacteria and some strains of *Escherichia coli*

— is shuttled through several organelles in the infected cell and eventually shuts down cellular protein production. Somshuvra Mukhopadhyay and Adam Linstedt at Carnegie Mellon University in Pittsburgh, Pennsylvania, fluorescently tagged the toxin and found that, in cells treated with manganese, the toxin was rerouted to the cell's degradative compartment and destroyed. Manganese targets a protein called GPP130 — which is normally required for the trafficking of the toxin — preventing the toxin from binding to it.

Mice injected with the toxin and treated with manganese stayed healthy throughout the six-day study, whereas untreated mice died within four days.

Science 335, 332–335 (2012)

ECOLOGY

Ready for the toxic toads

Exposure to an exotic plant seems to have pre-adapted a native Australian lizard to the toxins of an invasive animal.



The American cane toad (*Rhinella marina*), an exotic introduced to Australia within the past century, is generally toxic to native predators.

But Richard Shine and his colleagues at the University of Sydney observed that bluetongue skinks (*Tiliqua scincoides*; pictured) in some areas can tolerate the toad's toxins. The toxins are similar to those produced by another exotic species, the Madagascan 'mother of millions' plant (*Bryophyllum* spp.).

The authors tested the resistance of skinks from

COMMUNITY CHOICE

The most viewed papers in science

CLIMATE CHANGE

Warming, but not as much

HIGHLY READ
on www.agu.org
the week beginning 16 January

The climate system may be less sensitive to greenhouse-gas warming than many models have predicted.

Nathan Gillett and his co-workers at Environment Canada in Victoria, British Columbia, analysed how well the latest Canadian Earth System Model tracked temperature changes attributable to volcanoes, man-made aerosols and rising greenhouse-gas emissions. They adjusted the model using temperature records from 1851 to 2010 — 60 years of data more than most previous analyses. The model predicted a short-term increase of 1.3–1.8 °C for a doubling of atmospheric carbon dioxide levels, which is low in the range of estimates from previous forecasts.

Under various scenarios, the authors' model forecasts warming of 1.2–4.3 °C by the end of the century compared with pre-industrial times.

Geophys. Res. Lett. <http://dx.doi.org/10.1029/2011GL050226> (2012)

various regions of Australia to either the toad or plant toxin. They found that skinks from areas where the plant is abundant were better able to tolerate both. Moreover, skinks readily eat both the plants and the toads. The findings suggest that the plants have selected for skinks that could tolerate the toad toxins. *Am. Nat.* <http://dx.doi.org/10.1086/664184> (2012)

NEURODEVELOPMENT

Mutation and infection to blame

A combination of genetic and environmental factors may act synergistically to boost the risk of certain neurodevelopmental disorders.

In humans, mutations in *NURR1* — a gene vital for the normal development of neurons that produce a neurotransmitter called dopamine — are thought to slightly raise the risk of neurodevelopmental disorders. The risk is similarly increased by infection in the mother during pregnancy. To test the combined effect of these two factors, Urs Meyer at the Swiss

Federal Institute of Technology in Zurich and his colleagues activated the immune system of pregnant mice that had only one copy of the *Nurr1* gene.

They found that dopaminergic development in key parts of the brain was impaired in *Nurr1*-deficient pups born to immune-activated mothers. As adults, these mice were unable to sustain or shift attention normally, a characteristic of neurodevelopmental diseases such as schizophrenia and attention-deficit hyperactivity disorder.

J. Neurosci. 32, 436–451 (2012)

CORRECTION

In the Research Highlight 'Magnetic switch for memory' (*Nature* 481, 241; 2012), the authors switched the magnetic states of antiferromagnetic iron atoms by applying a voltage, not a current, of more than 7 millivolts.

NATURE.COM

For the latest research published by Nature visit:
www.nature.com/latestresearch

SEVEN DAYS

The news in brief

POLICY

Leap-second vote

A decision about whether to ditch the leap second — a move that would pull reference time out of sync with the rising and setting of the Sun — has been deferred until 2015. Delegates to the World Radiocommunication Assembly of the International Telecommunication Union in Geneva, Switzerland, were supposed to vote on the issue last week, but couldn't reach a consensus. See go.nature.com/tucaxg for more.

Untreatable TB?

India's government has dismissed reports that a form of incurable tuberculosis has arrived in the country. Last year, researchers at the Hinduja National Hospital in Mumbai reported 12 cases of totally drug-resistant tuberculosis (Z. F. Udwadia *et al.* *Clin. Infect. Dis.* <http://doi.org/hpd;2011>). This would have made India the third country, after Italy and Iran, in which an untreatable form of the disease had emerged. But in a 17 January statement, the health ministry said doctors had found that seven of the patients were responding to treatment, and that the disease was in fact extensively-drug-resistant tuberculosis. See go.nature.com/hygn2o for more.

West Bank rebuke

The European Commission and London's venerable Natural History Museum are facing criticism for working with a company that has facilities inside Israeli settlements in the West Bank occupied territories — settlements that international law has determined are illegal. The company, Israeli cosmetics firm Ahava Dead Sea Laboratories, is part of



A. HARRER/BLOOMBERG/GETTY

Tar sands pipeline pulled

US President Barack Obama has blamed politics for his rejection of an application to build a 2,700-kilometre-long pipeline to carry oil from tar sands in Alberta, Canada, to the coast of Texas. Congress had forced a deadline of 21 February for the decision, which did not

leave time for the state department to assess the project, Obama said on 18 January. The decision pleased environmental campaigners, but TransCanada, the Canadian company hoping to build the Keystone XL pipeline, said that it would reapply.

a €5.19-million (US\$6.7-million) research project on the toxicity of nanoparticles. On 17 January, 21 academics and public figures wrote to the British newspaper *The Independent* decrying the museum's involvement with the firm. See go.nature.com/vxuwwm for more.

NIH salary cut

The maximum salary that institutions can pay to a biomedical researcher out of a grant from the US National Institutes of Health has been cut by 10% to \$179,700. The agency told grant recipients about the tightened salary cap (which applies to grants won after 22 December) on 20 January. Academic medical centres will have to dig into other budgets if they wish to keep wages high. The cut

could have been worse — last October, Congress was considering legislating a 17% cut. See go.nature.com/jdk9gh for more.

Genome reshuffle

Genome scientists and genetics societies have expressed support for a planned reorganization of the US National Human Genome Research Institute. At a public teleconference on 18 January, biologists welcomed the changes, which create new divisions to help the institute shift the focus of its research from understanding the structure and biology of genomes, to translating this information into better medical care. (Priorities were laid out in a planning paper last year; see E. D. Green *et al.* *Nature* **470**, 204–213; 2011.) Another

public meeting will be held on 13 February. See go.nature.com/s6sgw8 for more.

BUSINESS

Stem-cell promise

Two clinical trials testing retinal cells derived from human embryonic stem cells have reported positive preliminary results. Advanced Cell Technology, a biotechnology firm in Marlborough, Massachusetts, says that the cells seem to be safe 4 months after being injected into the eyes of two patients with differing forms of blindness (S. D. Schwartz *et al.* *Lancet* [http://dx.doi.org/10.1016/S0140-6736\(12\)60028-2](http://dx.doi.org/10.1016/S0140-6736(12)60028-2); 2012). The trials — which are testing safety, not efficacy — will eventually enrol a dozen

patients each, with final results expected in 2013. See go.nature.com/g3mjg7 for more.

EVENTS

Nuclear looting

Radioactive material was stolen last week from a nuclear power plant being built in Egypt, highlighting the dangers of nuclear looting during social upheaval. The International Atomic Energy Agency said that low-level radioactive sources were taken from a lab at the El Dabaa nuclear plant on Egypt's Mediterranean coast. This is not the first example of such theft: for instance, looters stole caesium and cobalt radioactive sources from a nuclear centre in Baghdad in 2003, after the US-led invasion of Iraq. See go.nature.com/u6g8se for more.

PEOPLE

European funder

Teresa Riera Madurell (**pictured**), a Spanish politician and former computer scientist, will be the rapporteur for Europe's enormous 2014–20 research funding programme (Horizon 2020), *Nature* has learned. As rapporteur, Riera will shepherd committee reports on the programme through the European Parliament, and will influence decisions about its funds and structure. Under



proposals currently being considered, the programme would distribute around €80 billion (US\$104 billion) for research.

Brazilian minister

Brazil's new science minister is Marco Antonio Raupp, formerly head of the Brazilian space agency. From 24 January, he replaces Aloizio Mercadante, who moves to the education ministry in a cabinet reshuffle. The announcement was made on 18 January.

Crafoord winners

Astrophysicist Reinhard Genzel, at the Max Planck Institute for Extraterrestrial Physics in Garching, Germany, and astronomer Andrea Ghez, at the University of California, Los Angeles (UCLA), have won the 2012 Crafoord Prize in Astronomy for their work showing that there is probably a black hole at the centre of the Milky Way. The prize, worth 4 million Swedish kronor (US\$590,000), rotates through

several disciplines. This year, a separate mathematics prize was given to mathematicians Terence Tao at UCLA and Jean Bourgain at the Institute for Advanced Study in Princeton, New Jersey, for their work in areas including harmonic analysis, partial differential equations and ergodic theory of dynamical systems.

Early-career grants

The Howard Hughes Medical Institute in Chevy Chase, Maryland, will dole out a total of more than US\$20 million to 28 international scientists who are beginning their independent careers. The medical-research giant announced on 24 January that the investigators come from 12 countries, with China, Portugal and Spain leading the way. Each person, selected from the 760 applicants, will receive \$650,000 over 5 years.

RESEARCH

A chip off Mars

A meteorite that fell to Earth last July in Morocco has proven to be a rare chunk of Mars. Only a handful of Martian meteorites are known, and only five (including the new find) were seen falling to Earth — an important factor because it tells scientists how much time the meteorites have had to pick up contamination on the ground. The last witnessed

COMING UP

26 JANUARY

To inform its priorities in tackling climate change, the UK government publishes a study that weighs up climate risks according to their financial, social and environmental cost.

fall was in 1962. About a dozen pieces of meteorite were recovered from Morocco in December, and were certified on 17 January as coming from Mars. See go.nature.com/9scfwq for more.

Bat scourge

Between 5.7 million and 6.7 million bats have been killed by white-nose syndrome in North America since 2006, biologists agreed on 17 January, after a meeting of the Northeast Bat Working Group in Carlisle, Pennsylvania. A 2009 estimate had put the death toll at 1 million. The deadly disease, caused by a fungus, was first documented in February 2006 in a cave in New York, and has spread to at least 16 other US states and 4 Canadian provinces. Mortality rates in surveyed bat colonies range from 70% to more than 90%.

Altering embryos

Researchers at Newcastle University, UK, have received £5.8 million (US\$9 million) from the university and the Wellcome Trust in London to assess the safety of techniques that transfer genetic material between human eggs to produce embryos free of inherited mitochondrial diseases. The award was announced on 19 January. On the same day, British regulators launched a public consultation on the procedures, a step towards legalizing their clinical use. See page 419 for more.

➔ **NATURE.COM**

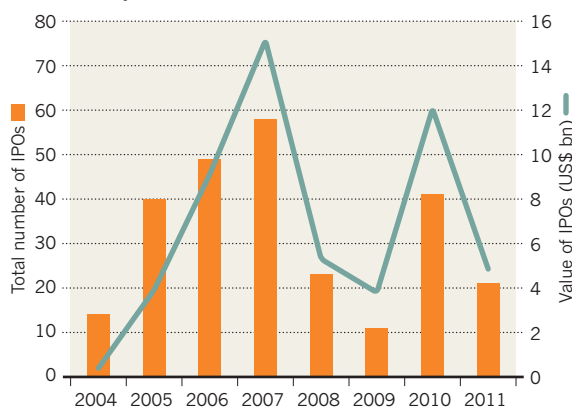
For daily news updates see:
www.nature.com/news

TREND WATCH

Biodiesel firm Renewable Energy, based in Ames, Iowa, made the first US initial public offering (IPO) of 2012, raising US\$72 million on 19 January. Companies hope to improve on 2011, which saw only 21 clean-energy IPOs globally, say analysts Bloomberg New Energy Finance. The sector's three largest IPOs last year were Chinese firms: Sinovel Wind Group (\$1.4 billion); wind-energy firm Huaneng Renewables (\$850 million); and photovoltaic maker Beijing Jingyuntong Technology (\$394 million).

THE IPO ROLLERCOASTER

Initial public offerings (IPOs) in clean energy stuttered in 2011 after a recovery in 2010.



NEWS IN FOCUS

GENE THERAPY Britain maps route to genetic modification of eggs **p.419**

US ELECTIONS Presidential candidates abandon earlier views on science **p.421**

ARCHAEOLOGY Robots boost the hunt for Bronze Age shipwrecks **p.426**



TECHNOLOGY Is it time to turn the page on the lab notebook? **p.430**

C. ANAND/AP



Countries with endemic H5N1 avian flu, such as India, often have limited resources to control the virus.

BIOSAFETY

Caution urged for mutant flu work

Public-health benefits of controversial research questioned.

BY DECLAN BUTLER

Why would scientists deliberately create a form of the H5N1 avian influenza virus that is probably highly transmissible in humans? In the growing debate about research that has done precisely that¹, a key question is whether the public-health benefits of the work outweigh the risks of a potential pandemic if the virus escaped from the lab.

For the scientists who have created the

mutated strains of the H5N1 virus, the justifications are clear. Surveillance of flu viruses could, they argue, allow health organizations to monitor birds and other animals for the mutations that would provide an early warning of a pandemic and enable authorities to act quickly to contain the virus.

That claim is meeting with scepticism, however. More than a dozen flu experts contacted by *Nature* say they believe that the work opens up important vistas in basic research, and that it sends a valuable warning about the potential

for the virus to spark a human pandemic. But they caution that virus surveillance systems are ill-equipped to detect such mutations arising in flu viruses. As such, work on the viruses is unlikely to offer significant, immediate public-health benefits, they say.

That tips the balance of risk-benefit assessment in favour of a cautious approach, says Michael Osterholm, who heads the University of Minnesota's Center for Infectious Disease Research and Policy in Minneapolis, and who is a member of the US National Science Advisory Board for Biosecurity (NSABB).

In a paper submitted to *Science*, Ron Fouchier's team at Erasmus Medical Center in Rotterdam, the Netherlands, found that just five mutations allowed avian H5N1 to spread easily among ferrets, which are a good proxy for how flu behaves in other mammals, including humans. All five mutations have been spotted individually — although not together — in wild viruses. Yoshihiro Kawaoka of the University of Wisconsin-Madison and his colleagues have submitted similar work to *Nature*, which is partially described in an online Comment published this week².

Acting on advice from the NSABB, the US government last month asked *Science* and *Nature* to publish only the broad conclusions of the two studies, and not to reveal the scientific details, in order to limit the risk that uncontrolled proliferation of such research might lead to accidental or intentional release of similar mutant viruses. The journals and the authors have agreed to this redaction, provided that a mechanism is established to disseminate the data to flu researchers and public-health officials on a need-to-know basis. The US government, the World Health Organization (WHO) and other bodies are now trying to put this mechanism together, along with a framework for international oversight of such research.

Last week, in a statement jointly published in *Nature* and *Science*³, 39 flu researchers declared a 60-day pause in the creation of lab mutant strains of the H5N1 avian flu virus. The hiatus, they hope, should give scientists and policymakers time to debate how such research might best proceed, and what safety measures should

be required of labs that handle the virus. The signatories to the statement, including the key authors behind the controversial research, plan to bring ▶

➔ **NATURE.COM**
For all of *Nature's* mutant flu coverage, see:
go.nature.com/mhmibi

► together some 50 experts at a WHO-hosted meeting in Geneva, Switzerland, next month to discuss these thorny issues.

Scientists contacted by *Nature* say that basic research on such mutated strains may eventually yield insight relevant to developing pandemic countermeasures such as drugs and vaccines. And they all agree that the new research has done the world a service by showing that H5N1 seems capable of evolving the ability to spread rapidly among humans, in contrast to what some scientists have claimed.

Fouchier's study "raises a red flag," says Ilaria Capua, an animal-flu expert at the Experimental Animal Health Care Institute of Venice in Legnaro, Italy. "That is the real, and most important message, of this whole exercise." It should prompt donors and international organizations to ramp up their funding of efforts to control outbreaks of the H5N1 virus in poultry, and so give the virus fewer opportunities to evolve into a human pathogen, she says. Other scientists add that it should force governments to rethink existing vaccine technologies, which are only capable of supplying vaccine six months after a pandemic starts, and of producing enough vaccine for a small fraction of the world population.

PATCHY SURVEILLANCE

But the notion that the research offers a guide to dangerous variants that could be stamped out before they spread is unrealistic, say Osterholm and other researchers. "In order to even consider the possibility of reducing the animal reservoir of an emerging pandemic virus, one would need rapid and complete detection of virus in all geographical areas," Osterholm says. Yet surveillance of H5N1 in poultry worldwide is patchy, particularly in poorer countries, where the virus is prevalent. It is also largely geared towards simply detecting and monitoring outbreaks, and few of the viral samples collected are ever sequenced.

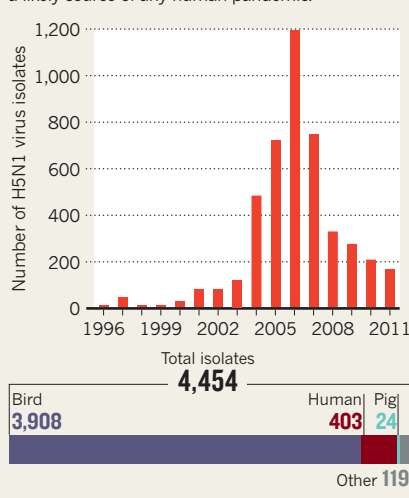
Last year, global surveillance resulted in partial sequences from just 160 H5N1 isolates being submitted to GenBank, the main repository of such data (see 'Sequence shortfall'). And virus isolates are often sequenced months or years after they are collected — hardly the swift turnaround of a pandemic alert system. "Could we pick up a mutation in real time and stop a pandemic?" asks Capua. "Not with the surveillance we have now."

Moreover, if H5N1 surveillance in poultry

is poor, the situation is far worse in pigs, where there is almost no systematic surveillance, even in richer countries. H5N1 infections in pigs are uncommon and cause only mild illness, creating little economic incentive to monitor them⁴. GenBank contains partial sequences from just 24 pig H5N1 isolates. Yet pigs are a likely source of a human pandemic H5N1 virus because they are susceptible to both human and avian viruses, creating opportunities for genetic reassortment in co-infected animals.

SEQUENCE SHORTFALL

The number of H5N1 virus isolates sequenced and deposited in the GenBank database has waned in recent years. It holds very few sequences from pigs, a likely source of any human pandemic.



Fouchier argues that many countries collect more, and more-timely, sequence data than those deposited in GenBank. "That some outbreak countries are not yet fully capable of making optimal use of such data should not lead to the fatalistic conclusion not to generate and share the data as they emerge," he says. "Warnings weeks after dangerous viruses have emerged in poultry, or mammals, may be better than no warnings at all."

But even if a candidate pandemic H5N1 virus was detected in poultry, culling flocks to eliminate it would be no mean feat. H5N1 has become endemic in many countries, including China, Vietnam, Indonesia, Bangladesh, India and Egypt, and the United Nations' Food and Agriculture Organization estimates that, with current resources, it would take at least a decade

to stamp out the virus in such countries.

The relative ease of making H5N1 transmissible between mammals in the lab should now prompt the world to address these glaring inadequacies in surveillance, says Jeremy Farrar, director of the Oxford University Clinical Research Unit in Ho Chi Minh City, Vietnam. Molecular technologies need to be made more easily available and affordable to countries at risk, and genetic surveillance more comprehensive and timely. But building such systems would require sustained political will, financial resources, and overcoming major logistical hurdles in the field.

OTHER MUTATIONS

Even if such a revolution occurred, looking only for the mutations reported by Fouchier and Kawaoka would be short-sighted, says Marc Lipsitch, an epidemiologist at the Harvard School of Public Health in Boston, Massachusetts. "There are many, many, other ways that the virus could become transmissible," he says. "It would be very unfortunate if people say that if we don't see these mutations, we don't need to worry," he adds. Moreover, says Farrar, H5N1 is far from being the only flu virus that poses a pandemic threat. But he believes that more extensive genetic surveillance could eventually pay off. "The research points us to where we need to go, rather than where we are today," he says. "Before this research, we were all guessing what changes might be needed. This work pushes that forward."

Asked whether there were any areas in which the mutant flu research could provide immediate public-health benefits, Anthony Fauci, director of the US National Institute of Allergy and Infectious Diseases, replies: "I would say that, in a perfect world, the immediate benefit would be in surveillance. But from a logistics standpoint, in the world we live in, that will be difficult to do."

Because the value of these studies is more likely to emerge in the longer term, it makes sense to take time to consider how such research can proceed safely, he says. "What's the rush?" he asks. "I am very much in favour of having a pause in the research." ■

1. *Nature* **480**, 421–422 (2011).
2. Kawaoka, Y. *Nature* <http://dx.doi.org/10.1038/nature10884> (2012).
3. Fouchier, R. A. M. *et al.* *Nature* **481**, 443 (2012).
4. *Nature* **459**, 894–895 (2009).



TOP STORY

Study challenges existence of arsenic-based life
go.nature.com/1sazol



MORE NEWS

- Victory for crowdsourced biomolecule as Foldit offers route to better enzyme go.nature.com/xkz2v3
- Rat helps pinpoint pain molecule go.nature.com/fiylkt
- The neuroscience of magic mushrooms go.nature.com/bznocy

ON THE BLOG



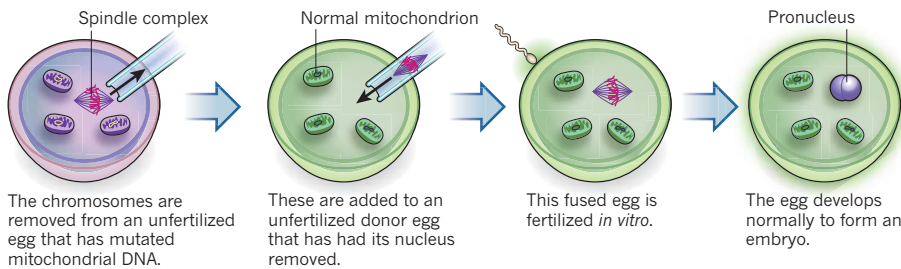
Wider Panama Canal could cut shipping emissions worldwide
go.nature.com/kryocl

SOURCE: HFEA

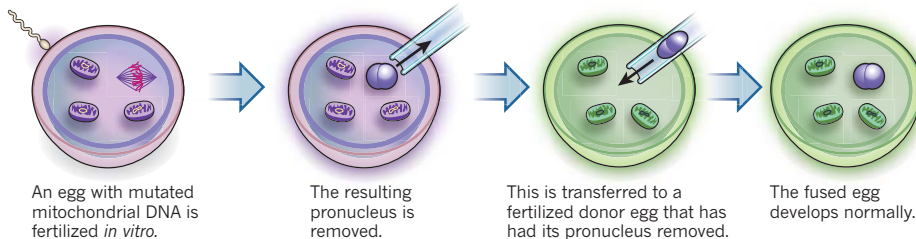
TWO WAYS TO CRACK AN EGG

Researchers are studying two ways to fuse a diseased egg with a healthy one to prevent rare mitochondrial diseases.

Maternal spindle transfer



Pronuclear transfer



EMBRYOLOGY

UK sets sights on gene therapy in eggs

Public consultation and safety assessment would pave the way for embryo manipulation to treat genetic diseases.

BY EWEN CALLAWAY

Britain has set out a road map towards the first clinical tests of reproductive techniques that combine parents' genes with DNA from a third party. The approach raises ethical questions, but could spare children from inheriting some rare diseases, including forms of muscular dystrophy and neurodegenerative disorders that affect around 1 in 5,000 people.

These conditions are caused by defects in the mitochondria, the 'power packs' of the cell, which are inherited from a child's mother through the egg. Experiments on primates, and with defective human eggs, have already shown that genetic material can be removed from an egg that has faulty mitochondria and transferred to a healthy donor ovum, leaving the flawed mitochondrial DNA behind. In principle, the resulting egg could then develop into a healthy child carrying both the parents' nuclear genes and mitochondrial DNA from the donor. But the work amounts to genetic modification of embryos — which is currently illegal in the United Kingdom — and also involves destroying fertilized eggs.

On 19 January, the UK government's Human Fertilisation and Embryology Authority

(HFEA) announced a public consultation on the process, the first step towards making it legal. Simultaneously, the country's biggest biomedical charity, the Wellcome Trust, said that it would fund preclinical experiments to gauge the safety of the techniques. An independent bioethical review is also in progress. "It's a wonderful example of how regulation should work, because it's saying let's see the science, let's see the bioethics, let's find out what the public thinks," says Peter Braude, a reproductive biologist at King's College London.

Two procedures are being developed: pronuclear transfer and maternal spindle transfer (see 'Two ways to crack an egg'). US researchers have already used maternal spindle transfer to produce two healthy rhesus monkeys (M. Tachibana *et al. Nature* **461**, 367–372; 2009). Meanwhile, neurologist Douglass Turnbull of Newcastle University, UK, and his team have performed pronuclear transfer on defective human eggs, and found that normal development occurred in a small minority (L. Craven *et al. Nature* **465**, 82–85; 2010).

In 2011, Braude co-authored a report for the HFEA that concluded that the nuclear transfer procedures seem safe on the basis of current research. The report outlined several studies

that it deemed "critical" before either procedure could be used to create a child. These include experiments on healthy human eggs, and proof that the pronuclear transfer technique can conceive healthy monkeys.

The Wellcome Trust has now awarded Turnbull £4.4 million (US\$6.8 million), which his university has topped up with another £1.4 million, to perform the procedures on healthy human eggs. Turnbull and his team hope to determine whether the embryos can safely reach the 100-cell blastocyst stage, when implantation occurs. Yet they have no plans to test pronuclear transfer in monkeys, and it is unclear who would conduct such experiments.

Shoukhrat Mitalipov, a reproductive biologist at Oregon Health and Science University near Portland, who led the work on rhesus monkeys, says that his lab uses the maternal spindle transfer technique because it is easier to perform. Mitalipov has begun experiments on human eggs in a privately funded lab. Such work is barred from receiving federal funds because it involves the destruction of human embryos.

NO SCRAMBLE

Turnbull is agnostic about which, if any, procedure is likely to reach the clinic first. One technique may prove more efficient than the other, or may shuttle fewer mutant mitochondria to the donor egg. "We've got to be careful that this is not a race," Turnbull says. Taking the technique beyond the lab would also require a change in the law. Nuclear transfer procedures are banned under the UK Human Fertilisation and Embryology Act, but the government could amend the law for procedures used to treat mitochondrial diseases.

Meanwhile, the Nuffield Council on Bioethics in London has begun an independent review of the procedures. Science writer Geoff Watts, chairman of the working group behind the review, believes that it will inform the government's decision. It will consider issues such as whether the procedures should be used to conceive only males, who will not pass on any donor mitochondria to their children. The council says that it will deliver a report in the summer.

Braude worries that, outside the United Kingdom, "somebody will be a cowboy" and attempt the procedures without regulatory oversight. Yet government hurdles could prevent the techniques from being adopted quickly elsewhere. In Australia, for example, a government review in 2011 recommended continuing a ban on such techniques. In the United States, the Food and Drug Administration would be responsible for approving them. Such restrictions, combined with the US ban on federal funding of human embryo work, mean that the first clinical trials of nucleus-swapping procedures will almost certainly occur in the United Kingdom.

"We've moved to the stage where we think that the preliminary evidence is very supportive," says Turnbull, "and we think it's a very good idea that they consider this." ■ SEE EDITORIAL P.410

SCIENCE INVESTMENT

Research in Asia heats up

US indicators reveal challenges and opportunities as science momentum shifts to China.

BY EUGENIE SAMUEL REICH

It is a mantra that plays readily to US competitive fears: Asia, led by China, is on track to displace the United States as the world's science and technology powerhouse. That message is loud and clear in the 2012 edition of *Science and Engineering Indicators*, a nearly 600-page snapshot of the state of global research that looks at education, academic infrastructure, the knowledge-based workforce and international markets. Yet some policy experts say that the trends reveal opportunities for partnerships that could benefit the United States.

"Our country needs to worry about science and innovation when so much is being done out of the country. Long-term, this might be harmful to our competitiveness," says Ray Bowen, chairman of the US National Science Board, which produced the report and oversees one of the US government's main research funding agencies, the National Science Foundation (NSF).

The report, released on 17 January, finds that by 2009, the combined research and development (R&D) investment from a group of ten Asian economies including China and India, had caught up with that of the United States (see 'Rising influence'). "One hopes that the new data will help to reinforce the message that the US government (as well as industry) needs to keep R&D investments at the top of its priorities, despite current fiscal constraints," says Claude Canizares, vice-president for research at the Massachusetts Institute of Technology in Cambridge.

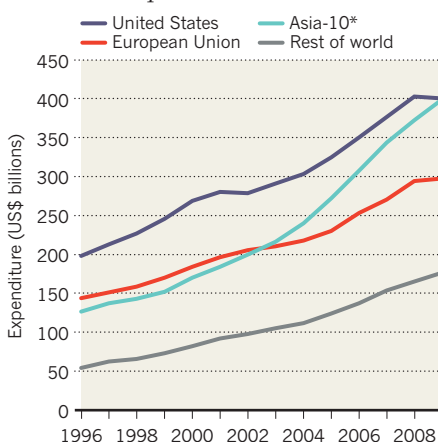
Yet Ron Hira, an engineer and science-policy expert at the Rochester Institute of Technology in New York, says that the real problem is that the United States invests too little in R&D, but that its ability to channel that investment into high-tech manufacturing has been declining since 2000. Hira says that India and China have been more proactive in protecting and fostering high-tech industries. In the United States, "we have a surplus of researchers doing endless postdocs," he says. "The worry is how that translates into economic growth."

Henry Sauermann, who studies science and innovation at the Georgia Institute of Technology in Atlanta, says that the United States may need to alter its perspective. The indicators suggest that intellectual property and trained personnel are increasingly likely to come from Asia and developing countries. The United

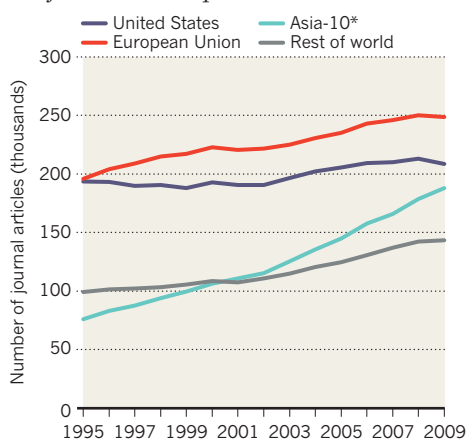
RISING INFLUENCE

Research and development investment in ten Asian economies has tripled in the past 15 years (1), as has the number of journal articles (2). Collaborations between US and Asian researchers have been roughly constant since 2000 (3), suggesting that the United States could do more to take advantage of Asian research. The trend looks set to continue, with the numbers of science degrees in China rising rapidly (4).

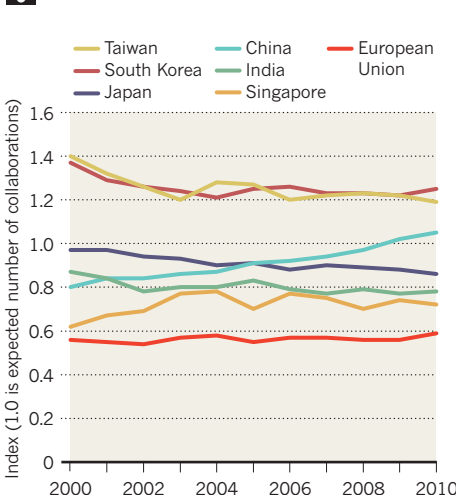
1 Spending on research and development



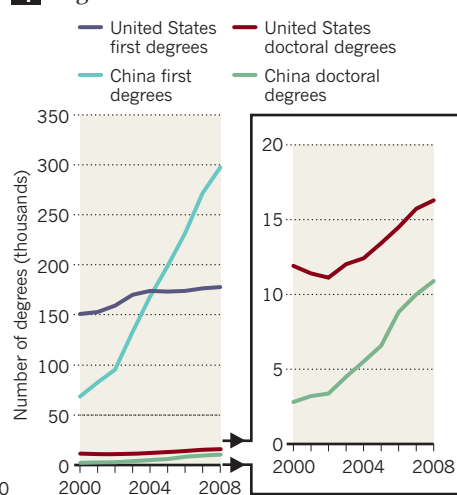
2 Number of science and engineering journal articles produced



3 US collaborations



4 Degrees in natural sciences



*Asia-10: China, India, Indonesia, Japan, Malaysia, Philippines, Singapore, South Korea, Taiwan, Thailand

States should take advantage of Asian ideas and expertise rather than thinking of itself as a producer of value that may be lost, says Sauermann. For example, US researchers could make greater efforts to read Chinese publications and collaborate with Chinese institutions. "Increasingly we see China paying for research and putting it out there for everyone to use. That's an opportunity."

Caroline Wagner, a science-policy expert at Ohio State University in Columbus, says that it is important to be aware that much of

the science done in developing countries is not captured by the report, which covers only research published in journals that are indexed by Thomson-Reuters — fewer than 10% of the world total, she estimates. The remainder is likely to be in languages other than English, and benefits its country of origin — through research on Brazilian fruit trees or fungus in China, for example — but not necessarily other members of the global economy, such as the United States. "There's an awful lot of unseen science," she says. ■

SOURCE: NSF



Mitt Romney (left) and Newt Gingrich have shifted their views on the threat posed by climate change.

US ELECTION

Candidates play to the right on science

Rivals for the Republican nomination laud research but take a hard line on embryonic stem cells and climate.

BY SUSAN YOUNG

US presidential elections do not tend to revolve around science. But thanks to the latest twist in the race for the Republican candidacy, the unusual topic of mining the Moon looks set to be up for discussion. Lunar resources and the space programme in general are popular themes with former US House speaker Newt Gingrich. Following his decisive victory over the Republican frontrunner, former Massachusetts governor Mitt Romney, in the South Carolina primary on 21 January, Gingrich — whose fortunes have zigzagged during the campaign — is back in the media spotlight.

Romney and Gingrich now dominate an unsettled contest. Both are taking staunchly conservative positions on controversial science issues: they are against regulating carbon emissions and oppose embryonic stem-cell research. Yet both have held more moderate views in the past. And, with concern growing about unemployment and international competition (see page 420), the state of US research and its role as an economic driver could have more resonance than usual in this year's presidential race.

"The public supports science strongly," says Mary Woolley, president of the medical-science advocacy group Research!America, based in Alexandria, Virginia. "They can connect the dots between science and better jobs for themselves, their children, their grandchildren. They don't want to be part of a country that's not making progress in science at the level we used to."

Last November, the group sent a list of research-oriented questions to all candidates, including US President Barack Obama, against whom the winner of the Republican contest will face off later this year. So far, only Gingrich and Obama have responded. In keeping with Republican ideology, Gingrich credits the US private sector as the key driver of technical innovation and success. But his tone is urgent. "We are on the cusp of an explosion of new science that will create new opportunities in health, agriculture, energy, and materials technology," he writes. "We must move quickly and decisively so we will be the creators of this innovation, not just the recipients of it." Now, with the race moving on to the Florida primary on 31 January, Gingrich has promised to deliver a visionary speech on the US space programme, in the tradition of Democratic president John F. Kennedy.

Yet, on stem cells, Gingrich leans firmly ►

► to the right, mindful that many social conservatives in the United States equate research on human embryos with abortion. In 2009, Obama lifted a ban imposed by former Republican president George W. Bush that limited federal funding for human embryonic stem-cell research to just a handful of existing cell lines. By contrast, Gingrich says he would “oppose at every turn any process of destroying embryos”. That could mean a freeze on the approval of new lines, or possibly an end to federal funding for such work altogether.

Romney’s history on the issue is more complex. As a candidate for governor in 2002, he voiced general support for stem-cell science. But, once in office, he vetoed a 2005 bill that allowed cloning to create human embryonic stem cells for research. Romney was overruled by the state’s legislature, but the following year his administration set down regulations that could have criminalized the work of scientists using human embryonic stem cells. However, no scientists were prosecuted under the regulations, and the bill was amended when the next governor took over.

The positions that Romney and Gingrich now espouse suggest that if either were to be

in the White House with a Congress similar to today’s, US stem-cell policy would take a hard right turn. “It would be very likely that there would be a reduction or elimination of funding for embryonic stem-cell research”, says Alta Charo, a professor of law and bioethics at the University of Wisconsin–Madison.

“Any time a scientist stands up in a public forum and says climate change is real and we need to do something about it, there are immediate repercussions.”

grounds, from a regional initiative in which several northeastern states banded together to reduce emissions.

Gingrich’s turn on climate has been even more abrupt. In 2008, he teamed up with Democrat and then House speaker Nancy Pelosi in a television advert promoting political action on climate change. He has since been chastised for

Romney’s stance on climate has also shifted. In 2004, he issued a ‘climate protection plan’, with targets for reducing carbon dioxide emissions from the state’s power plants. However, by December 2005 he backed away, on economic

this by conservative commentators. Gingrich now says he regrets the ad and, in recent weeks, has further distanced himself from his proactive former stance. After he was criticized on right-wing talk radio for involving Katharine Hayhoe, a climate scientist at Texas Tech University in Lubbock, in a book project on environment entrepreneurship, Gingrich said he would drop Hayhoe’s chapter from the book. Hayhoe supports the idea that human activity is driving climate change. “Any time a scientist stands up in a public forum and says climate change is real and we need to do something about it, there are immediate repercussions,” Hayhoe says.

Yet whoever becomes the Republican candidate — and whoever ultimately becomes president — these disputes may not mean much for the support of science as a whole. Since the cold war, both Republican and Democratic administrations have a steady record of support for basic science. And with the US electorate focused on the economy and unemployment, it seems likely that if science is discussed at all in this year’s campaign it will be in the context of jobs and competitiveness — issues on which all candidates, no matter what their ideology, see a need for action. ■

GENETICS

French institute prepares for gene-therapy push

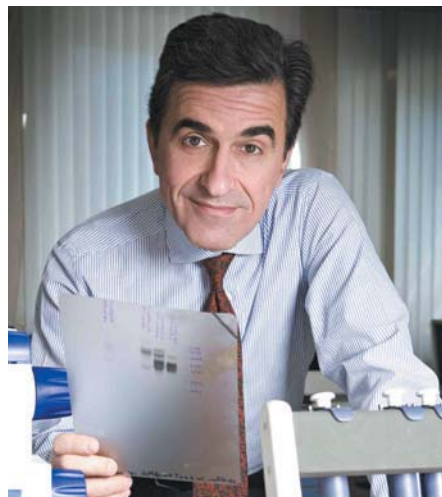
Genethon relaunches itself as a force for translational medicine.

BY ALISON ABBOTT

The French biotechnology institute Genethon is perhaps best known for its unusual funding source — annual television appeals — and for its mapping of the human genome in the early 1990s (I. Chumakov *et al.* *Nature* **359**, 380–387; 1992). Now, after spending years in the scientific doldrums, it plans to become known as the European centre that can speed up the process of getting gene therapy for rare genetic disorders into routine clinical practice.

Scientific director Fulvio Mavilio, a molecular biologist who took office earlier this month, has a mandate to sharpen the research profile of the institute, which employs 180 scientific staff at its base just outside Paris. One of his main strategies is to create international clinical networks for gene therapy around Genethon. The institute should become particularly attractive to international partners later this year, when it opens what will be the world’s biggest plant for

producing large volumes of clinical-grade viral vectors — used to transfer therapeutic genes into the cells of patients.



Fulvio Mavilio is Genethon’s new scientific director.

“Getting vectors is a bottleneck for us,” says Adrian Thrasher, director of the gene-therapy programme at University College London’s Institute of Child Health, and a Genethon collaborator. “Genethon’s new strategy is realistic.”

The first gene-therapy trials involved a handful of children in Italy and France who had rare and fatal immunodeficiency disorders, and showed that healthy genes could be transferred stably into patients to reverse their symptoms.

The early successes spawned a period of hype that came to an abrupt end with the 1999 death of Jesse Gelsinger, a teenager in the United States who had a profound immune reaction to his gene therapy, as well as the emergence of cancers in some immunodeficient children who had been treated. Progress has been slow and cautious ever since. More than a thousand proof-of-principle clinical studies have been done around the world (see ‘Gene promise’), and dozens have shown positive results, but as yet no form of gene ►

► therapy has been approved for routine use by the US Food and Drug Administration or the European Medicines Agency. That situation must change, according to the board of directors of the French Muscular Dystrophy Association, which created Genethon in 1990 and has funded it ever since through its annual telethons.

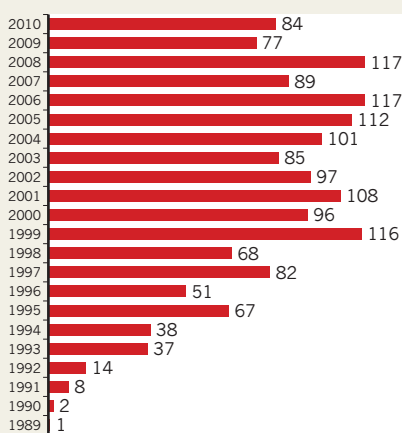
BROAD POTENTIAL

Although the best-known gene-therapy trials have been done in children with immune deficiencies, the technique could tackle a much wider array of diseases. Most of the current clinical studies are in cancer, with researchers trying to introduce genes that will kill the cancer cells directly, or prod the patient's immune system into attacking them. And on 6 January, the American Society of Gene and Cell Therapy sent the director of the US National Institutes of Health a list of the diseases it believes will benefit most in the next six years from investment in translating basic research to the clinic. It included rare immunodeficiency and eye disorders, as well as more common blood disorders, two cancers and Parkinson's disease.

Mavilio worked on the world's first gene-therapy trial, which treated children with the immunodeficiency disorder ADA-SCID at the San Raffaele Scientific Institute in Milan.

GENE PROMISE

Dozens of gene-therapy clinical trials are now approved by regulatory authorities every year.



Another 141 trials have been approved at unspecified times.

Pharmaceutical giant GlaxoSmithKline last year forged a multi-million-euro alliance with the institute to develop similar gene therapy for rare diseases, becoming the first pharmaceutical giant to invest significantly in the field.

"The disadvantage of Genethon compared to the San Raffaele is that it does not have its own hospital," Mavilio says. "We will be very

proactive in forging collaborations with top clinicians in Europe and beyond so that we can become a major hub for gene-therapy networks."

The vector-production facility will be a huge asset for this, he says. "But it won't be enough. To get good collaborations, we also have to be known as a force in science." Genethon moved away from basic research in 2006, to focus on vector production. It now gets more than 90% of its money from the Telethon, but Mavilio wants this to be significantly supplemented by competitive research grants.

Philippe Moullier, director of the French national biomedical research agency's gene-therapy unit in Nantes, and a Genethon adviser, warns that the firm needs "to remain humble and move slowly — I don't know if we can demand to become a European hub". Thrasher, at least, is enthusiastic about the institute's ambitions, predicting that "Genethon will probably become our first port of call". ■

CORRECTION

The photo caption in the News story 'Gemini's twin telescopes reboot' (*Nature* **481**, 251; 2012) incorrectly identified the Gemini North telescope as Gemini South.

SOURCE: J. GENEMED.



HUNT FOR THE ANCIENT MARINER

Armed with high-tech methods, researchers are scouring the Aegean Sea for the world's oldest shipwrecks.

BY JO MARCHANT

Brendan Foley peels his wetsuit to the waist and perches on the side of an inflatable boat as it skims across the sea just north of the island of Crete. At his feet are the dripping remains of a vase that moments earlier had been resting on the sea floor, its home for more than a millennium. "It's our best day so far," he says of his dive that morning. "We've discovered two ancient shipwrecks."

Foley, a marine archaeologist at the Woods Hole Oceanographic Institution in Massachusetts, and his colleagues at Greece's Ephorate of Underwater Antiquities in Athens have spent the day diving near the cliffs of the tiny island of Dia in the eastern Mediterranean. They have identified two clusters of pottery dating from the first century BC and fifth century AD. Together with other remains that the team has discovered on the island's submerged slopes, the pots reveal that for centuries Greek, Roman and Byzantine traders used Dia as a refuge during storms, when they couldn't safely reach Crete.

It is a nice archaeological discovery, but Foley was hoping for something much older. His four-week survey of the waters around Crete last October is part of a long-term effort to catalogue large numbers of ancient shipwrecks in the Aegean Sea. And the grand prize would be a wreck from one of the most influential and enigmatic cultures of the ancient world — the Minoans, who ruled these seas more than 3,000 years ago.

Some researchers believe that quest to be close to impossible. But Foley and a few competitors are using high-tech approaches such as autonomous robots and new search strategies that they say have a good chance of locating the most ancient of shipwrecks. If they succeed, they could transform archaeologists' understanding of a crucial period in human history, when ancient mariners first ventured long distances across the sea.

Archaeologists have precious little information about the seagoing habits of the Minoan civilization, which erected the palace of Knossos on Crete — linked to the Greek myth of the Minotaur. Minoans far exceeded their neighbours in weaponry, literacy and art, and formed "part of the roots of what went on to become European civilization", says Don Evly, an archaeologist at the British School at Athens, and curator of Knossos. Archaeologists are keen to understand what made the Minoans so successful and how they interacted with nearby cultures such as the Egyptians.

Although researchers have studied scores of Roman ships, finding a much older Minoan wreck "would add 100% new knowledge", says Shelley Wachsmann, an expert in ancient seafaring at Texas A&M University in College Station.

UNDERWATER TREASURE

A Bronze Age wreck called Ulu Burun shows how the remains of a single ship can transform archaeologists' understanding of an era. Discovered in 1982, it lies about 9 kilometres southeast of Kaş in southern Turkey, and dates from around 1300 BC, a century or two after the Minoans disappeared.

Christos Agourides, secretary-general of the Hellenic Institute of Marine Archaeology in Athens, describes it as "the dream of every marine archaeologist". It took ten years to excavate, and researchers are still studying the nearly 17 tonnes of treasures recovered. The vast cargo includes ebony, ivory, ostrich eggs, resin, spices, weapons, jewellery and textiles as well as ingots of copper, tin and glass.

But what really stunned archaeologists was that the artefacts on this one vessel came from at least 11 different cultures¹ — from a gold scarab bearing the name of the Egyptian queen Nefertiti to copper from



A sixteenth-century-BC Minoan wall mural from the Greek island of Santorini depicts some of the ships used by the Bronze-Age seafarers.

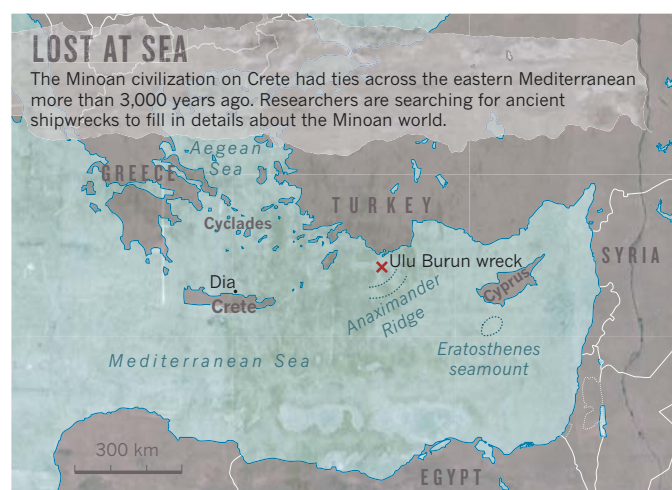
Cyprus and tin from central Asia.

The wreck provided tangible evidence of an astonishing array of contacts and trade between the different cultures of the Mediterranean and Near East in the late Bronze Age. The Ulu Burun ship sailed at around the time that Tutankhamun ruled Egypt, and “it is far more important than Tutankhamun’s tomb as a contribution to our understanding of the period”, according to Wachsmann. “This goes to the nitty gritty of the world. It’s Wall Street in a ship.”

The earlier Minoans set the stage for such a widespread trading network through their domination of the eastern Mediterranean. Their seafaring abilities were still celebrated 1,000 years later by Greek historian Thucydides, who credited the Minoans with building the world’s first navy and ridding the seas of pirates. Although other contemporary Mediterranean cultures were starting to travel across the sea, the Minoans ventured farther than others, reaching distant ports in Syria, Cyprus, the Cyclades and Egypt (see map). Wachsmann describes them as the “Christopher Columboes of the Bronze Age”.

Researchers have already found one potential Minoan wreck site by the island of Pseira, off the northeast coast of Crete. In 2003, archaeologist Elpida Hatzidaki of the Ephorate of Underwater Antiquities discovered a large collection of underwater pottery dating to around 1800 BC.

But at this site and a few even older ones, no portion of the ship itself survives, and it is hard to determine whether the pottery came from a wreck, was simply thrown overboard, or washed into the sea from the nearby coast. Even those who believe the Pseira site does represent a Minoan wreck admit that the pottery itself — everyday ware of local origin — doesn’t reveal much new information. What archaeologists crave is an equivalent of Ulu Burun, a long-distance trading ship packed with valuable cargo that would reveal how different cultures interacted.



“Ships were the way that people communicated and moved about the ancient world,” says Foley. “So if we can find these ancient wrecks, we get a much clearer view of the very dim past.”

That dream lured Foley and his team to Crete last year, and they brought a new tool that they hope will significantly raise the chances of finding an ancient shipwreck. In the past, archaeologists have explored the sea floor using divers and, more recently, remotely operated vehicles (ROVs) that are controlled by pilots on ship. Foley’s team tested an autonomous diving robot that could search the ocean bottom for hours under its own command. The REMUS 100 vehicle (for Remote Environmental Monitoring Underwater System) is equipped with Global Positioning System technology, side-scan sonar and a video camera. The Woods Hole researchers worked on the project with Greek archaeologists led by Theotokis Theodoulou of the Ephorate of Underwater Antiquities.

ROBOT ROVERS

The torpedo-shaped robot, nicknamed Gudgeon after a Second World War submarine, spent the first month of the field campaign surveying the entire sea floor north of Crete’s main harbour, Heraklion, for any lumps and bumps that might signal an ancient wreck.

Foley had high hopes for the area because it had been a port for millennia and had never been surveyed by archaeologists. But the search came up empty handed. Close to shore, there was no hope of finding ancient wrecks because the sea floor was covered in a thick pile of sediments that had washed off the island. Farther out, the researchers found furrows left by trawl fishermen, who had scraped the sea floor clean, even in areas where trawling is supposedly forbidden.

So Foley’s team moved its search to Dia, which lies just north of Heraklion. In 1976, the ocean explorer Jacques Cousteau found some ancient remains there, and Foley suspected that Dia might be a fertile site for shipwrecks because its steep cliffs could be lethal to vessels caught in a storm.

The team took a two-pronged approach to exploring around Dia. The Gudgeon crew prowled Dia’s bays, where the ocean bottom is smooth and artefacts are more likely to show up in sonar images. Near shore, where the bottom is too rocky for Gudgeon, Foley and his team of divers made a circuit of the bays at about 40 metres depth.

Almost immediately, the divers located five ancient wrecks, ranging from around the second century BC to the ninth century AD. The discoveries confirmed Cousteau’s impression that now-deserted Dia was used for centuries as an anchorage. And Foley was convinced that the Minoans must have been here too, with the evidence perhaps on the deeper floor of Dia’s bays. But Gudgeon’s sonar images from those sites kept coming back disappointingly clear.

On the penultimate day of the field season, Greg Packard and Mark Dennett of Woods Hole stood on the stern of their small research vessel, and swung Gudgeon overboard. The miniature explorer descended to the bottom and spent the morning cruising back and forth along

preprogrammed gridlines. Later that evening, when Packard examined the sonar data, he spied a potential target — a patch of bright speckles amid the smooth dark image. The team debated whether it could be a heap of pottery on the sand.

The next day, Foley took his crew of divers out to the suspect site. Some 15 minutes later, they came back with disheartening news: the sonar signal was a collection of plastic water bottles that must have been dumped overboard from a modern boat. And footage from Gudgeon's video camera explained the absence of archaeological remains — furrows in the sand showed that trawlers had cleaned out even these tiny bays. If a Minoan ship ever sank here, it has long since been destroyed. "It's such a waste," says Foley, clearly disappointed. "I bet they're not even trawling for fish. I bet they're trawling for antiquities."

DIVING DEEPER

Wachsmann says that he isn't surprised by what Foley saw. From 2007 to 2009, he led the Danaos project, using sonar-equipped ROVs to survey hundreds of square kilometres of sea floor on a suspected ancient trading route between Crete and Egypt. In three seasons, he didn't find a single ancient wreck from any period, and only a scattering of artefacts.

Wachsmann found that sedimentation was a problem even far from shore — up to a metre per millennium in some areas. This means that although some Greek and Roman remains might still be visible, a Minoan ship would be buried under 3 or 4 metres of sand. And even at 500–600 metres depth, he saw clear evidence of trawling. "It was almost like somebody had swept the sea in front of me," he says. On the basis of his experiences, Wachsmann now believes that the chance of finding a Minoan equivalent of Ulu Burun "approaches zero".

The effect of bottom trawling is "devastating" for archaeologists, agrees Robert Ballard, an oceanographer based at the University of Rhode Island in Narragansett, who has pioneered deep-sea exploration and discovered the wreck of the *Titanic* in 1985. "Most of the Aegean has been destroyed," he says.

Ballard has spent years searching for ancient wrecks and says that he has learned the importance of finding areas beyond the reach of fishermen — below about 600 metres, say, or close to undersea cables, which trawlers avoid. He has also opened up his search area. Historians once assumed that the number of wrecks in the deep sea was negligible because ancient ships must have hugged the coastlines, but in the 1990s Ballard found eight ancient wrecks far from shore between the islands of Sicily and Sardinia² (Foley was Ballard's graduate student at the time). "The ancient mariner was not afraid of going out to sea," says Ballard.

Since 2008, Ballard has been exploring the eastern Mediterranean, the Aegean and the Black Sea with a suite of ROVs. Although he is finding large numbers of ancient wrecks, he hasn't yet uncovered anything from the Bronze Age. But, like Foley, he believes Minoan ships are waiting to be discovered. The key to finding the oldest wrecks, he says, is locating "relic surfaces" that have escaped being buried by sediment, which flows downhill and covers the deep sea floor³. "What you want is a shipwreck that came down on a mountain," he says, because sediment can't accumulate on a steep slope.

Last year, Ballard investigated the Eratosthenes seamount, a 700-metre-deep tabletop south of

Cyprus, and says it does indeed seem to represent a relic surface. He is now applying for permits to return to Eratosthenes to search for shipwrecks next year. Another area he would like to investigate is the submerged Anaximander mountains south of Turkey. It would be difficult to distinguish a wreck site from such rocky terrain using sonar, so he plans to use video cameras to conduct a painstaking visual search over smaller areas. "It's very hard hunting," he says.

Foley is also now looking to the deep sea, but has a different strategy. Instead of targeting particular sweet spots, he wants to cover as large an area as possible. He has raised more than US\$1 million towards the \$1.8 million that he needs to return to the Mediterranean next year, this time with two of Gudgeon's more powerful cousins, REMUS 6000s owned by the Waitt Institute in La Jolla, California.

To maximize the chances of finding ancient wrecks, the team will hunt on open, flat areas in the lowest reaches of the sea, up to 6,000 metres deep. Foley estimates that the two REMUS vehicles can cover up to 5,000 square kilometres in one month, equivalent to 1% of the entire Aegean Sea. The recent field trial around Dia encouraged Foley because it should be easier for the sonar surveys to pick out vases than it was to find plastic water bottles, which are poor sonar reflectors, he says.

Both Ballard and Foley are ultimately hoping to use their surveys to catalogue large numbers of wrecks of all ages across great swathes of the Mediterranean and the Black Sea. Through a combination of sonar and high-resolution digital photography, they can compile detailed three-dimensional maps of a wreck site and answer questions about the date, origin and cargo of a ship without bringing up a single artefact.

Foley estimates that hundreds of thousands of ships must have sunk in ancient times — including thousands in the Bronze Age alone — and that a significant proportion of those are still sitting at the bottom of the deep sea. If he's right, then perhaps researchers will eventually have not just one Minoan ship, but hundreds. With enough wrecks, says Foley, "it ought to allow us to draw new conclusions about this absolutely formative period in human experience."

That could shift marine archaeologists into an era in which they can use statistical data gathered from hundreds or thousands of wrecks to build up a bigger picture of trade routes, migration and warfare throughout history. "We'd rather find 500 ships than excavate one," says Ballard.

Such a dream seems a long way off as Foley's team packs up its gear at the end of its campaign. Packard and Dennett carefully lower Gudgeon into a crate for its long trip back to Woods Hole, while Foley eyes one of the artefacts he retrieved from Dia's waters — a bulbous Byzantine amphora covered in deposits left by worms.

It's not the find Foley hoped for, but he is undaunted — this is just the beginning of what he knows could be a long search. "I'd like to be doing this every year for the next 20 or 30 years," he says. "Until I'm too old to go to sea." ■

Jo Marchant is author of *Decoding the Heavens: Solving the Mystery of the World's First Computer* (William Heinemann, 2008).

1. Pulak, C. in *Beyond Babylon: Art, Trade, and Diplomacy in the Second Millennium B.C.* (eds Aruz, J., Benzel, K. & Evans, J. M.) 289–310 (Yale Univ. Press, 2008).
2. Ballard, R. D. et al. *Deep Sea Res.* **47**, 1591–1620 (2000).
3. Canals, M. et al. *Rapp. Comm. Int. Mer Médit.* **38**, 47 (2007).



Divers investigate a first-century-AD wreck near the Greek island of Dia.

B. FOLEY

➔ **NATURE.COM**
For a slideshow of images related to this feature, see:
go.nature.com/lnz2yb



THE DIGITAL LAB

Lab-management software and electronic notebooks are here — and this time, it's more than just talk.

BY JIM GILES

The basement room in the James H. Clark Center contains all the trappings of a modern imaging laboratory. An X-ray scanner hums away in a corner. A miniature magnetic resonance imaging (MRI) machine, designed to scan the brains of mice, sits nearby. It's the kind of set-up that researchers at well-funded institutions such as Stanford University in California, the centre's home, have come to expect.

One piece of equipment, however, is conspicuous by its absence: the humble paper notebook. Michelle James uses her iPad to jot down notes, check protocols and monitor the progress of her experiments on techniques for the early detection of Alzheimer's disease. Since she first brought the device into the lab around four months ago, it has essentially replaced her former hardback notebook. "Paper has nothing to offer me," declares James.

It's a refrain heard in more and more labs. Some groups have ditched notebooks in favour of software from Google, such as free-to-use tools for sharing documents, spreadsheets and calendars. Others are finding that software designed specifically for lab workers has evolved to the point where it can reliably do a range of tasks, from tracking reagent supplies to sharing protocols. The era of the paperless lab, decades in the making, seems finally to have arrived.

Now that it's here, adopters say that a paperless laboratory seems to offer real advantages. Bench researchers say that digital notebooks help them track their experiments in more detail. Lab heads report being able to follow and focus projects more efficiently when documentation is tailored to their needs, accessible online and shared among colleagues. In some cases, digital notebooks could even help researchers to find connections or extract results from systematically stored data. "The efficiency thing is nice," says Jonathan Hirsch, founder of Syapse, a

company based in Palo Alto, California, that develops the software James uses to manage and share her results. "But understanding your data better is what gets people really excited."

GOING PAPERLESS, AGAIN

If these claims sound familiar, that may be because the paper notebook's obituary has been written many times before. The paperless laboratory was "nascent" ten years ago, according to one American Chemical Society journal. Electronic notebooks are "ready for prime time", said Douglas Perry, a bioinformatics expert, in a *Nature News* Feature from 2005 (see *Nature* **436**, 20–21; 2005).

Yet most early notebook-software programs had limited impact, often because they weren't easy enough to use. Some worked only with specific file types, for example, or had cumbersome data-entry mechanisms. Such drawbacks have not stopped digital notebooks from taking off within the pharmaceutical industry, where companies have the funds to customize the

ANNITHEA LEWIS: SHUTTERSTOCK

systems and can mandate that employees use them. But for academics, these shortcomings were deal-breakers. “Everything we tried was really crappy,” says Sriram Kosuri, a bioengineer at Harvard Medical School (HMS) in Boston, Massachusetts, who experimented with many of the older packages.

Things have changed, thanks in part to the arrival of free or cheap sharing tools that are easy to use and configure. These tools, from storage systems such as Dropbox to the products offered by Google and others, rely on fast and reliable Internet connections and cloud-based storage. They provide a quick and cheap way to set up a basic lab infrastructure for sharing methods, data and other records.

At William Shih’s synthetic-biology lab at HMS, researchers store records on a password-protected network of interlinked pages that any group member can edit. His team built it using MediaWiki, the free-to-use software that powers Wikipedia. A page for an ongoing experiment, for example, can easily be updated to note changes in a protocol or to include a graph of the latest results.

Team members log on to the site through laptops or their iPads, which they wrap in ziplock bags before venturing to the bench. “Even with a finger in a glove we can still get touch-screen sensitivity,” says Shih. When researchers want to sketch out an idea — an essential process in a lab working on self-assembling nanostructures — they use Adobe Ideas, software that, for US\$10 or less, makes it possible to construct detailed images on touch-screen devices.

But these general-purpose tools don’t always satisfy researchers’ needs. Some note-taking software, for example, does not handle tables well. And although MediaWiki is very flexible, some users say that it has a clunky interface for putting in text. This means that the race to create a good digital notebook — one that is both flexible and tailored to researchers’ requirements — is still on.

GETTING PLUGGED IN

Jonathan Gross is one of the front runners in that competition. Gross began creating lab software when he was a plant-biology researcher at the Hebrew University of Jerusalem. The tools he built gained a following among his colleagues and, in 2007, he quit the lab to found BioData, a company based in Rosh Ha’ayin, Israel, that develops lab-management software. (BioData was purchased in 2010 by Digital Science, a sister company to Nature Publishing Group.)

Alex Kentsis, a paediatric oncologist and haematologist at HMS, is an early adopter of Gross’s software. “Prior to BioData we had a makeshift operation,” he says. His group used

➔ **NATURE.COM**
Tell us if you’ve
gone paperless by
commenting at:
go.nature.com/3pdphb

to swap files over shared drives, and Kentsis kept track of the lab’s progress using an Excel spreadsheet in which each column represented a

project and each row an activity. It worked, but only kind of. External collaborators could not access the shared drives, and the spreadsheet required constant maintenance and was hard to interpret.

BioData’s software, which was relaunched last December as Labguru, tackles those problems. It’s an online home for any information associated with scientific research, from protocols and results to images and related papers. The material is grouped by project, which Gross says makes it easy to track progress

“UNDERSTANDING YOUR DATA BETTER IS WHAT GETS PEOPLE REALLY EXCITED.”

and to assemble the components of a paper. A tagging system makes it possible to group experiments that share a common component, such as a specific gene or cell line. External collaborators can use a password to access a specific project, which can be done from anywhere because the data are stored in the cloud.

Gross plans to add new functions: he says he is in discussions about integrating his system with *Nature Protocols*, a journal dedicated to recipes for lab procedures, and Addgene, a repository of information on genetic-research tools called plasmids. The hope is that Labguru users can seamlessly pull information from the external databases. “It’s about making researchers’ lives as easy as possible,” says Gross.

Labguru is aimed at life-science labs, but there are alternatives for other fields. Andrew Phillips, a chemist at Yale University in New Haven, Connecticut, uses iLabber, a product from Stockholm-based Contur Software. The selling point for Phillips was iLabber’s ability to handle a chemist’s daily tasks, such as drawing molecular structures and calculating expected yields. “It’s chemically savvy,” says Phillips, who says he pays \$150 per user per year. Labguru charges academic labs a similar fee.

At Syapse, Hirsch also has ambitious plans. The company’s software, Syapse Discovery, is undergoing testing in around 45 US labs. It combines the project-based structure of iLabber and Labguru with a layer of semantic technology that ‘knows’ the data that researchers upload. For example, the Syapse software can automatically recognize that data are from a particular lab machine, such as a microarray or MRI, and apply ‘time’ and other appropriate headings to it. For other data, Syapse Discovery has a system that allows researchers to quickly select labels from a drop-down list.

With the tagging in place, researchers can use the software to run complex tasks that would generally require coding skills. Users might ask it to scan multiple experiments and to build a table that combines all results on a specific gene. Or, in a clinical setting, they might ask it how an experimental drug is affecting patients with a particular constellation of symptoms. “We want to give people the ability to access this information without them having to learn programming,” says Hirsch.

END OF AN ERA?

All of this hints at a future in which iPads and other devices do more than just replace notebooks. Kentsis points to a study of his into a therapy for acute myeloid leukaemia. Only when he looked at the milestones he had highlighted in BioData did he realize that a key piece of evidence — additional results on the extent to which drug resistance developed — was missing. The task could have been done using pen and paper, but BioData made it quicker. “It’s been easier to see project arcs and to direct research towards more important questions,” says Kentsis.

Digital notebooks may also help researchers to probe correlations that are too time-consuming to pursue using paper-based records. Archana Shenoy, a stem-cell biologist at the University of California, San Francisco, has been using Syapse Discovery for six months. She thinks that it can help to shed light on one of the frustrations of her field: cell lines that die without apparent cause.

With a paper notebook it is almost impossible to correlate the myriad factors that might affect cell survival. But with Syapse Discovery, Shenoy can quickly record data ranging from the carbon dioxide levels in a cell incubator to the date when a new batch of reagents arrives. When the search capability is up and running, she will be able to look for correlations between these factors and the fate of her cells. “It’s something everybody wonders about,” she says. “What is causing these little changes?”

Yet it’s unclear how much impact the new programs will have. Expense is one issue: not every lab can afford to equip its members with laptops or iPads. Practicality is another: some labs don’t allow laptops near the bench because of the risk of spills. But ultimately, these tools, like the earlier iterations of digital notebooks, will live or die on the basis of their usability.

The greatest challenge for Syapse, BioData and their rivals is not to create a tool that can do everything, but one that, like the intuitive software produced by Apple, is fundamentally easy to use. The initial feedback from James and others suggests that the latest generation of lab software might be able to do both. If so, it might finally be time to turn the page on the notebook. ■

Jim Giles is a freelance writer based in San Francisco, California.



COMMENT

FUNDING Asking the right questions can revitalize research **p.436**

BIOGRAPHY Joseph Rotblat's crusade for nuclear disarmament **p.438**

COSMOLOGY How to create the Universe from a sea of nothing **p.440**

OBITUARY James Crow, genetic pioneer and accomplished musician **p.444**

K. JAMES/BLOOMBERG/GETTY



Production at oil fields globally, including at the Kern River oil field in Bakersfield, California, is declining at about 4–6% a year.

Oil's tipping point has passed

The economic pain of a flattening supply will trump the environment as a reason to curb the use of fossil fuels, say **James Murray** and **David King**.

In many parts of the world, particularly the United States, continuing debates about the quality of climate-change science and doubts about the scale of negative environmental impacts have held back political action against rising greenhouse-gas emissions. But there is a potentially more persuasive argument for lowering global emissions: the impact of dwindling oil supplies on the economy.

There is less fossil-fuel production available to us than many people believe. From 2005 onwards, conventional crude-oil production has not risen to match increasing demand. We argue that the oil market has

tipped into a new state, similar to a phase transition in physics: production is now 'inelastic', unable to respond to rising demand, and this is leading to wild price swings. Other fossil-fuel resources don't seem capable of making up the difference.

Such major spikes in fuel price can cause economic crises, and contributed to the one the world is recovering from now. The future economy is unlikely to be able to bear what oil prices have in store. Only by moving away from fossil fuels can we both ensure a more robust economic outlook and address the challenges of climate change. This will be a decades-long transformation¹

that needs to start immediately.

Production of crude oil increased along with demand from 1988 to 2005. But then something changed. Production has been roughly constant for the past seven years, despite an increase in price of around 15% per year² (at Brent crude (London) prices) from about US\$15 per barrel in 1998 to more than \$140 per barrel in 2008 (see 'Oil production hits a ceiling'). The price still reflects demand: it declined to about \$35 per barrel in 2009 thanks to the 2008–09 recession, and recovered along with the upturn in the global economy to \$120 per barrel before declining to its value today of \$111. But ►

► the supply chain has been unable to keep pace with rising demand and prices.

The idea of 'peak oil' — that global production will reach a peak and then decline — has been around for decades, with academics arguing about whether this peak has already passed or is yet to come. The typical industry response is to point to increasing assessments of global reserves — the amount known to be in the ground that can be produced commercially. But this is misleading. The true volume of proven global reserves is clouded by secrecy; forecasts by state oil companies are not audited and seem to be exaggerated³. More importantly, reserves often take 6–10 years to drill and develop before they become part of supply, by which time older fields have become depleted. It is far more sensible to look instead at actual production records, which are less encouraging. Even while reserves are apparently increasing, the percentage available for production is going down. In the United States, for example, production as a percentage of reserves has steadily decreased from 9% in 1980 to 6% today². Production at existing oil fields around the world is declining at rates of about 4.5% (ref. 4) to 6.7% per year⁵. Only by adding in production from new wells is overall global production holding steady.

In 2005, global production of regular crude oil reached about 72 million barrels per day. From then on, production capacity seems to have hit a ceiling at 75 million barrels per day. A plot of prices against production from 1998 to today² shows this dramatic transition, from a time when supply could respond elastically to rising prices caused by increased demand, to when it could not (see 'Phase shift'). As a result, prices swing wildly in response to small changes in demand. Other people have remarked on this step change in the economics of oil around the year 2005, but the point needs to be lodged more firmly in the minds of policy-makers.

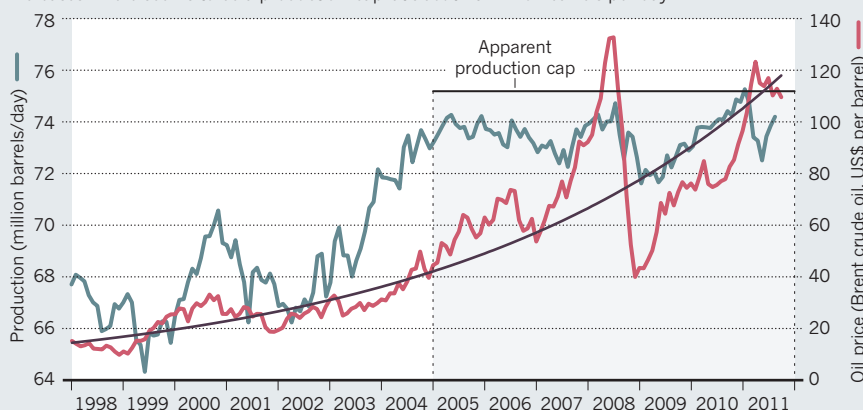
EASY ACCESS

We are not running out of oil, but we are running out of oil that can be produced easily and cheaply. The US Energy Information Administration optimistically projects a 30% increase in oil production between now and 2030 (ref. 2). All of that increase is in the form of unidentified projects — in other words, oil yet to be discovered. Even if production at existing fields miraculously stopped declining, such an increase would require 22 million barrels per day of new oil production by 2030. If realistic declines of 5% per year continue, we would need new fields yielding more than 64 million barrels per day — roughly equivalent to today's total production. In our view, this is very unlikely to happen.

Non-conventional oil won't make up the difference. Production of oil derived from Canada's tar sands — sometimes called the

OIL PRODUCTION HITS A CEILING

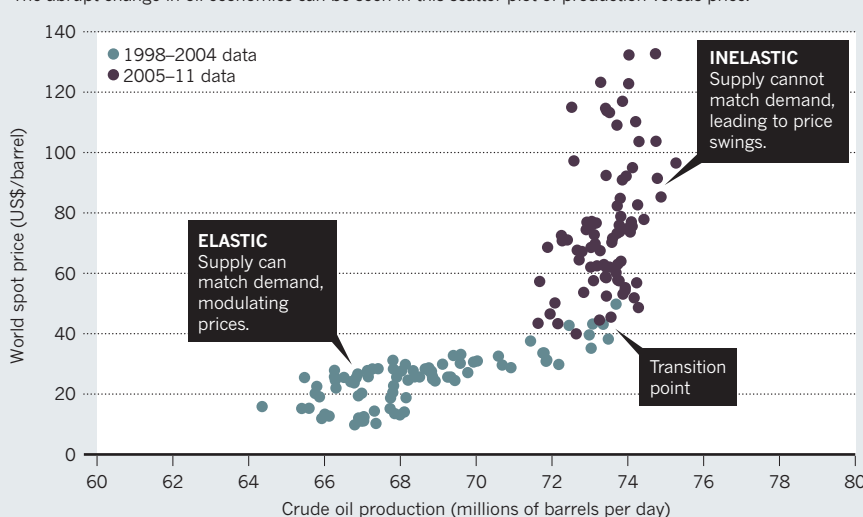
Production followed demand until 2005, when it levelled off despite continued price increases. There seems to be a production 'cap' at about 75 million barrels per day.



SOURCE: REF. 2

PHASE SHIFT

The abrupt change in oil economics can be seen in this scatter plot of production versus price.



'oil junkie's last fix' — is expected to reach just 4.7 million barrels per day by 2035 (ref. 6). Production from Venezuela's tar sands is currently less than 2 million barrels per day⁷, with little prospect of a dramatic increase.

Many believe that coal will be the solution to our energy needs, and will stay cheap for decades. But several recent studies suggest that available coal is less abundant than has been assumed. US coal production peaked in 2002, and world coal-energy production is projected to peak as early as 2025 (ref. 8). Whenever coal-reserve figures are updated, the estimates are usually revised downwards: estimates of world reserves (79% of which are held in the United States, Russia, India, China, Australia and South Africa) were decreased by more than 50% in 2005, to 861 gigatonnes (ref. 9). That study put the ultimate production of coal (the total amount that humanity will be able to extract from the ground) at 1,163 gigatonnes. A 2011 independent estimate of ultimate production came to just 680 gigatonnes (ref. 10), some 40% lower

than the 2005 figure and about five times less than assumed by some older, high-coal-consumption scenarios of the Intergovernmental Panel on Climate Change. The US National Research Council's Committee on Coal Research, Technology, and Resource Assessments to Inform Energy Policy noted in 2007 that "present estimates of coal reserves are based upon methods that have not been reviewed or revised since their inception in 1974 ... updated methods indicate that only a small fraction of previously estimated reserves are actually mineable reserves."¹¹

Natural gas is still abundant and large discoveries have been made recently, notably in Israel and Mozambique last year. Power plants using natural gas provide 25%, and rising, of electricity generation in the United States. Production of conventional natural gas in North America peaked in 2001 (ref. 2), but energy companies have worked hard to promote the idea that hydraulic fracturing of shale rock will lead to 'the age of natural gas'. There is no doubt that US shale-gas

resources are immense, but recent reports suggest that both reserves and future production rates have been substantially overstated¹². For sites such as the Barnett and Fayetteville shales, where a long production history can be studied, there has been an extremely large annual decline in production rates. Geological consultant Arthur Berman, director of Labyrinth Consulting Services in Sugar Land, Texas, and a world expert on shale gas, has put this decline in the range of 60–90%. For shale-gas wells that are more than five years old, about 30% are sub-commercial because of rapid decline combined with the low price of gas.

STUNTED GROWTH

What does this mean for the global economy, which is so closely tied to physical resources? Of the 11 recessions in the United States since the Second World War, 10, including the most recent, were preceded by a spike in oil prices¹³. It seems clear that it wasn't just the 'credit crunch' that triggered the 2008 recession, but the rarely-talked-about 'oil-price crunch' as well. High energy prices erode family budgets and act as a head wind against economic recovery.

The United States and Europe each spends \$1 billion per day on oil imports. The average price of petrol in the United States increased from 75 cents per litre in 2010 to 95 cents per litre in 2011. Because the United States consumes about 1.4 billion litres per day, the nation spent about \$280 million a day more on petrol in 2011, leaving less for discretionary items.

Another powerful example of the effect of increasing oil prices can be seen in Italy. In 1999, when Italy adopted the euro, the country's annual trade surplus was \$22 billion. Since then, Italy's trade balance has altered dramatically and the country now has a deficit of \$36 billion. Although this shift has many causes, including the rise of imports from China, the increase in oil price was the most important. Despite a decrease in imports of 388,000 barrels per day compared with 1999, Italy now spends about \$55 billion a year on imported oil, up from \$12 billion in 1999. That difference is close to the current annual trade deficit. The price of oil is likely to have been a large contributor to the euro crisis in southern Europe, where countries are completely dependent on foreign oil.

The International Energy Agency has made it very clear that the global economy is at risk when oil prices are greater than \$100 per barrel — as they have been in recent years, and will surely continue to be, given the inelastic response of global production.

Historically, there has been a tight link between oil production and global economic growth. If oil production can't grow, the implication is that the economy can't grow either. This is such a frightening prospect

that many have simply avoided considering it. The International Monetary Fund, for example, still projects economic growth of 4% of gross domestic product for the next five years: near the top of the historical range since 1980. Yet to achieve that will require either a heroic increase in oil production of 3% per year, increased efficiency of oil use, more energy-efficient growth or rapid substitution of other fuel sources. Economists and politicians continually debate policies that will lead to a return to economic growth. But because they have failed to recognize that the high price of energy is a central problem, they haven't identified the necessary solution: weaning society off fossil fuel.

The UK Industry Taskforce on Peak Oil and Energy Security and the UK government's Department of Energy and Climate

"The price of oil is likely to have been a large contributor to the euro crisis in southern Europe."

Change are very aware of these risks, and have made a commitment to work together to protect the United Kingdom and its economy from rising oil prices. The task force, formed in 2008,

warned that Britain must not be caught out by the oil crunch, and said that policies to address 'peak oil' must be made a priority. In 2011, its chairman, John Miles of architects and design engineers Arup in London, said: "We must define the risks and develop sensible contingency plans. This means thinking critically about what we should be doing now if we knew that the oil price would soar over the next five years." Such joint industry/federal government recognition of the problem does not exist in the United States, where action has largely been at the state or city level. The UK government has embedded by parliamentary statute a commitment to decrease carbon dioxide emissions by 80% by 2050 compared with 1990 levels. The US Congress has rejected any such commitment.

FASTER ACTION

Climate change and changes in fossil-fuel production are generally seen as separate phenomena. But they are closely linked. The risk of fossil-fuel supply limitation should be included when considering the uncertainties of future climate change. The approaches needed for tackling the economic impacts of resource scarcity and climate change are the same: moving away from a dependence on fossil-fuel energy sources. Whereas the implications of climate change have driven only slow policy responses, economic consequences tend to drive shorter-term action. We know from the historical record that when there are oil-price spikes, the economy begins to respond within a year. Governments that fail to plan for the decline in

fossil-fuel production will be faced with potentially major blows to their economies even before rising sea levels flood their coasts or crops begin to fail catastrophically.

The solutions are not secret or mysterious. Globally we get 55×10^{18} joules of useful energy from 475×10^{18} joules of primary energy from fossil fuels, biomass and nuclear power plants. The difference is due to energy losses and inefficiencies in the conversion and transmission processes. By increasing the efficiency, we could get the same useful energy by burning less fuel. We need to specify conservation goals for improving the efficiency of use of fossil-fuel energy. These include taxing oil to keep prices high and to encourage a reduction in energy use; encouraging nuclear energy; questioning if and how economic growth can continue without an increase in fossil fuels; lowering speed limits on roads and encouraging public transport; or redirecting tax credits towards renewable-energy development. The transformation will take decades, so we must begin as soon as possible. Emphasizing the short-term economic imperative from oil prices must be enough to push governments into action now. ■

James Murray is in the School of Oceanography, University of Washington, Seattle, Washington 98195, USA. He was founding director of the University of Washington's Program on Climate Change. David King is director of the Smith School of Enterprise and the Environment, University of Oxford, Oxford OX1 2BQ, UK, and senior science adviser to the bank UBS. He served as chief scientific adviser to the UK government in 2000–07. e-mail: jmmurray@u.washington.edu

1. Hirsch, R. L., Bezdek, R. & Wendling, R. *Peaking of World Oil Production: Impacts, Mitigation, & Risk Management* (US Department of Energy, 2005).
2. US Energy Information Administration *Annual Energy Outlook 2011* (DOE/EIA, 2011).
3. Owen, N. A., Inderwildi, O. R. & King, D. A. *Energy Policy* **38**, 4743–4749 (2010).
4. Cambridge Energy Research Associates *Finding the Critical Numbers: What Are the Real Decline Rates for Global Oil Production?* (IHS/CERA, 2007).
5. International Energy Agency *World Energy Outlook 2008* (IEA, 2008).
6. Canadian Association of Petroleum Producers *Report of the Dialogues on the Oil Sands* (CAPP, 2011).
7. Hirsch, R. L., Bezdek, R. H. & Wendling, R. M. *The Impending World Energy Mess: What it is and What it Means to You!* (Apogee Prime Press, 2010).
8. Energy Watch Group *Coal: Resources and Future Production*, EWG-Series No. 1/2007 (EWG, 2007).
9. World Energy Council *2010 Survey of Energy Resources* (WEC, 2010).
10. Rutledge, D. *Int. J. Coal Geol.* **85**, 23–33 (2011).
11. National Research Council *Coal: Research and Development to Support National Energy Policy* (National Academies Press, 2007).
12. Hughes, D. *Will Natural Gas Fuel America in the 21st Century?* (Post Carbon Institute, 2011).
13. Hamilton, J. D. *Causes and Consequences of the Oil Shock of 2007–08*. Brookings Papers on Economic Activity, 215–259 (2009).



Provocative questions in cancer research

Harold Varmus and Ed Harlow explain how an innovative initiative is opening up neglected areas of oncology.

What is the best way for large research organizations to guide the expenditure of their funds? Governmental funding agencies, major philanthropic foundations and industrial firms bear a primary allegiance to those who pay for them — taxpayers, benefactors and shareholders, respectively. They are also dedicated to long-term goals — solving problems posed by disease, environmental change or national defence.

The issue is hotly debated. At one end of the spectrum, organizations place decisions about the direction of research on the shoulders of individual investigators who conceive new proposals and the peers who judge their value. At the other, they define the research programmes and direct them towards their goals from the top down.

As the director of the US National Cancer Institute (NCI) and a senior adviser to the director, we and others have developed a different way to manage a significant portion of the agency's research portfolio. Our Provocative Questions initiative asks investigators

to propose intriguing questions in cancer research that need attention but would usually find it difficult to get. The initiative does not replace the NCI's traditional reliance on the imaginations of individual investigators; nor does it intend to restate obvious goals. Instead, it aims to engage a diverse range of scientists in a challenging intellectual exercise to define then solve the major unsolved or neglected problems in oncology.

The initiative builds on a rich history of scientific discoveries that have stemmed from well conceived questions. Such questions recognize the role of natural phenomena, reflect technical feasibility and convey the importance of a satisfactory answer. They point to alternative directions in research, new uses of technologies, forgotten observations or under-studied but important problems. They bypass the obvious and emphasize the provocative. Properly constructed and phrased, they excite curiosity, stimulate ideas and inspire progress.

Similar strategies in disciplines ranging

from mathematics to global health serve as precedents. These efforts have tended to set goals (the United Nations' Millennium Development Goals¹) or post challenges (David Hilbert's Grand Challenges in Mathematics² or the Gates Foundation's Grand Challenges in Global Health³). For the NCI, however, we chose to pose questions because we believe that good questions lie behind much of the best work in science. How does something work? Where are the key points of control? How can we explain unexpected observations or apparently contradictory findings in mechanistic terms?

Over the past 18 months, we have developed the Provocative Questions initiative from a concept into a pragmatic strategy for supporting new grants. We have hosted community-wide activities to gather questions; evolved ways to refine and select the most powerful ones; and solicited proposals to answer them.

To develop a list of key questions related to cancer, the NCI conducted 16 day-long workshops on the National Institutes

of Health (NIH) campus in Bethesda, Maryland, and at several other locations throughout the United States. Around 30 investigators from different scientific disciplines and at varying stages of their careers posed and discussed questions and judged their importance. We then moulded the most appealing ones into a format that explains the importance of the question, the likelihood that it will be answered and the ramifications of doing so. The workshops have been revelatory in another, less expected way. Minimally structured, they were immensely enjoyable, offering hours of uninhibited and unconventional exchanges.

To extend this exercise beyond the small number of people who could attend the workshops, the NCI has created a website (provocativequestions.nci.nih.gov). There, anyone can learn about the motivations behind the initiative, and people have been able to propose additional questions and comment on those suggested at workshops or online. The site now lists more than 100 questions and has been visited by more than 35,000 scientists throughout the world, at a rate of roughly 1,800 hits per day.

To formalize the initiative, the NCI has issued a request for applications and provisionally set aside US\$15 million from the budget for fiscal year 2012 to support the best ideas for answering any of the questions chosen from a list of 24. Applications for funding will be judged by special NCI study sections, the members of which will be asked to assess the relative power of the proposed ideas, rather than the supporting preliminary data or the reputation of an applicant.

Four examples of under-studied areas chosen for funding are outlined below. Detailed descriptions can be found at the website.

FOUR EXAMPLES

Drug mechanisms: Although conventional chemotherapy is often regarded as a sub-optimal treatment strategy, with high toxicity and less than curative outcomes in common adult cancers, there are several well documented situations (such as germ-line or paediatric cancers) in which these therapies can provide complete cures⁴. For example, cisplatin cures most patients with advanced testicular cancer and has been the standard treatment for decades. Perhaps because it has been so successful, few studies of this drug response are being conducted. Yet knowing why this drug and others can produce such durable cures could illuminate the search for similar opportunities for cancers that are less successfully treated.

Cancer evolution: The emergence of tumours resistant to both traditional chemotherapies and newer targeted treatments involves selection of cancer-cell variants that have acquired properties that block

or sidestep the action of the drug⁵. As an evolutionary biologist pointed out during one workshop, little attention has been directed to the application of ideas about how Darwinian selection by massive cell killing might drive the emergence of drug-resistant tumour cells. Applying such a strong selective pressure may not be the best way to undermine the behaviour of cancer cells.

Obesity risk: Epidemiologists have established that obesity dramatically increases the risk of developing some cancers, and in some cases the risk rivals that for tobacco^{6–8}. One of the Provocative Questions asks scientists to consider how obesity promotes tumour development. Uncovering the molecular mechanisms by which this happens could help to identify new approaches to cancer prevention or treatment. Such an effort would be a powerful example of how to link risk identification to the molecular steps that drive carcinogenesis.

Ageing and cancer: Cancers are commonly considered to be associated with ageing, presumably because of the accumulation of mutations affecting cancer genes. However, some cancers peak in childhood, adolescence, young adulthood or middle age. Moreover, the occurrence of cancers does not correlate well with the lifespan of an animal: mice, which have a two-year life expectancy, are much more prone to cancer than are turtles or marine mammals that live longer than human beings. What accounts for these discrepancies? Does our understanding of the process of ageing help to explain the patterns of carcinogenesis as a function of age?

MEASURING SUCCESS

Because the Provocative Questions initiative is an experiment, the NCI is using a combination of subjective and objective assessments to measure its success. The workshops were welcomed enthusiastically: almost all invitations to participate were accepted, and we received many testimonials afterwards. The response to the request for applications has also been strong — perhaps not surprising at a time when success rates for new grants are at an all-time low across the NIH. We have processed more than 750 applications, with every question receiving interest from multiple investigators. The response suggests that the initiative is meeting a pent-up demand for more imaginative funding opportunities.

Of course, the proof of principle — finding satisfying answers to a significant number of Provocative Questions or developing sustained research programmes to expand the pursuit of answers — will take years to accomplish. In the meantime, we plan to expand the list of questions through additional workshops and the website, to invite requests for applications annually for at least

another two years and to consider whether to expand the initiative in the more distant future.

We believe that the Provocative Questions model will help funding agencies in other fields. The approach helps to define the boundaries between the known and unknown; it takes advantage of new developments to refocus a discipline's attention on historically intractable problems; and it highlights perplexing issues that may be raised by new evidence about traditional topics.

An initiative of this type combats the pressures for 'safe havens', which are common in eras of budgetary stringency. Reductions in funding tend to prompt all parts of the research community to become more conservative. Grant writers look to the safest harbours for research ideas and often converge on similar subjects, narrowing research portfolios. In turn, reviewers respond conservatively; popular ideas are likely to score well, again narrowing the scope of approaches.

By pooling the imaginations of the research community to address understudied areas, an initiative such as ours provides a useful compromise between two traditional approaches of funding agencies: one that focuses on goals set by portfolio managers and another that is entirely unstructured.

The benefits will also be evident in fields that are progressing rapidly. In our research area of oncology, we are witnessing an explosion of knowledge about the genetic basis and underlying biology of many cancers, matched by the development of powerful technologies for expanding and applying that knowledge to the classification and management of disease⁹. Under these circumstances it is easy to become overconfident in the progress that is occurring. Provocative Questions are welcome antidotes, as well as productive guides to future research. ■

Harold Varmus is the director of the US National Cancer Institute and **Ed Harlow** is a senior adviser to the director.
e-mail: harold.varmus@nih.gov

1. Annan, K. *We the Peoples: The role of the United Nations in the 21st Century* (United Nations, 2000).
2. Hilbert, D. *Bull. Am. Math. Soc.* **8**, 437–479 (1902).
3. Varmus, H. et al. *Science* **302**, 398–399 (2003).
4. Guminski, A. D., Harnett, P. R. & deFazio, A. *Lancet Oncol.* **3**, 312–318 (2002).
5. McCormick, F. *J. Surg. Oncol.* **103**, 464–467 (2011).
6. Calle, E. E., Rodriguez, C., Walker-Thurmond, K. & Thun, M. J. *N. Engl. J. Med.* **348**, 1625–1638 (2003).
7. Adams, T. D. et al. *N. Engl. J. Med.* **357**, 753–761 (2007).
8. Renehan, A. G., Soerjomataram, I. & Leitzmann, M. F. *Eur. J. Cancer* **46**, 2581–2592 (2010).
9. National Research Council. *Toward Precision Medicine: Building a Knowledge Network for Biomedical Research and a New Taxonomy of Disease* (National Academies Press, 2011).



Joseph Rotblat shared the Nobel Peace Prize for his efforts to rid the world of nuclear weapons.

NUCLEAR PHYSICS

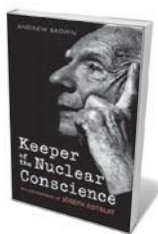
Arms and the man

Martin Rees applauds a biography of the physicist who kickstarted the Pugwash Conferences for arms control.

The physicists who developed nuclear weapons during the Second World War mostly returned to academic pursuits when peace was declared. But some did what they could, however little, to control the powers that they had helped to unleash. The most committed and idealistic of these was Joseph Rotblat — the instigator and driving force behind the Pugwash Conferences on Science and World Affairs, which aim to reduce the danger of armed conflict through global cooperation.

Radiation oncologist Andrew Brown's fine biography, *Keeper of the Nuclear Conscience*, chronicles a life spanning almost the entire twentieth century and moulded by its turmoil and horrors. Rotblat was born in Poland in 1908, and his family suffered severe privations in the First World War. But he was energetic and persistent — a lifelong trait — and, by the age of 30, had achieved international standing in radioactivity research.

In 1939 he left the Warsaw Radiological Laboratory in Poland to take up a short-term



Keeper of the Nuclear Conscience: The Life and Work of Joseph Rotblat

ANDREW BROWN
Oxford University Press: 2012. 368 pp.
£18.99, \$29.95

this UK effort was subsumed into the US Manhattan Project in 1943, Chadwick used his influence to enable Rotblat to move to the Los Alamos Laboratory in New Mexico, despite his Polish citizenship.

Since 1940, nuclear physicists had feared

post with physicist James Chadwick at the University of Liverpool, UK. This was a fortunate move: the Warsaw lab was destroyed a year later, and few of its staff survived the Nazi occupation. Rotblat quickly became Chadwick's trusted lieutenant. Chadwick was part of a team studying the feasibility of a fission weapon under the code names Maud and Tube Alloys. When

a nightmare scenario in which Adolf Hitler developed atomic weapons. For Rotblat, this was the only moral justification for the Allies' bomb project. He was, famously, the only scientist to leave the Manhattan Project when, by 1944, this threat no longer seemed realistic. He recounted that the trigger was a comment by Leslie Groves, the military head of the project, that the bomb could be used against the Soviet Union. But Brown elaborates the complex motives and personal turmoil behind this decision. Rotblat had heard nothing from his wife since 1939, and learnt only later that she had perished in a concentration camp. And he was mindful that US authorities were concerned that his secret knowledge might reach Poland and fall into the hands of the Nazis or Soviets.

Rotblat returned to Liverpool, helping to rebuild the physics department, but moved in 1950 to a position in radiation medicine attached to St Bartholomew's Hospital in London. He first gained public prominence in 1954. By analysing radioactive dust from a Japanese fishing boat that strayed too close to a US thermonuclear test, he inferred key features of the bomb's design. He also appeared, with British philosopher Bertrand Russell, in an early *Panorama* programme on BBC television, highlighting the hazards of nuclear fallout. Russell subsequently prepared a manifesto against nuclear weapons, signed by Albert Einstein and other eminent scientists, which declared that the signatories were speaking "not as members of this or that nation, continent, or creed, but as human beings, members of the species Man, whose continued existence is in doubt".

Bolstered by this initiative, in 1957 Rotblat arranged for a select group of Eastern and Western scientists to meet in the Canadian village of Pugwash, Nova Scotia, for private discussions of how to control nuclear arms. Thus began the Pugwash conferences and workshops. There have now been around 300; Rotblat attended almost all of them before his death in 2005. Funding was a continual challenge, especially because it was crucial to avoid sponsorship from propagandist bodies.

BAN BROKER

How much influence did these non-governmental gatherings have? During the 1960s, the Pugwash Conferences undoubtedly offered crucial back-channel contact between the United States and the Soviet Union. This eased the path for the Partial Test Ban Treaty of 1963, and the subsequent anti-ballistic missile and non-proliferation treaties. The Pugwash agenda later broadened to include biological weapons and problems of the developing world. Brown argues that the

➔ **NATURE.COM**
For more on Joseph Rotblat and Pugwash:
go.nature.com/lj6nn2

conferences thereby became less distinctive, and that their influence was diluted.

Brown also notes the tension between those who wished to promote piecemeal progress and those, such as Rotblat, who did not wish to lose sight of the long-term aim to rid the world of nuclear weapons. This latter view was widely derided as woolly idealism. But it gradually gained broader establishment support. In his later years, for instance, Robert McNamara, defence secretary to US presidents John F. Kennedy and Lyndon Johnson, attended several Pugwash meetings. This might have seemed incongruous, as did Rotblat's friendship with Soviet Union President Mikhail Gorbachev. But these men came together with the realization that eliminating nuclear weapons should be an eventual goal. This view has become mainstream, espoused recently by the US 'gang of four' (former secretaries of state Henry Kissinger and George Schultz, former defence secretary William Perry and former Senator Sam Nunn) and proclaimed in President Barack Obama's 2009 speech in Prague.

When the Pugwash Conferences were recognized by the 1995 Nobel Peace Prize, half of the award went to the organization and half to Rotblat personally. It was characteristic that he donated his half of the prize money to the organization.

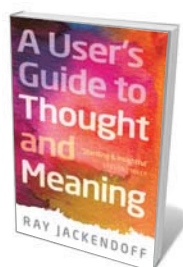
That was also the year of Rotblat's absurdly overdue election to the Royal Society — recognition that meant a lot to him. In a memorable speech, he warned against exchanging the ivory tower for secret work. He quoted Solly Zuckerman, long-term adviser on nuclear policy to the UK government: "When it comes to nuclear weapons... it is he, the technician, not the commander in the field, who is at the heart of the arms race".

Until his last few months (he died aged 96), Rotblat travelled the world with the resilience of a man half his age. He was concerned about the hazards that could stem from the misuse of twenty-first-century science, so was keen to convey his disquiet beyond the Pugwash community, and to a younger generation. He favoured a 'Hippocratic oath' whereby scientists would pledge to use their talents for human benefit. Whether or not such an oath would have substance, there can be no doubt of his success at raising awareness. Even in his nineties, he could still captivate students.

Brown's balanced and comprehensive biography is welcome. Rotblat's inspiring life — against a backdrop of tragedy and hardship, with idealism but without illusions — deserves to be better known. ■

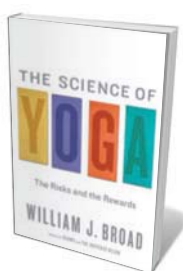
Martin Rees is master of Trinity College, Cambridge, UK; former president of the Royal Society; and author of *From Here to Infinity: Scientific Horizons*. He has attended several Pugwash meetings. e-mail: mjr36@cam.ac.uk

Books in brief



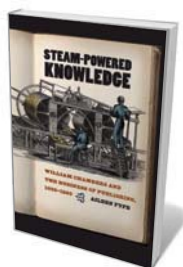
A User's Guide to Thought and Meaning

Ray Jackendoff OXFORD UNIVERSITY PRESS 288 pp. £16.99 (2012)
Linguist Ray Jackendoff wends his way through thorny questions around language and thought, hedge-clippers in hand. Covering words and meaning, consciousness and perception, reference, rationality and intuition, he reveals the split between how we experience the world and how perception and language are organized. His conclusion is that rational thought rests on intuition — and that meaning and thought are almost completely unconscious. The book is a multi-perspective journey into the hinterlands of the 'problem of knowledge'.



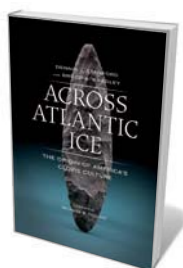
The Science of Yoga: The Risks and the Rewards

William J. Broad SIMON & SCHUSTER 336 pp. £16.63 (2012)
Whether it is hatha, ashtanga or kundalini, yoga is swathed in hype. This ancient discipline is a vast and growing industry in the West, and ripe for investigation. Science writer William Broad, a two-time Pulitzer prizewinner and experienced yoga practitioner, has spent five years researching the teaching and practice. The result is illuminating and often unnerving. Yoga has proven physical and psychological benefits, yet Broad shows how even ordinary poses, poorly taught to the unfit, can lead to strokes, serious hip-joint damage and worse.



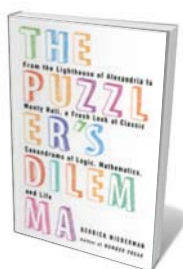
Steam-Powered Knowledge: William Chambers and the Business of Publishing, 1820–1860

Aileen Fyfe UNIVERSITY OF CHICAGO PRESS 336 pp. \$50 (2012)
As e-books rise, it is salutary to recall another technological revolution in bringing words to mind: the steam-powered printing press. Historian Aileen Fyfe focuses on Edinburgh publishing firm W. & R. Chambers to reveal how the cheap print that flooded both sides of the Atlantic in the 1800s transformed the dissemination of knowledge. This chronicle of great endeavour is studded with small pleasures, from the horror over 'sordid' railway literature to engineer Charles Babbage's awe of printing speeds at *The Times*.



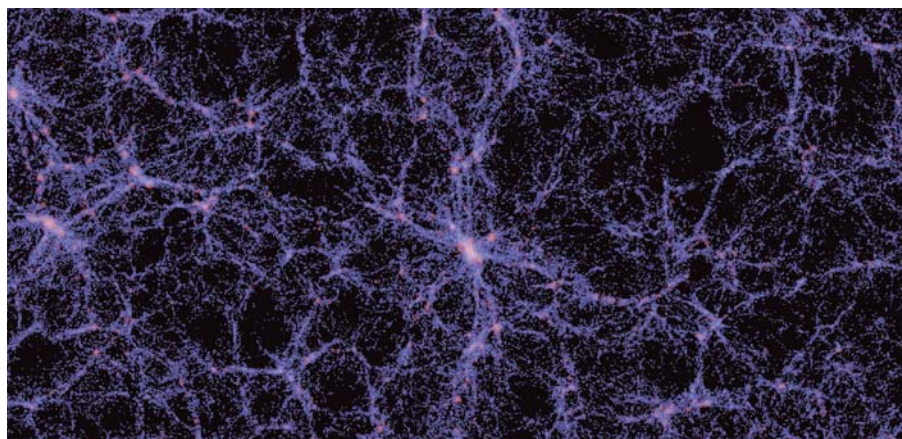
Across Atlantic Ice: The Origin of America's Clovis Culture

Dennis J. Stanford and Bruce A. Bradley UNIVERSITY OF CALIFORNIA PRESS 336 pp. \$34.95 (2012)
North America's first peoples were long thought to be Asians who migrated over the Bering land bridge some 12,000 years ago, bringing with them the tools of the Clovis culture. Now archaeologists Dennis Stanford and Bruce Bradley have radically recast the story. Drawing on climatic, genetic and archaeological evidence, they argue that the roots of Clovis culture rest in the Solutrean people of Spain and France, who sent some of their number across the Atlantic in boats 18,000 years ago.



The Puzzler's Dilemma: From the Lighthouse of Alexandria to Monty Hall, a Fresh Look at Classic Conundrums of Logic, Mathematics, and Life

Derrick Niederman DUCKWORTH 216 pp. £14.99 (2012)
Mathematician Derrick Niederman takes classic logic puzzles and weaves them into a fiendish brain-teaser of a narrative. He covers 'kangaroo' puzzles that contain their own answers, lateral-thinking posers, and even riddles that abide by Sherlock Holmes's great technique — eliminating the impossible so that "whatever remains, however improbable, must be the truth".



The cooling Universe enabled galaxies to form, as this simulation shows.

COSMOLOGY

Plucked from the vacuum

A tale of multiverses, cosmic inflation and dark energy grips **Caleb Scharf**.

In less than 100 years, humanity has seen the predictions of fundamental physics converge with the observation of nature on cosmic scales. The result is an increasingly convincing picture that we, and the Universe as a whole, owe our existence to the instability of 'empty' space at a quantum level. Moreover, space and the laws of physics may be just one variant among many possible ways to assemble universes, separated by dimension or by scale.

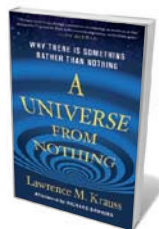
How physicists came up with the current model of the cosmos is quite a story, and to tell it in his elegant *A Universe From Nothing*, physicist Lawrence Krauss walks a carefully laid path. The evolving Universe of finite age has pushed physicists to tackle ever more profound and challenging questions using some of the most innovative tools ever forged.

Krauss begins in 1916, when Albert Einstein fudged the field equations in his general theory of relativity to ensure that they modelled a static Universe. To do this he added a small constant repulsive force, equivalent to endowing empty space with energy. Within a few years, Edwin Hubble and other astronomers demonstrated that, in fact, the Universe is expanding and dynamic. Einstein removed the force from his equations. In the following decades came the recognition that most matter is dark and only weakly interacting, and that the observed cosmic mix of light elements, such as hydrogen, helium and

lithium, is the result of primordial nucleosynthesis in the first minutes after the Big Bang, when newly stable protons and neutrons combined in a frenzy of nuclear fusion.

Another milestone in the story is the measurement, in 1992, of hot and cold patches in the sea of microwave radiation that was scattered as the plasma of a 380,000-year-old Universe cooled enough to form atoms. These patterns reveal the seeds of galactic structures in today's Universe and offer striking confirmation of current cosmological theories. But just as all seemed to be fitting together well, astronomers turning their telescopes to distant, dimmed supernovae saw that the expansion of the space between the stars was accelerating rather than decelerating. Like Einstein, physicists are again stepping back to look for a way to tie the strands together.

Mathematical investigations of the atomic and subatomic world provide a plausible solution. The overall smoothness and geometrical regularity of the Universe could have resulted from its rapid inflation from



A Universe from Nothing: Why There Is Something Rather Than Nothing
LAWRENCE M. KRAUSS
Free Press: 2012.
224 pp. \$24.99,
£17.99

quantum scales during its earliest stages. The later accelerating expansion might be driven by the 'dark energy' of the vacuum itself — a seething ocean of virtual particle pairs popping in and out of existence as a result of quantum uncertainty.

Furthermore, Krauss points out, our Universe seems to have a net gravitational energy that is suspiciously close to zero: its existence may 'cost' nothing, requiring no energy input. This raises the possibility of the ultimate free lunch — of a cosmos that is merely a piece of borrowed stuff, having appeared spontaneously, like a virtual particle, and been filled with matter and radiation simply as a consequence of the energy of empty space. Ours may be one of an infinite array of universe-like things, just one instance in a multiverse.

It would be easy for this remarkable story to revel in self-congratulation, but Krauss steers it soberly and with grace, taking time to let the reader digest the material. His discussion of the multiverse is a good example: he lays out the possibilities and scientific and philosophical implications without beating the drum for any one hypothesis. His asides on how he views each piece of science and its chances of being right are refreshingly honest.

He notes that a number of vital empirical discoveries are, ominously, missing from our cosmic model. Dark matter is one. Despite decades of astrophysical evidence for its presence, and plausible options for its origins, physicists still cannot say much about it. We don't know what this major mass component of the Universe is, which is a bit of a predicament. We even have difficulty accounting for every speck of normal matter in our local Universe. This does not mean that something is wrong with the current picture, but that we astronomers should be uncomfortable about embracing a phenomenon such as dark energy when we still have a mess to tidy up elsewhere.

Krauss eases such concerns by showing that the Universe's accelerating expansion fits astonishingly well with a host of its other characteristics. He shows how the theories of the physical sciences — from the subatomic to the cosmological — unite sublimely.

What does this mean for humanity? In a provocative afterword, evolutionary biologist and atheist Richard Dawkins writes that the apparent near-inevitability of something arising out of unstable nothingness, as described by Krauss, is devastating for theologians and creationists. Dawkins is right. But it is also invigorating for the rest of us, because in this nothingness there are many wonderful things to see and understand. ■

Caleb Scharf is director of astrobiology at Columbia University, New York, USA. His forthcoming book is *Gravity's Engines*. e-mail: caleb@astro.columbia.edu

FILM

Science gets real at Sundance

This year's crop of research-related films moves away from 'mad genius' mode, finds **Jascha Hoffman**.

Hollywood likes its science catastrophic and its researchers portrayed as either reckless geniuses or crazed loners. Will we ever have a realistic rendering of the benign innovators at work in a lab near you? The answer could be a qualified yes, judging from the lineup at this year's Sundance Film Festival in Utah.

The cinematic celebration, now in its 34th year, promotes US film outside Hollywood and has launched the career of directors such as Steven Soderbergh, whose epidemiological thriller *Contagion* did well last year. For 2012, the festival has embraced the bright side of science in its documentary-heavy programme.

"Most of these films are positive in their view of science as a means to improve our lives," said John Nein, a film programmer at the Sundance Institute in Los Angeles, California. Many of the festival's 100 or so features bear out Nein's words.

Among a handful of documentaries concerned with climate, energy and the environment, one stands out for its sheer ambition.

GO NATURE.COM
For Isabella Rossellini's take on science and film: go.nature.com/urek25

Chasing Ice, directed by Jeff Orlowski, follows dogged *National Geographic*

Sundance Film Festival
Park City, Utah.
Until 29 January.

photographer James Balog as he deploys 30 cameras on three continents to gather time-lapse footage of glaciers melting and ice shelves collapsing. The result is a graphic portrait of global warming. Director Mark Kitchell's *A Fierce Green Fire* is a sweeping history of environmental activism in the past half-century, with biologist E. O. Wilson as adviser. *The Atomic States of America*, directed by Don Argott and Sheena Joyce, sounds a warning of the health and environmental costs of nuclear energy.

Also on the factual front is a set of documentaries showing how science improves public life through education, medicine and criminal justice. In *The D Word: Understanding Dyslexia* (directed by James Redford, son of Sundance president and founder Robert Redford), physicians from the Yale Center for Dyslexia and Creativity in New Haven, Connecticut, explain the neurological underpinnings of dyslexia, revealing how some of its features may account for the success of entrepreneur Richard Branson and others with the condition.

David France's *How to Survive a Plague* explores the controversial efforts of AIDS activists in the 1980s and 1990s to push

experimental treatments through the drug pipeline. And *West of Memphis*, directed by Amy Berg and co-produced by *The Hobbit* director Peter Jackson, delves into the finer points of forensic science. It tells the story of three Arkansas teenagers who, convicted of murdering three boys, were released two decades later on the basis of DNA evidence.

Other offerings are more personal and research-focused. Homing in on freshwater biology, Chris Peters's *The Diatom* is a meditative glimpse of a microbiologist tracking the unicellular organisms that thrive in Utah's remote mountain reservoirs. *Valley of Saints*, directed by Musa Syeed, follows a biologist and the boatman she falls in love with as they discover serious pollution in a pristine lake in Kashmir.

Two star-studded films offer comic relief. Director Jake Schreier's dramatic comedy *Robot and Frank* recounts the budding friendship between an elderly thief and the household robot that cooks and cleans for him, and claims to illuminate "the implications of humankind's ever-changing relationship with technology". *Red Lights*, by director Rodrigo Cortés, features a research duo played by Sigourney Weaver and Cillian Murphy as a pair of sceptics who debunk clairvoyants. Until, that is, they discover a blind psychic, unaccountably played by Robert De Niro, whose apparent powers threaten their faith in reason.

Festival-goers may be lured from their seats for conversations on the future of film-making. A talk that questions 'the new future normal' speculates on tomorrow's beneficial technologies, from camera contact lenses to regularly upgraded 'hyperhumanity'. A panel on good science in films, sponsored by the Alfred P. Sloan Foundation, will ask what would happen if robots or viruses helped humanity instead of wiping it out. Panellists include biologists Helen Fisher and Robert Full, and *Contagion* screenwriter Scott Burns.

Science fiction and allegorical drama also get a look-in. *Beasts of the Southern Wild*, directed by Benh Zeitlin, is a moody film about a six-year-old girl in a flooded world rife with prehistoric creatures. Director Colin Trevorrow's *Safety Not Guaranteed* is a romantic comedy hinging on time travel. There are even classic blood-spattered forays. In Jon Wright's monster feature *Grabbers*, "giant, bloodsucking, tentacled aliens" rise from the sea to prey on boozy Irish villagers, despite the efforts of a marine biologist and two local police officers.

There's always room for a little bone-crunching horror — if only for contrast to the nuanced, realistic cinematic science we see dawning at Sundance. ■

Jascha Hoffman is a journalist based in San Francisco, California.
e-mail: jascha@jaschahoffman.com



Time-lapse footage of melting glaciers in *Chasing Ice* offers a graphic glimpse of global warming in action.

J. BALOG/EXTREME ICE SURVEY

Correspondence

Pause on avian flu transmission studies

The continuous threat of an influenza pandemic represents one of the biggest challenges in public health. Influenza pandemics are known to be caused by viruses that evolve from animal reservoirs, such as birds and pigs, and can acquire genetic changes that increase their ability to transmit in humans. Pandemic preparedness plans have been implemented worldwide to mitigate the impact of influenza pandemics. A major obstacle in preventing influenza pandemics is that little is known regarding what makes an influenza virus transmissible in humans. As a consequence, the potential pandemic risk associated with the many different influenza viruses of animals cannot be assessed with any certainty.

Recent research breakthroughs identified specific determinants of transmission of H5N1 influenza viruses in ferrets. Responsible research on influenza virus transmission using different animal models is conducted by multiple laboratories in the world using the highest international standards of biosafety and biosecurity practices that effectively prevent the release of transmissible viruses from the laboratory. These standards are regulated and monitored closely by the relevant authorities. This statement is being made by the principal investigators of these laboratories.

In two independent studies conducted in two leading influenza laboratories at the University of Wisconsin-Madison and Erasmus MC in Rotterdam, the Netherlands, investigators have proved that viruses possessing a haemagglutinin (HA) protein from highly pathogenic avian H5N1 influenza viruses can become transmissible in ferrets. This is critical information that advances our understanding

of influenza transmission. However, more research is needed to determine how influenza viruses in nature become human pandemic threats, so that they can be contained before they acquire the ability to transmit from human to human, or so that appropriate countermeasures can be deployed if adaptation to humans occurs.

Despite the positive public-health benefits these studies sought to provide, a perceived fear that the ferret-transmissible H5 HA viruses may escape from the laboratories has generated intense public debate in the media on the benefits and potential harm of this type of research. We would like to assure the public that these experiments have been conducted with appropriate regulatory oversight in secure containment facilities by highly trained and responsible personnel to minimize any risk of accidental release. Whether the ferret-adapted influenza viruses have the ability to transmit from human to human cannot be tested.

We recognize that we and the rest of the scientific community need to clearly explain the benefits of this important research and the measures taken to minimize its possible risks. We propose to do so in an international forum in which the scientific community comes together to discuss and debate these issues. We realize that organizations and governments around the world need time to find the best solutions for opportunities and challenges that stem from the work. To provide time for these discussions, we have agreed on a voluntary pause of 60 days on any research involving highly pathogenic avian influenza H5N1 viruses leading to the generation of viruses that are more transmissible in mammals. In addition, no experiments with live H5N1 or H5 HA reassortant viruses already shown to be transmissible in ferrets will be

conducted during this time. We will continue to assess the transmissibility of H5N1 influenza viruses that emerge in nature and pose a continuing threat to human health.

Ron A. M. Fouchier *Erasmus MC, Rotterdam, the Netherlands.*

Adolfo García-Sastre *Mount Sinai School of Medicine, New York, USA.*

Yoshihiro Kawaoka *University of Tokyo, Japan; and University of Wisconsin-Madison, Wisconsin, USA.*

kawaokay@svm.vetmed.wisc.edu
For a full list of co-authors, see go.nature.com/mwqvoo

Train local experts to help conserve forests

The management of tropical forests by indigenous communities requires a formal intervention plan based on quantitative inventories, growth studies and permanent monitoring systems. But in our 30 years of experience, few such communities, if any, would be able to produce a plan on their own. This shortcoming needs to be rectified.

One answer would be to train village-based resource managers, who could use their knowledge and skills in forestry, ecology, ethnobotany, economics and anthropology to help local communities manage forests and interact with the state, commercial markets and the global conservation community. This would reduce dependency on external inputs, draw on local skills, promote community organization and self-governance, and help to implement ways of reducing emissions from deforestation and degradation.

Crucially, community-owned forests would then stay in the hands of those who have lived in, used and looked after them for so long.

Charles M. Peters *The New York Botanical Garden, New York, USA.*
cpeters@nybg.org
Miguel Alexiades *University of*

Kent, Canterbury, UK.

Sarah A. Laird *People and Plants International, Bristol, Vermont, USA.*

Biobank donors should have a say

Our findings from a qualitative survey of patients, health-care providers, researchers and other members of the public in Switzerland support suggestions that the views of prospective tissue donors should be taken into account in securing biobank samples (*Nature* **478**, 312–313; 2011).

In 2009–10, we interviewed 90 people in focus groups, using fictitious case studies to explore perceptions about the use of human tissue.

Those professionals who preferred blanket consent from donors commonly expressed fears that providing information on tissue use to patients could make them reluctant to donate samples. The general population and patient groups, by contrast, usually wanted to be informed and have the opportunity to give consent.

Among patients, the need to be informed was linked to a wish to be appraised of their medical condition and to be a partner in the therapeutic process. Cancer patients were particularly enthusiastic about the use of their tissues because it helped them to make sense of their illness and could potentially benefit others.

Brenda Spencer, Daria Koutaissoff, Hans-Anton Lehr *Lausanne University Hospital, Switzerland.*
brenda.spencer@chuv.ch

CONTRIBUTIONS

Correspondence may be sent to correspondence@nature.com after consulting the guidelines at go.nature.com/cmchno. Readers can also comment online: www.nature.com/nature.

James Crow

(1916–2012)

Population geneticist who studied mutation, selection and random drift.

Much about James Franklin Crow, who died on 4 January two weeks short of his 96th birthday, challenges our sense of scale. Over seven decades, he contributed to an astonishing array of topics in genetics, and the list of his students and postdocs reads like a who's who. One of them, the pioneering geneticist Motoo Kimura, wrote that getting Crow as his adviser after a period of uncertainty was such a joy it was like "meeting Buddha in Hell". Crow also played the viola for 45 years with the Madison Symphony Orchestra. He once performed with the great violin soloist Yehudi Menuhin.

Crow is primarily known for his work in theoretical population genetics. He developed a concept of genetic load — a measure of how fitness may be reduced by selection — and applied it widely, in particular to calculating how quickly natural selection would remove deleterious mutations from a population. With Kimura in 1965, he quantified how sex accelerates the accrual of beneficial mutations in an evolving population. He refined the concept of effective population size and provided simple connections between selection at the genetic level (genotype) and at the physically observed level (phenotype).

Crow's expertise drew him into the public-health sphere. He served on a National Academy of Sciences committee to assess genetic damage caused by radiation in victims of the atomic weapons dropped on Hiroshima and Nagasaki. And he advised the US government in the 1980s and 1990s on forensic DNA tests, leading to their widespread adoption in the courts.

Born in 1916, in Phoenixville, Pennsylvania, Crow grew up in Wichita, Kansas, where his father taught biology at Friends University. Crow took a bachelor's degree there and moved to the University of Texas at Austin for his PhD in genetics, which he earned in 1941. After several years at Dartmouth College in Hanover, New Hampshire, he moved to the University of Wisconsin-Madison in 1948, where he remained for the rest of his career.

He was interested in the pursuit of truth, and never advocated a particular opinion.

This must be one reason why Crow and Kimura's 1970 textbook *An Introduction to Population Genetics Theory* has had a lasting role in the development of the field.

Most of Crow's experimental work was concerned with deleterious mutations, both *de novo* and segregating within populations. In addition, his lab made two landmark discoveries in *Drosophila* genetics: a locus called segregation distorter, which can manipulate Mendelian genetic segregation in meiosis, found by Yuichiro Hiraizumi and Larry Sandler; and P elements, which can cause high

do little — causing a slight increase in blood pressure, for instance. But cumulatively their effect could prove fatal. Unlike some other prominent geneticists, Crow was always careful to separate science and policy and never advocated simplistic approaches to dealing with this problem.

After his retirement in 1986, Crow largely devoted himself to writing about the early history of genetics and evolutionary biology. He was well placed, having had close long-term acquaintance with many pioneers — including Sewall Wright, Ronald Fisher,

J. B. S. Haldane and Hermann Muller. His command of the subject and fondness for it, his benevolence and fairness, attention to detail and beautiful prose mean that Crow's publications remain required reading for anybody interested in this crucial phase.

Crow was famous for his kindness, which coexisted with the firmness of his views. There was no better person to point out a grave error in your work — making him always in demand and appreciated by his undergraduate students. My dentist in Madison once completely forgot about my filling, when he realized that I worked in Crow's laboratory. He still spoke of "Dr Crow" with awe some 25 years after taking one of Crow's courses during pre-medical training.

Those who knew Crow well will thoroughly miss his low-key benign humour, often directed towards himself. When asked about his religious views, he always cheerfully replied that the Bible is "important if true". Still, he cherished the ethics of his Quaker heritage. Crow also explained to an insistent advocate of a healthy lifestyle that exercise prolongs life only by as much time as one spends exercising, so he did not see a point in it. He always remained active — and died in his sleep.

To borrow Crow's phrase, originally about Wright: "They don't make them like that any longer". ■

Alexey Kondrashov is in the Department of Ecology and Evolutionary Biology, University of Michigan, Ann Arbor, Michigan 48109, USA. He was a long-time collaborator with Crow.
e-mail: kondrash@umich.edu



rates of mutation, found by William Engels (and independently by Margaret Kidwell, then at Brown University in Providence, Rhode Island). P elements are now widely used for genetic modification of fruitflies.

CLEAR JUSTIFICATION

Characteristically, Crow declined to be a co-author of papers reporting these two discoveries: he did not feel that providing a good working environment and sage advice was sufficient to warrant it. It was often hard to convince Crow to put his name on a paper even when this was clearly justified.

Crow was very concerned about the negative impact on human health of mildly deleterious alleles that, due to advances in medicine, can accumulate almost unchecked by natural selection. Individually, these may

FORUM Neuroscience

Spikes timed through inhibition

Purkinje cells in the brain region known as the cerebellum act by inhibiting their target neurons. A paper in this issue provides an explanation for how this inhibition might be used to control the timing of action potentials. But experts are not equally convinced about the functional relevance of this finding. SEE LETTER P.502

THE PAPER IN BRIEF

- Purkinje cells regulate the entire output of the cerebellar cortex — a brain area responsible for generating precise movement.
- They do so by sending inhibitory signals to nuclei (groups of neurons) lying deep within the cerebellum.
- So, while Purkinje cells are firing, the downstream nuclear neurons should be inhibited.
- However, the firing rate of Purkinje cells and nuclear neurons do not

always vary inversely.

- Person and Raman¹ (page 502) propose that the answer to this conundrum lies in synchrony of firing.
- Through *in vitro* experiments, they find that, as expected, random firing of Purkinje neurons powerfully inhibits nuclear cells.
- But when a small number of Purkinje cells fire synchronously, nuclear neurons fire action potentials that are 'time-locked' to the gaps between the inhibitory Purkinje inputs (Fig. 1).

Time for action

JAVIER F. MEDINA

Person and Raman¹ identify the conditions that allow Purkinje cells to control the timing of spikes (action potentials) in their target cerebellar nuclear neurons with millisecond precision. This is very exciting news for several reasons.

From a purely computational standpoint, the paper reveals a time-locking mechanism (Fig. 1) for neurons receiving inhibitory input from groups of cells that fire action potentials at high and irregular rates. This mechanism, which may be applicable to other inhibitory circuits in the brain, stands in stark contrast to the precise regulation of spike timing in another brain region — the cerebral cortex — by synchronous inputs that depolarize the neuronal membrane. It relies on several idiosyncratic features of cerebellar nuclear neurons that were previously unknown, including a high intrinsic firing rate, ultra-fast inhibitory synapses (neuronal connections) and, as also suggested by others², some degree of synchronous activity in the Purkinje-cell input.

The findings are equally intriguing for our understanding of how the brain controls movement, especially given that a time-locking mechanism seems perfectly suited to contribute to one of the most notable functions

ascribed to the cerebellum — coordinating muscles with utmost accuracy and temporal precision. But does the cerebellum really use time-locking to control movement? After all, years of research have shown that much of the information sent to motor areas from the cerebellum is conveyed by a rate code³ — a modulation in the firing frequency of neurons in which the precise timing of the spikes is irrelevant because the rate is averaged over tens to hundreds of milliseconds.

Clearly, modulation of firing frequency has a crucial role in cerebellar processing.

The findings are equally intriguing for our understanding of how the brain controls movement.

But before discarding time-locking of nuclear neurons as a computationally elegant, but otherwise functionally irrelevant, mechanism, let's remember that codes based on the timing or the rate of spikes are not mutually exclusive. Previous work has demonstrated that spikes in Purkinje cells less than 100 micrometres apart can be precisely synchronized^{4,5}, and that the level of synchrony is dynamically regulated⁴. So, at least in theory³, this would allow inputs from different groups of Purkinje cells to become synchronized for brief periods of time, and, when a high degree of temporal precision is required (for instance, at the beginning

or end of a movement), to control the exact timing of spikes in nuclear neurons. To control other aspects of movement, such as amplitude or speed, the cerebellum might switch Purkinje cells back to the asynchronous mode and modulate their firing frequency up or down, thus regulating the firing rate of nuclear neurons.

As with every landmark paper, several questions remain. For example, in addition to inhibitory synapses from Purkinje cells, nuclear neurons receive excitatory inputs from mossy and climbing fibres of neurons in other parts of the brain. How does the cerebellum process such opposing signals to achieve its goals? Examining the patterns of excitatory and inhibitory inputs *in vivo*, and understanding how they are integrated in nuclear neurons, should provide an answer.

Another question arises from work⁶ showing that cerebellar nuclear neurons can be classified into different functional groups according to not only the proteins they express or their particular anatomical connectivities, but also their electrical properties. Do these cell groups also differ in the way they process the inputs they receive?

Finally, Person and Raman's findings reveal what nuclear neurons can do, but not what they actually do. Does synchronization of Purkinje cells result in the spiking activity of nuclear neurons during normal cerebellar processing? The answer may come from whole-cell recordings in awake animals to check whether the membrane-voltage signature of individual nuclear cells *in vivo* is consistent with a spike-generating mechanism based on membrane repolarization after synchronous inhibition. As for the question of whether time-locking is part of the cerebellar code used for motor control, it will be necessary to record from many nuclear cells simultaneously, and to examine the timing and synchronization of their spikes relative to movement when the animal is active.

Javier F. Medina is in the Department of Psychology, University of Pennsylvania, Philadelphia, Pennsylvania 19104-6241, USA. e-mail: jmed@sas.upenn.edu

Sync or sink?

KAMRAN KHODAKHAH

Elucidating the principles by which neurons and neuronal circuits 'compute' remains a cardinal objective in neuroscience. Through an ingenious set of experiments, Person and Raman¹ describe one such computational principle: how a (nuclear) neuron decodes the temporal structure of its synchronous (Purkinje cell) inhibitory inputs while ignoring the asynchronous ones. The question is how relevant this temporal decoding mechanism is to cerebellar processing.

Person and Raman demonstrate *in vitro* that synchronous activity of even two Purkinje-cell inputs is sufficient to modestly entrain (time-lock) the activity of their target nuclear neuron. They posit that temporal decoding is the mechanism by which nuclear neurons encode information *in vivo*. But a confounding limitation of such temporal decoding is that the probability of firing entrained spikes is reduced so much that nuclear neurons cannot rate-code — that is, the persistent activity of the asynchronous inputs reduces the probability of a nuclear neuron firing entrained spikes to such an extent that it can no longer encode the firing rate of its synchronous inputs in its own firing rate¹. This is problematic, because it has been known^{3,7,8} for more than 40 years that the activity rates of individual nuclear and Purkinje neurons correlate with movement and thereby with each other.

Moreover, to date, no *in vivo* data have refuted the assertion that the firing rate of a nuclear neuron is inversely related to the average firing rate of its synaptically connected Purkinje cells⁹. Therefore, even if several Purkinje cells could be perfectly synchronized *in vivo*, it is doubtful that, as implied¹, nuclear neurons process and encode movement-related information through temporal decoding alone.

It is quite possible that some sort of temporal decoding occurs intermittently *in vivo*, for example during brief conditions when very precise timing of muscle movement is needed. However, the study¹ suggests that it often takes several spikes from synchronously active Purkinje cells (requiring tens to hundreds of milliseconds) to entrain a nuclear neuron. It is therefore questionable whether a rate-coding nuclear neuron can rapidly switch modes and transiently time-lock to a few synchronous Purkinje-cell spikes.

Because of the severely diminished probability of firing of entrained spikes, the authors often had to artificially depolarize the nuclear neurons to promote spiking. But what depolarizing inputs could permit temporal decoding *in vivo* without diminishing time-locking? A neuromodulator molecule may partially provide sustained depolarization free of synaptic

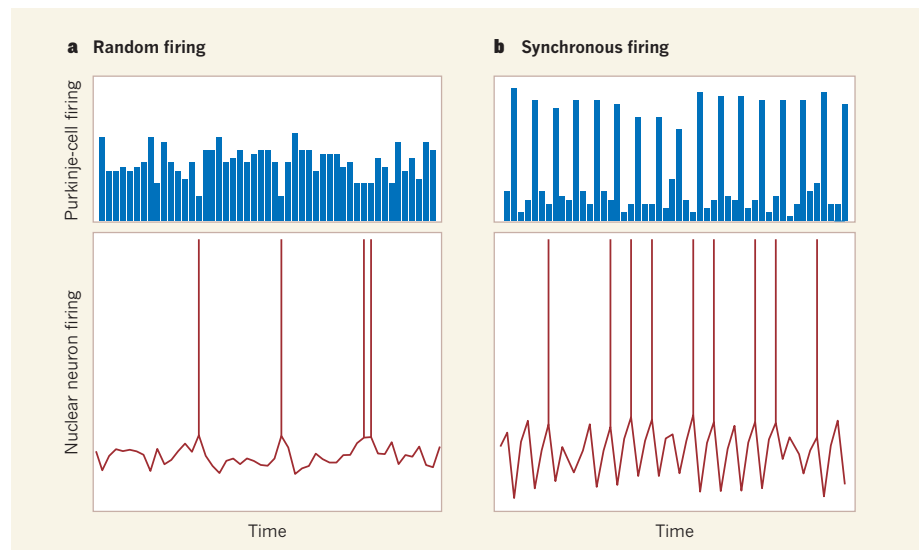


Figure 1 | Decoding Purkinje-cell inputs. a, Purkinje cells of the cerebellum send inhibitory inputs (blue bars) to their target nuclear neurons. Consequently, nuclear neurons get little chance to fire action potentials (red lines). b, Person and Raman¹ report that if two or more inhibitory inputs from Purkinje cells are synchronized (longer bars), it creates more opportunities for nuclear neurons to fire action potentials in the gaps between such 'bundles' of inhibitory inputs, entraining their spiking. (This graphic is not an exact representation of the authors' data.)

'noise', although there is no evidence for this premise. The most likely depolarizing source is the excitatory inputs from mossy and climbing fibres. These inputs powerfully modulate the firing of Purkinje cells *in vivo*, and their collateral synaptic inputs to nuclear neurons should also depolarize the latter. But the strength of

The question is how relevant this temporal decoding mechanism is to cerebellar processing.

these inputs changes with movement, and they will also generate synaptic noise. *In vivo*, these inputs are therefore likely to significantly diminish the precision of the modest time-locked spiking seen *in vitro*¹.

Linking *in vitro* and *in vivo* studies is always challenging, and in this case it is unclear whether nuclear neurons can temporally decode synchronous activity of a small number of Purkinje cells *in vivo*. With strong electrical stimulation of the cerebellar cortex, Person and Raman¹ could evoke time-locked responses. But estimating the number of activated Purkinje cells in these experiments is challenging, and electrical stimulation does not have any specificity for activating cell types or axonal processes of neurons. A more rigorous test of temporal decoding using the technique of optogenetics will allow selective, synchronous activation of a few Purkinje cells *in vivo*, while eliminating complications that arise from the unavoidable electrical activation of mossy and climbing fibres.

Lastly, even if a small number of synchronized Purkinje cells could modestly promote entrainment of nuclear neurons *in vivo*, complete synchronous activity of even two

Purkinje cells is improbable. When examined pairwise *in vivo* during brief periods of high synchrony, the correlation between the firing of two Purkinje cells is of the order of a few per cent^{10,11} — tenfold lower than the 100% synchrony assumed here¹. To what extent nuclear neurons can meaningfully entrain when a few Purkinje cells are only partially synchronized remains to be established.

The new computational principle described by Person and Raman unveils a powerful tool in the brain's information-processing tool kit. Future experiments will undoubtedly identify the circuits in which this tool is used, and may outline the conditions under which it contributes to motor coordination by the cerebellum. ■

Kamran Khodakhah is in the Dominick P. Purpura Department of Neuroscience, Albert Einstein College of Medicine, Bronx, New York 10461, USA.
e-mail: k.khodakhah@einstein.yu.edu

1. Person, A. L. & Raman, I. M. *Nature* **481**, 502–505 (2012).
2. Gauck, V. & Jaeger, D. J. *Neurosci.* **20**, 3006–3016 (2000).
3. De Zeeuw, C. I. et al. *Nature Rev. Neurosci.* **12**, 327–344 (2011).
4. Bell, C. C. & Grimm, R. J. *J. Neurophysiol.* **32**, 1044–1055 (1969).
5. Ebner, T. J. & Bloedel, J. R. *J. Neurophysiol.* **45**, 948–961 (1981).
6. Uusisaari, M. & Knöpfel, T. *Cerebellum* **10**, 637–646 (2011).
7. Thach, W. T. *J. Neurophysiol.* **31**, 785–797 (1968).
8. Armstrong, D. M. & Edgley, S. A. *J. Physiol.* **351**, 411–432 (1984).
9. McDevitt, C. J., Ebner, T. J. & Bloedel, J. R. *Brain Res.* **425**, 1–13 (1987).
10. Wise, A. K., Cerminara, N. L., Marple-Horvat, D. E. & Apps, R. J. *J. Physiol.* **588**, 2373–2390 (2010).
11. Heck, D. H., Thach, W. T. & Keating, J. G. *Proc. Natl Acad. Sci. USA* **104**, 7658–7663 (2007).

ASTRONOMY

A new class of planet

Three examples of a new family of planets, which orbit a pair of stars rather than a single one, have been discovered. The Milky Way may contain millions of these circumbinary planets. [SEE LETTER P.475](#)

JOHN SOUTHWORTH

Although more than 700 extrasolar planets have been detected, none was known to orbit more than one star until the recent discovery¹ of a circumbinary planet, which orbits a pair of stars. This concept was previously confined to theory — and to science fiction, for example the planet Tatooine in *Star Wars*. On page 475 of this issue, Welsh *et al.*² describe the discovery of two more such planets and provide insight into their frequency of occurrence. The previously discovered planet¹ and the new ones, each of which orbits its own system of two stars, were found using NASA's Kepler space telescope*.

For hundreds of years, scientists assumed that the Solar System is a typical example of a planetary system. That assumption was challenged in 1995 by the discovery³ of 51 Pegasi b, the first planet to orbit a normal star other than the Sun. Although this planet is probably a gas giant (the lower limit on its mass is 0.47 Jupiter masses), it orbits at only 0.052 astronomical units (AU) from its star (1 AU is the average distance between Earth and the Sun). This means that 51 Pegasi b is 100 times closer to its star than Jupiter is to the Sun.

Planet 51 Pegasi b was discovered through precise measurements of the velocity of its parent star, which revealed the motion induced in the star by the presence of the orbiting planet. This method has proved very successful for spotting planets, and can be credited with the discovery of roughly 400 so far. As observational programmes continue, they become sensitive to planets on wider orbits (longer orbital periods). The dominant population of extrasolar planets currently consists of objects that are more massive than Jupiter and are separated from their host stars by several astronomical units; many of these are in multi-planet systems.

The other very successful method for discovering planets is to look for those that periodically transit (eclipse) their parent star. These transiting planets are a gold mine of information: they are the only ones whose size can be obtained, by measuring the amount of starlight

*This article and the paper² under discussion were published online on 11 January 2012.

blocked during transit. This means that their surface gravities and mean densities can be calculated, ultimately allowing the investigation of their internal structure and formation process.

The transit method has led to the discovery of more than 200 planets, predominantly by teams that operate small wide-field robotic survey telescopes at observatories spread around the world, such as HATNet⁴ and SuperWASP⁵. These surveys are heavily biased towards large planets with small orbits. As a result, they are unparalleled sources of oddballs such as WASP-17 (ref. 6), the biggest and most rarefied planet known (up to twice the radius of Jupiter and only 6% as dense), and WASP-18 (ref. 7), which is ten times the mass of Jupiter and whirls around its host star every 23 hours (Jupiter's orbital period is 11.9 years).

The overriding aim of planetary research is to find one that might support life. Habitability most probably requires a rocky surface with liquid water, which, in turn, demands a planet no bigger than two Earth radii on an orbit with

a period of hundreds of days. The transits of such a body will not only be infrequent but will cause the light from the star to drop by a puny 0.01%. Such a signal is much too meagre to pick up with ground-based telescopes, which suffer from the blurring effect of Earth's atmosphere, as well as inevitable interruptions due to daylight and bad weather.

Finding a habitable planet requires a larger — and much more expensive — telescope outside Earth's atmosphere. Enter the Kepler spacecraft, the primary aim of which is to use the transit method to discover Earth-like planets. It monitors 150,000 stars in the constellations Cygnus and Lyra, and has already found more than 2,000 candidate transiting planets. Three of these have been confirmed to be circumbinary planets: Kepler-34 b (Fig. 1) and Kepler-35 b, which Welsh *et al.* describe in their study², and Kepler-16 b (ref. 1). Not only does each of these three planets transit both of its parent stars, but the stars themselves eclipse each other.

Although the discovery¹ of Kepler-16 b revealed that it was possible for such an object to exist, Welsh and colleagues' identification of two more circumbinary planets not only shows that such a planet is no freak object, but also allows an estimate of their prevalence to be made. The authors² find that, for short-period binary star systems, the frequency of occurrence of circumbinary planets is at least 1%. Taking into account the fraction of stars that are short-period binaries, this result implies that there are millions of such

planets distributed throughout the Galaxy. This analysis does not account for longer-period binary star systems, which are similarly plentiful in the Galaxy.

Some circumbinary planets may even be habitable, although the three known ones are not. Kepler-16 b is slightly too cold, and Kepler-34 b and Kepler-35 b are too hot. They also have extreme seasons because the light received from their parent stars changes not only during the stars' orbital periods (tens of days) and the planetary orbital period (hundreds of days), but also on much longer timescales through precession of the orbits due to three-body effects.

What common characteristics do these three planets have? The central binary systems have orbital separations of between 0.18 and 0.22 AU, and the planets orbit their hosts at distances of between 0.6 and 1.1 AU. They are thus all close to the smallest possible stable orbits, but the fact that such planets were the first to be found is at least partly an effect of the detection method. As Kepler continues to observe, it will become sensitive to planets on longer periods: these three systems may represent only the tip of the iceberg. ■

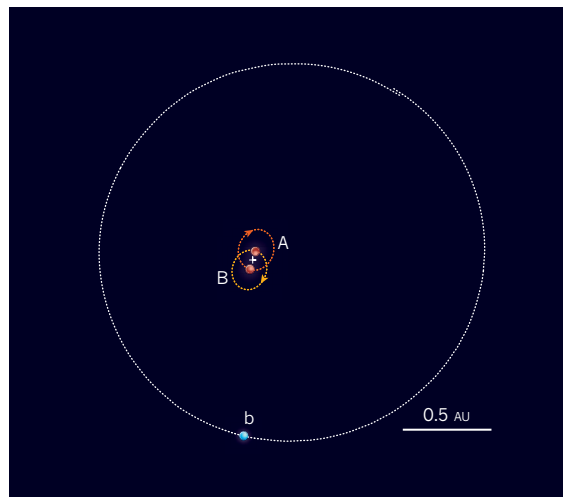


Figure 1 | Orbital configuration of the Kepler-34 system. The outer ellipse represents the orbital motion of the circumbinary planet Kepler-34 b, labelled b, around its host binary star system, which is composed of stars A and B in orbit around one another (as indicated by arrows). The plus sign shows the system's centre of mass. Spheres denote the orbital positions of the three bodies. One astronomical unit (AU) is the average distance between Earth and the Sun. Gravitational effects between the three bodies mean that this orbital configuration is gradually changing, so the bodies follow different paths on successive orbits. This is why the orbit of the planet shows a discontinuity in the upper part of the figure. Kepler-34 b is one of two circumbinary planets discovered by Welsh and colleagues². (Modified from ref. 2.)

John Southworth is in the *Astrophysics Group, Keele University, Newcastle-under-Lyme ST5 5BG, UK.*

e-mail: jkt@astro.keele.ac.uk

1. Doyle, L. R. *et al. Science* **333**, 1602–1606 (2011).
2. Welsh, W. F. *et al. Nature* **481**, 475–479 (2012).

3. Mayor, M. & Queloz, D. *Nature* **378**, 355–359 (1995).
4. Bakos, G. Á., Lázár, J., Papp, I., Sári, P. & Green, E. M. *Publ. Astron. Soc. Pacif.* **114**, 974–987 (2002).
5. Pollacco, D. L. *et al. Publ. Astron. Soc. Pacif.* **118**, 1407–1418 (2006).
6. Anderson, D. R. *et al. Astrophys. J.* **709**, 159–167 (2010).
7. Hellier, C. *et al. Nature* **460**, 1098–1100 (2009).

SOCIAL SCIENCE

Hunter–gatherer cooperation

A study of social networks in the hunter–gatherer Hadza people in Tanzania illuminates the evolutionary origins of humans’ unique style of cooperation in groups. [SEE LETTER P.497](#)

JOSEPH HENRICH

The social behaviour of humans poses a significant evolutionary puzzle. Influenced by ‘prosocial’ motivations, we routinely help our relatives and friends in ways big and small, from donating kidneys to sharing food. Perhaps most puzzlingly, and unlike other primates, we also help strangers and cooperate in large groups by, for example, giving blood, going to war, recycling and paying taxes. Yet human prosocial behaviour varies dramatically between groups — from societies with little cooperation beyond extended kin to the vast scales of cooperation found in many modern states^{1,2}.

Among the key challenges to understanding the origins of human cooperation are the difficult questions of what the social lives of our Palaeolithic ancestors were like, and how they shaped our psychology. Studying modern foraging populations who depend on tools and resources similar to those of our ancestors is one of the few means we have of glean-ing certain kinds of insight into the past³. On page 497 of this issue, Apicella *et al.*⁴ give us a glimpse into the social dynamics of one of the few remaining populations of nomadic hunter-gatherers, the Hadza of Tanzania (Fig. 1).

With its practical implications, human cooperation stands as a central question that spans the behavioural sciences. From an evolutionary perspective, the conundrum is how individuals sustain cooperation in the face of the ever-present forces of self-interest; in other words, how could natural selection favour actions that benefit others, or one’s group, but that also incur a personal cost? Theorists generally agree that the solution to this core dilemma requires assortative interaction, such that cooperators benefit other cooperators more than non-cooperators⁵. The challenge arises when one tries to delineate the processes that

sustain such assortative interactions against invasion by ‘free-riders’ — non-cooperators who siphon off collective benefits.

Through the 1970s and 1980s, many researchers assumed that hunter-gatherers tackle this core dilemma by relying on a combination of kinship and direct reciprocity. By targeting kin on the basis of shared genetic inheritance, cooperators are more likely to deliver benefits to fellow cooperators. Similarly, by reciprocating help with help, unrelated individuals can sustain tit-for-tat cooperation. However, by the twenty-first century it had become clear that although kinship and direct reciprocity can each explain some aspects of human prosociality, many domains

of cooperation, ranging from the sharing of meat within bands of hunter-gatherers to territorial defence, cannot be easily accounted for by these models¹.

To address this gap, researchers began to develop and apply new models. Gene–culture co-evolutionary models propose that, because social strategies are culturally learned, rapid cultural change tends to generate substantial variation in cooperation among groups while reducing variation within groups. In these models, cooperation is sustained by a process of cultural learning and the sanctioning of norm violators, which leads to the continuous reassortment of groups⁶. More cooperative groups tend to endure and expand, whereas less cooperative groups gradually break down. Another class of models, based on social selection, proposes that individuals cooperate competitively, as a means of attracting an inflow of partners who bring benefits⁷. A third approach proposes that cooperation can be sustained as individuals seek out those with different skills, resources or abilities. Here, assortment is based on complementarity rather than similarity⁸.

To illuminate how the Hadza tackle the core dilemma of cooperation, Apicella *et al.*⁴ gathered data on assortment and cooperative tendencies. The authors studied assortment within two social networks. To assemble the first (a campmate network), they asked adult Hadza from 17 different bands who they wanted to camp with when their next band formed. For the second network (a gift network), individuals received three honey sticks — Hadza love honey — and were asked to secretly specify who should get each stick. Finally, to measure cooperativeness, the researchers gave individuals from each band



Figure 1 | Helping hands. The Hadza people of Tanzania, such as these young men who are roasting birds they have caught, rely on hunting and gathering to obtain most of their food. By studying Hadza social networks, Apicella *et al.*⁴ illuminate the population dynamics that underpin the evolution of human cooperation.

PHOTOSTOCK-ISRAEL/ALAMY

four additional honey sticks, and told them that any stick that was contributed to a common pool for their band would be tripled and the sticks distributed equally among band members. The Hadza could anonymously contribute any number of these four sticks (from zero to four), thereby pitting self-interest against the common good. Cooperators contribute sticks to the pool whereas egotists contribute nothing and free-ride on others' contributions.

Let's begin by considering those models that are not supported by the authors' results. They find that Hadza do not preferentially pick more cooperative individuals as future campmates or stick-receivers. They also do not preferentially network with those possessing complementary attributes, at least as indicated by age, food preferences or various physical measures. Thus, these findings do not favour existing models based on social selection or complementarity.

On the positive side, the most striking findings emerge when the variation in cooperative behaviours is partitioned within and among the 17 Hadza bands. There is substantially more variation among the bands, and substantially less variation within them, than would be expected by chance. Despite the fluidity of band membership, it seems that some combination of similarity-based association, social learning and sanctioning establishes differences in cooperative tendencies among different bands. This pattern is particularly interesting in light of experiments⁹ showing that larger Hadza bands evince more fairness in anonymous interactions. Consistent with this, Apicella and co-workers' data from both the campmate and gift networks suggest that high contributors associate with other high contributors, and low contributors choose other low contributors. In fact, the gift-network results indicate that this extends to friends of friends: if your friend's friend is highly cooperative, you are likely to cooperate more, too.

As is the case in other primates¹⁰, Apicella *et al.* also found that kinship and reciprocity contribute to assortment in Hadza social networks. No surprises there.

The crucial insight from this work⁴ is that understanding distinct aspects of cooperation among these hunter-gatherers must incorporate an analysis of the dynamic processes at the population level that influence association, cultural transmission and band formation, instead of focusing tightly on purely individual actions within bands — the emphasis of much previous work. ■

Joseph Henrich is in the Departments of Psychology and of Economics, University of British Columbia, Vancouver V6 1V9, Canada.

e-mail: henrich@psych.ubc.ca

1. Henrich, N. & Henrich, J. *Why Humans Cooperate: A Cultural and Evolutionary Explanation* (Oxford Univ. Press, 2007).

2. Silk, J. B. *et al.* *Nature* **437**, 1357–1359 (2005).
3. Marlowe, F. W. *Evol. Anthropol.* **14**, 54–67 (2005).
4. Apicella, C. L., Marlowe, F. W., Fowler, J. H. & Christakis, N. A. *Nature* **481**, 497–501 (2012).
5. Hamilton, W. D. in *Biosocial Anthropology* (ed. Fox, R.) 133–156 (Malaby, 1975).
6. Boyd, R., Richerson, P. J. & Henrich, J. *Behav. Ecol. Sociobiol.* **65**, 431–444 (2011).

7. McNamara, J. M., Barta, Z., Fromhage, L. & Houston, A. I. *Nature* **451**, 189–192 (2008).
8. Tooby, J. & Cosmides, L. *Proc. Br. Acad.* **88**, 119–143 (1996).
9. Marlowe, F. W. in *Foundations of Human Sociality* (eds Henrich, J. *et al.*) 168–193 (Oxford Univ. Press, 2004).
10. Silk, J. B. *et al.* *Behav. Ecol. Sociobiol.* **61**, 197–204 (2010).

NANOTECHNOLOGY

Shape matters

The ligand-mediated binding of colloid particles to each other is more effective if the particles are flat rather than curved. This finding opens up opportunities for the design of self-assembling materials.

SHARON C. GLOTZER

From the invention of the wheel to the stacking of cannonballs and the design of stealth aircraft, humans have long known that shape matters. On a much smaller scale, the shapes of molecules affect their ability to form crystals, and enzyme shape is central to the binding of their substrates. Writing in the *Journal of the American Chemical Society*, Mirkin and colleagues¹ report a way in which shape can also affect the binding forces that hold nanometre-scale particles together — a discovery that suggests new approaches for constructing potentially useful architectures from these tiny building blocks.

Metallic and semiconductor nanoparticles grow as tiny crystals from solutions of precursor ions. Facets arise naturally from the anisotropic (directionally dependent) growth of the nanocrystals, producing particles that have a range of convex and concave shapes. These nanocrystals can be stabilized by coating them with small organic ligand molecules, or modified by the attachment of larger molecules such as DNA. Ligand coatings can conspire with the atoms in nanoparticles to produce net inter-particle forces (either attractive or repulsive) through van der Waals, hydrophobic and electrostatic interactions. DNA modification can also confer specificity on inter-particle forces — particles to which single-stranded

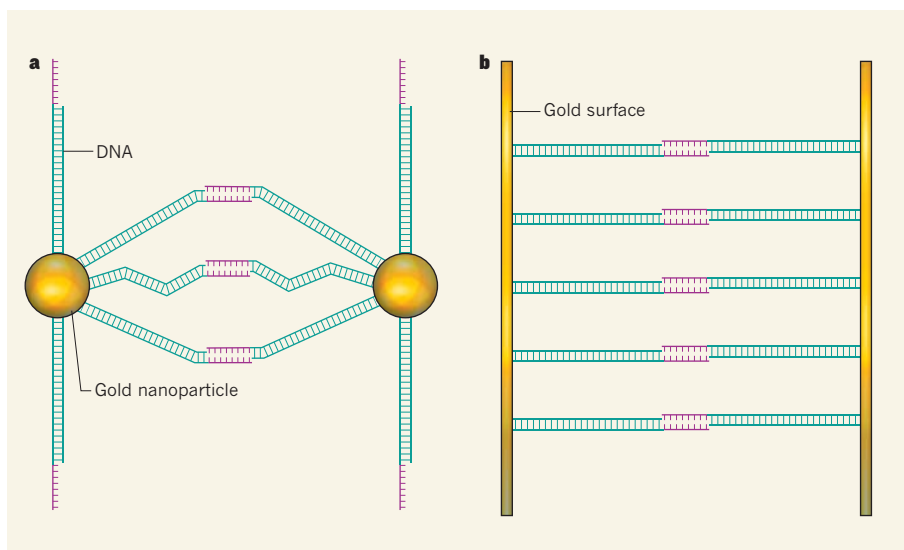


Figure 1 | DNA-mediated binding of nanoparticles. Mirkin and colleagues¹ prepared nanoscale gold particles of different shapes to which DNA molecules were attached. Although the main bodies of these molecules were duplexes (turquoise), the free ends of the DNA were single-stranded 'sticky ends' (pink). These could bind the particles together by forming duplexes with complementary sticky ends on other particles. The authors observed that particles with flat surfaces bound to each other more strongly than did spherical nanoparticles. This effect depends on how easily the sticky ends on different particles can approach each other. **a**, On spherical particles, relatively few sticky ends can come together to form duplexes, and the DNA molecules need to bend to allow duplex formation. **b**, When attached to flat surfaces, the DNA molecules can align so that more sticky ends form duplexes, without any bending.

DNA is attached bind only to other particles that have complementary DNA sequences appended, because of the resulting DNA duplex formation.

Depending on their interactions, anisotropically shaped nanoparticles can serve as building blocks for self-assembled materials suitable for many applications, including solar cells, computer chips and even camouflage. There are various recent examples of nanoparticles whose anisotropic shape controls the structures that assemble from them: octopods², cuboctahedra (shapes formed by cutting the corners off a cube to create a polyhedron that has only squares and triangles for faces) and related polyhedra³, and rounded squares and cubes^{4–6}, to name just a few.

Mirkin and co-workers¹ now add to our knowledge of the shape dependence of nanoparticle self-assembly. They made triangular gold nanoprisms — essentially, two-dimensional triangular objects — whose faces were modified with a layer of single-stranded DNA. When the authors combined these nanoprisms with others bearing complementary DNA, the particles ‘hybridized’ quickly and strongly with their counterparts. The researchers observed that particle–particle binding was several million times stronger, and happened 100 times faster, than in the case of similarly modified gold nanospheres.

The reason the triangular-shaped particles bind so much better to each other than do the spheres is just what one might expect. Mirkin and colleagues found that the large, flat faces of triangles align to allow many more DNA–DNA binding interactions than are possible for the curved surfaces of the spheres (Fig. 1). Additionally, the authors observed that the binding affinity of each DNA molecule for its complementary strand seems to be higher for the flat particles than for the round ones, so that greater numbers of duplex linkers can form per unit area. Finally, they found that flat surfaces allow many complementary DNAs to form duplexes without first having to bend; such bending is necessary for the binding of multiple ligands of similar length attached to two curved surfaces. It is remarkable that simple geometrical principles are at play even on such small length scales.

Intuitively, plate-like particles of any shape should be just as effective as triangles in maximizing the available interaction area for the ligands. In fact, any particles that have flat facets should bind together more easily using ligands than do spheres. And it is not just ligands such as DNA — which bind to each other through a precise combination of interactions — that should be able to maximize ligand–ligand interactions, and thus particle–particle interactions, when attached to flat surfaces. Ligands of any sort that attract each other should similarly benefit.

Mirkin and co-workers demonstrated this generality using ligands that terminate in

carboxylic acid groups (COOH) in place of DNA. In this case, hydrogen bonds between the acid groups allow particle–particle association. The authors again observed that inter-particle attraction was considerably stronger for triangular gold particles than for spherical ones. Faceted particles could thus offer a new way of making ‘patchy’ particles⁷, which contain interaction sites in patches at prescribed locations. By varying the patterns of the patches, the self-assembly of such particles can be controlled to make particular structures.

Shape is also beginning to be used to control depletion interactions, which occur when entropy effects cause small particles or polymers to be excluded from the spaces between larger colloid particles. This exclusion increases the osmotic pressure outside — and so provides an effective attraction between — the larger particles. Micrometre-scale discs stack up⁸ readily into columns when mixed with nanometre-scale micelles in water, demonstrating that the discs bind more strongly face to face through depletion, rather than edge to edge or edge to face. Similar principles have been used for the assembly of nanoscale octahedra³. The idea of matching the shapes of colloid particles to maximize the strength of depletion interactions between them has also been applied to particles that have curved surfaces, allowing the preparation of Pac-Man-shaped particles that specifically bind smaller spheres in their dimple-shaped ‘mouths’⁹.

Shape and the alignment of facets are crucial factors in particle assembly, even when the only interactions between particles are those that prevent them from overlapping. For example, computer simulations have shown that hard, regular tetrahedrons¹⁰ and triangular bipyramids¹¹ each self-assemble into quasicrystals (aperiodic crystals) once the fraction of space occupied by the particles within a given volume exceeds roughly one-half.

The thermodynamically stable assemblies of truncated tetrahedra — a series of polyhedra formed when the four tips of a tetrahedron are progressively truncated until an octahedron is produced — are also dramatically influenced by the precise shape of the objects¹². The resulting crystals can be quasicrystalline, or can have a similar structure to the atomic structures of diamond, of the metallic form of tin (β -tin) or of high-pressure lithium. They can also form what are known as body-centred cubic crystals. Taken together, these assemblies represent the most complex and diverse set of structures ever predicted to form from hard shapes.

In contrast to the alignment of nanoprisms discovered by Mirkin and colleagues¹, which is driven by the minimization of potential energy, the faces of hard polyhedra align to maximize entropy. This results in entropically ‘sticky’ patches that effectively provide attraction between particles without the need for ligand binding. Such behaviour is

possible only when the particles are confined to a fixed volume or pressure, but it serves as another recently discovered example of how shape matters.

In fields ranging from biology to engineering, the importance of shape has long been appreciated, but not always fully understood. Through work such as that of Mirkin and co-workers, we are starting to get a sense of how shape affects objects on the nanoscale — and so a glimpse of the shapes of things to come. ■

Sharon C. Glotzer is in the Departments of Chemical Engineering and of Materials Science and Engineering, University of Michigan, Ann Arbor, Michigan 48109, USA. e-mail: sglotzer@umich.edu

1. Jones, M. R., Macfarlane, R. J., Prigodich, A. E., Patel, P. C. & Mirkin, C. A. *J. Am. Chem. Soc.* **133**, 18865–18869 (2011).
2. Misztal, K. *et al. Nature Mater.* **10**, 872–876 (2011).
3. Henzie, J. *et al. Nature Mater.* <http://dx.doi.org/10.1038/nmat3178> (2011).
4. Zhao, K., Bruinsma, R. & Mason, T. G. *Proc. Natl*

- Acad. Sci. USA* **108**, 2684–2687 (2011).
5. Rossi, L. *et al. Soft Matter* **7**, 4139–4142 (2011).
6. Zhang, Y., Lu, F., van der Lelie, D. & Gang, O. *Phys. Rev. Lett.* **107**, 135701 (2011).
7. Zhang, Z. & Glotzer, S. C. *Nano Lett.* **4**, 1407–1413 (2004).
8. Mason, T. G. *Phys. Rev. E* **66**, 060402 (2002).
9. Sacanna, S., Irvine, W. T. M., Chaikin, P. M. & Pine, D. J. *Nature* **464**, 575–578 (2010).
10. Haji-Akbari, A. *et al. Nature* **462**, 773–777 (2009).
11. Haji-Akbari, A., Engel, M. & Glotzer, S. C. *Phys. Rev. Lett.* **107**, 215702 (2011).
12. Damasceno, P. F., Engel, M. & Glotzer, S. C. *ACS Nano* <http://dx.doi.org/10.1021/nn204012y> (2011).

LASER SCIENCE

Even harder X-rays

With the laser just over half a century old, another dream of the pioneers of this light source has been fulfilled. An atomic X-ray laser with unprecedentedly high photon energy has been demonstrated. [SEE LETTER P.488](#)

JON MARANGOS

Writing in this issue, Rohringer *et al.*¹ report the first demonstration of atomic X-ray lasing at a photon energy of 849 electronvolts. The X-ray laser emission in this case is based on atomic population inversion, which arises when more members of an ensemble of atoms exist in a higher-energy state than in lower-energy states. Rohringer and colleagues created population inversion in a sample of neon gas using a device known as an X-ray free-electron laser, operating at 960 eV. Although its photon energy falls in the ‘soft’ X-ray part of the electromagnetic spectrum, the authors’ X-ray source paves the way to making practical

atomic lasers in the ‘hard’ X-ray regime (energies beyond 5 keV).

The X-ray free-electron laser (FEL) used by Rohringer and colleagues was the Linac Coherent Light Source (LCLS) at the SLAC National Accelerator Laboratory in Menlo Park, California. The LCLS, which is based on self-amplified spontaneous X-ray emission from a high-quality, high-energy (up to 14 GeV) electron beam, was essential for creating the population inversion; that is, for ‘pumping’ the new atomic X-ray laser.

But doesn’t the need to use an X-ray FEL somewhat undermine the authors’ new laser demonstration? Yes and no. The LCLS has already generated² laser-like X-rays of unprecedented brightness — having a photon energy

that can be tuned from 500 eV to more than 8 keV in pulses lasting 5–80 femtoseconds (1 femtosecond is 10^{-15} s) and containing up to 10^{13} photons. The LCLS has enabled the first laboratory studies^{3,4} of matter exposed to intense keV-energy X-rays, and has been used to image single nanocrystals⁵ and viruses⁶. Nevertheless, like any FEL based on self-amplified spontaneous X-ray emission, the LCLS has inherent limitations in the quality of its output radiation. These limitations are principally due to the stochastic nature of the process, which leads to poor temporal coherence (meaning that the waves comprising the X-ray field are not well synchronized) and strong spectral and temporal jitter from sequential laser pulses.

It has long been common practice to use one type of visible-light laser to provide the energy for pumping the population inversion needed to operate another laser that has different optical properties. For example, nanosecond visible lasers are regularly used to pump femtosecond visible lasers. In their study (page 488), Rohringer *et al.* extend this idea to the X-ray region of the spectrum. Earlier X-ray lasers operating at lower photon energies, from 20 to 300 eV (ref. 7), have been pumped by physical processes, such as electron

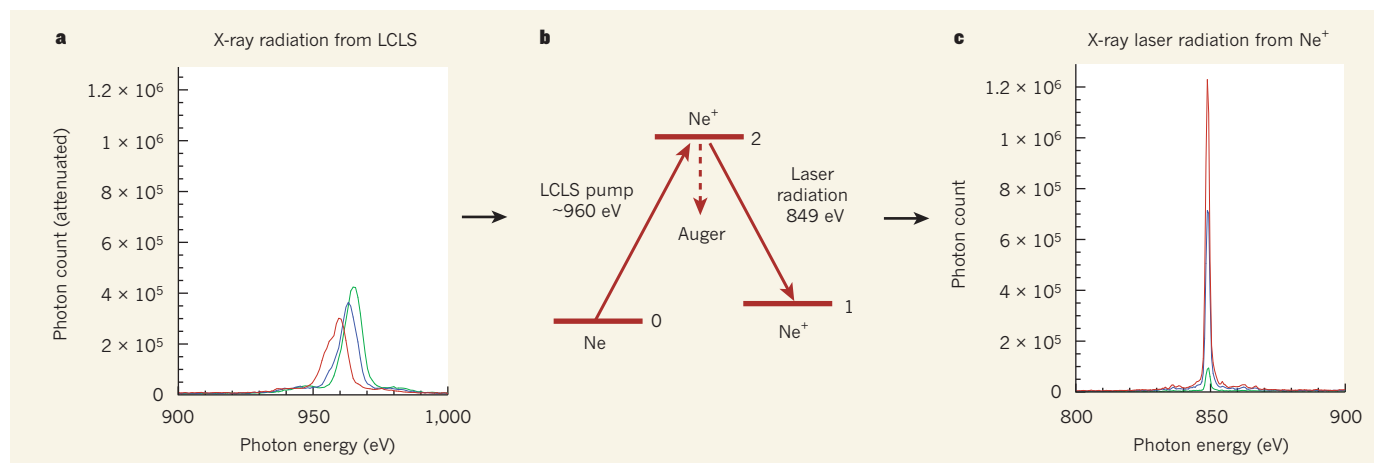


Figure 1 | Atomic X-ray lasing. Rohringer *et al.*¹ have demonstrated X-ray lasing at a photon energy of 849 electronvolts by creating atomic population inversion in a sample of neon gas using the Linac Coherent Light Source (LCLS), which is an X-ray free-electron laser. **a**, The LCLS X-ray radiation has a large spread in photon energy and considerable fluctuation in the average photon energy (about 960 eV) obtained from sequential laser pulses (shown in different colours). Photon count is measured after transmission through

the neon sample and is strongly attenuated. **b**, The LCLS ‘pumps’ many of the neon atoms from the ground state (state 0) into a higher-energy state of ionized neon (state 2). Most of the ions in this excited state decay through an Auger process, but some will make the radiative transition to a state (state 1) that has a lower energy than state 2. This transition is accompanied by the emission of laser radiation that has a precise average photon energy (849 eV). **c**, The laser radiation has a smaller energy spread than that of the LCLS.

collision, recombination or photoionization, in plasma media that are created by either electrical discharges or high-intensity visible lasers. These laser systems are limited because the energy density needed to pump population inversion scales as the cube of the laser photon energy. Therefore, a very high energy density is required to reach the harder X-ray range. Indeed, population-inversion hard X-ray lasers pumped by the extremely high energy density produced in thermonuclear explosions were the target of the Excalibur national-defence project at the Lawrence Livermore National Laboratory in the 1980s⁸. But these X-ray sources are of rather restricted general application.

In their experiment, Rohringer and colleagues focused LCLS X-ray pulses each containing more than 10^{12} 960-eV photons and lasting just 40 fs into a beam a few micrometres across that impinged on a dense sample of neon atoms. This produced the energy density required to pump many of the atoms from the ground state (state 0) into a higher-energy state of ionized neon (state 2) and attain population inversion. Most of the ions in the excited state decay by a mechanism known as an Auger process on a timescale of about 2.7 fs. But some of them make the radiative transition to a state (state 1) that has a lower energy than state 2. Because the applied LCLS X-ray radiation leads to the sudden creation of a large population of neon ions in state 2 and an equally rapid depletion of state 1, there is a transient population inversion between 2 and 1 that leads to lasing (Fig. 1).

The most important property of the authors' laser is that the emitted X-ray pulses have a precise central energy that has a spread of less than 1 eV and that is tied to the atomic properties of the neon ions. These properties are a result of the rules of quantum mechanics and so do not vary from pulse to pulse. By contrast, the energy spread of the LCLS X-ray pulses that impinge on and are transmitted through the neon gas is 8 eV on any given pulse, and nearer to 15 eV when averaged over many pulses (Fig. 1). The authors' modelling of the process suggests that the energy spread is consistent with the physical limit set by the short duration (about 5 fs) of the pulses emitted from the neon sample. The smaller energy spread of the emitted X-rays means that the temporal coherence of the 849-eV X-rays is more than tenfold greater than that of the LCLS pulses.

Although Rohringer and colleagues' X-ray laser has a lower output power than that of LCLS radiation, the greatly improved coherence and reduced energy spread will open new areas of research that demand a well-defined X-ray energy. Examples of these areas include the study of physical processes such as photoionization and inelastic X-ray scattering, which can be used to study ultra-fast changes in matter. Moreover, the authors' X-ray laser

pulses and the LCLS pulses are closely synchronized and so can be used in experiments in which two X-ray fields of differing photon energy are required to interact simultaneously with a sample.

Not only does the authors' X-ray-FEL-pumped scheme operate at a much higher photon energy than achieved by other approaches to producing X-ray lasers based on population inversion, but also the repetition rate (the rate at which X-ray pulses are produced) is as high as that of the FEL used. The LCLS has a repetition rate of up to 120 hertz, which is more than 100-fold higher than that of any previous X-ray laser. Although the new laser is more difficult

to operate than the LCLS, its photon-energy range, stability and repetition rate make it of considerable potential utility in time-resolved structural studies of matter. ■

Jon Marangos is in the *Blackett Laboratory, Imperial College London, London SW7 2AZ, UK.* e-mail: j.marangos@imperial.ac.uk

1. Rohringer, N. *et al. Nature* **481**, 488–491 (2012).
2. Emma, P. *et al. Nature Photon.* **4**, 641–647 (2010).
3. Marangos, J. P. *Contemp. Phys.* **52**, 551–569 (2011).
4. Young, L. *et al. Nature* **466**, 56–61 (2010).
5. Chapman, H. N. *et al. Nature* **470**, 73–77 (2011).
6. Seibert, M. M. *et al. Nature* **470**, 78–81 (2011).
7. Elton, R. C. *X-ray Lasers* (Academic, 1990).
8. Ritson, D. M. *Nature* **328**, 487–490 (1987).

STEM CELLS

The right neighbour

Different cell types produce signals that regulate the activity of blood-forming stem cells. A study shows that certain rare mesenchymal cells surrounding blood vessels are the main source of one such signal in mice. SEE ARTICLE P.457

ILYA A. SHESTOPALOV & LEONARD I. ZON

Coping with a lifetime of tissue function, injury and disease requires replenishment of the cells that make up organs. Replacement cells originate from adult-tissue stem cells such as haematopoietic stem cells, which continually form all types of blood cell. The growth and activity of tissue stem cells is regulated by neighbouring cells that comprise the stem-cell niche — a microenvironment containing regulatory signalling molecules. Identifying, controlling and mimicking the niche signals represent challenges for the emerging field of regenerative medicine. On page 457 of this issue, Ding *et al.*¹ identify the cells that produce a signal called stem-cell factor, which is essential for the generation of new blood cells from haematopoietic stem cells in embryonic and adult mice.

The bone-marrow niche contains small blood vessels called sinusoids (Fig. 1) made up of endothelial cells together with a variety of immune cell and the axonal processes of peripheral neurons². The rest of the bone marrow is filled with mesenchymal cells of various functions. For example, some (the stromal cells) provide connective tissue, others (osteoblasts) replenish or remodel the inner bone surface. Unlike the majority of stromal cells, a rare subset that originates from the neural-crest tissue of the embryo expresses the protein nestin and influences the function of haematopoietic stem cells (HSCs)³.

To understand the niche microenvironment, it is necessary to identify the cell types that provide the regulatory signals and to establish which signals each produces. For example,

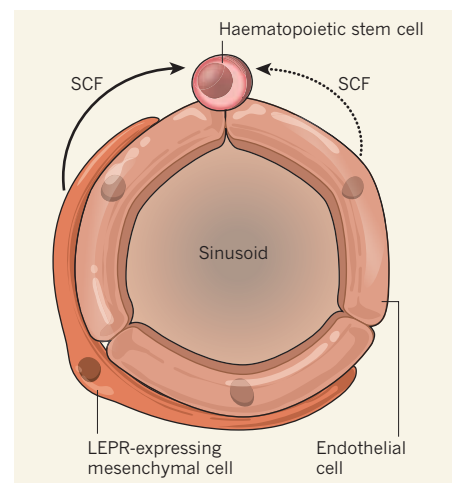


Figure 1 | A home for blood-forming cells. Haematopoietic stem cells (HSCs) generate all types of blood cell. In mammals, they reside in the bone marrow, where blood vessels made of endothelial cells form microscopic cavities called sinusoids. Endothelial cells are surrounded by connective tissue composed of different mesenchymal cells, which can produce molecular signals that control HSC growth. Ding *et al.*¹ find that in mouse bone marrow, the molecular signal stem-cell factor (SCF), which is required to sustain HSCs, is primarily produced by a type of mesenchymal cell that expresses the leptin receptor (LEPR). Endothelial cells also contribute some SCF.

stem-cell factor (SCF)⁴ is secreted by endothelial cells, osteoblasts and nestin-expressing stromal cells^{3,5,6}. Although previous research⁷ has shown that depletion of many cell types in the bone-marrow niche produces measurable effects on HSCs, the causality of the observed

TECHNOLOGY

A deeper peek into living organisms

In two papers in this issue, Lechene and colleagues^{1,2} report the first use of an approach called multi-isotope imaging mass spectrometry (MIMS) in living organisms (see pages 516 and 520). This technique has outstanding resolution: it provides data in the sub-micrometre range, allowing analysis of structures as small as cellular regions.

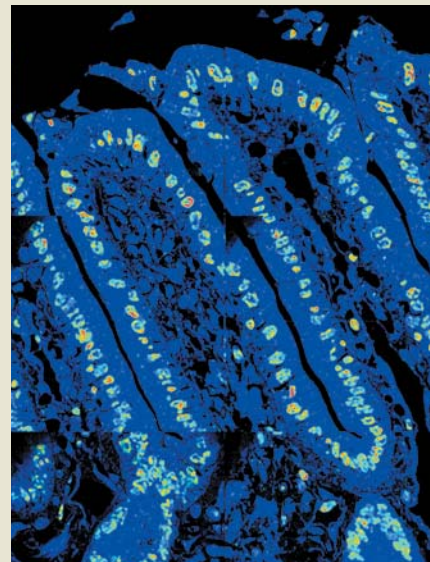
MIMS involves labelling living tissues with stable isotopes. The isolated sample surface is then bombarded with a beam of ions, and the ejected 'secondary' ions are measured with a mass spectrometer to determine the sample's molecular composition. The technique can distinguish between ions of very similar mass, providing a precise measurement of isotope labels, which can be imaged simultaneously.

Lechene and co-workers used MIMS to test the immortal-strand hypothesis, which proposes that asymmetrically dividing stem cells also segregate their DNA asymmetrically. That is, the daughter cells that will remain stem cells retain the older DNA template, whereas those that are committed to differentiation inherit newly synthesized DNA strands. The authors

disprove this proposal, showing that DNA strands segregate randomly in proliferating crypt cells of the mouse small intestine (pictured). This finding should further our understanding of tissue homeostasis.

The researchers also analysed protein turnover in the mechanosensory hair cells in the inner ear of frogs and mice. During most vertebrates' lifetime, hair cells are not replaced, but their degraded proteins are. One kind of structure within these cells is the stereocilia, each of which is made up of hundreds of filaments of the protein actin. Lechene and collaborators quantified actin turnover in both adult and neonatal hair cells and report that, with the exception of the filaments' tips, this protein's turnover is particularly slow throughout stereocilia. This observation differs from previous findings³ that stereocilium actin has a rapid turnover time. According to Lechene and co-authors, this discrepancy may be due to differences in experimental conditions between the two studies.

The team also demonstrates successful use of MIMS for human studies. They thus not only further prove the broad applicability of their technique, but also



open the door to its use for investigations of metabolism and cell-lineage tracking in humans. **Francesca Cesari and Deepa Nath**

1. Steinhäuser, M. L. *et al.* *Nature* **481**, 516–519 (2012).
2. Zhang, D.-S. *et al.* *Nature* **481**, 520–524 (2012).
3. Rządzińska, A. K. *et al.* *J. Cell Biol.* **164**, 887–897 (2004).

changes has been difficult to ascertain.

To establish the relative importance of the various SCF-producing cells in HSC growth, Ding *et al.*¹ developed a mouse model in which the *Scf* gene could be replaced with a gene encoding green fluorescent protein, in all or in selected cell types, at different times during the animal's life. In this way, cells that would normally express *Scf* became fluorescent instead. Using this mouse model, Ding *et al.* found that, when they abolished SCF production in all cell types, HSCs disappeared from the bone marrow. The authors then removed *Scf* from specific cell types in the HSC niche, and found that loss of *Scf* from blood cells, osteoblasts and nestin-expressing mesenchymal cells did not alter HSC abundance in the bone marrow. Mice with *Scf*-lacking endothelial cells, however, had fewer HSCs during embryonic development, and only some HSCs remained in these mice during adulthood.

The researchers went on to identify a type of mesenchymal cell that surrounds sinusoids in adult bone marrow and that, in contrast to other niche cells, expresses the gene *Lepr*, which encodes the leptin receptor. The LEPR protein regulates fat metabolism in some cell types, but its function in bone-marrow mesenchymal cells is unknown. Ding *et al.* observed that loss of SCF from *Lepr*-expressing mesenchymal cells

reduced HSC abundance in adult mice. Moreover, when the authors deleted the *Scf* gene from both endothelial and *Lepr*-expressing cells, nearly all HSCs disappeared from adult mice. These results indicate that, in the bone marrow of adult mice, SCF comes primarily from *Lepr*-expressing mesenchymal cells that envelop sinusoids, with a smaller contribution of SCF expression from sinusoid endothelial cells.

Future studies are needed to characterize the functions of the *Lepr*-expressing mesenchymal cells in the HSC niche. According to Ding and colleagues' gene-expression data¹, these cells produce another HSC-regulating signal, stromal-cell-derived factor 1 (SDF1), along with the enzyme alkaline phosphatase, which makes them similar to previously described mesenchymal cells that also surround blood vessels in the bone marrow⁸. But the *Lepr*-expressing cells do not produce nestin, which underscores the diversity among mesenchymal stromal cells. Because several genetic tools are available to control gene expression of specific cells in mice, a next logical step should be determining whether *Lepr*-expressing mesenchymal cells are one of the main sources of other HSC-regulating signals.

Different vertebrates have HSC niches in different tissues, and the location of the HSC niche can change during an organism's

lifetime⁹. In mammals, HSCs are found first in the aorta, then in the liver and, finally, in the bone marrow. In fish, HSCs also start out in the aorta, but then go on to occupy tissue in the tail and, eventually, the kidneys. All of these seemingly unrelated vertebrate tissues have vascular endothelial cells surrounded by mesenchymal cells, which — as Ding *et al.*¹ now highlight — are required for regulating HSCs in mice. It remains unclear, however, whether different tissue-specific cell types that make up the bone marrow, liver and kidneys provide similar signals to regulate HSC activity.

At present, clinically useful HSCs cannot be efficiently cultured in the lab. The presence of mesenchymal cells in HSC cultures has occasionally been linked to enhanced HSC growth¹⁰, but which mesenchymal cell types are responsible for this effect has been difficult to determine. Robust HSC growth could perhaps be achieved by culturing them on top of mesenchymal 'feeder' cells that express specific markers such as LEPR or nestin. According to Ding and colleagues' results¹, only one in 8,000 bone-marrow cells expresses LEPR, yet these rare cells are the primary source of the SCF needed to support HSCs. Unfortunately, culturing LEPR- or nestin-expressing cells is not an easy task, so more robust conditions should be developed to culture such cells.

The approach used by Ding *et al.*¹ to identify the main sources of SCF in the haematopoietic niche, although labour-intensive, sets a standard of rigour for researchers studying the bone marrow, and should also be applied to other signals that affect HSCs. Analysis of the gene-expression signatures of specific cells that express other major signalling molecules involved in HSC regulation may allow the identification of marker genes in addition to *Lepr*. These marker genes could be used to isolate cells that support HSC growth from the mesenchymal milieu of the bone marrow. Understanding the complex HSC niche will one day make it possible to create a synthetic microenvironment capable of sustaining long-term HSC growth. ■

Ilya A. Shestopalov and Leonard I. Zon
are in the Stem Cell Program and Division of

Hematology/Oncology, Children's Hospital
Boston, Boston, Massachusetts 02115, USA.
e-mails: ishestopalov@enders.tch.harvard.edu;
zon@enders.tch.harvard.edu

1. Ding, L., Saunders, T. L., Enikolopov, G. & Morrison, S. J. *Nature* **481**, 457–462 (2012).
2. Yamazaki, S. *et al.* *Cell* **147**, 1146–1158 (2011).
3. Méndez-Ferrer, S. *et al.* *Nature* **466**, 829–834 (2010).
4. McCarthy, K. F., Ledney, G. D. & Mitchell, R. *Cell Tissue Kinet.* **10**, 121–126 (1977).
5. Aye, M. T. *et al.* *Exp. Hematol.* **20**, 523–527 (1992).
6. Bilbe, G., Roberts, E., Birch, M. & Evans, D. B. *Bone* **19**, 437–445 (1996).
7. Mercier, F. E., Ragu, C. & Scadden, D. T. *Nature Rev. Immunol.* **12**, 49–60 (2012).
8. Omatsu, Y. *et al.* *Immunity* **33**, 387–399 (2010).
9. Orkin, S. H. & Zon, L. I. *Cell* **132**, 631–644 (2008).
10. Weisel, K. C., Gao, Y., Shieh, J. H. & Moore, M. A. *Exp. Hematol.* **34**, 1505–1516 (2006).

L.I.Z. declares competing financial interests.
See go.nature.com/lrttdji for details.

DRUG DISCOVERY

Chemical beauty contest

Most drug candidates fail clinical trials, in many cases because the compounds have less than optimal physico-chemical properties. A new method for assessing the 'drug-likeness' of compounds might help to remedy the situation.

PAUL LEESON

Experienced medicinal chemists develop a sense of chemical aesthetics — a feel for how drug-like any particular molecule is. But is it possible to measure such chemical beauty? Reporting this week in *Nature Chemistry*, Hopkins and colleagues¹ provide a quantitative estimate of drug-likeness that assesses a combination of a molecule's physical properties. Unlike the commonly used descriptions of drug-likeness, their approach allows a single, continuous scale to be defined, so that molecules can be ranked in order of desirability.

Drugs are developed from the optimization of 'lead' molecules, which are frequently found through the biological screening of compound collections. Before being finally accepted into use by regulatory and paying bodies, an optimized drug candidate must undergo years of intensive toxicological and clinical-efficacy studies. Most orally active drugs that survive these arduous developmental pressures have a set of physico-chemical properties that fall within a certain range of values — they are said to lie in a defined physical and chemical 'drug-like space'^{2–5}. Until now, this drug-like space has been defined using cut-off values for permissible physical properties, perhaps most notably the values defined by the medicinal chemist Christopher Lipinski and his colleagues in the 'rule of five'² (Box 1).

Hopkins and co-workers¹ point out that Lipinski's rule can be misleading, because undesirable compounds could pass the drug-likeness test by only just meeting all four cut-off criteria, whereas better compounds could fail because they just miss one of the cut-offs. The application of the rule in this unintended way may help to explain why the compounds in current patents from pharmaceutical companies are, on average, significantly less drug-like than marketed drugs^{6–8}.

Taking a cue from a study⁹ that used mathematical 'desirability functions' to assess how suitable a range of compounds would be as drugs that act in the central nervous system, Hopkins and co-workers¹ used a similar approach to analyse the drug-likeness of a set of 771 oral drugs approved by the US Food and Drug Administration. The authors defined desirability functions for eight physical properties proposed to be important for oral drugs, including the four Lipinski properties. They also took into account the number of aromatic rings and rotatable bonds in a molecule, the polar surface area (a measure of how hydrophilic a molecule is) and the number of groups in the molecule known to cause toxicity. The functions captured the full distribution of each physical property and provided a continuous quantitative estimate of drug-likeness (QED) on a scale from most to least drug-like.

Because the bulk physical properties of compounds are known to correlate with each other



50 Years Ago

It is the purpose of this article to show that a group of compounds related to lysergic acid diethylamide (LSD-25) produces surfacing behaviour of carp with the movement directed towards the surface ... It has been shown previously from work in this laboratory that very small quantities of derivatives of lysergic acid, like lysergic acid diethylamide (LSD-25) and lysergic acid ethylamide (LAE-32), have a surfacing effect on small Siamese fighting fish ... After the fish had been exposed to LSD-25 for 10 min., they showed signs of LSD-25 activity. After 30 min. all three fish in the tank containing LSD-25 were at the surface of the liquid in a nose up—tail down position ... For the next hour the fish in the tank containing LSD-25 remained at the surface, from time to time moving and even swimming backwards ... The fish were returned to the running-water pool after 1.5 hr. In the pool they continued to stay at the surface, moving about but not going to the bottom at all. 2 hr. later they were still at the surface ... Experiments in larger tanks, and field trials, are planned.

From *Nature* 27 January 1962

100 Years Ago

I have repeatedly observed the brilliancy of cats' eyes in the dark in particularly favourable circumstances. I have a brilliant incandescent light in my hall, and several cats on the premises. The entrance drive is in a line with the door and the hall lamp. When I call a cat in the chances are that if there she simply sits and looks at me, presenting the spectacle of two small incandescent lights glowing out of the darkness. Light, observer, and cat are all three in line, as observed by Colonel Herschel.

From *Nature* 25 January 1912

to some extent, Hopkins and colleagues used different property weightings to maximize the overall information content of the combined QED values for each drug. This weighting system will be controversial to some, because it may not reflect the importance of each property to drug-likeness. For example, there is a strong case to be made for lipophilicity as the dominant drug-like property, because it is important for a molecule's absorption, metabolism, promiscuity (binding to unwanted targets), toxicity and survival in the drug-development pipeline^{3,4,6,7}. Nevertheless, the benefits of the authors' strategy are clear: their method not only computes drug-likeness on a single quantitative scale, but, more importantly, it reveals that drugs that fail the Lipinski criteria have distributions of drug-likeness that overlap with drugs that pass the criteria (Fig. 1).

Hopkins and colleagues went on to show that their QED approach is better at differentiating drugs from non-drugs than the Lipinski rule and other schemes based on cut-off values. They further validated the discriminatory power of their method by comparing QED scoring with the results of a study¹ in which 79 medicinal chemists decided which of 17,117 molecules were attractive starting points for optimization as drugs, on the basis of only visual inspection of the molecular structures. Impressively, the QED scores for molecules considered to be attractive by the chemists were significantly higher than those for molecules considered unattractive. This suggests that the QED method may, at least in part, capture a sense of the chemical aesthetics that medicinal chemists develop through knowledge, experience and intuition¹⁰.

Finally, Hopkins and co-workers used their method to predict the drug-likeness of 167,045 ligand compounds that bind to 1,729 proteins (on the basis of binding information from ChEMBL, a database of biologically active compounds¹¹). This allowed them to

BOX 1

The Lipinski rule of five

The medicinal chemist Christopher Lipinski and his colleagues analysed² the physico-chemical properties of more than 2,000 drugs and candidate drugs in clinical trials, and concluded that a compound is more likely to be membrane permeable and easily absorbed by the body if it matches the following criteria:

- Its molecular weight is less than 500.
- The compound's lipophilicity, expressed as a quantity known as log P (the logarithm of the partition coefficient between water and 1-octanol), is less than 5.
- The number of groups in the molecule that can donate hydrogen atoms to hydrogen bonds (usually the sum of hydroxyl and amine groups in a drug

molecule) is less than 5.

- The number of groups that can accept hydrogen atoms to form hydrogen bonds (estimated by the sum of oxygen and nitrogen atoms) is less than 10.

The rules, based on the 90-percentile values of the drugs' property distributions, apply only to absorption by passive diffusion of compounds through cell membranes; compounds that are actively transported through cell membranes by transporter proteins are exceptions to the rule. Due in no small part to their simplicity, the Lipinski criteria are widely used by medicinal chemists to predict not only the absorption of compounds, as Lipinski originally intended, but also overall drug-likeness.

determine which proteins had the most drug-like set of ligands. Proteins whose ligands had the highest QED scores should be the most chemically tractable targets for drug discovery, because their known ligands are the most drug-like.

QED is not the final word in understanding the underlying features of chemical beauty and drug-likeness, but it does provide a holistic, more balanced assessment than previous approaches. It is also customizable, highly flexible and seems to be straightforward to implement. Any combination of physical properties can be chosen to define desirability functions, and users can set the relative weightings for properties as desired. QED should therefore find immediate use in replacing cut-off rules for the selection of oral-drug-like compounds for screening. The method can also be applied

to control sets other than oral drugs, such as lead-like molecules¹², compounds that belong to specific target and therapeutic classes, and drugs that are administered non-orally.

The widest long-term impact of Hopkins and colleagues' method¹ should be on the optimization of lead compounds, where it will help medicinal chemists to prioritize which drug-like compounds to prepare. It is to be hoped that the implementation of improved guidelines for drug-likeness, such as QED, at this stage of drug discovery will improve the quality⁷ of candidate drug molecules, and eventually help to reduce the 96% attrition rate of compounds that enter clinical trials¹³. ■

Paul Leeson is at the GlaxoSmithKline Medicines Research Centre, Stevenage SG1 2NY, UK.
e-mail: paul.d.leeson@gsk.com

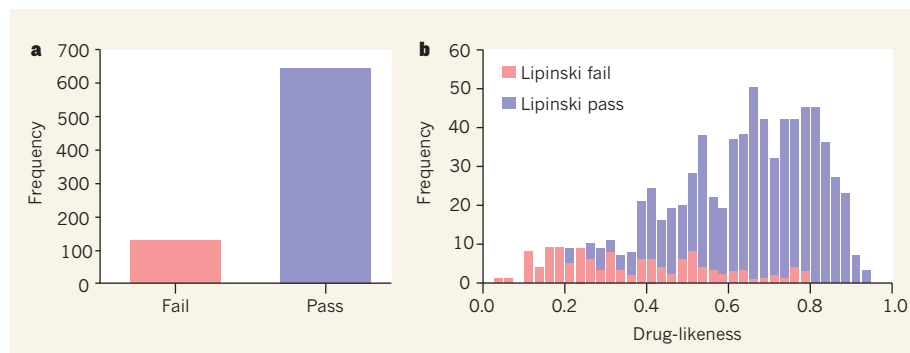


Figure 1 | Assessments of 'drug-likeness'. Physico-chemical criteria, such as those defined by the Lipinski rule of five, are typically used to predict whether a compound is drug-like or not. **a**, The bar chart shows the number of oral drugs that fail or pass the Lipinski rule, based on a set of 771 drugs approved by the US Food and Drug Administration. **b**, Hopkins and colleagues' report a method for predicting the drug-likeness of compounds on a scale of 0 (not drug-like) to 1 (drug-like). The chart shows the distribution of drug-likeness calculated using this method for the same drugs depicted in **a**. The analysis shows an overlap of Lipinski passes and failures for a range of drug-likenesses. Notably, some very drug-like molecules fail the Lipinski rule, whereas some very un-drug-like compounds pass it.

1. Bickerton, G. R., Paolini, G. V., Besnard, J., Muresan, S. & Hopkins, A. L. *Nature Chem.* **4**, 90–98 (2012).
2. Lipinski, C. A., Lombardo, F., Dominy, B. W. & Feeney, P. J. *Adv. Drug Delivery Rev.* **23**, 3–25 (1997).
3. Wenlock, M. C., Austin, R. P., Barton, P., Davis, A. M. & Leeson, P. D. *J. Med. Chem.* **46**, 1250–1256 (2003).
4. Hughes, J. D. *et al. Bioorg. Med. Chem. Lett.* **18**, 4872–4875 (2008).
5. Luker, T. *et al. Bioorg. Med. Chem. Lett.* **21**, 5673–5679 (2011).
6. Leeson, P. D. & Springthorpe, B. *Nature Rev. Drug Discov.* **6**, 881–890 (2007).
7. Leeson, P. D. & St-Gallay, S. A. *Nature Rev. Drug Discov.* **10**, 749–765 (2011).
8. Hann, M. M. *Med. Chem. Commun.* **2**, 349–355 (2011).
9. Wager, T. T. *et al. ACS Chem. Neurosci.* **1**, 435–449 (2010).
10. Lajiness, M. S., Maggiora, G. M. & Shanmugasundaram, V. J. *Med. Chem.* **47**, 4891–4896 (2004).
11. www.ebi.ac.uk/chembl
12. Teague, S. J., Davis, A. M., Leeson, P. D. & Oprea, T. *Angew. Chem. Int. Edn* **38**, 3743–3748 (1999).
13. Bunnap, M. E. *Nature Chem. Biol.* **7**, 335–339 (2011).

Endothelial and perivascular cells maintain haematopoietic stem cells

Lei Ding¹, Thomas L. Saunders², Grigori Enikolopov³ & Sean J. Morrison¹

Several cell types have been proposed to create niches for haematopoietic stem cells (HSCs). However, the expression patterns of HSC maintenance factors have not been systematically studied and no such factor has been conditionally deleted from any candidate niche cell. Thus, the cellular sources of these factors are undetermined. Stem cell factor (SCF; also known as KITL) is a key niche component that maintains HSCs. Here, using *Scf*^{gfp} knock-in mice, we found that *Scf* was primarily expressed by perivascular cells throughout the bone marrow. HSC frequency and function were not affected when *Scf* was conditionally deleted from haematopoietic cells, osteoblasts, nestin-*cre*- or nestin-*creER*-expressing cells. However, HSCs were depleted from bone marrow when *Scf* was deleted from endothelial cells or leptin receptor (*Lepr*)-expressing perivascular stromal cells. Most HSCs were lost when *Scf* was deleted from both endothelial and *Lepr*-expressing perivascular cells. Thus, HSCs reside in a perivascular niche in which multiple cell types express factors that promote HSC maintenance.

Stem cells are maintained in specialized microenvironments in tissues—termed niches—in which supporting cells secrete factors that promote stem cell maintenance¹. In most mammalian tissues, including the haematopoietic system, the identities of the cells that promote stem cell maintenance remain uncertain^{1,2}. One popular model of the HSC niche proposed that osteoblasts express many factors that promote HSC maintenance³, including SCF, CXCL12, angiopoietin 1 and thrombopoietin^{4–7}. However, none of these factors have been conditionally deleted from osteoblasts, so there is no direct evidence that osteoblasts are a functionally important source of these factors.

We found that most HSCs localize adjacent to sinusoidal blood vessels throughout the bone marrow^{8,9}. This led us to hypothesize that the HSC niche is perivascular^{2,9}. Others found that perivascular stromal cells secrete high levels of CXCL12 and other factors proposed to regulate HSC maintenance^{10,11}. Nestin-expressing mesenchymal stem cells also localize adjacent to blood vessels in the bone marrow and express factors thought to promote HSC maintenance¹². Ablation of the *Cxcl12*-expressing cells or the nestin-expressing cells reduced HSC frequency^{12,13}. Administration of antibodies against endothelial cells *in vivo* impairs HSC engraftment and transformed endothelial cells promote HSC expansion in culture^{14,15}. Nonetheless, no factor that promotes HSC maintenance has been conditionally deleted from any perivascular cell, so there is no direct evidence that endothelial or perivascular cells are functionally important sources of factors for HSC maintenance *in vivo*.

SCF is non-cell autonomously required for HSC maintenance *in vivo*^{16–19}. Differential splicing and proteolytic cleavage lead to the expression of a membrane-bound form and a soluble form of SCF. HSCs are depleted in *Sl/Sl*^d mutant mice²⁰, which express soluble SCF but lack the membrane-bound form, indicating that membrane-bound SCF is particularly important for HSC maintenance²¹. Mice with a mixture of wild-type and *Sl/Sl*^d stromal cells only exhibit normal haematopoiesis in the immediate vicinity of the wild-type cells, demonstrating that SCF acts locally in creating the niche²².

Scf has been suggested to be expressed by endothelial cells, bone marrow fibroblasts, osteoblasts, *Cxcl12*-expressing perivascular stromal cells and nestin-expressing mesenchymal stem cells^{5,12,13,23–25},

but *Scf* has not been conditionally deleted to test which source(s) are functionally important for HSC maintenance. We generated *Scf*^{gfp} and *Scf*^{fl} mice to systematically examine *Scf* expression and to conditionally delete *Scf* from subpopulations of bone marrow cells.

Scf is expressed by perivascular cells

We generated *Scf*^{gfp} knock-in mice by inserting enhanced green fluorescent protein (*gfp*) into the endogenous *Scf* locus (Supplementary Fig. 1a–c). *Scf*^{gfp/gfp} mice died perinatally (Fig. 1a and Supplementary Fig. 1f, g) with severe anaemia (Fig. 1b and Supplementary Fig. 2c), as observed in mice with a strong loss of SCF/c-Kit function¹⁷. By quantitative reverse transcription–polymerase chain reaction (qRT–PCR), *Scf* transcripts were nearly undetectable in *Scf*^{gfp/gfp} newborn liver (Fig. 1c).

The overall cellularity of the newborn liver was reduced about twofold in *Scf*^{gfp/+} and about fivefold in *Scf*^{gfp/gfp} mutant mice compared to *Scf*^{+/+} controls (Fig. 1d). The frequency of HSCs (CD150⁺ CD48[–] CD41[–] Sca1⁺ cKit⁺ cells^{9,26}) in the newborn liver was reduced about eightfold in *Scf*^{gfp/gfp} mutant mice compared to littermate *Scf*^{gfp/+} or *Scf*^{+/+} controls (Fig. 1e). Consistent with this, newborn *Scf*^{gfp/gfp} liver cells gave significantly lower levels of donor cell reconstitution in irradiated mice compared to *Scf*^{gfp/+} or *Scf*^{+/+} controls (Fig. 1f and Supplementary Fig. 2d). *Scf*^{gfp/gfp} mice therefore have a severe loss of SCF function.

Using flow cytometry we determined that only rare (0.027 ± 0.0099%, mean ± standard deviation (s.d.)) enzymatically dissociated bone marrow cells were positive for GFP. The actual frequency of GFP⁺ cells in the bone marrow may be somewhat higher as our dissociation conditions may not have recovered all of the GFP⁺ stromal cells. These GFP⁺ cells were negative for CD45 and Ter119, indicating a non-haematopoietic source of SCF (Fig. 1g). Endogenous *Scf* transcripts were highly enriched in GFP⁺ stromal cells and highly depleted in GFP[–] stromal cells (Supplementary Fig. 2f, g), suggesting that GFP expression faithfully reflected endogenous *Scf* expression.

GFP was mainly expressed by cells surrounding sinusoids throughout the *Scf*^{gfp/+} bone marrow, with some expression by cells surrounding venules and arterioles (Fig. 1h–m and Supplementary Fig. 2h, i).

¹Howard Hughes Medical Institute, Children's Research Institute, Department of Pediatrics, University of Texas Southwestern Medical Center, Dallas, Texas 75390, USA. ²Transgenic Animal Model Core, University of Michigan, Ann Arbor, Michigan 48109-2216, USA. ³Cold Spring Harbor Laboratory, Cold Spring Harbor, New York 11724, USA.

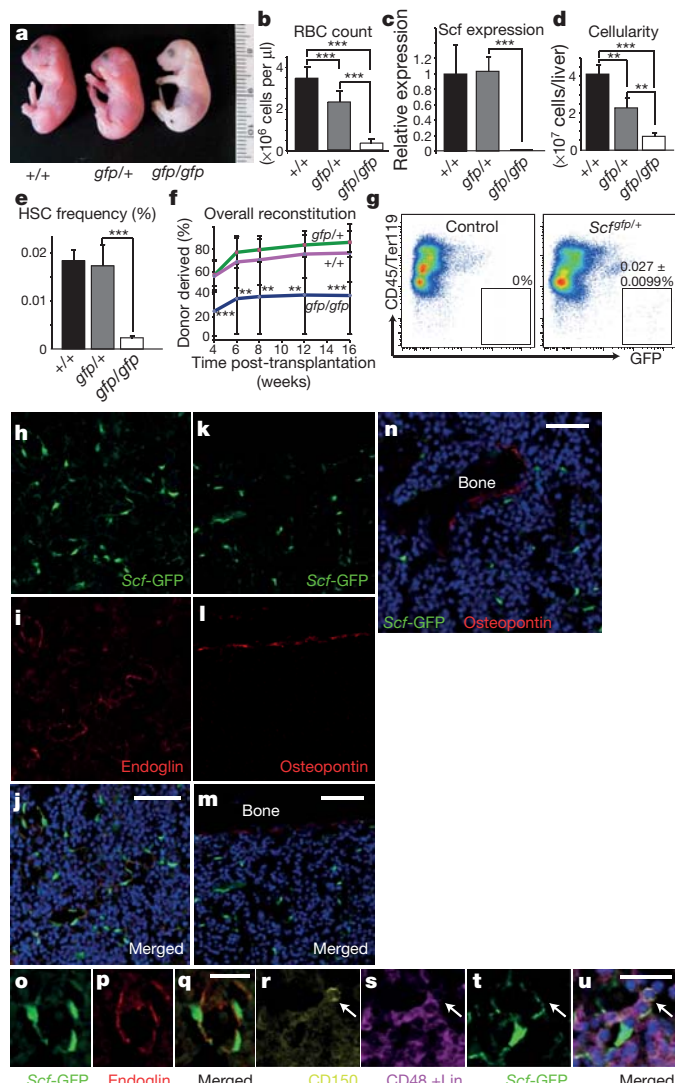


Figure 1 | *Scf*^{gfp} is a strong loss-of-function allele and *Scf* is primarily expressed by perivascular cells in the bone marrow. **a**, **b**, *Scf*^{gfp/gfp} homozygous mice died perinatally and were severely anaemic ($n = 4-20$). RBC, red blood cell. **c**, *Scf* transcripts in livers from newborn mice by qRT-PCR ($n = 3$). **d**, **e**, Newborn liver cellular density and HSC frequency ($n = 4$). **f**, Irradiated mice (CD45.1⁺) were transplanted with 3×10^5 newborn liver cells from *Scf*^{gfp/gfp}, *Scf*^{gfp/+} or *Scf*^{+/+} donor (CD45.1⁺) mice along with 3×10^5 recipient (CD45.1⁺) bone marrow cells (3–4 experiments with 13–18 mice per genotype). **g**, *Scf*-GFP was expressed by rare non-haematopoietic stromal cells ($n = 8$). **h–j**, GFP was primarily expressed by perivascular cells in the bone marrow of *Scf*^{gfp/+} mice. Endothelial cells were stained with an anti-endoglin antibody. **k–n**, GFP was not detected in bone-lining osteoblast lineage cells (osteopontin) in the diaphysis (**k–m**) or in trabecular bone (**n**). **o–q**, Higher magnification images of a sinusoid. **r–u**, A CD150⁺ CD48[−] lineage[−] candidate HSC (arrow) localized adjacent to a GFP-expressing perivascular cell. Nuclei were stained with 4',6-diamidino-2-phenylindole (DAPI; in blue). All data represent mean \pm s.d. Two-tailed Student's *t*-tests were used to assess statistical significance. ** $P < 0.01$, *** $P < 0.001$. Scale bars in **j**, **m** and **n** are 50 μ m. Scale bars in **q** and **u** are 20 μ m.

GFP partially overlapped with endothelial marker staining (Fig. 1h–j, o–q and Supplementary Fig. 2i), suggesting that both endothelial and perivascular stromal cells express *Scf*. In contrast, GFP was not concentrated near the endosteum (Supplementary Fig. 2h) and we did not detect any GFP expression by bone-lining cells that expressed osteoblast markers in either the diaphysis (Fig. 1k–m) or trabecular bone (Fig. 1n). Perivascular stromal and endothelial cells therefore appeared to represent the major sources of SCF in bone marrow.

We isolated *Scf*-GFP⁺ cells by flow cytometry and performed gene expression profiling. Several mesenchymal stem/stromal cell markers,

including *Cxcl12*, alkaline phosphatase, *Vcam1*, *Pdgfra* and *Pdgfrb* were highly elevated in *Scf*-GFP⁺ cells relative to whole bone marrow cells (Supplementary Table 1). This indicates that *Scf*-GFP⁺ cells included mesenchymal stem/stromal cells²⁷ and *Cxcl12*-expressing perivascular stromal cells¹⁰. Nestin was not detected in *Scf*-GFP⁺ perivascular cells (Supplementary Table 1).

As we observed previously^{8,9}, CD150⁺ CD48[−] lineage[−] candidate HSCs were mainly found adjacent to sinusoidal blood vessels throughout the bone marrow. Sixty-five per cent (47/73) of all CD150⁺ CD48[−] lineage[−] cells were immediately adjacent to GFP-expressing stromal cells (Fig. 1r–u). Almost all of the remaining cells (30%; 22/73) were within five cell diameters of GFP-expressing cells. This suggests that *Scf*-GFP-expressing cells form a perivascular niche for HSCs.

Scf is required by adult HSCs

We generated a floxed allele of *Scf* (*Scf*^{fl}) to conditionally delete *Scf* from candidate niche cells (Supplementary Fig. 3a–c). Mice homozygous for the germline recombined allele of *Scf*—*Scf*^{−/−}—were perinatally lethal and anaemic (Fig. 2a), similar to other *Scf*-deficient mice (Fig. 1a)¹⁷. Recombination of the *Scf*^{fl} allele therefore led to a strong loss of SCF function. We were unable to amplify *Scf* transcripts by PCR from the liver of *Scf*^{−/−} newborns (Fig. 2b).

We generated *Ubc-creER*; *Scf*^{fl/fl} mice to ubiquitously delete *Scf* upon tamoxifen administration. We administered tamoxifen-containing chow to *Ubc-creER*; *Scf*^{fl/fl} mice and littermate controls for 1–2 months beginning at 8 weeks of age, and then killed them for analysis. Some of the mice became anaemic and ill during tamoxifen administration. The *Ubc-creER*; *Scf*^{fl/fl} mice had significantly lower red blood cell counts than controls (Fig. 2c) and a trend towards lower

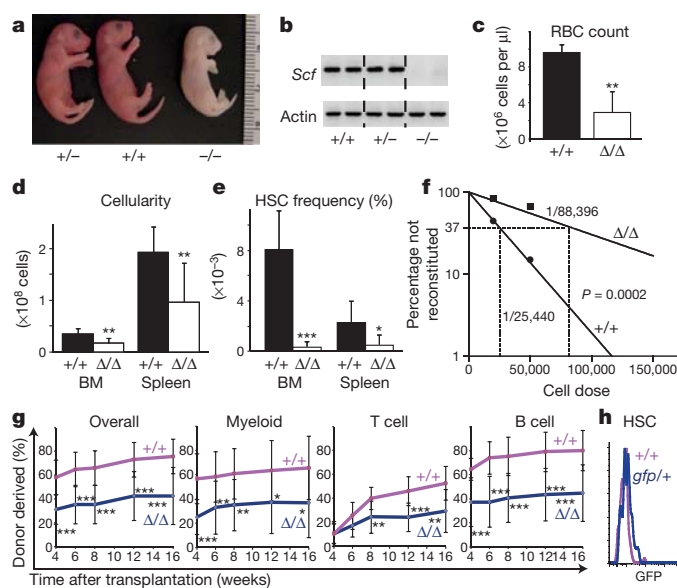


Figure 2 | *Scf* is required for adult HSC maintenance. **a**, Homozygous *Scf*^{−/−} mutant mice generated from germline recombination of the *Scf*^{fl} allele were perinatally lethal and anaemic. **b**, *Scf* transcripts amplified by RT-PCR from the livers of newborn mice. **c**, Global deletion of *Scf* in *Ubc-creER*; *Scf*^{fl/fl} mice led to anaemia ($n = 5-6$). **d**, **e**, Global deletion of *Scf* in adult mice significantly reduced cellular density and HSC frequency in bone marrow (two femurs and two tibias) and spleen ($n = 8-10$). BM, bone marrow. **f**, To perform a limit dilution analysis⁴², three doses of donor bone marrow cells were competitively transplanted into irradiated mice. ELDA software (<http://bioinf.wehi.edu.au/software/elda/>) was used to calculate HSC frequency and assess statistical significance (two experiments). **g**, 3×10^5 donor bone marrow cells were transplanted with 3×10^5 recipient bone marrow cells into irradiated recipient mice (three experiments with a total of 12–14 recipients per genotype). **h**, HSCs did not express *Scf*-GFP by flow cytometry. Δ , recombined *Scf*^{fl} allele; +, wild-type allele of *Scf*. All data represent mean \pm s.d. * $P < 0.05$, ** $P < 0.01$, *** $P < 0.001$.

white blood cell and platelet counts (Supplementary Fig. 3d). *Ubc-creER*; *Scf^{fl/fl}* mice exhibited approximately twofold reductions in the overall cellularity of bone marrow and spleen compared to controls (Fig. 2d).

CD150⁺ CD48[−] Lin[−] Sca1⁺ c-Kit⁺ HSCs were also depleted in the bone marrow and spleen of *Ubc-creER*; *Scf^{fl/fl}* mice compared to controls treated concurrently with tamoxifen (Fig. 2e). Limit dilution analysis demonstrated that long-term multilineage reconstituting cells were 3.5-fold less frequent in the bone marrow of *Ubc-creER*; *Scf^{fl/fl}* mice compared to controls upon transplantation into irradiated mice (Fig. 2f). Bone marrow cells from *Ubc-creER*; *Scf^{fl/fl}* mice gave significantly lower levels of donor cell reconstitution in irradiated mice (Fig. 2g). These data confirmed that SCF is required for HSC maintenance in adult mice.

CD150⁺ CD48[−] Lin[−] Sca1⁺ c-Kit⁺ HSCs from *Scf^{fl/+}* mice did not express GFP by flow cytometry (Fig. 2h). This is consistent with prior studies^{17,21,22} in suggesting that *Scf* non-cell autonomously regulates HSC maintenance. To test the role of other haematopoietic cells we conditionally deleted *Scf* using *Vav1-cre*. As expected²⁸, *Vav1-cre* recombined a conditional *loxP-EYFP* reporter²⁹ in virtually all HSCs, CD45⁺ and Ter119⁺ haematopoietic cells (Fig. 3a and Supplementary Fig. 4a). Eight-week-old *Vav1-cre*; *Scf^{fl/−}* mice exhibited normal blood cell counts, bone marrow composition (Supplementary Fig. 4b, c), and bone marrow and spleen cellularity (Fig. 3b). *Scf^{fl/+}* heterozygous mice exhibited a twofold decline in the frequency of CD150⁺ CD48[−] Lin[−] Sca1⁺ c-Kit⁺ HSCs relative to wild-type littermates. However, deletion of the second allele of *Scf* from haematopoietic cells in *Vav1-cre*; *Scf^{fl/−}* mice did not further reduce HSC frequency in the bone marrow or spleen (Fig. 3c). Bone marrow cells from adult *Vav1-cre*; *Scf^{fl/−}* mice had a normal capacity to reconstitute irradiated mice (Fig. 3d and Supplementary Fig. 4d) and to form colonies in methylcellulose (Supplementary Fig. 4e, f). Therefore, *Scf* expression by haematopoietic cells is not required for HSC maintenance in adult bone marrow.

HSCs do not require SCF from osteoblasts

Col2.3-Cre recombines genes in fetal and postnatal osteoblasts³⁰. Consistent with this, we found strong enhanced yellow fluorescent protein (EYFP) expression among bone-lining cells in *Col2.3-cre*; *loxP-EYFP* mice (Fig. 3e). To test whether osteoblasts produce SCF for HSC maintenance, we analysed 8-week-old *Col2.3-cre*; *Scf^{fl/−}* mice. *Col2.3-cre*; *Scf^{fl/−}* mice had normal blood counts (Supplementary Fig. 5a), normal lineage composition in the bone marrow and spleen (Supplementary Fig. 5b) and normal bone marrow and spleen cellularity (Fig. 3g). Although *Scf^{fl/+}* germline heterozygous mice exhibited a twofold decline in the frequency of CD150⁺ CD48[−] Lin[−] Sca1⁺ c-Kit⁺ HSCs relative to wild-type littermates, conditional deletion of the second allele of *Scf* from osteoblasts in *Col2.3-cre*; *Scf^{fl/−}* mice did not further reduce HSC frequency in the bone marrow or spleen (Fig. 3h). Bone marrow cells from *Col2.3-cre*; *Scf^{fl/−}* mice had a normal capacity to reconstitute irradiated mice (Fig. 3i and Supplementary Fig. 5c) and to form colonies in methylcellulose (Supplementary Fig. 5d, e). Therefore, *Scf* expression by osteoblasts is not required for HSC maintenance in adult bone marrow.

HSCs do not require SCF from nestin⁺ cells

In *nestin-cre*; *loxP-EYFP* mice we found rare EYFP-expressing perivascular stromal cells around larger blood vessels, not sinusoids, in the bone marrow (Fig. 3f). These cells exhibited a very different distribution than *Scf*-expressing cells (compare Fig. 3f to Fig. 1h–m and Supplementary Fig. 2h, i). Eight-week-old *nestin-cre*; *Scf^{fl/−}* mice had normal blood cell counts (Supplementary Fig. 6b), normal lineage composition and cellularity in the bone marrow and spleen (Supplementary Fig. 6c and Fig. 3j). Comparing *nestin-cre*; *Scf^{fl/−}* mutants with *Scf^{fl/+}* controls, deletion of *Scf* from *nestin-cre*-expressing cells did not reduce HSC frequency in the bone marrow (Fig. 3k).

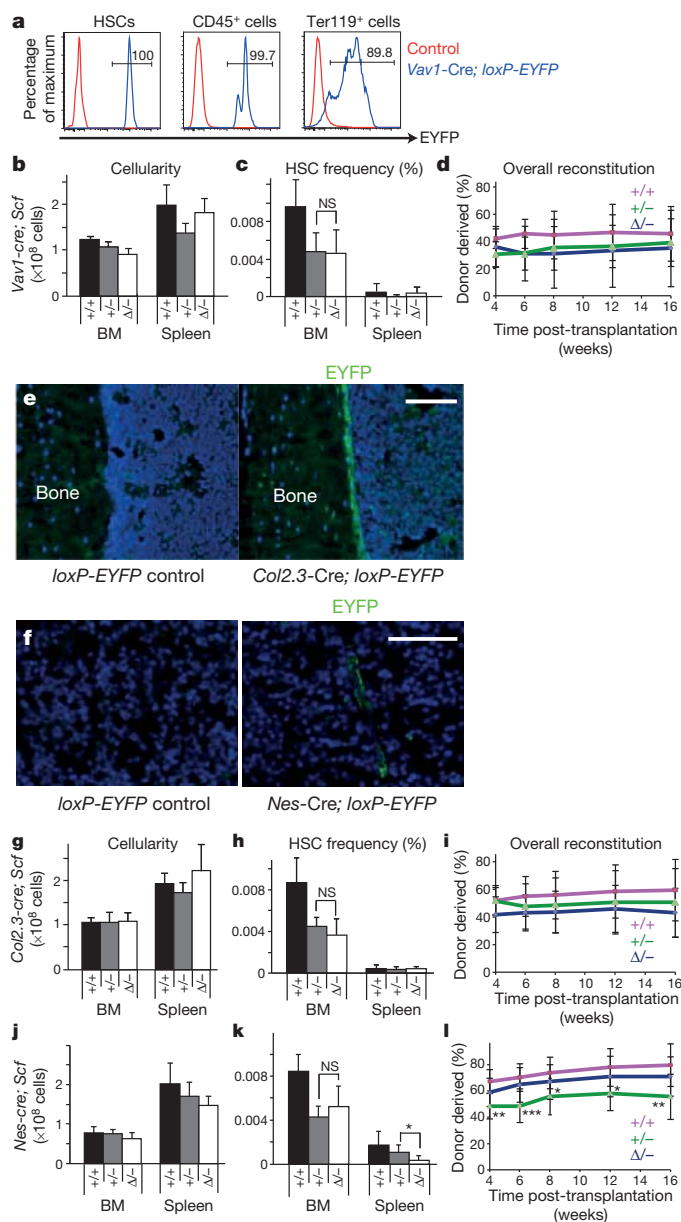


Figure 3 | SCF from haematopoietic cells, osteoblasts and nestin-Cre-expressing stromal cells is not required for HSC maintenance. **a**, *Vav1-Cre* recombined the *loxP-EYFP* reporter in virtually all HSCs, CD45⁺ and Ter119⁺ haematopoietic cells. **b**, **c**, Deletion of *Scf* from haematopoietic cells did not significantly affect bone marrow or spleen cellularity or HSC frequency ($n = 4$). **d**, A competitive reconstitution assay with *Vav1-cre*; *Scf^{fl/−}*, *Scf^{fl/+}* and *Scf^{+/+}* bone marrow cells (2 experiments with a total of 10 recipients per genotype). **e**, *Col2.3-Cre* recombined the *loxP-EYFP* reporter in bone-lining osteoblast lineage cells. **f**, Nestin-Cre recombined the *loxP-EYFP* reporter in rare stromal cells around larger blood vessels. **g**, **h**, Bone marrow and spleen cellularity (**g**) and HSC frequency (**h**) in *Col2.3-cre*; *Scf^{fl/−}* mice relative to controls ($n = 5–6$). **i**, A competitive reconstitution assay with *Col2.3-cre*; *Scf^{fl/−}*, *Scf^{fl/+}* and *Scf^{+/+}* bone marrow cells (3–5 experiments with a total of 14–22 recipients per genotype). **j**, **k**, Bone marrow and spleen cellularity (**j**) and HSC frequency (**k**) in *nestin-cre*; *Scf^{fl/−}* mice relative to controls ($n = 5–7$). **l**, 3×10^5 donor bone marrow cells from *nestin-cre*; *Scf^{fl/−}* and *Scf^{fl/+}* mice gave similar levels of donor cell reconstitution in irradiated mice. Reconstitution levels from *Scf^{fl/+}* cells were modestly but significantly lower (3–5 experiments with a total of 14–24 recipient mice per genotype). Δ , recombined *Scf^{fl}* allele; +, wild-type allele; −, germline deleted allele. Scale bar is 100 μ m in **e** and 50 μ m in **f**. All data represent mean \pm s.d. NS, not significant. * $P < 0.05$, ** $P < 0.01$, *** $P < 0.001$.

Nestin-*cre*; *Scf*^{fl/-} mice did exhibit a significant decline in HSC frequency in the spleen (Fig. 3k), raising the possibility that nestin-*cre*-expressing cells are a component of the HSC niche in the spleen. Bone marrow cells from adult nestin-*cre*; *Scf*^{fl/-} mice had a normal capacity to reconstitute irradiated mice (Fig. 3l and Supplementary Fig. 6d). Conditional deletion of *Scf* by administering tamoxifen for 2–5 months to adult nestin-*creER*; *Scf*^{fl/fl} mice also did not affect haematopoiesis, HSC frequency, or reconstituting capacity in irradiated mice (Supplementary Fig. 7). Therefore, *Scf* expression by nestin-*cre*-expressing or nestin-*creER*-expressing perivascular cells is not required for the maintenance of HSCs in adult bone marrow.

Because nestin-GFP-expressing bone marrow cells express *Scf*^{Δ2}, we independently characterized nestin-GFP expression. Consistent with the prior report¹², we observed strong nestin-GFP staining along larger vessels in the bone marrow (Supplementary Fig. 8; see supplementary figure 1 from ref. 12). Nestin-GFP was also observed in perisinusoidal stromal cells in a pattern that resembled *Scf*-GFP⁺ expression (Supplementary Fig. 8a). This appeared to be different from the nestin-*cre* expression pattern, which we detected only around larger blood vessels in the bone marrow (Fig. 3f). In nestin-*Cherry* and nestin-GFP double transgenic mice we detected nestin-*Cherry* expression around larger vessels but not around sinusoids, whereas nestin-GFP was detected around both (Supplementary Fig. 8). Thus, different nestin transgenes seem to be expressed by different subpopulations of perivascular stromal cells. Nestin-GFP appears to exhibit more expression in perisinusoidal stromal cells than other nestin transgenes. Our data are therefore consistent with the possibility that nestin-GFP-expressing stromal cells contribute to the HSC niche as previously suggested¹², even though conditional deletion of *Scf* with nestin-*cre* and nestin-*creER* did not affect HSC frequency.

HSCs require SCF from endothelial cells

We conditionally deleted *Scf* from endothelial cells using *Tie2-cre*³¹. *Tie2-Cre* recombined in endothelial (Fig. 4a) and haematopoietic cells

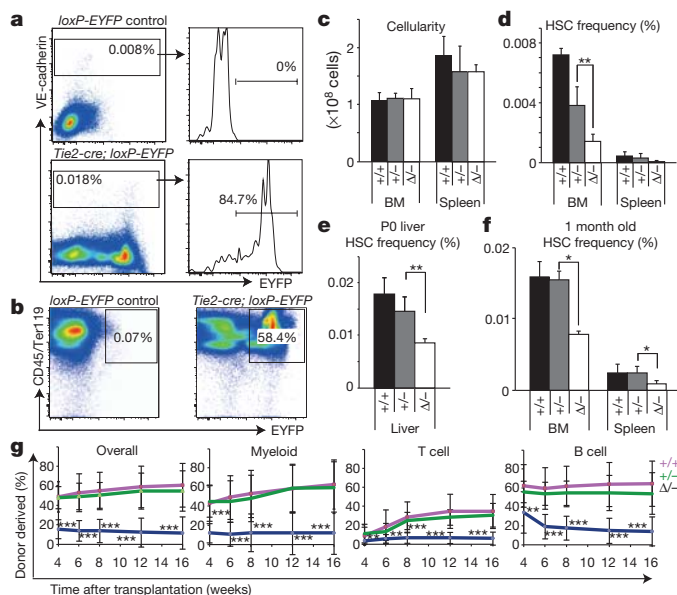


Figure 4 | Deletion of *Scf* from endothelial cells depletes HSCs. **a, b,** *Tie2-Cre* recombined the *loxP-EYFP* conditional reporter in VE-cadherin⁺ endothelial cells and in haematopoietic cells in the bone marrow. **c,** Bone marrow and spleen cellularity in *Tie2-cre*; *Scf*^{fl/-} mice and littermate controls (*n* = 4–7). **d,** HSC frequency in *Tie2-cre*; *Scf*^{fl/-} mice and controls (*n* = 4–7). **e,** HSC frequency in the liver of newborn *Tie2-cre*; *Scf*^{fl/-} mice and controls (*n* = 3–6). P0, postnatal day 0. **f,** HSC frequency in 1-month-old *Tie2-cre*; *Scf*^{fl/-} mice and controls (*n* = 3–4). **g,** Bone marrow cells from *Tie2-cre*; *Scf*^{fl/-} mice gave significantly lower levels of reconstitution relative to cells from *Scf*^{+/+} and *Scf*^{+/+} mice (3–5 experiments with a total of 15–25 recipients per genotype). All data represent mean ± s.d. **P* < 0.05, ***P* < 0.01, ****P* < 0.001.

(Fig. 4b) but not in mesenchymal stem/stromal cells from the bone marrow (Supplementary Fig. 9d, e). Because haematopoietic cells do not express *Scf* (Fig. 1g and Fig. 2i) and conditional deletion of *Scf* from haematopoietic cells did not affect HSC frequency (Fig. 3a–d), the use of *Tie2-cre* allowed us to test whether SCF expression by endothelial cells regulates HSC frequency.

Eight-week-old *Tie2-cre*; *Scf*^{fl/-} mice exhibit normal blood cell counts (data not shown), bone marrow and spleen cellularity (Fig. 4c). However, the frequency of CD150⁺ CD48⁺ Lin⁺ Sca1⁺ c-Kit⁺ HSCs in the bone marrow was significantly reduced in *Tie2-cre*; *Scf*^{fl/-} mice relative to controls (Fig. 4d). Consistent with this, 300,000 bone marrow cells from *Tie2-cre*; *Scf*^{fl/-} mice gave significantly lower levels of donor reconstitution upon transplantation into irradiated mice (Fig. 4g). In 5 independent experiments, 24 of 25 recipients of *Scf*^{+/+} cells, 15 of 15 recipients of *Scf*^{fl/-} cells, and only 7 of 21 recipients of *Tie2-cre*; *Scf*^{fl/-} cells were long-term multilineage reconstituted. By Poisson statistics this corresponds to an HSC frequency in control bone marrow of at least 1/93,200 cells but only 1/739,900 in *Tie2-cre*; *Scf*^{fl/-} mice. Endothelial cells are therefore an important source of SCF for HSC maintenance.

The HSC depletion in *Tie2-cre*; *Scf*^{fl/-} mice probably reflects an ongoing need for SCF expression by endothelial cells in adult bone marrow, because when HSCs are depleted as a consequence of reduced SCF/c-Kit signalling, HSC frequencies return to normal levels upon restoration of normal SCF/c-Kit signalling^{19,21}. Nonetheless, we also examined whether SCF expression by endothelial cells during development is required by HSCs. We found a 1.7–2.1-fold reduction in HSC frequency in the liver of newborn *Tie2-cre*; *Scf*^{fl/-} mice (Fig. 4e) and a twofold reduction in HSC frequency in the bone marrow of 1-month-old *Tie2-cre*; *Scf*^{fl/-} mice (Fig. 4f) relative to *Scf*^{+/+} and *Scf*^{+/+} controls. The magnitude of HSC depletion in adult bone marrow seemed to increase, as we found a 2.7-fold and 5.2-fold reduction in HSC frequency in the bone marrow of 8-week-old *Tie2-cre*; *Scf*^{fl/-} mice relative to *Scf*^{+/+} and *Scf*^{+/+} controls, respectively (Fig. 4d). These data suggest that ongoing SCF expression by endothelial cells in adult bone marrow contributes to HSC maintenance; however, HSC depletion in adult bone marrow may reflect a loss of SCF expression by endothelial cells during development.

HSCs require SCF from perivascular cells

We found that *Lepr* is highly restricted in its expression within the bone marrow to *Scf*-GFP-expressing perivascular stromal cells (Supplementary Table 1). Consistent with this, *Lepr-cre*; *loxP-EYFP* mice exhibited EYFP expression in perivascular stromal cells (Fig. 5b, e) but not in haematopoietic cells (Fig. 5b, c, e), bone-lining cells (Fig. 5c), or endothelial cells (Fig. 5d).

Consistent with the gene expression profile of *Scf*-GFP⁺ cells (Supplementary Table 1), EYFP⁺ cells from *Lepr-cre*; *loxP-EYFP* mice did not detectably express nestin but did express mesenchymal stem/stromal cell markers including *Cxcl12*, alkaline phosphatase, PDGFRα and PDGFRβ (Supplementary Fig. 9a–c). These data indicate a mesenchymal identity for the *Lepr*-expressing stromal cells; however, the lack of EYFP expression in bone-lining cells from *Lepr-cre*; *loxP-EYFP* mice suggests that the *Lepr-cre*-expressing perivascular cells did not give rise to osteoblasts during normal development. Future studies will be required to assess the relationship between *Lepr-cre*-expressing perivascular cells, mesenchymal stem cells, and other perivascular stromal cells.

Bone marrow cellularity was significantly reduced in *Lepr-cre*; *Scf*^{fl/gfp} mice compared to *Scf*^{+/+} controls, but not compared to *Scf*^{+/gfp} controls (Fig. 5g). Spleen size (Fig. 5f) and cellularity were significantly increased in *Lepr-cre*; *Scf*^{fl/gfp} mice (Fig. 5g). Sections through the spleen revealed increased extramedullary haematopoiesis in *Lepr-cre*; *Scf*^{fl/gfp} mice (data not shown). The frequency of CD150⁺ CD48⁺ Lin⁺ Sca1⁺ c-Kit⁺ HSCs was significantly reduced in the bone marrow of *Lepr-cre*; *Scf*^{fl/gfp} mice, but significantly increased in the spleen (Fig. 5h). The total number of bone marrow and spleen HSCs

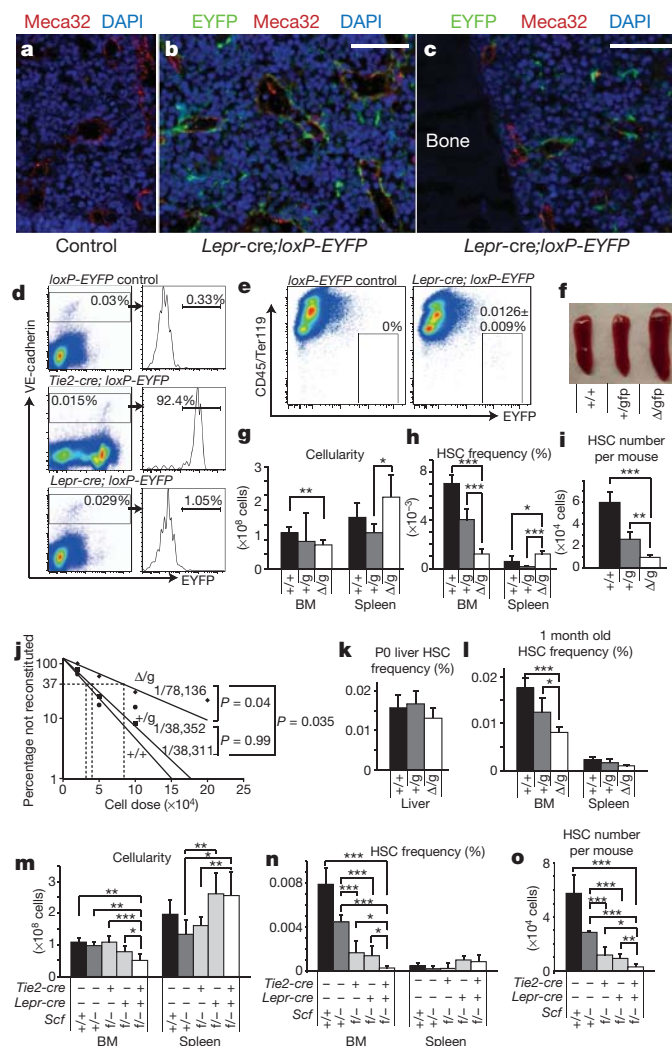


Figure 5 | Deletion of *Scf* from *Lepr-cre*-expressing perivascular stromal cells depletes HSCs in the bone marrow. **a–c**, *Lepr-cre* recombined the *loxP-EYFP* reporter in perisinusoidal stromal cells in the bone marrow but not in bone-lining or haematopoietic cells. **d**, *Lepr-cre* did not recombine in VE-cadherin⁺ endothelial cells. **e**, 0.013 ± 0.009% (mean ± s.d.; *n* = 3) of bone marrow cells from *Lepr-cre; loxP-EYFP* mice were EYFP⁺. **f**, **g**, Spleen size (**f**) and bone marrow and spleen cellularity (**g**) (*n* = 4–7). **h**, HSC frequency (*n* = 4–7). **i**, Total HSC numbers (including bone marrow and spleen) in *Lepr-cre; Scf^{fl/gfp}* mice (*n* = 4–7). **j**, Limit dilution analysis⁴² of the frequency of long-term multilineage reconstituting cells in the bone marrow of *Lepr-cre; Scf^{fl/gfp}* mice relative to controls (two experiments). **k**, HSC frequency in the newborn liver (*n* = 4–11). **l**, HSC frequency in 1-month-old *Lepr-cre; Scf^{fl/gfp}* mice and controls (*n* = 3–6). **m**, *Tie2-cre; Lepr-cre; Scf^{fl/-}* mice had significantly reduced bone marrow cellularity and increased spleen cellularity compared to *Scf^{fl/+}* or *Tie2-cre; Scf^{fl/-}* controls (*n* = 4–11). **n**, Deletion of *Scf* from endothelial and perivascular stromal cells in *Tie2-cre; Lepr-cre; Scf^{fl/-}* mice greatly depleted HSCs from adult bone marrow (*n* = 4–11). **o**, Total HSC number was significantly reduced in *Tie2-cre; Lepr-cre; Scf^{fl/-}* mice compared to *Tie2-cre; Scf^{fl/-}* or *Lepr-cre; Scf^{fl/-}* mice (*n* = 4–11). **g** or **gfp**, *Scf^{gfp}* allele; **f**, *Scf^{fl}* allele. Scale bars are 50 μm. All data represent mean ± s.d. **P* < 0.05, ***P* < 0.01, ****P* < 0.001.

per mouse was significantly reduced in *Lepr-cre; Scf^{fl/gfp}* mice (Fig. 5i). *Lepr-cre*-expressing cells thus promote HSC maintenance in the bone marrow, but not in the spleen, by producing SCF.

In limit dilution transplantation studies the frequency of long-term multilineage reconstituting cells in *Scf^{fl/+}* and *Scf^{fl/gfp}* control cells was 1/38,311 and 1/38,352, respectively (Fig. 5j). In *Lepr-cre; Scf^{fl/gfp}* bone marrow cells the frequency of long-term multilineage reconstituting cells was 1/78,136, significantly lower than in *Scf^{fl/+}* and *Scf^{fl/gfp}* controls (Fig. 5j). Thus conditional deletion of *Scf* from

Lepr-cre-expressing perivascular stromal cells depletes HSCs from adult bone marrow. The frequency of GFP⁺ cells in the bone marrow of *Lepr-cre; Scf^{fl/gfp}* mice did not significantly differ from *Scf^{fl/gfp}* controls (Supplementary Fig. 10), suggesting that *Scf* deletion did not lead to the death of *Lepr*-expressing cells.

The HSC depletion observed in *Lepr-cre; Scf^{fl/gfp}* mice did not reflect a developmental effect of SCF expression by *Lepr-cre*-expressing cells as no HSC depletion was detected in the liver of newborn *Lepr-cre; Scf^{fl/gfp}* mice (Fig. 5k). Furthermore, the magnitude of the HSC depletion increased with time in the adult bone marrow (Fig. 5h, l).

To test whether deletion of *Scf* from endothelial and *Lepr*-expressing perivascular cells has additive effects on HSC depletion we analysed 8-week-old *Tie2-cre; Lepr-cre; Scf^{fl/-}* mice. Bone marrow cellularity was significantly reduced in *Tie2-cre; Lepr-cre; Scf^{fl/-}* mice compared to *Tie2-cre; Scf^{fl/-}* and *Lepr-cre; Scf^{fl/-}* mice (Fig. 5m). Spleen cellularity was significantly increased in *Tie2-cre; Lepr-cre; Scf^{fl/-}* mice compared to *Scf^{fl/-}* or *Tie2-cre; Scf^{fl/-}* mice (Fig. 5m). HSC frequency was significantly reduced in the bone marrow of *Tie2-cre; Lepr-cre; Scf^{fl/-}* mice compared to *Tie2-cre; Scf^{fl/-}* or *Lepr-cre; Scf^{fl/-}* mice (Fig. 5n). The frequency and absolute number of HSCs in the bone marrow of *Tie2-cre; Lepr-cre; Scf^{fl/-}* mice was less than 5% of wild-type levels (Fig. 5m–o). This suggests that endothelial and *Lepr*-expressing perivascular stromal cells are the major sources of SCF for HSC maintenance in normal adult bone marrow and that deletion of *Scf* from each cell population has additive effects on HSC depletion.

qRT-PCR revealed that endothelial and *Lepr-cre*-expressing perivascular cells expressed both long and short splice isoforms of *Scf*, rendering both cell types capable of expressing membrane-bound and soluble SCF (Supplementary Fig. 11). The levels of both isoforms of *Scf* in the two cell populations were significantly higher than in whole bone marrow cells, although *Lepr-cre*-expressing cells expressed much higher levels of both isoforms compared to endothelial cells (Supplementary Fig. 11).

Discussion

Our data demonstrate that HSCs reside in a perivascular niche in which endothelial and *Lepr*-expressing perivascular stromal cells are two functionally important components of the niche (Supplementary Fig. 12). The simplest interpretation of our data is that both cell types produce SCF for the maintenance of HSCs in adult bone marrow; however, endothelial cells also produce SCF for HSC maintenance/expansion during development so it is possible that the depletion of bone marrow HSCs in adult *Tie2-cre; Scf^{fl/-}* mice reflects a developmental effect of endothelial SCF. Endothelial cells and perivascular stromal cells are probably not the only components of the HSC niche, as other cell types probably contribute through mechanisms other than SCF production (for example, refs 32, 33).

Lepr-cre-expressing stromal cells did not express endogenous nestin (Supplementary Fig. 9c). Nestin-*cre*- or nestin-*creER*-mediated deletion of *Scf* did not deplete HSCs (Fig. 3j–l and Supplementary Figs 6 and 7). However, *Lepr-cre*-expressing perisinusoidal cells do partially overlap with nestin-GFP-expressing perivascular cells (Supplementary Fig. 8 and Supplementary Fig. 9a–c). The *Lepr-cre*-expressing stromal cells therefore include stromal cells that express certain nestin transgenes, consistent with previous work¹², and may also include *Cxcl12*-abundant reticular cells¹⁰. Perivascular stromal cells are probably heterogeneous and may include multiple cell types that contribute to HSC maintenance through different mechanisms.

Although we have partially characterized the bone marrow niche for HSCs in adult mice under homeostatic conditions, other studies will be required to functionally characterize HSC niches in other haematopoietic tissues and after haematopoietic stress.

METHODS SUMMARY

Targeting vectors for making *Scf^{gfp}* and *Scf^{fl}* mice were constructed by recombineering³⁴. The *Frt*-flanked *Neo* cassette was removed by mating with *Flpe*

mice³⁵. *Scf^{flp}* and *Scf^{fl}* mice were backcrossed onto a C57BL/Ka background before analysis. Mice used in this study included *Ubc-creER³⁶*, *CMV-cre³⁷*, *Vav1-cre²⁸*, *nestin-cre³⁸*, *Tie2-cre³¹*, *Lepr-cre³⁹* and *loxP-EYFP²⁹* (all from the Jackson Laboratory), *Col2.3-cre³⁰*, *nestin-creER⁴⁰* and *nestin-GFP⁴¹*. All were maintained on a C57BL/Ka background. Unless otherwise indicated, data always reflect mean \pm s.d. and two-tailed Student's *t*-tests were used to assess statistical significance (**P* < 0.05, ***P* < 0.01, ****P* < 0.001).

Full Methods and any associated references are available in the online version of the paper at www.nature.com/nature.

Received 5 August; accepted 12 December 2011.

- Morrison, S. J. & Spradling, A. C. Stem cells and niches: mechanisms that promote stem cell maintenance throughout life. *Cell* **132**, 598–611 (2008).
- Kiel, M. J. & Morrison, S. J. Uncertainty in the niches that maintain haematopoietic stem cells. *Nature Rev. Immunol.* **8**, 290–301 (2008).
- Wilson, A. & Trumpp, A. Bone-marrow haematopoietic-stem-cell niches. *Nature Rev. Immunol.* **6**, 93–106 (2006).
- Arai, F. *et al.* Tie2/angiopoietin-1 signaling regulates hematopoietic stem cell quiescence in the bone marrow niche. *Cell* **118**, 149–161 (2004).
- Calvi, L. M. *et al.* Osteoblastic cells regulate the haematopoietic stem cell niche. *Nature* **425**, 841–846 (2003).
- Kollet, O. *et al.* Osteoclasts degrade endosteal components and promote mobilization of hematopoietic progenitor cells. *Nature Med.* **12**, 657–664 (2006).
- Yoshihara, H. *et al.* Thrombopoietin/MPL signaling regulates hematopoietic stem cell quiescence and interaction with the osteoblastic niche. *Cell Stem Cell* **1**, 685–697 (2007).
- Kiel, M. J., Radice, G. L. & Morrison, S. J. Lack of evidence that hematopoietic stem cells depend on N-cadherin-mediated adhesion to osteoblasts for their maintenance. *Cell Stem Cell* **1**, 204–217 (2007).
- Kiel, M. J., Yilmaz, O. H., Iwashita, T., Terhorst, C. & Morrison, S. J. SLAM family receptors distinguish hematopoietic stem and progenitor cells and reveal endothelial niches for stem cells. *Cell* **121**, 1109–1121 (2005).
- Sugiyama, T., Kohara, H., Noda, M. & Nagasawa, T. Maintenance of the hematopoietic stem cell pool by CXCL12-CXCR4 chemokine signaling in bone marrow stromal cell niches. *Immunity* **25**, 977–988 (2006).
- Sacchetti, B. *et al.* Self-renewing osteoprogenitors in bone marrow sinusoids can organize a hematopoietic microenvironment. *Cell* **131**, 324–336 (2007).
- Méndez-Ferrer, S. *et al.* Mesenchymal and haematopoietic stem cells form a unique bone marrow niche. *Nature* **466**, 829–834 (2010).
- Omatsu, Y. *et al.* The essential functions of adipo-osteogenic progenitors as the hematopoietic stem and progenitor cell niche. *Immunity* **33**, 387–399 (2010).
- Butler, J. M. *et al.* Endothelial cells are essential for the self-renewal and repopulation of Notch-dependent hematopoietic stem cells. *Cell Stem Cell* **6**, 251–264 (2010).
- Kobayashi, H. *et al.* Angiocrine factors from Akt-activated endothelial cells balance self-renewal and differentiation of haematopoietic stem cells. *Nature Cell Biol.* **12**, 1046–1056 (2010).
- Broudy, V. C. Stem cell factor and hematopoiesis. *Blood* **90**, 1345–1364 (1997).
- Russell, E. S. Hereditary anemias of the mouse: a review for geneticists. *Adv. Genet.* **20**, 357–459 (1979).
- Ogawa, M. *et al.* Expression and function of c-kit in hemopoietic progenitor cells. *J. Exp. Med.* **174**, 63–71 (1991).
- Czechowicz, A., Kraft, D., Weissman, I. L. & Bhattacharya, D. Efficient transplantation via antibody-based clearance of hematopoietic stem cell niches. *Science* **318**, 1296–1299 (2007).
- Barker, J. E. *Sl/Sl^{fl}* hematopoietic progenitors are deficient *in situ*. *Exp. Hematol.* **22**, 174–177 (1994).
- Barker, J. E. Early transplantation to a normal microenvironment prevents the development of Steel hematopoietic stem cell defects. *Exp. Hematol.* **25**, 542–547 (1997).
- Wolf, N. S. Dissecting the hematopoietic microenvironment. III. Evidence for a positive short range stimulus for cellular proliferation. *Cell Tissue Kinet.* **11**, 335–345 (1978).
- Heinrich, M. C. *et al.* Constitutive expression of steel factor gene by human stromal cells. *Blood* **82**, 771–783 (1993).
- Blair, H. C., Julian, B. A., Cao, X., Jordan, S. E. & Dong, S. S. Parathyroid hormone-regulated production of stem cell factor in human osteoblasts and osteoblast-like cells. *Biochem. Biophys. Res. Commun.* **255**, 778–784 (1999).
- Kimura, Y. *et al.* c-Kit-mediated functional positioning of stem cells to their niches is essential for maintenance and regeneration of adult hematopoiesis. *PLoS ONE* **6**, e26918 (2011).
- Kim, I., He, S., Yilmaz, O. H., Kiel, M. J. & Morrison, S. J. Enhanced purification of fetal liver hematopoietic stem cells using SLAM family receptors. *Blood* **108**, 737–744 (2006).
- Morikawa, S. *et al.* Prospective identification, isolation, and systemic transplantation of multipotent mesenchymal stem cells in murine bone marrow. *J. Exp. Med.* **206**, 2483–2496 (2009).
- de Boer, J. *et al.* Transgenic mice with hematopoietic and lymphoid specific expression of Cre. *Eur. J. Immunol.* **33**, 314–325 (2003).
- Srinivas, S. *et al.* Cre reporter strains produced by targeted insertion of EYFP and ECFP into the ROSA26 locus. *BMC Dev. Biol.* **1**, 4 (2001).
- Liu, F. *et al.* Expression and activity of osteoblast-targeted Cre recombinase transgenes in murine skeletal tissues. *Int. J. Dev. Biol.* **48**, 645–653 (2004).
- Koni, P. A. *et al.* Conditional vascular cell adhesion molecule 1 deletion in mice: impaired lymphocyte migration to bone marrow. *J. Exp. Med.* **193**, 741–754 (2001).
- Adams, G. B. *et al.* Stem cell engraftment at the endosteal niche is specified by the calcium-sensing receptor. *Nature* **439**, 599–603 (2006).
- Yamazaki, S. *et al.* Nonmyelinating schwann cells maintain hematopoietic stem cell hibernation in the bone marrow niche. *Cell* **147**, 1146–1158 (2011).
- Liu, P., Jenkins, N. A. & Copeland, N. G. A highly efficient recombineering-based method for generating conditional knockout mutations. *Genome Res.* **13**, 476–484 (2003).
- Rodriguez, C. I. *et al.* High-efficiency deleter mice show that FLPe is an alternative to Cre-loxP. *Nature Genet.* **25**, 139–140 (2000).
- Ruzankina, Y. *et al.* Deletion of the developmentally essential gene *ATR* in adult mice leads to age-related phenotypes and stem cell loss. *Cell Stem Cell* **1**, 113–126 (2007).
- Schwenk, F., Baron, U. & Rajewsky, K. A cre-transgenic mouse strain for the ubiquitous deletion of loxP-flanked gene segments including deletion in germ cells. *Nucleic Acids Res.* **23**, 5080–5081 (1995).
- Tronche, F. *et al.* Disruption of the glucocorticoid receptor gene in the nervous system results in reduced anxiety. *Nature Genet.* **23**, 99–103 (1999).
- DeFalco, J. *et al.* Virus-assisted mapping of neural inputs to a feeding center in the hypothalamus. *Science* **291**, 2608–2613 (2001).
- Balordi, F. & Fishell, G. Hedgehog signaling in the subventricular zone is required for both the maintenance of stem cells and the migration of newborn neurons. *J. Neurosci.* **27**, 5936–5947 (2007).
- Mignone, J. L., Kukekov, V., Chiang, A. S., Steindler, D. & Enikolopov, G. Neural stem and progenitor cells in nestin-GFP transgenic mice. *J. Comp. Neurol.* **469**, 311–324 (2004).
- Hu, Y. & Smyth, G. K. ELDA: extreme limiting dilution analysis for comparing depleted and enriched populations in stem cell and other assays. *J. Immunol. Methods* **347**, 70–78 (2009).

Supplementary Information is linked to the online version of the paper at www.nature.com/nature.

Acknowledgements This work was supported by the Howard Hughes Medical Institute (HHMI) and the National Heart, Lung and Blood Institute (5R01HL097760). L.D. was supported by a Helen Hay Whitney Foundation Fellowship and by the HHMI. G.E. was supported by the National Institute of Aging (R01AG040209) and NYSYSTEM. We thank M. White and D. Adams for flow cytometry, E. Hughes at the UM transgenic core for helping to generate *Scf^{flp}* and *Scf^{fl}* mice, M. Purkey for technical assistance, J. Peyer and M. Lim for discussion, and C. Mountford, S. Grove and R. Coolon for managing the mouse colony. This work was initiated in the Life Sciences Institute at the University of Michigan then completed at Children's Research Institute at UT Southwestern.

Author Contributions L.D. performed all of the experiments. T.L.S. helped to design and generate the *Scf^{fl}* and *Scf^{flp}* mice. G.E. generated the nestin-*Cherry* transgenic mice. L.D. and S.J.M. designed the experiments, interpreted the results and wrote the manuscript.

Author Information The microarray data were deposited in the Gene Expression Omnibus (<http://www.ncbi.nlm.nih.gov/geo/>) under accession number GSE33158. Reprints and permissions information is available at www.nature.com/reprints. The authors declare no competing financial interests. Readers are welcome to comment on the online version of this article at www.nature.com/nature. Correspondence and requests for materials should be addressed to S.J.M. (Sean.Morrison@UTSouthwestern.edu).

METHODS

Mice. Targeting vectors for making *Scf^{flp}* and *Scf^{fl}* mice were constructed by recombineering³⁴. Linearized targeting vector was electroporated into W4 (*Scf^{flp}*) or Bruce4 (*Scf^{fl}*) embryonic stem (ES) cells. Positive clones were identified by Southern blotting and injected into B6 or C57BL/6-Tyr^{c-2j} blastocysts. Chimaeric mice were bred with B6 or C57BL/6-Tyr^{c-2j} mice to obtain germline transmission. The *Frt*-flanked *Neo* cassette was subsequently removed by mating with *Flpe* mice³⁵. *Scf^{flp}* mice were backcrossed at least five times and *Scf^{fl}* mice were backcrossed at least three times onto a C57BL/Ka background before analysis. Note that *Scf^{fl}* mice were backcrossed fewer times before analysis because Bruce4 ES cells were from a substantially C57BL/6 background. *Ubc-creER*³⁶, *CMV-cre*³⁷, *Vav1-cre*³⁸, *nestin-cre*³⁸, *Tie2-cre*³¹, *Lepr-cre*³⁹ and *loxP-EYFP*²⁹ mice were obtained from the Jackson Laboratory and maintained by crossing with C57BL/Ka mice. *Col2.3-cre* mice on a C57BL/6 background were provided by B. Cream and F. Liu³⁰. *Nestin-creER* mice were obtained from G. Fishell and backcrossed onto a C57BL/Ka background⁴⁰. *Nestin-GFP* mice were as previously described⁴¹. C57BL/6-SJL (CD45.1) mice were used as recipients in transplantation experiments. All mice were housed in the Unit for Laboratory Animal Medicine at the University of Michigan. All protocols were approved by the University of Michigan Committee on the Use and Care of Animals. Unless otherwise indicated, data are mean \pm s.d. and two-tailed Student's *t*-tests were used to assess statistical significance (**P* < 0.05, ***P* < 0.01, ****P* < 0.001).

Genotyping PCR. Primers for genotyping *Scf^{flp}* were: OLD291, 5'-CCCGC AGCTCTGGTATATTTGC-3'; OLD292, 5'-CGGACAGCTGAACCTGTGG-3'; and OLD360, 5'-AAGCACTTCAGATTCTAGGG-3'. Primers for genotyping *Scf^{fl}* were: OLD301, 5'-GGAAAAGAACCAAGTGAAGTC-3'; and OLD302, 5'-GTCCGCAGCAAGCTCACCAGC-3'. Primers for genotyping *Scf* were: OLD301, 5'-GGAAAAGAACCAAGTGAAGTC-3'; and OLD304, 5'-ACGG GGAAAGACCTCCGGTCC-3'. Primers for genotyping *Tie2-cre* were: OLD438, 5'-CCTGTGCTCAGACAGAAATG-3'; and OLD435, 5'-GGCAAA TTTTGGTGTACGGTC-3'. Primers for genotyping *Lepr-cre* were: OLD434, 5'-CATTGTATGGGATCTGATCTGG-3'; and OLD435, 5'-GGCAAATTTTG GTGTACGGTC-3'.

Tamoxifen administration. Tamoxifen citrate (Sigma or Spectrum Chemical) was administered in chow at 400 mg kg⁻¹ with 5% sucrose (Harlan). Mice were fed tamoxifen chow for 1–5 months before being analysed.

Long-term competitive reconstitution assay and limit dilution assay. Adult recipient mice were lethally irradiated by a Cesium 137 GammaCell40 Irradiator (MDS Nordia) at 300 rad per minute with two doses of 540 rad (total 1,080 rad) delivered at least 2 h apart. Cells were transplanted by retro-orbital sinus injection of anaesthetized mice. 3×10^5 fetal liver or bone marrow cells were transplanted along with 3×10^5 recipient bone marrow cells into each irradiated mouse unless otherwise indicated. Mice were maintained on antibiotic water (neomycin sulphate 1.11 g l⁻¹ and polymyxin B 0.121 g l⁻¹) for 14 days then switched to regular water. Recipient mice were periodically bled to assess the level of donor-derived blood lineages, including myeloid, B and T cells for at least 16 weeks. Blood was subjected to ammonium chloride potassium red cell lysis before antibody staining. Antibodies including anti-CD45.2 (104), anti-CD45.1 (A20), anti-Gr1 (8C5), anti-Mac-1 (M1/70), anti-B220 (6B2) and anti-CD3 (KT31.1) were added to stain cells. Stained samples were analysed by flow cytometry. For limit dilution assay on *Ubc-creER*; *Scf^{fl/fl}* mice, three doses of donor bone marrow cells (2×10^4 , 5×10^4 and 1.5×10^5) along with 3×10^5 recipient bone marrow cells were transplanted into irradiated mice. For limit dilution assay on *Lepr-cre*; *Scf^{fl/gfp}* mice, 2×10^4 , 5×10^4 or 1×10^5 bone marrow cells along with 3×10^5 recipient bone marrow cells were competitively transplanted into irradiated mice. After 16 weeks, the percentage of mice that were not multilineage reconstituted by donor haematopoietic cells was plotted against cell dose. ELDA software was used to calculate HSC frequency and statistical significance (<http://bioinf.wehi.edu.au/software/elda/>).

Flow cytometry. Bone marrow cells were isolated by flushing the long bones or by crushing the long bones with mortar and pestle in Ca²⁺ and Mg²⁺ free HBSS with 2% heat-inactivated bovine serum. Spleen cells were obtained by crushing the spleen between two glass slides. The cells were drawn by passing through a 25G needle several times and filtered with a 70 μ m nylon mesh. The following

antibodies were used to stain HSCs: anti-CD150 (TC15-12F12.2), anti-CD48 (HM48-1), anti-CD41 (MWReg30), anti-Sca-1 (E13-161.7), anti-cKit (2B8), lineage markers (anti-Ter119, anti-B220 (6B2), anti-Gr1 (8C5), anti-CD2 (RM2-5), anti-CD3 (17A2), anti-CD5 (53-7.3) and anti-CD8 (53-6.7). DAPI was used to exclude dead cells. For flow cytometric analysis of *Scf*-GFP⁺ or *Lepr-cre*; *loxP-EYFP*⁺ stromal cells, bone marrow was flushed using HBSS with 2% bovine serum. Then whole bone marrow was digested with Collagenase IV (200 U ml⁻¹) and DNase I (200 U ml⁻¹) at 37 °C for 15 min. Samples were then stained with antibodies and analysed by flow cytometry. Anti-CD140a (APAs), anti-CD140b (APB5), anti-CD45 (30F-11) and anti-Ter119 antibodies were used to stain perivascular stromal cells. For analysis of bone marrow endothelial cells, mice were intravenously injected with 10 μ g per mouse Alexa Fluor 647 conjugated anti-VE-cadherin antibody (BV13, eBiosciences)¹⁴. Ten minutes later, the long bones were removed and bone marrow was flushed, digested and stained as above. Samples were run on FACSaria II or FACSCanto II flow cytometers. Data were analysed by FACSDiva (BD) or FlowJo (Tree Star) software.

Methylcellulose culture. Cells were sorted into methylcellulose culture medium (3434, Stemcell Technology) and incubated at 37 °C as described⁸.

Bone sectioning and immunostaining. Freshly dissected long bones were fixed in a formalin-based fixative at 4 °C for 3 h. Then the bones were embedded in 8% gelatin in PBS. Samples were snap frozen with liquid nitrogen and stored at -80 °C. Bones were sectioned using CryoJane (Instrumedics). Sections were dried overnight at room temperature (~22 °C) and stored at -80 °C. Sections were re-hydrated in PBS for 5 min before immunostaining. 5% goat serum in PBS was used for blocking. Primary antibodies were applied to the slides for 1 h at room temperature followed by secondary antibody incubation for 30 min at room temperature with repetitive washes in between. Slides were mounted with anti-fade prolong gold (Invitrogen) and images were acquired on an Olympus IX81 microscope or a Leica SP5 confocal microscope. Primary antibodies were: chicken-anti-GFP (Aves), rat-anti-endoglin (eBioscience), goat-anti-osteopontin (R&D), rat-anti-mouse pan-endothelial cell antigen (Meca32, Biolegend) and rabbit-anti-Cherry (Clontech).

qRT-PCR. Cells were sorted directly into Trizol. Total RNA was extracted according to manufacturer's instructions. Total RNA was subjected to reverse transcription or amplification using the WT-Ovation Pico RNA Amplification System (Nugen). Quantitative real-time PCR was run using SYBR green on a LightCycler 480 (Roche). β -Actin was used to normalize the RNA content of samples. Primers used in this study were: *Scf*: OLD405, 5'-TTGTACCT TCGCACAGTGG-3'; and OLD406, 5'-AATTCAGTGCAGGGTTCACA-3'; *Cxcl12*: OLD35, 5'-TGCATCAGTGCAGGTAAACCA-3'; and OLD36, 5'-GTTGTTCTTCAGCCGTGCAA-3'; *Alpl*: OLD164, 5'-TTGTGCCAGAGAAA GAGAGAGA-3'; and OLD165, 5'- GTTTCAGGGCATTTTTCAAGGT-3'; *Tie2*: OLD158, 5'-ATGTGGAAGTCGAGAGGCGAT-3'; and OLD159, 5'-CGAATAGCCATCCACTATTGTCC-3'; *Lepr*: OLD418, 5'-TGATGTGTCA GAAATTCTATGTGG-3'; and OLD419, 5'- TGCCAGGTTAAGTGCA GCTAT-3'; *Scf* long form: 5'- GCCAGAACTAGATCCTTTACTCCTGA-3'; and 5'-ACATAAATGGTTTTGTGACACTGACTCTG-3'; *Scf* short form: 5'-CCCAGAAAAGGAAAGCCG-3'; and 5'-ATTCTCTCTCTTCTGTTGCAA CATACTT-3'; β -actin: OLD27, GCTCTTTCCAGCCTTCCTT-3'; and OLD28, 5'-CTTCTGATCCTGTCAGCAA-3'.

Gene expression profiling. Three independent, fresh isolated aliquots of approximately 5,000 *Scf*-GFP⁺ cells or whole bone marrow cells were flow cytometrically sorted into Trizol. Total RNA was extracted and amplified using the WT-Ovation Pico RNA Amplification system (Nugen) following manufacturer's instructions. Sense strand cDNA was generated using the WT-Ovation Exon Module (Nugen). Then, cDNA was fragmented and labelled using FL-Ovation DNA Biotin Module V2 (Nugen). The labelled cDNA was hybridized to Affymetrix Mouse Gene ST 1.0 chips following the manufacturer's instructions. Expression values for all probes were normalized and determined using the robust multi-array average (RMA) method⁴³.

43. Irizarry, R. A. *et al.* Exploration, normalization, and summaries of high density oligonucleotide array probe level data. *Biostatistics* **4**, 249–264 (2003).

A PGC1- α -dependent myokine that drives brown-fat-like development of white fat and thermogenesis

Pontus Boström¹, Jun Wu¹, Mark P. Jedrychowski², Anisha Korde¹, Li Ye¹, James C. Lo¹, Kyle A. Rasbach¹, Elisabeth Almer Boström³, Jang Hyun Choi¹, Jonathan Z. Long¹, Shingo Kajimura⁴, Maria Cristina Zingaretti⁵, Birgitte F. Vind⁶, Hua Tu⁷, Saverio Cinti⁵, Kurt Højlund⁶, Steven P. Gygi² & Bruce M. Spiegelman¹

Exercise benefits a variety of organ systems in mammals, and some of the best-recognized effects of exercise on muscle are mediated by the transcriptional co-activator PPAR- γ co-activator-1 α (PGC1- α). Here we show in mouse that PGC1- α expression in muscle stimulates an increase in expression of FNDC5, a membrane protein that is cleaved and secreted as a newly identified hormone, irisin. Irisin acts on white adipose cells in culture and *in vivo* to stimulate UCP1 expression and a broad program of brown-fat-like development. Irisin is induced with exercise in mice and humans, and mildly increased irisin levels in the blood cause an increase in energy expenditure in mice with no changes in movement or food intake. This results in improvements in obesity and glucose homeostasis. Irisin could be therapeutic for human metabolic disease and other disorders that are improved with exercise.

PGC1- α is a transcriptional co-activator that mediates many biological programs related to energy metabolism. Originally described as a co-activator of PPAR- γ that modulated expression of uncoupling protein 1 (UCP1) and thermogenesis in brown fat¹, it has also been shown to control mitochondrial biogenesis and oxidative metabolism in many cell types. PGC1- α is induced in muscle by exercise and stimulates many of the best-known beneficial effects of exercise in muscle: mitochondrial biogenesis, angiogenesis and fibre-type switching². It also provides resistance to muscular dystrophy and denervation-linked muscular atrophy³. The health benefits of elevated muscle expression of PGC1- α may go beyond the muscle tissue itself. Transgenic mice with mildly elevated muscle PGC1- α are resistant to age-related obesity and diabetes and have a prolonged lifespan⁴. This suggests that PGC1- α stimulates the secretion of factors from skeletal muscle that affect the function of other tissues. Here we show that PGC1- α stimulates the expression of several muscle gene products that are potentially secreted, including FNDC5. The *Fndc5* gene encodes a type I membrane protein that is processed proteolytically to form a newly identified hormone secreted into the blood, termed irisin. Irisin is induced in exercise and activates profound changes in the subcutaneous adipose tissue, stimulating browning and UCP1 expression. Importantly, this causes a significant increase in total body energy expenditure and resistance to obesity-linked insulin resistance. Thus, irisin action recapitulates some of the most important benefits of exercise and muscle activity.

Muscle PGC1- α transgenics

Mice with transgenically increased PGC1- α in muscle are resistant to age-related obesity and diabetes⁴, suggesting that these animals have a fundamental alteration in systemic energy balance. We therefore analysed the adipose tissue of the PGC1- α transgenic mice for expression of genes related to a thermogenic gene program and genes characteristic

of brown fat development. There were no significant alterations in the expression of brown-fat-selective genes in the interscapular brown adipose tissue or in the visceral (epididymal) white adipose tissue (Fig. 1a). However, the subcutaneous fat layer (inguinal), a white adipose tissue that is particularly prone to 'browning' (that is, formation of multilocular, UCP1-positive adipocytes), had significantly increased levels of *Ucp1* and *Cidea* messenger RNAs (Fig. 1b). We also observed increased UCP1 protein levels and more UCP1-positive stained multilocular cells in transgenic mice compared to controls (Fig. 1c, d). There are recent reports that exercise causes a mild increase in the expression of a thermogenic gene program in the visceral adipose tissue, a depot that has minimal expression of these genes⁵. As it is the subcutaneous white adipose depot that has the greatest tendency to turn on a thermogenic gene program and alter the systemic energy balance of mice⁶, we re-investigated this with regard to browning of the white adipose tissues in two types of exercise. Similar to what has been reported⁵, a twofold increase in *Ucp1* mRNA expression was observed in the visceral, epididymal fat with 3 weeks of wheel running (Supplementary Fig. 1). However, a much larger change (approximately 25 fold) was seen in the same mice in the subcutaneous inguinal fat depot. Similarly, a small increase in *Ucp1* mRNA expression was seen in the epididymal fat with repeated bouts of swimming in warm (32 °C) water (Supplementary Fig. 1); however a very large increase (65 fold) was observed in the inguinal white depot (Supplementary Fig. 1). Thus, muscle-specific expression of PGC1- α drives browning of subcutaneous white adipose tissue, possibly recapitulating part of the exercise program.

Media from PGC1- α -expressing myocytes

The effect on browning of the adipose tissues from PGC1- α -expressing muscle could be due to direct muscle-fat signalling or to another,

¹Dana-Farber Cancer Institute and Harvard Medical School, 3 Blackfan Circle, CLS Building, Floor 11, Boston, Massachusetts 02115, USA. ²Department of Cell Biology, Harvard Medical School, Boston, Massachusetts 02115, USA. ³Renal Division, Brigham and Women's Hospital, Harvard Medical School, Boston, Massachusetts 02115, USA. ⁴UCSF Diabetes Center and Department of Cell and Tissue Biology, University of California, San Francisco, California 94143, USA. ⁵Department of Experimental and Clinical Medicine, Università Politecnica delle Marche, Electron Microscopy Unit-Azienda Ospedali Riuniti, Ancona 60020, Italy. ⁶Diabetes Research Center, Department of Endocrinology, Odense University Hospital, DK-5000, Odense, Denmark. ⁷LakePharma, Inc., 530 Harbor Blvd, Belmont, California 94002, USA.

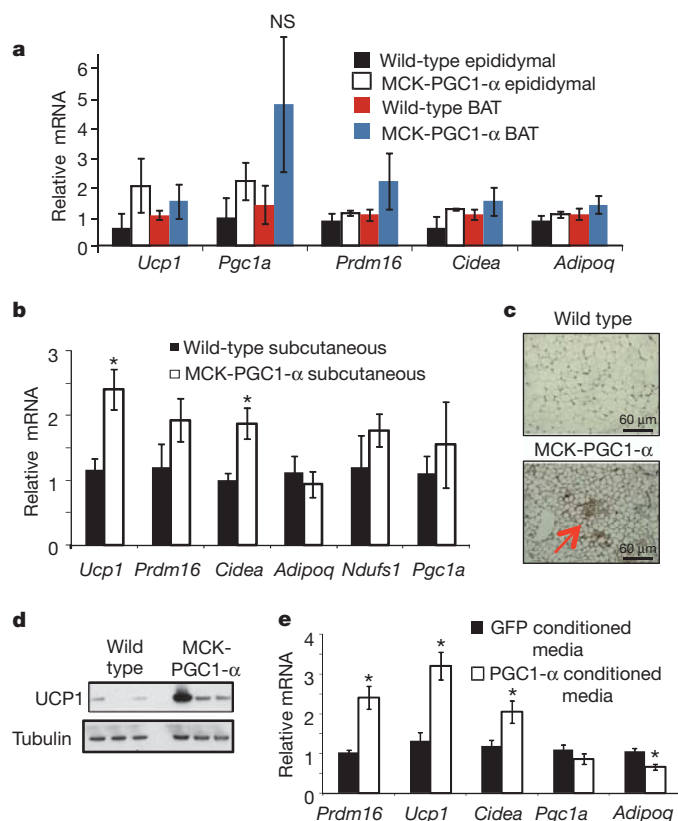


Figure 1 | Muscle-specific PGC1- α transgenic mice have increased brown/beige fat cells in the subcutaneous depot. **a**, **b**, Quantitative polymerase chain reaction (qPCR) against brown fat and thermogenic genes in epididymal fat, BAT (**a**) and subcutaneous, inguinal (**b**) fat depots in muscle creatine kinase promoter (MCK)-PGC1- α transgenic mice or littermate controls. $n = 7$ for each group, repeated in a separate cohort with similar results. **c**, Representative immunohistochemistry against UCP1 in the inguinal depot from indicated mice. **d**, Western blot against UCP1 in the inguinal fat depot ($n = 3$ and repeated in an independent cohort with similar results). **e**, qPCR against indicated genes in adipocytes differentiated for 6 days from stroma vascular fraction (SVF) cells. This was done in the presence of conditioned media from primary myocytes with forced expression of GFP or PGC1- α (representative for three independent experiments). Data are presented as mean \pm s.e.m., and $*P < 0.05$ compared to control group. Student's t -test was used for single comparisons. NS, not significant.

indirect mechanism. To investigate this, we treated cultured primary subcutaneous adipocytes with serum-free media conditioned by myocytes expressing PGC1- α or cells expressing green fluorescent protein (GFP). As shown in Fig. 1e, the media from cells expressing ectopic PGC1- α increased the mRNA levels of several brown-fat-specific genes (Fig. 1e). This suggested that PGC1- α causes the muscle cells to secrete a molecule(s) that can induce a thermogenic gene program in the cells.

Candidate, secreted PGC1- α -dependent proteins

We used a combination of Affymetrix-based gene expression arrays and an algorithm that predicts protein secretion to search for proteins that could mediate the browning of adipose tissues under the control of muscle PGC1- α (Methods). Proteins with mitochondrial targeting sequences were excluded, and all candidates were validated in gain-of-function systems for PGC1- α *in vivo* (Methods). Five proteins were identified as PGC1- α target genes in muscle and as likely to be secreted: IL-15, FNDC5, VEGF- β , LRG1 and TIMP4 (Fig. 2a). Conversely, expression of these genes was reduced in mice with muscle-specific deletion of PGC1- α (Supplementary Fig. 2). Furthermore, they were also found to be increased at the mRNA level in muscle from exercised mice (Fig. 2b). The expression of this same set of genes was also examined in muscle biopsies from human subjects before and after

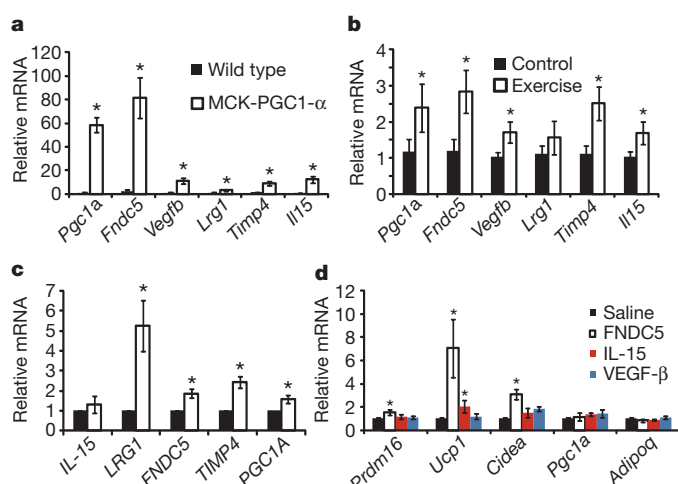


Figure 2 | FNDC5 is induced with forced PGC1- α expression or exercise, and turns on brown/beige fat gene expression. **a**, qPCR against indicated genes in skeletal muscle from MCK-PGC1- α transgenic mice or littermate controls ($n = 7$ from each group). **b**, qPCR against indicated genes in skeletal muscle from sedentary mice or mice given 3 weeks of free wheel running ($n = 10$ from each group). Mice were rested for 12 h before being killed. **c**, mRNA expression levels from human muscle biopsies before and after 10 weeks of endurance exercise training (8 subjects included). All data points are normalized to baseline levels. **d**, SVF from the inguinal fat depot, differentiated into adipocytes for 6 days in the presence of saline or recombinant FNDC5 (20 nM), IL-15 (10 μ M) or VEGF- β (50 μ M). The graph shows normalized mRNA levels of indicated genes. This experiment was repeated three times with similar results. For **d**, we performed one-way ANOVA tests where $*P < 0.05$ for the effect of FNDC5 on *Ucp1* and *Cidea* expression. All other statistics were performed using Student's t -test, and bar graphs are mean \pm s.e.m.

a controlled period of endurance exercise⁷ (Fig. 2c). *FNDC5*, *VEGFB* and *TIMP4* mRNAs were all significantly induced in humans with exercise. IL-15 has previously been reported as being secreted from muscle under the influence of exercise⁸, while the regulation of FNDC5, VEGF- β , LRG1 and TIMP4 by exercise has not been described. *FNDC5* mRNA and brown fat markers in subcutaneous fat were not regulated by acute exercise, and *FNDC5* mRNA was not induced by exposure to cold (4 $^{\circ}$ C) for 6 h (Supplementary Fig. 2).

Fndc5 induces a browning in vitro

Several of the proteins encoded by these genes were commercially available, so they were applied directly to primary subcutaneous white adipocytes during differentiation. Factors such as IL-15 or VEGF- β had minimal effects on the expression of *Ucp1* and other brown fat genes at concentrations of 200 nM or higher. However, FNDC5 promoted a sevenfold induction of *Ucp1* mRNA at a concentration of 20 nM (Fig. 2d). The transcriptional changes induced by FNDC5 were addressed on a global scale using gene expression arrays (Supplementary Fig. 3). Notably, *Ucp1* and three other known brown fat genes, *Elovl3*, *Cox7a1* and *Otop1*, were among the eight most upregulated genes (Supplementary Fig. 4). Conversely, genes characteristic of white fat development were downregulated, such as leptin (Supplementary Fig. 3). These data indicate that the activation of browning and thermogenic genes by FNDC5 is a major part of the action of this polypeptide on these cells.

The effects of FNDC5 treatment were remarkably robust; *Ucp1* mRNA was increased 7–500 fold in more than ten experiments using FNDC5 at a concentration of 20 nM (Fig. 3a and Supplementary Fig. 5). Moreover, we could demonstrate a clear dose-dependence, with an effective range between 20–200 ng ml⁻¹ (1.5–15 nM) (Fig. 3b). In contrast, BMP7, reported as a potent inducer of browning⁹, had a much smaller effect (maximum of twofold) on the same cells at 3.3 μ M (Fig. 3a).

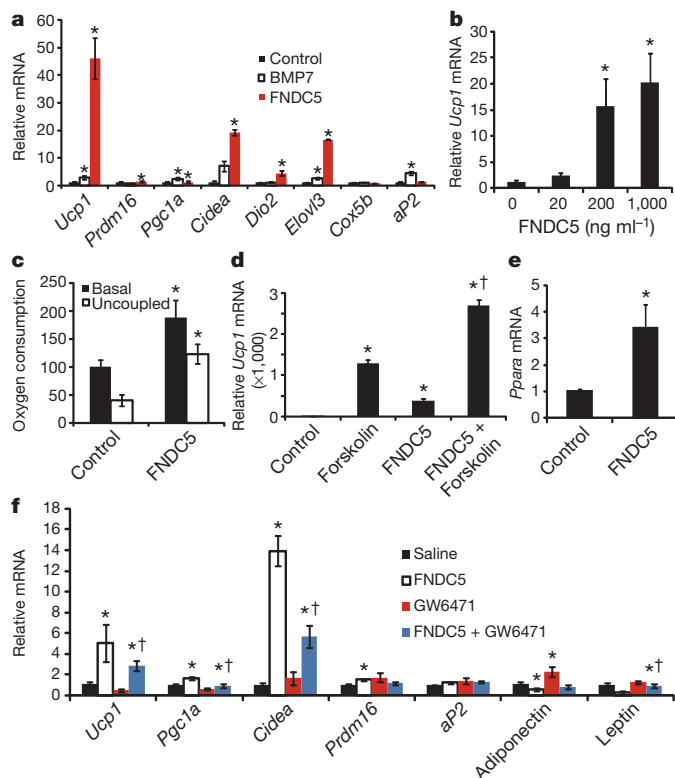


Figure 3 | FNDC5 is a potent inducer of the brown/beige fat gene program
a, SVF from the inguinal fat depot was differentiated into adipocytes for 6 days in the presence of saline, recombinant FNDC5 (20 nM) or BMP7 (3.3 μ M). The graph shows normalized mRNA levels for indicated genes. Similar results were obtained in more than 10 experiments with the fold induction of *Ucp1* between 7–500 fold. **b**, mRNA levels of *Ucp1* from inguinal-derived SVF treated with FNDC5 for 6 days at indicated doses. **c**, Clark electrode measurements of oxygen consumption in SVF from the inguinal fat depot, differentiated into adipocytes for 6 days in the presence of saline or recombinant FNDC5 (20 nM). Data are representative for three independent experiments and normalized to total cellular protein. **d**, qPCR of *Ucp1* mRNA from SVF, differentiated into adipocytes, and treated with FNDC5 or saline for 6 days followed by addition of forskolin for 8 h. $\dagger P < 0.05$ compared to forskolin treatment. **e**, qPCR of *Ppara* after 6 days of FNDC5 treatment (20 nM) during differentiation of primary SVF. **f**, SVF differentiated into adipocytes and treated with FNDC5 and/or GW6471 for 6 days. The graph shows qPCR of indicated genes. $\dagger P < 0.05$ compared to FNDC5 treatment. For **d** and **f**, combined one- and two-way ANOVA was used. $*P < 0.05$. All other statistics were performed using Student's *t*-test, and bar graphs are mean \pm s.e.m.

We also used immunohistochemistry to study cells treated with FNDC5 and observed a robust increase in UCP1-positive adipocytes with multilocular lipid droplets (Supplementary Fig. 4). Electron microscopic analysis of FNDC5-treated cells showed a higher density of mitochondria compared to control cells, consistent with a brown-fat-like phenotype and elevated mitochondrial gene expression (Supplementary Fig. 5). The sizes of mitochondria, however, were similar between groups (Supplementary Fig. 4). Lastly, measurements of oxygen consumption provided functional evidence of increased energy expenditure with FNDC5 exposure. Total oxygen consumption was greatly increased (100%) by 20 nM of FNDC5, and the majority of this respiration was uncoupled (Fig. 3c). Thus, FNDC5 potently induces thermogenesis and a brown-fat-like gene program in cultured adipocytes. In marked contrast, FNDC5 showed little or no effects on the classical brown fat cells isolated from the interscapular depot (Supplementary Fig. 4).

We sought to define the timeframe during the differentiation process when FNDC5 was effective. FNDC5 was applied to cells in 2-day windows from day 0–6, and this was compared to cells to which the protein was added during the entire 6-day differentiation process. As

shown in Supplementary Fig. 5, treatment during days 3–6 was effective at inducing *Ucp1* mRNA, although not as effective as when FNDC5 was present throughout the differentiation process. Furthermore, treatment during the initial 2 days had no effect on *UCP1* levels, suggesting that FNDC5 acts mainly during the differentiation process of cells committed to the adipocyte lineage. Cyclic AMP (cAMP) is an important signalling pathway in thermogenesis, promoting the brown-fat gene program downstream of β -adrenergic stimulation. We therefore asked whether FNDC5 effects were additive or redundant with cAMP signalling. As shown in Fig. 3d, FNDC5-exposed cells increase UCP1 expression in an additive manner when exposed to forskolin, an adenylyl cyclase activator. Two-way ANOVA tests demonstrated that there was a significant ($P < 0.01$) interaction between FNDC5 and forskolin treatment, indicating synergistic effects.

PPAR- α acts downstream of *Fndc5*

A key question is how FNDC5 is able to stimulate a thermogenic gene program. One potentially important transcription factor induced by FNDC5, identified using gene expression arrays, was PPAR- α . This nuclear receptor has been shown to drive *Ucp1* expression and several other genes involved in browning of adipose cells¹⁰. *Ppara* is increased threefold at the mRNA level by FNDC5 treatment (Fig. 3e). Importantly, the FNDC5-mediated increase in UCP1 was significantly reduced when cells were simultaneously subjected to the selective PPAR- α antagonist GW6471 (Fig. 3f). The functional interaction between the FNDC5 and GW6471 treatments on *UCP1* expression was confirmed using two-way ANOVA ($P < 0.05$). Conversely, the PPAR- α antagonist normalized the reduction seen in white adipose genes leptin and adiponectin after FNDC5 treatment. Together, these data indicate that FNDC5 acts to induce *Ucp1* gene expression, at least in part, via PPAR- α .

Irisin is a cleaved and secreted fragment of *Fndc5*

FNDC5 (also known as FRCP2 and PeP), was previously shown to have a signal peptide, two fibronectin domains and one hydrophobic domain that is likely to be membrane inserted^{11,12} (Fig. 4a). Previous studies did not investigate whether part of this protein might be secreted^{11,12}. With this structure in mind, we considered the possibility that FNDC5 might be synthesized as a type I membrane protein, followed by proteolytic cleavage and release of the amino (N)-terminal part of the protein into the extracellular space. Thus, any carboxy (C)-terminal or N-terminal tags would be lost during processing of the mature protein or interfere with localization. Indeed, expression of a C-terminally Flag-tagged FNDC5 (Fig. 4a) did not result in any Flag immunoreactivity in the media from cells expressing this construct (Fig. 4b). However, when we immunoblotted the same samples with an antibody that recognizes the endogenous FNDC5 protein, we could easily detect substantial amounts of FNDC5 in the media at approximately 32 kilodalton (kDa): this is slightly larger than the cellular FNDC5 (Fig. 4b). These data indicate that FNDC5 is C-terminally cleaved, secreted and possibly further modified.

Western blot of media fractions with antibodies against wild-type FNDC5 showed multiple bands, suggestive of glycosylation, a common feature of secreted proteins. Treatment of supernatants from FNDC5-expressing cells with peptide N-glycosidase F (PNGase F) resulted in a significant size decrease as detected by SDS-polyacrylamide gel electrophoresis (SDS-PAGE), from 32 kDa to 20 kDa (Fig. 4c).

Mass spectrometry was used to determine the sequence of the FNDC5-derived polypeptide found in the media (Methods). To do this, we fused the N terminus of FNDC5 (without the signal peptide) to the C terminus of the crystallisable fragment (Fc) domain of immunoglobulin G (IgG). After purification and enzymatic deglycosylation of the secreted material, mass spectrometry analyses indicated that secreted FNDC5 was truncated at glutamic acid 112 (not including the signal sequence), as shown in Fig. 4e. The secreted portion of FNDC5 has remarkable conservation between species, with 100% identity between

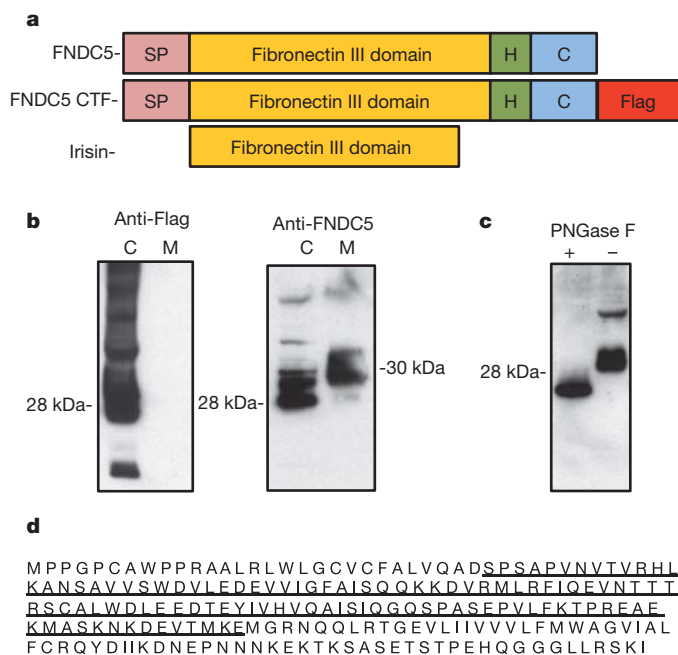


Figure 4 | FNDC5 is proteolytically cleaved and secreted from cells.

a, Schematic representation of the FNDC5 protein structure (top), Flag-tagged FNDC5 protein (middle) and irisin (bottom). C, C-terminal domain; H, hydrophobic domain; SP, signal peptide. **b**, HEK 293 cells transfected with a vector expressing the C-terminal Flag-tagged FNDC5 (CTF-F5, third panel from **a**), followed by isolation of cell and culture media protein. Samples were adjusted for protein content and western blots were performed against the Flag antigen (left) or FNDC5 (right). This was repeated in several experiments with similar results. Adjusting for volume (instead of protein content) also gave similar results. C, cell fraction; M, media fraction. Arrows indicate molecular weight. **c**, HEK 293 cells transfected with a vector expressing FNDC5-CTF, followed by isolation of cell and media protein. Respective protein fraction was then treated with PNGase F followed by western blot against FNDC5 after SDS-PAGE. **d**, Representation of the full-length FNDC5 and the irisin fragment mapped by mass spectrometry (underlined).

mice and humans (Supplementary Fig. 6). Because this distinct, secreted polypeptide has not been previously described and signals from muscle to other tissues we named it irisin, after Iris, the Greek messenger goddess.

The ability of the anti-FNDC5 antibodies to react with irisin allowed us to investigate the contribution made by irisin to the browning activity caused by muscle cells expressing PGC1- α . Media conditioned by muscle cells that had forced expression of PGC1- α were incubated with control or anti-FNDC5 antibodies before they were applied to the fat cell cultures. As shown in Supplementary Fig. 6, the FNDC5 antibody caused a marked reduction in the ability of the PGC1- α conditioned media to induce *Ucp1* and *Cidea* mRNA in the primary inguinal cells. This suggests that irisin accounts for a significant fraction of this activity found in secreted media from muscle cells with forced PGC1- α expression. We cannot, however, exclude the possibility that other factors might also contribute to this response.

Irisin is present in mouse and human plasma

We next analysed levels of irisin in plasma from wild-type mice, using intravenous adenoviral delivery of full-length FNDC5 as a positive control. This method results in strong forced expression from the liver and potential secretion to the plasma, where we detected irisin using western blot after albumin/IgG-depletion and deglycosylation. As seen in Fig. 5a, FNDC5-expressing virus resulted in a clear increase in an immunoreactive band at 22 kDa. Importantly, this was the only band altered on these blots. Using western blots of purified FNDC5 protein as a quantitative standard, irisin is present in the plasma of control mice at a concentration of approximately 40 nM. We also

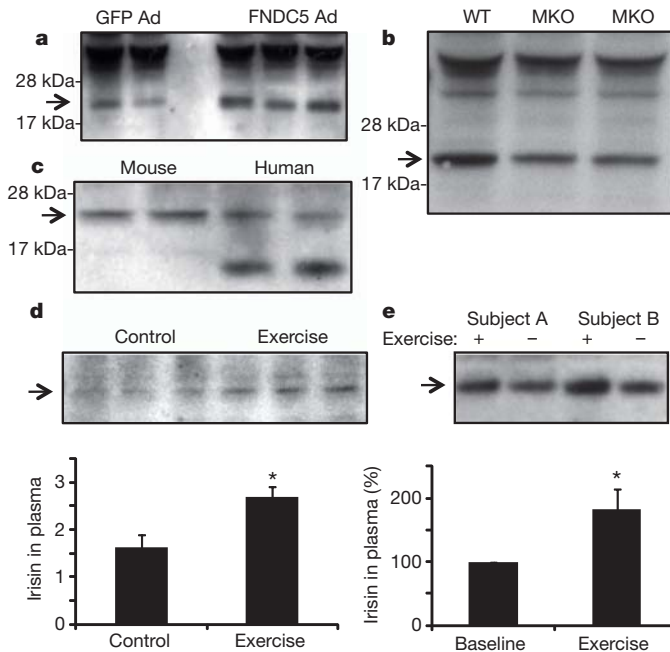


Figure 5 | Detection of irisin in mouse and human plasma. **a**, Plasma from mice injected intravenously with adenoviral vectors (Ad) expressing FNDC5 or GFP was subjected to western blot against FNDC5. **b**, Western blot against irisin in plasma from muscle-specific PGC1- α knockout (MKO) mice or control littermates (flox/flox). WT, wild type. **c**, Western blot against irisin in plasma from wild-type mice or two healthy human subjects (representative for 8 subjects analysed identically). **d**, Western blot against irisin in serum from control or 3 weeks exercised mice, followed by 12 h rest. Bottom panel shows quantification of the bands. **e**, Western blot analysis of irisin in plasma from human subjects before and after 10 weeks of endurance exercise. Eight subjects in total were analysed; quantification after internal normalization is displayed in bottom panel. For all plasma analyses, samples were depleted for albumin/IgG, and deglycosylated using PNGase F. Arrow indicated irisin band. Data are presented as mean \pm s.e.m., and $*P < 0.05$ compared to control group. Student's *t*-test was used for single comparisons.

analysed plasma of PGC1- α muscle-specific knockout mice as a negative control, and the irisin band at 22 kDa was decreased by 72% in these animals (Fig. 5b). Furthermore, an immunoreactive band of identical electrophoretic mobility was found in plasma from healthy human subjects (Fig. 5c). This band was greatly diminished when the anti-FNDC5 antibody was neutralized with an excess of antigen (Supplementary Fig. 7).

We examined blood levels of irisin after exercise in mice and human subjects. Mice had significantly elevated (65%) plasma concentrations of irisin after they were subjected to 3 weeks of free wheel running (Fig. 5d). Similar analyses in healthy adult humans subjected to supervised endurance exercise training for 10 weeks revealed a twofold increase in the circulating irisin levels compared to the non-exercised state (Fig. 5e). Thus, irisin is present in mouse and human plasma, and is increased with exercise. The increase in circulating protein in both species is roughly proportional to the increases observed at the mRNA level in muscle (Fig. 2c).

Irisin reduces obesity and insulin resistance

We used adenoviral vectors to express full-length FNDC5 (or a control GFP) and examined its biological and therapeutic effects. This method resulted in a 15-fold increase in liver *Fndc5* mRNA, although the liver expresses very low endogenous levels of this mRNA. Plasma levels of irisin were increased 3–4 fold (Fig. 5a). The mice did not display any adverse reaction, and upon gross pathological examination, there was no apparent toxicity in any major organ system. There was also no increase in plasma AST levels, and inflammatory genes were not significantly altered in the liver when the two groups were compared

(Supplementary Fig. 8). Ten days after injection, *Ucp1* mRNA was increased by 13-fold in the subcutaneous depot relative to the same depot in mice receiving the virus expressing GFP (Fig. 6a,b); *Cidea* was also significantly upregulated (Fig. 6a). There were no changes in expression of UCP1 in the interscapular classical brown fat (BAT), but we did observe a minor elevation in *Prdm16* and *Pgc1a* mRNA (Supplementary Fig. 8). The changes in gene expression in the subcutaneous adipose tissues were accompanied by a clear increase in the number of UCP1-positive, multilocular adipocytes (Fig. 6c). We did not, however, detect any change in body weight in the GFP versus FNDC5 groups of animals. We observed similar results in young C57BL/6 mice (Supplementary Fig. 9). Thus, moderate increases in circulating irisin can induce browning of white adipose tissues *in vivo*, including increased expression of UCP1.

As activation of the classical brown fat or browning of white fat has been shown to improve obesity and glucose homeostasis *in vivo*^{6,13}, we delivered FNDC5-expressing adenovirus to mice rendered obese and insulin-resistant by feeding a high fat diet. We chose C57BL/6 mice for these experiments because they are highly prone to diet-induced obesity and diabetes. The expression of irisin increased *Ucp1* gene expression to the same degree as in lean mice (Supplementary Fig. 9).

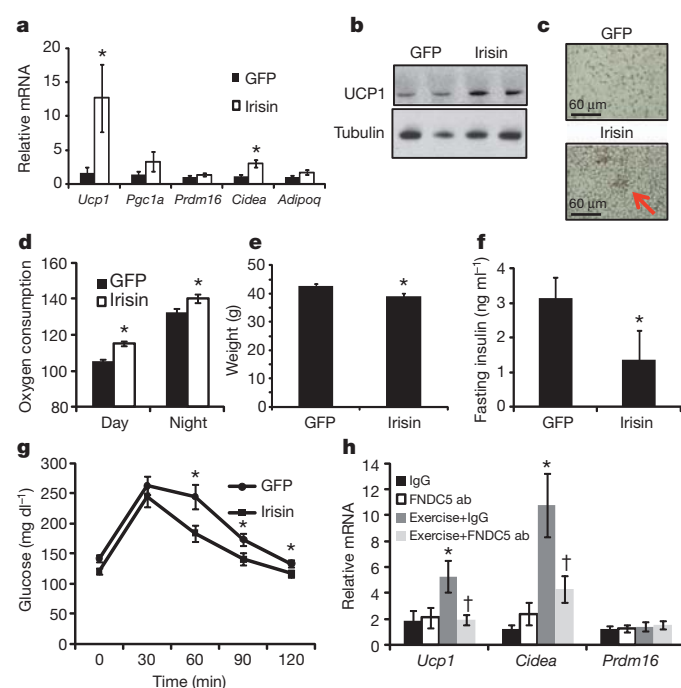


Figure 6 | Irisin induces browning of white adipose tissues *in vivo* and protects against diet-induced obesity and diabetes. a–c, Wild-type BALB/c mice were injected with 10^{10} GFP- or FNDC5-expressing adenoviral particles intravenously ($n = 7$ for each group). a, b, Animals were killed after 10 days and inguinal/subcutaneous fat pads were collected and analysed using qPCR analysis of indicated mRNAs (a) and western blot against UCP1 (b). c, Representative images from immunohistochemistry against UCP1 in these mice. All results in a–c were repeated two times with similar results. d–g, C57BL/6 mice fed a 60% kcal high-fat diet for 20 weeks were intravenously injected with GFP- or FNDC5-expressing adenovirus and all analyses were done 10 days thereafter ($n = 7$ for both groups). d, Oxygen consumption at day and night. e, Body weights of mice 10 days after injection with indicated adenovirus. f, Fasting plasma insulin measured using enzyme-linked immunosorbent assay (ELISA). g, Intraperitoneal glucose tolerance test. h, Mice were injected intraperitoneally with 50 μ g of rabbit IgG or a rabbit anti-FNDC5 antibody (ab) and were either subjected to swimming for 7 days or kept sedentary ($n = 10$ for all groups). Data show mRNA expression levels from inguinal white adipose tissue. All data in d–j were performed at least twice in a separate mouse cohort with similar results. $\dagger P < 0.05$ compared to exercise and IgG. One-way ANOVA was used for statistics in h. All other statistics were performed using Student's *t*-test, and bar graphs are mean \pm s.e.m.

There was also an elevation in expression of several mitochondrial genes (Supplementary Fig. 8). Notably, these changes occurred with only moderately increased irisin blood levels, threefold compared to the GFP-expressing mice. This effect was accompanied with a large increase in oxygen consumption (Fig. 6d), consistent with the gene expression data, and body weights of the irisin-expressing mice were slightly reduced after 10 days compared to GFP-expressing controls (Fig. 6e). These effects of irisin on mitochondrial gene expression in the fat were not seen in skeletal muscle *in vivo* or in cultured myocytes (Supplementary Fig. 10). Irisin expression in the mice fed a high fat diet caused a significant improvement in glucose tolerance when compared to the control mice expressing GFP. In addition, fasting insulin was also reduced (Fig. 6f,g). These data illustrate that even moderately increased levels of circulating irisin potentially increase energy expenditure, reduce body weight and improve diet-induced insulin resistance.

Finally, we asked whether irisin is required for the exercise-induced effects on the subcutaneous white fat. Injection of anti-FNDC5 antibodies into mice before 10 days of swim training dramatically reduced the effect of this exercise on *Ucp1* and *Cidea* gene expression, compared to injection of control antibodies (Fig. 6h). In contrast, *Prdm16* mRNA levels were not increased with exercise and were also not affected by the anti-FNDC5 antibodies. Thus, irisin is required for a substantial part of the effect of exercise on these gene expression events in the browning of white fat.

Discussion

Exercise has the capacity to improve metabolic status in obesity and type 2 diabetes, but the mechanisms are poorly understood. Importantly, exercise increases whole body energy expenditure beyond the calories used in the actual work performed¹⁴. However, the relative contribution of the adipose tissues to this phenomenon has not been clarified. Because transgenic mice expressing PGC1- α selectively in muscle showed a remarkable resistance to age-related obesity and diabetes⁴, we sought factors secreted from muscle under the control of this co-activator that might increase whole body energy expenditure. We describe a new polypeptide hormone, irisin, which is regulated by PGC1- α , secreted from muscle into blood and activates thermogenic function in adipose tissues. Irisin is remarkable in several respects. First, it has powerful effects on the browning of certain white adipose tissues, both in culture and *in vivo*. Nanomolar levels of this protein increase UCP1 in cultures of primary white fat cells by 50 fold or more, resulting in increased respiration. Perhaps more remarkable, viral delivery of irisin that causes only a moderate increase (~ 3 fold) in circulating levels stimulates a 10–20 fold increase in UCP1, increased energy expenditure and an improvement in the glucose tolerance of mice fed a high fat diet. As this is in the range of increases seen with exercise in mouse and man, it is likely that irisin is responsible for at least some of the beneficial effects of exercise on the browning of adipose tissues and increases in energy expenditure. It is important to note that the evidence provided here does not exclude a role for other tissues besides muscle in the biological regulation and secretion of irisin.

Second, the cleaved and secreted portion of FNDC5, the hormone irisin, is highly conserved in all mammalian species sequenced. Mouse and human irisin are 100% identical, compared to 85% identity for insulin, 90% for glucagon and 83% identity for leptin. This certainly implies a highly conserved function that is likely to be mediated by a cell surface receptor. The identity of such a receptor is not yet known.

On the basis of the gene structure of *Fndc5*, with a signal peptide that was evidently missed in previous studies¹², we considered that FNDC5 might be a secreted protein. Indeed, we have observed that the signal peptide is removed, and the mature protein is further proteolytically cleaved and glycosylated, to release the 112-amino-acid polypeptide irisin. The cleavage and secretion of irisin is similar to the release/shedding of other transmembrane polypeptide hormones and hormone-like molecules such as epidermal growth factor (EGF) and transforming growth factor- α (TGF- α).

As the conservation of calories would probably provide an overall survival advantage for mammals, it seems paradoxical that exercise would stimulate the secretion of a polypeptide hormone that increases thermogenesis and energy expenditure. One explanation for increased irisin expression with exercise in mouse and man may be that it evolved as a consequence of muscle contraction during shivering. Muscle secretion of a hormone that activates adipose thermogenesis during this process might provide a broader, more robust defence against hypothermia.

The therapeutic potential of irisin is obvious. Exogenously administered irisin induces the browning of subcutaneous fat and thermogenesis, and it presumably could be prepared and delivered as an injectable polypeptide. Increased formation of brown or beige/brite fat has been shown to have anti-obesity, antidiabetic effects in multiple murine models⁶, and adult humans have significant deposits of UCP1-positive brown fat¹⁵. Data presented here show that even relatively short treatments of obese mice with irisin improves glucose homeostasis and causes a small weight loss. Whether longer treatments with irisin and/or higher doses would cause more weight loss remains to be determined. The worldwide, explosive increase in obesity and diabetes renders attractive the therapeutic potential of irisin in these and related disorders.

Another potentially important aspect of this work relates to other beneficial effects of exercise, especially in some diseases for which no effective treatments exist. The clinical data linking exercise with health benefits in many other diseases suggests that irisin could also have significant effects in these disorders.

METHODS SUMMARY

Primary mouse stromal vascular fractions from adipose tissues were differentiated as described⁶. FNDC5/irisin were purchased from ABNOVA (GST fused), or produced from Syd Laboratories (GST fused) or LakePharma (Fc fusions). Hydrodynamic injections¹⁶, electron microscopy¹⁷ and treadmill running¹⁸ were performed as previously described. Unless otherwise stated, bar graph data are presented as mean \pm s.e.m., and $*P < 0.05$ compared to control group. Student's *t*-test was used for single comparisons and one-way ANOVA for multiple.

Full Methods and any associated references are available in the online version of the paper at www.nature.com/nature.

Received 14 August; accepted 13 December 2011.

Published online 11 January 2012.

1. Puigserver, P. *et al.* A cold-inducible coactivator of nuclear receptors linked to adaptive thermogenesis. *Cell* **92**, 829–839 (1998).
2. Handschin, C. & Spiegelman, B. M. The role of exercise and PGC1 α in inflammation and chronic disease. *Nature* **454**, 463–469 (2008).
3. Sandri, M. *et al.* PGC-1 α protects skeletal muscle from atrophy by suppressing FoxO3 action and atrophy-specific gene transcription. *Proc. Natl Acad. Sci. USA* **103**, 16260–16265 (2006).
4. Wenz, T., Rossi, S. G., Rotundo, R. L., Spiegelman, B. M. & Moraes, C. T. Increased muscle PGC-1 α expression protects from sarcopenia and metabolic disease during aging. *Proc. Natl Acad. Sci. USA* **106**, 20405–20410 (2009).

5. Xu, X. *et al.* Exercise ameliorates high-fat diet-induced metabolic and vascular dysfunction, and increases adipocyte progenitor cell population in brown adipose tissue. *Am. J. Physiol. Regul. Integr. Comp. Physiol.* **300**, R1115–R1125 (2011).
6. Seale, P. *et al.* Prdm16 determines the thermogenic program of subcutaneous white adipose tissue in mice. *J. Clin. Invest.* **121**, 96–105 (2011).
7. Vind, B. F. *et al.* Impaired insulin-induced site-specific phosphorylation of TBC1 domain family, member 4 (TBC1D4) in skeletal muscle of type 2 diabetes patients is restored by endurance exercise-training. *Diabetologia* **54**, 157–167 (2011).
8. Nielsen, A. R. & Pedersen, B. K. The biological roles of exercise-induced cytokines: IL-6, IL-8, and IL-15. *Appl. Physiol. Nutr. Metab.* **32**, 833–839 (2007).
9. Tseng, Y. H. *et al.* New role of bone morphogenetic protein 7 in brown adipogenesis and energy expenditure. *Nature* **454**, 1000–1004 (2008).
10. Komatsu, M. *et al.* Multiple roles of PPAR α in brown adipose tissue under constitutive and cold conditions. *Genes Cells* **15**, 91–100 (2010).
11. Teufel, A., Malik, N., Mukhopadhyay, M. & Westphal, H. *Frcp1* and *Frcp2*, two novel fibronectin type III repeat containing genes. *Gene* **297**, 79–83 (2002).
12. Ferrer-Martínez, A., Ruiz-Lozano, P. & Chien, K. R. Mouse PEP: a novel peroxisomal protein linked to myoblast differentiation and development. *Dev. Dyn.* **224**, 154–167 (2002).
13. Cederberg, A. *et al.* *FOXC2* is a winged helix gene that counteracts obesity, hypertriglyceridemia, and diet-induced insulin resistance. *Cell* **106**, 563–573 (2001).
14. Speakman, J. R. & Selman, C. Physical activity and resting metabolic rate. *Proc. Nutr. Soc.* **62**, 621–634 (2003).
15. Enerbäck, S. Human brown adipose tissue. *Cell Metab.* **11**, 248–252 (2010).
16. Bell, J. B., Aronovich, E. L., Schreifels, J. M., Beadnell, T. C. & Hackett, P. B. Duration of expression and activity of *Sleeping Beauty* transposase in mouse liver following hydrodynamic DNA delivery. *Mol. Ther.* **18**, 1796–1802 (2010).
17. Cinti, S., Zingaretti, M. C., Cancelli, R., Ceresi, E. & Ferrara, P. Morphologic techniques for the study of brown adipose tissue and white adipose tissue. *Methods Mol. Biol.* **155**, 21–51 (2001).
18. Wu, J. *et al.* The unfolded protein response mediates adaptation to exercise in skeletal muscle through a PGC-1 α /ATF6 α complex. *Cell Metab.* **13**, 160–169 (2011).

Supplementary Information is linked to the online version of the paper at www.nature.com/nature.

Acknowledgements This study was supported by National Institutes of Health grants DK54477, DK31405, DK61562 to B.M.S. P.B. and E.A.B. were supported by the Wenner-Gren Foundation, Swedish Heart and Lung Foundation and the 'Svenska Sällskapet för Medicinsk Forskning'. J.W. was supported by a postdoctoral fellowship from the American Heart Association (Founders Affiliate #09POST2010078). The animal procedures were in accordance with Institutional Animal Use and Care Committee protocols 110-2008 and 056-2009. The authors thank S. Loffredo and M. Kirschner for discussions and suggestions on the manuscript.

Author Contributions P.B. and B.M.S. planned the majority of experiments and wrote the paper, and P.B. executed most of the experiments. J.W. performed a subset of cultured cell experiments and contributed valuable materials. M.P.J. and S.P.G. performed the peptide fingerprinting identification of irisin cleavage. A.K. contributed with technical assistance and L.Y. and S.K. performed the CLARK electrode experiments. E.A.B. assisted with the hydrodynamic injections. J.C.L. assisted with intravenous injections and K.A.R. with bioinformatics. J.Z.L. and J.H.C. performed *in vitro* experiments. P.B. and H.T. and LakePharma designed and provided Fc fusion proteins. K.H. and B.F.V. performed the human cohort study, and M.C.Z. and S.C. performed the electron microscopy studies.

Author Information Reprints and permissions information is available at www.nature.com/reprints. The authors declare no competing financial interests. Readers are welcome to comment on the online version of this article at www.nature.com/nature. Correspondence and requests for materials should be addressed to B.M.S. (bruce_spiegelman@dfci.harvard.edu).

METHODS

Materials. Antibodies against UCP1, tubulin and FNDC5 were from Abcam. Forskolin, insulin, dexamethasone, rosiglitazone, GW6471 and antibody against Flag were from Sigma. Primers for all qPCR experiments are listed in Supplementary Table 1. Recombinant FNDC5, LRG1, IL-15, VEGF- β and TIMP4 were from ABNOVA (Taiwan). Coomassie staining kit and Lipofectamine 2000 were from Invitrogen.

Identification of PGC1- α -dependent secreted proteins. All PGC1- α -induced genes as judged from gene expression analysis in MCK-PGC1- α muscle with a fold change of at least 2 and $P < 0.05$ were subjected to the following analysis. The protein sequence of the longest transcript were analysed in the SignalP-software¹⁹ (<http://www.cbs.dtu.dk/services/SignalP/>). Sequences with positive S, C, Y and D scores were considered positive for a signal sequence. All positive proteins were then screened for mitochondrial target sequences (<http://www.cbs.dtu.dk/services/TargetP/>) whereas positive sequences were removed. All remaining hit proteins were then analysed using qPCR in muscle from MCK-PGC1- α mice and myocytes overexpressing PGC1- α .

Primary cell cultures and recombinant protein treatments. The SVF from inguinal fat depots of 8–12-week-old BALB/C mice were prepared and differentiated for 6 days as previously described²⁰. Rosiglitazone was used for the two first days of differentiation. For all experiments, unless otherwise indicated, recombinant FNDC5 was added to the culture media at a concentration of $1 \mu\text{g ml}^{-1}$ for the last 4 days of differentiation. Primary myoblasts were cultured and differentiated as described previously²¹.

Preparation of protein fractions from cells and media. 293HEK or primary myocytes were transfected by standard methods or transduced with adenovirus at a multiplicity of infection (m.o.i.) of 20 as indicated. Twenty-four hours after transfection, media was removed, and cells were washed in large volumes of PBS five times, followed by incubation in Freestyle serum-free media (GIBCO) for 24 h. The cells and media were then collected separately, and media were centrifuged three times at 2,000g to pellet debris. Thereafter, a quarter volume of ice-cold TCA was added and precipitated protein was pelleted at 6,000g and washed three times in acetone. Pellet was then dried and resuspended in SDS-containing lysis buffer. Protein concentration was measured in both cell and media fraction and adjusted either by protein or volume as indicated.

RT-PCR. qPCR was carried out after Trizol-based RNA extraction using RNeasy (Invitrogen) and thereafter SYBR green. All data were normalized to TBP, 18S or indicated in-house genes and quantitative measures were obtained using the $\Delta\Delta C_T$ method.

Western blot and quantification. Protein amounts from all samples were assessed using the BCA-kit (Thermo Scientific) followed by protein concentration normalization before all western blot experiments. Western blot was carried out following standard procedure and final band intensity (QL-BG) was quantified using BioPix iQ²². All data were normalized to background and loading controls.

Additional methods. CLARK electrode measurements, energy expenditure *in vivo*, interaperitoneal glucose tolerance test (IGTT) and immunohistochemistry against UCP1 were performed as described previously⁶, with the exception that CLARK output was normalized to total cell protein. Fc-fusion construction and protein purification was performed by LakePharma.

Comprehensive laboratory animal monitoring system. C57/Bl6J mice were fed a high fat (60% kcal) diet (D12492, Research Diets) for 20 weeks, starting at 6 weeks of age. Mice were then injected with indicated doses of adenovirus expressing GFP or FNDC5, and comprehensive laboratory animal monitoring system (CLAMS; Columbia Instruments)-cage analysis was performed as described previously⁶. Briefly, mice were acclimated in metabolic chambers for 2 days before analysis in order to minimize stress. CO₂ and O₂ levels were then collected every 36 min for a period of 3 days. Data on activity, heat generation and food intake were measured at more frequent intervals. Circadian rhythm was observed for most parameters. Data were not normalized to body weights unless otherwise stated.

Mass spectrometry and peptide fingerprinting. Gel bands were digested with sequencing grade trypsin (Promega) or ASP-N (Sigma-Aldrich) as per manufacturer's instructions. Extracted in-gel protein digests were resuspended in 8 μl 5% formic acid/5% acetonitrile, and 4 μl were analysed by microcapillary liquid chromatography electrospray ionization tandem mass spectrometry (LC-MS/MS). Analyses were done on a LTQ Orbitrap Velos mass spectrometer (Thermo Fisher Scientific) equipped with a Thermo Fisher Scientific nanospray source, an Agilent 1100 Series binary HPLC pump and a Famos autosampler. Peptides were separated on a 100 m \times 16 cm fused silica microcapillary column with an in-house made needle tip. The column was packed with MagicC18AQ C₁₈ reversed-phase resin (particle size, 5 μm ; pore size, 200 Å; Michrom Bioresources). Separation was achieved through applying a 30 min gradient from

0–28% acetonitrile in 0.125% formic acid. The mass spectrometer was operated in a data-dependent mode essentially as described previously²³ with a full MS scan acquired with the Orbitrap, followed by up to ten LTQ MS/MS spectra on the most abundant ions detected in the MS scan. Mass spectrometer settings were: full MS (automated gain control, 1×10^6 ; resolution, 6×10^4 ; m/z range, 375–1,500; maximum ion time, 1,000 ms); MS/MS (AGC, 5×10^3 ; maximum ion time, 120 ms; minimum signal threshold, 4×10^3 ; isolation width, 2 Da; dynamic exclusion time setting, 30 s). After MS data acquisition, RAW files were converted into mzXML format and processed using a suite of software tools developed in-house for analysis. All precursors selected for MS/MS fragmentation were confirmed using algorithms to detect and correct errors in monoisotopic peak assignment and refine precursor ion mass measurements. All MS/MS spectra were then exported as individual DTA files and searched with no enzyme using the Sequest algorithm. These spectra were then searched against a database containing sequence of mouse FNDC5 in both forward and reversed orientations. The following parameters were selected to identify FNDC5: 10 p.p.m. precursor mass tolerance, 0.8 Da product ion mass tolerance, fully tryptic or ASP-N digestion, and up to two missed cleavages. Variable modifications were set for methionine (+15.994915). In addition, a fixed modification for the carbamidomethylation for cysteine (+57.021464) was used as well. The C-terminal fragment for FNDC5 was identified (KDEVTMKKE) by trypsin digestion and reconfirmed by a separate ASP-N digestion.

Preparation of plasma samples for western blot. Thirty-five microlitres of mouse or human plasma were precleared for albumin/IgG using the ProteoExtract-kit (CalBiochem) as recommended by the manufacturer. Samples were then concentrated to approximately 100 μl and $>8 \mu\text{g} \mu\text{l}^{-1}$, followed by deglycosylation of 150 μg using PNGase F (New England Biolabs). Totally, 80 μl were then prepared containing $1 \times$ sample buffer with reducing agent and $1.7 \mu\text{g} \mu\text{l}^{-1}$ protein, sonicated, boiled and analysed using western blot against FNDC5 or indicated antibody.

Construction of adenoviral vectors. The FNDC5 expression vector was purchased with a C-terminal Flag-tag from OriGene. The QuickChange Multi Site XL Directed Mutagenesis Kit (Aligent Technologies) was used to introduce a Flag tag downstream of the signal sequence and to mutate the C-terminal Flag tag, thus resulting in the N-terminal Flag (NTF)-FNDC5 construct (Fig. 5a). The NTF and CTF FNDC5 constructs were then subcloned into the pENTR1a vector (Invitrogen) and recombined into the pAd-CMV-DEST-V5 vector (Invitrogen) and adenovirus was produced using the virapower system (Invitrogen), including three rounds of amplification. Thereafter, virus was concentrated using the Vivapure adenopack 100 (Sartorius Stedim Biotech) and buffer exchanges to saline reaching a concentration of 9–10 i.f.u. μl^{-1} . A GFP-containing adenovirus previously used was prepared in parallel.

Transgenic mice. The MCK-PGC1- α transgenic and muscle-specific PGC1- α knockout mice have been described previously²⁴.

Exercise protocols. Twelve-week-old B6 mice were exercised either using swimming²⁵ or using free wheel running, as described previously²⁶.

Human material and exercise training program. Blood samples and skeletal muscle biopsies were obtained from eight male non-diabetic individuals before and after 10 weeks of aerobic training as described previously⁷. In brief, the exercise-training program consisted of cycling on stationary bikes with 4–5 sessions of 20–35 min per week at an average intensity of $\sim 65\%$ of maximal oxygen consumption. Informed consent was obtained from all volunteers before participation. The study was approved by the Local Ethics Committee and was performed in accordance with the Helsinki Declaration.

- Emanuelsson, O., Brunak, S., von Heijne, G. & Nielsen, H. Locating proteins in the cell using TargetP, SignalP and related tools. *Nature Protocols* **2**, 953–971 (2007).
- Kajimura, S. *et al.* Initiation of myoblast to brown fat switch by a PRDM16-C/EBP- β transcriptional complex. *Nature* **460**, 1154–1158 (2009).
- Rasbach, K. A. *et al.* PGC-1 α regulates a HIF2 α -dependent switch in skeletal muscle fiber types. *Proc. Natl Acad. Sci. USA* **107**, 21866–21871 (2010).
- Bostrom, P. *et al.* The SNARE protein SNAP23 and the SNARE-interacting protein Munc18c in human skeletal muscle are implicated in insulin resistance/type 2 diabetes. *Diabetes* **59**, 1870–1878 (2010).
- Villén, J. & Gygi, S. P. The SCX/IMAC enrichment approach for global phosphorylation analysis by mass spectrometry. *Nature Protocols* **3**, 1630–1638 (2008).
- Handschin, C. *et al.* Skeletal muscle fiber-type switching, exercise intolerance, and myopathy in PGC-1 α muscle-specific knock-out animals. *J. Biol. Chem.* **282**, 30014–30021 (2007).
- Boström, P. *et al.* C/EBP β controls exercise-induced cardiac growth and protects against pathological cardiac remodeling. *Cell* **143**, 1072–1083 (2010).
- Chinsomboon, J. *et al.* The transcriptional coactivator PGC-1 α mediates exercise-induced angiogenesis in skeletal muscle. *Proc. Natl Acad. Sci. USA* **106**, 21401–21406 (2009).

X-ray structures of LeuT in substrate-free outward-open and apo inward-open states

Harini Krishnamurthy¹ & Eric Gouaux^{1,2}

Neurotransmitter sodium symporters are integral membrane proteins that remove chemical transmitters from the synapse and terminate neurotransmission mediated by serotonin, dopamine, noradrenaline, glycine and GABA (γ -aminobutyric acid). Crystal structures of the bacterial homologue, LeuT, in substrate-bound outward-occluded and competitive inhibitor-bound outward-facing states have advanced our mechanistic understanding of neurotransmitter sodium symporters but have left fundamental questions unanswered. Here we report crystal structures of LeuT mutants in complexes with conformation-specific antibody fragments in the outward-open and inward-open states. In the absence of substrate but in the presence of sodium the transporter is outward-open, illustrating how the binding of substrate closes the extracellular gate through local conformational changes: hinge-bending movements of the extracellular halves of transmembrane domains 1, 2 and 6, together with translation of extracellular loop 4. The inward-open conformation, by contrast, involves large-scale conformational changes, including a reorientation of transmembrane domains 1, 2, 5, 6 and 7, a marked hinge bending of transmembrane domain 1a and occlusion of the extracellular vestibule by extracellular loop 4. These changes close the extracellular gate, open an intracellular vestibule, and largely disrupt the two sodium sites, thus providing a mechanism by which ions and substrate are released to the cytoplasm. The new structures establish a structural framework for the mechanism of neurotransmitter sodium symporters and their modulation by therapeutic and illicit substances.

Chemical neurotransmission in the central nervous system is terminated through re-uptake of neurotransmitters from the synapse into surrounding neuronal and glial cells, a process first characterized in 1961 (ref. 1). Transmitter uptake is mediated by neurotransmitter sodium symporters (NSSs)^{2,3}, integral membrane proteins that exploit energetically favourable Na^+ electrochemical gradients for the thermodynamically uphill transport of neurotransmitters. Members of the NSS family include transporters for GABA, glycine, noradrenaline, serotonin and dopamine—chemical transmitters that have fundamental roles in the function of the nervous system. Accordingly, dysfunction of these transporters is implicated in diseases such as depression^{4,5}, schizophrenia⁴, epilepsy⁶ and Parkinson's disease⁴, and they are targets for therapeutic drugs including tricyclic antidepressants (TCAs) and selective serotonin re-uptake inhibitors (SSRIs) as well as addictive substances such as cocaine and amphetamines⁷. Understanding the substrate translocation mechanism of NSSs is central to the development of accurate models of substrate and drug complexes and to the discovery of new therapeutic agents.

The mechanism of NSS transport is generally described by the thermodynamically coupled binding of substrate and ion(s) to a central binding site that is alternately accessible to either side of the membrane^{8,9} (Supplementary Fig. 1). Crystal structures of LeuT, a bacterial NSS homologue, elucidated the architecture of NSS proteins, demonstrated the existence of a substrate- and ion-bound occluded conformation, and illustrated how competitive and non-competitive inhibitors stabilize an outward-facing conformation^{10–14}. LeuT is, at present, the best template for modelling the structure of NSSs and their complexes with therapeutic and illicit drugs. However, our understanding of

mechanism and structure/function relationships in NSSs is incomplete due to the absence of LeuT structures in outward-open and inward-open states.

In the absence of structural knowledge of transporter intermediates, general mechanisms of transport have been proposed based on structures of other secondary transporters bearing the LeuT fold and crystallized in distinct conformational states^{15–19}. However, low amino acid sequence identity compromises the extent to which this approach can generate a detailed and accurate mechanism for NSSs. Concomitantly, spectroscopic and computational methods have focused on characterization of conformational changes accompanying substrate and ion association/dissociation events in LeuT^{20–23}. Although these approaches have yielded new insights into localized movements, they have not revealed the three-dimensional, atomic-level details of conformational changes associated with substrate binding, isomerization of the transporter to the inward-open conformation, and release of substrate and sodium ion(s). Here, we present crystal structures of the outward-open and inward-open states of LeuT and thereby establish the structural basis for transport in the NSS family and provide accurate templates for modelling eukaryotic NSSs and their complexes with substrates, ions and drugs.

Substrate-free and inward-open conformations

To stabilize the substrate-free and inward-open states of LeuT, we mutated residues in transmembrane domains (TMs) 3 and 8, helices comprising part of the 'scaffold' domain (TMs 3, 4, 8 and 9) and in TM6, one of the 'core' domain helices (TMs 1, 2, 6 and 7)^{10,22,24} in the background of the wild-type-like K288A variant (LeuT^K)²⁵ (Supplementary Table 1 and Supplementary Fig. 2). To enhance

¹Vollum Institute, Oregon Health and Science University, 3181 SW Sam Jackson Park Road, Portland, Oregon 97239, USA. ²Howard Hughes Medical Institute, Oregon Health and Science University, 3181 SW Sam Jackson Park Road, Portland, Oregon 97239, USA.

crystallization behaviour, we raised conformation-specific antibodies, exploiting fluorescence-detection size-exclusion chromatography (FSEC)²⁶ to select the antibodies and to demonstrate state-dependent binding. Well-diffracting crystals of substrate-free LeuT were obtained using the Tyr 108 to Phe mutant in TM3 (LeuT^K(Y108F))²⁵ and the 2B12 antibody fragment (Fab). Stabilization of LeuT in an inward-open conformation required weakening of the sodium 2 (Na2) site¹⁰ by mutation of Thr 354 to Val and Ser 355 to Ala (TM8), as well as the cytoplasmic gate by changing Tyr 268 to Ala (TM6; LeuT^K(TSY))^{23,27,28}, together with the 6A10 Fab.

Sodium-bound state is outward-open

The substrate-free LeuT^K(Y108F) structure (Supplementary Table 2 and Supplementary Fig. 3) adopts an outward-open conformation as a consequence of hinge-like movements in TMs 1b, 2a (residues 41–55), and 6a, relative to the outward-occluded state (Fig. 1a–c, e). Extracellular loop 3 (EL3) and TM11 are displaced by as much as 2.8 Å and 2.2 Å, respectively, due to the movements of TM1b and TM6a (Fig. 1a). Notably, TMs 1b, 2a and 6a pivot at Val 23, Gly 55 and Leu 257, respectively, suggesting that when substrate no longer forges interactions between the core and scaffold domains, constraints on TM1b and TM6a are released, allowing them to move outward and the transporter to adopt an outward-open conformation. The LeuT^K(Y108F) structure is similar to the previously reported Trp-bound LeuT structure¹² with a root mean squared deviation (r.m.s.d.) value of 0.4 Å for all C α atoms (Supplementary Fig. 4), supporting the

general principle that inhibitors bind to conformational states populated by the wild-type transporter.

The ‘thin’ extracellular gate¹⁹ of the outward-occluded state is ruptured in the LeuT^K(Y108F) structure. Residues that bridge TM1b/TM6a to TM3/TM10 in the outward-occluded state have separated, opening a pathway to the extracellular solution (Fig. 1d, e). Arg 30 no longer forms a water-mediated salt bridge with Asp 404 (TM10) and the side chain of Phe 253 has rotated away from the binding site by a $\sim 90^\circ$ rotation about the χ_1 dihedral angle, in agreement with molecular dynamics simulations^{21,29}. The coordinated movement of Arg 30 and Phe 253 enables the retention of an important cation- π interaction between their respective guanidinium and phenyl groups. The phenyl ring of residue 253 now occupies the same position as the indole ring of Trp 602 bound to the extracellular vestibule in the Trp-bound LeuT complex¹².

Prominent electron density peaks (4.0 σ) observed in the Na1 and Na2 sites together with ion-oxygen distances of ~ 2.4 Å (ref. 30) are consistent with sodium occupancy of these sites, although higher resolution diffraction data will be required to confirm their identity (Fig. 2). Most importantly, the outward-open structure suggests that the presence of sodium ions keeps the intracellular thick gate¹⁹ closed by bridging interactions between the intracellular halves of the core and scaffold domains. Even though the Na1 site is located close to the pivot points for TM1b and TM6a (Fig. 2a), the concerted movement of the helices allows for retention of ion coordination geometry, excepting the loss of the carboxylate oxygen from the absent substrate.

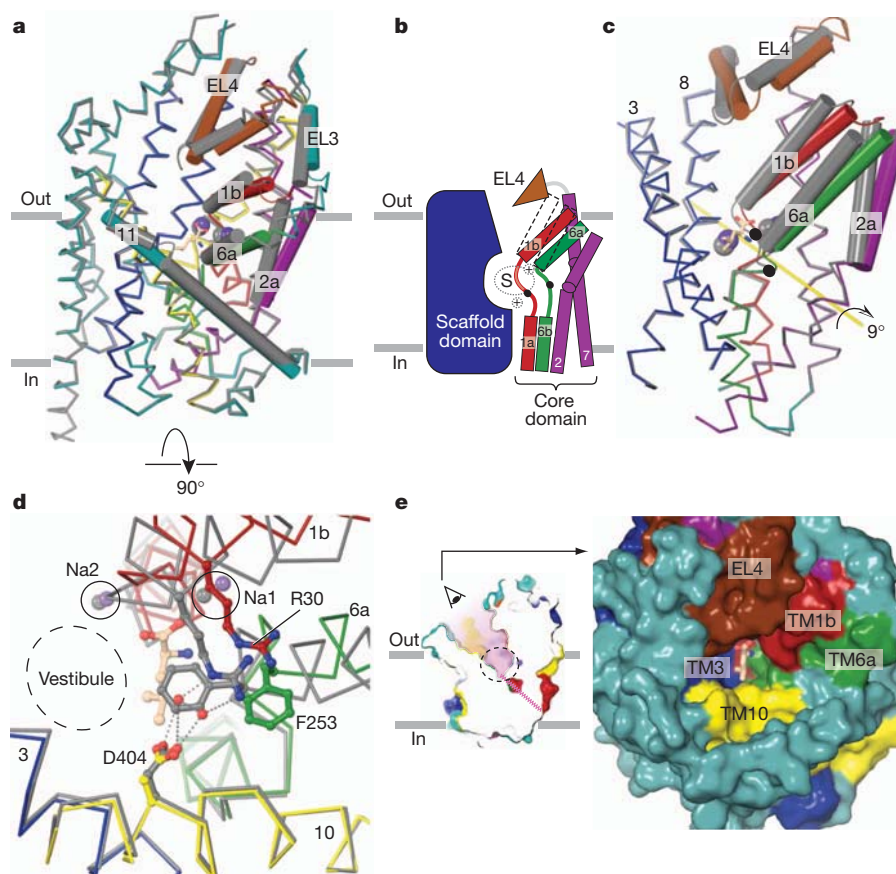


Figure 1 | The substrate-free, Na⁺-bound state is outward-open.

a, Superposition of the outward-open and leucine-bound outward-occluded conformations. Outward-open structure is coloured with Na⁺ ions as purple spheres. The outward-occluded structure with Na⁺ ions (spheres) is grey and leucine is shown in stick representation. **b**, Schematic of scaffold and core domains, EL4, the pivot points of hinge movements in TMs 1 and 6 (solid black circles) and the substrate (S) and sodium sites (+). **c**, Superposition, as in panel **a**, illustrating that a $\sim 90^\circ$ rotation about an axis passing through the middle of

the core domain (yellow arrow) describes the conformational change associated with opening to the outside. Pivot points are shown as in panel **b**. **d**, Rupture of extracellular gate interactions (grey dashed lines) in the outward-open structure. Two water molecules that bridge Arg 30 and Asp 404 in the outward-occluded state are shown as red spheres. **e**, Surface representation of the outward-open structure with the zig-zag pink line indicating a closed intracellular pathway. Leucine, where shown, is from the outward-occluded Leu-bound structure.

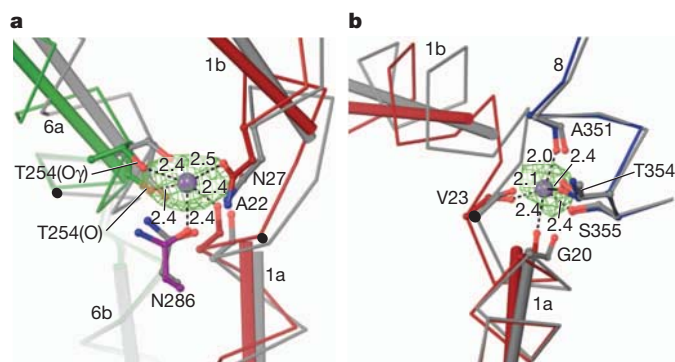


Figure 2 | Sodium sites in the outward-open state. **a**, The Na1 site showing positions of the coordinating residues within the framework of global changes in the outward-open structure. **b**, The Na2 site. $F_o - F_c$ omit density is contoured at 4σ and represented as green mesh. Colour scheme and representations are the same as in Fig. 1. Dashed lines indicate interactions between sodium ions and coordinating atoms with distances in Å, solid black circles are approximate pivot points for hinge movement of helices and red and green cylinders define the TM1 and six helix axes, respectively.

Binding of Na^+ at this site may precede substrate binding, as also suggested by simulation studies²⁹, thereby stabilizing local conformations of TMs 1 and 6 and engaging the main-chain carbonyl oxygen of Ala 22 (TM1a) with side-chain oxygens of Asn 27 (TM1b) and Thr 254 (TM6a). The Na2 site is located towards the intracellular region of TM1, stitching TM1a to TM8 through the main-chain carbonyls of Gly 20 and Val 23 (Fig. 2b). Thus, the Na^+ ions, through their interaction with TM1a, stabilize an intracellular-closed conformation, a finding supported by single-molecule Förster resonance energy transfer (FRET) studies²³.

Structure of the inward-open conformation

We hypothesized that weakening of the Na2 binding site by mutation of Thr 354 and Ser 355 to valine and alanine, respectively, and perturbation of the intracellular gate by mutation of Tyr 268 to Ala²⁷,

together yielding the LeuT^K(TSY) variant, would shift the conformational equilibrium of LeuT towards the inward-open state (Supplementary Discussion and Supplementary Figs 2, 5, 8 and 9). We proceeded to crystallize the LeuT^K(TSY)-6A10 Fab complex in the presence of lipids and solved the structure by molecular replacement at 3.2 Å resolution (Supplementary Table 2 and Supplementary Figs 10 and 11). Electron density for LeuT residues 1–10 was not observed and that for amino acids 11–24 was weak (mean B factor of 158.0 Å^2 versus 121.2 Å^2 for the rest of LeuT). The Fab fragment binds on the intracellular side of LeuT^K(TSY) (Supplementary Fig. 11).

LeuT^K(TSY) adopts an inward-open conformation as a consequence of large hinge-like movements within the core domain relative to the scaffold domain, and shifts in extracellular loops (Figs 3a–c). Perhaps the most notable change involves TM1a. Tilted by $\sim 45^\circ$ from its position in the closed state, it protrudes into the predicted location of the membrane. TM6b, in comparison, is rotated away from the central binding site by only 17° . In contrast to the uncoupled movements of TMs 1a and 6b, TMs 1b and 6a tilt by a similar extent (24° and 21° , respectively) towards the scaffold domain, blocking the extracellular pathway. Because TM1 and TM6 do not move as a unit, we superimposed the inward-open and outward-occluded structures using only the scaffold domain, resulting in an r.m.s.d. in $\text{C}\alpha$ positions of 3.0 Å. Helices buttressing TM1 and TM6, namely TM2, TM7 and TM5, also undergo substantial rearrangements but their extracellular and intracellular halves move to significantly different extents (Fig. 3c). Thus, these helices bend, rather than tilt as rigid bodies, facilitated by either a glycine or proline residue located in their midsections. Movement of TM7 causes EL4 to dip down further into the extracellular vestibule, thus closing off the extracellular solvent pathway. To make room for TM6a, TM11 moves away from the centre of the transporter, a direction opposite to that seen in the outward-open state (Fig. 3b).

Access to the substrate-binding site

In the inward-open LeuT structure, formation of a thick extracellular gate cuts off solvent access from the extracellular side while the thick

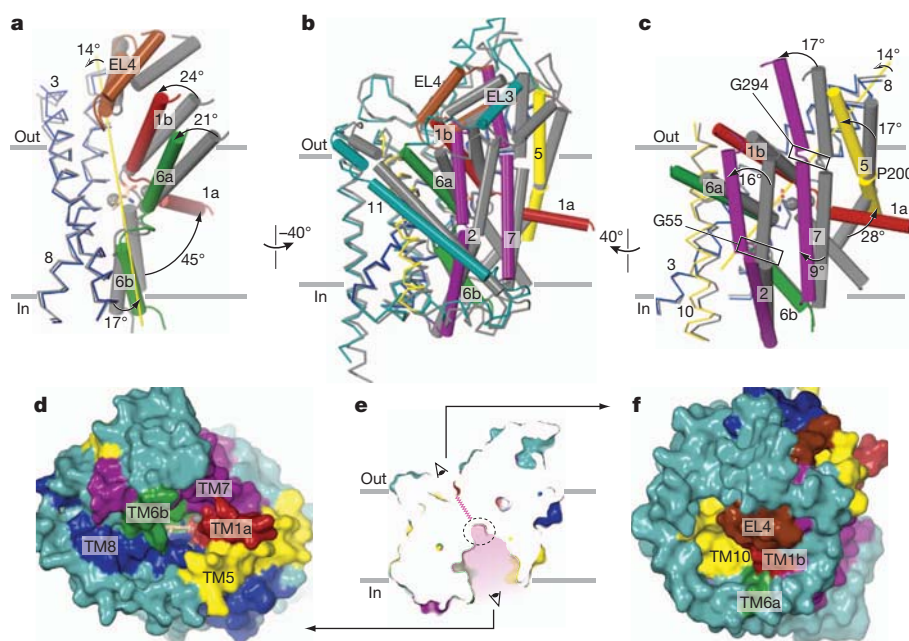


Figure 3 | Inward-open conformation. **a–c**, Superposition of inward-open and outward-occluded state structures using the scaffold domain. The overall changes shown in **b** are divided in two parts, **a** and **c**, for clarity. The extent of rotation for the key TMs between the outward-occluded and inward-open conformations are indicated in **a** and **c**. The axis of rotation of core domain with the exclusion of TM1a is depicted in yellow. **d**, Surface representation of the

inward-open structure looking 'up' into the binding site from the intracellular side, as depicted in **e**, **f**. Surface representation of the inward-open structure showing the elements forming the extracellular thick gate. Colour coding and representations are as in Fig. 1. Leucine and sodium, where shown, are from the outward-occluded Leu-bound structure.

intracellular gate opens, allowing access to the substrate binding site from the inside (Figs 3d–f). Consistent with cysteine accessibility studies on the serotonin (SERT)^{22,31,32} and GABA (GAT-1)³³ transporters, TM1a, TM5 and TM8 line the intracellular cavity. In particular, residues Leu 14 and Ala 19 of TM1a are solvent accessible, in line with the marked increase in reactivity observed for the corresponding residues in SERT in the inward-open conformation²². Accessibility and cross-linking studies also indicate that TM1b and TM6a move closer to TM3 (ref. 34) and, together with EL4, become inaccessible in the absence of sodium^{35–38}. Consistent with its essential role in substrate transport³⁹, EL4 occludes the extracellular pathway by packing tightly against TM1b and TM7 on one side and TM3, TM8 and EL2 on the other side, making extensive contacts that include hydrophobic interactions and a hydrogen bond between Asp 401 (TM10) and Ala 319 (EL4).

The collapse of the extracellular vestibule in the inward-open state is central to our understanding of how therapeutic agents, including TCAs and SSRIs, inhibit NSSs. Large, bulky molecules such as tryptophan¹², the cocaine analogue 2 β -carbomethoxy-3 β -(4-iodophenyl)tropane³¹ and SKF-8997A⁴⁰ arrest LeuT, SERT and GAT-1, respectively, in the outward-facing conformation by blocking collapse of the extracellular vestibule, which in turn precludes opening of the intracellular gate. The inward-open LeuT structure now provides a new template for designing novel therapeutic agents that arrest NSS transporters in the inward-facing conformation. Ibogaine, shown to bind in the intracellular vestibule of SERT⁴¹, is the only known inhibitor of this type.

The closure of the extracellular gate radically changes the nature of the proposed S2 substrate-binding site, which is hypothesized to be occupied by substrate in occluded and inward-facing conformational states^{42,43}. Residues Ile 111 and Leu 400, stated to line the S2 site, are now deeply buried (Supplementary Fig. 12). Although we do see a

small non-protein electron density feature near EL4, it is probably not a substrate molecule, not only because no substrates were included in the protein preparation, but also because the density cannot be well fit by leucine or a related amino acid. We suggest that the density is due to buffer, detergent or several water molecules.

Rupture and formation of gating interactions

The extracellular gate of the inward-open state is closed through interactions between residues of TM1b (Arg 30) and TM10 (Asp 404, Gly 408, Thr 409), EL4 (Ala 319) and TM10 (Asp 401) (Fig. 4a) and TM6a (Asp 240) and TM11 (Tyr 471). The guanidinium group of Arg 30, riding 'on top' of the aromatic ring of Phe 253 (TM6a), makes multiple interactions with TM10 that include a direct salt bridge with Asp 404 and hydrogen bonds to Thr 409 and the carbonyl oxygen of Gly 408. In GAT-1, conservative mutation to Lys of the residue equivalent to Arg 30 severely compromises uptake activity⁴⁴, an outcome in accord with the manner in which interactions of Arg 30 are modulated in the outward-open, outward-occluded and inward-open states of LeuT (Fig. 4a, b).

In contrast to the extracellular gate, a network of interactions within the thick intracellular gate of outward-facing and outward-occluded states is disrupted (Fig. 4b, c). Ionic interactions linking the N terminus and TM1a (Arg 5, Trp 8) to TM6b (Ser 267, Tyr 268) and TM8 (Gln 361, Asp 369) on the intracellular side no longer exist. The splaying apart of TM5, TM7 and TM1a also abrogates interactions between Lys 196 and Thr 10 and between Ser 278 and Arg 11. Consistent with the disruption of these interactions, mutation of residues homologous to Arg 5 or Trp 8 (ref. 45), Tyr 268 (refs 27, 28), Asp 369, Lys 196 and Ser 278 (refs 46, 47) in eukaryotic transporters alters substrate uptake and shifts the conformational equilibrium of the transporter towards an inward-open state.

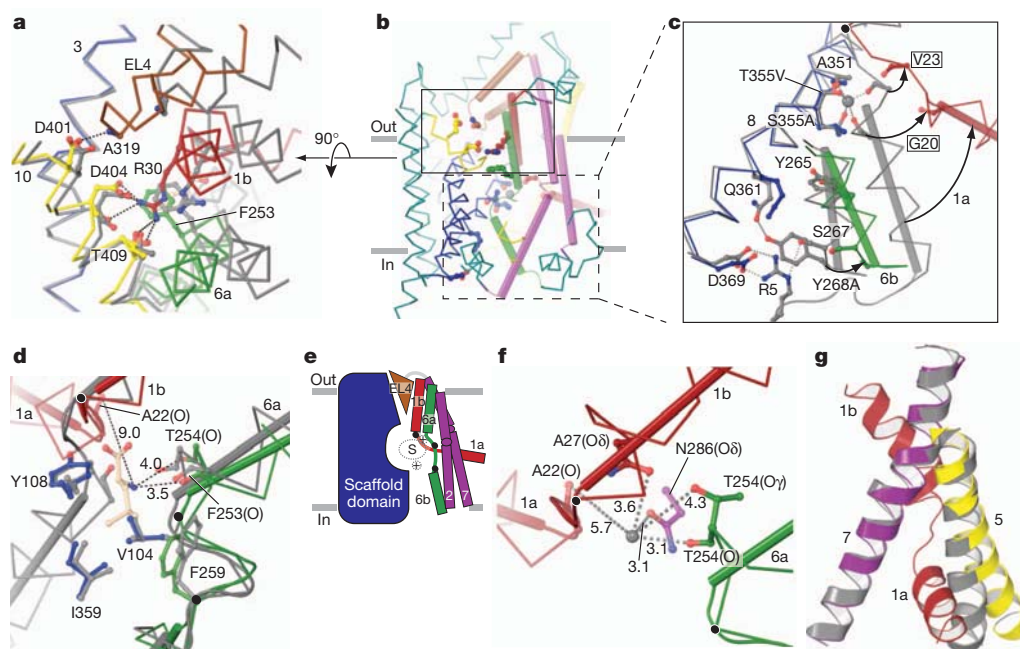


Figure 4 | Changes in gate, substrate and ion site interactions and coupling to helix movements. **a**, Comparison of the extracellular gating interactions in the inward-open and outward-occluded structures. View is from extracellular side. Polar contacts in the inward-open structure are shown as black dashed lines. **b**, Overall view of inward-open structure showing closed extracellular gate (box with solid lines) and open intracellular gate (box with dashed lines). **c**, Comparison of the intracellular gating interactions in the inward-open and outward-occluded structures. Interactions forming the intracellular gate in the outward-occluded state are shown as grey dashed lines. **d**, Changes in the central substrate-binding site. In comparing the outward-occluded and inward-

open structures, A22, T254 and F253 move away from the binding site. Distances were measured relative to leucine from the outward-occluded structure. **e**, A cartoon representing changes in the core domain relative to the scaffold domain and the location of hinges relative to the position of substrate- and ion-binding sites is shown. **f**, Changes in the Na1 site. Distances of the coordinating residues from the sodium ion of the outward-occluded structure are shown. **g**, Superposition of the inward-open and outward-occluded structures using TM7. TM1a of only the inward-open structure is shown for clarity. Colour scheme is as in Fig. 1. Location of TM1 and TM6 hinges are shown as black spheres in c–f.

Perturbation of ion and substrate sites

The location of hinges for the conformational changes in TM1 and TM6 of the inward-open state has profound consequences for the substrate and sodium ion sites. The hinge for TM1a is located at Leu 25, considerably 'above' the Na2 site, leading to separation of residues on TM1a and TM8 that define this site, thus demonstrating how the release of sodium from the Na2 site, the movement of TM1a and the opening of the transporter to the cytoplasm are coupled (Fig. 4c), a mechanism that has also been suggested for the *Vibrio parahaemolyticus* sodium/galactose transporter (vSGLT)⁴⁸. There are two hinges in TM6, Ser 256 for TM6a and Phe 259 for TM6b, while TM1b also pivots at Leu 25. Because these residues are all close to the substrate-binding site but further away from the Na1 site (Fig. 4e), there is minimal perturbation of the former (Fig. 4d) but considerable weakening of the latter (Fig. 4e, f). Thus, although changes in TM1 and TM6 affect residues coordinating the α -amino group of leucine and cause small shifts in the side chains of Phe 253 and Phe 259, residues from TM3 and TM8 that engage the aliphatic moiety of the substrate maintain their positions. Consequently, an important portion of the substrate-binding pocket is retained in the inward-open state, preserving the ability of the transporter to bind substrate under conditions of reversed substrate flux.

Structural principles of transporter mechanism

The pseudo two-fold symmetric relationship of TMs 1–5 and 6–10 together with the organization of TMs 1, 2, 6 and 7 as a four-helix bundle led to the rocking bundle mechanism of transport, in which the core moves as a unit about a rotation axis oriented approximately parallel to the membrane and intersecting the substrate-binding site²². Detailed analysis of the inward-open state, however, indicates that only a portion of the core moves as a unit and that there is not strict adherence to the pseudo two-fold symmetry. The conformational transition from the outward-occluded to the inward-open state is brought about by multiple adjustments in individual TM helices, including the bending of TM2 and TM7 at conserved glycine residues and the independent movements of TMs 1a and 6b. Indeed, the core domains in the inward-open and outward-occluded states align with a r.m.s.d. of 3.5 Å (C α atoms), whereas the scaffold domains align with a r.m.s.d. of 0.7 Å. If TM1a is excluded from consideration, however, the core domain helices superpose with a r.m.s.d. of 0.83 Å (C α atoms), thus demonstrating that a portion of the core helices do reorient as a unit, undergoing a rotation of $\sim 14^\circ$ about an axis passing through Leu 25 and Phe 259 in the plane of the membrane (Fig. 3a, c). The intracellular loop 1 (IL1) and EL4 are also related by the pseudo two-fold symmetry axis, yet whereas EL4 undergoes large relative movements, the position of IL1 is constant.

The structural rearrangement of TM1a in the inward-open conformation of LeuT is different from that seen in Mhp1 (refs 15, 18), in which TM1 moves as a rigid body (Supplementary Fig. 13)²². At present it is unclear whether the extent to which TM1a is seen to tilt away from its position in the occluded state reflects its true position in a native membrane environment. The fact that TM1a is neither involved in crystal contacts nor interacts with the Fab (Supplementary Fig. 11) diminishes the possibility that its position is a crystallization artefact. The weak density of TM1a suggests that it is highly flexible in the detergent/lipid micelles in which LeuT^K(TSY) was crystallized. Indeed, the apparent mobility and large extent of movement of TM1a are in general agreement with findings of single-molecule FRET studies and molecular dynamics simulations^{23,49,50}.

Coupling of binding sites and helix movements

The inward-open structure of LeuT suggests the manner by which changes in the sodium- and substrate-binding pockets are coupled to the larger structural changes that simultaneously open the intracellular side and close the extracellular side. The location of the TM1 hinge at Leu 25 in the inward-open state, at a position extracellular to the

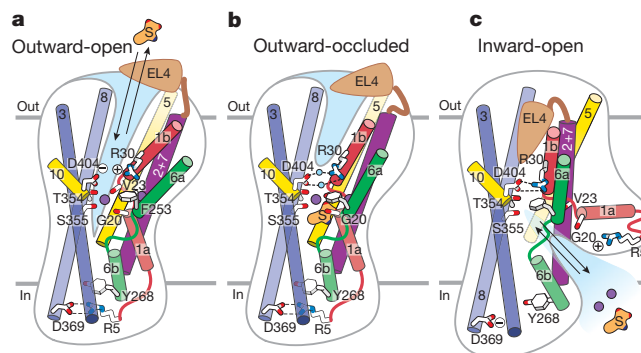


Figure 5 | Schematic of transport in LeuT. a–c, Shown are structural elements and gating residues instrumental to conformational changes associated with the transition from the outward-open (a) to the outward-occluded state (b) and the inward-open state (c). At present there is no crystal structure for an inward-occluded state and thus no schematic is provided.

substrate and sodium sites, is consistent with the observation that in the absence of Na⁺ ions TM1a moves away from the scaffold domain and TM6b, not only initiating conformational changes that open an intracellular pathway, but also resulting in the disruption of the sodium ion sites. We propose that it is energetically unfavourable for TM1a to remain in an intracellular gate 'closed' conformation without the compensating contributions from bound Na⁺. We further suggest that the movement of TM1a initiates a cascade of structural rearrangements that result in closure of the extracellular gate as follows. A change in the position of TM1a requires movement of the intracellular region of TM5 (Fig. 4g). Yet because TM5 lacks the hinge-like regions of TM1 and TM6, the entire helix tilts, 'pushing' TM7 and TM1b and closing the extracellular gate (Fig. 3c). Similar structural adjustments involving TM2 and TM6a also occur, ensuring that the intracellular gate cannot open without simultaneous closure of the extracellular gate.

Mechanism

Crystal structures of LeuT captured in three distinct conformational states show how both local conformational changes and rigid body movements of groups of helices are associated with the transport mechanism (Fig. 5). Opening and closure of the extracellular and intracellular gates exploit hinge-like bending of helices at pivot points within short non-helical regions halfway across the bilayer, together with the rigid body rotation of helical bundles, movements of extracellular loops and flexing of numerous transmembrane helices (Supplementary Movie). General principles emerging from these studies are that local hinge-like movements of transmembrane helices are coupled to the formation and disruption of substrate- and sodium-binding sites, which are translated through nearly rigid body movements of groups of helices and loops into opening and closing of the 'thick' extracellular and intracellular gates. Most importantly, the relative locations of substrate/ion-binding sites and hinge pivots define the extent to which hinge motions perturb the sites. More broadly, these structures demonstrate how the overall conformation and shape of LeuT changes during the transport cycle, thereby providing a general mechanistic framework to understand how substrates, ions, mutations and drugs modulate the conformational equilibria and transport activity of LeuT and related NSS proteins.

METHODS SUMMARY

LeuT mutants were expressed as previously described¹⁰, monoclonal antibodies and Fab fragments were generated by standard methods, and X-ray crystal structures of the Fab complexes were solved by molecular replacement. Final models were obtained by an iterative process of manual model building and refinement against X-ray diffraction data. The functional properties of LeuT mutants were examined using scintillation proximity binding assays and uptake or exchange assays with LeuT reconstituted into proteoliposomes.

Full Methods and any associated references are available in the online version of the paper at www.nature.com/nature.

Received 5 August; accepted 28 November 2011.

Published online 9 January 2012.

- Hertting, G. & Axelrod, J. Fate of tritiated noradrenaline at the sympathetic nerve-endings. *Nature* **192**, 172–173 (1961).
- Nelson, N. The family of Na⁺/Cl[−] neurotransmitter transporters. *J. Neurochem.* **71**, 1785–1803 (1998).
- Saier, M. H. J. A functional-phylogenetic classification system for transmembrane solute transporters. *Microbiol. Mol. Biol. Rev.* **64**, 354–411 (2000).
- Hahn, M. K. & Blakely, R. D. Monoamine transporter gene structure and polymorphisms in relation to psychiatric and other complex disorders. *Pharmacogenomics J.* **2**, 217–235 (2002).
- Klimek, V. *et al.* Reduced levels of norepinephrine transporters in the locus coeruleus in major depression. *J. Neurosci.* **17**, 8451–8458 (1997).
- Richerson, G. B. & Wu, Y. Role of the GABA transporter in epilepsy. *Adv. Exp. Med. Biol.* **548**, 76–91 (2004).
- Amara, S. G. & Sonders, M. S. Neurotransmitter transporters as molecular targets for addictive drugs. *Drug Alcohol Depend.* **51**, 87–96 (1998).
- Mitchell, P. A general theory of membrane transport from studies of bacteria. *Nature* **180**, 134–136 (1957).
- Jardetzky, O. Simple allosteric model for membrane pumps. *Nature* **211**, 969–970 (1966).
- Yamashita, A., Singh, S. K., Kawate, T., Jin, Y. & Gouaux, E. Crystal structure of a bacterial homologue of Na⁺/Cl[−]-dependent neurotransmitter transporters. *Nature* **437**, 215–223 (2005).
- Singh, S., Yamashita, A. & Gouaux, E. Antidepressant binding site in a bacterial homologue of neurotransmitter transporters. *Nature* **448**, 952–956 (2007).
- Singh, S. K., Piscitelli, C. L., Yamashita, A. & Gouaux, E. A competitive inhibitor traps LeuT in an open-to-out conformation. *Science* **322**, 1655–1661 (2008).
- Zhou, Z. *et al.* LeuT-desipramine structure reveals how antidepressants block neurotransmitter uptake. *Science* **317**, 1390–1393 (2007).
- Zhou, Z. *et al.* Antidepressant specificity of serotonin transporter suggested by three LeuT–SSRI structures. *Nature Struct. Mol. Biol.* **16**, 652–657 (2009).
- Weyand, S. *et al.* Structure and molecular mechanism of a nucleobase–cation–symport-1 family transporter. *Science* **322**, 709–713 (2008).
- Faham, S. *et al.* The crystal structure of a sodium galactose transporter reveals mechanistic insights into Na⁺/sugar symport. *Science* **321**, 810–814 (2008).
- Shaffer, P. L., Goehring, A., Shankaranarayanan, A. & Gouaux, E. Structure and mechanism of a Na⁺-independent amino acid transporter. *Science* **325**, 1010–1014 (2009).
- Shimamura, T. *et al.* Molecular basis of alternating access membrane transport by the sodium-hydantoin transporter Mhp1. *Science* **328**, 470–473 (2010).
- Krishnamurthy, H., Piscitelli, C. L. & Gouaux, E. Unlocking the molecular secrets of sodium-coupled transporters. *Nature* **459**, 347–355 (2009).
- Shaikh, S. A. & Tajkhorshid, E. Modeling and dynamics of the inward-facing state of a Na⁺/Cl[−]-dependent neurotransmitter transporter homologue. *PLOS Comput. Biol.* **6**, e1000905 (2010).
- Claxton, D. P. *et al.* Ion/substrate-dependent conformational dynamics of a bacterial homolog of neurotransmitter:sodium symporters. *Nature Struct. Mol. Biol.* **17**, 822–829 (2010).
- Forrest, L. R. *et al.* Mechanism for alternating access in neurotransmitter transporters. *Proc. Natl Acad. Sci. USA* **105**, 10338–10343 (2008).
- Zhao, Y. *et al.* Single-molecule dynamics of gating in a neurotransmitter transporter homologue. *Nature* **465**, 188–193 (2010).
- Boudker, O. & Verdon, G. Structural perspectives on secondary active transporters. *Trends Pharmacol. Sci.* **31**, 418–426 (2010).
- Piscitelli, C. L., Krishnamurthy, H. & Gouaux, E. Neurotransmitter/sodium symporter orthologue LeuT has a single high-affinity substrate site. *Nature* **468**, 1129–1132 (2010).
- Kawate, T. & Gouaux, E. Fluorescence-detection size-exclusion chromatography for precrystallization screening of integral membrane proteins. *Structure* **14**, 673–681 (2006).
- Kniazef, J. *et al.* An intracellular interaction network regulates conformational transitions in the dopamine transporter. *J. Biol. Chem.* **283**, 17691–17701 (2008).
- Loland, C. J., Norregaard, L., Litman, T. & Gether, U. Generation of an activating Zn²⁺ switch in the dopamine transporter: mutation of an intracellular tyrosine constitutively alters the conformational equilibrium of the transport cycle. *Proc. Natl Acad. Sci. USA* **99**, 1683–1688 (2002).
- Celik, L., Schiott, B. & Tajkhorshid, E. Substrate binding and formation of an occluded state in the leucine transporter. *Biophys. J.* **94**, 1600–1612 (2008).
- Harding, M. M. Small revisions to predicted distances around metal sites in proteins. *Acta Crystallogr. D* **62**, 678–682 (2006).
- Zhang, Y.-W. & Rudnick, G. The cytoplasmic substrate permeation pathway of serotonin transporter. *J. Biol. Chem.* **281**, 36213–36220 (2006).
- Rudnick, G. The cytoplasmic permeation pathway of neurotransmitter transporters. *Biochemistry* **50**, 7462–7475 (2011).
- Ben-Yona, A. & Kanner, B. I. Transmembrane domain 8 of the γ -aminobutyric acid transporter GAT-1 lines a cytoplasmic accessibility pathway into its binding pocket. *J. Biol. Chem.* **284**, 9727–9732 (2009).
- Tao, Z., Zhang, Y. W., Agyiri, A. & Rudnick, G. Ligand effects on cross-linking support a conformational mechanism for serotonin transport. *J. Biol. Chem.* **284**, 33807–33814 (2009).
- Rosenberg, A. & Kanner, B. I. The substrates of the γ -aminobutyric acid transporter GAT-1 induce structural rearrangements around the interface of transmembrane domains 1 and 6. *J. Biol. Chem.* **283**, 14376–14383 (2008).
- Henry, L. K., Adkins, E. M., Han, Q. & Blakely, R. D. Serotonin and cocaine-sensitive inactivation of human serotonin transporters by methanethiosulfonates targeted to transmembrane domain I. *J. Biol. Chem.* **278**, 37052–37063 (2003).
- Zomot, E. & Kanner, B. I. The interaction of the γ -aminobutyric acid transporter GAT-1 with the neurotransmitter is selectively impaired by sulfhydryl modification of a conformationally sensitive cysteine residue engineered into extracellular loop IV. *J. Biol. Chem.* **278**, 42950–42958 (2003).
- Mitchell, S. M., Lee, E., Garcia, M. L. & Stephan, M. M. Structure and function of extracellular loop 4 of the serotonin transporter as revealed by cysteine-scanning mutagenesis. *J. Biol. Chem.* **279**, 24089–24099 (2004).
- Smicun, Y., Campbell, S. D., Chen, M. A., Gu, H. & Rudnick, G. The role of external loop regions in serotonin transport. Loop scanning mutagenesis of the serotonin transporter external domain. *J. Biol. Chem.* **274**, 36058–36064 (1999).
- Hirayama, B. A., Diez-Sampedro, A. & Wright, E. M. Common mechanisms of inhibition for the Na⁺/glucose (hSGLT1) and Na⁺/Cl[−]/GABA (hGAT1) cotransporters. *Br. J. Pharmacol.* **134**, 484–495 (2001).
- Jacobs, M. T., Zhang, Y. W., Campbell, S. D. & Rudnick, G. Ibogaine, a noncompetitive inhibitor of serotonin transport, acts by stabilizing the cytoplasm-facing state of the transporter. *J. Biol. Chem.* **282**, 29441–29447 (2007).
- Shi, L., Quick, M., Zhao, Y., Weinstein, H. & Javitch, J. A. The mechanism of a neurotransmitter:sodium symporter-inward release of Na⁺ and substrate is triggered by a substrate in a second binding site. *Mol. Cell* **30**, 667–677 (2008).
- Zhao, Y. *et al.* Substrate-modulated gating dynamics in a Na⁺-coupled neurotransmitter transporter homologue. *Nature* **474**, 109–113 (2011).
- Pantanowitz, S., Bendahan, A. & Kanner, B. I. Only one of the charged amino acids located in the transmembrane α -helices of the γ -aminobutyric acid transporter (subtype A) is essential for its activity. *J. Biol. Chem.* **268**, 3222–3225 (1993).
- Bennett, E. R., Su, H. & Kanner, B. I. Mutation of arginine 44 of GAT-1, a (Na⁺ + Cl[−])-coupled γ -aminobutyric acid transporter from rat brain, impairs net flux but not exchange. *J. Biol. Chem.* **275**, 34106–34113 (2000).
- Loland, C. J., Granas, C., Javitch, J. A. & Gether, U. Identification of intracellular residues in the dopamine transporter critical for regulation of transporter conformation and cocaine binding. *J. Biol. Chem.* **279**, 3228–3238 (2004).
- Chen, N., Rickey, J., Berfield, J. L. & Reith, M. E. Aspartate 345 of the dopamine transporter is critical for conformational changes in substrate translocation and cocaine binding. *J. Biol. Chem.* **279**, 5508–5519 (2004).
- Watanabe, A. *et al.* The mechanism of sodium and substrate release from the binding pocket of vSGLT. *Nature* **468**, 988–991 (2010).
- Quick, M. *et al.* State-dependent conformations of the translocation pathway in the tyrosine transporter Tyt1, a novel neurotransmitter:sodium symporter from *Fusobacterium nucleatum*. *J. Biol. Chem.* **281**, 26444–26454 (2006).
- Shi, L. & Weinstein, H. Conformational rearrangements to the intracellular open states of the LeuT and ApcT transporters are modulated by common mechanisms. *Biophys. J.* **99**, L103–L105 (2010).

Supplementary Information is linked to the online version of the paper at www.nature.com/nature.

Acknowledgements We thank D. Cawley for monoclonal antibody production, L. Vaskalis for help with illustrations and the staff at the Advanced Photon Source beamline 24-ID-E and at the Advanced Light Source beamline 5.0.2 for their assistance with X-ray data collection and processing. We are grateful to E. Haddadian, T. Sosnick and K. Freed for assistance in refining the backbone torsional and side-chain angles using their unpublished TOP algorithm. We thank all Gouaux laboratory members, especially C. Piscitelli and S. K. Singh, for discussions and helpful suggestions throughout the project. This work was supported by the National Institutes of Health. E.G. is an investigator with the Howard Hughes Medical Institute.

Author Contributions H.K. and E.G. contributed to all aspects of the project.

Author Information Atomic coordinates and structure factors have been deposited with the Protein Data Bank under accession codes 3TT1, 3TT3 and 3TU0 for the LeuT^K(Y108F)–2B12 complex, the LeuT^K(TSY)–6A10 complex and the LeuT^K(TS) complex with alanine, respectively. Reprints and permissions information is available at www.nature.com/reprints. The authors declare no competing financial interests. Readers are welcome to comment on the online version of this article at www.nature.com/nature. Correspondence and requests for materials should be addressed to E.G. (gouauxe@ohsu.edu).

METHODS

Purification of LeuT mutants. The site-directed mutants LeuT^K(Y108F), LeuT^K(TS) and LeuT^K(TSY) were produced by polymerase chain reaction (PCR) and subcloned into a pET16b plasmid containing a thrombin-cleavage site and a C-terminal octa-histidine tag. All mutants were verified by DNA sequencing. The resulting proteins were expressed and purified as previously described^{10,25} with the following modifications. To obtain leucine-free transporter, buffers for purification did not contain sodium salts and membranes were washed three times in sodium-free buffer to ensure that no endogenously bound leucine was carried along. LeuT mutants were solubilized with *n*-dodecyl- β -D-maltopyranoside (C₁₂M) and purified by Ni-affinity chromatography. Protein for functional and biochemical assays was further purified by gel filtration in buffer containing C₁₂M.

Monoclonal antibodies and Fab fragments. Mouse monoclonal antibodies against LeuT^K(Y108F) and LeuT^K(TSY) were raised by standard methods using corresponding purified protein in detergent as antigen. Antibodies recognizing a conformational epitope in LeuT^K(Y108F) were selected using FSEC²⁶ and western blot analysis, resulting in the identification of the 2B12 monoclonal antibody. Antibodies specific to the inward-facing mutant LeuT^K(TSY) were selected based on their relative affinities for LeuT^K(TSY) and wild-type LeuT as determined by FSEC. From these screens we isolated the 6A10 monoclonal antibody. All FSEC analysis relied on C-terminal GFP fusions of the LeuT variants. Antibodies were purified from hybridoma supernatants using a SP sepharose cation-exchange column. Fab fragments were generated by papain digestion at 37 °C in 50 mM sodium phosphate pH 7.2, 1 mM EDTA and a papain to monoclonal antibody ratio of 1:20 w/w (2B12) or 1:100 w/w (6A10). Cysteine at 10 mM final concentration was added to the digestion reaction for 6A10. Digestion of 2B12 was stopped with 30 mM iodoacetamide after 4 h, while digestion of 6A10 was quenched by transferring the reaction to 4 °C after 2 h. Fab fragments were purified on a Protein A column, followed by ion-exchange chromatography. DNA encoding the light and heavy chains of 2B12 (IgG2a, κ) and 6A10 (IgG1, κ) Fab fragments were cloned and sequenced from hybridoma cells using rapid amplification of 5' complementary DNA ends (5'-RACE).

Purification of Fab complexes for crystallization. The His-tag of LeuT destined for crystallization was cleaved by thrombin. Transporter was then mixed with excess Fab and the complex was subjected to gel filtration in *n*-octyl- β -D-thioglycoside (C₈SG)-containing buffer. The buffer consisted of 20 mM Tris, pH 8.0, 50 mM (LeuT^K(TSY)-Fab) or 100 mM (LeuT^K(Y108F)-Fab) KCl and 12 mM (LeuT^K(TSY)-Fab) or 15 mM (LeuT^K(Y108F)-Fab) C₈SG. For crystallization of LeuT^K(TSY)-Fab complex, the protein was then supplemented with a fivefold molar excess of 1,2-dimyristoyl-*sn*-glycero-3-phosphoethanolamine (DMPE) and incubated at 4 °C for 1 h before removing insoluble lipids by centrifugation. A 55 mM DMPE stock was prepared in 20% DMSO and 80% gel filtration buffer. Protein was concentrated to 3.0–3.2 mg ml⁻¹ (LeuT^K(Y108F)-Fab) or 4.5–5 mg ml⁻¹ (LeuT^K(TSY)-Fab) for crystallization.

Crystallization. Crystallization was carried out by vapour diffusion in hanging drops at 20 °C. LeuT^K(Y108F)-Fab crystals were grown in 40 mM Tris pH 7.5, 23–26% PEG 550 monomethyl ether and 50–100 mM NaCl, and cryo-protected in 35% PEG 550 monomethyl ether. Crystals were allowed to sit in the final cryo-solution for 4–5 h before flash freezing in liquid nitrogen.

Different crystal forms were obtained for the LeuT^K(TSY)-Fab complex in similar crystallization conditions with the best crystals belonging to space group C222₁. These crystals were grown in 100 mM HEPES pH 7.6, 0.1 M Mg(NO₃)₂, 12–14% PEG 1500 and 1.5% w/v trimethylamine *N*-oxide dehydrate in a protein to precipitant ratio of 1:2. LeuT^K(TSY)-Fab crystals were cryo-protected with 15% PEG 1500 and 20% glycerol before flash-freezing.

Crystals of alanine-bound LeuT^K(TS) were obtained from protein purified in 20 mM Tris pH 8.0, 100 mM L-Ala, 200 mM NaCl and 40 mM *n*-octyl- β -D-glucoside (β -OG). Purification and crystallization were carried out as described for wild-type LeuT¹⁰.

Data collection and structure determination. For the LeuT^K(Y108F)-Fab complex, X-ray diffraction data sets for the crystals were indexed, integrated and scaled using HKL2000 and the CCP4 suite of computer programs^{51,52}. The crystals diffract to ~3.1 Å resolution, belong to the space group *P*2₁2₁2₁ and harbour two LeuT^K(Y108F)-Fab complexes per asymmetric unit, giving a Matthews coefficient⁵³ of 3.9 Å Da⁻³. The structure was determined by molecular replacement using the program PHASER⁵⁴. The search probes were the tryptophan-bound LeuT structure (PDB accession 3F3A) and a Fab homology model built using SWISS-MODEL⁵⁵. The model was built using COOT⁵⁶ into 2F_o - F_c maps, cross-validated using simulated annealing composite omit maps and refined with PHENIX⁵⁷ using non-crystallographic symmetry, individual atomic displacement parameters and translation/libration/screw (TLS)⁵⁸ subdomains. Six TLS groups composed of two LeuT molecules, two Fab constant domains and two

Fab variable domains were defined. This iterative model building and refinement procedure yielded a structure with good crystallographic and stereochemical statistics. Regions of weak or no electron density were excluded from the model such that the final structure consists of LeuT residues 5–129 and 135–507, Fab light chain residues 1–215, and Fab heavy chain residues 1–135, 143–219.

For the LeuT^K(TSY)-Fab complex, the crystals diffract to ~3.2 Å resolution and belong to the space group C222₁. There is one complex in the asymmetric unit, resulting in a Matthews coefficient of 3.4 Å Da⁻³. Initial phases were derived from a molecular replacement solution using PHASER⁵⁴ in which a partial structure of leucine-bound LeuT (PDB accession 2A65) and a high-resolution IgG1 Fab structure (PDB accession 1Q9Q) were used as search probes. The partial LeuT search probe was obtained by deleting TMs 1, 6 and 12 from the 2A65 structure. Electron density maps calculated using the 'prime and switch' method⁵⁹ clearly showed the LeuT regions where there were deviations from the 2A65 structure. This initial molecular replacement solution was used as a starting point for automated building using Phenix. Further changes were made to the LeuT portion using COOT⁵⁶. At this stage, electron density for the Fab portion was poor, making it difficult for manual building. A homology model built using PDB accession 1EJO for the light chain and PDB accession 2Z4Q for the heavy chain by PHYRE⁶⁰ resulted in a substantial decrease in the crystallographic *R* factors, yielding *R*_{work} and *R*_{free} values of 0.33 and 0.36, respectively. This model and a 2F_o - F_c map calculated with exclusion of the test set of reflections (*R*_{free} set) were then submitted to a crystallographic refinement server (<http://godzilla.uchicago.edu>). The resulting model had improved stereochemistry and *R*_{work} and *R*_{free} values of 0.29 and 0.32, respectively.

Further improvements to the model were made until the *R*_{work}/*R*_{free} values converged to 0.26/0.30 and structure quality assessed using Molprobit⁶¹ was satisfactory. Throughout the model building procedure, bias-minimized 'prime and switch' maps⁵⁹ and simulated annealing composite omit maps were used. Individual isotropic *B* factors and TLS parameters were refined using 11 TLS groups identified using Phenix⁵⁷: three LeuT domains comprised of residues 11–184, 185–254 and 255–511, four Fab heavy-chain domains involving residues 1–83, 84–140, 141–180 and 181–219, together with residues 1–94, 95–131, 132–177 and 178–215 forming the 4 Fab light-chain domains. The final model consists of LeuT residues 11–511, Fab light-chain residues 1–216, Fab heavy-chain residues 1–102, 104–219, and several detergent molecules.

The changes in helix and domain orientation were analysed using the program Interhlx (K. Yap, University of Toronto) and DynDom, respectively, and molecular figures were prepared using PyMOL.

Saturation binding assays. Dissociation constants of LeuT mutants for leucine were determined by scintillation proximity assays as described previously²⁵ at a protein concentration of 1 μM in 20 mM Tris-MES pH 7.0, 200 mM NaCl and 1 mM C₁₂M. Non-specific binding was measured in duplicate using 1 mM L-leucine as cold competitor and total binding was measured in triplicate. Data were fit with GraphPad Prism.

Transport time course. LeuT mutants were reconstituted into liposomes as previously described²⁵, at a protein to lipid ratio of 1:100, and loaded with either Buffer 1 (20 mM Tris-MES pH 6.0 and 500 mM KCl) for uptake or Buffer 2 (20 mM Tris-MES pH 6.0, 500 mM NaCl and 10 mM L-leucine) for exchange. Transport was initiated at 27 °C by diluting proteoliposomes to 10 μg ml⁻¹ into external buffer (20 mM Tris-MES pH 6.0, 500 mM NaCl) containing either 200 nM (for LeuT^K(Y108F)) or 400 nM (for LeuT^K(TS) and LeuT^K(TSY)) or 10 nM [³H]-leucine. Uptake or exchange was followed by quenching 100 μl samples of the reaction mixture in 1.8 ml of ice-cold Buffer 1 for uptake or Buffer 2 for exchange. Background counts were measured with control reactions performed in the absence of sodium. Reactions were measured in replicates of 3–5 and analysed using GraphPad Prism.

FSEC. FSEC experiments²⁶ were carried out using a Superose 6 10/300 column with the mobile phase consisting of 20 mM Tris, pH 8.0, 1 mM C₁₂M, and either 200–400 mM NaCl and 10 mM leucine or 200 mM KCl for analyses of LeuT in substrate-bound and apo states, respectively. Fab-LeuT complexes were prepared by mixing LeuT and Fab in a molar ratio of 1:2. Elution was followed using tryptophan fluorescence with excitation and emission wavelengths at 280 nm and 335 nm, respectively.

- Otwinowski, Z. & Minor, W. Processing of X-ray diffraction data collected in oscillation mode. *Methods Enzymol.* **276**, 307–326 (1997).
- Collaborative Computational Project 4. The CCP4 suite: programs for protein crystallography. *Acta Crystallogr. D* **50**, 760–763 (1994).
- Matthews, B. W. Solvent content of protein crystals. *J. Mol. Biol.* **33**, 491–497 (1968).
- McCoy, A. J. Solving structures of protein complexes by molecular replacement with Phaser. *Acta Crystallogr. D* **63**, 32–41 (2007).
- Kopp, J. & Schwede, T. The SWISS-MODEL Repository: new features and functionalities. *Nucleic Acids Res.* **34**, D315–D318 (2006).

56. Emsley, P. & Cowtan, K. Coot: model-building tools for molecular graphics. *Acta Crystallogr. D* **60**, 2126–2132 (2004).
57. Adams, P. D. *et al.* PHENIX: building new software for automated crystallographic structure determination. *Acta Crystallogr. D* **58**, 1948–1954 (2002).
58. Painter, J. & Merritt, E. A. Optimal description of a protein structure in terms of multiple groups undergoing TLS motion. *Acta Crystallogr. D* **62**, 439–450 (2006).
59. Terwilliger, T. C. Using prime-and-switch phasing to reduce model bias in molecular replacement. *Acta Crystallogr. D* **60**, 2144–2149 (2004).
60. Kelley, L. A. & Sternberg, M. J. Protein structure prediction on the Web: a case study using the Phyre server. *Nature Protocols* **4**, 363–371 (2009).
61. Chen, V. B. *et al.* MolProbity: all-atom structure validation for macromolecular crystallography. *Acta Crystallogr. D* **66**, 12–21 (2010).

Transiting circumbinary planets Kepler-34 b and Kepler-35 b

William F. Welsh¹, Jerome A. Orosz¹, Joshua A. Carter², Daniel C. Fabrycky³, Eric B. Ford⁴, Jack J. Lissauer⁵, Andrej Prša⁶, Samuel N. Quinn^{2,7}, Darin Ragozzine², Donald R. Short¹, Guillermo Torres², Joshua N. Winn⁸, Laurance R. Doyle⁹, Thomas Barclay^{5,10}, Natalie Batalha^{5,11}, Steven Bloemen¹², Erik Brugamyer¹³, Lars A. Buchhave^{14,15}, Caroline Caldwell¹³, Douglas A. Caldwell⁹, Jessie L. Christiansen^{5,9}, David R. Ciardi¹⁶, William D. Cochran¹³, Michael Endl¹³, Jonathan J. Fortney¹⁷, Thomas N. Gautier III¹⁸, Ronald L. Gilliland¹⁹, Michael R. Haas⁵, Jennifer R. Hall²⁰, Matthew J. Holman², Andrew W. Howard²¹, Steve B. Howell⁵, Howard Isaacson²¹, Jon M. Jenkins^{5,9}, Todd C. Klaus²⁰, David W. Latham², Jie Li^{5,9}, Geoffrey W. Marcy²¹, Tsevi Mazeh²², Elisa V. Quintana^{5,9}, Paul Robertson¹³, Avi Shporer^{23,24}, Jason H. Steffen²⁵, Gur Windmiller¹, David G. Koch⁵ & William J. Borucki⁵

Most Sun-like stars in the Galaxy reside in gravitationally bound pairs of stars^{1,2} (binaries). Although long anticipated^{3–8}, the existence of a ‘circumbinary planet’ orbiting such a pair of normal stars was not definitively established until the discovery⁹ of the planet transiting (that is, passing in front of) Kepler-16. Questions remained, however, about the prevalence of circumbinary planets and their range of orbital and physical properties. Here we report two additional transiting circumbinary planets: Kepler-34 (AB)b and Kepler-35 (AB)b, referred to here as Kepler-34 b and Kepler-35 b, respectively. Each is a low-density gas-giant planet on an orbit closely aligned with that of its parent stars. Kepler-34 b orbits two Sun-like stars every 289 days, whereas Kepler-35 b orbits a pair of smaller stars (89% and 81% of the Sun’s mass) every 131 days. The planets experience large multi-periodic variations in incident stellar radiation arising from the orbital motion of the stars. The observed rate of circumbinary planets in our sample implies that more than ~1% of close binary stars have giant planets in nearly coplanar orbits, yielding a Galactic population of at least several million.

The new planets were identified using 671 days of data from the NASA Kepler spacecraft¹⁰. As part of its mission¹¹ to detect Earth-like planets via the transit method, Kepler is monitoring more than 2,000 eclipsing binary stars^{12,13}. From these, we selected a sample of 750 systems with orbital periods ranging from 0.9 to 276 days, and for which eclipses of both stars occur. For each system, we measured the eclipse times for both stars and searched for departures from strict periodicity, as would be produced by gravitational perturbations from a third body.

All 750 systems were searched by eye for planetary transits, with particular attention being paid to a subset (18% of the total) that exhibited significant differences between the periods derived from the deeper primary eclipses, and those derived from the shallower secondary eclipses (for details, see Supplementary Information). (Here ‘primary eclipse’ indicates the eclipse of the primary star by the secondary star.) This led to the discovery of Kepler-34 and

Kepler-35, and a candidate system KOI-2939. KOI-2939 (Kepler Input Catalog¹⁴ number 05473556) exhibited a single transit at BJD (barycentric Julian date) $2,454,996.995 \pm 0.010$ of duration 2.5 h and depth 0.18%. The transit duration constrains the size and velocity of the third body and is consistent with a Jovian planet transiting the secondary star, but we cannot verify its planetary nature. We defer discussion for a future investigation.

The stars of Kepler-34 (denoted A and B, where A is the brighter, more massive primary star) have an orbital period of 28 days, with a period difference between primary and secondary eclipses of 4.91 ± 0.59 s. Three transits were detected (Fig. 1), with the first and second being transits of the primary star, while the third is of the secondary star. Notably the transit durations are all different, ruling out the most common type of ‘false positive’, a background eclipsing binary. Circumbinary transits naturally vary in duration as a consequence of the changing velocity of the stars. The Kepler photometry was supplemented by spectroscopic observations of the radial-velocity variations of both stars (Fig. 1f), in order to determine the orbital scale and sizes of all three bodies. The photometric and spectroscopic data were fitted with a model^{9,15} that accounts for the three-body gravitational dynamics and the loss of light due to eclipses and transits (see Supplementary Information). The model fit confirms that the transiting body is a planet with 22% of the mass of Jupiter (69 Earth masses) and 76% of the radius of Jupiter (8.6 Earth radii). The primary and secondary stars are similar to the Sun. Using the spectra, we also measured the effective temperature and abundance of heavy elements (metallicity) of both stars. The observed stellar parameters match the Yonsei-Yale theoretical models of stellar evolution¹⁶ for an age of 5–6 Gyr. The parameters and uncertainties are given in Table 1, with details in Supplementary Information.

The stars of Kepler-35 (A and B) have an orbital period of 21 days, with a period difference between primary and secondary eclipses of 1.89 ± 0.48 s. Four transits were detected (Fig. 2 b–e). The first, second and fourth events are transits of the primary star, and the weaker third

¹Astronomy Department, San Diego State University, 5500 Campanile Drive, San Diego, California 92182, USA. ²Harvard-Smithsonian Center for Astrophysics, 60 Garden Street, Cambridge, Massachusetts 02138, USA. ³UCO/Lick Observatory, University of California, Santa Cruz, California 95064, USA. ⁴University of Florida, 211 Bryant Space Science Center, Gainesville, Florida 32611-2055, USA. ⁵NASA Ames Research Center, Moffett Field, California 94035, USA. ⁶Villanova University, Department of Astronomy and Astrophysics, 800 E. Lancaster Avenue, Villanova, Pennsylvania 19085, USA. ⁷Department of Physics and Astronomy, Georgia State University, PO Box 4106, Atlanta, Georgia 30302, USA. ⁸Massachusetts Institute of Technology, Physics Department and Kavli Institute for Astrophysics and Space Research, 77 Massachusetts Avenue, Cambridge, Massachusetts 02139, USA. ⁹Carl Sagan Center for the Study of Life in the Universe, SETI Institute, 189 Bernardo Avenue, Mountain View, California 94043, USA. ¹⁰Bay Area Environmental Research Institute, Inc., 560 Third Street West, Sonoma, California 95476, USA. ¹¹Department of Physics and Astronomy, San Jose State University, One Washington Square, San Jose, California 95192, USA. ¹²Instituut voor Sterrenkunde, Katholieke Universiteit Leuven, Celestijnenlaan 200D, B-3001 Leuven, Belgium. ¹³McDonald Observatory, The University of Texas at Austin, Austin, Texas 78712-0259, USA. ¹⁴Niels Bohr Institute, Copenhagen University, Juliane Maries Vej 30, DK-2100 Copenhagen, Denmark. ¹⁵Centre for Star and Planet Formation, Natural History Museum of Denmark, University of Copenhagen, DK-1350 Copenhagen, Denmark. ¹⁶NASA Exoplanet Science Institute/Caltech, 770 South Wilson Avenue, Pasadena, California 91125, USA. ¹⁷Department of Astronomy and Astrophysics, University of California, Santa Cruz, Santa Cruz, California 95064, USA. ¹⁸Jet Propulsion Laboratory, 4800 Oak Grove Drive, Pasadena, California 91109, USA. ¹⁹Space Telescope Science Institute, 3700 San Martin Drive, Baltimore, Maryland 21218, USA. ²⁰Orbital Sciences Corporation/NASA Ames Research Center, Moffett Field, California 94035, USA. ²¹Astronomy Department, University of California, Berkeley, California 94720, USA. ²²School of Physics and Astronomy, Tel Aviv University, Tel Aviv 69978, Israel. ²³Las Cumbres Observatory Global Telescope Network, 6740 Cortona Drive, Suite 102, Santa Barbara, California 93117, USA. ²⁴Department of Physics, Broida Hall, University of California, Santa Barbara, California 93106, USA. ²⁵Fermilab Center for Particle Astrophysics, MS 127, PO Box 500, Batavia, Illinois 60510, USA.

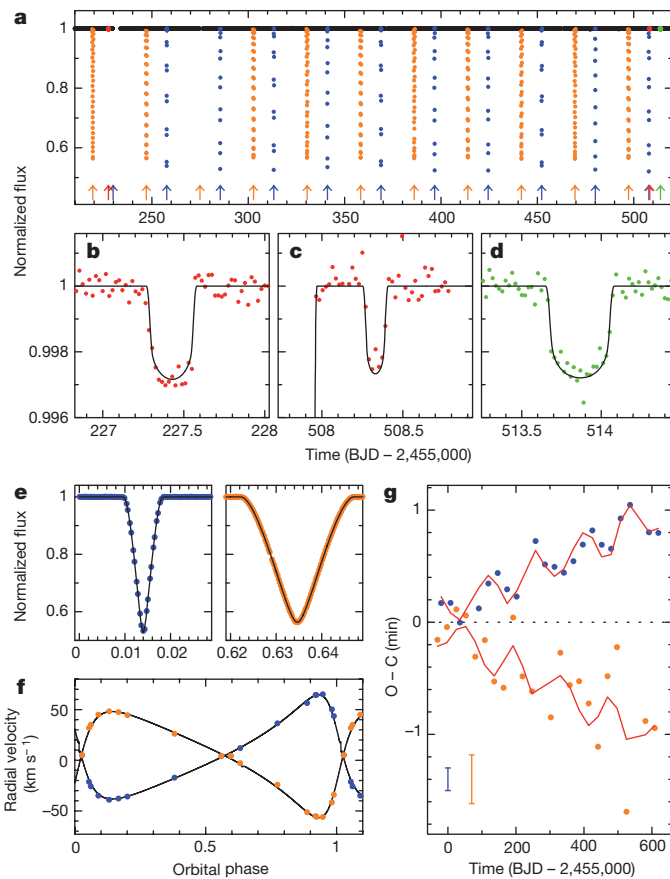


Figure 1 | Observations of Kepler-34. **a**, A portion of the normalized light curve, showing the relative brightness versus time (in units of barycentric Julian days, BJD). Low-frequency variations and instrumental drifts have been removed (Supplementary Information). The blue points show the primary eclipses (star B eclipses star A), orange points show the secondary eclipses, red points show the primary transits (planet transits star A), and green shows the secondary transit. The times of each event are indicated by the arrows. Owing to gaps in the observations, one primary and one secondary eclipse were missed. **b–d**, Close-up views of the three transit events. The solid curve is the photometric-dynamical model. Variations in transit widths are mainly due to differences in the transverse velocity of the stars during transit. The large drop before the transit in **c** is due to a primary eclipse. **e**, Close-up views of the phase-folded primary and secondary eclipses plotted versus orbital phase (time modulo the orbital period P , where $P = 27.795794795$ d and the time of periastron is BJD 2,455,007.5190). Only Kepler Quarter 4 data are shown. **f**, Radial velocities of the primary star (blue points), secondary (orange points), and the model curve, versus orbital phase. **g**, Observed (O) minus computed (C) diagram, showing the deviations between the measured eclipse times and those predicted assuming strict periodicity. Primary eclipses are shown as blue points, secondaries by orange points, and the corresponding models by the red curves. A period of 27.79578193 days and an epoch of BJD 2,454,979.72301 were used to compute the primary eclipse times, and a phase offset of 0.6206712 for the secondary eclipse times. The divergence indicates the primary and secondary periods are different. The two vertical bars in the lower left denote the median $\pm 1\sigma$ uncertainties of the primary and secondary eclipse times: 0.10 and 0.22 min.

event is a transit of the secondary star. Transits do not occur every planetary orbit, placing a strong constraint on the mutual orbital inclination and its evolution. The transits differ in duration, and the interval between transits is not constant, again signalling a circumbinary body. Modelling the photometry and radial velocities yields the system parameters given in Table 1. The transiting body is a planet with 13% of the mass and 73% of the radius of Jupiter (respectively 41 Earth

Table 1 | Circumbinary planet system parameters

	Kepler-34 (this work)	Kepler-35 (this work)	Kepler-16 (ref. 9)
Planetary properties			
Mass of planet, M_p (M_{Jupiter})	$0.220^{+0.011}_{-0.010}$	$0.127^{+0.020}_{-0.020}$	$0.333^{+0.016}_{-0.016}$
Radius of planet, R_p (R_{Jupiter})	$0.764^{+0.012}_{-0.014}$	$0.728^{+0.014}_{-0.014}$	$0.7538^{+0.0026}_{-0.0023}$
Mean density of planet, ρ_p (g cm^{-3})	$0.613^{+0.045}_{-0.041}$	$0.410^{+0.070}_{-0.069}$	$0.964^{+0.047}_{-0.046}$
Planet surface gravity, g_p (cm s^{-2})	936^{+57}_{-54}	596^{+98}_{-98}	$1,452^{+70}_{-69}$
Properties of the planetary orbit			
Reference epoch (BJD)	2,454,969.20000	2,454,965.85000	2,455,212.12316
Period, P (days)	$288.822^{+0.063}_{-0.081}$	$131.458^{+0.077}_{-0.105}$	$228.776^{+0.020}_{-0.037}$
Semi-major axis length, a (AU)	$1.0896^{+0.0009}_{-0.0009}$	$0.60347^{+0.00101}_{-0.00103}$	$0.7048^{+0.0011}_{-0.0011}$
Eccentricity, e	$0.182^{+0.016}_{-0.020}$	$0.042^{+0.007}_{-0.004}$	$0.00685^{+0.00101}_{-0.00146}$
$e \sin(\omega)$	$0.025^{+0.007}_{-0.007}$	$0.035^{+0.009}_{-0.011}$	$-0.00448^{+0.00088}_{-0.00090}$
$e \cos(\omega)$	$0.180^{+0.016}_{-0.021}$	$0.017^{+0.021}_{-0.018}$	$0.0051^{+0.0014}_{-0.0028}$
Mean longitude, $\lambda \equiv M + \omega$ (deg)	$106.5^{+2.1}_{-2.0}$	$136.4^{+2.1}_{-2.7}$	$106.51^{+0.32}_{-0.16}$
Inclination, i (deg)	$90.355^{+0.026}_{-0.018}$	$90.76^{+0.12}_{-0.09}$	$90.0322^{+0.0022}_{-0.0023}$
Relative nodal longitude, Ω (deg)	$-1.74^{+0.14}_{-0.16}$	$-1.24^{+0.24}_{-0.33}$	$0.003^{+0.013}_{-0.013}$
Properties of the stars in the stellar binary			
Mass of A, M_A (M_{Sun})	$1.0479^{+0.0033}_{-0.0030}$	$0.8877^{+0.0051}_{-0.0053}$	$0.6897^{+0.0035}_{-0.0034}$
Radius of A, R_A (R_{Sun})	$1.1618^{+0.0027}_{-0.0031}$	$1.0284^{+0.0020}_{-0.0019}$	$0.6489^{+0.0013}_{-0.0013}$
Mass of B, M_B (M_{Sun})	$1.0208^{+0.0022}_{-0.0022}$	$0.8094^{+0.0042}_{-0.0045}$	$0.20255^{+0.00066}_{-0.00065}$
Radius of B, R_B (R_{Sun})	$1.0927^{+0.0032}_{-0.0027}$	$0.7861^{+0.0020}_{-0.0022}$	$0.22623^{+0.00059}_{-0.00053}$
Flux ratio in the Kepler bandpass, F_B/F_A	$0.8475^{+0.0110}_{-0.0076}$	$0.3941^{+0.0011}_{-0.0010}$	$0.01555^{+0.00010}_{-0.00006}$
Properties of the stellar binary orbit			
Period, P (days)	$27.7958103^{+0.0000016}_{-0.0000015}$	$20.733666^{+0.000012}_{-0.000012}$	$41.079220^{+0.000078}_{-0.000077}$
Semi-major axis length, a (AU)	$0.22882^{+0.00019}_{-0.00019}$	$0.17617^{+0.00029}_{-0.00030}$	$0.22431^{+0.00035}_{-0.00035}$
Eccentricity, e	$0.52087^{+0.00052}_{-0.00055}$	$0.1421^{+0.0014}_{-0.0015}$	$0.15944^{+0.00061}_{-0.00062}$
$e \sin(\omega)$	$0.49377^{+0.00057}_{-0.00060}$	$0.1418^{+0.0014}_{-0.0015}$	$-0.15840^{+0.00063}_{-0.00061}$
$e \cos(\omega)$	$0.165828^{+0.000065}_{-0.000061}$	$0.0086413^{+0.0000031}_{-0.0000031}$	$-0.0181481^{+0.0000045}_{-0.0000044}$
Mean longitude, $\lambda \equiv M + \omega$ (deg)	$300.1970^{+0.0099}_{-0.0105}$	$89.1784^{+0.0011}_{-0.0012}$	$92.3520^{+0.0011}_{-0.0011}$
Inclination, i (deg)	$89.8584^{+0.0075}_{-0.0083}$	$90.4238^{+0.0076}_{-0.0073}$	$90.3401^{+0.0016}_{-0.0019}$

Results of the photometric-dynamical model for Kepler-34 (KIC 8572936) and Kepler-35 (KIC 9837578). The orbital parameters listed are the osculating Jacobian parameters, that is, the instantaneous Keplerian elements for the listed epoch. In general, unlike the simple two-body Keplerian case, the orbital elements are functions of time. In particular, the orbital period of Kepler-34 b varies from 280 to 312 days on secular timescales; the median period is ~ 291 days. See Supplementary Information for details. For direct comparison, values^a for Kepler-16 are listed. The mean longitude (λ) is the sum of the mean anomaly (M) and the argument of periastron (ω).

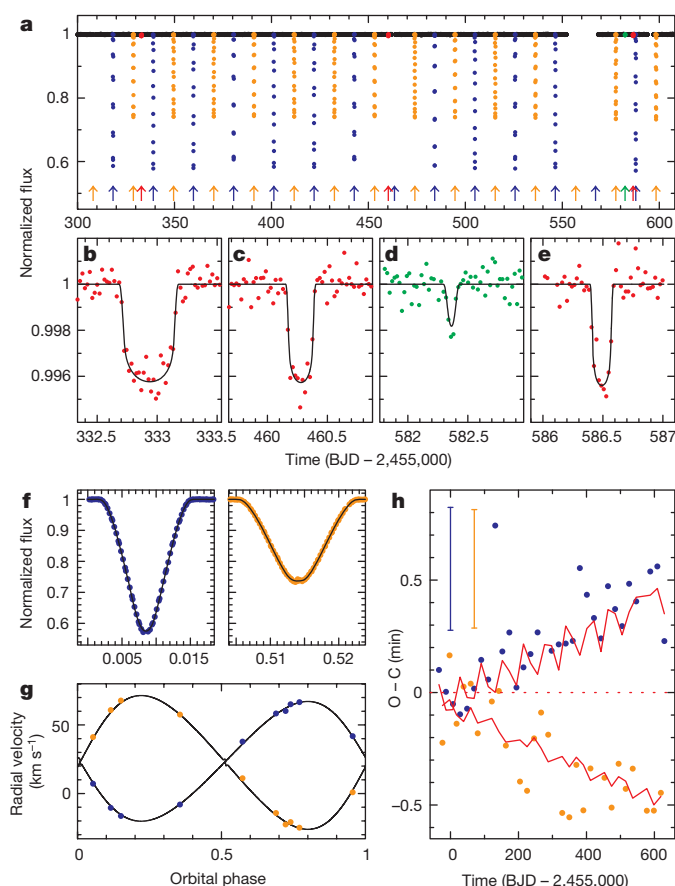


Figure 2 | Observations of Kepler-35. The representation of data is similar to that in Fig. 1. **a**, A portion of the light curve for Kepler-35. Owing to interruptions in the data acquisition, two primary and two secondary eclipses were not observed. **b–e**, Close-up views of the four transit events. Red points denote primary transits, green points denote a secondary transit. Note the differences in transit duration. **f**, Close-up views of the primary eclipses and secondary eclipses, plotted versus orbital phase where $P = 20.733762175$ days and the time of periastron passage is BJD 2,455,007.3131. Only Kepler Quarter 4 data are shown (BJD 2,455,183 through to 2,455,275). **g**, Radial velocities of the primary star (blue points), secondary (orange points) and model fit. **h**, Observed minus computed diagram, where a period of 20.73373997 days and an epoch of BJD 2,454,965.84579 were used to predict the primary eclipses, and a phase offset of 0.5055680 for the secondary eclipses. The two vertical bars in the upper left denote the median $\pm 1\sigma$ uncertainties of the primary and secondary eclipse times, 0.27 and 0.26 min, respectively

Kepler-16 b, but all are consistent with low-density gas-giant planets. Figure 3 gives a visual comparison of the systems' orbits. For all three systems, the planetary and stellar orbits are aligned to within 2° , suggesting that each system formed from a flat disk of material. The period ratios (planetary to stellar) for Kepler-34, Kepler-35 and Kepler-16 are 10.4, 6.3 and 5.6, respectively, only 21%, 24% and 14% larger than analytic estimates for stability against three-body interactions^{17–19}. Long-term integration of the equations of motion confirms that these two new systems are stable for at least 10 Myr (Supplementary Information). Note that the planets' locations bracket the habitable zone²⁰ (where liquid water would be stable on the surface of a rocky planet), with Kepler-34 b and Kepler-35 b lying interior to the habitable zone and Kepler-16 b lying exterior to it.

A simple argument suggests that circumbinary giant planets are not extremely rare, as three such objects have been seen in our sample of 750 systems. Given the orbital geometry of Kepler-34, Kepler-35 and Kepler-16, the probability²¹ that a randomly placed observer who sees stellar eclipses would also see planetary transits is approximately 12%, 14% and 21%, respectively (Supplementary Information). If this probability of roughly $\sim 15\%$ were constant across all 750 target systems, then the fraction of binaries with circumbinary gas giant planets at similar periods would be $(3/750) \times (0.15)^{-1}$, or a few per cent. However, this does not account for the period distribution of binaries in our sample, and the search is not complete; consequently a lower limit of $\sim 1\%$ is reasonable. With $\sim 2.6\%$ of all Sun-like stars in

masses and 8.2 Earth radii). Comparison to stellar-evolutionary models suggests a system age of $\sim 8\text{--}12$ Gyr, although, interestingly, the models do not provide a satisfactory match to the stellar masses and radii under the assumption of a common age and metallicity (Supplementary Information).

The mean densities of Kepler-34 b and Kepler-35 b are respectively 0.61 and 0.41 g cm^{-3} , somewhat lower than the 0.96 g cm^{-3} of

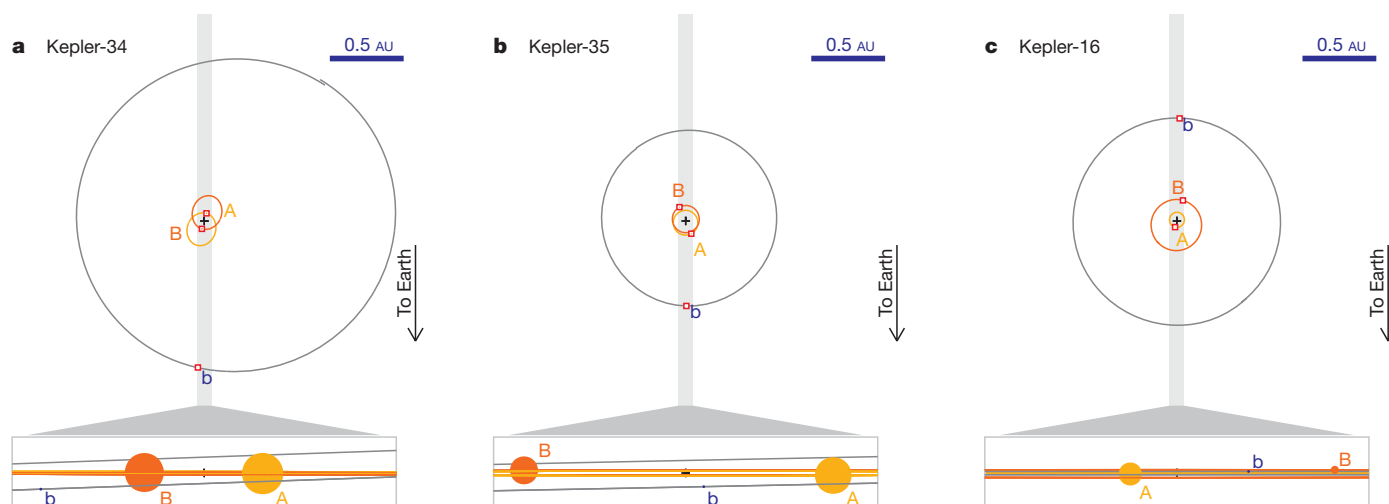


Figure 3 | Orbital configurations. **a**, Scale view of the orbits of the Kepler-34 system seen face-on (top) and also as seen from Earth (boxed, bottom). In the face-on view, the stars and planet are too small to be seen relative to their orbit curves, and so are represented as dots and marked with symbols A, B, and b denoting the primary star, secondary star, and planet. This view is correct for a given epoch (BJD 2,455,507.50). Because of the dynamical interactions between the three bodies, this orbital configuration will evolve. For example, the orbits precess, and hence the orbits do not actually close. The line-of-sight view shown

in the box depicts the stars and planet with correct relative sizes and orientation. More importantly, the orbits and the orbital tilts are accurately portrayed, showing how transits do not necessarily occur at every conjunction. The grey shaded area in the top panel denotes the limits of the view shown in the expanded bottom panel. **b**, As for **a**, but for Kepler-35 at epoch BJD 2,455,330.60. Note that the relative sizes of the bodies are drawn to scale for each panel (**a–c**), not just within a panel. **c**, As for **a**, but for Kepler-16 at epoch BJD 2,455,213.0.

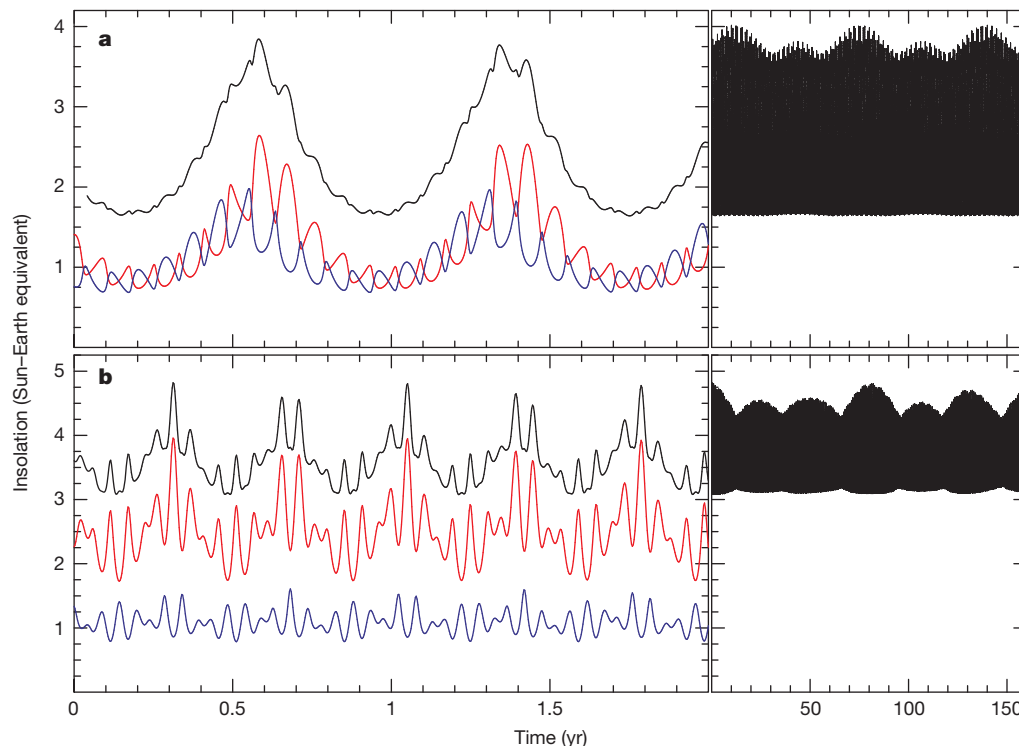


Figure 4 | Variations in insolation received by Kepler-34 b and Kepler-35 b. **a**, Left panel, the black curve shows the incident flux (insolation) received by Kepler-34 b from its two stars. The insolation is in units of the solar constant S (solar flux received at a distance of 1 AU; $S = 1.0$ for the Sun–Earth system). The contribution from star A is shown in red and the contribution from star B in

the Galaxy residing in binary star systems similar to the three discussed here^{2,22} (Supplementary Information), a conservative estimate yields millions of nearly coplanar circumbinary planets in the Galaxy like the ones reported here.

Orbital motion of the central stars causes complex time variations in stellar insolation for circumbinary planets. Figure 4 shows the calculated insolation for Kepler-34 b and Kepler-35 b. The variation is multi-periodic, with changes on the timescales of the stellar orbit, the planetary orbit, and the long-term precession of the orbits due to three-body effects. For Kepler-34 b and Kepler-35 b, the average insolation is (respectively) 2.4 and 3.6 times the Earth's insolation, with maximum-to-minimum ratios of 250% and 160%. By comparison, for Venus the insolation is 1.9 times the Earth's with only a 2.7% variation. These highly variable, multi-periodic fluctuations in insolation are unique to circumbinary planets, and can lead to complex climate cycles. It will be interesting to explore the effects of these swings in insolation on the atmospheric dynamics (Supplementary Information), and ultimately on the evolution of life on habitable circumbinary planets.

Received 15 November; accepted 5 December 2011.

Published online 11 January 2012.

1. Binnendijk, L. *Properties of Double Stars* (Univ. Pennsylvania Press, 1960).
2. Raghavan, D. *et al.* A survey of stellar families: multiplicity of solar-type stars. *Astrophys. J.* **190** (Suppl.), 1–42 (2010).
3. Schneider, J. & Chevreton, M. The photometric search for Earth-sized extrasolar planets by occultation in binary systems. *Astron. Astrophys.* **232**, 251–257 (1990).
4. Quintana, E. V. & Lissauer, J. J. Terrestrial planet formation surrounding close binary stars. *Icarus* **185**, 1–20 (2006).
5. Deeg, H.-J. *et al.* Extrasolar planet detection by binary stellar eclipse timing: evidence for the third body around CM Draconis. *Astron. Astrophys.* **480**, 563–571 (2008).
6. Haghighipour, N. *Planets in Binary Star Systems* (Astrophysics and Space Science Library, Vol. 366, Springer, 2010).
7. Sybilski, P., Konacki, M. & Kozłowski, S. Detecting circumbinary planets using eclipse timing of binary stars — numerical simulations. *Mon. Not. R. Astron. Soc.* **405**, 657–665 (2011).

blue. The most rapid variations are caused by the orbital motion of the stars. The slower variations are due to the orbital motion of the planet. Right panel, a longer timescale view of the insolation. The long-timescale quasi-periodicity is caused by the mutual precession of the orbits of the stars and planet, but is dominated by the precession of the planet. **b**, As for **a**, but for Kepler-35 b.

8. Schwarz, R. *et al.* Prospects of the detection of circumbinary planets with Kepler and CoRoT using the variations of eclipse timing. *Mon. Not. R. Astron. Soc.* **414**, 2763–2770 (2011).
9. Doyle, L. R. *et al.* Kepler-16: a transiting circumbinary planet. *Science* **333**, 1602–1606 (2011).
10. Koch, D. *et al.* Kepler mission design. *Astrophys. J.* **713**, L79–L86 (2010).
11. Borucki, W. J. *et al.* Kepler planet-detection mission: introduction and first results. *Science* **327**, 977–980 (2010).
12. Prša, A. *et al.* Kepler eclipsing binary stars. I. Catalog and principal characterization of 1879 eclipsing binaries in the first data release. *Astron. J.* **141**, 83–98 (2011).
13. Slawson, R. W. *et al.* Kepler eclipsing binary stars. II. 2165 Eclipsing binaries in the second data release. *Astron. J.* **142**, 160–173 (2011).
14. Brown, T. M. *et al.* Kepler input catalog: photometric calibration and stellar classification. *Astron. J.* **142**, 112–129 (2011).
15. Carter, J. A. *et al.* KOI-126: a triply eclipsing hierarchical triple with two low-mass stars. *Science* **331**, 562–565 (2011).
16. Yi, S. K. *et al.* Toward better age estimates for stellar populations: the Y^2 isochrones for solar mixture. *Astrophys. J. Suppl. Ser.* **136**, 417–437 (2001).
17. Holman, M. J. & Wiegert, P. A. Long-term stability of planets in binary systems. *Astron. J.* **117**, 621–628 (1999).
18. Eggleton, P. & Kiseleva, L. An empirical condition for stability of hierarchical triple systems. *Astrophys. J.* **455**, 640–645 (1995).
19. Doolin, S. & Blundell, K. M. The dynamics and stability of circumbinary orbits. *Mon. Not. R. Astron. Soc.* (in the press); preprint at <http://arXiv.org/abs/1108.4144> (2011).
20. Kasting, J. F., Whitmire, D. P. & Reynolds, R. T. Habitable zones around main sequence stars. *Icarus* **101**, 108–128 (1993).
21. Ragozzine, D. & Holman, M. J. The value of systems with multiple transiting planets. *Astrophys. J.* (submitted); preprint at <http://arXiv.org/abs/1006.3727> (2010).
22. Chabrier, G. Galactic stellar and substellar initial mass function. *Publ. Astron. Soc. Pacif.* **115**, 763–795 (2003).

Supplementary Information is linked to the online version of the paper at www.nature.com/nature.

Acknowledgements Kepler was selected as the tenth NASA Discovery mission with funding provided by NASA's Science Mission Directorate. We thank the many people who made the Kepler mission a reality. W.F.W., J.A.O., E.B.F., A.P., L.R.D., J.J.F., M.J.H., T.M. and J.H.S. were supported by the Kepler Participating Scientist Program. W.F.W., J.A.O., D.R.S. and G.W. were supported by the NSF. D.C.F. and J.A.C. acknowledge NASA support through Hubble Fellowship grants, awarded by STScI, operated by AURA. J.N.W. was supported by the NASA Origins programme. S.B. acknowledges funding from the European Research Council under the European Community's Seventh Framework Programme (PROSPERITY) and from the Research Council of KU Leuven.

Some of the reported computations were run on the Odyssey cluster supported by the FAS Science Division Research Computing Group at Harvard University. This Letter is based in part on observations made with the Nordic Optical Telescope (operated on the island of La Palma jointly by Denmark, Finland, Iceland, Norway and Sweden, in the Spanish Observatorio del Roque de los Muchachos of the Instituto de Astrofísica de Canarias), the W. M. Keck Observatory (operated by the University of California and the California Institute of Technology) and the Hobby-Eberly Telescope (HET; a joint project of the University of Texas at Austin, the Pennsylvania State University, Stanford University, Ludwig-Maximilians-Universität München, and Georg-August-Universität Göttingen).

Author Contributions W.F.W. led the research effort on these transiting circumbinary planets (CBPs) and wrote much of the Letter. J.A.O. led the ETV (eclipse timing variation) investigation, measured $O - Cs$, inspected light curves, measured EB (eclipsing binary) properties, measured radial velocities and flux ratios, generated Figs 1 and 2, and assembled the Supplementary Information. J.A.C. created and used the photometric-dynamical code to model the light curve and RVs (radial velocities), measured system parameters, and generated Table 1 and Fig. 3. D.C.F. produced initial dynamical models to interpret the timing of eclipse and transit events leading to the planet interpretation, and developed criteria for non-eclipsing CBP searches. E.B.F. contributed to interpretation and text, checked long-term stability, and did insolation calculations. J.J.L. contributed to interpretation and text, and initiated study of variations in insolation on CBPs. A.P. measured mass, radii and other properties of the EBs, including contamination and flux ratios. S.N.Q. obtained and analysed spectra, and determined stellar parameters and luminosity ratios. D.R. computed the estimated frequency of CBPs. D.R.S. developed the automated ETV code to measure eclipse times and $O - C$ deviations. G.T. contributed to the discussion of the stellar parameters and carried out the comparison with stellar evolution models. J.N.W. contributed to the text, estimated age via gyrochronology, and contributed to topics related to pseudosynchronicity. L.R.D. contributed to the habitable zone discussion and led the initial search for CBPs. T.B. examined pixel level data and contributed basis-vector corrected light curves. N.B. directed EB target selection and identification. S.B. contributed to the text and Supplementary Information. E.B. carried out an independent spectroscopic investigation to measure stellar parameters. L.A.B. gathered spectroscopic observations for the RV and spectroscopic parameter determination. C.C. contributed three nights of spectroscopic observations at the McDonald 2.7 m observatory. D.A.C. contributed to calibration of the Kepler

photometer and pipeline necessary for data acquisition. J.L.C. supported the science operations to collect and calibrate the Kepler data. D.R.C. coordinated ground-based follow-up observations. W.D.C. obtained the HET spectra, and processed all McDonald 2.7 m and HET spectra. M.E. contributed HET and McDonald 2.7 m spectra. J.J.F. contributed calculations and discussion regarding the characteristics of the planets' atmospheres. T.N.G. coordinated the Kepler follow-up observation effort. R.L.G. provided mission support and contributed to the text and discussion of results. M.R.H. led the effort to gather, process and distribute the data necessary for this investigation. J.R.H. contributed to the collection, validation and management of the Kepler data used here. M.J.H. contributed to the discussion of the dynamical stability. A.W.H. made spectroscopic observations using Keck-HIRES. S.B.H. contributed reconnaissance spectroscopy. H.I. obtained spectroscopic observations of targets. J.M.J. developed observation/analysis techniques and calibration software that enables the Kepler photometer to operate successfully. T.C.K. led the design and development of the Science Processing Pipeline Infrastructure needed to process the data used here. D.W.L. contributed spectroscopy and preparation of the Kepler Input Catalog. J.L. contributed to the development of the Data Validation component of the Kepler Science Operations Center pipeline necessary to obtain these data. G.W.M. obtained Keck-HIRES spectra. T.M. analysed the beaming effect in Kepler-35 and participated in the discussion of statistical inference and the spectroscopic light ratio. E.V.Q. developed calibration/validation software necessary for the Kepler data in this paper. P.R. contributed ten nights of spectroscopic observations at the McDonald 2.7m telescope. A.S. contributed ground-based follow-up imaging of the targets. J.H.S. contributed to the text, scope and interpretation. G.W. ran the ETV code, developed tools for analysing $O - C$ variations, and assisted with text. D.G.K. designed major portions of the Kepler photometer that acquired these data. W.J.B. led the design and development of the Kepler mission that acquired these data, and contributed to the text.

Author Information The Kepler light curves used in this work can be downloaded from the MAST (Multimission Archive at Space Telescope Science Institute) at <http://archive.stsci.edu/kepler/>. Reprints and permissions information is available at www.nature.com/reprints. The authors declare no competing financial interests. Readers are welcome to comment on the online version of this article at www.nature.com/nature. Correspondence and requests for materials should be addressed to W.F.W. (wfw@sciences.sdsu.edu) or J.A.C. (jacarter@cfa.harvard.edu), for questions regarding the photometric-dynamical modelling).

Generation of scaled protogalactic seed magnetic fields in laser-produced shock waves

G. Gregori^{1,2}, A. Ravasio³, C. D. Murphy¹, K. Schaar¹, A. Baird¹, A. R. Bell¹, A. Benuzzi-Mounaix³, R. Bingham^{2,4}, C. Constantin⁵, R. P. Drake⁶, M. Edwards¹, E. T. Everson⁵, C. D. Gregory⁷, Y. Kuramitsu⁸, W. Lau¹, J. Mithen¹, C. Niemann⁵, H.-S. Park⁹, B. A. Remington⁹, B. Reville¹, A. P. L. Robinson², D. D. Ryutov⁹, Y. Sakawa⁸, S. Yang¹, N. C. Woolsey⁷, M. Koenig³ & F. Miniati¹⁰

The standard model for the origin of galactic magnetic fields is through the amplification of seed fields via dynamo or turbulent processes to the level consistent with present observations^{1–3}. Although other mechanisms may also operate^{4,5}, currents from misaligned pressure and temperature gradients (the Biermann battery process) inevitably accompany the formation of galaxies in the absence of a primordial field. Driven by geometrical asymmetries in shocks⁶ associated with the collapse of protogalactic structures, the Biermann battery is believed to generate tiny seed fields to a level of about 10^{-21} gauss (refs 7, 8). With the advent of high-power laser systems in the past two decades, a new area of research has opened in which, using simple scaling relations^{9,10}, astrophysical environments can effectively be reproduced in the laboratory^{11,12}. Here we report the results of an experiment that produced seed magnetic fields by the Biermann battery effect. We show that these results can be scaled to the intergalactic medium, where turbulence, acting on timescales of around 700 million years, can amplify the seed fields^{13,14} sufficiently to affect galaxy evolution.

We conducted these experiments at the Laboratoire pour l'Utilisation de Lasers Intenses (LULI 2000) laser facility. The intense laser was used to illuminate a small carbon rod inside a low-pressure gas-filled interaction chamber. A full description of the experimental set-up, including details of the laser properties, is provided in Fig. 1. Because of the large energy density accumulated on the carbon target over the relatively short laser pulse duration, the heated solid matter initially underwent a ballistic expansion until the shocked mass was roughly equal to the ejected mass, and then the shock transitioned to a Sedov–Taylor blast wave^{15,16}. The shock evolution over time was monitored using optical diagnostics. The experimentally measured shock position for $t \lesssim 200$ ns was then compared with a one-dimensional radial radiation hydrodynamic simulation using the HELIOS-CR software package¹⁷ (Fig. 2). Given the quantitative agreement of the experimental measurements of the density values at $t \lesssim 200$ ns with the results of the HELIOS-CR code, we used the simulations to extrapolate the experimental results to later times, $t \approx 0.5$ – 1.5 μ s, when the shock arrived at the position of the magnetic-field probes but the plasma density was below the detection limit of the optical probe.

The measurement of the magnetic field was performed with three-axis magnetic induction coils¹⁸, giving both the magnetic-field components along the shock: normal (B_{\perp}) and perpendicular to the shock (B_{\parallel}), as indicated in Fig. 3. At a radius $r \approx 3$ cm from the initial blast, peak B_{\perp} values occurring at $t \approx 1$ – 2 μ s were in the range 10–30 G. The position of the first peak in B_{\perp} was in agreement with the shock arrival time estimates based on HELIOS-CR, and was also consistent with the time lags between different locations of the probe coils. Finally, shots

taken with no ambient gas (not plotted) showed no peak in B_{\perp} for $t \approx 0.5$ – 2 μ s, which further supports the inference that the magnetic field arrives with the shocked plasma.

It is well known that return currents driven by hot electrons can generate magnetic fields in laser-produced plasmas^{5,19}. However, at our laser intensity we expected the hot electrons to be distributed with temperature $T_{\text{hot}} \approx 5$ keV (ref. 20). If so, they would reach the coil position at $t \lesssim 3$ ns, much earlier than the measured peak in B_{\perp} . A magnetic field generated through vorticity by Biermann's battery⁷ is more plausible. We estimated it as²¹:

$$B_{\text{vort}} = \frac{m_{\text{ion}}}{e} \omega \approx \frac{(\rho - 1)^2}{\rho} \frac{m_{\text{ion}}}{e} \left| \frac{\partial \mathbf{v}_{\text{shock}}}{\partial S} \right| \quad (1)$$

where $\omega = \nabla \times \mathbf{v}$ is the vorticity, m_{ion} is the ion mass, e is the electron charge, $\rho \approx 3$ is the shock compression ratio (see Supplementary Fig. 1) and $\partial \mathbf{v}_{\text{shock}} / \partial S$ is the tangential gradient of the shock velocity. Since $\partial \mathbf{v}_{\text{shock}} / \partial S \approx \kappa \mathbf{v}_{\text{shock}} / r$, where $\kappa \approx 0.1$ – 0.3 (Fig. 3a), at $r \approx 3$ cm we obtained $B_{\text{vort}} \approx 10$ – 30 G, in agreement with the measured values.

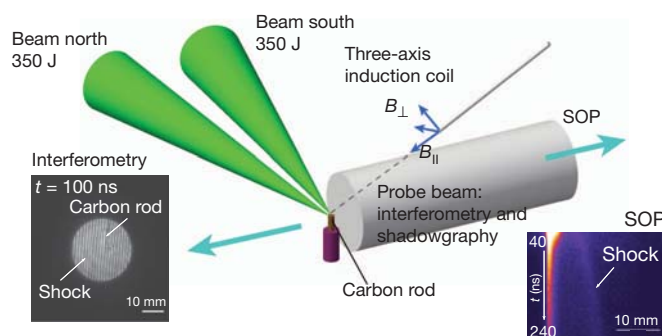


Figure 1 | Experimental set-up showing the laser beams and diagnostics configuration. Either one or two frequency-doubled (527 nm), 1.5-ns-long laser beams are focused on the tip of a 500- μ m-diameter carbon rod. At focus, each laser beam has a 400- μ m flat-top distribution, achieving a peak intensity of 2×10^{14} W cm⁻², delivering around 350 J. The interaction chamber is filled with helium gas at pressure $P = 0.8 \pm 0.3$ mbar or $P = 1.6 \pm 0.3$ mbar (with the error estimated from the uncertainty in the pressure readings inside the target chamber). The shock-wave evolution during times $t \lesssim 200$ ns (where $t = 0$ corresponds to the time of the laser pulse) was monitored using transverse interferometry and Schlieren shadowgraphy with an optical probe (with 532 nm wavelength and 6 ns gate width). The interferometer was of Mach–Zehnder type with an approximately 25-mm field of view, and it was used to provide the electron density. The inset on the left shows an example of an interferometric image. The inset on the right shows a streaked self-emission optical pyrometry (SOP) image in a narrow band at 450 ± 30 nm.

¹Department of Physics, University of Oxford, Parks Road, Oxford OX1 3PU, UK. ²Rutherford Appleton Laboratory, Chilton, Didcot OX11 0QX, UK. ³Laboratoire pour l'Utilisation de Lasers Intenses, UMR7605, CNRS CEA, Université Paris VI Ecole Polytechnique, 91128 Palaiseau cedex, France. ⁴Department of Physics, University of Strathclyde, Glasgow G4 0NG, UK. ⁵University of California Los Angeles, Los Angeles, California 90095, USA. ⁶Department of Atmospheric, Oceanic and Space Science, University of Michigan, 2455 Hayward Street, Ann Arbor, Michigan 48103, USA. ⁷Department of Physics, Heslington, University of York, YO10 5DD, UK. ⁸Institute of Laser Engineering, Osaka University, 2-6 Yamadaoka, Suita, Osaka 565-0871, Japan. ⁹Lawrence Livermore National Laboratory, PO Box 808, Livermore, California 94551, USA. ¹⁰Physics Department, Wolfgang-Pauli-Strasse 27, ETH-Zürich, CH-8093 Zürich, Switzerland.

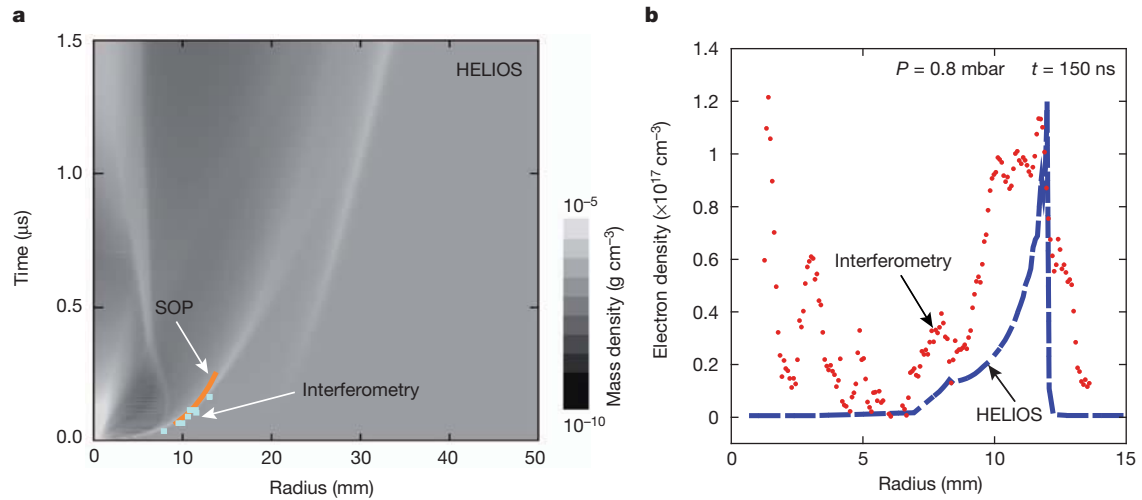


Figure 2 | Comparison between numerical simulations and optical diagnostics. **a**, HELIOS-CR simulations (done with a one-beam laser driver) and experimentally determined shock position using both interferometry and self-emission optical pyrometry. The laser energy deposition in the HELIOS-CR code was adjusted to 70% of the nominal value so that the simulated shock position would match the experimental values. The transition to a Sedov–

The range of measured magnetic-field strengths agreed with the observed shot-to-shot variations in the measured shock properties at early times, as indicated in the Supplementary Information. We observed that the peak of the measured magnetic energy density in the downstream plasma corresponds to a fraction of a per cent of that of the incoming flow: $\varepsilon_B = B^2 / \mu_0 n_{\text{gas}}^0 m_{\text{ion}} v_{\text{shock}}^2 \approx 0.1\%$, where n_{gas}^0 is the

Taylor blast wave occurs at distances $r < 10$ mm from the sample. **b**, Calculated electron density at $t = 150$ ns versus electron density values extracted from interferometric measurements via Abel inversion, which requires the assumption of cylindrical symmetry. Because observed differences in the shock wave radius are less than 20%, this gives the uncertainty in the density measurement.

upstream gas density (Supplementary Fig. 1). On the other hand, the magnetic-field energy density was significantly larger than the ram pressure of the incoming ionized plasma: $\varepsilon_B^{\text{ion}} = B^2 / \mu_0 n_e^0 m_{\text{ion}} v_{\text{shock}}^2 \gtrsim 0.1$ (with $n_e^0 \approx 10^{14} \text{ cm}^{-3}$ the inferred electron density ahead of the shock). This suggests that, in this experiment, the kinetic Weibel instability may not play an important part, given that one would expect it to produce a

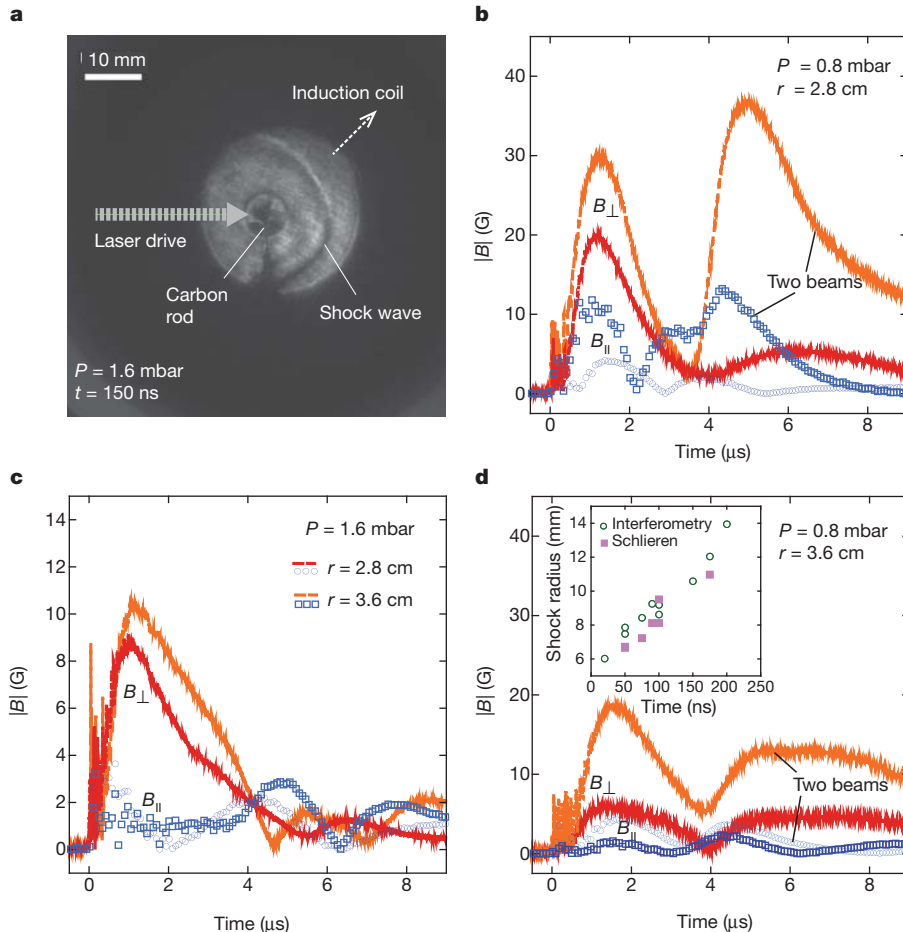


Figure 3 | Magnetic-field measurements from induction coils. **a**, Schlieren image, showing laser and magnetic pick-up coil configuration as well as the shock position. The Schlieren image indicates when the refractive index of the plasma changes rapidly, thus tracking the position of the shock. From the asymmetry in the shape of the shock wave we obtain an approximate value for κ of 0.1–0.3 in equation (1). The induction coils were placed at 2.8 cm and 3.6 cm from the carbon rod (that is, the centre of the initial blast). Each coil consisted of eight twisted pairs of coils wound around the axis of a $3.1 \text{ mm} \times 3.1 \text{ mm}$ plastic core. The voltage from the twisted-pair loops was then differentially amplified to remove any electric-field components, and the magnetic field was calculated using Faraday's law. The coils were protected from the surrounding plasma by a 1-mm-thick glass tube. Time resolution was better than 50 ns. We estimated the error associated to each magnetic-field trace to be about 15%. **b**, B_{\perp} (lines) and B_{\parallel} (symbols) traces taken at $P = 0.8$ mbar. The rise and gradual decay of B_{\perp} was consistent with the shock front crossing the coil and the subsequent evolution of the shocked material. The second peak at $t \approx 5 \mu\text{s}$ seen for the case of two beams illumination is probably associated with the ejecta material from the sample arriving at the coil. **c**, B_{\perp} (lines) and B_{\parallel} (symbols) traces for the one-beam laser driver at $P = 1.6$ mbar. **d**, Same as **b** but at $r = 3.6$ cm. The inset shows the measured shock radius along the laser axis for $P = 0.8$ mbar and single-beam illumination. We attribute shot-to-shot variations in the observed field values (up to $\sim 50\%$) to the stochastic generation of vorticity and to variations in the radius of curvature of the shock front (as large as $\sim 20\%$ at early times, as shown in the inset). Additional details are given in Supplementary Fig. 2.

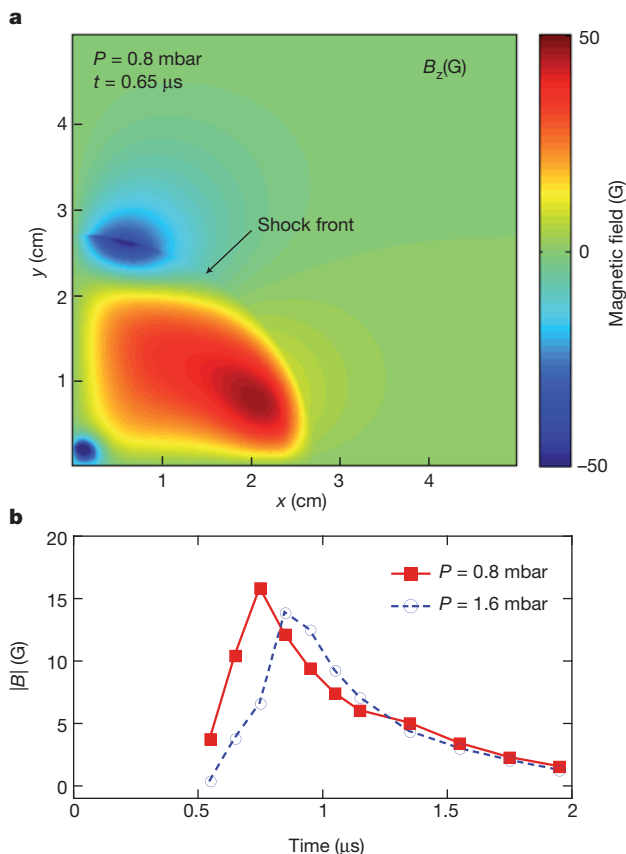


Figure 4 | Resistive magnetohydrodynamics simulations of the magnetic-field generation. The magnetohydrodynamics scheme is an implementation of ref. 25. The ionization state was computed using Saha equilibrium²⁶. Radiation transport, thermal conduction and laser coupling were not included in the magnetohydrodynamics code. Although radiation transport is important during the early stages of the laser drive (for a few nanoseconds), at the time when the shock has expanded and magnetic-field measurements are taken, the radiation cooling time exceeds the hydrodynamic timescale ($\tau_{\text{rad}}/\tau_{\text{hydro}} \approx 8 \times 10^3$), so radiative processes do not affect the hydrodynamic evolution. For the initial conditions we used the results from HELIOS-CR. At $t = 150$ ns (the time when the shock has swept about 1 cm from the initial carbon rod position), the system had uniform density and temperature, except for a central region ($r < 1$ cm) where the temperature is $T(x, y) = T_0 (1 + \delta \cos \theta)$, with $T_0 = 50$ eV and $\delta = 0.9$, and $\theta \in [0, 2\pi]$ is the polar angle. Therefore the scale coefficient κ is around $1/\pi$, in agreement with experimental estimates. The numerical grid consists of $2,000 \times 2,000$ cells with resolution $\Delta x = \Delta y = 0.005$ cm. **a**, Two-dimensional plot of the perpendicular component of the magnetic field obtained from magnetohydrodynamics simulations. Note that because of finite magnetic diffusion, the plasma was magnetized ahead of the shock front. **b**, Plot of the magnetic flux density at 2.7 cm from the centre of the domain ($x = 2.5$ cm, $y = 1$ cm).

much smaller field, that is, $e_B^{\text{ion}} \approx (m_e/m_{\text{ion}}) \approx 10^{-3}$ (refs 4 and 22), where m_e is the electron mass.

The vorticity-generated magnetic field is perpendicular to the shock normal, consistent with the experimental traces in Fig. 3 that show $B_{\perp} \gg B_{\parallel}$. We note that in a perfectly spherical shock no magnetic field can be produced because $\partial v_{\text{shock}}/\partial S = 0$. Magnetic fields can thus only be generated in non-spherical expansion shocks, which are expected to occur during structure formation in the pregalactic phase⁷. Our interpretation is reinforced by a computer calculation that solved the resistive magnetohydrodynamics equations in two dimensions (Fig. 4) with a baroclinic (Biermann) source term for the magnetic-field generation (that is, $-\nabla n_e \times \nabla p_e / en_e^2$, with n_e the electron density and p_e the electron pressure). The asymmetric expansion due to the initial temperature anisotropy of the laser illumination drove

Table 1 | Similarity scaling between the laboratory and the intergalactic medium

Scaling parameters	Definition	Laboratory (LULI) value	Intergalactic medium extrapolated value
Characteristic length scale of the system	$L \approx 2r/\kappa$	18.8 cm	1 Mpc
Characteristic timescale of the system	t	1 μs	0.7 Gyr
Electron temperature	T_e	2 eV	100 eV
Electron density	n_e	$5 \times 10^{15} \text{ cm}^{-3}$	10^{-4} cm^{-3}
Cyclotron frequency	$\Omega_B = \frac{eB}{m_{\text{ion}}}$	$4.8 \times 10^4 \text{ s}^{-1}$	$8.7 \times 10^{-18} \text{ s}^{-1}$
Reynolds number	Re	7.9×10^3	3.0×10^{13}
Peclet number	Pe	69.0	7.0×10^{11}
Magnetic Reynolds number	Re_M	16.5	3.9×10^{27}

The similarity between the astrophysical and the laboratory systems breaks down owing to viscous dissipation at laboratory spatial scales $h \lesssim \lambda_{\text{coll}}$, where λ_{coll} is the collisional mean free path⁹, and equally for thermal and magnetic dissipation. This implies that, for the conditions of our experiment, in which magnetic dissipation is the dominant effect, full similarity is achieved at macroscopic scales ($h \gtrsim 5 \mu\text{m}$), and the microphysics at the kinetic level will be different. The similarity given here roughly applies to the shocked intergalactic medium for scales of $L \gtrsim 25$ pc.

baroclinic generation of a magnetic field comparable in strength to what we measured in the laboratory.

We applied magnetohydrodynamics scaling techniques to investigate the importance of the Biermann battery for magnetic-field generation at high-Mach-number astrophysical shocks occurring in the intergalactic medium. Similarity in the magnetohydrodynamics equations is preserved if heat convection divided by conduction (the Peclet number), inertial forces divided by viscosity (the Reynolds number), and inertial forces divided by magnetic diffusivity (the magnetic Reynolds number) are all large in both systems (Table 1). From equation (1), the magnetic field generated by the Biermann mechanism is proportional to the shock generated vorticity. It follows that, on a given spatial scale L , which characterizes the velocity gradients, $\omega \approx v_{\text{shock}}/L \approx 1/t$ (see also Supplementary Information). Our laboratory results thus indicate that curved intergalactic shocks in protogalactic structures, with changing curvature at the level of a few tens of a per cent on scales of about one megaparsec, can generate magnetic fields with values of around 10^{-21} G.

The curvature radius, the asymmetry and the resulting magnetic field are all consistent with the scenario of protogalactic magnetic-field generation from the Biermann battery process modelled with numerical simulations in ref. 7. Thus we have experimentally verified such a process. Generation of these tiny magnetic fields precedes the formation of the galaxy. The magnetic field can quickly be amplified to about equipartition values by turbulent motions and can strongly affect the evolution of the galactic medium from its early stages^{13,14}. Indeed, astronomical observations show that dynamically strong magnetic fields are common even in young galaxies^{23,24}. This excellent agreement between our experiment and current theories of magnetic-field generation in the early Universe opens up the opportunity to investigate other effects that may influence the generation of seed fields.

Received 17 July; accepted 2 December 2011.

- Parker, E. N. Hydromagnetic dynamo models. *Astrophys. J.* **122**, 293–314 (1955).
- Zweibel, E. G. & Heiles, C. Magnetic fields in galaxies and beyond. *Nature* **385**, 131–136 (1997).
- Ryu, D., Kang, H., Cho, J. & Das, S. Turbulence and magnetic fields in the large-scale structure of the universe. *Science* **320**, 909–912 (2008).
- Schlickeiser, R. & Shukla, P. K. Cosmological magnetic field generation by the Weibel instability. *Astrophys. J.* **599**, L57–L60 (2003).
- Miniati, F. & Bell, A. R. Resistive magnetic field generation at cosmic dawn. *Astrophys. J.* **729**, 73, <http://dx.doi.org/10.1088/0004-637X/729/1/73> (2011).
- Miniati, F. *et al.* Properties of cosmic shock waves in large-scale structure formation. *Astrophys. J.* **542**, 608–621 (2000).
- Kulsrud, R. M., Cen, R., Ostriker, J. P. & Ryu, D. The protogalactic origin for cosmic magnetic fields. *Astrophys. J.* **480**, 481–491 (1997).

8. Xu, H. *et al.* The Biermann battery in cosmological MHD simulations of population III star formation. *Astrophys. J.* **688**, L57–L60 (2008).
9. Ryutov, D. D. *et al.* Similarity criteria for the laboratory simulation of supernova hydrodynamics. *Astrophys. J.* **518**, 821–832 (1999).
10. Ryutov, D. D., Drake, R. P. & Remington, B. A. Criteria for scaled laboratory simulations of astrophysical MHD phenomena. *Astrophys. J. Suppl. Ser.* **127**, 465–468 (2000).
11. Remington, B. A., Arnett, D., Drake, R. P. & Takabe, H. Modeling astrophysical phenomena in the laboratory with intense lasers. *Science* **284**, 1488–1493 (1999).
12. Remington, B. A., Drake, R. P. & Ryutov, D. D. Experimental astrophysics with high power lasers and Z pinches. *Rev. Mod. Phys.* **78**, 755–807 (2006).
13. Cho, J. & Vishniac, E. T. The generation of magnetic fields through driven turbulence. *Astrophys. J.* **538**, 217, <http://dx.doi.org/10.1086/309127> (2000).
14. Sur, S., Schleicher, D. R. G., Banerjee, R., Federrath, C. & Klessen, R. S. The generation of strong magnetic fields during the formation of the first stars. *Astrophys. J.* **721**, L134–L138 (2010).
15. Hansen, J. F. *et al.* Laboratory simulations of supernova shockwave propagation. *Astrophys. Space Sci.* **298**, 61–67 (2005).
16. Hansen, J. F. *et al.* Laboratory observation of secondary shock formation ahead of a strongly radiative blast wave. *Phys. Plasmas* **13**, 022105 (2006).
17. MacFarlane, J. J., Golovkin, I. E. & Woodruff, P. R. HELIOS-CR—a 1-D radiation-magnetohydrodynamics code with inline atomic kinetics modeling. *J. Quant. Spectrosc. Radiat. Transf.* **99**, 381–397 (2006).
18. Everson, E. T. *et al.* Design, construction, and calibration of a three-axis, high-frequency magnetic probe (B-dot probe) as a diagnostic for exploding plasmas. *Rev. Sci. Instrum.* **80**, 113505 (2009).
19. Bell, A. R. & Kingham, R. J. Resistive collimation of electron beams in laser-produced plasmas. *Phys. Rev. Lett.* **91**, 035003 (2003).
20. Reich, Ch, Gibbon, P., Uschmann, I. & Förster, E. Yield optimization and time structure of femtosecond laser plasma K α sources. *Phys. Rev. Lett.* **84**, 4846–4849 (2000).
21. Hayes, W. D. The vorticity jump across a gasdynamic discontinuity. *J. Fluid Mech.* **2**, 595–600 (1957).
22. Medvedev, M. V. Weibel turbulence in laboratory experiments and GRB/SN shocks. *Astrophys. Space Sci.* **307**, 245–250 (2007).
23. Bernet, M. L., Miniati, F., Lilly, S. J., Kronberg, P. P. & Dessauges-Zavadsky, M. Strong magnetic fields in normal galaxies at high redshift. *Nature* **454**, 302–304 (2008).
24. Murphy, E. J. The far-infrared-radio correlation at high redshifts: physical considerations and prospects for the square kilometer array. *Astrophys. J.* **706**, 482–496 (2009).
25. Ziegler, U. A central-constrained transport scheme for ideal magnetohydrodynamics. *J. Comput. Phys.* **196**, 393–416 (2004).
26. Zel'dovich, Ya. B. & Raizer, Yu. P. *Physics of Shock Waves and High-Temperature Hydrodynamic Phenomena* (Academic, 1966).

Supplementary Information is linked to the online version of the paper at www.nature.com/nature.

Acknowledgements We thank the LULI technical team for their support during the experiments. The research leading to these results has received funding from the European Research Council under the European Community's Seventh Framework Programme. This work was also supported by the EU programme Laserlab-Europe. Partial support from the Science and Technology Facilities Council (the Central Laser Facility and the Centre for Fundamental Physics) and the Engineering and Physical Sciences Research Council of the United Kingdom is also acknowledged.

Author Contributions G.G. and F.M. conceived the project. G.G., A.R., C.D.M., A.B.-M., M.E., C.D.G., Y.K., J.M., H.-S.P., N.C.W. and M.K. carried out the LULI experiment. The paper was written by G.G., A.R., A.R.B., R.P.D., B.R. and F.M. The data was analysed by G.G., A.R., C.D.M., K.S. and C.D.G. Preparatory diagnostics work was conducted by A.B., C.C., E.T.E., C.N., W.L. and S.Y. Numerical simulations were performed by G.G. and A.P.L.R. Additional experimental and theoretical support was provided by A.R.B., R.B., R.P.D., B.A.R., B.R., D.D.R., Y.S. and F.M.

Author Information Reprints and permissions information is available at www.nature.com/reprints. The authors declare no competing financial interests. Readers are welcome to comment on the online version of this article at www.nature.com/nature. Correspondence and requests for materials should be addressed to G.G. (ggregori1@physics.ox.ac.uk) or F.M. (fm@phys.ethz.ch).

Light-cone-like spreading of correlations in a quantum many-body system

Marc Cheneau¹, Peter Barmettler², Dario Poletti², Manuel Endres¹, Peter Schauß¹, Takeshi Fukuhara¹, Christian Gross¹, Immanuel Bloch^{1,3}, Corinna Kollath^{2,4} & Stefan Kuhr^{1,5}

In relativistic quantum field theory, information propagation is bounded by the speed of light. No such limit exists in the non-relativistic case, although in real physical systems, short-range interactions may be expected to restrict the propagation of information to finite velocities. The question of how fast correlations can spread in quantum many-body systems has been long studied¹. The existence of a maximal velocity, known as the Lieb–Robinson bound, has been shown theoretically to exist in several interacting many-body systems (for example, spins on a lattice^{2–5})—such systems can be regarded as exhibiting an effective light cone that bounds the propagation speed of correlations. The existence of such a ‘speed of light’ has profound implications for condensed matter physics and quantum information, but has not been observed experimentally. Here we report the time-resolved detection of propagating correlations in an interacting quantum many-body system. By quenching a one-dimensional quantum gas in an optical lattice, we reveal how quasiparticle pairs transport correlations with a finite velocity across the system, resulting in an effective light cone for the quantum dynamics. Our results open perspectives for understanding the relaxation of closed quantum systems far from equilibrium⁶, and for engineering the efficient quantum channels necessary for fast quantum computations⁷.

Lieb–Robinson bounds have already found a number of fundamental applications^{8,9}. For example, they enable a rigorous proof of a long-standing conjecture that linked the presence of a spectral gap in a lattice system to the exponential decay of correlations in the ground state^{10,11}. They also provide fundamental scaling laws for entanglement entropy, which is an indicator of the computational cost of simulating strongly interacting systems¹². Despite intensive theoretical work, the extent to which Lieb–Robinson bounds for interacting spins on a lattice^{2–5} can be generalized remains however an open question^{13–16}.

In the context of quantum many-body systems, the existence of a Lieb–Robinson bound can be probed by recording the dynamics following a sudden parameter change (a quench) in the Hamiltonian. In that case, a simple picture has been suggested: quantum-entangled quasiparticles emerge from the initially highly excited state and propagate ballistically³, carrying correlations across the system. Ultracold atomic gases offer an ideal test bed for exploring such quantum dynamics owing to their almost perfect decoupling from the environment and their fast tunability¹⁷. In addition, the recently demonstrated technique of single-site imaging in an optical lattice^{18,19} offers the resolution and sensitivity necessary to reveal the dynamical evolution of a many-body system at the single-particle level.

Our system consists of ultracold bosonic atoms in an optical lattice and is well described by the Bose–Hubbard model^{20,21}. This model is parameterized by two energy scales: the on-site interaction, U , and the tunnel coupling between adjacent sites, J . Driven by the competition of these two parameters, a quantum phase transition between a superfluid and a Mott-insulating phase occurs in homogeneous systems where each lattice site is filled by an integer number of atoms, \bar{n} . In

the one-dimensional geometry considered here, the critical point of this transition is located at $(U/J)_c \approx 3.4$ (ref. 22). We observed the time evolution of spatial correlations after a fast decrease of the effective interaction strength U/J , from an initial value deep in the Mott-insulating regime, with filling $\bar{n} = 1$, to a final value closer to the critical point (Fig. 1a). After such a quench, the initial many-body state $|\Psi_0\rangle$ is highly excited and acts as a source of quasiparticles. In order to elucidate the nature and the dynamics of these quasiparticles, we have developed an analytical model in which the occupancy of each lattice site is restricted to $n = 0, 1$ or 2 (Supplementary Information). For large interaction strengths, the quasiparticles consist of either an excess particle (‘doublon’) or a hole (‘holon’) on top of the unity-filling background. The quasiparticles inherit the bosonic nature of the atoms, but they can be turned into fermions (fermionized) using a Jordan–Wigner transformation. This allows us to partially eliminate the non-physical states in which a lattice site would be occupied by two quasiparticles. To first order in J/U , we then find that the many-body state at time t after the quench reads:

$$|\psi(t)\rangle \approx |\psi_0\rangle + i\sqrt{8}\frac{J}{U} \sum_k \sin(ka_{\text{lat}}) \left[1 - e^{-i[\epsilon_d(k) + \epsilon_h(-k)]t/\hbar}\right] \hat{a}_k^\dagger \hat{h}_{-k}^\dagger |\psi_0\rangle \quad (1)$$

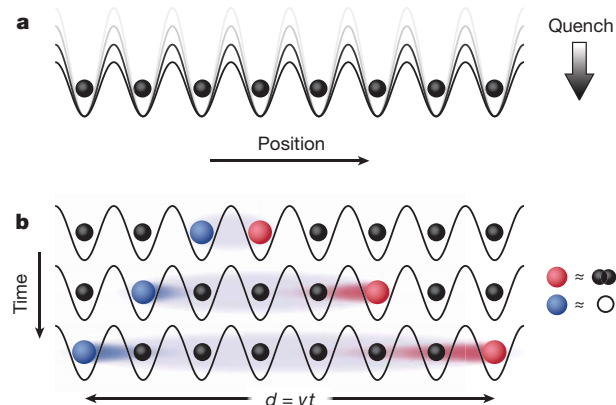


Figure 1 | Spreading of correlations in a quenched atomic Mott insulator.

a, A one-dimensional ultracold gas of bosonic atoms (black balls) in an optical lattice is initially prepared deep in the Mott-insulating phase with unity filling. The lattice depth is then abruptly lowered (arrow at right), bringing the system out of equilibrium. **b**, Following the quench, entangled quasiparticle pairs emerge at all sites. Each of these pairs consists of a doublon and a holon (red and blue ball, respectively; see key at right) on top of the unity-filling background that propagate ballistically in opposite directions. It follows that a correlation in the parity of the site occupancy builds up at time t between any pair of sites separated by a distance $d = vt$, where v is the relative velocity of the doublons and holons.

¹Max-Planck-Institut für Quantenoptik, 85748 Garching, Germany. ²Département de physique théorique, Université de Genève, 1211 Genève, Switzerland. ³Ludwig-Maximilians-Universität, 80799 München, Germany. ⁴Centre de physique théorique, École Polytechnique, CNRS, 91128 Palaiseau, France. ⁵University of Strathclyde, SUPA, Glasgow G4 0NG, UK.

The operators \hat{d}_k^\dagger and \hat{h}_{-k}^\dagger create a doublon with momentum k and energy $\varepsilon_d(k)$, and a holon with momentum $-k$ and energy $\varepsilon_h(-k)$, respectively. k belongs to the first Brillouin zone and a_{lat} is the lattice period. Quasiparticles thus emerge at any site in the form of entangled pairs, consisting of a doublon and a holon with opposite momenta. Some of these pairs are bound on nearest-neighbour sites while the others form wave packets, owing to their peaked momentum distribution. The wave packets propagate in opposite directions with a relative group velocity v determined by the dispersion relation $\varepsilon_d(k) + \varepsilon_h(-k)$ (Fig. 1b). The propagation of quasiparticle pairs is reflected in the two-point parity correlation functions²³:

$$C_d(t) = \langle \hat{s}_j(t) \hat{s}_{j+d}(t) \rangle - \langle \hat{s}_j(t) \rangle \langle \hat{s}_{j+d}(t) \rangle \quad (2)$$

where j generally labels the lattice sites and d denotes the distance between the two sites considered. The operator $\hat{s}_j(t) = e^{i\pi[\hat{n}_j(t) - \bar{n}]}$ measures the parity of the occupation number $\hat{n}_j(t)$. It yields $+1$ in the absence of quasiparticles (odd occupancy) and -1 if a quasiparticle is present (even occupancy). Because the initial state is close to a Fock state with one atom per lattice site, we expect $C_d(t=0) \approx 0$. After the quench, the propagation of quasiparticle pairs with relative velocity v results in a positive correlation between any pair of sites separated by a distance $d = vt$.

The experimental sequence started with the preparation of a two-dimensional degenerate gas of ^{87}Rb confined in a single antinode of a vertical optical lattice^{19,23} (z axis, $a_{\text{lat}} = 532$ nm). The system was then divided into about 10 decoupled one-dimensional chains by adding a second optical lattice along the y axis and by setting both lattice depths to $20.0(5) E_r$ (the number in parenthesis denotes the uncertainty of the last digit; see Methods), where $E_r = (2\pi\hbar)^2 / (8ma_{\text{lat}}^2)$ is the recoil energy of the lattice and m the atomic mass of ^{87}Rb . The effective interaction strength along the chains was tuned via a third optical lattice along the x axis. The number of atoms per chain ranged between 10 and 18, resulting in a lattice filling $\bar{n} = 1$ in the Mott-insulating domain. The initial state was prepared by adiabatically increasing the x -lattice depth until the interaction strength reached a value of $(U/J)_0 = 40(2)$. At this point, we measured the temperature to be $T \approx 0.1 U/k_B$ (k_B is the Boltzmann constant) following the method described in ref. 19. We then brought the system out of equilibrium by lowering the lattice depth, typically within $100 \mu\text{s}$, which is fast compared to the inverse tunnel coupling \hbar/J , but still adiabatic with respect to transitions to higher Bloch bands. The final lattice depths were in the Mott-insulating regime, close to the critical point. After a variable evolution time, we ‘froze’ the density distribution of the many-body state by rapidly raising the lattice depth in all directions to $\sim 80 E_r$. Finally, the atoms were detected by fluorescence imaging using a microscope objective with a resolution of the order of the lattice spacing and a reconstruction algorithm extracted the occupation number at each lattice site¹⁹. Because inelastic light-assisted collisions during the imaging led to a rapid loss of atom pairs, we directly detected the parity of the occupation number.

Our experimental results for the time evolution of the two-point parity correlations after a quench to $U/J = 9.0(3)$ show a clear positive signal propagating with increasing time to larger distances d (Fig. 2). In addition, the propagation velocity of the correlation signal is constant over the range $2 \leq d \leq 6$ (Fig. 2 inset), demonstrating that the correlations spread along an effective light cone. We also found similar dynamics for quenches to $U/J = 5.0(2)$ and $7.0(3)$ (Supplementary Fig. 1). We note that the observed signal cannot be attributed to a simple density wave because such an excitation would result in $\langle \hat{s}_j \hat{s}_{j+d} \rangle = \langle \hat{s}_j \rangle \langle \hat{s}_{j+d} \rangle$. We compared the experimental results to numerical simulations of an infinite, homogeneous system at $T = 0$ using the adaptive time-dependent density matrix renormalization group algorithm^{24,25}. In the simulation, the initial and final interaction strengths were fixed at the experimentally determined values and the quench was considered to be instantaneous, at $t = 0$. We found

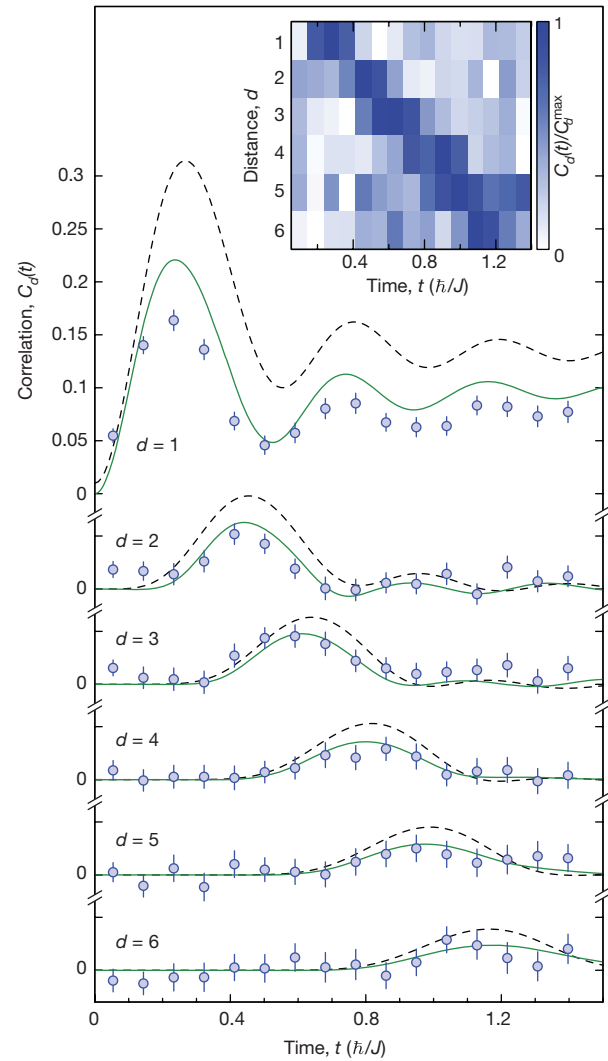


Figure 2 | Time evolution of the two-point parity correlations. After the quench, a positive correlation signal propagates with increasing time to larger distances. Main figure, the experimental values for a quench from $U/J = 40$ to $U/J = 9.0$ (open circles) are in good agreement with the corresponding numerical simulation for an infinite, homogeneous system at zero temperature (continuous green line). Our analytical model (dashed black line) also qualitatively reproduces the observed dynamics. Inset, experimental data displayed as a colour map (colour scale at right), revealing the propagation of the correlation signal with a well defined velocity. The experimental values result from the average over the central N sites of more than 1,000 chains, where N equals 80% of the length of each chain. Error bars, s.d.

remarkable agreement between the experiment and theory over all explored distances and times, despite the finite temperature and the harmonic confinement with frequency $\nu = 68(1)$ Hz that characterize the experimental system. The observed dynamics is also qualitatively reproduced by our analytical model for $U/J = 9.0$. For lower values of U/J , however, the model breaks down owing to the increasing number of quasiparticles.

We extracted the propagation velocity v from the time of the correlation peak as a function of the distance d (Fig. 3a). A linear fit restricted to $2 \leq d \leq 6$ yields $v\hbar/(Ja_{\text{lat}}) = 5.0(2)$, $5.6(5)$ and $5.0(2)$ for $U/J = 5.0(2)$, $7.0(3)$ and $9.0(3)$, respectively. The points for $d = 1$ were excluded from the fit, as they result from the interference between propagating and bound quasiparticle pairs (see equation (1)). A comparison of the experimental velocities with those obtained from numerical simulations (Fig. 3b) shows agreement within the error bars. The measured velocities can also be compared with two limiting cases: on the one hand, they are significantly larger than the spreading

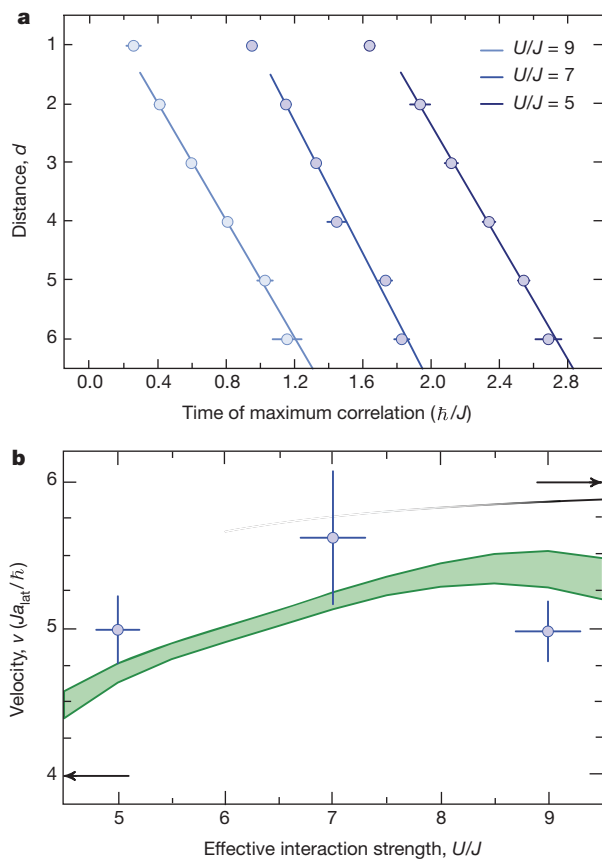


Figure 3 | Propagation velocity. **a**, Determination of the propagation velocity for the quenches to $U/J = 5.0$ (open circles, dark blue), 7.0 (medium blue) and 9.0 (light blue). The time of the maximum of the correlation signal is obtained from fits to the traces $C_d(t)$ for distances $d = 1$ to 6 . Error bars, the 68% confidence interval of these fits. We then extract the propagation velocities from weighted linear fits restricted to $2 \leq d \leq 6$ (lines). The data for $U/J = 5.0$ and 7.0 have been offset horizontally for clarity. **b**, Comparison of the experimental velocities (open circles) at different interaction strengths to those obtained from numerical simulations for an infinite, homogeneous system at zero temperature (green shaded area). The shaded area and the vertical error bars denote the 68% confidence interval of the fit. The horizontal error bars represent the uncertainty due to the calibration of the lattice depth. The black line (top right) corresponds to the bound v_{max} predicted by our effective model (the fading indicates the breakdown of this model). The arrows mark the maximum velocity expected in the non-interacting case (left) and the asymptotic value derived from our model when $U/J \rightarrow \infty$ (right).

velocity of non-interacting particles, $v = 4 Ja_{\text{lat}}/\hbar$, and twice the velocity of sound in the superfluid phase²⁶, on the other hand, they remain below the maximum velocity predicted by our analytical model, $v_{\text{max}} \approx (6Ja_{\text{lat}}/\hbar)[1 - 16J^2/(9U^2)]$, which can be interpreted as a Lieb–Robinson bound (Fig. 3b). In the limit $U/J \rightarrow \infty$, this bound corresponds to doublons and holons propagating with respective group velocities $4 Ja_{\text{lat}}/\hbar$ and $2 Ja_{\text{lat}}/\hbar$. The higher velocity of doublons simply reflects their Bose-enhanced tunnel coupling.

We have presented the first (to our knowledge) experimental observation of an effective light cone for the spreading of correlations in an interacting quantum many-body system. Although the observed dynamics can be understood within a fermionic quasiparticle picture that is valid deep in the Mott-insulating regime, we note that our experimental data cover a region close to the critical point, for which only *ab initio* numerical simulations are available so far¹³. Our work opens interesting perspectives, such as revealing the entanglement carried by the quasiparticle pairs or investigating the quantum dynamics in higher dimensions, where little is known about Lieb–Robinson bounds and the scaling of entanglement. For example, the experiment can be extended to study correlation propagation in two

dimensions, where existing numerical and analytical approaches suffer from severe limitations. Furthermore, the production rate of excitations and the formation of domains when tuning the effective interaction strength slowly across the critical point can be investigated, thereby exploring a quantum analogue to the Kibble–Zurek mechanism^{6,27,28}.

METHODS SUMMARY

We calibrated the lattice depths by performing amplitude modulation spectroscopy of the transition between the zeroth and second Bloch band in a one-dimensional degenerate gas for the x and y axes, and in a two-dimensional degenerate gas for the z axis. We estimate the calibration uncertainty to be 1–2%.

The quench was performed by lowering the lattice depth along the x axis in an exponential way (Supplementary Information). Numerical simulations showed that the origin $t = 0$ of the time evolution can be defined as the moment when the effective interaction strength reaches the value $U/J \approx 17$. We used the same phenomenological criterion to locate the moment at which the dynamics stops when raising the lattice depth to $\sim 80 E_r$.

We extracted the time of the maximum of the correlation signal as a function of the distance, for both the experiment and the theory, by fitting an offset-free Gaussian profile to the traces $C_d(t)$. For the numerical data, we filtered out frequency components above $3 J/\hbar$ before the fit in order to isolate the envelope of the signal. For the experimental data, we fixed the width of the Gaussian profile to the value obtained from the numerical data, keeping only the amplitude and time as free parameters.

The numerical simulations relied on matrix product states²⁹ to represent infinite homogenous systems³⁰. Initial states were obtained using the DMRG (density matrix renormalization group) algorithm. For the time evolution, we used a second-order Suzuki–Trotter decomposition^{24,25}. We achieved quasi-exact results on the relevant timescale $t/\hbar \approx 2$ by choosing a small enough Trotter time step (~ 0.002) and retaining a few thousand states.

Received 6 October; accepted 1 December 2011.

- Lieb, E. H. & Robinson, D. W. The finite group velocity of quantum spin systems. *Commun. Math. Phys.* **28**, 251–257 (1972).
- Bravyi, S., Hastings, M. B. & Verstraete, F. Lieb–Robinson bounds and the generation of correlations and topological quantum order. *Phys. Rev. Lett.* **97**, 050401 (2006).
- Calabrese, P. & Cardy, J. Time dependence of correlation functions following a quantum quench. *Phys. Rev. Lett.* **96**, 136801 (2006).
- Eisert, J. & Osborne, T. J. General entanglement scaling laws from time evolution. *Phys. Rev. Lett.* **97**, 150404 (2006).
- Nachtergaele, B., Ogata, Y. & Sims, R. Propagation of correlations in quantum lattice systems. *J. Stat. Phys.* **124**, 1–13 (2006).
- Polkovnikov, A., Sengupta, K., Silva, A. & Vengalattore, M. Nonequilibrium dynamics of closed interacting quantum systems. *Rev. Mod. Phys.* **83**, 863–883 (2011).
- Bose, S. Quantum communication through spin chain dynamics: an introductory overview. *Contemp. Phys.* **48**, 13–30 (2007).
- Hastings, M. B. Lieb–Schultz–Mattis in higher dimensions. *Phys. Rev. B* **69**, 104431 (2004).
- Nachtergaele, B. & Sims, R. Much ado about something: why Lieb–Robinson bounds are useful. Preprint at <http://arXiv.org/abs/1102.0835> (2011).
- Nachtergaele, B. & Sims, R. Lieb–Robinson bounds and the exponential clustering theorem. *Commun. Math. Phys.* **265**, 119–130 (2006).
- Hastings, M. B. & Koma, T. Spectral gap and exponential decay of correlations. *Commun. Math. Phys.* **265**, 781–804 (2006).
- Eisert, J., Cramer, M. & Plenio, M. B. Area laws for the entanglement entropy. *Rev. Mod. Phys.* **82**, 277–306 (2010).
- Läuchli, A. M. & Kollath, C. Spreading of correlations and entanglement after a quench in the one-dimensional Bose–Hubbard model. *J. Stat. Mech.* P05018 (2008).
- Nachtergaele, B., Raz, H., Schlein, B. & Sims, R. Lieb–Robinson bounds for harmonic and anharmonic lattice systems. *Commun. Math. Phys.* **286**, 1073–1098 (2009).
- Cramer, M., Serafini, A. & Eisert, J. in *Quantum Information and Many Body Quantum Systems* Vol. 8 (eds Ericsson, M. & Montangero, S.) 51–72 (Edizioni della Normale, Pisa, 2008).
- Eisert, J. & Gross, D. Supersonic quantum communication. *Phys. Rev. Lett.* **102**, 240501 (2009).
- Bloch, I., Dalibard, J. & Zwerger, W. Many-body physics with ultracold gases. *Rev. Mod. Phys.* **80**, 885–964 (2008).
- Bakr, W. S., Gillen, J. I., Peng, A., Fölling, S. & Greiner, M. A quantum gas microscope for detecting single atoms in a Hubbard-regime optical lattice. *Nature* **462**, 74–77 (2009).
- Sherson, J. F. *et al.* Single-atom resolved fluorescence imaging of an atomic Mott insulator. *Nature* **467**, 68–72 (2010).
- Fisher, M. P. A., Weichman, P. B., Grinstein, G. & Fisher, D. S. Boson localization and the superfluid-insulator transition. *Phys. Rev. B* **40**, 546–570 (1989).

21. Jaksch, D., Bruder, C., Cirac, J. I., Gardiner, C. W. & Zoller, P. Cold bosonic atoms in optical lattices. *Phys. Rev. Lett.* **81**, 3108–3111 (1998).
22. Kühner, T. D., White, S. R. & Monien, H. One-dimensional Bose–Hubbard model with nearest neighbor interaction. *Phys. Rev. B* **61**, 12474–12489 (2000).
23. Endres, M. *et al.* Observation of correlated particle-hole pairs and string order in low-dimensional Mott insulators. *Science* **334**, 200–203 (2011).
24. Daley, A. J., Kollath, C., Schollwöck, U. & Vidal, G. Time-dependent density-matrix renormalization-group using adaptive effective Hilbert spaces. *J. Stat. Mech.* P04005 (2004).
25. White, S. R. & Feiguin, A. E. Real-time evolution using the density matrix renormalization group. *Phys. Rev. Lett.* **93**, 076401 (2004).
26. Kollath, C., Schollwöck, U., von Delft, J. & Zwirger, W. One-dimensional density waves of ultracold bosons in an optical lattice. *Phys. Rev. A* **71**, 053606 (2005).
27. Kibble, T. W. B. Topology of cosmic domains and strings. *J. Phys. Math. Gen.* **9**, 1387–1398 (1976).
28. Zurek, W. H. Cosmological experiments in superfluid helium? *Nature* **317**, 505–508 (1985).
29. Schollwöck, U. The density-matrix renormalization group in the age of matrix product states. *Ann. Phys.* **326**, 96–192 (2011).
30. Vidal, G. Classical simulation of infinite-size quantum lattice systems in one spatial dimension. *Phys. Rev. Lett.* **98**, 070201 (2007).

Supplementary Information is linked to the online version of the paper at www.nature.com/nature.

Acknowledgements We thank C. Weitenberg and J. F. Sherson for their contribution to the design and construction of the apparatus. We also thank D. Baeriswyl, T. Giamarchi, V. Gritsev and S. Huber for discussions. C.K. acknowledges previous collaboration on a related subject with A. Läuchli. We acknowledge funding by MPG, DFG, EU (NAMEQUAM, AQUTE, Marie Curie Fellowship to M.C.), JSPS (Postdoctoral Fellowship for Research Abroad to T.F.), ‘Triangle de la physique’, ANR (FAMOUS) and SNSF (under division II and MaNEP). Financial support for the computer cluster on which the calculations were performed was provided by the Fondation Ernst et Lucie Schmidheiny.

Author Contributions M.C. performed the experiment. P.B. performed the numerical simulations. P.B., D.P. and C.K. developed the analytical model. M.C. and P.B. carried out the data analysis. All authors contributed to designing the study, to interpreting the data and to writing the manuscript.

Author Information Reprints and permissions information is available at www.nature.com/reprints. The authors declare no competing financial interests. Readers are welcome to comment on the online version of this article at www.nature.com/nature. Correspondence and requests for materials should be addressed to M.C. (marc.cheneau@mpq.mpg).

Atomic inner-shell X-ray laser at 1.46 nanometres pumped by an X-ray free-electron laser

Nina Rohringer^{1†}, Duncan Ryan², Richard A. London¹, Michael Purvis², Felicie Albert¹, James Dunn¹, John D. Bozek³, Christoph Bostedt³, Alexander Graf¹, Randal Hill¹, Stefan P. Hau-Riege¹ & Jorge J. Rocca²

Since the invention of the laser more than 50 years ago, scientists have striven to achieve amplification on atomic transitions of increasingly shorter wavelength^{1–7}. The introduction of X-ray free-electron lasers^{8–10} makes it possible to pump new atomic X-ray lasers^{11–13} with ultrashort pulse duration, extreme spectral brightness and full temporal coherence. Here we describe the implementation of an X-ray laser in the kiloelectronvolt energy regime, based on atomic population inversion and driven by rapid K-shell photo-ionization using pulses from an X-ray free-electron laser. We established a population inversion of the K α transition in singly ionized neon¹⁴ at 1.46 nanometres (corresponding to a photon energy of 849 electronvolts) in an elongated plasma column created by irradiation of a gas medium. We observed strong amplified spontaneous emission from the end of the excited plasma. This resulted in femtosecond-duration, high-intensity X-ray pulses of much shorter wavelength and greater brilliance than achieved with previous atomic X-ray lasers. Moreover, this scheme provides greatly increased wavelength stability, monochromaticity and improved temporal coherence by comparison with present-day X-ray free-electron lasers. The atomic X-ray lasers realized here may be useful for high-resolution spectroscopy and nonlinear X-ray studies.

The emergence of short-wavelength X-ray free-electron lasers^{8–10} (XFELs), delivering femtosecond X-ray pulses that exceed the peak brilliance of synchrotron sources by many orders of magnitude, has potential to open a pathway to studying nonlinear interactions of X-rays with matter^{15–21}. Especially appealing are ideas of transferring nonlinear spectroscopic techniques to the X-ray regime, to study photoinduced charge transfer, nuclear dynamics, chemical reactions, valence wavepacket propagation in molecules or phase transitions in solids at high temporal and spatial resolution. Nonlinear techniques to study these effects, such as X-ray stimulated coherent Raman spectroscopy^{19,20} or four-wave mixing^{18,21}, would, however, require ultrashort (preferably subfemtosecond), temporally coherent, synchronized two-colour X-ray sources. Present-day XFELs are based on self-amplified spontaneous emission (SASE) and start from noise. Although they are of unprecedented brightness, the pulses of SASE free-electron lasers have a fluctuating spectrum and limited temporal coherence²². A way to improve SASE pulses and to create a synchronized two-colour source in the X-ray regime is to use a SASE pulse to pump an atomic X-ray laser (XRL)^{11–13}.

Soft-X-ray lasers were first realized in 1984 at wavelengths near 20 nm (refs 2,3). In the soft-X-ray/vacuum-ultraviolet regime, population inversion is typically achieved by collisional excitation or recombination into excited states of highly ionized atoms in a hot, dense plasma^{4–7}. The first XRL in the kiloelectronvolt regime was proposed in 1967 and is based on establishing a population inversion by rapid photo-ionization of an inner-shell electron¹. In 1983 this scheme was demonstrated at optical wavelengths²³, and a few years later a

similar scheme was demonstrated in the vacuum ultraviolet using Auger-decay pumping following inner-shell photo-ionization²⁴. The photo-ionization scheme was extensively studied in theory for different gain materials and pump sources in the X-ray regime^{14,25–27}. Notably, detailed calculations for the neon K α transition pumped by laser-produced plasma X-rays were presented in 1991¹⁴. However, the lack of sufficiently fast and intense X-ray sources has so far precluded the realization of the photo-ionization scheme in the X-ray regime. More recently, calculations for neon pumped by XFEL radiation, which served as the design basis for this experiment, have been presented¹³.

When irradiated by X-rays slightly higher in energy than the ionization edge of an inner electronic shell, photo-ionization of an atom proceeds from the inside out, creating short-lived core-excited ions, which subsequently relax by means of Auger or radiative decay. At intensities achievable with XFELs, inner-shell photo-ionization happens on a timescale comparable to the lifetime of core-excited states, so that states of high ionic charge can be reached within a few femtoseconds and double-core-excited ‘hollow’ ions can be created²⁸. Moreover, rapid photo-ionization results in short-lived population inversions, which can be exploited for lasing from the valence to the core level.

In our experiment, which was carried out at the Linac Coherent Light Source⁸ (LCLS) of the SLAC National Accelerator Laboratory, XFEL pulses of 960-eV photon energy were focused into a volume of neon gas at ~ 500 torr to spot sizes of 1–2- μ m radius, to create a long, narrow column of transiently core-excited ions (Fig. 1). XFEL pulse energies on target were between 0.02 and 0.27 mJ, and the pulse duration was 40–80 fs. This resulted in intensities up to 2×10^{17} W cm⁻² and an inverse photo-ionization rate of ~ 4 fs, which is comparable to the Auger lifetime of the 1s core hole, namely 2.4 fs. Although the decay of the core-excited state is dominated by the Auger process, there is a small probability (1.8%) that the ion will undergo a spontaneous radiative decay, emitting a photon with an energy of 849 eV. Photons that are spontaneously emitted near the front end of the plasma column generate exponentially amplified stimulated emission along the direction of the XFEL pulse, which prepares atoms in the excited state, just as the atomic line radiation from previously excited atoms reaches them. In traditional plasma-based XRLs, the width of the transition is determined by Doppler, lifetime and collisional broadening. In the present scheme, the density is low and the plasma remains cold, with the result that the transition is mainly lifetime-broadened by Auger decay. The line profile of the spontaneous emission before strong amplification by stimulated emission is therefore Lorentzian with a width of 0.27 eV.

A grazing-incidence grating spectrometer with a CCD detector was used to monitor the spectrum of the transmitted XFEL pump source and the atomic XRL radiation. The raw single-shot image shown in Fig. 1b provides strong evidence of lasing. The relatively broad line (Fig. 1b, bottom) is the transmitted XFEL pulse. The narrow atomic line radiation is visible at 849 eV, with peak intensities one order of

¹Lawrence Livermore National Laboratory, 7000 East Avenue, Livermore, California 94551, USA. ²Colorado State University and NSF Engineering Research Center for Extreme Ultraviolet Science and Technology, Fort Collins, Colorado 80523, USA. ³LCLS, SLAC National Accelerator Laboratory, 2575 Sand Hill Road, Menlo Park, California 94025, USA. [†]Present address: Max Planck Advanced Study Group, Center for Free-Electron Laser Science, c/o DESY, Notkestrasse 85, 22607 Hamburg, Germany.

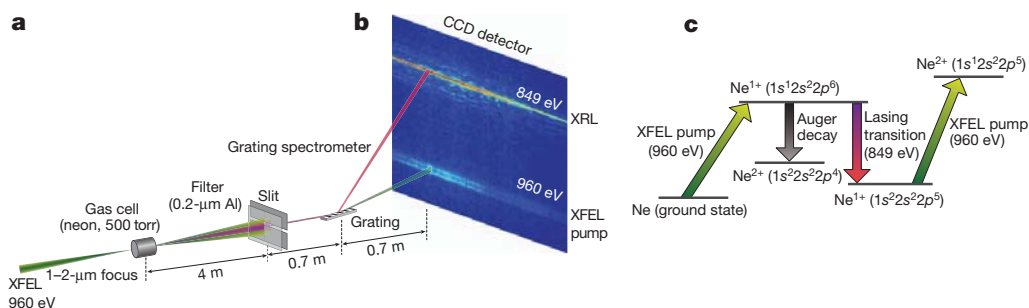


Figure 1 | Experimental scheme. **a**, The XFEL beam is focused into a gas cell filled with neon to a focus spot of radius 1–2 μm . A flat-field X-ray grating spectrometer was positioned ~ 4 m from the interaction region. **b**, The charge-coupled-device (CCD) image of the transmitted XFEL pump (bottom) and the XRL (top). **c**, Level scheme. Population inversion of the $1s^1 2s^2 2p^6$ -to- $1s^2 2s^2 2p^5$

magnitude higher than that of the strongly attenuated XFEL. Fluorescence would result in ~ 50 photons entering the spectrometer set-up, which is undetectable in the current configuration. Figure 2 shows line-outs of three different single-shot spectra for an XFEL energy of ~ 0.25 mJ. By contrast with the broad (full-width at half-maximum (FWHM) of 8 eV) and jittering (FWHM of 14 eV) spectra of the XFEL pulses, the atomic line has a reproducible spectral shape with narrow width and fixed centroid. The measured FWHM, of 2 eV, is limited by the resolution of the spectrometer.

To demonstrate exponential amplification on the atomic line transition, we varied the incoming XFEL energy. To average over the large statistical fluctuations in the XRL output, we gathered a set of 950 spectral images in a series of ten-shot integrations. Figure 3 shows the averaged number of photons in the neon $K\alpha$ line for each of the images as a function of the averaged pulse energy. Doubling the XFEL energy from 0.12 to 0.24 mJ results in an average increase in the XRL line energy by four orders of magnitude. The XRL pulse energy distribution is relatively broad at a given pump energy, reflecting the large shot-to-shot variation of the gain due to the stochastic properties of the SASE pulse. Also shown in Fig. 3 is a comparison to a one-dimensional, time-dependent, self-consistent gain model¹³ (see also Supplementary Information). There is good agreement between the calculated and measured energies in the neon $K\alpha$ line and in the transmitted XFEL pump (Supplementary Fig. 6).

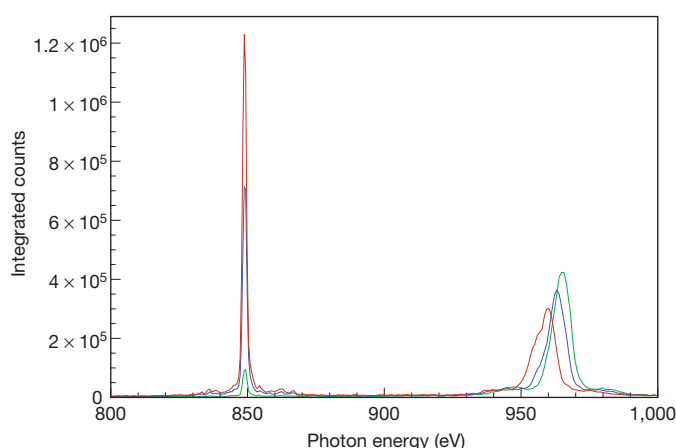


Figure 2 | Single-shot spectra of the atomic XRL line and transmitted XFEL pump. Horizontally integrated spectra for three shots with similar pulse energies, but slightly varying XFEL photon energies. The neon gas attenuates the XFEL and XRL lines by factors of 2.5×10^3 and 2, respectively. The neon $K\alpha$ line is centred at 849 eV and has a FWHM of 2 eV limited by instrument resolution. The neon $K\alpha$ line shows satellite peaks on both sides of the main peak. Their intensities closely follow that of the main peak and are most probably ghost lines from the spectrometer grating.

transition is created by K-shell photo-ionization of neutral neon. The Auger decay time of the inverted state (2.4 fs) dominates the kinetics of the system in the small-signal-gain regime. The lower lasing state is depleted by K-shell photo-ionization.

To estimate the influence of the fluctuating temporal profiles of the XFEL on the gain, we calculated the small-signal gain coefficient for an ensemble of 1,000 numerically generated SASE pulses (Fig. 4). The gain for this self-terminating scheme is characterized by a rise time of 5 fs and a peak of 64 cm^{-1} . The gain duration has a FWHM of 20 fs and is determined by the convolution of the rate to deplete the neutral atoms with the exponential Auger decay. The variation in the peak gain due to the SASE pump is considerable; the standard deviation is 30%.

The traditional method of determining the gain-length product (GL) is by measuring the output energy versus length. We estimate GL by comparing the measured value of the output energy with a simple theoretical estimate (Supplementary Information). For the single shot with the highest XRL output, $1.1 \pm 0.4 \mu\text{J}$, we estimate that $\text{GL} = 19.2\text{--}21.3$, whereas for average shots with 0.24-mJ XFEL energy we deduce $\text{GL} = 17\text{--}19.3$. This is consistent with $\text{GL} = 19$, the result calculated using our one-dimensional model. Owing to strong absorption of the XFEL, the gain coefficient decreases as a function of propagation depth, with a calculated decay length of 0.28 cm. This is somewhat longer than the expected attenuation length in neutral neon, of 0.22 cm, owing to bleaching. Assuming a gain region 0.28 cm in length, we estimate an effective gain coefficient of $61\text{--}70 \text{ cm}^{-1}$ at 0.24-mJ XFEL energy. Saturation of the exponential amplification cannot be discerned in the experimental data presented in Fig. 3. Our

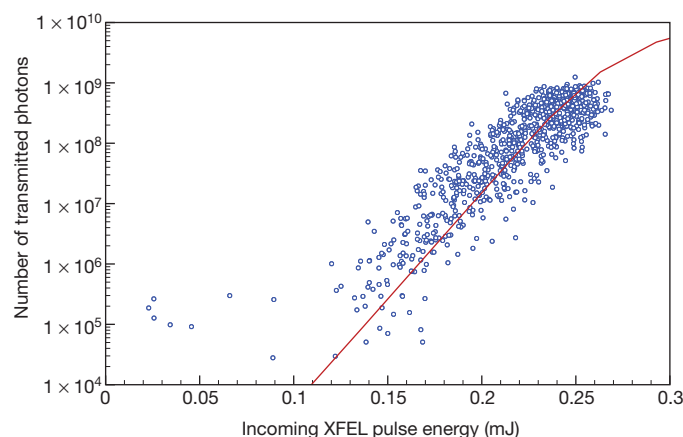


Figure 3 | Dependence of the XRL output on pump power. Average number of transmitted photons of the neon $K\alpha$ line for ten consecutive XFEL shots, as a function of the average XFEL pulse energy on target (s.d., ± 0.014 mJ). We assumed a beamline transmission of 18%. The determined number of $K\alpha$ photons has an error of $\sim 30\%$. The small linear signal below a pulse energy of 0.15 mJ results from spectral tails of the XFEL reaching into the 849-eV energy region of the XRL line. Results of a one-dimensional model are shown in red, assuming a density of $1.6 \times 10^{19} \text{ atoms cm}^{-3}$, an interaction length of 1.8 cm, a pulse duration of 40 fs and a focal radius of 2 μm .

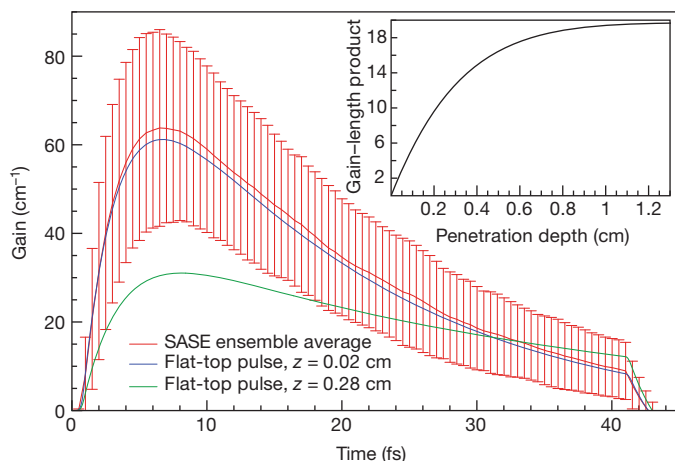


Figure 4 | Simulation of the gain. Temporal profile of the average gain (error bars, s.d.) at a density of 1.6×10^{19} atoms cm^{-3} for an ensemble of 1,000 SASE pulses of 40-fs pulse duration, an energy of 0.24 mJ and a coherence time of 0.3 fs. Also shown is the temporal profile of the gain as determined by the self-consistent gain calculations at penetration depths of $z = 0.02$ cm (blue) and 0.28 cm (green) for a flat-top pulse with a 0.5-fs Gaussian ramp on. Inset, integrated gain-length product as a function of the penetration depth in the medium.

simulations, however, suggest that we are close to the onset of saturation, which according to our model is reached at $GL = 22$. In traditional XRLs, saturation sets in at far lower values, of $GL \approx 15$ (ref. 5). In our scheme, the small angular divergence, the fast upper-state decay and the absence of refraction all contribute to the higher value of GL needed to reach saturation.

The measured output parameters of the neon XRL are a maximum single-shot energy of 1.1 ± 0.4 μJ and an angular divergence of 1 mrad (see spatial beam intensity profile in Supplementary Fig. 5). This energy corresponds to $\sim 8 \times 10^9$ photons in the neon $K\alpha$ line and an energy conversion efficiency of 4×10^{-3} . The geometry of the gain medium (radius, 1–2 μm ; length, 0.28 cm) results in a Fresnel number of ~ 1 , such that the XRL is expected to be transversely coherent⁴. Our model predicts an average pulse duration of 5-fs FWHM. The XRL, a gain-swept amplifier characterized by a fast build-up of the population inversion and a short upper-state lifetime, is expected to be nearly transform limited and longitudinally coherent²⁹. We estimate the spectral width to be 0.27 eV, resulting in a relative bandwidth of 0.03%, determined by Fourier transform of the square root of the temporal flux profile. To determine the spectral, temporal and coherence properties accurately, a Maxwell–Bloch approach is required. With the above parameters, we estimate the peak brilliance of the XRL to be $\sim 4 \times 10^{29}$ photons s^{-1} mrad^{-2} mm^{-2} within a relative spectral bandwidth of 0.1%. By comparison, the LCLS has a brilliance of $\sim 3 \times 10^{31}$ at a photon energy of 1 keV (ref. 8) and can be operated to produce pulses with durations of less than or equal to 10 fs. Considering the absolute bandwidth, the XRL has a spectral brightness only a factor of 30 smaller than that of the LCLS. Notably, the present inner-shell XRL is the shortest-wavelength atomic XRL demonstrated so far and its peak brilliance is greater by two to three orders of magnitude than those of laser-heated XUV plasma lasers³⁰.

The XRL photo-ionization scheme can be extended in several ways. The transverse coherence and the brilliance could be increased by lowering the gas density, thereby lengthening the gain region and reducing angular divergence. The output energy of the XRL could be increased significantly by a modest increase in the XFEL energy, as indicated by the theoretical curve in Fig. 3. By increasing the photon energy of the XFEL above the K edges of higher charge states, it should become possible to use hydrogen and helium-like neon as lasing ions¹³. This would result in lines of higher energies and of even narrower bandwidth ($\Delta\omega/\omega \approx 10^{-6}$), owing to the extended lifetime of the

upper state. An increase in the photon flux by a factor of ten and longer pulse durations, in the range of 150–200 fs, would be required to access these lines. The XRL photo-ionization scheme can be transferred to other elements and, thereby, to shorter or longer wavelengths. Lasing on a $K\alpha$ transition seems to be most promising for elements with atomic number $Z \leq 20$ (refs 14,25). According to a simplified gain model, the gain-length product scales like $GL \propto I\lambda^{2.2}$ as wavelength (λ) decreases (where I denotes the pump intensity). A numerical study published before XFELs were available showed that lasing in the $K\alpha$ transition in solid sulphur at 2.37 keV could be established with X-ray pulses nowadays achievable with XFELs²⁵. To achieve a gain-length product comparable to that of neon, an increase in the pump intensity by a factor of approximately ten is necessary, which could be achieved by tighter focusing. Another extension is to consider resonant excitation as a pumping mechanism¹⁸. This scheme, which is based on amplification of self-stimulated X-ray Raman scattering, has the potential of creating phase correlated two-colour X-ray/vacuum-ultraviolet sources suitable for coherent pump–probe applications.

The demonstrated XRL scheme enhances the capability of present-day XFEL sources. By contrast with the SASE XFELs, the atomic XRL is expected to be longitudinally coherent and has a stable wavelength centroid, that is, a highly reproducible spectrum and a much narrower bandwidth. These advantages could be exploited in applications of photoelectron spectroscopy or inelastic X-ray scattering. Moreover, the scheme directly provides a synchronized, that is, time-jitter free, two-colour source in the X-ray regime. Both the transmitted XFEL radiation and the atomic XRL radiation have of the order of 10^9 – 10^{10} photons per pulse and ultrashort pulse durations of 40 and 5 fs, respectively. The photon energy of the XFEL in this two-colour source is tunable, as long as the photon energy is greater than the K-edge energy of the gain medium. This scheme hence opens the way to two-colour pump–probe studies in the X-ray regime. Intriguing new directions realizable with this kind of source would for example be stimulated inelastic X-ray scattering for applications in solid-state and surface physics or time-resolved molecular spectroscopy by stimulated X-ray Raman scattering¹⁹.

METHODS SUMMARY

LCLS X-ray pulses with ~ 960 -eV photon energy were focused to an estimated focus spot of ~ 1 – 2 - μm radius in a gas cell of 1.4-cm length filled with neon at a pressure of 500 torr. The XFEL pulse energy was varied with a gas attenuator situated upstream and monitored by two upstream pulse-energy detectors. A flat-field grating spectrometer was positioned 4 m downstream of the gas cell to record the spectra of both the transmitted XFEL pump and the XRL line. The spectra were recorded with a conventional 20- μm -pixel back-illuminated X-ray CCD camera. The resolution of the spectrometer is ~ 2 eV at 1-keV photon energy. A triggered shutter allowed for both single-shot and integrated ten-shot measurements, at a repetition rate of the LCLS between 10 and 60 Hz. To estimate the signal and gain parameters of the XRL, we performed self-consistent gain calculations. The model is based on a set of atomic rate equations, determining the populations of a total of 63 configuration states of neon during interaction with an X-ray pulse, coupled to equations describing the propagation, absorption and amplification of the X-ray flux in a simplified one-dimensional geometry. The processes taken into account are photo-ionization of the valence and core shells, Auger decay, spontaneous and stimulated radiative decay, and absorption. We consider the forward-propagating X-ray flux at two discrete energies and assume a dispersion-free medium. Calculations for small signal gain were performed for a stochastic ensemble of SASE pulses, created by a Monte Carlo method. For comparison with the ten-shot data, we assumed flat-top pulses, representing the average temporal structure of the SASE ensemble.

Received 28 August; accepted 15 November 2011.

1. Duguay, M. A. & Rentzepis, G. P. Some approaches to vacuum UV and X-ray lasers. *Appl. Phys. Lett.* **10**, 350–352 (1967).
2. Matthews, D. L. *et al.* Demonstration of a soft X-ray amplifier. *Phys. Rev. Lett.* **54**, 110–113 (1985).
3. Suckewer, S., Skinner, S., Milchberg, C. H., Keane, C. & Voorhees, D. Amplification of stimulated soft X-ray emission in a confined plasma column. *Phys. Rev. Lett.* **55**, 1753–1756 (1985).

4. Elton, R. C. *X-ray lasers* (Academic, 1990).
5. Rocca, J. J. Table-top soft X-ray lasers. *Rev. Sci. Instrum.* **70**, 3799–3827 (1999).
6. Daido, H. Review of soft X-ray laser researches and developments. *Rep. Prog. Phys.* **65**, 1513–1576 (2002).
7. Suckewer, S. & Jaegle, P. X-ray lasers: past, present, future. *Laser Phys. Lett.* **6**, 411–436 (2009).
8. Emma, P. *et al.* First lasing and operation of an ångström-wavelength free-electron laser. *Nature Photon.* **4**, 641–647 (2010).
9. Ackermann, W. *et al.* Operation of a free-electron laser from the extreme ultraviolet to the water window. *Nature Photon.* **1**, 336–342 (2007).
10. Pile, D. X-rays: first light from SACLA. *Nature Photon.* **5**, 456 (2011).
11. Lan, K. Fill, E. & Meyer-ter-Vehn, J. Photopumping of XUV lasers by XFEL radiation. *Laser Part. Beams* **22**, 261–266 (2004).
12. Zhao, J. Dong, Q. L., Wang, S. J., Zhang, L. & Zhang, J. X-ray lasers from inner-shell transitions pumped by the free-electron laser. *Opt. Express* **16**, 3546–3559 (2008).
13. Rohringer, N. & London, R. A. Atomic inner-shell X-ray laser pumped by an X-ray free-electron laser. *Phys. Rev. A* **80**, 013809 (2009).
14. Kapteyn, H. C. Photoionisation-pumped X-ray lasers using ultrashort-pulse excitation. *Appl. Opt.* **31**, 4931–4939 (1992).
15. Rohringer, N. & Santra, R. X-ray nonlinear optical processes using a self-amplified spontaneous emission free-electron laser. *Phys. Rev. A* **76**, 033416 (2007).
16. Kanter, E. P. *et al.* Unveiling and driving hidden resonances with high-fluence, high-intensity X-ray pulses. *Phys. Rev. Lett.* **107**, 233001 (2011).
17. Doumy, G. *et al.* Nonlinear atomic response to intense ultrashort X-rays. *Phys. Rev. Lett.* **106**, 083002 (2011).
18. Sun, Y.-P., Liu, J.-C., Wang, C.-K. & Gel'mukhanov, F. Propagation of a strong X-ray pulse: pulse compression, stimulated Raman scattering, amplified spontaneous emission, lasing without inversion, and four-wave mixing. *Phys. Rev. A* **81**, 013812 (2010).
19. Schweigert, I. V. & Mukamel, S. Probing valence electronic wave-packet dynamics by all X-ray stimulated Raman spectroscopy: a simulation study. *Phys. Rev. A* **76**, 012504 (2007).
20. Tanaka, S. & Mukamel, S. Coherent X-ray Raman spectroscopy: a nonlinear local probe for electronic excitations. *Phys. Rev. Lett.* **89**, 043001 (2002).
21. Mukamel, S. Multiple core-hole coherence in X-ray four-wave-mixing spectroscopies. *Phys. Rev. B* **72**, 235110 (2005).
22. Vartanyants, I. A. *et al.* Coherence properties of individual femtosecond pulses of an X-ray free-electron laser. *Phys. Rev. Lett.* **107**, 144801 (2011).
23. Silfvast, W. T., Macklin, J. J. & Wood, O. R. II. High-gain inner-shell photoionisation laser in Cd vapor pumped by soft-X-ray radiation from a laser-produced plasma source. *Opt. Lett.* **8**, 551–553 (1983).
24. Kapteyn, H. C., Lee, R. W. & Falcone, R. W. Observation of short-wavelength laser pumped by Auger decay. *Phys. Rev. Lett.* **57**, 2939–2942 (1986).
25. Axelrod, T. S. Inner-shell photoionisation-pumped X-ray lasers. Sulfur. *Phys. Rev. A* **13**, 376–382 (1976).
26. Eder, D. C. *et al.* Tabletop X-ray lasers. *Phys. Plasmas* **1**, 1744–1752 (1994).
27. Strobel, G. L. *et al.* Innershell photoionized X-ray laser schemes. *Proc. SPIE* **1860**, 157–166 (1993).
28. Young, L. *et al.* Femtosecond electronic response of atoms to ultra-intense X-rays. *Nature* **466**, 56–61 (2010).
29. Hopf, F. A. & Meystre, P. Quantum theory of a swept-gain laser amplifier. *Phys. Rev. A* **12**, 2534–2548 (1975).
30. Rus, B. *et al.* Multimillijoule, highly coherent X-ray laser at 21 nm operating in deep saturation through double-pass amplification. *Phys. Rev. A* **66**, 063806 (2002).

Supplementary Information is linked to the online version of the paper at www.nature.com/nature.

Acknowledgements This work was performed under the auspices of the US Department of Energy by Lawrence Livermore National Laboratory (LLNL; DE-AC52-07NA27344) and was supported by LLNL's LDRD programme, 09-LW-044. Portions of this research were carried out at the Linac Coherent Light Source, a national user facility operated by Stanford University on behalf of the US Department of Energy, Office of Basic Energy Sciences. J.J.R., M.P. and D.R. were supported by the US Department of Energy Basic Energy Sciences AMOS Program. We thank M. J. Pivovarov and K. A. van Bibber for their encouragement and support for this project; R. W. Lee, T. Ditmire, L. Young, R. Falcone and S. Le Pape for discussions of the experimental design; J.-C. Castagna, C.-M. Tsai, S. Schorb, M. L. Swiggers and M. Messerschmidt for their assistance with the experiment; M. J. Bogan for the loan of the X-ray CCD camera and A. Barty for the design of Fig. 1. We also acknowledge support of the LCLS software engineers for the control and data acquisition. We are indebted to the LCLS operating team for their support during beam time in achieving the necessary pulse energies for this experiment.

Author Contributions N.R. and R.A.L. had the idea for the experiment, which was designed with J.J.R., J.D. and J.D.B. N.R. developed theory and models of the data. J.D.B. and C.B. were responsible for the AMO beamline at LCLS. R.H. designed the neon gas cell. D.R. and M.P. calibrated and installed the X-ray spectrograph. D.R., M.P., J.D.B., C.B., J.D., F.A., N.R., J.J.R. and R.A.L. carried out the experiment. S.P.H.-R. and R.A.L. performed hole-drilling tests on the gas-cell window materials. A.G. helped in the set-up of the experiment. J.D., R.A.L. and N.R. designed the filters. N.R., D.R. and R.A.L. analysed and interpreted the data. R.A.L. estimated the gain and gain-length product. N.R. wrote the paper with contributions from R.A.L., J.D., D.R. and J.J.R.

Author Information Reprints and permissions information is available at www.nature.com/reprints. The authors declare no competing financial interests. Readers are welcome to comment on the online version of this article at www.nature.com/nature. Correspondence and requests for materials should be addressed to N.R. (nina.rohringer@asg.mpg.de).

Pathway complexity in supramolecular polymerization

Peter A. Korevaar^{1,2}, Subi J. George², Albert J. Markvoort^{1,3}, Maarten M. J. Smulders^{1,2}, Peter A. J. Hilbers^{1,3}, Albert P. H. J. Schenning², Tom F. A. De Greef^{1,2,3} & E. W. Meijer^{1,2}

Self-assembly provides an attractive route to functional organic materials, with properties and hence performance depending sensitively on the organization of the molecular building blocks^{1–5}. Molecular organization is a direct consequence of the pathways involved in the supramolecular assembly process, which is more amenable to detailed study when using one-dimensional systems. In the case of protein fibrils, formation and growth have been attributed to complex aggregation pathways^{6–8} that go beyond traditional concepts of homogeneous^{9–11} and secondary^{12–14} nucleation events. The self-assembly of synthetic supramolecular polymers has also been studied and even modulated^{15–18}, but our quantitative understanding of the processes involved remains limited. Here we report time-resolved observations of the formation of supramolecular polymers from π -conjugated oligomers. Our kinetic experiments show the presence of a kinetically favoured metastable assembly that forms quickly but then transforms into the thermodynamically favoured form. Quantitative insight into the kinetic experiments was obtained from kinetic model calculations, which revealed two parallel and competing pathways leading to assemblies with opposite helicity. These insights prompt us to use a chiral tartaric acid as an auxiliary to change the thermodynamic preference of the assembly process¹⁹. We find that we can force aggregation completely down the kinetically favoured pathway so that, on removal of the auxiliary, we obtain only metastable assemblies.

The π -conjugated oligomer *S*-chiral oligo(*p*-phenylenevinylene) (SOPV, Fig. 1a) serves as a functional material in a variety of organic electronic devices, with performance critically dependent on the material's morphology²⁰. This morphology is determined by the assembly mechanisms that transform the molecularly dissolved monomers into the materials used in devices. The hydrogen-bonded dimers of SOPV self-assemble in apolar solvents via π - π interactions into one-dimensional helical stacks, and earlier circular dichroism (CD) and ultraviolet–visible spectroscopy studies under thermodynamic control revealed exclusive formation of left-handed *M*-type helical aggregates (*M*-SOPV) through a nucleated growth mechanism²¹. In practice, however, the assembly process is often under kinetic control—prompting us to examine in detail the supramolecular polymerization process under non-equilibrium conditions.

Upon rapid quenching of SOPV from the molecularly dissolved state to 273 K, we observed the formation of a mixture of *M*-SOPV and aggregates with opposite helicity, as evidenced by the opposite sign of the bisignated Cotton effect (Fig. 1b). At 298 K, these right-handed *P*-type aggregates (*P*-SOPV) slowly converted into thermodynamically stable *M*-SOPV aggregates (Supplementary Fig. 1). The observation of metastable *P*-SOPV aggregates indicated that the supramolecular polymerization of SOPV involves two different aggregation pathways, which we termed the on-pathway (leading to *M*-SOPV) and off-pathway (leading to *P*-SOPV) (Fig. 1c).

To study the aggregation mechanism of SOPV and quantify the self-assembly pathways under kinetic control, we conducted stopped-flow

experiments in which a concentrated solution of molecularly dissolved SOPV in chloroform was mixed with an excess of methylcyclohexane (MCH) to initiate self-assembly. The subsequent formation of helical SOPV aggregated in MCH was probed using CD spectroscopy (Supplementary Discussion 1). These kinetic experiments were conducted at 293 K and 308 K, with different concentrations of SOPV. At 293 K and the lowest SOPV concentrations, the rate of aggregate formation initially increased with time, characteristic of a lag phase (Fig. 2a, c). The time-dependent CD signal was always negative under these conditions, suggesting the direct formation of thermodynamically stable on-pathway *M*-SOPV aggregates. At higher concentrations ($\geq 9 \mu\text{M}$) a positive CD signal appeared in the initial stages of the assembly process and then developed into a negative CD signal at later times, suggesting the initial formation of off-pathway *P*-SOPV aggregates that then convert into thermodynamically stable *M*-SOPV aggregates. Remarkably, the time at which 50% of the aggregation process was completed ($t - 50$) is longer at $15 \mu\text{M}$ than at $10 \mu\text{M}$ (Fig. 2d). Analogous kinetic studies at 308 K also revealed the presence of a lag phase in experiments at the lowest concentrations (Fig. 2b, e) and an inverted dependence of $t - 50$ on concentration, although the shortest $t - 50$ time shifts to a higher SOPV concentration ($20 \mu\text{M}$; Fig. 2d). Detailed analyses unambiguously prove that both the on- and off-pathway are formed via a homogeneously nucleated growth mechanism (Supplementary Figs 5 and 6).

To rationalize the experimental aggregation kinetics, we extended models known in the field of protein fibrillization^{6,9,11} by incorporating two competing, nucleated assembly pathways in which prenucleus oligomers (oligomer aggregates below the critical nucleation size) and helical aggregates change size through monomer association and dissociation (Fig. 3a, Supplementary Discussion 2). For the *M*-SOPV aggregates, non-helical prenucleus oligomers change size with rate constants for association and dissociation of a and b , respectively. Once the critical nucleus (with size n) is reached, the helical aggregates are in the elongation regime and change size through monomer association with the same rate constant a , while dissociation proceeds with rate constant c . The steady-state concentration of the aggregates in the nucleation phase is determined by the nucleation equilibrium constant $K_n = a/b$, while in the elongation phase it is determined by the elongation equilibrium constant $K_e = a/c$. The nucleated growth of off-pathway *P*-SOPV aggregates is described analogously, with nucleus size n^* , rate constants a^* , b^* and c^* , and equilibrium constants K_n^* and K_e^* . An essential model assumption is that the transition from metastable to thermodynamically stable aggregates occurs via depolymerization of *P*-SOPV aggregates and subsequent growth of *M*-SOPV aggregates. This is justified by the high helix reversal penalty ($8.1 k_B T$, where k_B is the Boltzmann constant and T is temperature), obtained by ‘majority rules’ experiments, which rules out intrastack stereomutation as an alternative transition mechanism (Supplementary Fig. 8)²².

¹Institute for Complex Molecular Systems, Eindhoven University of Technology, PO Box 513, 5600 MB, Eindhoven, The Netherlands. ²Laboratory of Macromolecular and Organic Chemistry, Eindhoven University of Technology, PO Box 513, 5600 MB, Eindhoven, The Netherlands. ³Biomodeling and Bioinformatics Group, Eindhoven University of Technology, PO Box 513, 5600 MB, Eindhoven, The Netherlands.

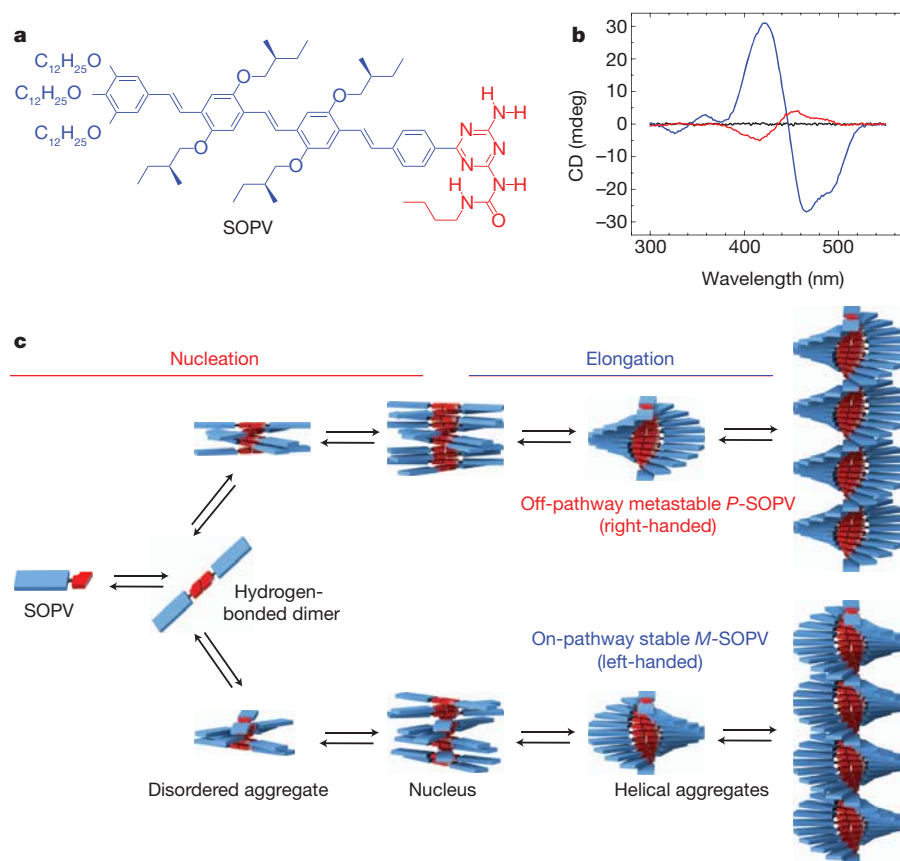


Figure 1 | Pathway complexity in supramolecular polymerization of SOPV. **a**, Molecular structure of SOPV with S-chiral butoxy side chains. **b**, CD spectra of SOPV in MCH in disassembled state (343 K, black line), thermodynamically stable *M*-SOPV (273 K, blue line) and mixture of *M*-SOPV and metastable *P*-SOPV (273 K, red line). **c**, Schematic representation of the aggregation pathways of SOPV, including the growth of two competing assemblies. Self-

assembly of SOPV in apolar solutions is initiated by formation of a quadruply hydrogen-bonded dimer. The hydrogen-bonded dimer further self-assembles into helical stacks via a nucleation–elongation growth mechanism. Right-handed *P*-helices form quickly but are less stable than the left-handed *M*-helices, which form more slowly.

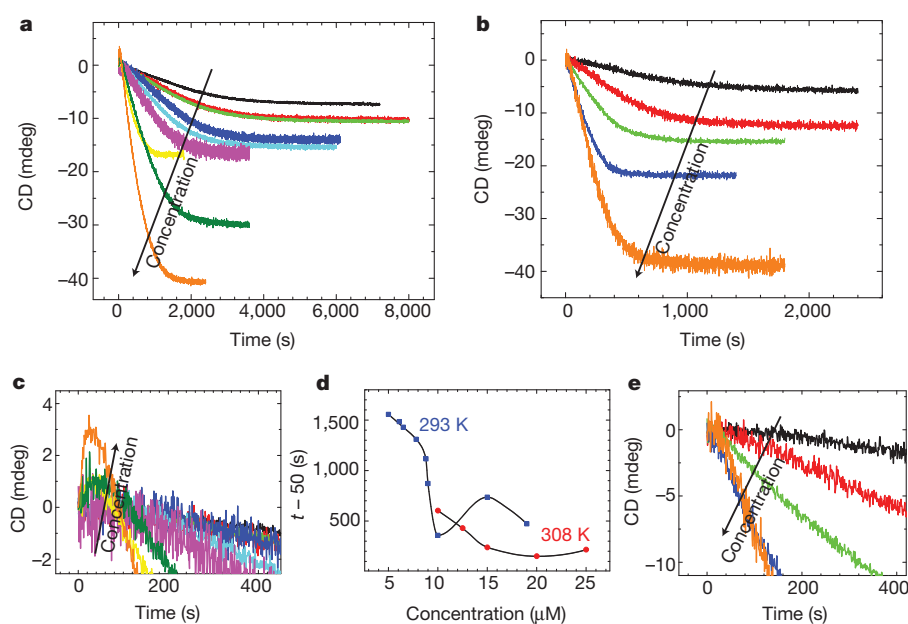


Figure 2 | Experiments under kinetic control. Stopped-flow studies on self-assembly of SOPV. **a**, Concentration-dependent kinetics at 293 K. SOPV concentrations (black arrow shows increasing concentration) are colour-coded as follows: 5 μM (black), 6.1 μM (red), 6.5 μM (light green), 7.8 μM (dark blue), 8.7 μM (light blue), 9 μM (pink), 10 μM (yellow), 15 μM (dark green) and 19 μM (orange). **b**, Concentration-dependent kinetics at 308 K. SOPV

concentrations are 10 μM (black), 12.5 μM (red), 15 μM (green), 20 μM (blue) and 25 μM (orange). **c**, Zoom in for initial stages of growth process studied at 293 K in panel **a**. **d**, Time at which 50% of final CD intensity is reached ($t = 50$) versus concentration at 293 K and 308 K. The lines serve to guide the eye. **e**, Zoom in for initial stages of growth process studied at 308 K in panel **b**.

Simulations with this model showed that off-pathway *P*-SOPV aggregates only appear in the initial stages of the self-assembly process if sufficient monomers are present and *P*-SOPV formation is kinetically favoured over that of *M*-SOPV. Specifically, the total monomer concentration (c_{tot}) has to exceed the critical concentration of *P*-SOPV ($c_{\text{tot}} > K_e^{*-1}$), which depends on the elongation equilibrium constant of this species. Moreover, the initial formation of *P*-SOPV is kinetically favoured when the forward rate constant of nucleation and elongation is larger for the off-pathway aggregates ($a^* > a$) or if the pre-nucleus oligomers of *P*-SOPV are kinetically more stable ($K_n^* > K_n$, or $a^*/b^* > a/b$) (Supplementary Fig. 9). As a result, off-pathway *P*-SOPV aggregates can only self-assemble at high concentrations and low temperatures (high K_e^*), as was observed experimentally. With $a^* > a$, the kinetic model successfully described the experimental kinetic data, including the initial formation of *P*-SOPV (Fig. 3b). The calculated Gibbs free energy diagram revealed that the *P*-SOPV nucleus is thermodynamically less unstable than the *M*-SOPV nucleus (that is, $K_n^* > K_n$), whereas *M*-SOPV is more stable in the elongation phase (Fig. 3c). Kinetic studies on protein fibrillation have shown that for the initial stages of homogeneously nucleated aggregation involving a thermodynamically unstable nucleus, the conversion to the stable product is proportional to time squared, t^2 (ref. 9). In our experiments with the lowest SOPV concentrations, the changes of the CD signal in the lag phases indeed can be described as being proportional to t^2 , demonstrating homogeneous nucleation in the aggregation of SOPV (Supplementary Fig. 10).

To corroborate the proposed involvement of two aggregation pathways, we further analysed the concentration dependence of the kinetic data and found that the changes in the $t - 50$ values with concentration can only be rationalized by taking off-pathway aggregation into account (Fig. 3d, e): the relatively large amount of metastable *P*-type aggregates formed at higher concentrations sequester monomers and lower their solution concentration, thereby hampering the formation of the thermodynamically stable *M*-type aggregates. Our simulations did not show a further decrease of $t - 50$ at higher

concentrations with reasonable model parameters. Because our model only considers monomer addition and dissociation, oligomer reactions and fragmentation¹⁴—which become more important at higher concentrations—may explain this difference between simulated and observed behaviour. Simulations exploring the effect of temperature showed that the maximum in the aggregation rate shifts to higher concentrations and the aggregation rate gets faster (that is, $t - 50$ values get lower) on increasing temperature, as was observed experimentally (Supplementary Fig. 11).

The discovery of these two different assembly pathways, producing structurally different aggregates, encouraged us to attempt to direct the assembly of SOPV towards metastable products. To force the assembly of SOPV into exclusively *P*-type aggregates instead of the mixture obtained upon fast cooling (see above), we used a two-step non-covalent synthetic method (Fig. 4a, b) inspired by previous assembly control experiments¹⁹. The earlier work involved achiral oligo(*p*-phenylenevinylene) monomers that assemble into chiral helical architectures of equal energy, and showed that the addition of chiral auxiliaries transforms an initially racemic mixture of these structures so that one of the two possible chiral helical architectures dominates¹⁹. Here, we used a chiral auxiliary to direct the assembly so that, upon removal of the auxiliary, we obtain the thermodynamically unstable *P*-type aggregates.

In the first step, *S*-chiral dibenzoyl tartaric acid (DTA) was used to dictate its chirality to the SOPV monomer via two-fold hydrogen bonding, orthogonal to the SOPV dimerization (Supplementary Discussion 3). Aggregates having opposite helicity (*P*-DTA-SOPV) compared to equilibrium conditions (*M*-SOPV) are formed, as demonstrated by the opposite CD spectrum (Fig. 4c). In the second step, the complete removal of DTA from the SOPV aggregates by aqueous extraction at 273 K using ethylene diamine resulted in the formation of transiently stable *P*-SOPV aggregates at this temperature (Supplementary Fig. 12). The exclusive formation of *P*-SOPV is demonstrated by the absolute ellipticity of *P*-SOPV, which equals the ellipticity of a solution containing exclusively *M*-SOPV aggregates

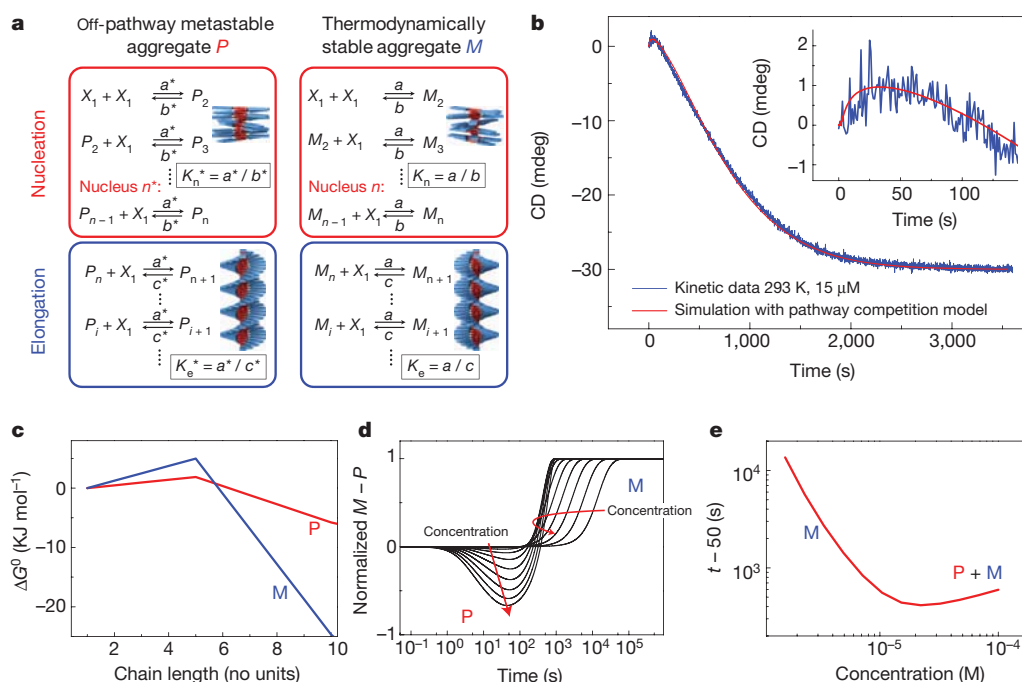


Figure 3 | Analysis aggregation pathway competition with kinetic model. **a**, Schematic representation of reversible kinetic model for nucleated supramolecular polymerization, including a metastable off-pathway and a thermodynamically stable on-pathway competing for free monomer. **b**, Kinetic trace of the self-assembly of SOPV and a simulated kinetic trace using the

pathway competition model. The inset to **b** shows a zoom in for the initial stages of the growth process. **c**, Calculated Gibbs free energy diagram for formation of *P*-SOPV and *M*-SOPV. **d**, Concentration-dependent simulation of kinetics with pathway competition model. **e**, $t - 50$ versus SOPV hydrogen-bonded dimer concentration obtained from simulated concentration-dependent kinetics.

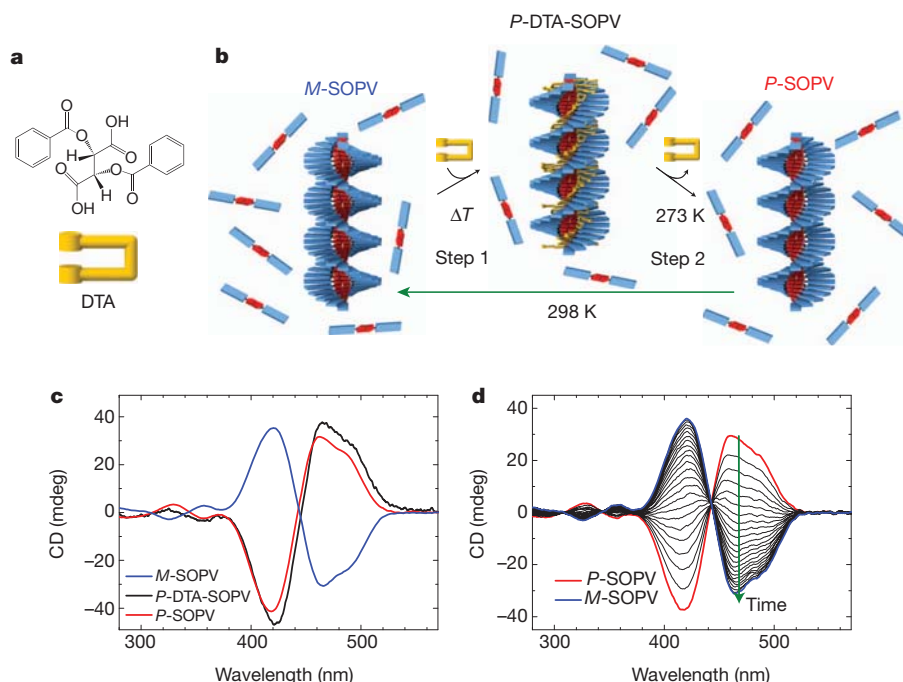


Figure 4 | Controlled formation of exclusively metastable aggregates via a two-step non-covalent synthetic methodology. **a**, Molecular structure of S-chiral dibenzoyl tartaric acid. **b**, Schematic representation of preparation of pure P-SOPV via a two-step non-covalent synthetic methodology. **c**, CD

spectra of M-SOPV, P-DTA-SOPV and P-SOPV. **d**, CD spectra acquired during conversion from metastable P-SOPV towards M-SOPV upon annealing at 298 K.

under equilibrium conditions. The kinetic lability of P-SOPV is demonstrated by annealing at 298 K, resulting in a time-dependent stereomutation of the CD spectra indicative of a conversion from P-SOPV towards M-SOPV aggregates (Fig. 4d). The single isosbestic point in these time-dependent CD spectra and their apparent first-order kinetics (Supplementary Fig. 13) indeed indicated that two distinct states are involved in the conversion process: P-SOPV and M-SOPV.

Our observations established that the aggregation of SOPV involves two competing pathways leading to assemblies with opposite helicity, one of which is favoured kinetically and the other thermodynamically. We note that kinetically controlled formation of one-dimensional supramolecular aggregates has been reported^{23–26}, but the metastable states involved have so far only been probed in terms of their static properties (such as morphology or photophysical properties). Our kinetic studies, by probing the full aggregation process starting from free monomers, reveal that the influence of the metastable state—the off-pathway aggregates—on the overall assembly process is mediated through the equilibrium with free monomers. This effect is a common mechanism for one-dimensional supramolecular systems. We also note that almost all organic materials used in functional devices are processed starting from solutions of the molecularly dissolved components. This means that by influencing the subtleties of the self-assembly process generating these materials, through tuning of the on-pathway or off-pathway mechanisms, the resulting morphologies could potentially be controlled to arrive at optimized self-assembled functional materials.

METHODS SUMMARY

Thermodynamically stable M-SOPV (MCH, 100 μ M) is obtained upon slow cooling from the molecularly dissolved state (60 K h^{−1}) to 273 K, and equilibrium conditions are verified by time-dependent measurements, showing no changes in time. Metastable P-SOPV (MCH, 100 μ M) is obtained upon quenching molecularly dissolved SOPV to 273 K (ice bath). Stopped-flow experiments are performed by mixing a concentrated SOPV solution in chloroform with MCH (1:50 volume ratio, Berger ball mixer, mixing time <10 ms). The subsequent formation of helical aggregates is probed by a CD spectrometer (466 nm) connected in-line with the stopped-flow instrument. The absence of (oligomeric) SOPV aggregates at the start

of the experiment is verified by ¹H nuclear magnetic resonance (NMR) studies. The nucleated aggregation pathway competition model describes the kinetic data with parameters $n = n^* = 5$; $a = 2.9 \times 10^4 \text{ M}^{-1} \text{ s}^{-1}$; $K_e = 1.52 \times 10^6 \text{ M}^{-1}$, $K_n/K_e = 0.0526$, $K_n^*/K_n = 1.38$, $K_e^*/K_e = 0.164$ and $a^*/a = 3.79$ (Matlab, ode15s solver). The value of K_e used is independently assessed by melting experiments. Alternatively, models using diffusion-controlled kinetics afford unrealistic values of $K_n/K_e < 10^{-4}$. The Gibbs free energy as a function of chain length i is calculated using $\Delta G_{(i-1) \rightarrow i}^0 = -RT \ln(K_{\text{tot}})$, where R is the gas constant. To obtain P-DTA-SOPV, DTA and SOPV are mixed in chloroform (1:1). Subsequently chloroform is evaporated; the residual DTA-SOPV complex is dissolved in MCH (100 μ M) on heating above the critical elongation temperature. Cooling from the molecularly dissolved state to 293 K results in P-DTA-SOPV aggregates. On adding an equal volume of aqueous ethyl diamine solution (0.15 M) at 273 K, vigorous mixing of the water and MCH phase (1 min) and full separation of both phases, the top MCH layer containing metastable P-SOPV is isolated.

Full Methods and any associated references are available in the online version of the paper at www.nature.com/nature.

Received 7 February; accepted 11 November 2011.

Published online 18 January 2012.

1. Yamamoto, Y. *et al.* Photoconductive coaxial nanotubes of molecularly connected electron donor and acceptor layers. *Science* **314**, 1761–1764 (2006).
2. Percec, V. *et al.* Self-organization of supramolecular helical dendrimers into complex electronic materials. *Nature* **417**, 384–387 (2002).
3. Würthner, F. *et al.* Supramolecular p–n-heterojunctions by co-self-organization of oligo(*p*-phenylene vinylene) and perylene bisimide dyes. *J. Am. Chem. Soc.* **126**, 10611–10618 (2004).
4. Capito, R. M., Azevedo, H. S., Velichko, Y. S., Mata, A. & Stupp, S. I. Self-assembly of large and small molecules into hierarchically ordered sacs and membranes. *Science* **319**, 1812–1816 (2008).
5. Dankers, P. Y. W., Harmsen, M. C., Brouwer, L. A., Van Luyn, M. J. A. & Meijer, E. W. A modular and supramolecular approach to bioactive scaffolds for tissue engineering. *Nature Mater.* **4**, 568–574 (2005).
6. Powers, E. T. & Powers, D. L. Mechanisms of protein fibril formation: nucleated polymerization with competing off-pathway aggregation. *Biophys. J.* **94**, 379–391 (2008).
7. Baskakov, I. V., Legname, G., Baldwin, M. A., Prusiner, S. B. & Cohen, F. E. Pathway complexity of prion protein assembly into amyloid. *J. Biol. Chem.* **277**, 21140–21148 (2002).
8. Mulder, A. M. *et al.* Visualizing ribosome biogenesis: parallel assembly pathways for the 30S subunit. *Science* **330**, 673–677 (2010).
9. Ferrone, F. A. Analysis of protein aggregation kinetics. *Methods Enzymol.* **309**, 256–274 (1999).

10. Oosawa, F. & Kasai, M. A theory of linear and helical aggregations of macromolecules. *J. Mol. Biol.* **4**, 10–21 (1962).
11. Powers, E. T. & Powers, D. L. The kinetics of nucleated polymerizations at high concentrations: amyloid fibril formation near and above the “supercritical concentration”. *Biophys. J.* **91**, 122–132 (2006).
12. Bishop, M. F. & Ferrone, F. A. Kinetics of nucleation-controlled polymerization. *Biophys. J.* **46**, 631–644 (1984).
13. Xue, W.-F. Homans, S. W. & Radford, S. E. Systematic analysis of nucleation-dependent polymerization reveals new insights into the mechanism of amyloid self-assembly. *Proc. Natl Acad. Sci. USA* **105**, 8926–8931 (2008).
14. Knowles, T. P. J., *et al.* An analytical solution to the kinetics of breakable filament assembly. *Science* **326**, 1533–1537 (2009).
15. De Greef, T. F. A. *et al.* Supramolecular polymerization. *Chem. Rev.* **109**, 5687–5754 (2009).
16. Cui, H. Chen, Z. Zhong, S., Wooley, K. L. & Pochan, D. J. Block copolymer assembly via kinetic control. *Science* **317**, 647–650 (2007).
17. Lund, R., *et al.* Structural observation and kinetic pathway in the formation of polymeric micelles. *Phys. Rev. Lett.* **102**, 188301 (2009).
18. Pasternack, R. F., *et al.* A nonconventional approach to supramolecular formation dynamics: the kinetics of assembly of DNA-bound porphyrins. *J. Am. Chem. Soc.* **120**, 5873–5878 (1998).
19. George, S. J., *et al.* Helicity induction and amplification in an oligo(*p*-phenylenevinylene) assembly through hydrogen-bonded chiral acids. *Angew. Chem. Int. Edn Engl.* **46**, 8206–8211 (2007).
20. Hoebe, F. J. M. Jonkhøj, P. Meijer, E. W. & Schenning, A. P. H. J. About supramolecular assemblies of π -conjugated systems. *Chem. Rev.* **105**, 1491–1546 (2005).
21. Jonkhøj, P. Van der Schoot, P. Schenning, A. P. H. J. & Meijer, E. W. Probing the solvent-assisted nucleation pathway in chemical self-assembly. *Science* **313**, 80–83 (2006).
22. Van Gestel, J. Amplification of chirality in helical supramolecular polymers: the majority-rules principle. *Macromolecules* **37**, 3894–3898 (2004).
23. Pashuck, E. T. & Stupp, S. I. Direct observation of morphological transformation from twisted ribbons into helical ribbons. *J. Am. Chem. Soc.* **132**, 8819–8821 (2010).
24. Lohr, A. & Würthner, F. Evolution of homochiral helical dye assemblies: involvement of autocatalysis in the “majority-rules” effect. *Angew. Chem. Int. Edn Engl.* **47**, 1232–1236 (2008).
25. Wolfs, M., *et al.* The role of heterogeneous nucleation in the self-assembly of oligothiophenes. *Chem. Commun.* 4613–4615 (2008).
26. Ajayaghosh, A. Varghese, R. Praveen, V. K. & Mahesh, S. Evolution of nano- to micro-sized spherical assemblies of a short oligo(*p*-phenylene-ethynylene) into superstructured organogels. *Angew. Chem. Int. Edn Engl.* **45**, 3261–3264 (2006).

Supplementary Information is linked to the online version of the paper at www.nature.com/nature.

Acknowledgements We thank Ž. Tomović for providing the SOPV. We are grateful to R. M. Kellogg (Syncom, Groningen, The Netherlands) for providing the tartaric acid derivative. We also thank H. W. H. van Roekel and R. de Bruijn for discussions. Artwork was provided by K. Pieterse. The research leading to these results has received funding from the European Research Council under the European Union’s Seventh Framework Programme (FP/2007-2013)/ERC grant agreement number 246829, and from the Netherlands Organization for Scientific Research.

Author Contributions P.A.K. and M.M.J.S. performed the stopped-flow experiments. P.A.K., A.J.M. and T.F.A.D.G. analysed the data and developed the kinetic model. S.J.G. performed the experiments with DTA and SOPV. E.W.M., T.F.A.D.G., A.P.H.J.S. and P.A.J.H. supervised the research. P.A.K., T.F.A.D.G. and E.W.M. wrote the manuscript. All authors discussed the results and commented on the manuscript.

Author Information Reprints and permissions information is available at www.nature.com/reprints. The authors declare no competing financial interests. Readers are welcome to comment on the online version of this article at www.nature.com/nature. Correspondence and requests for materials should be addressed to T.F.A.D.G. (t.f.a.d.greef@tue.nl) or E.W.M. (e.w.meijer@tue.nl).

METHODS

Materials. The synthesis of SOPV has been described previously²⁷. All solvents were used as received.

Instrumentation. CD, linear dichroism and corresponding ultraviolet–visual spectra were recorded using a Jasco J-815 CD spectrometer. Sensitivity, response time and scanning speed were chosen appropriately. The temperature was controlled using a Jasco Peltier temperature controller with a range of 263–383 K and adjustable temperature slope. Stopped-flow studies were performed using a Biologic SFM 400 stopped-flow setup with Berger Ball mixer, Biologic TC 100 cuvet (optical path length 1 cm), and Biologic MPS-60 controller unit. The stopped-flow cuvet was connected in-line with a Jasco J-815 CD spectrometer. To control the temperature of the cuvet and syringes, SFM 400 was connected to a Julabo F12 temperature controller (ethylene glycol bath with thermostat). ¹H-NMR spectra were recorded at 298 K on a Varian Unity Inova (500 MHz), in CDCl₃ (Cambridge Isotope Laboratories). Fluorescence measurements were performed on an Edinburgh Instruments FS920 double-monochromator luminescence spectrometer using a Peltier-cooled red-sensitive photomultiplier. Ultraviolet–visual spectra acquired on the complexation of α -cyclodextrin with *p*-nitrophenolate were recorded on a Perkin Elmer L40 photospectrometer.

Experiments under kinetic control. Thermodynamically stable *M*-SOPV (100 μ M) in methylcyclohexane (MCH, spectroscopic grade, Sigma-Aldrich) was obtained upon slow cooling (60 K h^{−1}) from the molecularly dissolved state (343 K) to 273 K; equilibrium conditions were verified by time-dependent measurements, showing no further change in time. Metastable *P*-SOPV (MCH, 100 μ M) was obtained upon quenching molecularly dissolved SOPV from 343 K to 273 K (ice bath). The optical path length for the reported spectra was 1 mm. The fraction of *P*-SOPV and *M*-SOPV obtained upon quenching SOPV (MCH, 13 μ M) from different temperatures was evaluated from the CD spectra by simulation of a linear combination of the spectra corresponding to a solution consisting of pure *P*-SOPV (obtained via the two-step non-covalent synthetic methodology) and a solution containing *M*-SOPV exclusively. The fraction of free SOPV monomer present before quenching was derived from the CD spectra under equilibrium conditions assuming $\phi_{\text{monomer}} = 1 - \phi_{\text{helical aggregate}}$. The optical path length of the reported spectra for these quenching experiments was 1 cm.

Stopped-flow experiments. To probe the kinetics of the supramolecular polymerization of SOPV, SOPV in chloroform (spectroscopic grade, Sigma-Aldrich) was mixed with MCH (50:1; 1,508 μ l:30 μ l, injection rate 8–9 ml s^{−1}, mixing time <10 ms), after which CD was followed in time (λ = 466 nm; $\Delta\lambda$ = 1 nm; Δt = 1 s; standard sensitivity; high tension voltage adjusted to get a direct-current voltage around 1 V). The SOPV concentration and the duration of the measurement were adjusted appropriately. The absence of (oligomeric) SOPV aggregates at the start of the experiment was verified by ¹H-NMR studies. Kinetic curves were averaged over multiple stopped-flow experiments as follows. At 293 K: 5 μ M, 9; 6.1 μ M, 2; 6.5 μ M, 6; 7.8 μ M, 1; 8.7 μ M, 4; 9 μ M, 2; 10 μ M, 9; 15 μ M, 3; 19 μ M, 6. At 308 K: 10 μ M, 6; 12.5 μ M, 6; 15 μ M, 11; 20 μ M, 9; 25 μ M, 6. After the measurement, the concentration was verified using CD (466 nm) and

ultraviolet–visual (438 nm) spectra. To test the mixing in the stopped-flow setup, the complexation of α -cyclodextrin and *p*-nitrophenolate was measured. Stopped-flow experiments were performed upon 100:1 mixing of an α -cyclodextrin (Across) and a *p*-nitrophenolate (Merck) solution. Both solutions were buffered at pH = 11 (HPO₄^{2−}/PO₄^{3−} buffer). Settings: injection volumes (100:1) 2,011 μ l:20 μ l, injection rate 7 ml s^{−1}, mixing time <10 ms, λ = 410 nm, $\Delta\lambda$ = 1 nm, l = 1 cm, Δt = 1 s, standard sensitivity, high tension voltage = 300 V; data averaged over 5 injections.

Aggregation pathway competition kinetics model. The kinetic model describes the competing nucleated aggregation pathways of both *P*-SOPV and *M*-SOPV via a sequence of differential equations. Each differential equation describes monomer association and dissociation to the respective aggregate with length *i*. Assuming that for $i > N$, with $N \gg n$ (N = 100), $[X_{i+1}] = \alpha[X_i]$, the required number of differential equations was reduced to $2(N+2)$. The resulting system of differential equations is solved using the ode15s solver in Matlab. The aggregation pathway competition model describes the kinetic data with parameters $n = n^* = 5$; $a = 2.9 \times 10^4 \text{ M}^{-1} \text{ s}^{-1}$; $K_e = 1.52 \times 10^6 \text{ M}^{-1}$, $K_n/K_e = 0.0526$, $K_i^*/K_n = 1.38$, $K_e^*/K_e = 0.164$ and $a^*/a = 3.79$. The value of K_e used was independently assessed by melting experiments. Alternatively, models using diffusion-controlled kinetics afforded unrealistic values of $K_n/K_e < 10^{-4}$. The Gibbs free energy diagram was calculated via $\Delta G_{(i-1) \rightarrow i}^0 = -RT \ln(K_{i \text{ tot}})$, with gas constant *R*, temperature *T*, equilibrium constant $K = K_n$ for $i \leq n$ and $K = K_e$ for $i > n$ and assuming the total SOPV hydrogen-bonded dimer concentration c_{tot} as the reference state, whereas the standard state was defined²⁸ at 1 M. The role of temperature on the aggregation pathway competition was rationalized by performing kinetic simulations at different temperatures. The temperature-dependency of the forward rate constant was described by the well-known Arrhenius equation: $a = A \exp(-E_{\text{act}}/RT)$, where *A* is the kinetic prefactor and E_{act} the activation energy. The temperature-dependency of K_e was described using the Van't Hoff equation: $K_e = \exp(-(\Delta H_e^0 - T\Delta S_e^0)/RT)$, where ΔH_e^0 and ΔS_e^0 represent the standard enthalpy and entropy of elongation, respectively. The other rate constants are defined via temperature-independent ratios.

Two-step non-covalent synthetic methodology. To obtain *P*-DTA-SOPV, the DTA (provided by Syncom) and SOPV were mixed in chloroform (1:1). Subsequently, chloroform was evaporated by purging with nitrogen gas; the residual DTA-SOPV complex (red colour) was dissolved in MCH (100 μ M) upon sonication and heating until the sample turned green, indicating molecular dissolution. Cooling from this molecularly dissolved state to 293 K resulted in *P*-DTA-SOPV aggregates. On adding an equal volume of aqueous ethyl diamine solution (0.15 M) at 273 K, vigorous mixing of the water and MCH phase (1 min) and full separation of both phases, the top MCH layer containing metastable *P*-SOPV could be isolated.

27. Jonkheijm, P. *et al.* Transfer of π -conjugated columnar stacks from solution to surfaces. *J. Am. Chem. Soc.* **125**, 15941–15949 (2003).

28. Xue, W.-F., Homans, S. W. & Radford, S. E. Systematic analysis of nucleation-dependent polymerization reveals new insights into the mechanism of amyloid self-assembly. *Proc. Natl Acad. Sci. USA* **105**, 8926–8931 (2008).

Social networks and cooperation in hunter–gatherers

Coren L. Apicella^{1,2}, Frank W. Marlowe³, James H. Fowler^{4,5} & Nicholas A. Christakis^{1,2,6,7}

Social networks show striking structural regularities^{1,2}, and both theory and evidence suggest that networks may have facilitated the development of large-scale cooperation in humans^{3–7}. Here, we characterize the social networks of the Hadza, a population of hunter-gatherers in Tanzania⁸. We show that Hadza networks have important properties also seen in modernized social networks, including a skewed degree distribution, degree assortativity, transitivity, reciprocity, geographic decay and homophily. We demonstrate that Hadza camps exhibit high between-group and low within-group variation in public goods game donations. Network ties are also more likely between people who give the same amount, and the similarity in cooperative behaviour extends up to two degrees of separation. Social distance appears to be as important as genetic relatedness and physical proximity in explaining assortativity in cooperation. Our results suggest that certain elements of social network structure may have been present at an early point in human history. Also, early humans may have formed ties with both kin and non-kin, based in part on their tendency to cooperate. Social networks may thus have contributed to the emergence of cooperation.

Humans are unusual as a species in the extent to which they form longstanding, non-reproductive unions with unrelated individuals—that is, we have friends. Cooperation is a defining feature of these friendships⁹. Humans also learn from and influence each other, evincing an exceptional reliance on cultural transmission¹⁰. These facts contribute to the propensity of humans to form social networks, which can range in size from dozens to millions of people¹.

Social networks display certain empirical regularities—in settings as diverse as villages, schools, and workplaces—in terms of variation in the degree distribution (number of social ties), transitivity (the likelihood that two of a person's friends are in turn friends), degree assortativity (the tendency of popular people to befriend other popular people), reciprocity (the increased likelihood of an outbound tie to be reciprocated with an inbound tie from the same person), and homophily (the tendency of similar people to form ties). Some properties (such as a fat-tailed degree distribution) may be seen in many contexts (such as neuronal, electronic and social networks). Other properties are more distinctively social, and may have adaptive significance. For instance, degree assortativity may constrain the spread of pathogens¹¹, high transitivity may help reinforce social norms (although it can also reduce the flow of new information), and homophily may facilitate collective action¹².

However, technological advances (such as in communication, transportation and agricultural systems), demographic changes (such as in population density, inter-group marriage and dispersal), and social innovations (such as in formal institutions) have all changed the social landscape of humans from that in which they evolved. This raises the question of whether features observed in modernized social networks are ancient or contemporary in origin. Yet the observed regularities in social networks, coupled with the fact that networks can affect diverse individual-level outcomes, suggests that natural selection may have played a part in the formation of human networks. Indeed, some egocentric network attributes, such as the number or kind of friends

a person has, or a person's tendency to be central in a network, may have a partially genetic basis^{13,14}.

The evolutionary relevance of social networks is also suggested by their role in cooperation. Evolutionary theories of cooperation rely on explicit or implicit assumptions regarding social structure³. Direct reciprocity assumes that the same individuals will encounter each other repeatedly⁴. Similar conclusions have been reached regarding indirect reciprocity¹⁵. Other theoretical models of kin selection, generalized assortativity⁵, group competition⁶ and social networks⁷ have also explicitly recognized the importance of population structure, showing that cooperation can evolve if individuals tend to interact with others of the same type (cooperators with cooperators and defectors with defectors). If real-world interactions do not exhibit such assortativity, then none of these theories can explain the widespread cooperation in humans that we observe today.

To discover the possibly adaptive origins of human social networks, and their relationship to cooperation, we wanted to examine network features in an evolutionarily relevant setting, that is, in a population whose way of life is thought to resemble that of our early ancestors⁸. Although cooperation is widespread in human societies, modern hunter-gatherers possibly exemplify this feature best—extensively sharing food, labour and childcare. It is likely that the high levels of cooperation observed in modern hunter-gatherers were also present in early humans¹⁶. Thus far, little work has focused on networks in hunter-gatherers. Related topics have included estimation of the total size of hierarchical social units¹⁷, examination of the role of resource production in social organization and residence patterns¹⁸, and evaluation of food sharing¹⁹. We know of no study that has attempted to map the complete social network of a foraging population to study its dyadic building blocks (ties between pairs of people) and macroscopic structure, as well as the role of cooperation.

Therefore, we performed a comprehensive, socio-centric network study of the Hadza hunter-gatherers of Tanzania. Connections between individuals were identified in two ways: subjects were asked with whom they would like to live in the next camp (the 'campmate network'), and to whom they would give an actual gift of honey (the 'gift network') (see Methods). We studied 205 individuals, and there were 1,263 campmate ties and 426 gift ties. By measuring a comprehensive set of statistics, we evaluated whether Hadza networks differ quantitatively from random networks in the same ways that modernized networks do.

Cumulative distributions of in-degree (the number of times an individual is nominated) are shown in Fig. 1a. As is typical of networks², the degree distributions have significantly fatter tails than a similarly sized group composed of individuals randomly forming the same number of social ties (Kolmogorov–Smirnov test, $P < 10^{-15}$ for all comparisons). Degree distributions for the male and female campmate networks did not differ (Kolmogorov–Smirnov test, $P = 0.86$ for in-degree and 0.59 for out-degree).

As in modernized societies²⁰, we find that the probability of a social tie decreases with increased geographic distance (see Supplementary Fig. 6a). Of significance to kin selection theory, we also find that the

¹Institute for Quantitative Social Science, Harvard University, Cambridge, Massachusetts 02138, USA. ²Department of Health Care Policy, Harvard Medical School, Boston, Massachusetts 02115, USA.

³Department of Anthropology, Cambridge University, Cambridge, CB2 3DZ, UK. ⁴Medical Genetics Division, University of California, San Diego, California 92093, USA. ⁵Political Science Department, University of California, San Diego, California 92093, USA. ⁶Department of Sociology, Harvard University, Cambridge, Massachusetts 02138, USA. ⁷Department of Medicine, Harvard Medical School, Boston, Massachusetts 02115, USA.

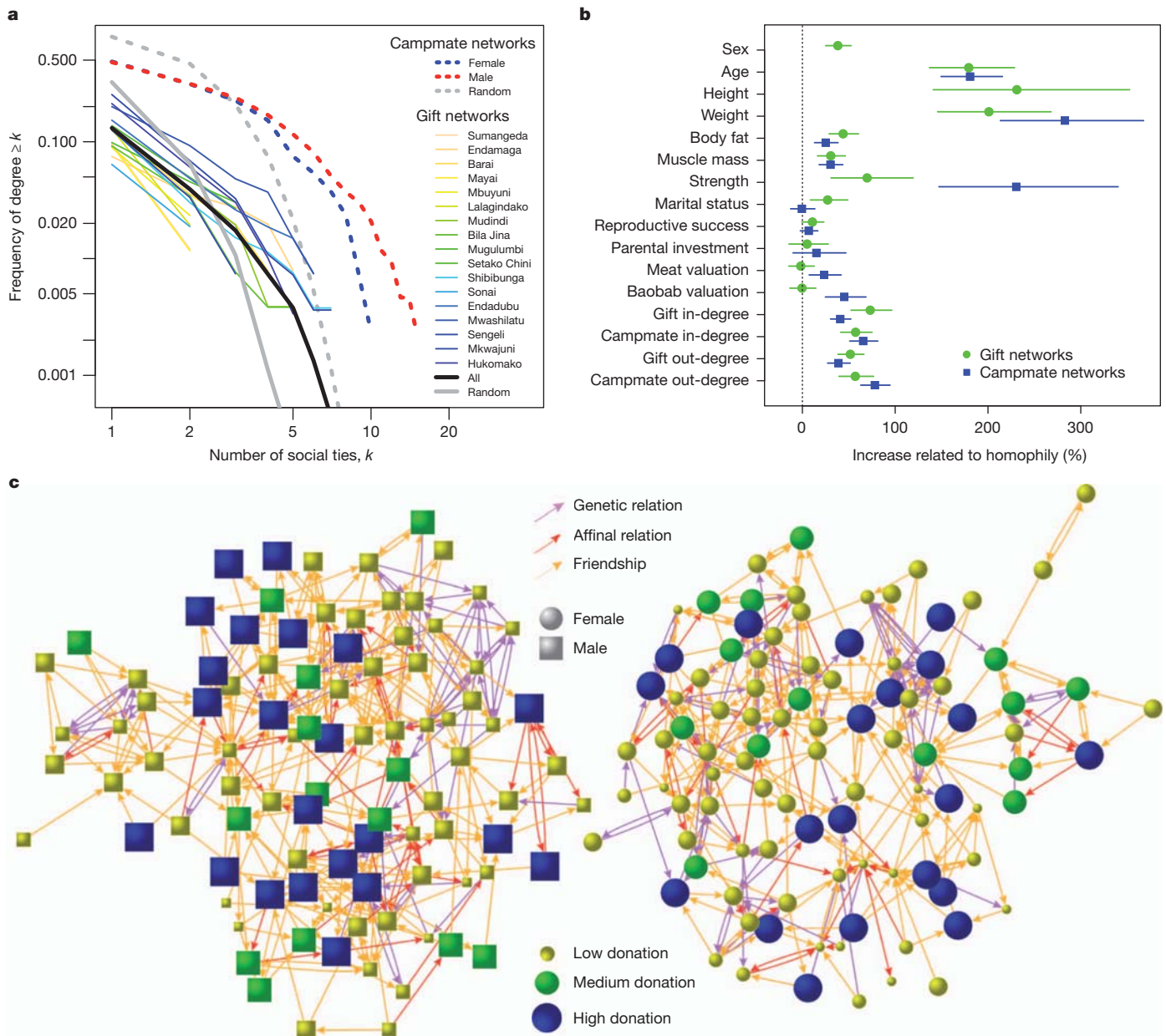


Figure 1 | Structural features of modern social networks also exist in Hadza networks. **a**, Cumulative in-degree distributions show the fraction of the population that has at least k social ties. The distributions for the campmate and gift networks are significantly different from random networks with the same number of nodes and edges (Kolmogorov–Smirnov test, $P < 10^{-15}$) and have fatter tails; the random distributions are shown separately for campmate and gift networks (in grey). The gift networks within each camp (ordered by size of camp from smallest, yellow, to largest, blue) show similar distributions of in-degree. **b**, Estimates based on dyadic models of social ties (see Supplementary Information) show that a 1-s.d. change in similarity in characteristics between two people significantly increases the likelihood of a social tie (homophily).

Horizontal lines indicate 95% confidence intervals. For the campmate networks, sex is not included because all ties are same-sex; homophily for height is not shown because it does not fit on the scale (the estimate is 801%, 95% confidence interval 549–1,148%), and homophily for cooperation is shown in Fig. 2c. **c**, Graphs of the campmate networks show that cooperators tend to be connected to cooperators and cluster together (see also Fig. 2b). Node colour and size indicates donation, shape indicates sex. Arrows point from an ego (the naming person) to an alter (the named person). Arrow colours indicate whether the ego and alter are related genetically, affinally (by marriage) or not at all (friendship).

probability that two individuals are connected increases as the genetic relatedness between the pair increases, in both the campmate and the gift networks (see Supplementary Fig. 6b).

We used regression analysis to evaluate the relationship between personal characteristics and degree (see Supplementary Information). In both the campmate and gift networks, age, height, weight and marital status are positively and significantly related to both out-degree and in-degree (see Supplementary Fig. 7a, b). For example, in the gift network, an 8.7-cm (one standard deviation, 1 s.d.) increase in height is associated with a 125% increase in out-degree and a 173% increase in

in-degree, suggesting that taller people are both more socially active and more socially attractive. The significance of these associations survives when we add numerous controls to the models, including camp-level fixed effects, geographic distance, genetic and affinal relationships, spouse relationships, age and sex (see Supplementary Information). Other characteristics associated with degree in at least one of the models include body fat, muscle mass, handgrip strength, the value placed on meat, and reproductive success, but none of these survive controls in both the campmate and gift networks, except body fat for in-degree and handgrip strength for out-degree (see Supplementary Information).

The selection of physically fit reproductive partners (in both traditional and modernized societies) makes sense from an evolutionary perspective, given the gains in resources and genetic benefits that can be passed on to offspring. But hunter-gatherers also prefer to form connections to non-reproductive partners who are physically fit, suggesting that this tendency might also be both common and ancient in origin. Food acquisition and processing in foragers is labour and time-intensive, requiring strength and stamina, as well as skill and knowledge²¹. Thus, forming connections with physically fit individuals probably translates into increased resources.

Hadza networks also resemble modernized human networks insofar as they too differ from random networks with respect to reciprocity^{16,22}. An 'ego' (the naming person) is 44.2 times (95% confidence interval 37.6–51.4) more likely to name an 'alter' (the named person) in the campmate network, and 14.3 times (95% confidence interval 12.2–16.4) more likely to name an alter in the gift network, if the alter reciprocated the social tie by also naming the ego as a friend (indeed, this happens even though nominations are private). Reciprocity remains significant even when controlling for genetic and non-genetic family ties, suggesting that reciprocity also exists between unrelated individuals.

Hadza networks also evince degree assortativity. People with higher in-degree name more social contacts, and people with higher out-degree are more likely to be named (see Supplementary Fig. 7a, b), even in models with controls (including a control for reciprocity). In other words, individuals who nominate more friends are popular even among those they themselves did not nominate.

Yet another property Hadza networks have in common with modernized human networks is that they have higher transitivity than expected in random networks²³. In the campmate networks, transitivity is 0.17 for females and 0.16 for males, while in the gift networks, the average transitivity is 0.41 (see Supplementary Fig. 7c). By comparison, in random networks with the same number of nodes and edges, transitivity is always less than 0.01.

Turning to homophily (Fig. 1b), in both the campmate and gift networks, social ties are significantly more likely when two people are similar in age, height, weight, body fat and handgrip strength. Thus, as in other human networks, hunter-gatherers who are socially connected tend to resemble one another. For example, a 7.5-kg (1 s.d.) increase in the similarity of weight is associated with a tripling of the probability (+201%) that two people are connected. There is also evidence of homophily on marital status, muscle mass, and the value placed on meat and baobab, but these relationships do not survive in the models with controls, except for the value of meat in the campmate network (see Supplementary Information).

Hunter-gatherer life is characterized by imbalances in productivity and consumption (for example, owing to differences in strength, which varies across an individual's lifetime), and this is reflected in divisions of labour²⁴. Thus, one might expect that choices of campmates would reflect complementarity (heterophily) rather than homophily. On the other hand, homophily may facilitate collective action because similar individuals are more likely to share assumptions, experiences and goals²⁵, and also because similarity increases empathy, which in turn facilitates cooperation¹². We find no significant heterophily on any attribute examined.

We also directly compared the measured Hadza parameters to values for 142 sociocentric networks of adolescent students in the USA and to two sociocentric networks of adult villagers in Honduras. The Hadza parameters fall within the observed ranges in these other networks, often near the centre of the distribution (see Supplementary Information). However, comparison of the precise values is limited by, among other things, variation in how ties were ascertained. Further research will be needed to clarify how details of human social network structure might vary across settings, if at all.

Graphs of the Hadza social networks (Fig. 1c) show that they tend to be structured in a way that is relevant for cooperative behaviour, as

elicited in public goods games. In particular, there is homophily on cooperation: cooperators tend to be connected to other cooperators, and non-cooperators to non-cooperators.

Although natural selection is said to favour defection in unstructured populations where all individuals have an equal chance of interacting with one another, cooperation can evolve if population structure permits clustering⁵. This feature allows cooperators to increase in the population because they benefit from the public goods provided by fellow cooperators with whom they interact. A key prediction of some evolutionary models is thus that there should be relatively more variance in cooperative behaviour between groups as compared to within groups⁶. But it was not known whether such assortment in cooperative behaviour actually exists in populations thought to resemble our early human ancestors.

In Fig. 2a, we show a comparison of the observed variance in donations to the public good to the variance obtained when we keep the population structure fixed and randomly reshuffle the observed distribution of donations across all individuals. Compared to chance, there is significantly more between-camp variation ($P = 0.01$) and significantly less within-camp variation ($P = 0.01$) in cooperative behaviour.

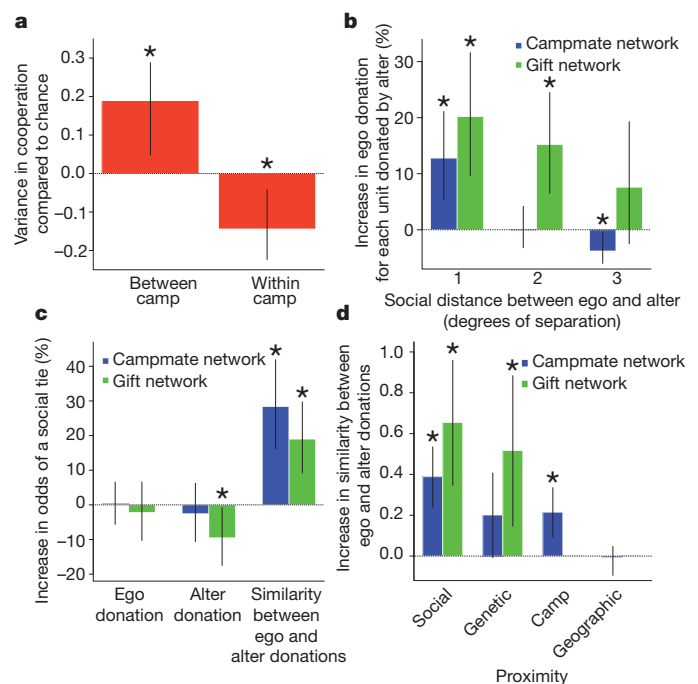


Figure 2 | Donations in the public goods game are associated with social network characteristics. **a**, A comparison of variance in observed donations with variance in 1,000 simulations in which donations were randomly shuffled between all individuals in the population shows that between-group variance in cooperation is significantly higher than expected, and within-group variance is significantly lower than expected, at the camp level. **b**, An analysis of cooperative behaviour across all camps shows that correlation in cooperation extends to one degree of separation in the campmate networks and two degrees (to one's friend's friends) in the gift networks. Moreover, there is anti-correlation at three degrees of separation in the campmate network, suggesting polarization between cooperators and non-cooperators. **c**, Correlation in behaviour cannot be explained by cooperators being more likely to form or attract social ties. Instead, subjects with similar levels of giving are significantly more likely to be connected at the dyadic level. **d**, Finally, several measures of proximity are independently associated with similarity in donations, but social proximity (the inverse of the degree of separation between two people in the network) appears to be just as important as genetic proximity (relatedness) and physical proximity (residence in the same camp) in a multivariate test. (Gift networks are defined only within camps and so are not presented for 'camp' and 'geographic' proximity in Fig. 2d.) Vertical lines indicate 95% confidence intervals and asterisks indicate estimates with $P < 0.05$. See the Supplementary Information for details of the models.

We investigated the role of network connections with respect to group-level variation in cooperation by studying the tendency of cooperative individuals to be connected to other cooperators. We regressed public-good donations on the donations of a person's friends (see Supplementary Information). Each extra stick of honey donated is associated with an extra 0.13 sticks (95% confidence interval 0.05–0.21) donated by each friend in the campmate networks and an extra 0.21 sticks (95% confidence interval 0.10–0.32) donated by each friend in the gift networks. Moreover, in the gift networks, the association extends to two degrees of separation; each friend's friend donates an extra 0.15 sticks (95% confidence interval 0.07–0.25) for every stick a person donates (Fig. 2b). And, interestingly, at three degrees of separation, there is significant anti-correlation in the campmate networks (-0.04 sticks, 95% confidence interval -0.00 to -0.06), suggesting that cooperative and non-cooperative clusters tend to be polarized (though this might also reflect a finite-size effect, given the small size of Hadza society).

Dyadic analyses of social ties show that people who donate more do not have higher out-degree or in-degree (Fig. 2c). In fact, in the gift networks, there is a weakly significant negative association between donations and in-degree, though this relationship does not survive in the models with controls (see Supplementary Information). This suggests that we can reject the hypothesis that hunter-gatherers unconditionally prefer to form ties with cooperators. However, there is significant homophily on cooperation in both the campmate and gift networks, and the relationship survives in the model with controls for the campmate network: cooperators are preferentially connected to other cooperators.

To determine whether social network structure may help to explain variation in cooperative behaviour, we considered three different kinds of proximity that could be generating the similarity: geographic, genetic and social. If the physical environment is an important source of variation, then geographic proximity should help to predict similarity in cooperative behaviour. Additionally, people who live in the same camp should be more similar than those who do not. If genes are an important source of variation, then genetic proximity (measured as relatedness) should help to predict similarity in cooperative behaviour. But if social networks are a source of variation, then social proximity (measured separately for the campmate networks and gift networks by the inverse of the degrees of separation between two people) should help to predict similarity in cooperation. In separate regression models, each kind of proximity is significantly related to similarity in cooperation (see Supplementary Information). In contrast, age and sex similarity are not significant predictors. However, when we include all the proximity measures in one model, geographic proximity ceases to matter (Fig. 2d). Moreover, social proximity, as measured in both the campmate networks and the gift networks, appears to be just as important as genetic proximity and camp co-residence, suggesting that cooperative behaviour may be best understood as a process influenced by a combination of not only genes and environment, but also social networks.

The Hadza represent possibly one of the most extreme departures from life in industrialized societies, and they remain relatively isolated from modern cultural influences. Yet all the examined properties of social networks seen in modernized societies also appear in the Hadza. Compared with random networks, Hadza networks, like modernized networks, exhibit a characteristic degree distribution, greater degree assortativity, transitivity, reciprocity and homophily than would be expected from chance, and a decay with geographic distance.

To the extent that the Hadza represent our late Pleistocene ancestors⁸, the network properties and social preferences in the Hadza may indeed reflect elements of human sociality along with which high levels of human cooperation evolved. Whether certain aspects of human social network structure existed still further back in our hominid past is unclear. Evaluating the resemblances between non-human and human primate networks is difficult, in part because the qualitative nature of dyadic ties can vary considerably across species²⁶. Nevertheless, some

network properties may be quite old. For instance, age and sex predict both the quantity and quality of many primate interactions, and primate networks may demonstrate homophily²⁶. Possibly, certain aspects of social network structure might appear in any vertebrate species that forms social networks²⁷, because particular structural features might facilitate the solution of problems common to such species (for example, those related to coordinated action, infection resistance and information transmission).

Humans' ability to trace descent bilaterally and form strong relationships with both sets of kin not only maximizes their kin ties but also increases their ability to move freely; once an organism is able to recognize paternal kin, potential inbreeding can be avoided without the need for evolution to favour a sex-biased dispersal pattern. Whereas chimpanzee females disperse and males typically spend their lives in their natal community, hunter-gatherers of both sexes can stay in or leave their natal group¹⁸, with individuals changing camp membership throughout their lives. It is thus possible that relaxed constraints on social mobility patterns provided humans a greater opportunity to make friends, which in turn allowed cooperators more opportunities to form ties with other cooperators and break ties with defectors.

Although the Hadza have a preference for kin as both campmates and gift recipients (indicating a potential for kin selection), the Hadza also actively form many ties with non-kin. In fact, recent work examining co-residence patterns across hunter-gatherer societies suggests that first-order relatives make up less than 10% of residential camps¹⁸, raising the question of how high levels of cooperation are maintained in groups of mostly unrelated individuals. The pervasive sharing of food that characterizes hunter-gatherer life is one plausible evolutionary mechanism²⁴, but theories of kin selection and reciprocal altruism, used to explain food sharing, have been criticized on the grounds that they require producer control over resource distribution²⁴. On the other hand, regardless of whether foragers have producer rights, they do maintain flexibility in choosing their friends and campmates, thus providing some control over resource distribution.

In summary, Hadza networks are structured in a way that is consistent with the evolution of cooperative behaviour. Cooperators tend to be connected to cooperators at both the dyadic and network level, conditions necessary to sustain cooperation²⁸. This phenomenon cannot be explained by camp-level differences in the contextual environment because it persists in a model that controls for camp-level fixed effects. However, it might be explained by two alternative hypotheses. One is that cooperators tend to form ties preferentially with other cooperators, leaving defectors no choice but to form ties to the remaining non-cooperators²⁹. Another is that people may influence the cooperative behaviour of their networks, as demonstrated in experimental studies³⁰. But regardless of the causal mechanism, homophily on cooperation and selective formation of network ties create conditions that would make it easier for cooperative behaviour to evolve²⁸. This suggests that social networks may have co-evolved with the widespread cooperation in humans that we observe today.

METHODS SUMMARY

We surveyed 205 adults in 17 Hadza camps. Cooperation was elicited by examining subjects' contributions to a public good using sticks of honey. Both women and men donated slightly more than half of their endowment.

We collected network data at both the population level and the camp level. We discerned same-sex network ties across the entire Hadza population by asking each individual: "With whom would you like to live after this camp ends?" We call this the 'campmate network'. On average, women chose 6.0 (± 1.9 s.d.) campmates and men chose 7.1 (± 2.1 s.d.) campmates. To facilitate this, we used posters containing facial photographs of a census of 517 adult Hadza (see Supplementary Information).

We discerned network ties in an additional way. Every adult in each camp (100%) was given three sticks of honey, which they could anonymously distribute to other adults, of either sex, in their camp. Participants could give all the honey to one person or distribute it to up to three different people. We call this the 'gift network'. On average, both women and men chose to give to 2.2 (± 0.8 s.d.) recipients.

Anthropometry measures were also collected, as well as marital status, reproductive histories, and many other measurements, and we computed the genetic relatedness of all pairs of people. The data were analysed with regression models and other methods (see Supplementary Information).

Full Methods and any associated references are available in the online version of the paper at www.nature.com/nature.

Received 1 June; accepted 25 November 2011.

1. Onnela, J. P. *et al.* Structure and tie strengths in mobile communication networks. *Proc. Natl Acad. Sci. USA* **104**, 7332–7336 (2007).
2. Barabási, A. L. & Albert, R. Emergence of scaling in random networks. *Science* **286**, 509–512 (1999).
3. Nowak, M. A., Tarnita, C. & Wilson, E. O. The evolution of eusociality. *Nature* **466**, 1057–1062 (2010).
4. Boyd, R. & Richerson, P. J. The evolution of reciprocity in sizable groups. *J. Theor. Biol.* **132**, 337–356 (1988).
5. Eshel, I. & Cavalli-Sforza, L. L. Assortment of encounters and evolution of cooperativeness. *Proc. Natl Acad. Sci. USA* **79**, 1331–1335 (1982).
6. Bowles, S. Group competition, reproductive levelling, and the evolution of human altruism. *Science* **314**, 1569–1572 (2006).
7. Ohtsuki, H., Hauert, C., Lieberman, E. & Nowak, M. A. A simple rule for the evolution of cooperation on graphs and social networks. *Nature* **441**, 502–505 (2006).
8. Marlowe, F. W. *The Hadza: Hunter-gatherers of Tanzania* (University of California Press, 2010).
9. Hruschka, D. J. *Friendship: Development, Ecology, and Evolution of a Relationship* (University of California Press, 2010).
10. Boyd, R. & Richerson, P. J. Why culture is common but cultural evolution is rare. *Proc. Br. Acad.* **88**, 73–93 (1996).
11. Badham, J. & Stocker, R. The impact of network clustering and assortativity on epidemic behaviour. *Theor. Popul. Biol.* **77**, 71–75 (2010).
12. Krebs, D. Empathy and altruism. *J. Pers. Soc. Psychol.* **32**, 1134–1146 (1975).
13. Fowler, J. H., Dawes, C. T. & Christakis, N. A. Model of genetic variation in human social networks. *Proc. Natl Acad. Sci. USA* **106**, 1720–1724 (2009).
14. Fowler, J. H., Settle, J. E. & Christakis, N. A. Correlated genotypes in friendship networks. *Proc. Natl Acad. Sci. USA* **108**, 1993–1997 (2011).
15. Boyd, R. & Richerson, P. J. The evolution of indirect reciprocity. *Soc. Networks* **11**, 213–236 (1989).
16. Bowles, S. & Gintis, H. The evolution of strong reciprocity: cooperation in heterogeneous populations. *Theor. Popul. Biol.* **65**, 17–28 (2004).
17. Hamilton, M. J. *et al.* The complex structure of hunter-gatherer social networks. *Proc. R. Soc. Lond. B* **274**, 2195–2203 (2007).
18. Hill, K. R. *et al.* Co-residence patterns in hunter-gatherer societies show unique human social structure. *Science* **331**, 1286–1289 (2011).
19. Gurven, M., Hill, K. & Kaplan, H. From forest to reservation: transitions in food sharing behavior among the Ache of Paraguay. *J. Anthropol. Res.* **58**, 93–120 (2002).
20. Onnela, J. P., Arbesman, S., Gonzalez, M. C., Barabasi, A. L. & Christakis, N. A. Geographic constraints on social network groups. *PLoS ONE* **6**, e16939 (2011).
21. Smith, E. A. *et al.* Wealth transmission and inequality among hunter-gatherers. *Curr. Anthropol.* **51**, 19–34 (2010).
22. Fehr, E. & Fischbacher, U. The nature of human altruism. *Nature* **425**, 785–791 (2003).
23. Davis, J. A. Clustering and hierarchy in inter-personal relations: testing two graph theoretical models in 742 sociomatrixes. *Am. Sociol. Rev.* **35**, 843–851 (1970).
24. Kaplan, H. & Gurven, M. in *Moral Sentiments and Material Interests: The Foundations of Cooperation in Economic Life* (eds Gintis, H., Bowles, S., Boyd, R. & Fehr, E.) 75–113 (MIT Press, 2005).
25. Cole, T. & Teboul, B. J. C. Non-zero-sum collaboration, reciprocity, and the preference for similarity: developing an adaptive model of close relational functioning. *Personal Relationships* **11**, 135–160 (2004).
26. Brent, L. J. H., Lehmann, J. & Ramos-Fernández, G. Social network analysis in the study of nonhuman primates: a historical perspective. *Am. J. Primatol.* **73**, 720–730 (2011).
27. Whitehead, H. *Analyzing Animal Societies: Quantitative Methods for Vertebrate Social Analysis* (University of Chicago Press, 2008).
28. Nowak, M. A. Five rules for the evolution of cooperation. *Science* **314**, 1560–1563 (2006).
29. Rand, D., Arbesman, S. & Christakis, N. A. Dynamic social networks promote cooperation in experiments with humans. *Proc. Natl Acad. Sci. USA* **108**, <http://dx.doi.org/10.1073/pnas.1108243108> (2011).
30. Fowler, J. H. & Christakis, N. A. Cooperative behavior cascades in human social networks. *Proc. Natl Acad. Sci. USA* **107**, 5334–5338 (2010).

Supplementary Information is linked to the online version of the paper at www.nature.com/nature.

Acknowledgements This work was supported by grant P01-AG031093 from the National Institute on Aging and by the Science of Generosity Initiative of the University of Notre Dame (supported by the John Templeton Foundation). We are grateful for comments from S. Bowles, D. Eisenberg, F. Fu, H. Gintis, J. Henrich, P. Hooper, D. Hruschka, M. Nowak, D. Rand, P. Richerson and C. Tarnita. We thank A. Mabulla, I. Mabulla, M. Peterson, C. Bauchner and L. Meneades for help with data collection and preparation. We are grateful to D. Stafford and A. Hughes for sharing data regarding two villages in Honduras, as used in the Supplementary Information.

Author Contributions C.L.A., J.H.F. and N.A.C. designed the study and experiments. C.L.A. and F.W.M. collected data. C.L.A., J.H.F. and N.A.C. analysed the data. C.L.A., J.H.F. and N.A.C. wrote the manuscript. F.W.M. provided technical support. J.H.F. and N.A.C. secured funding.

Author Information Reprints and permissions information is available at www.nature.com/reprints. The authors declare no competing financial interests. Readers are welcome to comment on the online version of this article at www.nature.com/nature. Correspondence and requests for materials should be addressed to N.A.C. (christakis@hcp.med.harvard.edu).

METHODS

Over a two-month period during the summer of 2010, we surveyed 205 adults (18–65 years old, 103 women and 102 men) by visiting 17 distinct Hadza camps within approximately 3,825 square kilometres (see map in Supplementary Information).

Cooperation was elicited by examining all subjects' voluntary contributions to a public good within each camp. Subjects were endowed with four sticks of honey, the favourite food of the Hadza³¹, and they then faced the decision of how to divide their endowment into a private account and a public account where the goods would be distributed evenly with all other adult camp members who also played the game (with N substantially greater than 4). Subjects were instructed that they could give any amount to the public good or keep any amount for themselves, and their choices were secret (see Supplementary Information). They were told that the researcher would triple any amount contributed to the public good, and that, only after all adult camp members played the game, they would receive both the honey in their private account as well as their share of honey from the aggregate contributions to the public good. Both women (mean = 2.32, standard error = 0.12) and men (mean = 2.22; standard error = 0.12) donated slightly more than half of their endowment. This is the first public-good experiment conducted with the Hadza, and, similarly to other small-scale societies, we find that Hadza behaviour is not governed by pure self-interest³².

We collected network data at both the population level and the camp level using a different 'name generator' for each³³. The Hadza live in camps consisting of approximately 30 individuals (including both adults and children)⁸; we include only adults here (an average of 11.7 (± 6.0 s.d.) adults live in each camp). Camps shift location every 4–6 weeks and individual membership in camps is fluid⁸. Because food that is brought into camp is widely shared³⁴, and because sharing of food is thought to be one of the main benefits of group living owing to the high variance in individual food returns³⁵, choosing with whom to live is consequential. Hence, we discerned same-sex network ties across the entire Hadza population by asking each individual: "With whom would you like to live after this camp ends?" We call this the 'campmate network'. The participants were instructed that they could choose up to a maximum of ten individuals, either currently living in their camp or outside their camp. On average, women chose 6.0 (± 1.9 s.d.) campmates and men chose 7.1 (± 2.1 s.d.) campmates (and 3% of women and 21% of men chose the maximum of 10). To facilitate this process and eliminate potential data

collection errors, we used posters containing full-frontal facial photographs of a census of 517 adult Hadza (see Supplementary Information).

At the camp level, we discerned network ties in an additional, novel way. Every adult in each camp (100%) was given three sticks of honey, which they could anonymously distribute to other adults, of either sex, currently living in their camp. Participants were told that they could give all the sticks of honey to one person or distribute them to up to three different people, but, unlike in the procedures used to elicit cooperation (which were administered separately), they could not keep the sticks for themselves. We call this the 'gift network'. The network discerned this way yields a maximum out-degree of 3, but it is also a weighted network, because people could choose to give more honey to certain alters. On average, both women and men chose to give to 2.2 (± 0.8 s.d.) recipients. While, ordinarily, gifts among the Hadza are not anonymous and involve reputation effects, the Hadza do understand the importance and feasibility of a gift given anonymously. We elected to measure ties this way because it was objective and could characterize phenomena such as reciprocity with limited bias.

Finally, anthropometry measures (including height, weight, body fat percentage, muscle mass and hand-grip strength) were collected, as well as marital status, reproductive histories, and other measurements; we also computed the genetic relatedness of all pairs of people (see Supplementary Information). The data were analysed with GEE regression models^{36,37}, and confirmatory analyses were also done using other methods (see Supplementary Information).

31. Berbesque, J. C. & Marlowe, F. W. Sex differences in food preferences of Hadza hunter-gatherers. *Evol. Psychol.* **7**, 601–616 (2009).
32. Henrich, J. *et al.* In search of *Homo economicus*: behavioral experiments in 15 small-scale societies. *Am. Econ. Rev.* **91**, 73–78 (2001).
33. Campbell, K. E. & Lee, B. A. Name generators in surveys of personal networks. *Soc. Networks* **13**, 203–221 (1991).
34. Hawkes, K., O'Connell, J. F. & Blurton Jones, N. Hadza meat sharing. *Evol. Hum. Behav.* **22**, 113–142 (2001).
35. Smith, E. A. in *Hunter Gatherers Vol. 1 History, Evolution and Social Change* (eds Ingold, T., Riches, D. & Woodburn, J.) 222–251 (Berg, 1988).
36. Liang, K. Y. & Zeger, S. Longitudinal data analysis using generalized linear models. *Biometrika* **73**, 13–22 (1986).
37. Scholdcrout, J. S. Regression analysis of longitudinal binary data with time-dependent environmental covariates: bias and efficiency. *Biostatistics* **6**, 633–652 (2005).

Purkinje neuron synchrony elicits time-locked spiking in the cerebellar nuclei

Abigail L. Person^{1†} & Indira M. Raman¹

An unusual feature of the cerebellar cortex is that its output neurons, Purkinje cells, release GABA (γ -aminobutyric acid). Their high intrinsic firing rates¹ (50 Hz) and extensive convergence^{2,3} predict that their target neurons in the cerebellar nuclei would be largely inhibited unless Purkinje cells pause their spiking, yet Purkinje and nuclear neuron firing rates do not always vary inversely⁴. One indication of how these synapses transmit information is that populations of Purkinje neurons synchronize their spikes during cerebellar behaviours^{5–11}. If nuclear neurons respond to Purkinje synchrony, they may encode signals from subsets of inhibitory inputs^{7,12–14}. Here we show in weanling and adult mice that nuclear neurons transmit the timing of synchronous Purkinje afferent spikes, owing to modest Purkinje-to-nuclear convergence ratios ($\sim 40:1$), fast inhibitory postsynaptic current kinetics ($\tau_{\text{decay}} = 2.5$ ms) and high intrinsic firing rates (~ 90 Hz). *In vitro*, dynamically clamped asynchronous inhibitory postsynaptic potentials mimicking Purkinje afferents suppress nuclear cell spiking, whereas synchronous inhibitory postsynaptic potentials entrain nuclear cell spiking. With partial synchrony, nuclear neurons time-lock their spikes to the synchronous subpopulation of inputs, even when only 2 out of 40 afferents synchronize. *In vivo*, nuclear neurons reliably phase-lock to regular trains of molecular layer stimulation. Thus, cerebellar nuclear neurons can preferentially relay the spike timing of synchronized Purkinje cells to downstream premotor areas.

During cerebellar behaviours, on-beam Purkinje cells fire synchronous simple spikes with millisecond-scale precision^{5–8}, and microbands of Purkinje cells fire synchronous complex spikes^{9–11}. The extent to which cerebellar nuclear neurons respond to synchrony depends on the magnitude, convergence and kinetics of Purkinje inputs. We therefore measured these properties before assessing the consequence of Purkinje synchrony on nuclear firing *in vitro* and *in vivo*.

We first recorded IPSC amplitudes evoked in nuclear neurons by stimulating Purkinje axons in mouse cerebellar slices (Fig. 1a, b). Maximal stimulation evoked inhibitory postsynaptic currents (IPSCs) up to ~ 200 nS (mean \pm s.e.m., 108.3 ± 13.0 nS; $n = 17$). Minimal stimulation evoked either failures or successes of 9.4 ± 1.0 nS ($n = 30$), the amplitudes of which resembled tetrodotoxin-sensitive spontaneous IPSCs¹⁵, consistent with activation of a single fibre. The high unitary amplitude suggests that individual Purkinje-to-nuclear contacts are quite strong¹⁶. The maximal-to-minimal conductance ratio indicates that functional convergence in the slice is about 12, or maximally ~ 22 . Because both slicing and incomplete recruitment of afferents probably limit maximal IPSC amplitudes, this estimate represents a lower bound on functional convergence in the intact cerebellar nuclei.

We obtained a second convergence estimate by considering structural constraints on innervation (see Supplementary Discussion for calculations). In mouse, the Purkinje-innervated surface of a large nuclear cell with four dendrites ($3,130 \mu\text{m}^2$) maximally accommodates 1,250 Purkinje boutons, each with a $2.5 \mu\text{m}^2$ surface area; comparable numbers (600–1,200) are estimated for cat¹⁷. Multiple boutons must

arise from a single Purkinje cell, however, because the quantal content of a unitary Purkinje IPSC^{15,16} is 12–18. Given a bouton release probability¹⁸ of 0.5, each Purkinje cell must contribute ~ 24 –36 boutons per target, predicting 34–52 Purkinje cells per nuclear cell.

A third convergence estimate was derived from the maximal GABA_A receptor conductance per nuclear neuron¹⁹, which yielded a mean convergence of ~ 20 (maximum, ~ 30) (Supplementary Discussion). The estimates from these three separate measures can be reconciled with classical histological measurements of 860 Purkinje cells per nuclear cell in the cat³, by the observation that each Purkinje bouton has 9–10 synaptic densities^{2,18}. Correcting for this factor reduces the predicted convergence to 86–96, on the order of magnitude of the present estimates. Thus, multiple approaches indicate a functional convergence in the intact cerebellum of tens of Purkinje neurons per nuclear neuron, probably 20–50 in the rodent.

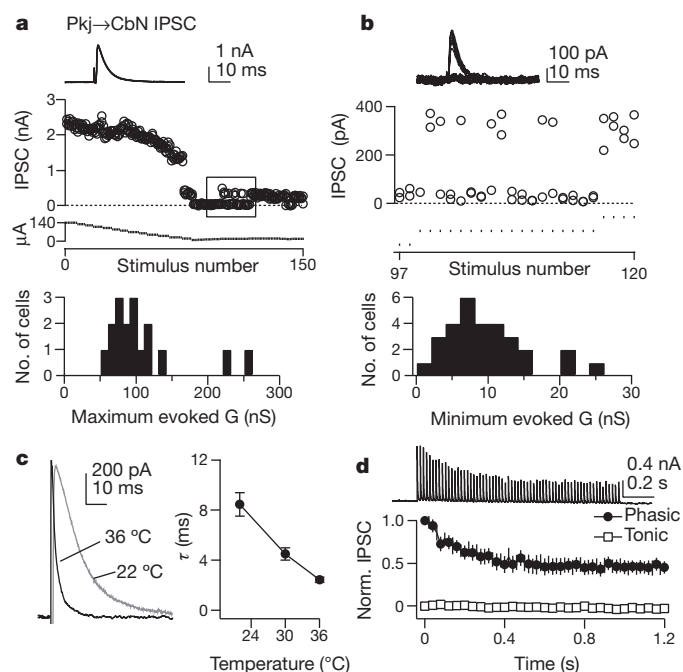


Figure 1 | Purkinje cell convergence and fast IPSCs in the cerebellar nuclei.

a, IPSCs evoked by maximal stimulation. Holding potential, -57 mV (junction potential corrected). Top: five overlaid IPSCs. Middle: IPSC amplitudes as stimulus strength was reduced. Bottom: maximal conductances calculated from measured IPSC reversal potentials ($n = 17$, mean $E_{\text{Cl}} = -75$ mV). Bin width, 10 nS. CbN, cerebellar nuclei; Pkj, Purkinje. **b**, IPSCs evoked by minimal stimulation (range 16–20 μA). Top: 20 overlaid IPSCs. Middle: expansion of box in **a**. Events near the zero line fell within the noise. Bottom: minimal conductances ($n = 30$). Bin width, 2 nS. **c**, Left: scaled IPSCs in one cell at 22°C and 36°C . Right: temperature dependence of IPSC decay τ ($n = 7$). **d**, Top: 50-Hz train of IPSCs at 36°C . Bottom: depression of phasic IPSCs and absence of tonic current during train. Data are mean \pm s.e.m.

¹Department of Neurobiology, Northwestern University, Evanston, Illinois 60208, USA. [†]Present address: Department of Physiology and Biophysics, University of Colorado School of Medicine, Aurora, Colorado 80045, USA.

Additional determinants of the efficacy of inhibition are the intrinsic firing rates and IPSC kinetics. In 17–26-day-old mice (P17–P26), nuclear neurons fired spontaneously at 91.5 ± 7.4 spikes s^{-1} , significantly faster than in P13 animals recorded under identical conditions¹⁵ (22.0 ± 5.0 spikes s^{-1} ; Supplementary Fig. 1), indicating a developmental increase in intrinsic firing rate. At near-physiological temperature (36°C), the τ_{decay} of evoked IPSCs was 2.4 ± 0.2 ms (Fig. 1c), making corticonuclear IPSCs among the fastest known GABA_A-receptor-mediated currents²⁰. This value is >5 -fold briefer than the τ_{decay} of 13.6 ms of IPSCs at room temperature²¹, which appears in previous corticonuclear models^{12–14}. When unitary IPSCs were mimicked with dynamic clamp, the duration of inhibition of spontaneously firing nuclear cells varied directly with τ_{decay} ^{15,21,22}, and the first post-inhibitory spike was well-timed relative to the stimulus^{12,23} (Supplementary Fig. 2). Thus, brief IPSCs minimize inhibition.

When synchronous IPSCs were evoked at 50 Hz at 36°C , peak IPSCs were depressed by 55% ($n = 6$), but the current decayed fully between stimuli (Fig. 1d), resulting in no accumulation of ‘tonic’ current¹⁵. Because tonic current is largely responsible for suppressing nuclear cell spiking, synchronous and asynchronous IPSCs may differentially modulate nuclear cell output. As a preliminary test of this idea, we delivered trains of dynamically clamped inhibitory postsynaptic potentials (dynIPSPs) from eight afferents, each with an amplitude of 10 nS and a rate of 50 Hz, which were either desynchronized (equivalent to one non-depressing input at 400 Hz) or synchronized (Fig. 2a). Not surprisingly, desynchronized dynIPSPs strongly inhibited spontaneous firing. In contrast, upon synchronization of dynIPSPs, nuclear neuron firing rates jumped instantaneously, but only when τ_{decay} was brief (Fig. 2b). Moreover, with physiological τ_{decay} , nuclear cell spiking entrained to the synchronous input, evident as a match between the instantaneous firing rate and the stimulus rate (Fig. 2a). Likewise, IPSPs evoked by Purkinje stimulation nearly perfectly entrained nuclear neuron spiking between 60 and 80 Hz (Fig. 2c, d); in contrast, desynchronized dynIPSPs suppressed firing at all stimulus rates (Fig. 2d). Thus, in the extreme case of low convergence, the output of nuclear neurons is determined by both the rate and synchrony of inhibition.

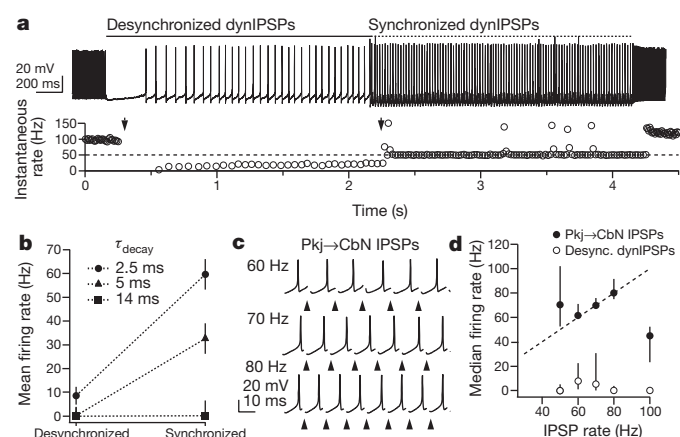


Figure 2 | Entrainment of nuclear neuron spiking to synchronous IPSPs. **a**, Top: response to desynchronized and synchronized dynIPSPs from 8 inputs at 50 Hz, $\tau_{\text{decay}} = 2.5$ ms. Bottom: instantaneous firing rates of neuron in **a**, showing entrainment during synchrony. Arrows indicate onset of desynchronized (left) and synchronized (right) dynIPSPs. Tall spikes reflect overlapping dynIPSPs and spikes. **b**, Firing rates during desynchronized and synchronized 50-Hz trains with different dynIPSP kinetics ($\tau_{\text{decay}} = 2.5, 5, 14$ ms, $n = 25, 18, 10$). **c**, Entrainment to corticonuclear IPSPs (36°C) between 60 and 80 Hz. Arrowheads indicate stimulation times. **d**, Median firing rates (± 1 quartile) in response to evoked IPSPs (closed symbols) and desynchronized dynIPSPs (open symbols). From 50–100 Hz, evoked, $n = 8, 8, 8, 7, 3$; simulated, $n = 25, 10, 10, 9, 14$. Dashed line indicates unity. Data are mean \pm s.e.m., unless noted.

Synchronous Purkinje firing occurs *in vivo*^{5–11}, but the proportion of convergent Purkinje cells that synchronize is probably $<100\%$. We therefore mimicked 40 Purkinje afferents with dynamic clamp, reflecting a realistic functional convergence, and tested whether synchronizing only a subpopulation of inputs can affect cerebellar nuclear output. To account for synaptic depression and mimic irregular spiking *in vivo*^{23,24}, each input was 5 nS, and inter-IPSP intervals were drawn from Gaussian distributions (coefficient of variation (CV) = 1), yielding a mean of 50 IPSPs s^{-1} . After 1 s of asynchronous inhibition, a fixed number of inputs (2–20, or 5–50%) was synchronized at 20–125 Hz, while the remaining inputs continued to provide asynchronous inhibition, each at 50 IPSPs s^{-1} (Fig. 3a, b). Asynchronous dynIPSPs greatly slowed nuclear cell firing. Firing rates, however, increased with fractional synchrony (Fig. 3a, c). The averaged voltage trajectories of synchronous dynIPSPs preceding and lacking a spike did not differ in the depth of hyperpolarization (Supplementary Fig. 3). Thus, the action potentials are not low-threshold spikes that follow unusually large inhibitory stimuli.

During trains of synchronous dynIPSPs, distinct temporal patterns of spiking emerged. For all frequencies tested, interspike interval distributions clustered at multiples of the interstimulus intervals of the synchronous dynIPSPs (Fig. 3d), reflecting phase locking of spikes to the regular stimulus train. The data were combined across stimulus

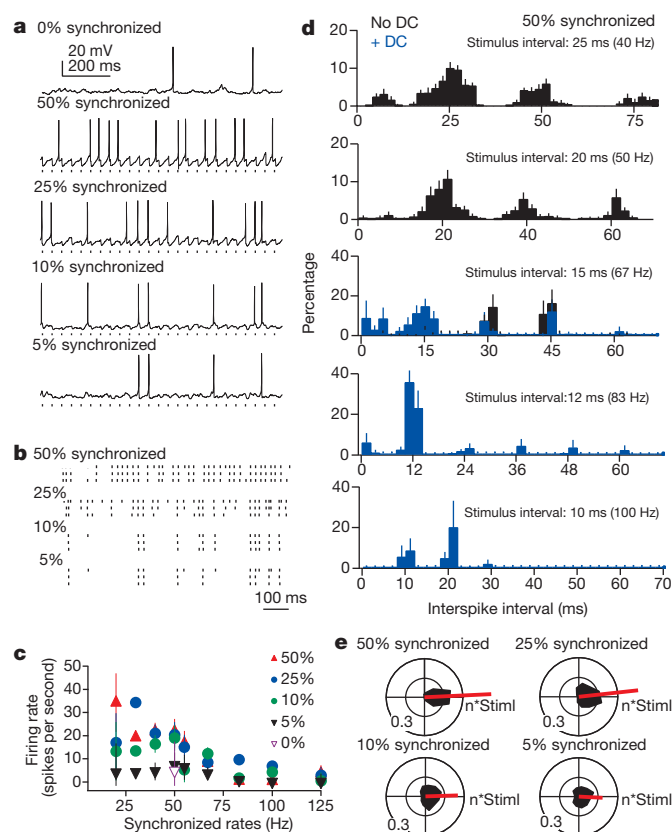


Figure 3 | The synchronous subpopulation of Purkinje inputs sets spike timing of nuclear neurons. **a**, Nuclear neuron responses to dynIPSPs from 40 asynchronous or partially synchronized inputs, as labelled. **b**, Spike rasters during dynIPSP trains with 50–5% synchrony. **c**, Firing rates during 20–125-Hz trains with 0–50% synchrony (‘Synchronized rates’). **d**, Normalized interspike interval distributions during 50% synchrony, from 40 to 100 Hz. Abscissa tick marks indicate multiples of the interstimulus intervals. Bin width, 2 ms. Black, no current injection; blue, with 200 pA direct current (DC) applied to increase spike number during inhibition. **e**, Black: polar histograms of interspike intervals during 50–5% synchrony for 50, 55, 67, 83, 100 and 125 Hz input. Each cycle is one interstimulus interval (StimI). Red: net vectors of interspike interval histograms. (For 50%, 25%, 10%, 5% synchrony, $n = 14, 9, 7, 7$.) Data are mean \pm s.e.m.

frequency by plotting interspike intervals as normalized polar histograms, with 0° representing multiples of the interstimulus interval (Fig. 3e). A net vector magnitude of 1 indicates perfect phase locking, and 0 indicates randomly occurring spikes. For all fractions of synchrony, the net vector was oriented close to 0° ($2^\circ \pm 2^\circ$) with a non-zero magnitude (0.18, 0.25, 0.45 and 0.52 for 5%, 10%, 25% and 50% synchrony), illustrating the temporal restructuring of spike patterns according to stimulus interval.

To test whether conditions *in vivo* permit phase locking, we recorded single units from the cerebellar nuclei in anaesthetized adult mice (Fig. 4a). Purkinje spiking was partially synchronized by stimulating the molecular layer²³. Indeed, for stimuli from 20–120 Hz, phase locking was robust in all neurons confirmed histologically to be within the nuclei (10 cells in 10 mice; Fig. 4a, b). No phase locking was apparent in two neurons located outside the nuclei. The net vector of the mean polar histogram combined across frequencies was oriented at -3° (Fig. 4c). Its magnitude (0.33) was between those for 10% and 25% synchrony *in vitro*, and was greater than that of baseline (0.09, $P < 0.05$, within-cell comparisons of vector magnitudes; direction 257°).

Stimulation modulated the mean firing rates of individual neurons ($P < 0.05$ versus baseline, within-cell comparisons). Like the results for different fractional synchrony *in vitro*, however, spike rates decreased in some cells ($n = 7$) and increased in others ($n = 3$; Supplementary Fig. 4), yielding no net change across cells ($P > 0.05$; Fig. 4d). Thus, the firing rate of nuclear cells, which is probably affected by both basal excitation and the fractional synchrony induced by the stimulus, does not obviously encode information about the rate of inhibitory inputs.

To evaluate whether stimulation directly excited nuclear neurons, we compared stimulus-to-spike latencies across conditions. *In vivo* latencies were 20.2 ± 2.2 ms, >5 -fold greater than excitatory post-synaptic potential (EPSP)-to-spike latencies *in vitro* (3.5 ± 0.5 , inhibition blocked), making direct excitation seem unlikely. Instead, *in vivo* latencies were closer to IPSP-to-spike latencies (11.9 ± 1.4 ms, excitation blocked) and synchronous dynIPSP-to-spike latencies with background inhibition (13.5 ± 0.6 ms; Fig. 4e), consistent with sequential parallel fibre and Purkinje cell activation²³. Given the similarity of phase locking *in vivo* and *in vitro* with excitation blocked, these results suggest that the *in vivo* stimulation synchronizes Purkinje cell simple spikes, which in turn set the timing of nuclear cell spikes. The reliability of phase locking to regular trains of inhibitory stimuli *in vivo* further suggests that the spike patterns of a synchronized Purkinje subpopulation can be transmitted with fidelity by cerebellar nuclear neurons.

These experiments address the long-standing question in cerebellar physiology of how nuclear neurons encode signals from convergent, inhibitory Purkinje cells firing at high basal rates¹. The intrinsic tendency of nuclear neurons to fire permits time-locked spiking during the transient reduction in inhibition after a few brief IPSCs overlap. Even synchrony of only two afferents (5%) can influence the timing of nuclear cell spiking. The results provide an alternative to the idea that nuclear cell firing requires pauses that permit low-threshold rebound spikes after prolonged Purkinje activity: not only would such a mechanism discard information present in graded Purkinje firing rates, but it would also introduce ~ 100 -ms delays in cerebellar processing that are not evident²⁵.

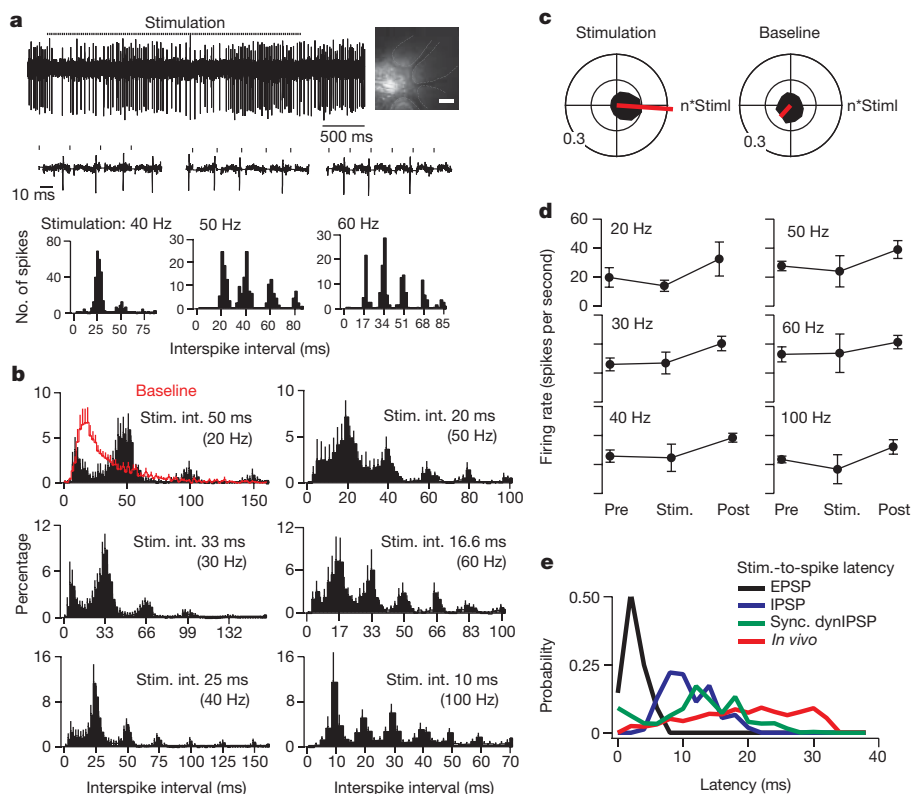


Figure 4 | Nuclear neurons phase-lock to molecular layer stimulation *in vivo*. **a**, Upper trace: response of a nuclear neuron to 40-Hz molecular layer stimulation (bar). Inset, recording site in the cerebellar nuclei recovered after focal Alexa 568 injection. Dashed lines demarcate cerebellar folia. Scale bar, 200 μ m. Lower traces: expanded segments of spikes during 40-, 50- and 60-Hz stimulation (ticks), showing the long stimulus-to-spike latency. Stimulus artefacts are set to zero. Plots show interspike interval histograms for responses above. **b**, Mean normalized interspike interval distributions during molecular layer stimulation from 20 to 100 Hz for 4, 9, 9, 7, 5, and 7 cells respectively.

Abscissa tick marks indicate multiples of the interstimulus interval. Red baseline histogram includes intervals before and after stimulation. Peaks at multiples of 8.3 ms were evident in 2 out of 2 cells stimulated at 120 Hz (not shown). Bin width, 2 ms. **c**, Black: polar histograms of interspike intervals during stimulation across rates (left) or during baseline periods. Red: net vectors of polar histograms. **d**, Mean firing rates before (Pre, 1 s), during (Stim., 3 s) and after (Post) stimulation. **e**, Stimulus-to-spike latencies for pharmacologically isolated EPSPs (black), IPSPs (blue) and dynIPSPs during partial synchrony (green) and *in vivo* (red). Data are mean \pm s.e.m.

The extent to which time locking occurs during natural cerebellar processing will depend on the fractional synchrony of converging Purkinje cells, the precision of this synchrony, and the variance of ongoing excitation of nuclear neurons¹³. Supporting the idea that synchronized Purkinje neurons converge, simple spike synchrony is observed in neighbouring on-beam Purkinje cells^{5,6}, and closely spaced Purkinje cells probably converge on a common nuclear neuron²⁶. Moreover, neighbouring Purkinje cells appear to be functionally related, as trans-synaptic tracing from muscles labels discrete strips of Purkinje cells²⁷.

A remaining question is how time-locked nuclear cell spikes are processed downstream. In the red nucleus, each interpositus axon makes parasagittally ramifying contacts²⁸, and about 50 interpositus neurons converge onto each target, producing EPSPs with little short-term plasticity²⁹. Therefore, summation of EPSPs in the red nuclei may drive spiking that follows the firing pattern of the synchronized Purkinje subpopulation. More generally, time locking by cerebellar nuclear neurons may be a mechanism whereby the rate and timing of signals from varying groups of synchronized Purkinje cells are preferentially transmitted to premotor areas and other cerebellar targets.

METHODS SUMMARY

Procedures conformed to institutional guidelines for animal care and use.

In vitro electrophysiology. Parasagittal cerebellar slices from both sexes of C57BL/6 13–29-day-old mice were cut¹⁵ in artificial cerebrospinal fluid (ACSF; 35 °C). Recordings from large nuclear neurons were made¹⁵ at 35–37 °C, unless noted, with a Multiclamp 700B amplifier and pClamp acquisition software. IPSCs were evoked in 6,7-dinitroquinoxaline-2,3-dione (DNQX; 5 μ M), (RS)-3-(2-carboxypiperazin-4-yl)-propyl-1-phosphonic acid (CPP; 10 μ M) and strychnine (2 μ M) by 0.1-ms pulses delivered through a concentric bipolar electrode in the white matter surrounding the cerebellar nuclei. Evoked IPSCs were considered minimal when a fixed intensity stimulus elicited responses and failures with approximately equal likelihood, and maximal when increasing intensity produced no larger IPSCs. Dynamic clamp was implemented with an SM-2 (Cambridge Conductance) and a P25M real-time DSP board sampling between 10 and 25 kHz. Simulated IPSCs had a rise time and τ_{decay} of 0.1 and 2.5 ms, 0.5 and 5 ms, or 1 and 14 ms, and reversed at –75 mV. Desynchronized inputs had dynIPSP intervals distributed uniformly. Asynchronous dynIPSP intervals were drawn from a Gaussian distribution, created offline in IgorPro 5.05, with CV = 1. Forty independent trains were merged.

In vivo electrophysiology. Adult C57BL/6 mice were anaesthetized with ketamine (80–100 mg kg^{–1}) and xylazine (5–10 mg kg^{–1}). A glass recording electrode containing 2 M NaCl was targeted to the cerebellar nuclei. A bipolar stimulating electrode (~300 μ m between poles) was placed stereotactically in the molecular layer, flanking the recording electrode. Three-second stimulus trains were delivered once every 15 s, repeated 4–20 times per frequency. Data were analysed in IgorPro.

Full Methods and any associated references are available in the online version of the paper at www.nature.com/nature.

Received 8 December 2010; accepted 23 November 2011.

Published online 25 December 2011.

1. Thach, W. T. Discharge of Purkinje and cerebellar nuclear neurons during rapidly alternating arm movements in the monkey. *J. Neurophysiol.* **31**, 785–797 (1968).
2. Chan-Palay, V. *Cerebellar Dentate Nucleus: Organization, Cytology, and Transmitters* (Springer, 1977).
3. Palkovits, M., Mezeke, E., Hamori, J. & Szentagothai, J. Quantitative histological analysis of the cerebellar nuclei in the cat. I. Numerical data on cells and on synapses. *Exp. Brain Res.* **28**, 189–209 (1977).
4. McDevitt, C. J., Ebner, T. J. & Bloedel, J. R. Relationships between simultaneously recorded Purkinje cells and nuclear neurons. *Brain Res.* **425**, 1–13 (1987).
5. Bell, C. C. & Grimm, R. J. Discharge properties of Purkinje cells recorded on single and double microelectrodes. *J. Neurophysiol.* **32**, 1044–1055 (1969).
6. Heck, D. H., Thach, W. T. & Keating, J. G. On-beam synchrony in the cerebellum as the mechanism for the timing and coordination of movement. *Proc. Natl Acad. Sci. USA* **104**, 7658–7663 (2007).

7. de Solages, C. et al. High-frequency organization and synchrony of activity in the Purkinje cell layer of the cerebellum. *Neuron* **58**, 775–788 (2008).
8. Wise, A. K., Cerminara, N. L., Marple-Horvat, D. E. & Apps, R. Mechanisms of synchronous activity in cerebellar Purkinje cells. *J. Physiol.* **588**, 2373–2390 (2010).
9. Welsh, J. P., Lang, E. J., Sugihara, I. & Llinas, R. Dynamic organization of motor control within the olivocerebellar system. *Nature* **374**, 453–457 (1995).
10. Ozden, I., Sullivan, M. R., Lee, H. M. & Wang, S. S. Reliable coding emerges from coactivation of climbing fibers in microbands of cerebellar Purkinje neurons. *J. Neurosci.* **29**, 10463–10473 (2009).
11. Schultz, S. R., Kitamura, K., Post-Uiterweer, A., Krupic, J. & Häusser, M. Spatial pattern coding of sensory information by climbing fiber-evoked calcium signals in networks of neighboring cerebellar Purkinje neurons. *J. Neurosci.* **29**, 8005–8015 (2009).
12. Gauck, V. & Jaeger, D. The control of rate and timing of spikes in the deep cerebellar nuclei by inhibition. *J. Neurosci.* **20**, 3006–3016 (2000).
13. Gauck, V. & Jaeger, D. The contribution of NMDA and AMPA conductances to the control of spiking in neurons of the deep cerebellar nuclei. *J. Neurosci.* **23**, 8109–8118 (2003).
14. Kistler, W. M. & De Zeeuw, C. I. Time windows and reverberating loops: a reverse-engineering approach to cerebellar function. *Cerebellum* **2**, 44–54 (2003).
15. Telgkamp, P. & Raman, I. M. Depression of inhibitory synaptic transmission between Purkinje cells and neurons of the cerebellar nuclei. *J. Neurosci.* **22**, 8447–8457 (2002).
16. Pedroarena, C. M. & Schwarz, C. Efficacy and short-term plasticity at GABAergic synapses between Purkinje and cerebellar nuclei neurons. *J. Neurophysiol.* **89**, 704–715 (2003).
17. Bengtsson, F., Ekerot, C.-F. & Jörntell, H. *In vivo* analysis of inhibitory synaptic inputs and rebounds in deep cerebellar nuclear neurons. *PLoS ONE* **6**, e18822 (2011).
18. Telgkamp, P., Padgett, D. E., Ledoux, V. A., Woolley, C. S. & Raman, I. M. Maintenance of high-frequency transmission at Purkinje to cerebellar nuclear synapses by spillover from boutons with multiple release sites. *Neuron* **41**, 113–126 (2004).
19. Pugh, J. R. & Raman, I. M. GABA_A receptor kinetics in the cerebellar nuclei: evidence for detection of transmitter from distant release sites. *Biophys. J.* **88**, 1740–1754 (2005).
20. Bartos, M. et al. Fast synaptic inhibition promotes synchronized gamma oscillations in hippocampal interneuron networks. *Proc. Natl Acad. Sci. USA* **99**, 13222–13227 (2002).
21. Anchisi, D., Scelfo, B. & Tempia, F. Postsynaptic currents in deep cerebellar nuclei. *J. Neurophysiol.* **85**, 323–331 (2001).
22. Uusisaari, M. & Knopfel, T. GABAergic synaptic communication in the GABAergic and non-GABAergic cells in the deep cerebellar nuclei. *Neuroscience* **156**, 537–549 (2008).
23. Hoebeek, F. E., Witter, L., Ruigrok, T. J. & De Zeeuw, C. I. Differential olivo-cerebellar cortical control of rebound activity in the cerebellar nuclei. *Proc. Natl Acad. Sci. USA* **107**, 8410–8415 (2010).
24. Goossens, H. H. L. M. et al. Simple spike and complex spike activity of floccular Purkinje cells during the optokinetic reflex in mice lacking cerebellar long-term depression. *Eur. J. Neurosci.* **19**, 687–697 (2004).
25. Mauk, M. D. & Buonomano, D. V. The neural basis of temporal processing. *Annu. Rev. Neurosci.* **27**, 307–340 (2004).
26. Sugihara, I. et al. Projection of reconstructed single Purkinje cell axons in relation to the cortical and nuclear aldolase C compartments of the rat cerebellum. *J. Comp. Neurol.* **512**, 282–304 (2009).
27. Ruigrok, T. J. H., Pijpers, A., Goedknecht-Sabel, E. & Coulon, P. Multiple cerebellar zones are involved in the control of individual muscles: a retrograde transneuronal tracing study with rabies virus in the rat. *Eur. J. Neurosci.* **28**, 181–200 (2008).
28. Shinoda, Y., Futami, T., Mitoma, H. & Yokota, J. Morphology of single neurons in the cerebello-rubrospinal system. *Behav. Brain Res.* **28**, 59–64 (1988).
29. Toyama, K., Tsukahara, N., Kosaka, K. & Matsunami, K. Synaptic excitation of red nucleus neurons by fibres from interpositus nucleus. *Exp. Brain Res.* **11**, 187–198 (1970).

Supplementary Information is linked to the online version of the paper at www.nature.com/nature.

Acknowledgements We are grateful to J. R. Pugh for new analysis of data from ref. 19 on whole-cell GABA conductances. We thank D. Ferster, D. McLean and C. Woolley for comments on the manuscript. This work was supported by NIH grants R01-NS39395 (I.M.R.) and F32-NS067831 (A.L.P.).

Author Contributions A.L.P. performed all experiments and analyses. A.L.P. and I.M.R. designed and interpreted experiments and wrote the manuscript.

Author Information Reprints and permissions information is available at www.nature.com/reprints. The authors declare no competing financial interests. Readers are welcome to comment on the online version of this article at www.nature.com/nature. Correspondence and requests for materials should be addressed to I.M.R. (i-raman@northwestern.edu) or A.L.P. (a-person@northwestern.edu).

METHODS

Tissue preparation. Parasagittal slices of the cerebellar nuclei were prepared as in ref. 15 in accordance with institutional guidelines for animal care and use. P13–P29 mice were deeply anaesthetized with isoflurane and transcardially perfused with warm (35 °C) ACSF containing (in mM): 123 NaCl, 3.5 KCl, 26 NaHCO₃, 1.25 NaH₂PO₄, 1.5 CaCl₂, 1 MgCl₂, 10 glucose and equilibrated with 95/5% O₂/CO₂. Mice were then rapidly decapitated and the brains removed into ACSF (35 °C). Slices (300 µm thick) were cut on a Vibratome (Leica VT 100S) and incubated in warmed (35 °C), oxygenated ACSF for at least 1 h before recording.

Electrophysiological recording. Cerebellar slices were transferred to a recording chamber perfused continuously with warmed (35–37 °C, unless noted), oxygenated ACSF at a flow rate of 2–4 ml min⁻¹. Slices were visualized with infrared differential interference contrast microscopy and recordings were made from large neurons (soma diameters >15 µm). Neurons all had fast decay constants (~2.5 ms at 36 °C) resembling the <5 ms τ_{decay} of glutamic acid decarboxylase (GAD)-negative large neurons at 34 °C rather than the ~10 ms τ_{decay} of GAD-positive neurons²². They are therefore likely to be excitatory projection neurons. Data were filtered at 6 kHz and sampled at 10–25 kHz.

Voltage- and current-clamp recordings were made with a Multiclamp 700B amplifier (Molecular Devices) and pClamp 10.0 data acquisition software (Molecular Devices). Borosilicate patch pipettes were pulled to tip resistances of 2–4 MΩ and filled with an internal solution containing (mM): 130 K-gluconate, 2 Na-gluconate, 6 NaCl, 10 HEPES, 2 MgCl₂, 0.1 or 1 EGTA, 14 Tris-creatine phosphate, 4 MgATP, 0.3 Tris-GTP and 10 sucrose. For experiments isolating GABA_A-receptor-mediated currents, DNQX (5 µM), CPP (10 µM) and strychnine (2 µM) were included in the bath solution and currents were evoked by stimulating the white matter surrounding the cerebellar nuclei with 0.1-ms current pulses (Isoflex Stimulus Isolation Unit; AMPI) delivered through a concentric bipolar electrode (FHC). Evoked IPSCs were considered minimal when a fixed amplitude stimulus strength elicited IPSCs or failures with approximately equal likelihood, indicating that stimulation was at threshold for a single input.

Dynamic clamp was implemented with a SM-2 system (Cambridge Conductance) with a P25M real-time DSP board (Innovative Integration) sampling between 10 and 25 kHz. Unitary conductances were set at either 10 or 5 nS and three kinetic profiles were used: 0.1-ms rise time and a single exponential τ_{decay} of 2.5 ms; 0.5-ms rise time and τ_{decay} of 5 ms (ref. 15); and 1-ms rise time and τ_{decay} 14 ms (ref. 21), with a reversal potential of -75 mV, accounting for a 7-mV measured liquid junction potential. In experiments manipulating synchrony between 0% and 100%, eight 10-nS convergent units were simulated. Desynchronized inputs were designed to distribute IPSP times uniformly during the inter-stimulus-interval,

such that each 'unit' was activated at a given rate but offset in time by (inter-stimulus-interval/8) milliseconds. Gaussian trains were created offline in IgorPro 5.05 (Wavemetrics). Spike times were drawn from a Gaussian distribution with a CV of 1. Forty independent trains were merged to represent a population of corticonuclear IPSP arrival times and applied to trigger inhibitory conductances.

In vivo electrophysiology. Adult C57BL/6 mice were anaesthetized with a cocktail of 80–100 mg kg⁻¹ ketamine and 5–10 mg kg⁻¹ xylazine intraperitoneally. A small craniotomy above the cerebellum was made with a dental drill. A glass recording electrode containing 2 M NaCl with 1% Alexa 568 10K dextran amine was targeted to the cerebellar nuclei (in mm: 2.6–3.0 posterior to Lambda, 1.0–1.3 lateral, 2.2–3.1 depth). A bipolar stimulating electrode (~300 µm between poles) was placed stereotactically in the cerebellar molecular layer, aligned approximately in the coronal plane (on-beam), flanking the recording electrode. Stimulus trains were 3 s, delivered once every 15 s, had pulse durations of 0.1 ms and amplitudes of 40 ($n = 1$), 200 ($n = 6$) or 360 µA ($n = 5$), after other studies that used 100–200 µA (ref. 23). A stimulus of 360 µA is expected to stimulate a sphere with <0.5 mm radius³⁰. Each stimulus rate was delivered between 4 and 20 times to each unit. After each recording, dye was pressure injected to mark the recording site. Only one cell was recorded from each mouse. Mice were transcardially perfused with physiological saline, brains were collected and fixed in 4% paraformaldehyde. Brains were cryoprotected in 30% sucrose, sectioned to 40 µm on a freezing microtome, and visualized on a Leica laser scanning confocal microscope.

Data analysis. Data were analysed offline in IgorPro 5.05 (Wavemetrics). Statistical analysis was done with paired or unpaired two-tailed *t*-tests as noted in the text, with significance taken as $P < 0.05$. Polar plots were constructed by binning interspike intervals with bin size = stimulus interval/12 for each stimulus frequency in each cell and averaging first across cells and then across frequencies. On each polar plot, one cycle is one interstimulus interval, such that a bar at 0° indicates spikes occurring at multiples of the interspike interval. Net vector magnitudes and directions were computed by summing the *x* and *y* values associated with the angle and radius values of the 12 vectors (histogram bars) that compose the mean polar plot. The null polar plot for the *in vivo* data was constructed from the interspike intervals of spikes occurring during non-stimulated periods, plotted with the same time bases as the stimulated interspike intervals. For statistical comparison of stimulated and null interspike intervals *in vivo*, vector magnitudes were calculated for data binned at 0.1 ms.

30. Tehovnik, E. J., Tolia, A. S., Sultan, F., Slocum, W. M. & Logothetis, N. K. Direct and indirect activation of cortical neurons by electrical microstimulation. *J. Neurophysiol.* **96**, 512–521 (2006).

Clonal evolution in relapsed acute myeloid leukaemia revealed by whole-genome sequencing

Li Ding^{1,2*}, Timothy J. Ley^{1,3,4*}, David E. Larson¹, Christopher A. Miller¹, Daniel C. Koboldt¹, John S. Welch³, Julie K. Ritchey³, Margaret A. Young³, Tamara Lamprecht³, Michael D. McLellan¹, Joshua F. McMichael¹, John W. Wallis^{1,2}, Charles Lu¹, Dong Shen¹, Christopher C. Harris¹, David J. Dooling^{1,2}, Robert S. Fulton^{1,2}, Lucinda L. Fulton^{1,2}, Ken Chen^{1,2}, Heather Schmidt¹, Joelle Kalicki-Veizer¹, Vincent J. Magrini^{1,2}, Lisa Cook¹, Sean D. McGrath¹, Tammi L. Vickery¹, Michael C. Wendl^{1,2}, Sharon Heath³, Mark A. Watson⁵, Daniel C. Link^{3,4}, Michael H. Tomasson^{3,4}, William D. Shannon⁶, Jacqueline E. Payton⁵, Shashikant Kulkarni^{2,4,5}, Peter Westervelt^{3,4}, Matthew J. Walter^{3,4}, Timothy A. Graubert^{3,4}, Elaine R. Mardis^{1,2,4}, Richard K. Wilson^{1,2,4} & John F. DiPersio^{3,4}

Most patients with acute myeloid leukaemia (AML) die from progressive disease after relapse, which is associated with clonal evolution at the cytogenetic level^{1,2}. To determine the mutational spectrum associated with relapse, we sequenced the primary tumour and relapse genomes from eight AML patients, and validated hundreds of somatic mutations using deep sequencing; this allowed us to define clonality and clonal evolution patterns precisely at relapse. In addition to discovering novel, recurrently mutated genes (for example, *WAC*, *SMC3*, *DIS3*, *DDX41* and *DAXX*) in AML, we also found two major clonal evolution patterns during AML relapse: (1) the founding clone in the primary tumour gained mutations and evolved into the relapse clone, or (2) a subclone of the founding clone survived initial therapy, gained additional mutations and expanded at relapse. In all cases, chemotherapy failed to eradicate the founding clone. The comparison of relapse-specific versus primary tumour mutations in all eight cases revealed an increase in transversions, probably due to DNA damage caused by cytotoxic chemotherapy. These data demonstrate that AML relapse is associated with the addition of new mutations and clonal evolution, which is shaped, in part, by the chemotherapy that the patients receive to establish and maintain remissions.

To investigate the genetic changes associated with AML relapse, and to determine whether clonal evolution contributes to relapse, we performed whole-genome sequencing of primary tumour–relapse pairs and matched skin samples from eight patients, including unique patient identifier (UPN) 933124, whose primary tumour mutations were previously reported³. Informed consent explicit for whole-genome sequencing was obtained for all patients on a protocol approved by the Washington University Medical School Institutional Review Board. We obtained >25× haploid coverage and >97% diploid coverage for each sample (Supplementary Table 1 and Supplementary Information). These patients were from five different French–American–British haematological subtypes, with elapsed times of 235–961 days between initial diagnosis and relapse (Supplementary Table 2a, b).

Candidate somatic events in the primary tumour and relapse genomes were identified^{4,5} and selected for hybridization capture-based validation using methods described in Supplementary Information. Deep sequencing of the captured target DNAs from skin (the matched normal tissue), primary tumour and relapse tumour specimens⁶ (Supplementary Table 3) yielded a median of 590-fold coverage per site. The average number of mutations and structural variants was 539 (range 118–1,292) per case (Fig. 1a).

The general approach for relapse analysis is exemplified by the first sequenced case (UPN 933124). A total of 413 somatic events from tiers

1 to 3 were validated (see ref. 7 for tier designations; Supplementary Fig. 1a and Supplementary Tables 4a and 5). Of these, 78 mutations were relapse-specific (63 point mutations, 1 dinucleotide mutation, 13 indels and 1 translocation; relapse-specific criteria described in Supplementary Information and shown in Supplementary Fig. 1b), 5 point mutations were primary-tumour-specific, and 330 (317 point mutations and 13 indels) were shared between the primary tumour and relapse samples (Fig. 1a, b and Supplementary Fig. 2). The skin sample was contaminated with leukaemic cells for this case (peripheral white blood cell count was 105,000 cells mm⁻³ when the skin sample was banked), with an estimated tumour content in the skin sample of 29% (Supplementary Information). In addition to the ten somatic non-synonymous mutations originally reported for the primary tumour sample³, we identified one deletion that was not detected in the original analysis (*DNMT3A* L723fs (ref. 8)) and three mis-sense mutations previously misclassified as germline events (*SMC3* G662C, *PDXDC1* E421K and *TTN* E14263K) (Fig. 1b, Table 1 and Supplementary Table 4b).

A total of 169 tier 1 coding mutations (approximately 21 per case) were identified in the eight patients (Table 1 and Supplementary Tables 4b and 6), of which 19 were relapse-specific. In addition to mutations in known AML genes such as *DNMT3A* (ref. 8), *FLT3* (ref. 9), *NPM1* (ref. 10), *IDH1* (ref. 7), *IDH2* (ref. 11), *WT1* (ref. 12), *RUNX1* (refs 13, 14), *PTPR* (ref. 3), *PHF6* (ref. 15) and *ETV6* (ref. 16) in these eight patients, we also discovered novel, recurring mutations in *WAC*, *SMC3*, *DIS3*, *DDX41* and *DAXX* using 200 AML cases whose exomes were sequenced as part of the Cancer Genome Atlas AML project (Table 1, Supplementary Table 4b and Supplementary Fig. 3; T.J.L., R.K.W. and The Cancer Genome Atlas working group on AML, unpublished data). Details regarding the novel, recurrently mutated genes are provided in Table 1, Supplementary Tables 4b and 7 and Supplementary Figs 3 and 4. Structural and functional analyses of structural variants are presented in the Supplementary Information (Supplementary Figs 5–10 and Supplementary Tables 2, 8 and 9).

The generation of high-depth sequencing data allowed us to quantify accurately mutant allele frequencies in all cases, permitting estimation of the size of tumour clonal populations in each AML sample. On the basis of mutation clustering results, we inferred the identity of four clones having distinct sets of mutations (clusters) in the primary tumour of AML1/UPN 933124 (Supplementary Information). The median mutant allele frequencies in the primary tumour for clusters 1 to 4 were 46.86%, 24.89%, 16.00% and 2.39%, respectively (Fig. 1b and Supplementary Table 5c). Clone 1 is the ‘founding’ clone (that is, the other subclones are derived from it), containing the cluster 1 mutations; assuming that nearly all of these mutations are heterozygous, they must

¹The Genome Institute, Washington University, St Louis, Missouri 63108, USA. ²Department of Genetics, Washington University, St Louis, Missouri 63110, USA. ³Department of Internal Medicine, Division of Oncology, Washington University, St Louis, Missouri 63110, USA. ⁴Siteman Cancer Center, Washington University, St Louis, Missouri 63110, USA. ⁵Department of Pathology and Immunology, Washington University, St Louis, Missouri 63110, USA. ⁶Division of Biostatistics, Washington University, St Louis, Missouri 63110, USA.

*These authors contributed equally to this work.

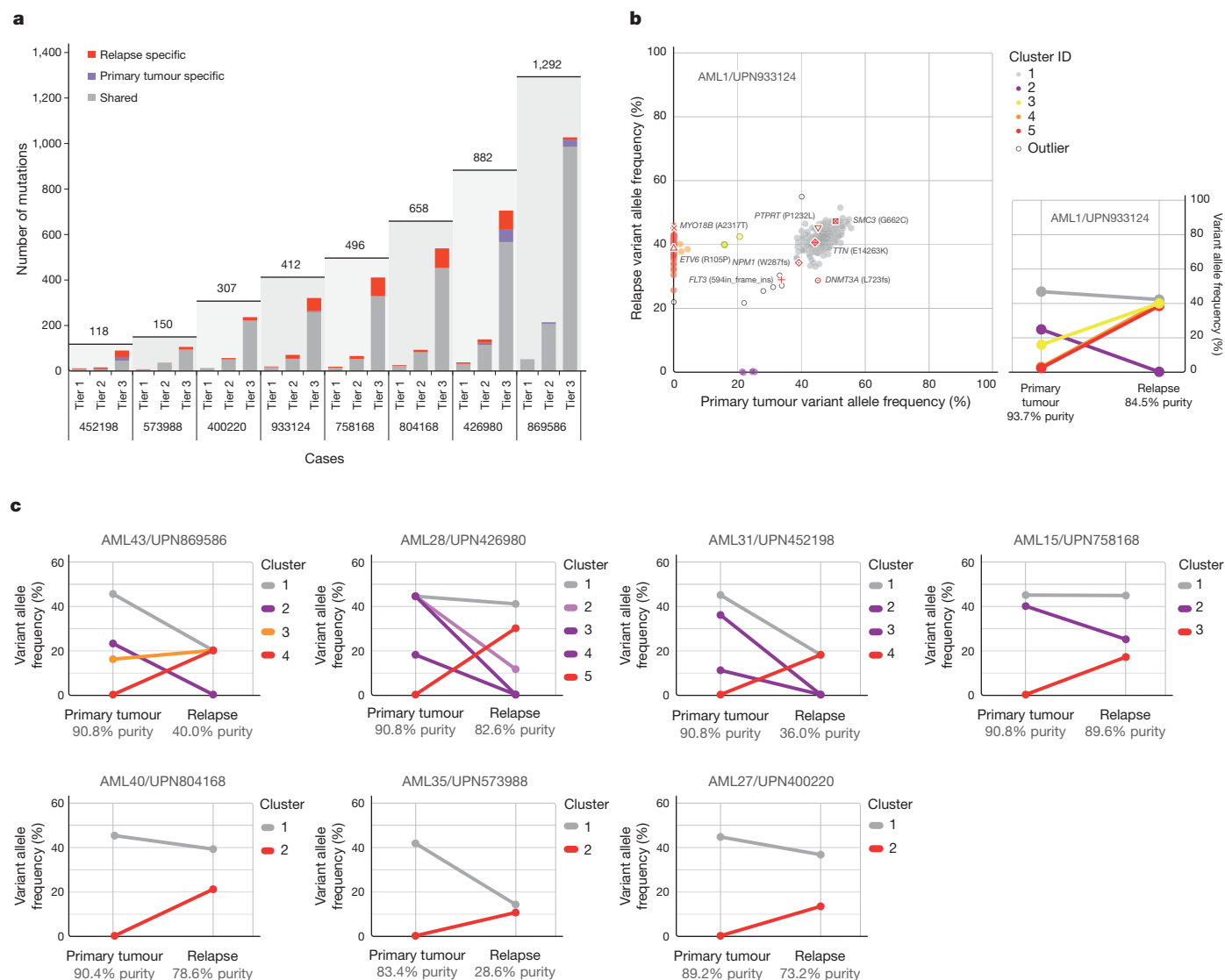


Figure 1 | Somatic mutations quantified by deep sequencing of capture validation targets in eight acute myeloid leukaemia primary tumour and relapse pairs. **a**, Summary of tier 1–3 mutations detected in eight cases (not including translocations). All mutations shown were validated using capture followed by deep sequencing. Shared mutations are in grey, primary tumour-specific mutations in blue and relapse-specific mutations in red. The total number of tier 1–3 mutations for each case is shown above the light-grey rectangle. **b**, Mutant allele frequency distribution of validated mutations from tier 1–3 in the primary tumour and relapse of case UPN 933124 (left). Mutant allele frequencies for five primary-tumour-specific mutations were obtained from a 454 deep read-count experiment. Four mutation clusters were identified

in the primary tumour, and one was found at relapse. Five low-level mutations in both the primary tumour and relapse (including four residing in known copy number variable regions) were excluded from the clustering analysis. Non-synonymous mutations from genes that are recurrently mutated in AML are shown. The change of mutant allele frequencies for mutations from the five clusters is shown (right) between the primary tumour and relapse. The orange and red lines are superimposed. **c**, The mutation clusters detected in the primary tumour and relapse samples from seven additional AML patients. The relationship between clusters in the primary tumour and relapse samples are indicated by lines linking them.

Table 1 | Coding mutations identified in eight primary tumour–relapse pairs

UPN	Total tier 1 mutations (primary/relapse)	Recurrently mutated genes in primary tumour	Relapse-specific non-synonymous somatic mutations
452198	9/9	<i>DNMT3A, NPM1, FLT3, IDH1</i>	None
573988	6/8	<i>NPM1, IDH2</i>	<i>STOX2</i>
804168	22/26	<i>FLT3, WT1, PHF6, FAM5C, TTC39A</i>	<i>SLC25A12, RIPK4, ABCD2</i>
933124	14/17	<i>DNMT3A, NPM1, FLT3, TTN, SMC3, PTPRT</i>	<i>ETV6*, MYO18B*, WAC*†, STK4</i>
400220	12/13	<i>FLT3, RUNX1, WT1, PLEKHH1</i>	None
426980	32/35	<i>IDH2, MYO1F, DDX4</i>	<i>GBP4, DCLK1, IDH2*, DCLK1*, ZNF260</i>
758168	15/19	<i>DNAH9, DIS3, CNTN5, PML-RARA†</i>	<i>ENSG00000180144, DAGLA*</i>
869586	51/50	<i>RUNX1, WT1, TTN, PHF6, NF1, SUZ12, NCOA7, EED, DAXX, ACSS3, WAC, NUMA1</i>	None

Tier 1 mutation counts exclude RNA genes.

* Recurrent mutations occurring in relapse sample.

† Translocations were not included in tier 1 mutation counts.

be present in virtually all the tumour cells at presentation and at relapse, as the variant frequency of these mutations is $\sim 40\text{--}50\%$. Clone 2 (with cluster 2 mutations) and clone 3 (with cluster 3 mutations) must be derived from clone 1, because virtually all the cells in the sample contain the cluster 1 mutations (Fig. 2a). It is likely that a single cell from clone 3 gained a set of mutations (cluster 4) to form clone 4: these survived chemotherapy and evolved to become the dominant clone at relapse. We do not know whether any of the cluster 4 mutations conferred chemotherapy resistance; although none had translational consequences, we cannot rule out a relevant regulatory mutation in this cluster.

Assuming that all the mutations detected are heterozygous in the primary tumour sample (with a malignant cellular content at 93.72% for the primary bone marrow sample, see Supplementary Information), we were able to calculate the fraction of total malignant cells in each clone. Clone 1 is the founding clone; 12.74% of the tumour cells contain only this set of mutations. Clones 2, 3 and 4 evolved from clone 1. The additional mutations in clones 2 and 3 may have provided a growth or survival advantage, as 53.12% and 29.04% of the tumour cells belonged to these clones, respectively. Only 5.10% of the tumour cells were from clone 4, indicating that it may have arisen last (Fig. 2a). However, the relapse clone evolved from clone 4. A single clone

containing all of the cluster 5 mutations was detected in the relapse sample; clone 5 evolved from clone 4, but gained 78 new somatic alterations after sampling at day 170. As all mutations in clone 5 appear to be present in all relapse tumour cells, we suspect that one or more of the mutations in this clone provided a strong selective advantage that contributed to relapse. The *ETV6* mutation, the *MYO18B* mutation, and/or the *WNK1-WAC* fusion are the most likely candidates, as *ETV6*, *MYO18B* and *WAC* are recurrently mutated in AML.

We evaluated the mutation clusters in the seven additional primary tumour–relapse pairs by assessing peaks of allele frequency using kernel density estimation (Supplementary Fig. 11 and Supplementary Information). We thus inferred the numbers and malignant fractions of clones in each primary tumour and relapse sample. Similar to UPN 933124, multiple mutation clusters (2–4) were present in each of the primary tumours from four patients (UPN 869586, UPN 426980, UPN 452198 and UPN 758168). However, only one major cluster was detected in each of the primary tumours from the three other patients (UPN 804168, UPN 573988 and UPN 400220) (Fig. 1c and Supplementary Table 10). Importantly, all eight patients gained relapse-specific mutations, although the number of clusters in the relapse samples varied (Fig. 1).

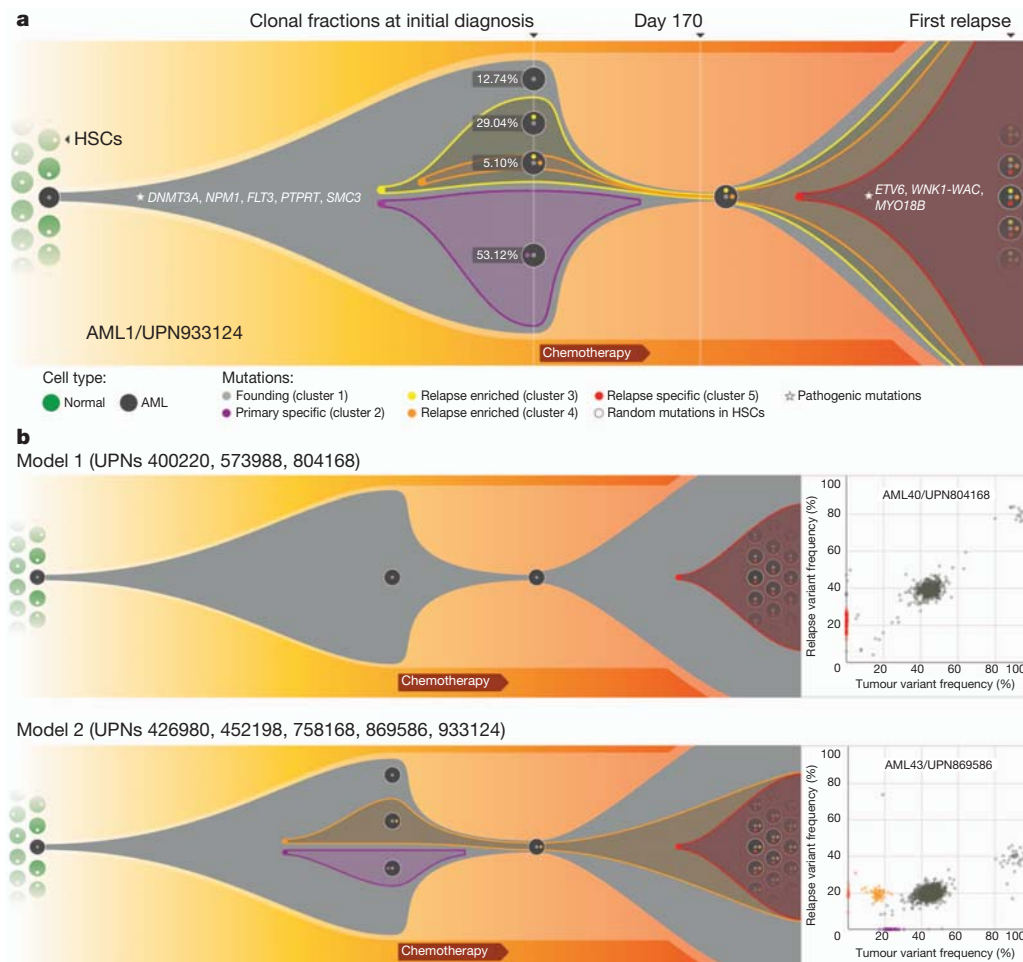


Figure 2 | Graphical representation of clonal evolution from the primary tumour to relapse in UPN 933124, and patterns of tumour evolution observed in eight primary tumour and relapse pairs. a, The founding clone in the primary tumour in UPN 933124 contained somatic mutations in *DNMT3A*, *NPM1*, *PTPRT*, *SMC3* and *FLT3* that are all recurrent in AML and probably relevant for pathogenesis; one subclone within the founding clone evolved to become the dominant clone at relapse by acquiring additional mutations, including recurrent mutations in *ETV6* and *MYO18B*, and a *WNK1-WAC* fusion gene. HSC, haematopoietic stem cell. **b,** Examples of the

two major patterns of tumour evolution in AML. Model 1 shows the dominant clone in the primary tumour evolving into the relapse clone by gaining relapse-specific mutations; this pattern was identified in three primary tumour and relapse pairs (UPN 804168, UPN 573988 and UPN 400220). Model 2 shows a minor clone carrying the vast majority of the primary tumour mutations survived and expanded at relapse. This pattern was observed in five primary tumour and relapse pairs (UPN 933124, UPN 452198, UPN 758168, UPN 426980 and UPN 869586).

Two major patterns of clonal evolution were detected at relapse (Fig. 2b and Supplementary Fig. 3): in cases with pattern 1, the dominant clone in the primary tumour gained additional mutations and evolved into the relapse clone (UPN 804168, UPN 573988 and UPN 400220). These patients may simply be inadequately treated (for example, elderly patients who cannot tolerate aggressive consolidation, like UPN 573988), or they may have mutations in their founding clones (or germline variants) that make these cells more resistant to therapy (UPN 804168 and UPN 400220). In patients with pattern 2, a minor subclone carrying the vast majority (but not all) of the primary tumour mutations survived, gained mutations, and expanded at relapse; a subset of primary tumour mutations was often eradicated by therapy, and were not detected at relapse (UPN 758168, UPN 933124, UPN 452198, UPN 426980 and UPN 869586). Specific mutations in a key subclone may contribute to chemotherapy resistance, or the mutations important for relapse may be acquired during tumour evolution, or both. Notably, in cases 426980 and 758168, a second primary tumour clone survived chemotherapy and was also present at relapse (Fig. 1c and Supplementary Fig. 3). Owing to current technical limits in our ability to detect mutations in rare cells (mostly related to currently achievable levels of coverage with whole genome sequencing), our models represent a minimal estimate of the clonal heterogeneity in AML.

All eight patients received cytarabine and anthracycline for induction therapy, and additional cytotoxic chemotherapy for consolidation; treatment histories are summarized in Supplementary Table 2 and described in Supplementary Information. To investigate the potential impact of treatment on relapse mutation types, we compared the six classes of transition and transversion mutations in the primary tumour with the relapse-specific mutations in all eight patients (Fig. 3a). Although C•G→T•A transitions are the most common mutations found in both primary and relapse AML genomes, their frequencies are significantly different between the primary tumour mutations (51.1%) and relapse-specific mutations (40.5%) ($P = 2.99 \times 10^{-7}$). Moreover, we observed an average of 4.5%, 5.3% and 4.2% increase in A•T→C•G ($P = 9.13 \times 10^{-7}$), C•G→A•T ($P = 0.00312$) and C•G→G•C ($P = 0.00366$) transversions, respectively, in relapse-specific mutations. Notably, an increased A•T→C•G transversion rate has also been observed in cases of chronic lymphocytic leukaemia with mutated immunoglobulin genes¹⁷. C•G→A•T transversions are the most common mutation in lung cancer patients who were exposed to tobacco-borne carcinogens¹⁸ (Fig. 3b and Supplementary Table 11). We

examined the 456 relapse-specific mutations and 3,590 primary tumour point mutations from all eight cases as a group, and found that the transversion frequency is significantly higher for relapse-specific mutations (46%) than for primary tumour mutations (30.7%) ($P = 3.71 \times 10^{-11}$), indicating that chemotherapy has a substantial effect on the mutational spectrum at relapse. Similar results were obtained when we limited the analysis to the 213 mutations that had 0% variant frequency in the primary tumour samples (Supplementary Fig. 1b); the transversion frequency for relapse-specific mutations was 50.4%, versus 31.4% for primary tumour samples ($P = 3.89 \times 10^{-9}$). Very few copy-number alterations were detected in the eight relapse samples, suggesting that the increased transversion rate is not associated with generalized genomic instability (Supplementary Fig. 12).

We first described the use of deep sequencing to define precisely the variant allele frequencies of the mutations in the AML genome of case 933124 (ref. 3), and here have refined and extended this technique to examine clonal evolution at relapse. The analysis of eight primary AML and relapse pairs has revealed unequivocal evidence for a common origin of tumour subpopulations; a dominant mutation cluster representing the founding clone was discovered in the primary tumour sample in all cases. The relationship of the founding clone (and subclones thereof) to the 'leukaemia initiating cell' is not yet clear—purification of clonal populations and functional testing would be required to establish this relationship. We observed the loss of primary tumour subclones at relapse in four of eight cases, suggesting that some subclones are indeed eradicated by therapy (Figs 1 and 2 and Supplementary Fig. 3). Some mutations gained at relapse may alter the growth properties of AML cells, or confer resistance to additional chemotherapy. Regardless, each tumour displayed clear evidence of clonal evolution at relapse and a higher frequency of transversions that were probably induced by DNA damage from chemotherapy. Although chemotherapy is required to induce initial remissions in AML patients, our data also raise the possibility that it contributes to relapse by generating new mutations in the founding clone or one of its subclones, which then can undergo selection and clonal expansion. These data demonstrate the critical need to identify the disease-causing mutations for AML, so that targeted therapies can be developed that avoid the use of cytotoxic drugs, many of which are mutagens.

This study extends the findings of previous studies^{19–21}, which recently described patterns of clonal evolution in ALL patients using fluorescence *in situ* hybridization and/or copy number alterations detected by SNP arrays, and it enhances the understanding of genetic changes acquired during disease progression, as previously described for breast and pancreatic cancer metastases^{22–25}. Our data provide complementary information on clonal evolution in AML, using a much larger set of mutations that were quantified with deep sequencing; this provides an unprecedented number of events that can be used to define precisely clonal size and mutational evolution at relapse. Both ALL and AML share common features of clonal heterogeneity at presentation followed by dynamic clonal evolution at relapse, including the addition of new mutations that may be relevant for relapse pathogenesis. Clonal evolution can also occur after allogeneic transplantation (for example, loss of mismatched HLA alleles via a uniparental disomy mechanism), demonstrating that the type of therapy itself can affect clonal evolution at relapse^{26,27}. Taken together, these data demonstrate that AML cells routinely acquire a small number of additional mutations at relapse, and suggest that some of these mutations may contribute to clonal selection and chemotherapy resistance. The AML genome in an individual patient is clearly a 'moving target'; eradication of the founding clone and all of its subclones will be required to achieve cures.

METHODS SUMMARY

Illumina paired-end reads were aligned to NCBI build36 using BWA 0.5.5 (<http://sourceforge.net/projects/bio-bwa/>). Somatic mutations were identified using SomaticSniper²⁸ and a modified version of the SAMtools indel caller. Structural

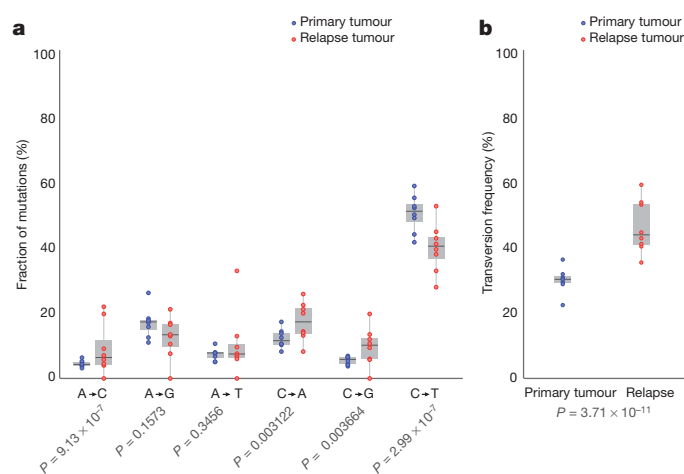


Figure 3 | Comparison of mutational classes between primary tumours and relapse samples. **a**, Fraction of the primary tumour and relapse-specific mutations in each of the transition and transversion categories. **b**, Transversion frequencies of the primary tumour and relapse-specific mutations from eight AML tumour and relapse pairs. 456 relapse-specific mutations and 3,590 primary tumour mutations from eight cases were used for assessing statistical significance using proportion tests.

variations were identified using BreakDancer⁵. All predicted non-repetitive somatic SNVs, indels and all structural variants were included on custom sequence capture arrays from Roche Nimblegen. Illumina 2 × 100-bp paired-end sequencing reads were produced after elution from capture arrays. VarScan⁶ and a read remapping strategy using Crossmatch (P. Green, unpublished data) and BWA were used for determining the validation status of predicted SNVs, indels and structural variants. A complete description of the materials and methods is provided in Supplementary Information. All sequence variants for the AML tumour samples from eight cases have been submitted to dbGaP (accession number phs000159.v4.p2).

Received 29 March; accepted 29 November 2011.

Published online 11 January 2012.

- Testa, J. R., Mintz, U., Rowley, J. D., Vardiman, J. W. & Golomb, H. M. Evolution of karyotypes in acute nonlymphocytic leukemia. *Cancer Res.* **39**, 3619–3627 (1979).
- Garson, O. M. *et al.* Cytogenetic studies of 103 patients with acute myelogenous leukemia in relapse. *Cancer Genet. Cytogenet.* **40**, 187–202 (1989).
- Ley, T. J. *et al.* DNA sequencing of a cytogenetically normal acute myeloid leukaemia genome. *Nature* **456**, 66–72 (2008).
- Li, H. *et al.* The Sequence Alignment/Map format and SAMtools. *Bioinformatics* **25**, 2078–2079 (2009).
- Chen, K. *et al.* BreakDancer: an algorithm for high-resolution mapping of genomic structural variation. *Nature Methods* **6**, 677–681 (2009).
- Koboldt, D. C. *et al.* VarScan: variant detection in massively parallel sequencing of individual and pooled samples. *Bioinformatics* **25**, 2283–2285 (2009).
- Mardis, E. R. *et al.* Recurring mutations found by sequencing an acute myeloid leukemia genome. *N. Engl. J. Med.* **361**, 1058–1066 (2009).
- Ley, T. J. *et al.* DNMT3A mutations in acute myeloid leukemia. *N. Engl. J. Med.* **363**, 2424–2433 (2010).
- Nakao, M. *et al.* Internal tandem duplication of the *flt3* gene found in acute myeloid leukemia. *Leukemia* **10**, 1911–1918 (1996).
- Falini, B. *et al.* Cytoplasmic nucleophosmin in acute myelogenous leukemia with a normal karyotype. *N. Engl. J. Med.* **352**, 254–266 (2005).
- Ward, P. S. *et al.* The common feature of leukemia-associated IDH1 and IDH2 mutations is a neomorphic enzyme activity converting alpha-ketoglutarate to 2-hydroxyglutarate. *Cancer Cell* **17**, 225–234 (2010).
- King-Underwood, L., Renshaw, J. & Pritchard-Jones, K. Mutations in the Wilms' tumor gene *WT1* in leukemias. *Blood* **87**, 2171–2179 (1996).
- Gao, J. *et al.* Isolation of a yeast artificial chromosome spanning the 8;21 translocation breakpoint t(8;21)(q22;q22.3) in acute myelogenous leukemia. *Proc. Natl Acad. Sci. USA* **88**, 4882–4886 (1991).
- Kirito, K. *et al.* A novel RUNX1 mutation in familial platelet disorder with propensity to develop myeloid malignancies. *Haematologica* **93**, 155–156 (2008).
- Van Vlierberghe, P. *et al.* PHF6 mutations in adult acute myeloid leukemia. *Leukemia* **25**, 130–134 (2011).
- Barjesteh van Waalwijk van Doorn-Khosrovani, S. *et al.* Somatic heterozygous mutations in ETV6 (TEL) and frequent absence of ETV6 protein in acute myeloid leukemia. *Oncogene* **24**, 4129–4137 (2005).
- Puente, X. S. *et al.* Whole-genome sequencing identifies recurrent mutations in chronic lymphocytic leukaemia. *Nature* **475**, 101–105 (2011).
- Ding, L. *et al.* Somatic mutations affect key pathways in lung adenocarcinoma. *Nature* **455**, 1069–1075 (2008).
- Mullighan, C. G. *et al.* Genomic analysis of the clonal origins of relapsed acute lymphoblastic leukemia. *Science* **322**, 1377–1380 (2008).
- Anderson, K. *et al.* Genetic variegation of clonal architecture and propagating cells in leukaemia. *Nature* **469**, 356–361 (2011).
- Notta, F. *et al.* Evolution of human BCR-ABL1 lymphoblastic leukaemia-initiating cells. *Nature* **469**, 362–367 (2011).
- Ding, L. *et al.* Genome remodelling in a basal-like breast cancer metastasis and xenograft. *Nature* **464**, 999–1005 (2010).
- Shah, S. P. *et al.* Mutational evolution in a lobular breast tumour profiled at single nucleotide resolution. *Nature* **461**, 809–813 (2009).
- Yachida, S. *et al.* Distant metastasis occurs late during the genetic evolution of pancreatic cancer. *Nature* **467**, 1114–1117 (2010).
- Navin, N. *et al.* Tumour evolution inferred by single-cell sequencing. *Nature* **472**, 90–94 (2011).
- Vago, L. *et al.* Loss of mismatched HLA in leukemia after stem-cell transplantation. *N. Engl. J. Med.* **361**, 478–488 (2009).
- Villalobos, I. B. *et al.* Relapse of leukemia with loss of mismatched HLA resulting from uniparental disomy after haploidentical hematopoietic stem cell transplantation. *Blood* **115**, 3158–3161 (2010).
- Larson, D. E. *et al.* SomaticSniper: identification of somatic point mutations in whole genome sequencing data. *Bioinformatics* (in the press).

Supplementary Information is linked to the online version of the paper at www.nature.com/nature.

Acknowledgements We thank the Analysis Pipeline group for developing the automated sequence analysis pipelines; the LIMS group for developing tools and software to manage samples and sequencing; the Systems group for providing the IT infrastructure and HPC solutions required for sequencing and analysis; and R. T. Demeter for experimental support. We also thank The Cancer Genome Atlas for allowing us to use unpublished data for this study, and the Washington University Cancer Genome Initiative for their support. This work was funded by grants to R.K.W. and the National Human Genome Research Institute (NHGRI U54 HG003079), and grants to T.J.L. from the National Cancer Institute (PO1 CA101937) and the Barnes-Jewish Hospital Foundation (00335-0505-02).

Author Contributions T.J.L., L.D., J.F.D., E.R.M. and R.K.W. designed the experiments. L.D. and T.J.L. led data analysis. L.D., D.E.L., C.A.M., D.C.K., J.S.W., M.D.M., J.W.W., C.L., D.S., C.C.H., K.C., H.S., J.K.-V., M.C.W., M.A.W., W.D.S., J.E.P. and S.K. performed data analysis. J.F.M., M.D.M. and L.D. prepared figures and tables. J.S.W., J.K.R., M.A.Y., T.L., R.S.F., L.L.F., V.J.M., L.S., L.C., S.D.M. and T.L.V. performed laboratory experiments. S.H. and P.W. provided samples and clinical data. D.J.D. provided informatics support. T.J.L., D.C.L., M.H.T., E.R.M., R.K.W. and J.F.D. developed project concept. L.D., T.J.L., M.J.W., T.A.G. and J.F.D. wrote the manuscript.

Author Information All sequence variants for the AML tumour samples from eight cases have been submitted to dbGaP under accession number phs000159.v4.p2. Reprints and permissions information is available at www.nature.com/reprints. This paper is distributed under the terms of the Creative Commons Attribution-Non-Commercial-Share Alike licence, and is freely available to all readers at www.nature.com/nature. The authors declare no competing financial interests. Readers are welcome to comment on the online version of this article at www.nature.com/nature. Correspondence and requests for materials should be addressed to T.J.L. (timley@wustl.edu).

Exercise-induced BCL2-regulated autophagy is required for muscle glucose homeostasis

Congcong He^{1,2,3*}, Michael C. Bassik^{4†}, Viviana Moresi⁵, Kai Sun^{2,6}, Yongjie Wei^{1,2,3}, Zhongju Zou^{1,2,3}, Zhenyi An^{1,2}, Joy Loh⁷, Jill Fisher⁴, Qihua Sun^{1,2}, Stanley Korsmeyer^{4‡}, Milton Packer⁸, Herman I. May², Joseph A. Hill², Herbert W. Virgin⁷, Christopher Gilpin⁹, Guanghua Xiao⁸, Rhonda Bassel-Duby⁵, Philipp E. Scherer^{2,6} & Beth Levine^{1,2,3,10}

Exercise has beneficial effects on human health, including protection against metabolic disorders such as diabetes¹. However, the cellular mechanisms underlying these effects are incompletely understood. The lysosomal degradation pathway, autophagy, is an intracellular recycling system that functions during basal conditions in organelle and protein quality control². During stress, increased levels of autophagy permit cells to adapt to changing nutritional and energy demands through protein catabolism³. Moreover, in animal models, autophagy protects against diseases such as cancer, neurodegenerative disorders, infections, inflammatory diseases, ageing and insulin resistance^{4–6}. Here we show that acute exercise induces autophagy in skeletal and cardiac muscle of fed mice. To investigate the role of exercise-mediated autophagy *in vivo*, we generated mutant mice that show normal levels of basal autophagy but are deficient in stimulus (exercise- or starvation)-induced autophagy. These mice (termed BCL2 AAA mice) contain knock-in mutations in BCL2 phosphorylation sites (Thr69Ala, Ser70Ala and Ser84Ala) that prevent stimulus-induced disruption of the BCL2–beclin-1 complex and autophagy activation. BCL2 AAA mice show decreased endurance and altered glucose metabolism during acute exercise, as well as impaired chronic exercise-mediated protection against high-fat-diet-induced glucose intolerance. Thus, exercise induces autophagy, BCL2 is a crucial regulator of exercise- (and starvation)-induced autophagy *in vivo*, and autophagy induction may contribute to the beneficial metabolic effects of exercise.

To investigate whether autophagy is induced by exercise, we analysed tissues of mice that transgenically express a green fluorescent protein (GFP)-labelled marker of autophagosomes, GFP-LC3 (LC3 is also known as MAP1LC3) (ref. 7), after treadmill exercise. In both skeletal and cardiac muscle, autophagosome (GFP-LC3 puncta) numbers increased after 30 min (~300 m) of running and reached a plateau at 80 min (~900 m) (Fig. 1a–c). This was observed in several muscle groups, including the vastus lateralis (thigh muscle) (Fig. 1a–c), soleus, tibialis anterior and extensor digitorum longus (Supplementary Fig. 1). Exercise also resulted in biochemical evidence of skeletal and cardiac muscle autophagy, including conversion of the non-lipidated form of LC3, LC3-I, to the autophagosome-membrane-associated lipidated form, LC3-II, and degradation of the autophagy substrate protein p62 (Fig. 1d). In addition, exercise induced autophagy in other organs involved in glucose and energy homeostasis, such as liver and pancreas, including islet β -cells (Supplementary Fig. 2a–f) and (based on LC3-II conversion) adipose tissue (Supplementary Fig. 2g). Thus, exercise is a newly defined stimulus that induces autophagy *in vivo*.

We found that exercise-induced autophagy *in vivo* involves disruption of the BCL2–beclin-1 complex. BCL2 is an anti-apoptotic and anti-autophagy protein that inhibits autophagy through a direct interaction with the BH3 domain of the autophagy protein beclin 1 at the endoplasmic reticulum⁸. Disruption of the BCL2–beclin-1 complex is crucial for stimulus-induced autophagy in mammalian cells⁸. Beclin 1 immunoprecipitation with BCL2 decreased in muscle within 15 min of exercise and was barely detectable after 30 min (Fig. 1e). Dissociation of the BCL2–beclin-1 complex was not associated with phosphorylation of kinases previously linked to BCL2 phosphorylation, such as JNK and p38 MAPK⁹ (Supplementary Fig. 3).

To study the physiological functions of exercise-induced autophagy *in vivo*, we constructed mutant mice that are deficient in stimulus-induced but not basal autophagy. As phosphorylation of three sites in the non-structured loop of human BCL2 is critical for stimulus-induced autophagy *in vitro*⁸, we generated knock-in (*Bcl2*^{AAA}) mice

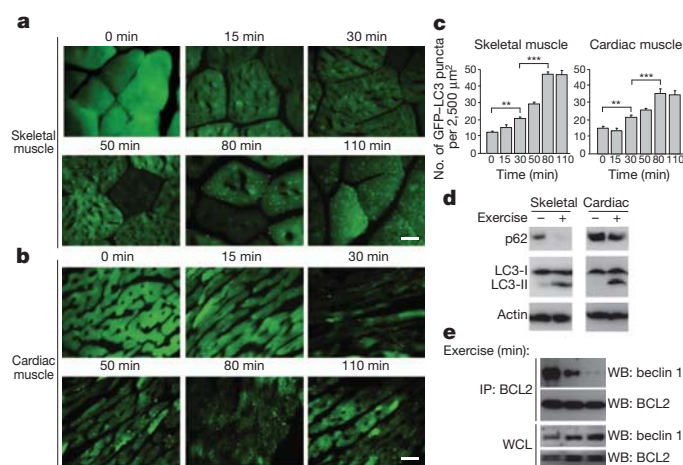


Figure 1 | Exercise induces autophagy in skeletal and cardiac muscle.

a, b, Representative images of GFP-LC3 puncta (autophagosomes) in skeletal (vastus lateralis) (**a**) and cardiac (**b**) muscle from GFP-LC3 transgenic mice at serial time points after exercise. Scale bar, 20 μ m. **c**, Quantification of data (mean \pm s.e.m. of 10 tissue sections) in **a** and **b**. ****** P < 0.01, ******* P < 0.001 (one-way ANOVA). **d**, Western blot analysis of LC3-I/II (non-lipidated and lipidated forms of MAP1LC3, respectively) and p62 levels in indicated tissue from mice at rest (–) or after maximal exercise (+). Skeletal and cardiac indicate skeletal and cardiac muscle, respectively. **e**, Co-immunoprecipitation of beclin 1 with BCL2 in muscle tissue from mice at indicated time points after exercise. IP, immunoprecipitate; WB, western blot; WCL, whole cell lysates.

¹Center for Autophagy Research, University of Texas Southwestern Medical Center, 5323 Harry Hines Boulevard, Dallas, Texas 75390, USA. ²Department of Internal Medicine, University of Texas Southwestern Medical Center, 5323 Harry Hines Boulevard, Dallas, Texas 75390, USA. ³Howard Hughes Medical Institute, University of Texas Southwestern Medical Center, 5323 Harry Hines Boulevard, Dallas, Texas 75390, USA. ⁴Dana-Farber Cancer Institute, Massachusetts 02115, USA. ⁵Department of Molecular Biology, University of Texas Southwestern Medical Center, 5323 Harry Hines Boulevard, Dallas, Texas 75390, USA. ⁶Touchstone Diabetes Center, University of Texas Southwestern Medical Center, 5323 Harry Hines Boulevard, Dallas, Texas 75390, USA. ⁷Department of Pathology and Immunology, Washington University School of Medicine, St Louis, Missouri 63110, USA. ⁸Department of Clinical Sciences, University of Texas Southwestern Medical Center, 5323 Harry Hines Boulevard, Dallas, Texas 75390, USA. ⁹Department of Cell Biology, University of Texas Southwestern Medical Center, 5323 Harry Hines Boulevard, Dallas, Texas 75390, USA. ¹⁰Department of Microbiology, University of Texas Southwestern Medical Center, 5323 Harry Hines Boulevard, Dallas, Texas 75390, USA. [†]Present address: University of California at San Francisco, San Francisco, California 94158, USA.

*These authors contributed equally to this work.

‡Deceased.

lacking three conserved phosphorylation residues in the non-structured loop region of mouse BCL2: Thr 69, Ser 70 and Ser 84 (homologous to human Ser 87) were replaced by alanines (BCL2 AAA) (Supplementary Fig. 4a–c). Homozygous *Bcl2*^{AAA} mice were viable and fertile, born in the expected Mendelian ratio, of normal size and weight, and displayed normal histology of major organs (data not shown). Steady-state levels of BCL2 AAA in *Bcl2*^{AAA} mice were similar to those of wild-type (WT) BCL2 in *Bcl2*^{WT} mice in skeletal and cardiac muscle, liver, adipose tissue and pancreas (Supplementary Fig. 4d).

Murine embryonic fibroblasts (MEFs) derived from BCL2 AAA mice showed a defect in stimulus-induced autophagy (Fig. 2a, b). In response to starvation, BCL2 underwent phosphorylation, BCL2 dissociated from beclin 1, and autophagy was induced in MEFs from isogenic wild-type mice. However, in BCL2 AAA MEFs, BCL2 phosphorylation was absent (as measured by p32 labelling), the BCL2–beclin-1 complex was not disrupted, and less autophagy was induced. Levels of basal autophagy were similar in wild-type and BCL2 AAA MEFs. Similar findings were observed *in vivo* in skeletal and cardiac muscle (Supplementary Fig. 5); autophagosome numbers were similar at baseline in wild-type and BCL2 AAA mice expressing GFP–LC3 but failed to increase in GFP–LC3 BCL2 AAA mice in response to 48 h starvation.

To evaluate whether BCL2 AAA mice are deficient in exercise-induced autophagy, we exercised GFP–LC3 wild-type mice and GFP–LC3 BCL2 AAA mice for a fixed time and fixed distance (80 min (~900 m)) and at 75% of their maximal running capacity (see Fig. 3a). Under both conditions, BCL2 AAA mice displayed marked impairment of exercise-induced upregulation of skeletal and cardiac muscle (as measured by numbers of GFP–LC3 puncta) (Fig. 2c, d and Supplementary Fig. 1b). BCL2 AAA mice also exhibited less exercise-induced LC3-II conversion and p62 degradation in skeletal and cardiac muscle (Fig. 2e), impaired autophagic responses in liver and pancreatic β -cells (Supplementary Fig. 2c, f), and defective exercise-induced dissociation of the BCL2–beclin-1 complex in muscle (Fig. 2f). Thus, non-phosphorylatable BCL2 does not alter basal autophagy *in vivo*, but prevents autophagy activation in response to starvation and exercise. This blockade of autophagy activation was not associated with increased cell death (Supplementary Fig. 6).

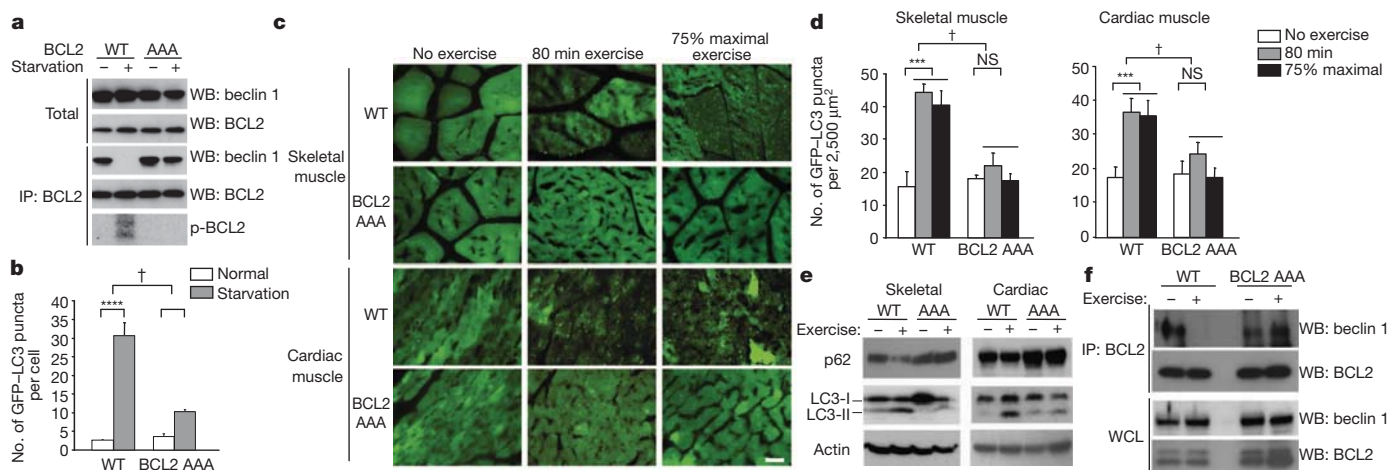


Figure 2 | Non-phosphorylatable BCL2 AAA knock-in mutations block BCL2 phosphorylation, BCL2–beclin 1 dissociation, and starvation- and exercise-induced autophagy. **a**, Analysis of BCL2 phosphorylation (detected by anti-BCL2 immunoprecipitation and autoradiography of ^{32}P -labelled cells) and beclin 1 co-immunoprecipitation with BCL2 in wild-type (WT) or BCL2 AAA MEFs grown in normal media or subjected to 4 h Earle's balanced salt solution (EBSS) starvation. p-BCL2, phospho-BCL2. **b**, Quantification of GFP–LC3 puncta (autophagosomes) in MEFs of indicated genotype in normal growth conditions or starvation conditions. Data represent mean \pm s.e.m. for 100 cells per well of triplicate samples per condition. Similar results were observed in three independent experiments. **c**, Representative images of GFP–LC3 puncta (autophagosomes) in skeletal and cardiac muscle of GFP–LC3

The deficient exercise-induced autophagy in BCL2 AAA mice was accompanied by lower maximal exercise capacity (Fig. 3a). BCL2 AAA mice had similar levels of serum lactate after maximal exercise, similar baseline muscle strength, and similar baseline cardiac function and size as wild-type mice (Supplementary Fig. 7). Characterization of various muscle groups (soleus, tibialis anterior and extensor digitorum longus) from wild-type and BCL2 AAA mice at baseline and after 80 min of exercise revealed no differences in weight, fibre cross-sectional area, morphology (haematoxylin and eosin staining), fibre type analysis, glycogen content, or mitochondrial content and functionality (Fig. 3b and Supplementary Figs 8–10). These analyses suggest that differences in baseline cardiac and skeletal muscle properties do not account for decreased exercise endurance in BCL2 AAA mice.

During strenuous exercise, mammals undergo metabolic changes to increase skeletal muscle glucose uptake/utilization efficiency, including increased insulin sensitivity and redistribution of glucose transporters, such as GLUT4 (also known as SLC2A4), to the plasma membrane^{10,11}, which is essential for exercise-stimulated glucose uptake¹². However, BCL2 AAA mice demonstrated impaired exercise-induced increase in insulin sensitivity, as reflected by less of a decline in plasma glucose (Fig. 3c) and plasma insulin (Fig. 3d) levels than in wild-type mice. Also, unlike wild-type mice, BCL2 AAA mice failed to exhibit increased plasma membrane GLUT4 localization in the vastus lateralis and soleus muscles following maximal or 80 min exercise, respectively (Fig. 3e and Supplementary Figs 11a and 12a) and they exhibited lower levels of radiolabelled glucose uptake in soleus muscle (Fig. 3h).

Adenosine monophosphate-activated protein kinase (AMPK) has a central role in enhanced GLUT4 plasma membrane localization and skeletal muscle glucose uptake during exercise¹³. BCL2 AAA mice had a notable decrease in AMPK activation, as measured by levels of phosphorylation at residue threonine 172, in both the vastus lateralis (Fig. 3f and Supplementary Fig. 11b) and in the soleus (Supplementary Fig. 12b) muscles. Phosphorylation of the downstream AMPK target acetyl-CoA carboxylase (ACC) paralleled AMPK phosphorylation (Supplementary Fig. 13), providing additional support for a defect in exercise-induced AMPK activation in BCL2 AAA mice.

wild-type and GFP–LC3 BCL2 AAA mice before exercise, after 80 min exercise, or after 75% of maximal exercise capacity. Scale bar, 20 μm . **d**, Quantification of data (mean \pm s.d. of 4 mice per experimental group) in **c**. **e**, Western blot analysis of LC3-I/II and p62 levels in indicated tissue from mice of indicated genotype at rest (–) or after maximal exercise (+). Skeletal and cardiac indicate skeletal and cardiac muscle, respectively. **f**, Co-immunoprecipitation of beclin 1 with BCL2 in muscle tissue from mice of indicated genotype at rest (–) or after 30 min of exercise. WCL, whole cell lysates. NS, not significant. * $P < 0.05$, ** $P < 0.01$, *** $P < 0.001$, one-way ANOVA for comparison between groups; † $P < 0.001$, two-way ANOVA for comparison of magnitude of changes between different groups in mice of different genotypes.

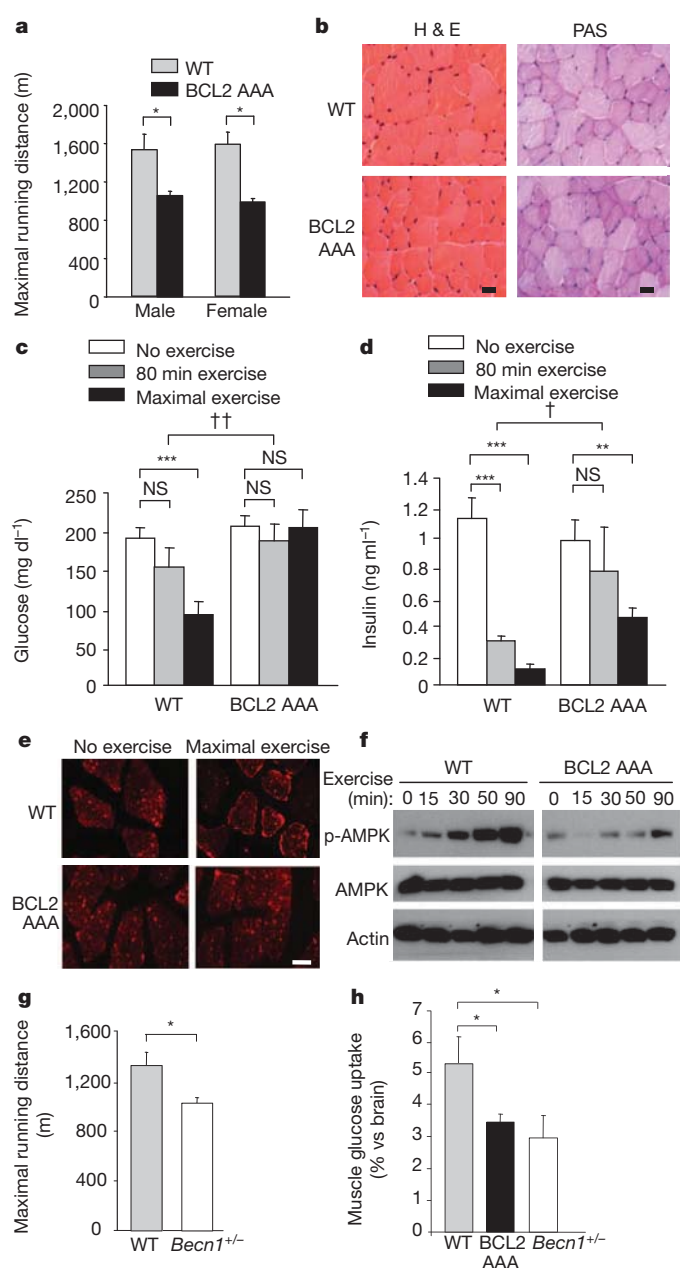


Figure 3 | BCL2 AAA mice show deficient exercise endurance and alterations in muscle glucose metabolism. **a**, Maximal treadmill running distance for mice of indicated genotype. Data represent mean \pm s.e.m. of 5 mice per group. **b**, Representative haematoxylin and eosin (H & E) and periodic acid-Schiff (PAS) staining in tibialis anterior muscle sections from mice of indicated genotype. Scale bar, 20 μ m. **c**, **d**, Plasma glucose (**c**) and insulin (**d**) levels in mice of indicated genotype at rest, after 80 min exercise (\sim 900 m), or maximal exercise. Data represent combined mean \pm s.e.m. for 9–11 mice per group from three independent cohorts; similar results were observed in each cohort. **e**, Representative images of GLUT4 immunofluorescence staining in vastus lateralis muscle of mice of indicated genotype before and after maximal exercise. Scale bar, 20 μ m. For **b** and **e**, similar results were observed in 3 mice per group. **f**, Western blot analysis of AMPK phosphorylation (p-AMPK (Thr 172)) in vastus lateralis muscle lysates from mice of indicated genotype at indicated time after exercise. **g**, Maximal treadmill running distance for mice of indicated genotype. Data represent mean \pm s.e.m. of 4–6 male mice per group. **h**, Soleus muscle 14 C-deoxyglucose uptake during treadmill exercise in mice of indicated genotype. Data represent mean \pm s.e.m. of 3 mice per group. * $P < 0.05$, ** $P < 0.01$, *** $P < 0.001$, one-way ANOVA for comparison between groups; † $P < 0.05$, †† $P < 0.01$, two-way ANOVA for comparison of magnitude of changes between different groups in mice of different genotypes. NS, not significant.

No differences were observed in phosphorylation of CaMK1, a downstream target of the Ca^{2+} -stimulated kinase CaMKK β (which is upstream of AMPK in certain contexts)¹³ (Supplementary Fig. 13b), suggesting that differences in levels of AMPK activation between wild-type and BCL2 AAA mice are not due to altered Ca^{2+} homeostasis. They are also probably unrelated to possible effects of BCL2 on mitochondrial function, because phosphorylated BCL2 resides at the endoplasmic reticulum¹⁴ and markers of mitochondrial function did not differ in the muscles of BCL2 AAA and wild-type mice (Supplementary Fig. 10). Differences in insulin signalling molecules also did not explain the altered glucose homeostasis in exercised BCL2 AAA mice, because at late time points during exercise, decreased (not increased) AKT activation and mTOR activation was observed in muscle of both wild-type and BCL2 AAA mice (Supplementary Fig. 13a). No differences were observed in muscle phosphorylation of the AKT substrate AS160 (also known as TBC1D4), or levels of the muscle-specific forkhead transcription factor target atrogin 1 (also known as FBXO32), in response to exercise or between genotypes.

To confirm that the observed defects in exercise-induced endurance and muscle glucose metabolism are due to defective autophagy, we examined mice with allelic loss of the autophagy gene beclin 1 (*Becn1*), which have decreased beclin 1 protein expression and decreased starvation-induced autophagy in skeletal muscle¹⁵. Similar to BCL2 AAA mice, *Becn1*^{+/-} mice exhibited deficient exercise-induced autophagy in skeletal muscle (Supplementary Fig. 14a, b), normal muscle strength (Supplementary Fig. 14c), decreased maximal treadmill running distance (Fig. 3g), impaired exercise-induced GLUT4 plasma membrane localization (Supplementary Fig. 14d) and muscle glucose uptake (Fig. 3h), and lower levels of exercise-induced muscle AMPK activation (phospho-AMPK and its target, phospho-ACC) (Supplementary Fig. 14e) than wild-type controls. The similarity of the phenotypes of BCL2 AAA and *Becn1*^{+/-} mice provides strong support for a role of deficient beclin 1 activity, rather than other BCL2-regulated functions, in the impairment of exercise endurance, glucose uptake and AMPK activation in BCL2 AAA mice.

AMPK activates autophagy in response to low energy conditions by sensing the cellular ratio of AMP to ATP¹³. Deficient AMPK activation in BCL2 AAA and *Becn1*^{+/-} mice during exercise raised the possibility that, similar to observations *in vitro*¹⁶, the autophagy pathway may function *in vivo* in a feed-forward manner in AMPK activation. To evaluate whether impaired exercise-induced AMPK activation *in vivo* is due to deficient autophagy, rather than potential autophagy-independent effects of the BCL2 AAA mutation or monoallelic loss of beclin 1, we examined exercise-induced AMPK activation in *Atg16l1*^{HM} mice that are hypomorphic for ATG16L1 (ref. 17), an essential autophagy protein that specifies the LC3 lipidation site for autophagosomal membrane biogenesis¹⁸. *Atg16l1*^{HM} mice had a significant reduction in ATG16L1 protein expression in skeletal muscle and a defect in exercise-induced autophagy in muscle lysates after 80 min of exercise (Supplementary Fig. 15a, b). This defect in exercise-induced autophagy was associated with decreased exercise-induced AMPK phosphorylation and ACC phosphorylation (Supplementary Fig. 15c).

Together, our *in vivo* studies in BCL2 AAA, *Becn1*^{+/-} and *Atg16l1*^{HM} mice suggest that cellular autophagy function is partially required for normal levels of exercise-induced muscle AMPK activation. The mechanism underlying this requirement is not yet known, but is unlikely to be caused by non-specific effects of the mouse mutations on AMPK activation as the direct AMPK activator, the AMP analogue 5-aminoimidazole-4-carboxamide riboside (AICAR), induced AMPK activation normally in BCL2 AAA, *Becn1*^{+/-} and *Atg16l1*^{HM} MEFs (Supplementary Fig. 16).

We next examined whether exercise-induced autophagy is required for the beneficial metabolic effects of long-term exercise training, using a high-fat diet (HFD) model of obesity and impaired glucose tolerance^{6,19}. Age-matched cohorts of wild-type and BCL2 AAA mice were fed a HFD

for four weeks; the HFD was continued for an additional 8 weeks either combined with 50 min of daily treadmill exercise or with no exercise (Supplementary Fig. 17a). In both wild-type and BCL2 AAA mice, HFD led to body weight gain (Supplementary Fig. 17b), which was probably due to increased fat mass (Supplementary Fig. 18a), as no differences in lean mass or muscle fibre size were observed (Supplementary Fig. 18). HFD led to modest suppression of baseline autophagy in skeletal and cardiac muscle as measured by levels of LC3-II conversion and p62 in tissue lysates (Supplementary Fig. 19). Ultrastructural analyses of the liver and pancreas did not reveal any differences in HFD versus regular diet animals, in wild-type versus BCL2 AAA mice, or in non-exercised versus exercised animals, except for hepatic lipid droplet accumulation in all HFD-fed groups (Supplementary Fig. 20). Although BCL2 AAA mice were more sensitive to HFD-induced obesity, 8 weeks of daily exercise reduced the magnitude of weight gain similarly in BCL2 AAA and wild-type mice (Supplementary Fig. 17b). Thus, the BCL2 AAA mutation did not alter the response of mice to HFD with respect to muscle fibre size, the morphology of liver and pancreas, or the effect of exercise on HFD-induced obesity.

However, BCL2 AAA mice failed to exhibit normal exercise-induced protection against HFD-induced impaired glucose tolerance. Before the administration of HFD, wild-type and BCL2 AAA mice had similar clearance rates in oral glucose tolerance tests (Fig. 4a). Four weeks of HFD led to impaired glucose tolerance in both genotypes versus regular diet control groups (Fig. 4b); the magnitude of this impairment was similar in BCL2 AAA and wild-type mice despite more weight gain in the BCL2 AAA mice. However, exercise training markedly improved glucose tolerance in HFD-fed wild-type mice but

not in autophagy-deficient BCL2 AAA mice (Fig. 4c and Supplementary Fig. 21). This failure of BCL2 AAA mice to show improved glucose tolerance is unlikely to be due to deficient insulin production, because at the end of the study HFD-fed wild-type and BCL2 AAA mice displayed similar circulating fasting insulin levels (Supplementary Fig. 22a), similar levels of insulin secretion in response to oral glucose challenge (Supplementary Fig. 22b), and similar pancreatic β -cell morphology (Supplementary Fig. 20b). These results suggest that BCL2-regulated functions are essential for chronic exercise-mediated protection against HFD-induced glucose intolerance. We speculate that, as in acute exercise, this may involve the dynamic interplay of autophagy induction and AMPK activation.

HFD-induced obesity is associated with several other metabolic changes, including increased levels of serum leptin, an appetite-inhibiting adipokine;²⁰ reduced levels of circulating adiponectin²¹, an antidiabetic adipokine^{22–24}; and increased serum triglycerides and cholesterol. In HFD-fed mice, baseline levels of leptin were higher in BCL2 AAA mice than in wild-type mice, and 8 weeks of exercise decreased serum leptin in wild-type but not in BCL2 AAA mice (Fig. 4d). Although adiponectin levels in HFD-fed mice were similar in the non-exercised wild-type and BCL2 AAA groups, they were significantly increased in the exercised wild-type mice versus the exercised BCL2 AAA mice (Fig. 4d). Both serum triglycerides and cholesterol increased in wild-type and BCL2 AAA HFD-fed mice; with exercise, the values returned to those observed in animals fed a regular diet in wild-type but not BCL2 AAA mice (Supplementary Fig. 23). Thus, the BCL2 AAA mutation impaired the beneficial effects of exercise on metabolic changes induced by a HFD.

The HFD-fed, daily exercised wild-type mice were more metabolically active than their BCL2 AAA counterparts, as demonstrated by elevated levels of oxygen consumption, CO₂ production and heat generation during a 12 h night interval when the mice were not exercised (Supplementary Fig. 24a). In addition, in vastus lateralis muscle, wild-type mice had elevated induction of messenger RNA for UCP1, *Ucp1*, a mitochondrial uncoupling protein mainly expressed in brown adipose tissue that contributes to thermogenesis and energy expenditure²⁵ (Supplementary Fig. 24d). These changes were probably due to improved metabolic fitness in response to exercise rather than alterations in food intake, spontaneous physical activity, or general mitochondrial function. No differences were observed in daily food intake in exercised HFD-fed wild-type and BCL2 AAA mice (Supplementary Fig. 24b). Spontaneous physical activity was similar in HFD-fed non-exercised wild-type and BCL2 AAA mice, although there was a trend towards decreased spontaneous physical activity in the exercised BCL2 AAA mice (Supplementary Fig. 24c). No changes were observed with exercise in either genotype in mRNA levels of the skeletal muscle-expressed uncoupling proteins UCP2 or UCP3, or the mitochondrial proteins cytochrome *b* and *c* (Supplementary Fig. 24d, e).

The HFD study suggests that increased autophagy triggered by exercise may be critical for improving impaired glucose tolerance and metabolism in diet-induced obesity. However, we cannot definitely conclude that lack of exercise-induced improvement in glucose tolerance in HFD-fed BCL2 AAA mice is caused by deficient exercise-induced autophagy; it is possible that other effects of the BCL2 AAA mutation are responsible for this phenotype. Nonetheless, given our findings in acute exercise (which demonstrate impaired muscle glucose uptake, GLUT4 plasma membrane localization and AMPK activation in autophagy-deficient animals), it seems plausible that alterations in exercise-induced skeletal muscle glucose metabolism in autophagy-deficient animals may also contribute to the failure of exercise to reverse HFD-induced metabolic abnormalities.

Our findings demonstrate that exercise is a potent inducer of autophagy, and that acute and chronic exercise enhances glucose metabolism in mice capable of inducing autophagy but not in autophagy-deficient mice. These beneficial metabolic effects (as well as exercise- and starvation-induced autophagy) are blocked by a

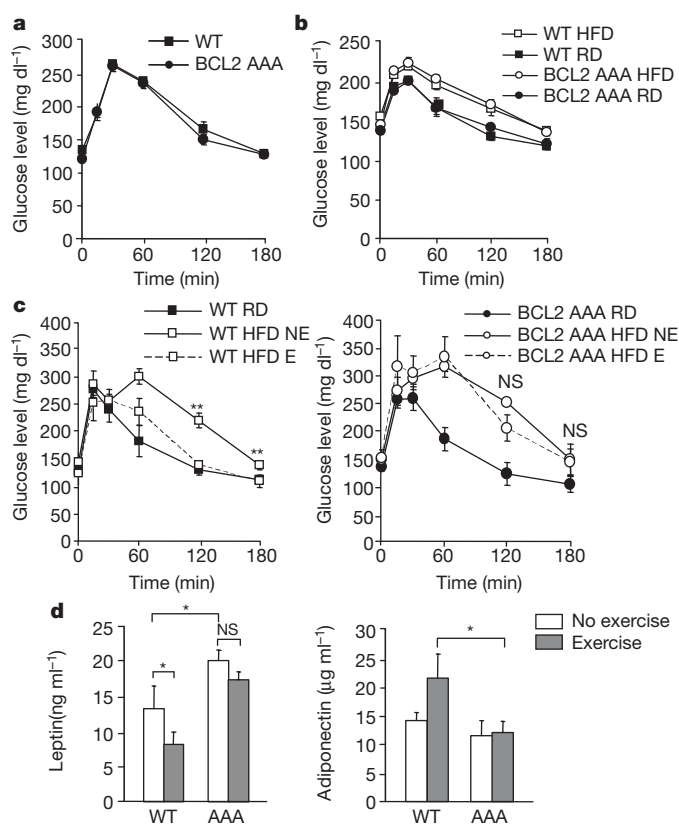


Figure 4 | Long-term exercise training protects wild-type but not BCL2 AAA mice from HFD-induced glucose intolerance. **a, b**, Oral glucose tolerance test (OGTT) before (**a**, week 0) and after (**b**, week 4) 4 weeks of HFD. **c, d**, OGTT (**c**) and serum leptin and adiponectin levels (**d**) after 8 weeks of daily exercise. For **a–d**, results represent the mean \pm s.e.m. for 4–5 mice per group. E, exercise; NE, no exercise; RD, regular diet. * $P < 0.05$, ** $P < 0.01$, (c, one-way ANOVA; d, Wilcoxon rank test). NS, not significant.

mutation in BCL2 that prevents its release from an inhibitory interaction with the autophagy protein beclin 1. Thus, BCL2 has previously undescribed essential roles in the *in vivo* regulation of stimulus-induced autophagy as well as glucose metabolism. We propose that BCL2-regulated autophagy activation contributes to the beneficial metabolic effects of exercise, and that manipulation of the autophagy pathway and/or the function of the autophagy inhibitory BCL2 protein may be a logical strategy to mimic the health effects of exercise and to prevent or treat impaired glucose metabolism. More broadly, on the basis of this newly discovered link between exercise, autophagy and altered metabolism, we speculate that autophagy may represent a cellular mechanism by which exercise prolongs life and protects against cancer, cardiovascular disorders and inflammatory diseases¹.

METHODS SUMMARY

Mouse strains. GFP–LC3 transgenic⁷, *Becn1*^{+/-} (ref. 15) and *Atg16l1*^{HM} (ref. 17) mice have been described. The generation of mice with a knock-in mutation in *Bcl2* that results in Thr69Ala, Ser70Ala and Ser84Ala mutations in BCL2 (BCL2 AAA) is described in Methods.

Exercise studies. Acute and chronic exercise studies were performed using a treadmill protocol described in Methods.

Autophagy assays. Autophagy was measured by visualizing GFP–LC3 puncta by fluorescence microscopy in MEFs or tissue sections from mice with transgenic expression of GFP–LC3, or by western blot analysis of LC3-II conversion and p62 levels in tissue lysates.

Metabolic analyses. Metabolic and blood parameters in the acute and chronic exercise studies were measured as described in Methods.

Full Methods and any associated references are available in the online version of the paper at www.nature.com/nature.

Received 22 September 2010; accepted 6 December 2011.

Published online 18 January 2012.

- Handschin, C. & Spiegelman, B. M. The role of exercise and PGC1 α in inflammation and chronic disease. *Nature* **454**, 463–469 (2008).
- Mizushima, N. & Levine, B. Autophagy in mammalian development and differentiation. *Nature Cell Biol.* **12**, 823–830 (2010).
- Kuma, A. & Mizushima, N. Physiological role of autophagy as an intracellular recycling system: with an emphasis on nutrient metabolism. *Semin. Cell Dev. Biol.* **21**, 683–690 (2010).
- Levine, B. & Kroemer, G. Autophagy in the pathogenesis of disease. *Cell* **132**, 27–42 (2008).
- Yang, L., Li, P., Fu, S., Calay, E. S. & Hotamisligil, G. S. Defective hepatic autophagy in obesity promotes ER stress and causes insulin resistance. *Cell Metab.* **11**, 467–478 (2010).
- Ebato, C. *et al.* Autophagy is important in islet homeostasis and compensatory increase of β cell mass in response to high-fat diet. *Cell Metab.* **8**, 325–332 (2008).
- Mizushima, N., Yamamoto, A., Matsui, M., Yoshimori, T. & Ohsumi, Y. *In vivo* analysis of autophagy in response to nutrient starvation using transgenic mice expressing a fluorescent autophagosome marker. *Mol. Biol. Cell* **15**, 1101–1111 (2004).
- He, C. & Levine, B. The Beclin 1 interactome. *Curr. Opin. Cell Biol.* **22**, 140–149 (2010).
- Wei, Y., Pattingre, S., Sinha, S., Bassik, M. & Levine, B. JNK1-mediated phosphorylation of Bcl-2 regulates starvation-induced autophagy. *Mol. Cell* **30**, 678–688 (2008).
- Goodyear, L. J. & Kahn, B. B. Exercise, glucose transport, and insulin sensitivity. *Annu. Rev. Med.* **49**, 235–261 (1998).
- Ryder, J. W., Chibalin, A. V. & Zierath, J. R. Intracellular mechanisms underlying increases in glucose uptake in response to insulin or exercise in skeletal muscle. *Acta Physiol. Scand.* **171**, 249–257 (2001).
- Zisman, A. *et al.* Targeted disruption of the glucose transporter 4 selectively in muscle causes insulin resistance and glucose intolerance. *Nature Med.* **6**, 924–928 (2000).
- Hardie, D. G. AMP-activated protein kinase: an energy sensor that regulates all aspects of cell function. *Genes Dev.* **25**, 1895–1908 (2011).
- Bassik, M. C., Scorrano, L., Oakes, S. A., Pozzan, T. & Korsmeyer, S. J. Phosphorylation of BCL-2 regulates ER Ca²⁺ homeostasis and apoptosis. *EMBO J.* **23**, 1207–1216 (2004).
- Qu, X. *et al.* Promotion of tumorigenesis by heterozygous disruption of the beclin 1 autophagy gene. *J. Clin. Invest.* **112**, 1809–1820 (2003).
- Malik, S. A. *et al.* BH3 mimetics activate multiple pro-autophagic pathways. *Oncogene* **30**, 3918–3928 (2011).
- Cadwell, K. *et al.* A key role for autophagy and the autophagy gene *Atg16l1* in mouse and human intestinal Paneth cells. *Nature* **456**, 259–263 (2008).
- Fujita, N. *et al.* The Atg16L complex specifies the site of LC3 lipidation for membrane biogenesis in autophagy. *Mol. Biol. Cell* **19**, 2092–2100 (2008).
- Asterholm, I. W. & Scherer, P. E. Enhanced metabolic flexibility associated with elevated adiponectin levels. *Am. J. Pathol.* **176**, 1364–1376 (2010).
- Zhang, Y. *et al.* Positional cloning of the mouse obese gene and its human homologue. *Nature* **372**, 425–432 (1994).
- Scherer, P. E., Williams, S., Fogliano, M., Baldini, G. & Lodish, H. F. A novel serum protein similar to C1q, produced exclusively in adipocytes. *J. Biol. Chem.* **270**, 26746–26749 (1995).
- Frederich, R. C. *et al.* Leptin levels reflect body lipid content in mice: evidence for diet-induced resistance to leptin action. *Nature Med.* **1**, 1311–1314 (1995).
- Van Heek, M. *et al.* Diet-induced obese mice develop peripheral, but not central, resistance to leptin. *J. Clin. Invest.* **99**, 385–390 (1997).
- Shetty, S., Kusminski, C. M. & Scherer, P. E. Adiponectin in health and disease: evaluation of adiponectin-targeted drug development strategies. *Trends Pharmacol. Sci.* **30**, 234–239 (2009).
- Almind, K., Manieri, M., Sivitz, W. I., Cinti, S. & Kahn, C. R. Ectopic brown adipose tissue in muscle provides a mechanism for differences in risk of metabolic syndrome in mice. *Proc. Natl Acad. Sci. USA* **104**, 2366–2371 (2007).

Supplementary Information is linked to the online version of the paper at www.nature.com/nature.

Acknowledgements We thank the UT Southwestern Mouse Metabolic Phenotyping Core and E. Berglund for assistance with metabolic measurements, J. Shelton for assistance with muscle stains, N. Mizushima for critical reagents, and B. D. Levine for expert advice. This work was supported by National Institutes of Health grants R01 CA109618 (B.L.), R01 HL080244 (J.A.H.), R01 HL090842 (J.A.H.), R01 AI084887 (H.W.V.), R01 DK086629 (P.E.S.), R01 CA112023 (P.E.S.) and 1P01 DK0887761 (P.E.S.).

Author Contributions C.H., M.C.B., V.M., K.S., S.K., M.P., J.A.H., H.W.V., R.B.-D., P.E.S. and B.L. designed the experiments. C.H., M.C.B., V.M., K.S., Y.W., Z.Z., Z.A., J.L., J.F., Q.S., H.I.M. and C.G. performed the experiments. G.X. performed statistical analyses. C.H. and B.L. wrote the manuscript.

Author Information Reprints and permissions information is available at www.nature.com/reprints. The authors declare no competing financial interests. Readers are welcome to comment on the online version of this article at www.nature.com/nature. Correspondence and requests for materials should be addressed to B.L. (beth.levine@utsouthwestern.edu).

METHODS

Mouse strains. GFP–LC3 transgenic, *Becn1*^{+/-} and *Atg16l1*^{HM} mice have been previously described^{7,15,17}. For the construction of a mouse strain with knock-in mutations in the phosphorylation sites in the non-structured loop of BCL2 (*Bcl2*^{AAA} mice), BAC clones (Incyte) were screened for the presence of *Bcl2* using the following primers: BCL2 5', GTGGGGCGGGAGTCGGGACT; BCL2 3', GACCCAGAATCCACTCACAC. The *Bcl2* BAC clone was digested by BglII, subcloned into pSP72, and a puromycin resistance marker flanked by FRT sites (SalI fragment of pPGKuro, cloned into pFRT) was blunt cloned into a BsaBI site 3' of exon II. A mutant allele was generated by subcloning a PstI fragment from the coding region. Amino acid residues Thr 69, Ser 70 and Ser 84 (homologous to human Ser 87) were changed to alanine in two steps using the Quickchange PCR (Stratagene) and the following primer sets: TSAA 5', GAGATGGAGTGCCAGGGCGGGCTCTCTCTCAGGCCCC; TSAA 3', GGGGCTGAGAGGAGCCGCCCTGGCAGCCATCTC; S84A 5', GCTGGGCTGCGCTCGCCCC TGTGC CACCATG; S84A 3', CATGGTGGCACAGGGGCGAGCGCAGGCCAGC. The targeting construct 7.1AAA was electroporated into RW4 embryonic stem cells (129 SvJ), and 36 h later, clones were selected with puromycin, picked and screened by Southern blot analysis with the probes indicated in Supplementary Fig. 4a. A 1.7 kb shift upwards indicative of the mutant allele was detected on Southern blots in 2/300 clones as the targeted locus (Supplementary Fig. 4b). These clones were tested for normal karyotype and used to inject blastocysts from C57BL/6J donors. Mice with germline transmission were bred to mice expressing FLP from the β -actin promoter (Jackson Laboratories: B6; SJLTgN(ACTFLPe)9205Dym), and offspring were screened for deletion of the puromycin selection marker. To screen for the presence of the mutation following excision of the selectable marker, PCR with 5' and 3' *Bcl2* primers was performed, and digestions were performed with BglI or AatII enzymes; BglI cuts the amplified fragment only if the T69AS70A site is present, while AatII cuts only the wild-type sequence for the same region (Supplementary Fig. 4c). Using this scheme, homozygous *Bcl2*^{AAA} mutants were identified by the presence of PCR fragments cleaved only by BglI and not AatII, whereas wild-type mice were identified by the presence of PCR fragments cleaved only by AatII and not BglI. *Bcl2*^{AAA} mice were backcrossed for more than ten generations to C57/B6 mice (Jackson Laboratories), and homozygous *Bcl2*^{AAA} and *Bcl2*^{WT} offspring were used in all studies.

Cell lines. Primary MEFs were established either from *Bcl2*^{AAA} and *Bcl2*^{WT} mice, the offspring of *Bcl2*^{AAA} and *Bcl2*^{WT} mice crossed with GFP–LC3 transgenic mice, *Becn1*^{+/-} and *Becn1*^{+/+} mice, and *Atg16l1*^{HM} and *Atg16l1*^{WT} at embryonic day 13.5 and cultured as described²⁶.

Radiolabelling and co-immunoprecipitation from MEFs. MEFs derived from *Bcl2*^{AAA} and *Bcl2*^{WT} mice were cultured overnight in labelling medium (phosphate-free DMEM with 10% dialysed FBS) and then cultured in starvation medium (EBSS minus phosphate) or labelling medium for 4 h containing 2 mCi ml⁻¹ ³²P-orthophosphate. Cells were lysed in lysis buffer containing 50 mM Tris (pH 7.9), 150 mM NaCl, 1 mM EDTA, 1% Triton X-100, proteinase inhibitor cocktail (Roche Applied Sciences) and halt phosphatase inhibitor cocktail (Thermo Scientific), and were subjected to immunoprecipitation with a monoclonal anti-BCL2 antibody (Santa Cruz Biotechnology, 1:50). Eluates were separated by SDS–PAGE and detected by anti-beclin 1 antibody (Santa Cruz Biotechnology, 1:200), anti-BCL2–HRP antibody (C2, Santa Cruz Biotechnology, 1:100) and autoradiography.

Co-immunoprecipitations from muscle tissue. Vastus lateralis (thigh muscle) was dissected and homogenized in lysis buffer containing 50 mM Tris (pH 7.9), 150 mM NaCl, 1 mM EDTA, 1% Triton X-100, proteinase inhibitor cocktail (Roche Applied Sciences) and halt phosphatase inhibitor cocktail (Thermo Scientific), and subjected to immunoprecipitation with a monoclonal anti-BCL2 antibody (Santa Cruz Biotechnology, 1:50). Eluates were separated by SDS–PAGE and detected by anti-beclin 1 antibody (Santa Cruz Biotechnology, 1:200) and anti-BCL2–HRP antibody (C2, Santa Cruz Biotechnology, 1:100) and autoradiography.

Mouse exercise studies. For acute exercise studies, 8-week-old (wild type, *BCL2*^{AAA} and *Atg16l1*^{HM}) or 12-week-old (*Becn1*^{+/-} and wild-type *Becn1*^{+/+} littermate) mice were acclimated to and trained on a 10° uphill Exer 3/6 open treadmill (Columbus Instruments) for 2 days. On day 1 mice ran for 5 min at 8 m min⁻¹ and on day 2 mice ran for 5 min at 8 m min⁻¹ followed by another 5 min at 10 m min⁻¹. On day 3, mice were subjected to a single bout of running starting at the speed of 10 m min⁻¹. Forty minutes later, the treadmill speed was increased at a rate of 1 m min⁻¹ every 10 min for a total of 30 min, and then increased at the rate of 1 m min⁻¹ every 5 min until mice were exhausted. Exhaustion was defined as the point at which mice spent more than 5 s on the electric shocker without attempting to resume running. Total running time was recorded and total running distance was calculated for each mouse.

For long-term exercise training, male *Bcl2*^{WT} or *Bcl2*^{AAA} mice (8 weeks old) were randomly divided into three cohorts, including: (1) mice fed a regular diet (Harlan Teklad) without daily exercise, (2) mice fed a HFD containing 60% fat

(Research Diets) without daily exercise, and (3) mice fed a HFD with daily exercise. Prior to initiation of exercise, mice were fed a HFD for 4 weeks. At the end of the fourth week, mice in the exercise groups were acclimated to treadmill running for 2 days as in the acute exercise studies, and then were trained on the treadmill with 10° uphill incline for 50 min d⁻¹, 5 d week⁻¹ at 17 m min⁻¹ for 8 weeks. Mice were given a HFD during the 8-week training period. All animal procedures were performed in accordance with institutional guidelines and with approval from the Institutional Animal Care and Use Committee.

Autophagy analyses. MEFs expressing GFP–LC3 were cultured in normal or starvation (EBSS, Earle's balanced salt solution) medium for 4 h, and GFP–LC3 puncta were quantified by fluorescence microscopy as described²⁷. For assessment of autophagy *in vivo* following starvation or exercise, 8-week-old *Bcl2*^{WT} or *Bcl2*^{AAA} GFP–LC3 mice or *Becn1*^{+/-} or *Becn1*^{+/+} GFP–LC3 mice were either subjected to starvation for 48 h or exercised for the indicated time period, anaesthetized by isoflurane, and perfused with 4% paraformaldehyde (PFA). Skeletal muscle (vastus lateralis, tibialis anterior, extensor digitorum longus and soleus), heart (left ventricle), pancreas and liver tissues were fixed in 4% PFA overnight, 15% sucrose for 4 h and 30% sucrose overnight before frozen sections were prepared. The number of GFP–LC3 puncta per unit area of tissue was quantified by fluorescence microscopy as described¹⁵. Autophagy in skeletal and cardiac muscle, liver, pancreas and adipose tissue during baseline conditions and after exercise was also analysed by western blot analysis of tissue extracts with antibodies against LC3 and p62 (see below for details).

Immunofluorescence studies. For immunofluorescence staining of frozen muscle and pancreatic sections, slides were heated at 50 °C for 10 min, rehydrated in 100%, 95% and 70% ethanol, washed 3 × 5 min in PBS, blocked with 1% goat serum and immunostained with a rabbit anti-mouse GLUT4 antibody (Alpha Diagnostic, 1:100 dilution) (muscle samples) and an Alexa Fluor 594 donkey anti-rabbit secondary antibody (Invitrogen, 1:1,000 dilution) or with a guinea pig anti-swine insulin antibody (Dako, 1:500 dilution) (pancreatic samples) and an Alexa Fluor 594 goat anti-guinea pig secondary antibody (Invitrogen, 1: 500 dilution). Immunofluorescence studies on skeletal muscle sections with anti-laminin and anti-type I myosin heavy chain antibodies were performed as previously described²⁸. Immunofluorescence images were taken using a Zeiss Axioplan2 microscope or Leica TCS SP5 confocal microscope.

Muscle morphology and function studies. Sections were stained with haematoxylin and eosin to visualize tissue architecture following standard protocols. Metachromatic ATPase staining and measurement of fibre cross-sectional area were performed as previously described²⁸. Periodic acid-Schiff staining for carbohydrates was performed according to standard protocols²⁹. Succinic dehydrogenase staining on cryosections was carried out using a 0.2 M phosphate buffer at pH 7.6. For staining, 270 mg succinic acid and 10 mg nitro blue tetrazolium were freshly dissolved in 10 ml phosphate buffer and incubated with sections for 1 h.

To measure muscle strength, a modified mesh grip assay was applied³⁰. Briefly, mice were placed on the wired mesh of cage tops. When they firmly grabbed the mesh, the cage top was flipped and held at a height of 30 cm above the bench until the mice released their grip. The time for each mouse to remain on the mesh was recorded. TUNEL staining of muscle sections to detect apoptosis was performed according to the manufacturer's instructions (ApopTag Peroxidase *In situ* Apoptosis Detection Kit, Millipore), using Sigma FAST 3,3'-diaminobenzidine (DAB) tablets as the peroxidase substrate.

Electron microscopy. Mice were euthanized, and liver and pancreas were rapidly fixed in 2.5% glutaraldehyde in 0.1 M cacodylate buffer. Electron microscopy was performed as previously described³¹.

Mouse metabolic studies and blood tests. Food intake, O₂ consumption, CO₂ production, heat production and physical activity were measured in TSE metabolic chambers (TSE Systems) over a 4 day period. Mice in the exercise group were removed from the chambers and allowed to run for 50 min daily as in the above protocol during the day (light period). Metabolic measurements were performed for 12 h daily during the dark period. Fat mass and lean tissue mass were determined using the Bruker Minispec mq10 scan system. Plasma glucose, lactate, cholesterol and triglycerides were measured using the Vitros 250 system (Ortho-Clinical Diagnostics). Plasma insulin (Crystal Chem), serum leptin (Crystal Chem) and adiponectin (Millipore) levels were determined using commercial ELISA kits. Glucose tolerance tests were performed by oral glucose injection (1 g kg⁻¹) after a 3 h fast. Blood was drawn from tail veins at the indicated time points after glucose injection and serum glucose levels were analysed using commercial glucose assay reagents (Sigma, Cat# 6918, P7119, F5803).

Echocardiography. Cardiac function was assessed by echocardiography, using a Visualsonic Vevo 2100 ultrasound machine equipped with a 30-Mhz transducer applied to the chest wall. Ventricular dimensions and ejection fraction were assessed using short axis view in two-dimensional and three-dimensional modes using the onboard VisualSonics cardiac analysis package.

Muscle glucose uptake assays. Surgical catheterization of the jugular vein was performed on each mouse. At day 4 after catheterization, mice were transferred to clean cages at 9:00 a.m. to begin a 4 h fast. Mice then ran on a treadmill for 50 min using the exercise protocol described above. At $t = 50$ min, a 13 μ Ci bolus of 14 C-deoxyglucose was injected intravenously and mice resumed running for another 25 min according to the exercise protocol described above before euthanasia. Skeletal muscle (soleus) and brain tissues were dissected and homogenized in 1.5 ml 0.5% perchloric acid. 14 C-deoxyglucose counts were determined in homogenized samples as previously described³² and muscle values were normalized to the counts in the brain.

Western blot analyses. Mouse tissue extracts were prepared by homogenizing tissues in lysis buffer containing 50 mM Tris (pH 7.9), 150 mM NaCl, 1 mM EDTA, 1% Triton X-100, proteinase inhibitor cocktail (Roche Applied Sciences) and halt phosphatase inhibitor cocktail (Pierce), and subjected to western blot analysis with anti-LC3 (Novus Biologicals, 1:500), anti-p62 (BD Biosciences, 1:500 dilution; Progen (C-terminal specific), 1:1,000 dilution). Anti-p-CaMKI (Santa Cruz Biotechnology, 1:100), anti-CaMKI (Santa Cruz Biotechnology, 1:300), anti-BCL2 (Santa Cruz Biotechnology, 1:100), anti-AMPK (Cell Signaling, 1:1,000), anti-p-AMPK (Cell Signaling, 1:1,000), anti-JNK (Cell Signaling, 1:400), anti-p-JNK (Cell Signaling, 1:500) anti-AS160 (Millipore, 1:400) anti-p-AS160 (Millipore, 1:100), anti-4E-BP1 (Cell Signaling, 1:1,000), anti-p-4E-BP1 (Cell Signaling, 1:1,000), anti-p-ACC (Millipore, 1:500) anti-AKT (Cell Signaling, 1:600), anti-p-AKT (Cell Signaling, 1:500), anti-p38 (Cell Signaling, 1:500), anti-p-p38 (Cell Signaling, 1:400), anti-atrogin-1 (ECM Biosciences, 1:400), ATG16L1 (Sigma, 1:1,000) and anti-actin (Santa Cruz Biotechnology, 1:3,000) antibodies.

For *in vitro* assessment of AMPK activation, MEFS derived from *Bcl2*^{AAA} and *Bcl2*^{WT} mice, *Becn1*^{+/-} and *Becn1*^{+/+} mice, and *Atg16l1*^{HM} and *Atg16l1*^{WT} mice were treated with 2 mM of the AMP analogue AICAR, or DMSO vehicle for 2 h. Whole-cell lysates were prepared, and AMPK and phospho-AMPK levels were determined by western blot analysis. For quantification, the relative intensity values of western blot bands were normalized to that of the first lane (set as 1) in the wild-type non-exercised group.

Statistical analyses. ANOVA approaches were used to compare values among different experimental groups for data that met the normality assumption. One-way ANOVA was used for comparison between two groups. Two-way ANOVA

was used for comparison of the magnitude of changes between two different groups in mice of two different genotypes. The normality assumption for the ANOVA model was checked using residual plots. When the assumption was violated, the data were log-transformed in order to meet the assumption. For data sets in which log transformation was inadequate to meet the analysis assumption, the non-parametric Wilcoxon rank-sum test was used.

Real-time PCR analyses. RNA isolation from muscle tissues and real-time RT-PCR were performed as previously described²⁸. The following Sybr Green primers were used: β -actin: forward, CTGGCTCCTAGCACCATGAAGAT; reverse, GGTGGACAGTGAGGCCAGGAT; UCP1: forward, TCAGGATTGGCCTCTACGAC; reverse, TAAGCCGGCTGAGATCTTGT; UCP2: forward, TGCCCGTAATGCCATTGTC; reverse, AGTGGAAGGGAGGTCATCT; cytochrome *c*: forward, GTCTGTTCGGGCGGAAGACAG; reverse, GGGGAGAGGATACCTGATGG; and cytochrome *b*: forward, ATTCATTGACCTACCTGCCC; reverse, TCTGATGTGTAGTGTATGGC. The following Tagman primers were used: PPARGC1 α (PGC1 α): Mm00447183_m1; myoglobin: Mm00442968_m1; PPARGC1 β (PGC1 β): Mm01258518_m1; MYH7 (MHC Type I): Mm00600555_m1; MYH1 (MHC Type IId/x): Mm01332488_g1; MYH2 (MHC Type IIa): Mm01332564_m1; and GAPDH: Mm99999915_g1.

26. Su, T. *et al.* Deletion of histidine triad nucleotide-binding protein 1/PKC-interacting protein in mice enhances cell growth and carcinogenesis. *Proc. Natl Acad. Sci. USA* **100**, 7824–7829 (2003).
27. Furuya, N., Yu, J., Byfield, M., Pattingre, S. & Levine, B. The evolutionarily conserved domain of Beclin 1 is required for Vps34 binding, autophagy and tumor suppressor function. *Autophagy* **1**, 46–52 (2005).
28. Moresi, V. *et al.* Myogenin and class II HDACs control neurogenic muscle atrophy by inducing E3 ubiquitin ligases. *Cell* **143**, 35–45 (2010).
29. Sheehan, D. C. & Hrapchak, D. C. *Theory and Practice of Histotechnology* 2nd edn, 162–166 (Battelle, 1980).
30. Butchbach, M., Edwards, J. & Burghes, A. Abnormal motor phenotype in the SMN $\Delta 7$ mouse model of spinal muscular atrophy. *Neurobiol. Dis.* **27**, 207–219 (2007).
31. Liang, X. H. *et al.* Induction of autophagy and inhibition of tumorigenesis by beclin 1. *Nature* **402**, 672–676 (1999).
32. Berglund, E. D. *et al.* Fibroblast growth factor 21 controls glycemia via regulation of hepatic glucose flux and insulin sensitivity. *Endocrinology* **150**, 4084–4093 (2009).

Multi-isotope imaging mass spectrometry quantifies stem cell division and metabolism

Matthew L. Steinhauser^{1,2}, Andrew P. Bailey³, Samuel E. Senyo^{1,2}, Christelle Guillermier^{2,4,5}, Todd S. Perlstein^{1,2}, Alex P. Gould³, Richard T. Lee^{1,2,6} & Claude P. Lechene^{2,4,5}

Mass spectrometry with stable isotope labels has been seminal in discovering the dynamic state of living matter^{1,2}, but is limited to bulk tissues or cells. We developed multi-isotope imaging mass spectrometry (MIMS) that allowed us to view and measure stable isotope incorporation with submicrometre resolution^{3,4}. Here we apply MIMS to diverse organisms, including *Drosophila*, mice and humans. We test the ‘immortal strand hypothesis’, which predicts that during asymmetric stem cell division chromosomes containing older template DNA are segregated to the daughter destined to remain a stem cell, thus insuring lifetime genetic stability. After labelling mice with ¹⁵N-thymidine from gestation until post-natal week 8, we find no ¹⁵N label retention by dividing small intestinal crypt cells after a four-week chase. In adult mice administered ¹⁵N-thymidine pulse-chase, we find that proliferating crypt cells dilute the ¹⁵N label, consistent with random strand segregation. We demonstrate the broad utility of MIMS with proof-of-principle

studies of lipid turnover in *Drosophila* and translation to the human haematopoietic system. These studies show that MIMS provides high-resolution quantification of stable isotope labels that cannot be obtained using other techniques and that is broadly applicable to biological and medical research.

MIMS combines ion microscopy with secondary ion mass spectrometry (SIMS), stable isotope reporters and intensive computation (Supplementary Fig. 1). MIMS allows imaging and measuring of stable isotope labels in cell domains smaller than one micrometre cubed. We tested the potential of MIMS to track DNA labelling quantitatively with ¹⁵N-thymidine *in vitro*. In proliferating fibroblasts, we detected label incorporation within the nucleus by an increase in the ¹⁵N:¹⁴N ratio above natural ratio (Fig. 1a). The labelling pattern resembled chromatin with either stable isotope-tagged thymidine or thymidine analogues (Fig. 1b). We measured dose-dependent incorporation of ¹⁵N-thymidine over three orders of magnitude (Fig. 1c and Supplementary Fig. 2). We

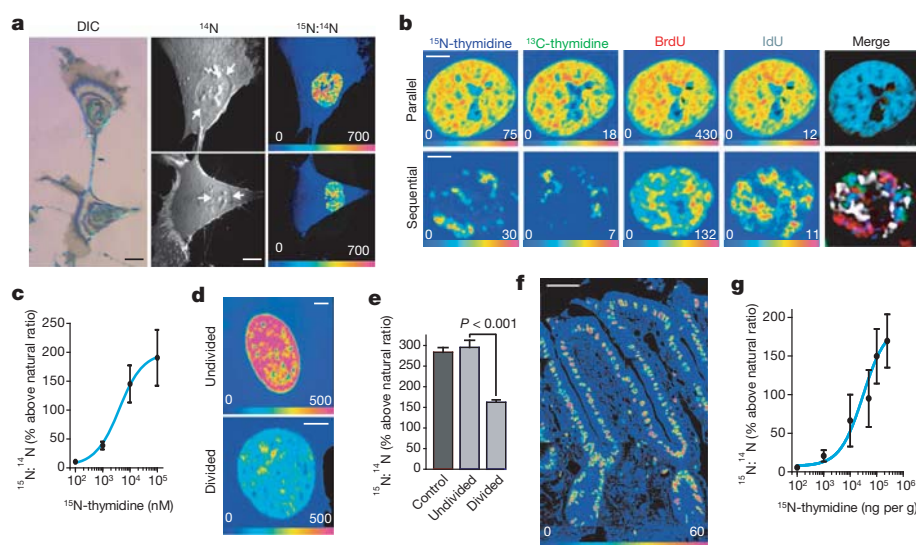


Figure 1 | MIMS quantification of stable isotope-labelled thymidine incorporation by dividing cells. **a**, Dividing fibroblast labelled with ¹⁵N-thymidine. The cell surface was sputtered to reach the nuclei. Left, differential interference contrast reflection microscopy. Middle, ¹⁴N image revealing subcellular details including the nucleus (white arrows) with nucleoli. Right, hue saturation intensity (HSI) image mapping the ¹⁵N:¹⁴N ratio. The rainbow scale ranges from blue, set to natural ratio (0.37%, expressed as 0% above natural ratio), to red, where the ratio is several fold above natural ratio (700%, eight times the natural ratio). ¹⁵N labelling is concentrated in the nucleus. Scale bars, 10 μ m. **b**, Fibroblast nuclei after serial or parallel DNA labelling with ¹⁵N-thymidine, ¹³C-thymidine, BrdU (⁸¹Br) or iododeoxyuridine (¹²⁷I). Parallel labelling (top row): colocalization of label confirmed by the merged image (far

right). Sequential labelling (bottom row): non-superimposable nuclear labelling. Scale bars, 5 μ m. **c**, Concentration-dependent nuclear ¹⁵N-labelling in ¹⁵N-thymidine treated fibroblasts. Pixel-by-pixel quantification of ¹⁵N-incorporation. Data are derived from the mean of intranuclear pixels. Sigmoidal dose response curve: $R^2 = 0.99$. **d**, Nuclei from ¹⁵N-thymidine-labelled human foreskin fibroblasts after 24-h chase (cycle approximately 18 h). Scale bars, 5 μ m. **e**, One group labelled similarly to control cells (undivided), the other with labelling that was approximately half that of control (divided). **f**, ¹⁵N:¹⁴N HSI image of the small intestine. ¹⁵N-thymidine labelling (one week) of nuclei extends from the crypts to the tips of the villi. Mosaic: 8 tiles, 80 μ m each. Scale bar, 30 μ m. **g**, Sigmoidal dose response curve: ¹⁵N-thymidine labelling after single subcutaneous injection ($R^2 = 0.99$).

¹Department of Medicine, Division of Cardiovascular Medicine, Brigham and Women's Hospital, Boston, Massachusetts 02115, USA. ²Harvard Medical School, Boston, Massachusetts 02115, USA.

³Division of Physiology and Metabolism, Medical Research Council National Institute for Medical Research, Mill Hill, London NW7 1AA, UK. ⁴National Resource for Imaging Mass Spectroscopy, 65

Landsdowne St, Cambridge, Massachusetts 02139, USA. ⁵Department of Medicine, Division of Genetics, Brigham and Women's Hospital, Boston, Massachusetts 02115, USA. ⁶Harvard Stem Cell Institute, Cambridge, Massachusetts 02138, USA.

also tracked fibroblast division after a 24-h label-free chase (Fig. 1d, e and Supplementary Fig. 3). Cells segregated into two populations, one indistinguishable from control cells suggesting no division, the other with halving of label, consistent with one division during the chase.

We found similar results by tracking cell division *in vivo* in the small intestine (Fig. 1f, g and Supplementary Figs 4–6). We measured dose-dependent ^{15}N -thymidine incorporation within nuclei of actively dividing crypt cells (Fig. 1g and Supplementary Fig. 4), down to a dose of $0.1\text{ }\mu\text{g per g}$ (Supplementary Fig. 2). The cytoplasm was slightly above natural ratio, probably due to low-level soluble ^{15}N -thymidine or mitochondrial incorporation (Supplementary Fig. 2). We measured halving of label with each division during label-free chase (Supplementary Fig. 6).

We then tested the ‘immortal strand hypothesis’, a concept that emerged from autoradiographic studies⁵ and that predicted long-term label retaining cells in the small intestinal crypt^{6,7}. It proposes that asymmetrically dividing stem cells also asymmetrically segregate DNA, such that older template strands are retained by daughter cells that will remain stem cells and newer strands are passed to daughters committed to differentiation (Supplementary Fig. 7)^{5,6}. Modern studies continue to argue both for^{8–12} or against^{13–16} the hypothesis, leading to the suggestion that definitive resolution of the debate will require a new experimental approach¹⁷.

Although prior evidence suggests a concentration of label-retaining cells in the +4 anatomic position^{7,8}, we searched for DNA label retention irrespective of anatomic position or molecular identity. We labelled mice with ^{15}N -thymidine for the first 8 weeks of life when intestinal stem cells are proposed to form⁸. After a 4-week chase, mice received bromodeoxyuridine (BrdU) for 24 h before euthanasia to identify proliferating cells (Fig. 2a and Supplementary Fig. 8, Experiment 1), specifically crypt base columnar (CBC) cells and transit amplifying cells (Supplementary Fig. 9), which cycle at a rate of one and two times per 24 h, respectively¹⁸ (Supplementary Fig. 10). All crypt cell nuclei were highly labelled upon completion of ^{15}N -thymidine; after a 4-week chase, however, we found no label retention by non-Paneth crypt cells (Fig. 2b–f; $n = 3$ mice, 136 crypts analysed). ^{15}N -labelling in $^{15}\text{N}^+/\text{BrdU}^-$ Paneth and mesenchymal cells was equivalent to that measured at pulse completion (Fig. 2b, c) indicating quiescence during the chase (values above $^{15}\text{N}:^{14}\text{N}$ natural ratio: Paneth pulse = $107.8 \pm 5.0\%$ s.e.m. $n = 51$ versus Paneth pulse-chase = $96.3 \pm 2.8\%$ s.e.m. $n = 218$; mesenchymal pulse = $92.0 \pm 5.0\%$ s.e.m. $n = 89$ versus mesenchymal pulse-chase = $90.5 \pm 2.2\%$ s.e.m. $n = 543$). The number of randomly selected crypt sections was sufficient to detect a frequency as low as one label-retaining stem cell per crypt irrespective of anatomic location within the crypt. Because each anatomic level contains approximately 16 circumferentially arrayed cells⁸, a two-dimensional analysis captures approximately one eighth of the cells at each anatomic position (one on each side of the crypt; Supplementary Fig. 9a). Therefore, assuming only one label-retaining stem cell per crypt we should have found 17 label-retaining cells in the 136 sampled crypts (one eighth of 136) but we found 0 (binomial test $P < 0.0001$). The significance of this result held after lowering the expected frequency of label-retaining cells by 25% to account for the development of new crypts, a process thought to continue into adulthood¹⁹. In three additional experiments, using shorter labelling periods and including *in utero* development, we also found no label-retaining cells in the crypt other than Paneth cells (Supplementary Fig. 8, Experiments 2–4).

To address the possibility that long-term thymidine exposure or frequent high-dose injections introduced pitfalls, we limited labelling to the previously reported peak time period of label-retaining stem cell formation⁸ and reduced the dose by 50-fold compared to prior experiments (Supplementary Fig. 8, Experiment 5). Approximately six label-retaining cells per intestinal circumference were observed previously⁸ with a similar protocol; with about 90 crypts per circumference, this translates to 1 label-retaining cell per 15 sectioned crypts. We analysed 330 crypts and observed 19 $^{15}\text{N}^+/\text{BrdU}^-$ Paneth cells (one per 17 crypt

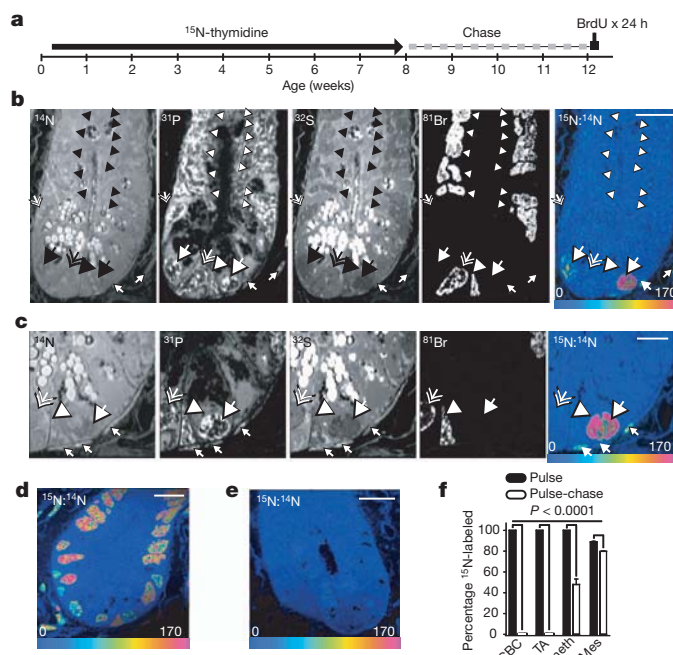


Figure 2 | No label-retaining stem cells in the small intestinal crypt. **a**, ^{15}N -thymidine administered from post-natal day 4 to week 8. After 4-week chase, BrdU was administered ($500\text{ }\mu\text{g}$ intraperitoneally every 6 h) for 24 h before euthanasia (see Supplementary Fig. 8). **b**, ^{14}N : crypt structure and intense signal in intracytoplasmic Paneth granules at the crypt base. ^{31}P : intense intranuclear signal. ^{32}S : intense signal within cytoplasmic Paneth cell granules. ^{81}Br : direct measure of BrdU incorporation. $^{15}\text{N}:^{14}\text{N}$: HSI image of ^{15}N -thymidine labelling within $^{15}\text{N}^+/\text{BrdU}^-$ Paneth cells (large arrow) and mesenchymal cells (small arrows). No other cells reveal ^{15}N retention. Large arrow head: recently formed ($\text{BrdU}^+/\text{BrdU}^-$) Paneth cell. Small hatched arrow (middle left side of the crypt): unlabelled Paneth cell, ($^{15}\text{N}^-/\text{BrdU}^-$). Scale bar, $15\text{ }\mu\text{m}$. **c**, Continued analysis of the same crypt after narrowing the acquisition field. High ^{15}N signal in a BrdU^- Paneth cell (large arrow) and mesenchymal cells closely associated with the crypt (small arrows). BrdU^+ CBC (hatched arrow) and Paneth cell (arrow head) are $^{15}\text{N}^-$. Scale bar, $5\text{ }\mu\text{m}$. **d**, $^{15}\text{N}:^{14}\text{N}$ HSI image of small intestinal crypt at the end of ^{15}N -thymidine pulse. All nuclei are labelled. Nuclei with lesser degrees of labelling likely represent cells born during a period of lower circulating ^{15}N -thymidine as expected given the different labelling protocols (Supplementary Fig. 8). Scale bar, $20\text{ }\mu\text{m}$. **e**, Unlabelled mouse image. The entire crypt contains the natural abundance of ^{15}N . Scale bar = $10\text{ }\mu\text{m}$. **f**, Mean % $^{15}\text{N}^+$ cells at the completion of pulse and after pulse-chase (\pm standard error of CBC, transit amplifying (TA), Paneth and mesenchymal (Mes) cells ($n = 3$ mice per group).

sections), but no non-Paneth label-retaining cells (expected, 21; observed, 0; binomial test $P < 0.0001$) or doubly labelled ($^{15}\text{N}^+/\text{BrdU}^+$) cells irrespective of cellular identity. Thus, after labelling during all potential periods of stem cell formation, spanning *in utero* through post-natal development, we found no label-retaining stem cells in the small intestinal crypt other than Paneth cells, which are largely quiescent. We conclude therefore that the phenomenon of label-retaining cells as described by others was most likely due either to reagent toxicity or to insufficient resolution with the consequent misidentification of labelled post-mitotic Paneth cell nuclei as label retaining +4 stem cells. MIMS minimizes these potential artefacts due to its ability to detect non-radioactive isotopes and the high imaging resolution both laterally and vertically. Although our data cannot directly exclude the migration of label-retaining stem cells into the crypt under non-homeostatic conditions such as radiation injury¹¹, prior examinations of crypt clones argue against contributions from either a resting stem cell population or from stem cells originating outside the crypt²⁰.

We also studied label release in adult mice after stem cell formation. These experiments are particularly relevant given the recent suggestion

that crypt stem cells exhibit monoclonal drift over 8 months^{21,22}, a model that is incompatible with lifetime survival of label-retaining stem cells but that does not exclude the possibility of biased template strand segregation. After administering ¹⁵N-thymidine for 2 weeks to label all proliferating crypt cells, ¹⁵N-thymidine was stopped and BrdU was administered for 24 h to label cells dividing during the ¹⁵N-thymidine-free chase (Fig. 3a). A consequence of the immortal strand hypothesis would be that a stem cell would produce a daughter in which ¹⁵N label was completely lost with the first division during chase (Supplementary Fig. 7). We observed no such BrdU⁺/¹⁵N⁻ crypt cells, even after extending the ¹⁵N-thymidine-free chase to 48 h (Fig. 3b and Supplementary Fig. 11). Proliferating (BrdU⁺) crypt cells ($n = 3$ mice; 563 cells analysed) diluted ¹⁵N-thymidine label (mean 71% above natural ratio) compared to undivided (BrdU⁻) cells (129% above natural ratio) or cells analysed at the end of ¹⁵N-thymidine pulse (128% above natural ratio), as expected of cells undergoing random chromosomal segregation (Fig. 3c). We also analysed crypt cell nuclei in late mitosis, finding ¹⁵N label and BrdU in both sets of segregating chromosomes (Fig. 3d and Supplementary Fig. 12, $n = 232$). Together, these data result from an analysis of 625 crypts, in which we did not find a single BrdU⁺ nucleus or chromosomal complement that was not ¹⁵N-labelled, indicating that dividing cells in the crypt uniformly dilute labelled DNA in a pattern consistent with random DNA strand segregation.

The broad applicability of MIMS is demonstrated by proof-of-principle studies in *Drosophila* and humans. *Drosophila* provides a model system in which to study the genetics of lipid metabolism, *in vivo*. Due to its small size, however, it is difficult to obtain sufficient material from specific tissue/cell types for measurement with conventional mass spectrometry. A previous study showed numerous lipid droplets in the enterocytes of a segment of the *Drosophila* larval intestine, the anterior midgut²³. We therefore used MIMS to measure the incorporation and turnover of diet-derived ¹³C-palmitate within these cells. After larval

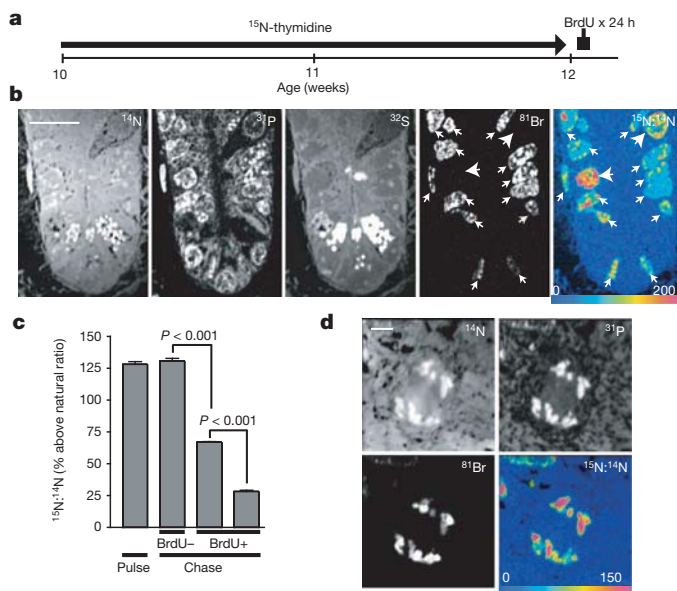


Figure 3 | Label-dilution in adult mice indicates random segregation of DNA strands. **a**, ¹⁵N-thymidine administered for 2 weeks to adult mice (osmotic mini-pump, 20 μg h⁻¹), then BrdU for 24 h before euthanasia (See Supplementary Fig. 8). **b**, Dividing cells (BrdU⁺) dilute ¹⁵N-thymidine label (small arrows) relative to undivided cells (BrdU⁻) (large arrows). Note two CBC cells with elongated nuclei at the crypt base. Scale bar, 10 μm. **c**, Divided crypt cells (BrdU⁺), residing in CBC or +4–10 positions, demonstrated ¹⁵N-dilution consistent with one or two rounds of division during the chase ($n = 3$ mice per group). **d**, Mitotic crypt cell. Segregating chromosomes are visible in ¹⁴N and ³¹P images. ¹⁵N-label and BrdU were measured in both segregating chromosomal complements consistent with symmetric chromosomal segregation. Scale bar, 2 μm.

exposure to dietary ¹³C-palmitate, label is incorporated into enterocyte lipid droplets with a subcellular pattern similar to that seen with a neutral lipid dye (compare Fig. 4a with supplementary Fig. 13). Dietary ¹³C-palmitate pulses of varying periods indicate that the rate of ¹³C label incorporation into lipid droplets is greater in anterior

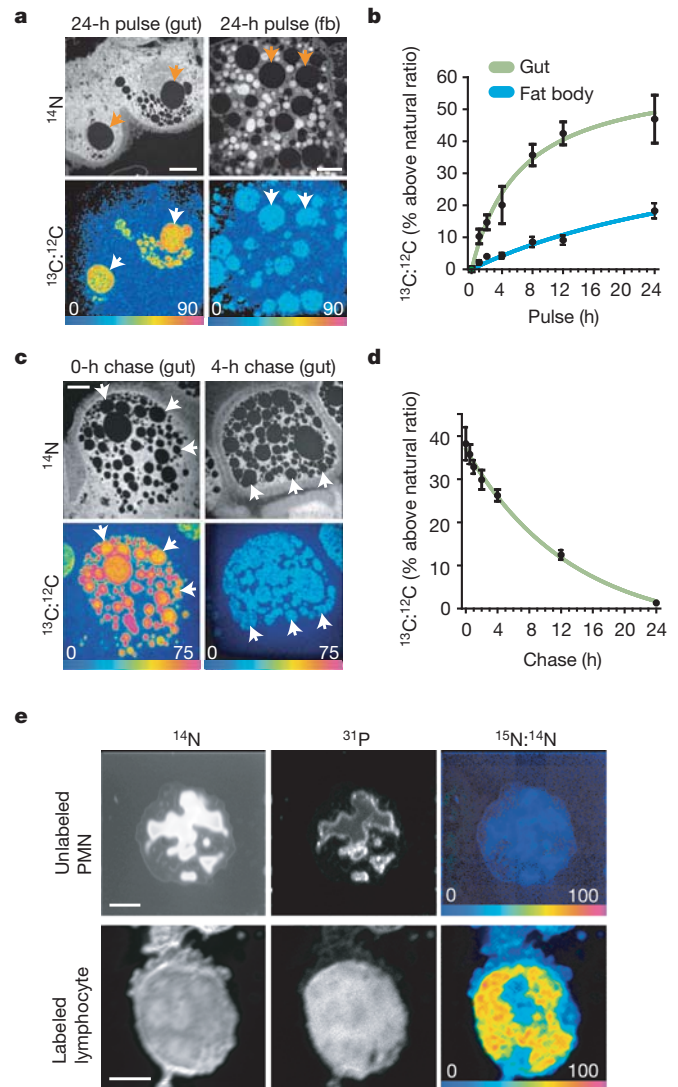


Figure 4 | Extending MIMS to *Drosophila* and human metabolism.

a, *Drosophila* anterior midgut enterocytes (gut, left panels) accumulate more ¹³C from 24-h exposure to dietary ¹³C-palmitate than adipocytes (fat body cells) (fb, right panels). Lipid droplets (arrows) have low nitrogen content and so appear dark in ¹⁴N images (top panels). The ¹³C:12C HSI images reveal ¹³C incorporation into lipid droplets. Scale bars, 10 μm. **b**, Time course of ¹³C incorporation into lipid droplets of anterior midgut enterocytes (gut) after larval dietary ¹³C-palmitate pulse-chase. Upper panels show ¹⁴N images and lower panels show corresponding ¹³C:12C HSI images, indicating strong ¹³C incorporation at the end of the pulse (bottom left) and rapid elimination during a 4-h chase (bottom right). Scale bar = 5 μm. **d**, ¹³C tracer dilution in the lipid droplets of anterior midgut enterocytes during a label-free chase fits an exponential decay curve ($R^2 = 0.90$, half-life = 9.1 h). **e**, ¹⁵N-thymidine administered for 48 h: no labelled white blood cell were found. After a 4-week chase we found few labelled lymphocytes. Top: unlabelled polymorphonuclear leukocyte (PMN) with multi-lobed nucleus. Bottom: ¹⁵N-labelled lymphocyte after chase. The round nucleus seen in the ³¹P image occupies the majority of the cell, as is typical for lymphocytes. Scale bars, 3 μm.

midgut enterocytes than in the adipocytes of the fat body, the major lipid storage depot in *Drosophila* (Fig. 4a, b). Pulse-chase experiments with dietary ^{13}C -palmitate also demonstrate a reproducible exponential decay ($R^2 = 0.9$) of the ^{13}C signal within enterocyte lipid droplets and provide an estimate for the half-life of approximately 9 h (Fig. 4c, d). These results demonstrate the utility of MIMS for precise measurement of *in vivo* lipid turnover at high resolution within individual *Drosophila* lipid droplets.

In the first MIMS human experiment, we administered ^{15}N -thymidine to a healthy volunteer by intravenous infusion for 48 h. We performed MIMS analysis on peripheral white blood cell smears. We found no labelled white blood cells at the end of the infusion (3,600 analysed). After a 4-week chase we found a few labelled white blood cells (Fig. 4c, 4 of approximately 2,000 cells analysed) consistent with a lag time before release from the bone marrow (chi-squared, $P < 0.01$). Radiolabelled thymidine has been administered to humans in numerous studies previously²⁴, but these studies were conducted primarily on cancer patients. There is no known risk to using stable isotopes²⁵. Thus, this experiment now opens the door to studies of metabolism and cell tracking in humans.

In conclusion, we provide direct evidence under physiological conditions against non-random template strand segregation in the small intestine. Our approach encompasses all potential stem cell populations in the crypt, those identifiable by known markers^{26–28} and putative ones not identified by a specific marker. We have demonstrated the power of MIMS to image and quantify cell metabolism in three different contexts: mammalian intestinal cell division, *Drosophila* lipid metabolism and human lymphopoiesis. We anticipate that the measuring and imaging power of MIMS will make it a major tool to study metabolism and cell fate in animals and humans.

METHODS SUMMARY

Data were acquired with the prototype (four detectors) and a second-generation instrument (NanoSIMS 50L, Cameca: seven detectors). Quantitative mass images were analysed with Open MIMS software, a plug-in to ImageJ (<http://www.nrims.harvard.edu/software.php>). Stable isotopes were obtained from Cambridge Isotopes (^{15}N -thymidine, ^{13}C -thymidine) and Sigma-Aldrich (^{13}C -palmitate).

Full Methods and any associated references are available in the online version of the paper at www.nature.com/nature.

Received 1 March; accepted 23 November 2011.

Published online 15 January 2012.

- Schoenheimer, R. & Rittenberg, D. The application of isotopes to the study of intermediary metabolism. *Science* **87**, 221–226 (1938).
- Schoenheimer, R. *et al.* The application of the nitrogen isotope N^{15} for the study of protein metabolism. *Science* **88**, 599–600 (1938).
- Lechene, C. *et al.* High-resolution quantitative imaging of mammalian and bacterial cells using stable isotope mass spectrometry. *J. Biol.* **5**, 20 (2006).
- Lechene, C. P., Luyten, Y., McMahon, G. & Distel, D. L. Quantitative imaging of nitrogen fixation by individual bacteria within animal cells. *Science* **317**, 1563–1566 (2007).
- Lark, K. G., Consigli, R. A. & Minocha, H. C. Segregation of sister chromatids in mammalian cells. *Science* **154**, 1202–1205 (1966).
- Cairns, J. Mutation selection and the natural history of cancer. *Nature* **255**, 197–200 (1975).
- Potten, C. S., Hume, W. J., Reid, P. & Cairns, J. The segregation of DNA in epithelial stem cells. *Cell* **15**, 899–906 (1978).
- Potten, C. S., Owen, G. & Booth, D. Intestinal stem cells protect their genome by selective segregation of template DNA strands. *J. Cell Sci.* **115**, 2381–2388 (2002).
- Shinin, V., Gayraud-Morel, B., Gomes, D. & Tajbakhsh, S. Asymmetric division and cosegregation of template DNA strands in adult muscle satellite cells. *Nature Cell Biol.* **8**, 677–682 (2006).

- Conboy, M. J., Karasov, A. O. & Rando, T. A. High incidence of non-random template strand segregation and asymmetric fate determination in dividing stem cells and their progeny. *PLoS Biol.* **5**, e102 (2007).
- Quyn, A. J. *et al.* Spindle orientation bias in gut epithelial stem cell compartments is lost in precancerous tissue. *Cell Stem Cell* **6**, 175–181 (2010).
- Rando, T. A. The immortal strand hypothesis: segregation and reconstruction. *Cell* **129**, 1239–1243 (2007).
- Kiel, M. J. *et al.* Haematopoietic stem cells do not asymmetrically segregate chromosomes or retain BrdU. *Nature* **449**, 238–242 (2007).
- Sotiropoulou, P. A., Candi, A. & Blanpain, C. The majority of multipotent epidermal stem cells do not protect their genome by asymmetrical chromosome segregation. *Stem Cells* **26**, 2964–2973 (2008).
- Schepers, A. G. *et al.* Lgr5 intestinal stem cells have high telomerase activity and randomly segregate their chromosomes. *EMBO J.* **30**, 1104–1109 (2011).
- Lansdorp, P. M. Immortal strands? Give me a break. *Cell* **129**, 1244–1247 (2007).
- Pech, M. F. & Artandi, S. E. TRAPping telomerase within the intestinal stem cell niche. *EMBO J.* **30**, 986–987 (2011).
- Cheng, H. & Leblond, C. P. Origin, differentiation and renewal of the four main epithelial cell types in the mouse small intestine. V. Unitarian theory of the origin of the four epithelial cell types. *Am. J. Anat.* **141**, 537–561 (1974).
- Totafurno, J., Bjerknes, M. & Cheng, H. The crypt cycle. Crypt and villus production in the adult intestinal epithelium. *Biophys. J.* **52**, 279–294 (1987).
- Bjerknes, M. & Cheng, H. Clonal analysis of mouse intestinal epithelial progenitors. *Gastroenterology* **116**, 7–14 (1999).
- Lopez-Garcia, C., Klein, A. M., Simons, B. D. & Winton, D. J. Intestinal stem cell replacement follows a pattern of neutral drift. *Science* **330**, 822–825 (2010).
- Snippert, H. J. *et al.* Intestinal crypt homeostasis results from neutral competition between symmetrically dividing Lgr5 stem cells. *Cell* **143**, 134–144 (2010).
- Gutierrez, E., Wiggins, D., Fielding, B. & Gould, A. P. Specialized hepatocyte-like cells regulate *Drosophila* lipid metabolism. *Nature* **445**, 275–280 (2007).
- Schick, P. *et al.* Labelling of human resting lymphocytes by continuous infusion of [^3H]thymidine. I. Characterization of cytoplasmic label. *J. Cell Sci.* **33**, 351–362 (1978).
- Stürup, S., Hansen, H. R. & Gammelgaard, B. Application of enriched stable isotopes as tracers in biological systems: a critical review. *Anal. Bioanal. Chem.* **390**, 541–554 (2008).
- Barker, N. *et al.* Identification of stem cells in small intestine and colon by marker gene *Lgr5*. *Nature* **449**, 1003–1007 (2007).
- Sangiorgi, E. & Capecchi, M. R. *Bmi1* is expressed *in vivo* in intestinal stem cells. *Nature Genet.* **40**, 915–920 (2008).
- Montgomery, R. K. *et al.* Mouse telomerase reverse transcriptase (mTert) expression marks slowly cycling intestinal stem cells. *Proc. Natl Acad. Sci. USA* **108**, 179–184 (2011).

Supplementary Information is linked to the online version of the paper at www.nature.com/nature.

Acknowledgements We thank A. Mudge, M. Raff and A. Aperia for critical reading of the manuscript; M. Raff for numerous enlightening discussions; T. Bloom for her strong support at the origin of MIMS development; M. Wang for MIMS analysis; J. Poczek and Z. Kaufman for MIMS analysis software development; L. Trakimas, C. MacGillivray, S. Clark and E. Hurst for histology; W. Wang for statistics advice. We thank Cambridge Isotope Laboratories for their generous gift of thymidine ($^{15}\text{N}_2$, 96–98%). M.L.S. is funded by the American Heart Association and Future Leaders in Cardiovascular Medicine. A.P.G. is funded by the Medical Research Council (U117584237). R.T.L. is funded by the National Institutes of Health (AG032977) and a grant from the Harvard Stem Cell Institute. C.P.L. is funded by the National Institutes of Health (EB001974, AG034641), the Ellison Medical Foundation and the Human Frontier Science Program.

Author Contributions M.L.S. designed the experiments to study the ‘immortal strand hypothesis’ in the small intestine with input from C.P.L.; M.L.S. performed *in vivo* mouse experiments with help from S.E.S.; A.P.B. and A.P.G. designed and performed the *Drosophila* experiments. M.L.S. designed the human experiment with input from R.T.L. and T.S.P.; M.L.S. and T.S.P. conducted the human protocol. S.E.S. was involved in study design. M.L.S. analysed the data with C.P.L. input. C.G. operated the instrument and assisted with analysis of *Drosophila* lipid droplets. M.L.S. and C.P.L. wrote the manuscript; A.P.B. and A.P.G. contributed the section on *Drosophila*. R.T.L. was involved in study design and provided critical feedback at all junctures. C.P.L. conceived of the general application of MIMS to metabolism, cell turnover and human experimentation. C.P.L. designed and performed *in vitro* experiments.

Author Information Reprints and permissions information is available at www.nature.com/reprints. The authors declare no competing financial interests. Readers are welcome to comment on the online version of this article at www.nature.com/nature. Correspondence and requests for materials should be addressed to C.P.L. (cpl@harvard.edu).

METHODS

Multi-isotope imaging mass spectrometry (MIMS). MIMS is based on secondary ion mass spectrometry (SIMS). An ionic beam sputters the surface atomic layer of a sample, resulting in the ionization of a small atomic fraction. In a SIMS instrument, secondary ions are separated by mass, and then used to derive a quantitative atomic mass image of the surface of the analysed sample. The instrument can simultaneously measure data from multiple isotopes from the same region. Data included in this study are derived from both the NanoSims prototype (ONERA, Université Paris Sud/Cameca) and a second-generation instrument (NanoSims 50L, Cameca). The second-generation instrument is fully automated and has the capacity to quantify seven masses simultaneously.

Quantitative image data extraction. For each pixel, the number of counts of a given secondary ion is stored in a computer file. The data are reconstructed into a grayscale image in which the pixel intensity is derived from the total number of counts of a given secondary ion within the area representing a given pixel. The lateral resolution is dependent on factors, including the beam size and the number of pixels per image acquisition area. A series of images based on the analysis of successive atomic layers can be summed. The incorporation of halogenated nucleotide analogues (BrdU, iododeoxyuridine) is assessed by directly quantifying the ionized halogen atoms (^{81}Br , ^{127}I), which are found at extremely low background concentrations in most tissues. Halogen enrichment within a given region of interest is expressed as the percent enrichment over natural background.

Hue saturation intensity ratio images. The localization of tracers enriched with rare stable isotopes (for example, ^{15}N -thymidine) is done by deriving quantitative ratio images. The ratio of a rare stable isotope and the common stable isotope is quantified on a pixel by pixel basis. Incorporation of a stable isotope within a region of interest is determined when the ratio of the rare stable isotope to the common stable isotope exceeds the natural ratio. Because quantitative images acquired with MIMS generate far more data than can be represented by a grayscale, we previously developed a method of visually representing ratio data based on a hue saturation intensity (HSI) transformation. With an HSI image, the scale can be set such that the lower bounds of the scale (blue colours) are assigned to pixels in which the corresponding rare-to-common stable isotope ratio is equivalent to the natural ratio. An important advantage of an HSI image is that the scale can be extended or compressed to provide an optimal colour representation of regions of differential stable isotope enrichment. However, any image manipulations, such as those resulting from scale changes, do not modify the quantitative data underlying the colour representation.

Data processing and export. MIMS images are viewed and processed using Open MIMS software, a custom-built plugin to the ImageJ software (<http://www.nrims.harvard.edu/software.php>). In the experiments contained herein, nuclei were manually identified as regions of interest within the crypts of the small intestine using a combination of ^{14}N and ^{31}P mass images. Cellular identity was assigned by an observer unaware of the labelling status of the cells. Paneth cells were identified on the basis of their characteristic cytoplasmic granules seen in ^{14}N and ^{32}S images, large round nuclei seen in ^{14}N and ^{31}P images, and their anatomic location at or near the base of the crypt (Supplementary Fig. 9). ^{15}N -labelled Paneth cells (Fig. 2 and Supplementary Fig. 8 Experiment 1) had a number of granules with a median of 8 (interquartile range = 5–11, $n = 218$). The granules were not separated from the nucleus by a plasma membrane, which would have been detected by MIMS. CBC cells were identified on the basis of their location between Paneth cells at the base of the crypt and their narrow, elongated nuclei. The +4 position was assigned

to the first non-Paneth cell superior to the Paneth zone at the base of the crypt. Cells in the +4 position and above (transit amplifying cells) typically had elliptical nuclei.

^{15}N -labelling is expressed as the $^{15}\text{N}:^{14}\text{N}$ ratio (percentage above natural ratio) obtained using the following equation:

$$^{15}\text{N}:^{14}\text{N}(\% \text{ above natural ratio}) = \frac{(^{15}\text{N}:^{14}\text{N} \text{ ratio}) - (\text{natural ratio})}{\text{natural ratio}} \times 100$$

Mosaic images. The maximum field size analysed in this study was $80 \mu\text{m} \times 80 \mu\text{m}$. The presentation of images from larger tissue swaths is made possible by the construction of mosaic images in which a series of adjacent fields are analysed. After MIMS acquisition, the full series of tiles is assembled to form a larger mosaic image.

Statistics. Data were analysed using JMP 8.0.1 and Prism 3.0 (GraphPad). Two-way *t*-tests were performed for comparisons of two experimental groups. For analyses of multiple experimental groups, one-way ANOVA and Bonferroni correction were used. Non-parametric data were analysed with a Kruskal–Wallis test and Dunn's multiple comparisons test. Binomial testing was used to compare observed versus predicted event frequencies.

Reagents. ^{15}N -thymidine and ^{13}C -thymidine were obtained from Cambridge Isotopes. ^{15}N -thymidine, used for human administration, was subjected to additional endotoxin and microbial limits testing before packaging. ^{13}C -palmitate was obtained from Sigma-Aldrich. Bromodeoxyuridine (BrdU) and iododeoxyuridine (IdU) were obtained from Sigma-Aldrich.

Cell culture. Human foreskin fibroblasts were grown in DMEM/Ham's F12 supplemented with 10% FBS, 1% penicillin/streptomycin/L-glutamine. For *in vitro* labelling experiments, fibroblasts were grown on silicon chips. Prior to MIMS analysis, cells were fixed and spun dry (Headway Research Spinner, PWM32) at 3,500 r.p.m. for 2 min.

Mice. C57B6 mice were used in accordance with the Guide for the Use and Care of Laboratory Animals and approved by the Harvard Medical School Standing Committee on Animals. Osmotic minipumps (Alzet) were implanted subcutaneously. Jejunal segments were fixed (4% paraformaldehyde) and embedded (LR white). Sections ($0.5 \mu\text{m}$) were mounted on silicon chips.

Drosophila. *Drosophila* larvae were fed a standard yeast/cornmeal diet²³ supplemented with 1% w/v ^{13}C -labelled palmitic acid-1 (Sigma-Aldrich). For chase experiments, larvae were collected at 72 h of development, following a label-free chase period of 0–24 h, using standard food supplemented with 1% unlabelled palmitic acid (Sigma-Aldrich). Following dissection, anterior midguts or fat bodies were fixed in 2% formaldehyde, post-fixed in 2% glutaraldehyde then 2% osmium tetroxide, embedded in Epon resin, sectioned (thickness = $2 \mu\text{m}$), and mounted on silicon chips.

Human protocol. The Partners Institutional Review Board approved the protocol. After obtaining informed consent, the subject was admitted to the Brigham and Women's Hospital clinical research unit. Prior to administration, ^{15}N -thymidine was resuspended in 500 ml 0.9% NaCl and passed through a $0.2 \mu\text{m}$ filter. The subject received ^{15}N -thymidine intravenously (30 mg bolus over 5 min, then 15 mg h^{-1} for 48 h) without adverse events. Peripheral blood was collected in an EDTA-containing tube at the conclusion of the infusion and after a 4-week chase. The blood sample was centrifuged (300g, 5 min), the buffy coat collected, and red blood cells lysed (ACK buffer, Invitrogen). The white blood cell suspension was smeared onto silicon chips and fixed with 4% paraformaldehyde.

Multi-isotope imaging mass spectrometry reveals slow protein turnover in hair-cell stereocilia

Duan-Sun Zhang^{1*}, Valeria Piazza^{1†*}, Benjamin J. Perrin², Agnieszka K. Rzadzinska³, J. Collin Poczatek⁴, Mei Wang⁴, Haydn M. Prosser³, James M. Ervasti², David P. Corey¹ & Claude P. Lechene⁴

Hair cells of the inner ear are not normally replaced during an animal's life, and must continually renew components of their various organelles¹. Among these are the stereocilia, each with a core of several hundred actin filaments that arise from their apical surfaces and that bear the mechanotransduction apparatus at their tips. Actin turnover in stereocilia has previously been studied² by transfecting neonatal rat hair cells in culture with a β -actin-GFP fusion, and evidence was found that actin is replaced, from the top down, in 2–3 days. Overexpression of the actin-binding protein espin causes elongation of stereocilia within 12–24 hours, also suggesting rapid regulation of stereocilia lengths³. Similarly, the mechanosensory 'tip links' are replaced in 5–10 hours after cleavage in chicken and mammalian hair cells^{4,5}. In contrast, turnover in chick stereocilia *in vivo* is much slower⁶. It might be that only certain components of stereocilia turn over quickly, that rapid turnover occurs only in neonatal animals, only in culture, or only in response to a challenge like breakage or actin overexpression. Here we quantify protein turnover by feeding animals with a ^{15}N -labelled precursor amino acid and using multi-isotope imaging mass spectrometry to measure appearance of new protein. Surprisingly, in adult frogs and mice and in neonatal mice, *in vivo* and *in vitro*, the stereocilia were remarkably stable, incorporating newly synthesized protein at <10% per day. Only stereocilia tips had rapid turnover and no treadmilling was observed. Other methods confirmed this: in hair cells expressing β -actin-GFP we bleached fiducial lines across hair bundles, but they did not move in 6 days. When we stopped expression of β - or γ -actin with tamoxifen-inducible recombination, neither actin isoform left the stereocilia, except at the tips. Thus, rapid turnover in stereocilia occurs only at the tips and not by a treadmilling process.

To understand protein turnover in the inner ear, we sought a method that could reveal new synthesis with high spatial resolution, in adult animals, *in vivo*, and without transfection of cells. We fed frogs with food containing L-leucine tagged with the stable isotope ^{15}N for up to 32 days, and killed them by cardiac perfusion. As leucine is an essential amino acid, newly synthesized protein would contain ^{15}N in nearly the same proportion as the food. To locate ^{15}N -tagged protein, plastic sections of frog saccules were placed onto silicon wafers or electron microscopy grids for multi-isotope imaging mass spectrometry (MIMS) imaging. We detected nitrogen as the CN^- ion, with the MIMS detectors set for the masses of ^{12}C , ^{13}C , $^{12}\text{C}^{14}\text{N}$ and $^{12}\text{C}^{15}\text{N}$, and calculated the $^{15}\text{N}/^{14}\text{N}$ ratio at each location in a field^{7,8} (see Methods).

A mass-26 ($^{12}\text{C}^{14}\text{N}$) image of the saccular macula, representing total protein, shows the apical surface of a hair cell with its hair bundle (Fig. 1a, left). Lateral resolution approaches 30 nm, and depth resolution is ~ 2 nm (ref. 7). The mass-27 channel ($^{12}\text{C}^{15}\text{N}$; not shown) revealed newly synthesized protein, and the mass-27/mass-26 ratio indicated

per cent incorporation. A ratio image (Fig. 1a, right, 32 days of feeding) shows that the stereocilia incorporate new protein more slowly than the cell body. We quantified turnover by summing the mass-26 and mass-27 counts for all pixels in each region of interest (ROI) and calculated per cent incorporation (Fig. 1c). Hair-cell cytoplasm and cuticular plates incorporated new protein at $\sim 0.5\%$ per day. But

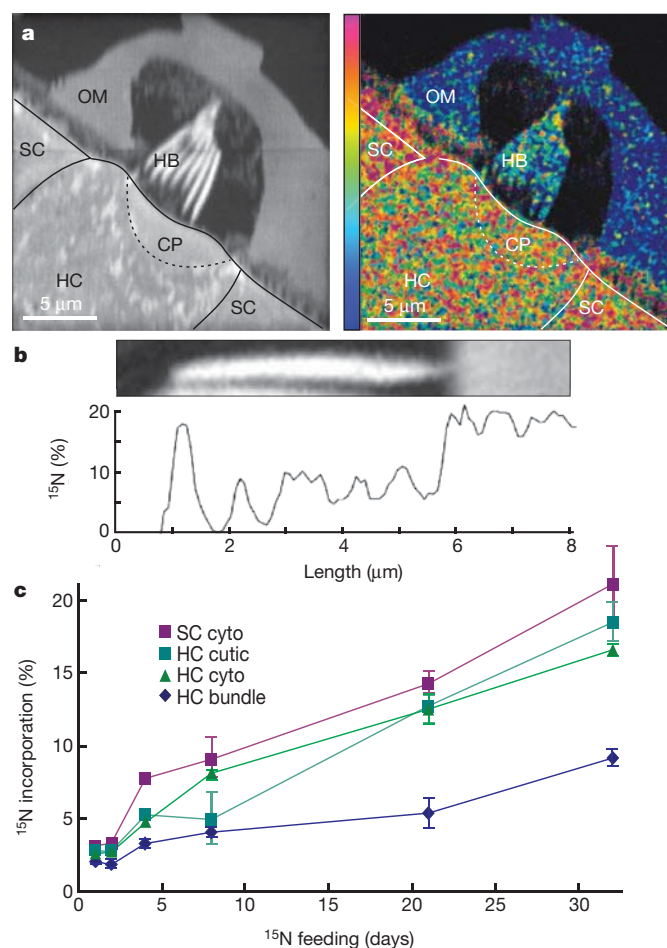


Figure 1 | Incorporation of ^{15}N into frog saccular epithelium. **a**, Left, mass-26 image for a hair cell (HC) and supporting cells (SC) at day 32. CP, cuticular plate; HB, hair bundle; OM, otolithic membrane. Right, image of mass-27/mass-26 ratio, revealing incorporation of ^{15}N . Colour scale represents 0–30% incorporation. Field is $20 \times 20 \mu\text{m}$. **b**, Top, mass-26 image of the shortest stereocilium in **a**. Bottom, profile of incorporation along its length. **c**, Turnover for days 1, 2, 4, 8, 21 and 32. cutic, cuticular plate; cyto, cytoplasm. Data are shown as mean \pm standard error of the mean (s.e.m.); N was typically 8–10.

¹Department of Neurobiology, Harvard Medical School and Howard Hughes Medical Institute, Boston, Massachusetts 02115, USA. ²Department of Biochemistry, Molecular Biology and Biophysics, University of Minnesota, Minneapolis, Minnesota 55455, USA. ³The Wellcome Trust Sanger Institute, Wellcome Trust Genome Campus, Hinxton, Cambridge CB10 1SA, UK. ⁴National Resource for Imaging Mass Spectrometry, Division of Genetics, Brigham and Women's Hospital and Harvard Medical School, Cambridge, Massachusetts 02139, USA. [†]Present address: Georg August University, D-37077 Göttingen, Germany.

*These authors contributed equally to this work.

stereocilia incorporated new protein at $<0.3\%$ per day, far lower than the 50% per day suggested for actin in mammalian cochlea². One difference is that MIMS assesses total protein; perhaps actin turns over rapidly but most other proteins are very stable. However, actin is 50–60% of the total protein in stereocilia^{9,10} and would account for the majority of the MIMS signal.

Surprisingly, incorporation seemed higher at the very tips of stereocilia (Fig. 1b). Incorporation at the tip almost equalled that of cytoplasm (Fig. 1c). In this bundle, incorporation at the tips of all stereocilia was 12.5%, compared to 6.1% in the shafts. We also measured incorporation in individual ROIs along the length of a stereocilium. Of 37 frog stereocilia, there was no correlation with height in 31 and positive correlation in just one, inconsistent with movement of the ^{15}N label from top to bottom.

Protein turnover in bullfrog stereocilia was much slower than that inferred for mouse and rat hair cells^{2,11}, leading us to wonder whether turnover is more rapid in mammals. We fed adult mice ^{15}N -leucine and killed them after 1, 2, 8, 32, 56 or 150 days. In the mouse vestibular

system, ^{15}N incorporation was faster in the cytoplasm of hair cells and supporting cells (Fig. 2a, b, e; $\sim 7\%$ per day initially) but still slow in stereocilia ($<3\%$ per day initially). This was not a peculiarity of actin-based structures: intestinal-brush-border microvilli showed more incorporation than the cytoplasm, and much more than stereocilia (Supplementary Fig. 2).

The MIMS instrument acquires repeated images, slowly etching the surface to create thousands of XY planes with a Z resolution of approximately 1 nm allowing the creation of a three-dimensional representation (Fig. 2c, d and Supplementary Movies 1 and 2). In mouse utricle, incorporation was again much higher in the tips than elsewhere in stereocilia. Although tip labelling would be expected in the initial phase of treadmilling, the high-turnover region never extended much below the top micrometre, which apparently represents a fixed zone that does not move down by treadmilling.

We then wondered whether turnover is more rapid in cochlear than vestibular hair cells. Apparently not: at 8, 32, 56 and 150 days (Fig. 2f–j), cochlear stereocilia had slower incorporation of new protein ($\sim 2\%$

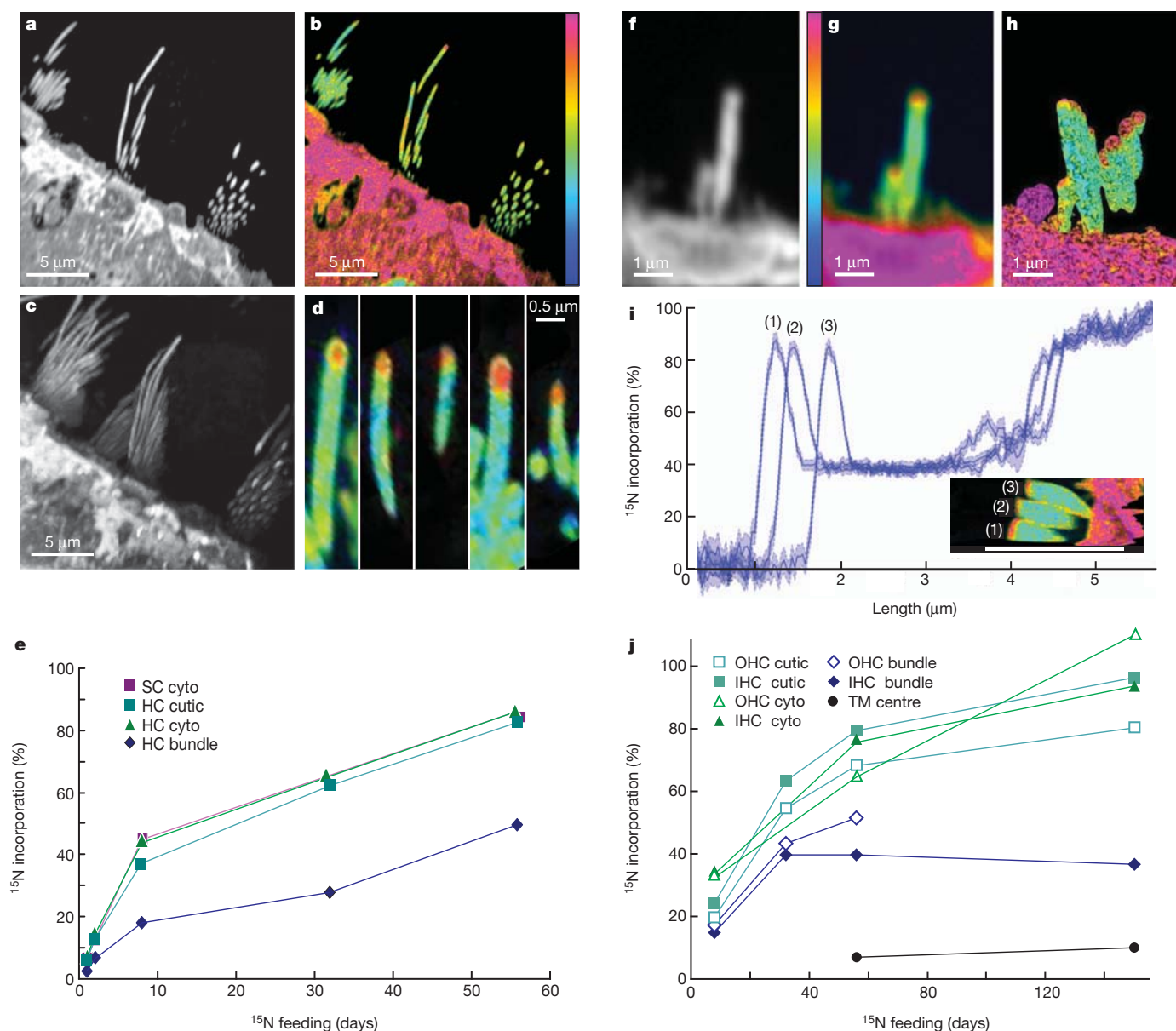


Figure 2 | Incorporation of ^{15}N into adult mouse hair cells. **a**, Mass-26 image of utricle; day 56. **b**, Mass-27/mass-26 ratio: low incorporation in stereocilia. **c**, Projection of a three-dimensional stack of **a**. **d**, Ratio image from **c**: high turnover at tips. **e**, Incorporation, days 1–56. cutic, cuticular plate; cyto,

cytoplasm; HC, hair cell; SC, supporting cell. **f**, Cochlear inner hair cell; day 56; mass 26. **g**, Ratio image. **h**, Three-dimensional reconstruction from 450 images. **i**, Incorporation along axis of stereocilia from **h**. Bar: plotted length. Line widths: 95% confidence. **j**, Incorporation after 8, 32, 56 or 150 days. Colour scale 0–100%.

initially) than did cell bodies or cuticular plates ($\sim 3.5\%$ initially). Moreover, adult stereocilia apparently have a pool of protein that is replaced exceedingly slowly: ^{15}N incorporation after 5 months was $<60\%$.

A three-dimensional image of cochlear hair bundles (Fig. 2h and Supplementary Movie 3) also showed high turnover in the distal micrometres of the stereocilia. At 56 days, ^{15}N incorporation was 40% along most of the length of individual stereocilia, but $>80\%$ at the tips (Fig. 2i). Except for the tips, we did not see a gradient of incorporation. In addition, the resolution of MIMS revealed higher turnover in the region of the cell membrane than in stereocilia cores (Fig. 2i, inset), perhaps reflecting rapid diffusion of some membrane proteins¹².

Elsewhere in the cochlea, ^{15}N incorporation varied considerably (Supplementary Fig. 1). Like the frog otolithic membrane, the mouse tectorial membrane was exceptionally stable, with $\sim 10\%$ ^{15}N incorporation in 5 months. Pillar cell shafts, containing stiff microtubule bundles, had just 23% incorporation. The reticular lamina, comprising the actin-rich cuticular plates of hair cells, terminal webs of Dieter's cells and their zonulae adherens, showed low turnover. Thus, low turnover occurred in structures that convey sound to stereocilia.

Protein turnover could be more rapid in neonatal mice. To test this, mice were moved at birth to surrogate mothers that had been fed ^{15}N for 24–28 days to raise the ^{15}N content of their milk; pups were nursed for 0–15 days before being killed. In a second group, mothers were fed ^{15}N before and during pregnancy. At birth, pups were moved to control nurse mothers, and protein turnover was measured as ^{15}N loss. Pups nursed by ^{15}N mothers showed a normal rise in ^{15}N in utricular cytoplasm (Supplementary Fig. 3), with 30–50% incorporation in 4 days. In stereocilia, protein turnover was slower, with 25% in 4 days (Supplementary Fig. 3b, g). A three-dimensional rendering also showed low turnover in stereocilia, except at the tips (Supplementary Fig. 3c).

A difficulty in interpretation is that about half the hair bundles in the mouse utricle develop postnatally¹³, so incorporation of new protein in the stereocilia might reflect development rather than turnover. Indeed, small bundles, presumably still developing, showed high incorporation (Supplementary Fig. 4), and were therefore excluded from the analysis in Supplementary Fig. 3g. Another difficulty is the assumption that tagged leucine is incorporated equally into proteins. Proteins with a lower abundance of leucine than the average (9.36%) would have a lower $^{15}\text{N}/^{14}\text{N}$ ratio, which might be interpreted as slow turnover. In fact, stereocilia proteins do have less leucine. The ten most abundant proteins of neonatal rat utricular stereocilia (P. Gillespie, personal communication), adjusted for abundance, have 8.53% leucine. This is not enough to account for low stereocilia incorporation, but we sought a different way to measure turnover.

We therefore measured the loss of ^{15}N in pups born to ^{15}N -fed mothers but nursed by controls, normalizing ^{15}N levels in each structure to that at postnatal day (P)0 (Supplementary Fig. 3h). Consistent with some postnatal bundle development, small bundles had little or no label, but full-sized hair bundles retained ^{15}N for many days, with 70% remaining at P4 (Supplementary Fig. 3d–f, h and Supplementary Fig. 4).

Perhaps turnover in stereocilia is more rapid *in vitro*. We cultured utricles from P0 pups and added ^{15}N -leucine after one day. Over four more days, hair bundles showed relatively low ^{15}N incorporation ($\sim 8\%$ per day versus 12–16% per day in cytoplasm; Supplementary Fig. 5).

Perhaps the fluorescence previously observed² was due to newly synthesized β -actin–GFP that was only a small fraction of the actin in the core—in essence a tracer for treadmilling, the bulk of which was driven by recycling of actin monomers that are only slowly replaced. To assess treadmilling with an alternative to MIMS, and with steady rather than transient expression of a tracer, we constructed mouse lines expressing β -actin–GFP under the myosin-7a promoter (Supplementary Fig. 6). Stereocilia were brightly fluorescent (Fig. 3). We dissected utricles at ages P0–P5 and cultured them for 1 day. In a confocal microscope, we selected a field in which the epithelium was tilted sideways, and bleached the GFP in a 1- μm -wide line mostly

perpendicular to the bundle axis, for 5–8 bundles (Fig. 3b, c). A three-dimensional confocal stack was acquired, and the utricle placed back into culture. Two, four and six days later, each utricle was returned for imaging (Fig. 3d). The bleached line was sometimes obscured if the bundle axis changed in culture, but the three-dimensional image could be used to reconstruct it. In all experiments, we saw no significant movement of the bleached line (Fig. 3f). On average, the line moved by $2 \pm 3\%$ of the bundle height in 6 days (Fig. 3g).

It is possible that our cultures were not healthy, and that treadmilling was impaired. However, in the same utricles, we observed the appearance and growth of new bundles. Moreover, both bleached and unbleached hair cells took up the fluorescent dye RH414, a marker for functional transduction (data not shown). Thus an independent method gave no evidence of treadmilling on a timescale of days.

The GFP tag could have inhibited treadmilling in *Myo7a::\beta*-actin:GFP mice. We therefore studied treadmilling by terminating β - or γ -actin expression and following the redistribution of actin with antibodies. Mice expressing a tamoxifen-inducible Cre under the β -actin promoter were crossed with mice carrying either a floxed β - or γ -actin gene¹⁴. At 3

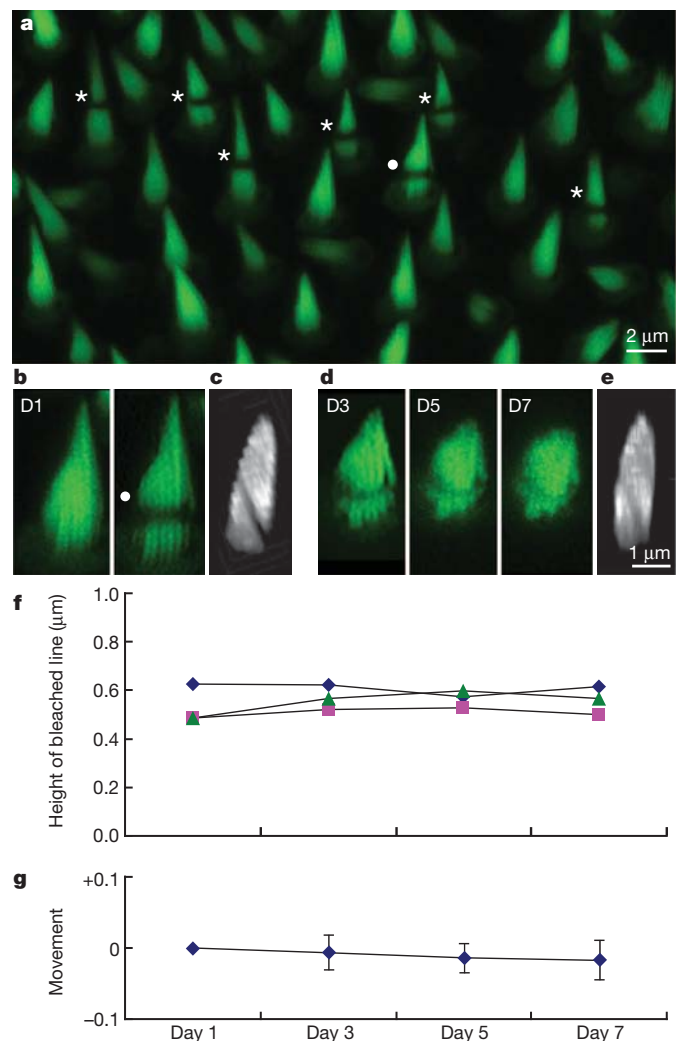


Figure 3 | Tracking treadmilling by bleaching GFP-tagged β -actin. **a**, Neonatal utricular macula in culture, hair cells expressed β -actin–GFP. Bleached bundles are indicated by asterisks. **b**, Projection of confocal planes before and after bleaching. **c**, Three-dimensional stack rotated to show oblique bleached line. **d**, Same bundle on days (D)3, 5 and 7. A shift in bundle orientation partially obscured the line. **e**, Rotation of the day-7 stack revealed the bleached line. **f**, Line positions for three bundles, as a proportion of bundle height. **g**, Average movement of bleached lines, as a proportion of bundle height. $N = 24$; mean \pm s.e.m.

weeks of age, after bundles had developed, mice were given tamoxifen to promote excision. One, three, eighteen or thirty-four weeks later, we fixed and removed cochleas, and used antibodies specific for β - and γ -actin.

In control mice without tamoxifen, β - and γ -actin were uniformly distributed (Fig. 4a). If there is rapid treadmilling in adults, β -actin protein should be lost from stereocilia soon after excision prevented β -actin gene expression. Similarly, γ -actin should be lost in mice with a floxed γ -actin gene. This occurred, but only for a 0.4- μ m region at stereocilia tips (Fig. 4a, b). The rest of the stereocilium retained the deleted actin isoform, and the region of isoform loss did not progress towards stereocilia bases, even after 34 weeks.

The MIMS method provides a new way to study protein stability in the inner ear⁷. MIMS is based on Schoenheimer's pioneering use of stable isotopes to reveal the dynamics of cellular components¹, but adds imaging with exceptional spatial resolution. ¹⁵N incorporation can be calculated with an accuracy that depends only on acquisition time. It does not rely on tagging any one protein species, or transfecting a specific cell type.

In contrast to previous studies², MIMS revealed unexpectedly low turnover of protein in hair-cell stereocilia. Incorporation of ¹⁵N in stereocilia occurred at <0.3% per day in frog, <2% per day in adult mouse and <9% per day in neonatal mice, incompatible with treadmilling in 2–3 days. By bleaching fluorescently labelled actin in bundles, we saw no significant movement of the actin. Finally, excision of the β - and γ -actin genes in mature mice showed loss of the excised actin from the stereocilia tips, but not a progressive loss from tip to base. We found no evidence for treadmilling of stereocilia cores, over

weeks or even months. It is possible that the previously observed treadmilling was produced by overexpression of β -actin, if the exogenous actin significantly exceeds endogenous actin. Or—at least in the vestibular system—addition of actin to hair bundles developing postnatally might have confused interpretation.

Nevertheless, there is a conspicuously dynamic turnover of protein at the tips of stereocilia, in the distal 0.3–0.5 μ m. This could represent turnover of transduction components, which can be replaced in hours when damaged^{4,5}. It could represent movement of proteins to the tips by hair-cell myosins, most of which climb from bases to tips. Or it may reflect a rapid regulation of actin filaments, which can change length by \sim 0.1 μ m when tip links are cut². If so, there might be both polymerization and depolymerization at the barbed end. Rapid but local regulation of filament length is not inconsistent with the limited growth of stereocilia induced by overexpression of *espin*³.

In long-lived vertebrates, the actin of stereocilia must be replaced. It may be that treadmilling does occur, but at a timescale far longer than that studied here. It may instead be that individual actin filaments do not extend the length of the stereocilium—that free ends can accept or shed monomers and that unsynchronized treadmilling occurs on a submicroscopic scale. Unlike filopodia, stereocilia seem to develop once, elaborating an intricate staircase of heights that persists for the life of an animal; in most of their length, they then replace individual proteins slowly and without disrupting this exquisite structure.

METHODS SUMMARY

Tissue preparation and ¹⁵N feeding. Adult bullfrogs (*Rana catesbeiana*) were maintained on a ¹⁵N-leucine diet, then fixed and treated with EDTA to dissolve otoconia before embedding and sectioning.

Adult mice (*Mus musculus*, CD1 strain) were maintained on a ¹⁵N-leucine diet before being killed and processed. For neonatal mice, mothers were maintained on ¹⁵N food before and during pregnancy; at birth, the pups were moved to a control surrogate mother. A second set was born to control mothers and moved at birth to a surrogate mother that had been maintained on ¹⁵N food.

Utricles were dissected, cultured overnight in DMEM-F12 with 1 or 6% FBS¹⁶ and maintained in ¹⁵N-enriched medium for up to 5 days.

MIMS analysis. MIMS was performed as described previously⁷. ¹⁵N incorporation was calculated by comparing counts for masses 27 and 26 to the natural abundance of ¹⁵N (0.37%) and the relative abundance of ¹⁵N in the food (1–2%).

Photobleaching of cultured mouse utricle. We constructed mice expressing a β -actin–GFP fusion under the myosin-7a promoter, integrated in the HPRT locus on the X chromosome (see Supplementary Fig. 6). Utricles from neonatal pups (mosaic for the transgene) were cultured as above. Hair bundles were bleached on day 1; images were taken on days 3, 5 and 7.

Conditional deletion of β - and γ -actin. *Actg1^{lox}* and *Actl^{lox}* mice, in which exons 3 and 4 were flanked by *loxP* sites¹⁴ were crossed to mice expressing Cre/*Esr1* recombinase driven by the chicken β -actin promoter coupled to the cytomegalovirus immediate-early enhancer. Mice were dosed with tamoxifen to induce recombination. Anti- γ -actin antibody clone 1-37 (ref. 15) IgG was conjugated to Alexa fluorescent dyes. FITC-labelled anti- β -actin antibodies (clone AC-15) were obtained from Abcam.

Full Methods and any associated references are available in the online version of the paper at www.nature.com/nature.

Received 25 July; accepted 1 December 2011.

Published online 15 January 2012.

- Schoenheimer, R. *The Dynamic State of Body Constituents* (Harvard Univ. Press, 1942).
- Rzadzinska, A. K. et al. An actin molecular treadmill and myosins maintain stereocilia functional architecture and self-renewal. *J. Cell Biol.* **164**, 887–897 (2004).
- Rzadzinska, A. et al. Balanced levels of *espin* are critical for stereociliary growth and length maintenance. *Cell Motil. Cytoskeleton* **62**, 157–165 (2005).
- Zhao, Y., Yamoah, E. N. & Gillespie, P. G. Regeneration of broken tip links and restoration of mechanical transduction in hair cells. *Proc. Natl Acad. Sci. USA* **93**, 15469–15474 (1996).
- Jia, S., Yang, S., Guo, W. & He, D. Z. Fate of mammalian cochlear hair cells and stereocilia after loss of the stereocilia. *J. Neurosci.* **29**, 15277–15285 (2009).
- Pickles, J. O., Billieux-Hawkins, D. A. & Rouse, G. W. The incorporation and turnover of radiolabelled amino acids in developing stereocilia of the chick cochlea. *Hear. Res.* **101**, 45–54 (1996).

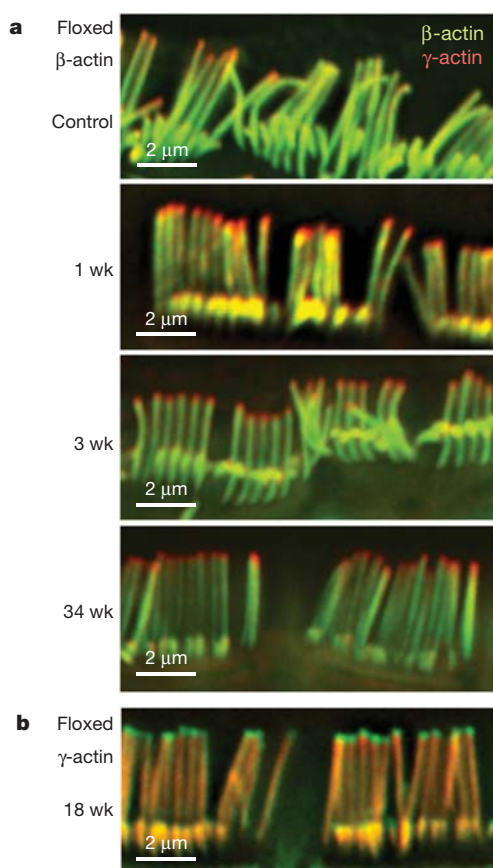


Figure 4 | Loss of actin from tips following knockout of actin genes. a, b, Adult (3-week-old) cochlear inner hair cells, labelled with antibodies to β -actin (green) or γ -actin (red). a, Floxed β -actin mouse crossed to Cagg-CreER, without tamoxifen (control), or 1, 3 or 34 weeks (wk) after tamoxifen. Loss of β -actin occurred only at tips of stereocilia. In control mice, a few hair cells displayed loss of β -actin at tips without tamoxifen, suggesting a leaky promoter. b, Floxed γ -actin mouse 18 weeks after tamoxifen. Loss of γ -actin occurred only at tips of stereocilia.

7. Lechene, C. *et al.* High-resolution quantitative imaging of mammalian and bacterial cells using stable isotope mass spectrometry. *J. Biol.* **5**, 20 (2006).
8. Lechene, C. P., Luyten, Y., McMahon, G. & Distel, D. L. Quantitative imaging of nitrogen fixation by individual bacteria within animal cells. *Science* **317**, 1563–1566 (2007).
9. Shepherd, G. M. G., Barres, B. A. & Corey, D. P. “Bundle Blot” purification and initial protein characterization of hair-cell stereocilia. *Proc. Natl Acad. Sci. USA* **86**, 4973–4977 (1989).
10. Shin, J. B. *et al.* Hair bundles are specialized for ATP delivery via creatine kinase. *Neuron* **53**, 371–386 (2007).
11. Schneider, M. E., Belyantseva, I. A., Azevedo, R. B. & Kachar, B. Rapid renewal of auditory hair bundles. *Nature* **418**, 837–838 (2002).
12. Grati, M. *et al.* Rapid turnover of stereocilia membrane proteins: evidence from the trafficking and mobility of plasma membrane Ca^{2+} -ATPase 2. *J. Neurosci.* **26**, 6386–6395 (2006).
13. Kirkegaard, M. & Nyengaard, J. R. Stereological study of postnatal development in the mouse utricular macula. *J. Comp. Neurol.* **492**, 132–144 (2005).
14. Perrin, B. J., Sonnemann, K. J. & Ervasti, J. M. β -actin and γ -actin are each dispensable for auditory hair cell development but required for stereocilia maintenance. *PLoS Genet.* **6**, e1001158 (2010).
15. Hanft, L. M. *et al.* Cytoplasmic γ -actin contributes to a compensatory remodeling response in dystrophin-deficient muscle. *Proc. Natl Acad. Sci. USA* **103**, 5385–5390 (2006).
16. Holt, J. R. *et al.* A chemical-genetic strategy implicates myosin-1c in adaptation by hair cells. *Cell* **108**, 371–381 (2002).

Supplementary Information is linked to the online version of the paper at www.nature.com/nature.

Acknowledgements C.P.L. thanks M. Raff for numerous discussions; T. Bloom for her insight, foresight and support at the origin of MIMS development. We thank D. Cotanche and G. Benichou for providing additional mouse cochlear samples, L. Trakimas for

histological assistance, Z. Kaufman for assisting data analysis, and J. Hill for electronic and mechanical maintenance of the prototype instrument. G. McMahon contributed to operating the instrument and data analysis. This work was supported by National Institutes of Health/National Institute of Biomedical Imaging and Bioengineering (NIH/NIBIB) grants P41RR14579, P41EB001974, NIH grants R01DC00033, R01DC03463, R01DC04179, R37DK39773, R01EY12963, R01GM47214 and R01D K58762, and National Science Foundation Division of Integrative Biology and Neuroscience (NSF/IBN) grant IBN-998298 to C.P.L., by NIH grant R01DC02281 to D.P.C., and by NIH grants F32DC009539 to B.J.P. and R01AR049899 to J.M.E., and by Wellcome Trust grant WT079643 to the Wellcome Trust Sanger Institute. Development of the SIMS instrument was supported by ONERA, CNRS, Université Paris Sud and Cameca (France). The work was also helped in part by software funded by the NIH National Center for Research Resources (NIH/NCRR) Center for Integrative Biomedical Computing, 2P41 RR0112553-12 and the Department of Energy SciDAC Visualization and Analytics Center for Enabling Technologies, DEFC0206ER25781. D.-S.Z. is a Research Associate, V.P. was a Research Associate and D.P.C. is an Investigator of the Howard Hughes Medical Institute.

Author Contributions D.-S.Z. carried out the ^{15}N experiments and the preparation of tissue for MIMS imaging. V.P. and A.K.R. conceived the photobleaching experiments; A.K.R. and H.M.P. made the β -actin–GFP mouse and V.P. did the experiments. B.J.P. and J.M.E. conceived the conditional actin deletion experiments; B.J.P. made the mice and carried out the experiments. C.P.L. and D.P.C. conceived the MIMS study of hair cells. C.P.L. developed the MIMS method, oversaw the MIMS imaging with M.W. and analysed the MIMS images with J.C.P. D.P.C. wrote the manuscript.

Author Information Reprints and permissions information is available at www.nature.com/reprints. The authors declare no competing financial interests. Readers are welcome to comment on the online version of this article at www.nature.com/nature. Correspondence and requests for materials should be addressed to C.P.L. (cpl@harvard.edu) or D.P.C. (dcorey@hms.harvard.edu).

METHODS

Tissue preparation and ^{15}N feeding. Adult bullfrogs (*Rana catesbeiana*) were fed an unlabelled control diet for 2–3 days, and were transferred at day 0 to a ^{15}N -rich diet. Food pellets contained ^{15}N -labelled leucine so that the ^{15}N content was 1.28%. Bullfrogs were fixed via cardiac perfusion with 4% formaldehyde + 0.1% glutaraldehyde. After decapitation, the sacculles were exposed and the head and carcass stored in 4% formaldehyde + 1% glutaraldehyde. Heads were transferred to PBS before dissection of the sacculles. Sacculles were then treated with EDTA for 2–10 days to dissolve otoconia before embedding in Epon and sectioning.

Adult mice (*Mus musculus*, CD1 strain) ate control food that contained no added ^{15}N , and then were switched to food with ^{15}N -leucine (either 1.28 or 1.23%) for up to 150 days. Neonatal mice were labelled in two ways. For one set, mothers were fed ^{15}N food for 4–8 days, mated, and continued on ^{15}N food until pups were delivered (^{15}N mother). At birth, the pups were moved to a surrogate mother that had been maintained on control food (^{14}N mother). A second set was born to ^{14}N mothers and moved at birth to a surrogate mother that had been maintained for 24–28 days and was continued on ^{15}N food. Pups were nursed by surrogate mothers for 0, 2, 4, 8 or 15 days before being killed and fixed. At least two animals (four inner ears) were prepared for each condition.

Cultured utricles were dissected by standard methods¹⁷. After removing the otolithic membranes, the maculae were plated on a sterile portion of ACLAR film (EMS) and incubated in DMEM-F12 containing 100 µg ml⁻¹ carbenicillin, with either 1 or 6% FBS. After an overnight incubation, the medium was replaced with ¹⁵N-enriched medium (¹⁵N, Cambridge Isotopes, 2.44 or 1.35% ¹⁵N). The cultures were then incubated at 37 °C for up to 5 days until fixation. Tissues were fixed in 4% formaldehyde + 0.1% glutaraldehyde in cacodylate buffer for 15 min at 22 °C, then overnight at 4 °C. Cultures were then moved to cacodylate buffer and held for 2–3 days at 4 °C, before processing in batches for plastic embedding, as above.

MIMS analysis. In the multi-isotope imaging mass spectrometer⁷, a ~30 nm beam of Cs⁺ ions, scanned across the sample, sputters atoms, atomic clusters or molecules from the surface, of which a small fraction are ionized. Negative secondary ions are accelerated back, then shaped with ion optics and analysed with a double sector mass spectrometer employing four detectors, each tuned to a specific mass. Because N₂ is not charged, ¹⁵N and ¹⁴N were detected as cyanide anions, ¹²C¹⁵N⁻ and ¹²C¹⁴N⁻, mass 27 and mass 26, respectively, and their ratio was calculated for each point in the raster scan.

We calculated the proportion of newly synthesized protein, for each pixel of the field, from the ratio of counts in the $^{12}\text{C}^{15}\text{N}$ and $^{12}\text{C}^{14}\text{N}$ images according to

$$\text{incorporation} = \frac{\frac{N_{27}}{N_{26}} - A_n}{A_f - A_n}$$

where N_{27} and N_{26} are the counts in each pixel for masses 27 and 26, A_n is the natural abundance of ^{15}N (0.37%), and A_f is the relative abundance of ^{15}N in the food (1–2%). Incorporation was displayed with a hue saturation intensity transformation (HSI) in which the hue corresponds to the ratio value, and the intensity is an index of statistical reliability⁸. Image analysis performed in Image/OpenMIMS (NIH/NRIMS). 3D reconstructions made in ImageVis3D (NIH/NCRR SCI/CIBC).

Photobleaching of cultured mouse utricles. To label endogenous actin, we constructed mice expressing a β -actin-GFP fusion under the myosin-7a promoter,

integrated in the HPRT locus on the X chromosome. Correct integration of the BAC was confirmed Southern blot using flanking probes. Details of the construction, using methods previously described¹⁷, are in Supplementary Fig. 6.

Neonatal pups (heterozygous and therefore mosaic for the transgene) were killed between P0 and P4, their utricles dissected and cultured as above. Dissection was performed on experimental day 0, then stereocilia were bleached on day 1 and images were taken on experimental days 3, 5 and 7. Each imaging day, the cells were transferred to DMEM-F12 without phenol red and then to the stage of an Olympus FV1000 confocal (upright configuration, LUMFL $\times 60$ immersion objective, 1.1 NA) with a warmed chamber. On day 1, a Z-stack of the selected field containing 20–50 hair cells was collected using confocal imaging of the GFP with a 488 nm laser. Target hair bundles were selected and bleached with one to three 300-ms flashes of a focused 405 nm laser at $20 \mu\text{s pixel}^{-1}$. Each selected bundle in the field was separately bleached. After bleaching, another Z-stack for the whole field was collected to confirm the bleached locations. The following experimental days one Z-stack per field was acquired. Movement of the bleached line was assessed by rotating the image stack to observe the line relative to the full length of the bundle.

Conditional deletion of β - and γ -actin. The *Actg1*^{fllox} and *Actb*^{fllox} mice, in which exons 3 and 4 were flanked by *loxP* sites¹⁴ were crossed to transgenic mice expressing Cre/Esr1 recombinase driven by the chicken β -actin promoter coupled to the cytomegalovirus immediate-early enhancer (Jackson Labs; stock number 004682). All mice were on the C57BL/6 background. Mice were dosed with tamoxifen once a day for 4 days to induce recombination (20 mg ml⁻¹ in corn oil, administered as 0.15 mg tamoxifen per gram of mouse by oral gavage). Esr1 control of Cre recombinase seemed to be leaky, in that 18-week-old mice that had not been given tamoxifen had the same actin-distribution phenotype as mice given tamoxifen; both were different from mice lacking CAG-Cre/Esr1. The phenotype was seen in a few cells of 3-week-old mice even in the absence of tamoxifen, so we restricted quantitative analysis to mice dosed with tamoxifen at 3 weeks.

Monoclonal mouse anti- γ -actin antibody clone 1-37 IgG (ref. 15) was purified from ascites using a T-gel Purification kit (Pierce) and conjugated to either Alexa-488 or Alexa-568 fluorescent dyes using a Monoclonal Antibody Labelling Kit (Invitrogen) following the manufacturer's instructions. FITC-labelled anti- β -actin antibodies (clone AC-15) were obtained from Abcam (validated in ref. 14).

For labelling, mice were perfused with 4% paraformaldehyde in PBS. Cochleas were then dissected and incubated in the same fixative for 2 h at room temperature (22 °C), washed in PBS and decalcified in 170 mM EDTA in PBS at 4 °C for 16 h. The organ of Corti was dissected, postfixed in 100% methanol at -20 °C for 10 min, rinsed in PBS and permeabilized in 0.5% Triton X-100 in PBS for 20 min at room temperature. Tissue was blocked for 1 h in 5% goat serum in PBS before incubation with the indicated antibodies. Samples were mounted in ProLong anti-fade reagent and viewed on a Deltavision PersonalDV deconvolution microscope equipped with a $\times 100$ 1.4 NA objective (Applied Precision). Stacks of images were collected at 0.20- μm intervals and deconvolved using Resolve3d software (Applied Precision).

17. Prosser, H. M., Rzadzinska, A. K., Steel, K. P. & Bradley, A. Mosaic complementation demonstrates a regulatory role for myosin VIIa in actin dynamics of stereocilia. *Mol. Cell. Biol.* **28**, 1702–1712 (2008).

Molecular recognition of a single sphingolipid species by a protein's transmembrane domain

F.-Xavier Contreras^{1*}, Andreas M. Ernst^{1*}, Per Haberkant^{1†}, Patrik Björkholm^{2,3}, Erik Lindahl^{2,4}, Başak Gönen¹, Christian Tischer⁵, Arne Elofsson^{2,3}, Gunnar von Heijne^{2,3}, Christoph Thiele⁶, Rainer Pepperkok⁵, Felix Wieland¹ & Britta Brügger¹

Functioning and processing of membrane proteins critically depend on the way their transmembrane segments are embedded in the membrane¹. Sphingolipids are structural components of membranes and can also act as intracellular second messengers. Not much is known of sphingolipids binding to transmembrane domains (TMDs) of proteins within the hydrophobic bilayer, and how this could affect protein function. Here we show a direct and highly specific interaction of exclusively one sphingomyelin species, SM 18, with the TMD of the COPI machinery protein p24 (ref. 2). Strikingly, the interaction depends on both the head-group and the backbone of the sphingolipid, and on a signature sequence (VXXTLXXIY) within the TMD. Molecular dynamics simulations show a close interaction of SM 18 with the TMD. We suggest a role of SM 18 in regulating the equilibrium between an inactive monomeric and an active oligomeric state of the p24 protein^{3,4}, which in turn regulates COPI-dependent transport. Bioinformatic analyses predict that the signature sequence represents a conserved sphingolipid-binding cavity in a variety of mammalian membrane proteins. Thus, in addition to a function as second messengers, sphingolipids can act as cofactors to regulate the function of transmembrane proteins. Our discovery of an unprecedented specificity of interaction of a TMD with an individual sphingolipid species adds to our understanding of why biological membranes are assembled from such a large variety of different lipids.

Lipidomics of Golgi-derived COPI vesicles unravelled a partial segregation of cholesterol and most sphingomyelin species except for one (*N*-stearoyl sphingomyelin) from the vesicle fraction⁵. To understand the molecular mechanisms of SM 18 enrichment in vesicles, we investigated *in vivo* binding of lipids to p24 and p23, membrane proteins involved in COPI vesicle biogenesis (Supplementary Fig. 1)⁶. Lipid crosslinking^{7,8} revealed a strong sphingolipid labelling of p24 (Fig. 1a, b, see also Supplementary Fig. 2), with a fivefold higher recovery of radioactivity per mole of protein compared to p23. To analyse if this interaction of p24 with sphingomyelin is specific for SM 18, we established a liposomal assay to study TMD–lipid interactions (see Supplementary Fig. 3). Maltose-binding protein (MBP) fusions of the TMDs of p23 and p24 were analysed in a liposomal Förster resonance energy transfer (FRET) system for their interaction with pentaenoyl-SM 18 (SM 18:5, as a fluorescently labelled analogue of endogenous SM 18:O (ref. 9), see Supplementary Information), pentaenoyl-ceramide 18, or pentaenoyl-phosphatidylcholine (PC) 18 (Fig. 1c). Distinct FRET was observed between the TMD of p24 and SM 18:5, but not with the TMD of p23. A mutant lacking the single Trp residue within the TMD (p24(TMD)W4A) did not trigger a FRET. With ceramide 18:5 no FRET was observed for any TMD. With PC 18:5 weak FRET was observed with the p24(TMD), and a slightly stronger signal was obtained with p23(TMD). Together these results show a marked specificity of p24 for

sphingomyelin, with both the hydrophobic moiety and the hydrophilic choline phosphate headgroup needed for the interaction. We next analysed the extent of FRET obtained between the TMDs of p24 and p23 and pentaenoyl-sphingomyelins covering the range of the major endogenous molecular species from C14 to C24. A remarkable specificity was observed for the interaction of p24 with SM 18 in liposomes composed of di-oleoyl-phosphatidylcholine/phosphatidylethanolamine/pentaenoyl-sphingomyelin (Fig. 1d, left panel). In liposomes more closely reflecting the lipid composition of the mammalian Golgi apparatus we again observed a striking specificity for SM 18, with weak but significant signals for SM 20 and SM 22 (Fig. 1d, right panel). In contrast, the TMD of p23 did not give rise to comparable FRET with any of the sphingomyelin species.

To define the structural prerequisites for SM 18 binding, we performed an Ala scan across the TMD of p24 starting with position 8 within the TMD, leaving three amino acids before and after W4 unchanged, to minimise a direct influence on the biophysical properties of the FRET donor. Two groups of mutants were observed, with a strong inhibition of FRET with Ala substitutions in positions 8, 10, 11, 12, 15, 19 and 20 (group 1), and less inhibition in positions 13, 16, 17, 18 and 21 (group 2) (Supplementary Fig. 4). Although group 1 mutants showed a strong inhibition of FRET, they maintained a high degree of specificity for SM 18:5 (for example, V11A, Supplementary Fig. 5a). In contrast, group 2 mutants V13, T16, L17 and Y21 showed strongly compromised species specificity (Supplementary Fig. 5c–f). Mutant G18A was not further investigated, because G18W had not shown an alteration of SM 18 binding (Supplementary Fig. 3d), indicating that G18 is not directly involved in the lipid–p24 interaction. From the above data we deduced that a carboxy-terminal motif made of amino acid residues V13, T16, L17 and Y21 of the p24 TMD (V181, T184, L185 and Y189 in the full-length protein) represents a structural determinant for the specific binding of SM 18 (see also Supplementary Discussion). An energy-minimised projection of the TMD yielded the structure depicted in Fig. 2a (left). In this model, a groove is formed from the Tyr residue in position 21 to the Val residue in position 13. Within the sphingomyelin-binding motif, the β -branched residue Ile is found in position 20 of the TMD. β -branched residues were shown to contribute to TMD–TMD interactions^{10,11} by conveying higher rigidity and thereby allowing for stronger London dispersion forces. In the model, this residue is part of the cavity and thus is likely to contribute to the binding motif. If this groove indeed accommodates the backbone of SM 18, the insertion of a bulky hydrophobic residue in position 17 should prevent lipid binding. To fill this cavity with minimal alterations of the helical structure¹² we introduced a Phe residue in position 17 of the TMD. FRET analysis showed that binding of SM 18 was completely inhibited (Fig. 2b). To challenge the existence of a C-terminal binding motif, we transferred the C-terminal half of the p24 TMD to the amino-terminal half of the non-sphingomyelin-binding TMD of p23. The

¹Heidelberg University Biochemistry Center, Im Neuenheimer Feld 328, 69120 Heidelberg, Germany. ²Center for Biomembrane Research, Department of Biochemistry and Biophysics, Stockholm University, SE-106 91 Stockholm, Sweden. ³Stockholm Bioinformatics Center, Science for Life Laboratory Stockholm University, Box 1031, SE-171 21 Solna, Sweden. ⁴Theoretical & Computational Biophysics, Royal Institute of Technology, AlbaNova University Centre, SE-106 91 Stockholm, Sweden. ⁵ALMF, EMBL, Meyerhofstrasse 1, 69117 Heidelberg, Germany. ⁶LIMES Life and Medical Sciences Institute, Carl-Troll-Strasse 31, 53115 Bonn, Germany. [†]Present address: Cell Biology and Biophysics Unit EMBL, Meyerhofstrasse 1, 69117 Heidelberg, Germany.

*These authors contributed equally to this work.

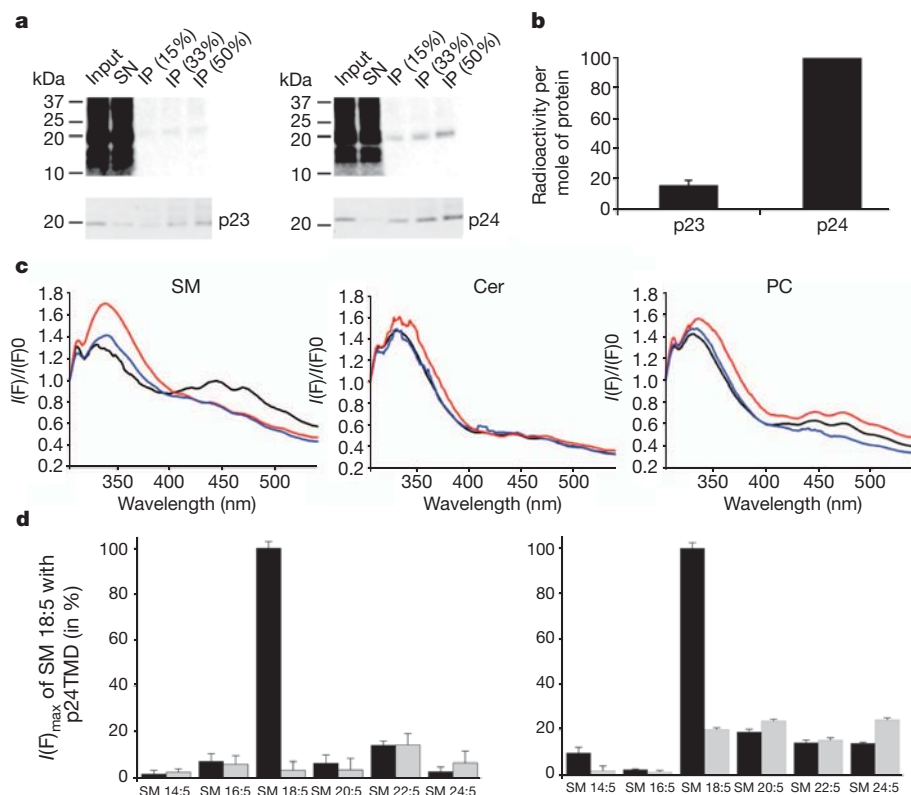


Figure 1 | p24 specifically interacts with SM 18.

a, CHO cells were grown in the presence of 200 μ Ci of [3 H]-photo-sphingosine. Cells were ultraviolet-irradiated, lysed and subjected to immunoprecipitation using antibodies against p23 or p24. Radioactivity recovered from input, supernatant (SN) and immunoprecipitation (IP) was visualized by autoradiography (upper panels). Lower panels, western blot analysis.

b, Quantification of immunoprecipitated radioactivity. **c**, *In vitro* FRET analysis of MBP-TMD fusion proteins and pentaenoyl-lipids. Proteoliposomes contained either SM 18:5, pentaenoyl-ceramide 18:5 (Cer) or PC 18:5. Red curve, p23(TMD); black curve, p24(TMD); blue curve, p24(TMD)W4A. **d**, Proteoliposomes were prepared in the presence of p24(TMD) (black bars) or p23(TMD) (grey bars) and 1 mol% of pentaenoyl-sphingomyelins, mimicking a liquid-disordered phase (left panel) or a mammalian Golgi membrane (right panel). Background-subtracted fluorescence data are normalized to SM 18:5, and are the mean \pm s.d. of three experiments.

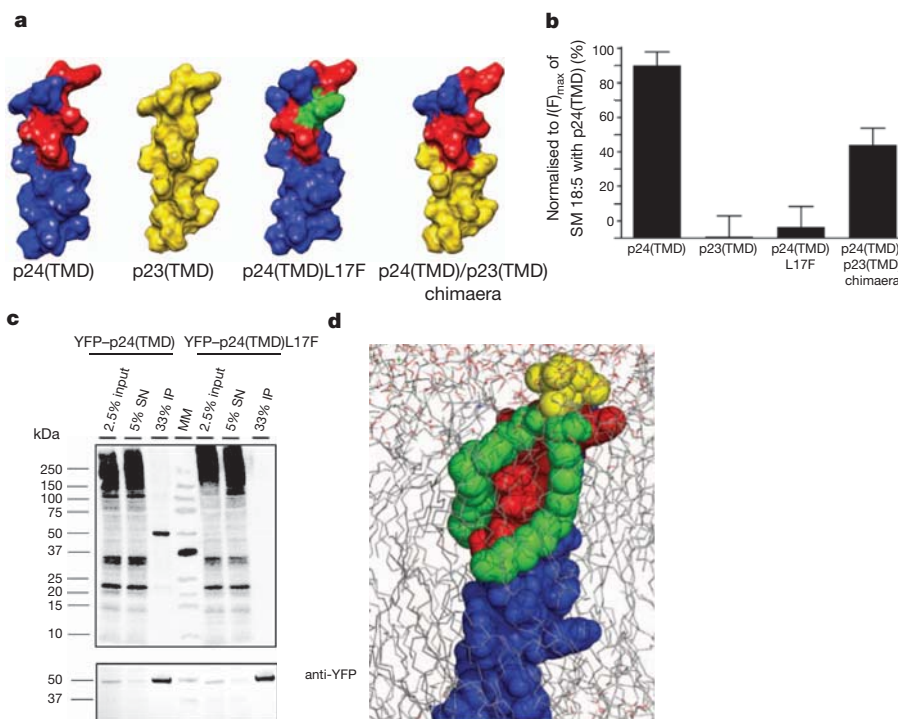


Figure 2 | Characterization of the sphingomyelin-binding pocket.

a, Energy-minimized structure of p24(TMD), p23(TMD), p24(TMD)L17F, and p24/p23 chimaeric TMD. Residues of p24 involved in SM 18 recognition are depicted in red, the L17F mutation is highlighted in green. **b**, Proteoliposomes containing p24(TMD), p23(TMD), p24(TMD)L17F or the p24(TMD)/p23(TMD) chimaera were prepared in the presence of 1 mol% of pentaenoyl-SM (18:5) (di-oleoyl-phosphatidylcholine/phosphatidylethanolamine/pentaenoyl-sphingomyelin, molar ratio 89:10:1).

FRET measurements were performed as described above. Data are the mean \pm s.d. of three independent experiments. **c**, *In vivo* binding of [3 H]-sphingolipids to YFP-p24 and YFP-p24L17F. Upper panel, autoradiography; lower panel, western blot. MM, molecular mass marker. **d**, Molecular dynamics simulations: snapshot of a SM 18-p24(TMD) interaction. The interacting lipid and residues displaying the signature are highlighted. Blue, p24(TMD); red, sphingomyelin-binding pocket, yellow; SM 18:0 head group; green, SM 18:0 backbone and N-acylated fatty acid.

chimaeric TMD yielded 50% of the level of FRET compared to the TMD of p24 (Fig. 2b). Interestingly, the chimaera shows promiscuity with regard to the sphingomyelin molecular species, binding significant amounts of SM 20 and SM 22 in addition to SM 18 (Supplementary Fig. 5b), pointing at a contribution of the N-terminal residues to the orientation of the sphingomyelin-binding pocket. The loss of FRET by mutant p24(TMD)L17F suggested a loss of SM 18 binding. To test loss of binding *in vivo*, full-length wild-type p24 and p24L17F were expressed as yellow fluorescent protein (YFP) fusion proteins (Supplementary Fig. 6a). Sphingolipid labelling showed that p24L17F has lost the capability to bind sphingomyelin *in vivo* (Fig. 2c). Sphingomyelin is known to be synthesized in the luminal leaflet; however, *in vitro* experiments suggest that sphingolipids can flip between the two leaflets stimulated by free ceramide that translocates from the cytoplasmic to the luminal leaflet of membranes¹³ (see also Supplementary Fig. 6b). In addition, *in vivo* analyses using the sphingomyelin-binding toxin equinatoxin II point to an occurrence of sphingomyelin in the cytoplasmic leaflet of the Golgi membrane¹⁴.

To understand binding selectivity at the molecular level, we compared the structural features of sphingomyelin molecular species (see Supplementary Fig. 7). Molecular dynamics simulations and monolayer experiments^{15–17} suggest that only the sphingomyelin species with a suitable dynamic volume would fit into the cavity of the p24 TMD formed by V13, T16 and L17, excluding lipids with larger dynamic volume (SM 14 and 16, see Supplementary Fig. 7). Sphingomyelin species with smaller dynamic volumes, however, would need to be excluded from the hydrophobic cavity by a different mechanism (see Supplementary Discussion).

We next investigated the binding signature through a series of five molecular simulations of the TMD of p24 embedded in a POPC bilayer including sphingomyelins with fatty acids of C14 to C22. By extending

all atomistic simulations to 1 μ s we observe spontaneous diffusion of sphingomyelins to the TMD and close interaction with the proposed binding site primarily for SM 18, and to a minor extent also SM 16 and SM 20 (Supplementary Fig. 8). The polar head group of sphingomyelin ‘wraps around’ the Y21 side chain, while the C18 chain continues down around the helix and packs in the groove between V13, T16 and L17 (Fig. 2d and Supplementary Movie 1). The sphingosine chain packs in the groove below V13. The other sphingomyelin molecular species also approach the p24 TMD, but steric effects seem to make interactions more difficult in these cases. For instance, the SM 14 lipid head group rather interacts with Y21 by packing mostly below the side chain, which rotates both lipid chains away from the helix and prevents efficient packing (Supplementary Movie 2). The lifetime of the SM 18–p24 (TMD) complex in the molecular dynamics simulation was of the order of 250 ns, which is five times longer than observed for the other sphingomyelin species. Likewise, as compared to SM 18, the relative dissociation constant of SM 14 was 6.5-fold higher (Supplementary Fig. 9). Notably, although the TMD of p24 is highly conserved in higher eukaryotes, it is not conserved in yeast, in agreement with the absence of sphingomyelin in this organism.

To search for other candidate sphingolipid-interacting proteins, we defined a binding signature where either a β -branched residue (I, T, V) or Leu is allowed in any of the first four positions, and an aromatic residue (F, W, Y) is allowed in the last position (Fig. 3a). The signature represents $4^4 \times 3 = 768$ unique sequence motifs, 13 of which were found to be overrepresented in a set of mammalian membrane proteins (see Full Methods in Supplementary Information). These 13 motifs identified 48 candidate proteins (Supplementary Table 1), mostly localized to the plasma membrane (Fig. 3b).

Three recombinant candidates and, as a negative control, the non-signature containing asialo-glycoprotein receptor, were expressed in

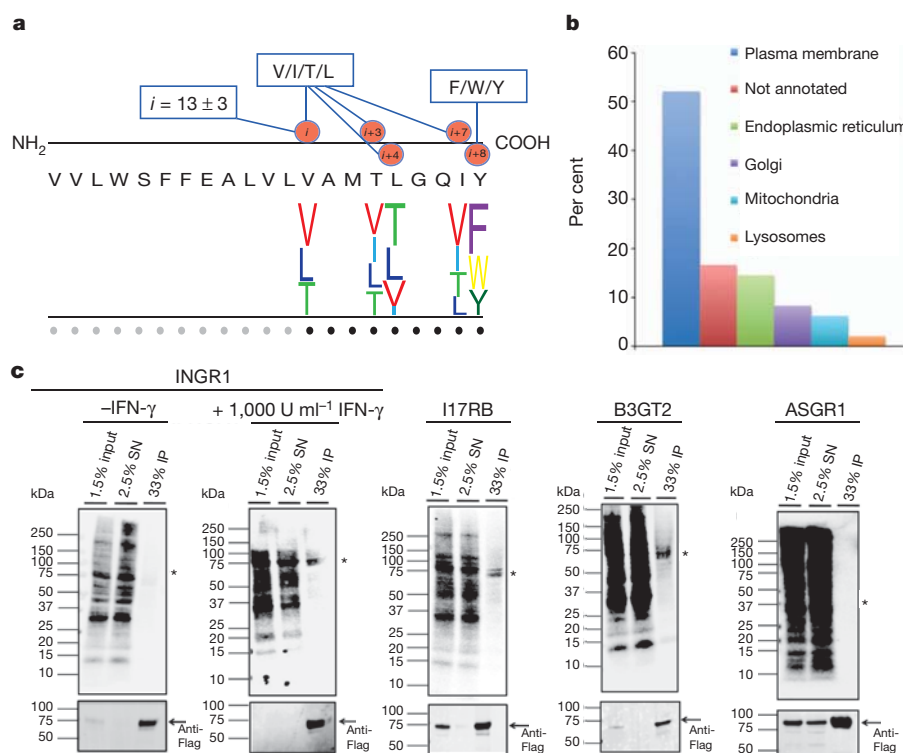


Figure 3 | A conserved sphingolipid binding signature. **a**, Signature patterns used for both randomization/shuffling approach and screening for potential sphingolipid-binding proteins (upper panel). All possible combinations were analysed for significant overrepresentations in TMDs. Motifs overrepresented with a P -value ≤ 0.05 were used to generate the sequence logo (lower panel). The letter size corresponds to the probability to find this amino acid at that position. Each dot below the line represents an amino acid position.

b, Intracellular distribution of signature-containing transmembrane protein candidates. **c**, *In vivo* labelling of Flag-tagged constructs of human INGR1, I17RB, B3GT2 and ASGR1. Cells were labelled with [3 H]-photo-sphingosine, ultraviolet-irradiated, lysed and subjected to IP using an antibody against the Flag tag. Radioactivity recovered with protein candidates was visualized by autoradiography. The corresponding proteins were detected by western blot analysis. Asterisk, expected size of proteins.

HeLa cells (Supplementary Fig. 10). In *in vivo* labelling all three candidates showed strong binding to a sphingolipid (Fig. 3c). Interestingly, INGR1 binds to a sphingolipid only upon activation by its ligand interferon γ .

What may be the function of the highly specific interaction of SM 18 with p24? As p24 acts as membrane machinery for the formation of COPI vesicles, we analysed if a loss of binding of SM 18 would affect transport of biosynthetic cargo^{18,19}. We analysed transport of vesicular stomatitis G (VSV-G) protein^{20,21} to determine the transport rates in HeLa cells stably transfected with full-length wild-type p24 or p24L17F, N-terminally fused to YFP. Expression of p24L17F caused an acceleration of VSV-G protein transport (Fig. 4a), resulting in a 2.5-fold increase of the fraction of total VSV-G that reached the plasma membrane at $t = 45$ min (see also Supplementary Fig. 11a, b).

How can a marked acceleration of transport be caused by a lack of binding of SM 18 to p24? A decrease in recycling efficiency would cause an increased anterograde transport of this cargo, and should affect Golgi export. To test this possibility, we measured Golgi export kinetics using fluorescence loss in photobleaching (FLIP). Whereas Golgi-associated fluorescence of YFP–wild-type p24 was reduced to 50% within 4.5 min, the half-life of Golgi residence of YFP–p24L17F was significantly prolonged to 7 min (Fig. 4b, for controls see Supplementary Fig. 11c). To analyse if indeed retrograde transport from the Golgi to the ER is affected we monitored trafficking to the

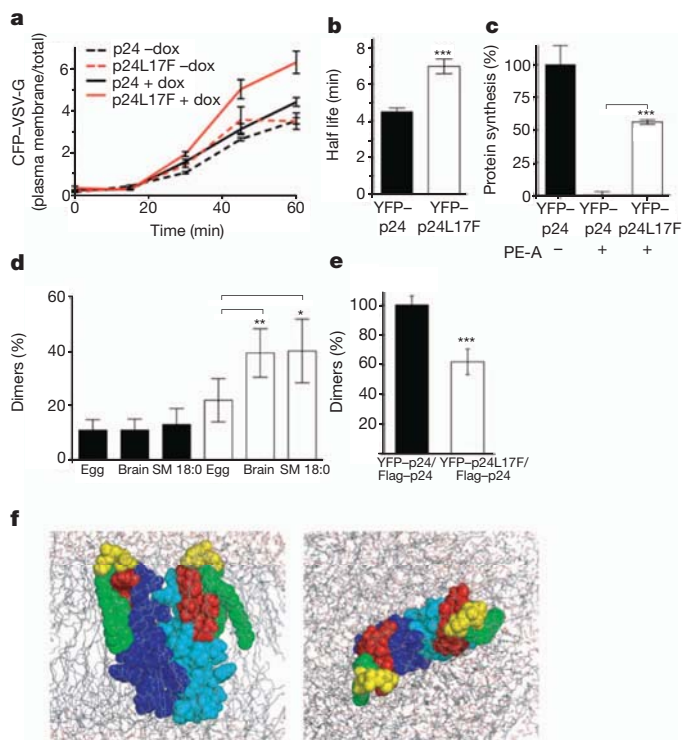


Figure 4 | Binding of SM 18 to p24(TMD) affects protein transport and triggers p24 dimerization. **a**, Expression of p24L17F accelerates transport of ts-O45-G protein. For each time point and experiment ($n = 3$), at least 600 cells were analysed. CFP–VSV-G, cyan-fluorescent-protein-tagged ts-O45-G protein. **b**, Comparison of the average half lives of decay in fluorescence in Golgi of YFP–p24 and YFP–p24L17F. Data represent the mean of $n = 22$ –24 experiments \pm s.e. P -value of two-tailed, unpaired t -test < 0.0001 (***) is given. **c**, Expression of YFP–p24L17F reduces toxicity of PE-A. Error bars, s.e.m. Statistics: two-tailed, unpaired t -test. **d**, SM 18:0 induces dimerization of p24(TMD) (white bars) but not of p23(TMD) (black bars). TMDs reconstituted into proteoliposomes with indicated sphingomyelin species subjected to chemical crosslinking ($n = 4$). Results of paired, two-tailed t -tests are given. **e**, Quantification of homodimers in CHO cells *in situ*. Error bars, s.e.m. Statistics: two-tailed, unpaired t -test. *** $P < 0.001$ **f**, Model of p24(TMD) SM 18 complexes. Left, side view; right, top view.

endoplasmic reticulum of *Pseudomonas aeruginosa* exotoxin A (PE-A). The toxin is transported from the Golgi to the endoplasmic reticulum in a COPI-dependent manner²². In contrast to cells expressing YFP–p24, YFP–p24L17F-cells showed a significant reduction of PE-A-dependent inhibition of protein biosynthesis, the readout for exotoxin transport to the endoplasmic reticulum (Fig. 4c, for controls see Supplementary Fig. 11d). Together, these data imply that efficient retrograde COPI-dependent transport depends on binding of p24 to sphingomyelin.

To test if binding to SM 18 might help organize the dimeric, transport active state of p24, by affecting its monomer/oligomer equilibrium via the TMD, we used a chemical crosslinking assay with proteoliposomes reconstituted from p24 family–TMD fusion proteins and sphingomyelins of various species compositions. Indeed, dimerization is significantly induced only in liposomes containing both SM 18 and p24 (Fig. 4d and Supplementary Fig. 12a–c). To analyse if dimerization of p24 is also affected *in vivo* in the presence of full-length p24L17F, we monitored dimerization of p24 using an *in situ* protein–protein interaction assay. Signals were significantly reduced in the presence of p24L17F (Fig. 4e, for representative images and western blots see Supplementary Fig. 12d). Similar results were obtained when cells expressing either YFP–p24 or YFP–p24L17F were subjected to chemical crosslinking (Supplementary Fig. 12e).

How might a complex of dimeric p24 and SM 18 be organized? We performed molecular dynamics simulations starting from different models based on the sphingomyelin-bound monomeric structures from the initial simulations. The most stable model was one with a rather polar dimerization interface not overlapping with the sphingomyelin binding site (Fig. 4f); this complex remained intact for at least 200 ns. Besides a direct role of sphingomyelin in stabilizing a p24 dimer, other mechanisms of sphingomyelin-triggered dimerization might apply, such as a sphingomyelin-dependent conformational change of p24 or build-up of high concentrations of p24 in SM 18 microdomains.

In summary, we have uncovered an unprecedented specificity of interaction between an individual sphingolipid species and a TMD, and have defined a structural signature within the TMD for this binding. Specific binding of individual lipid species to TMDs of membrane proteins may serve different functions and help to understand the need for the complexity of membrane lipid compositions at a functional level.

METHODS SUMMARY

***In vivo* photoaffinity labelling of CHO cells.** Cells were labelled with the different photoactivatable precursors as described^{7,8}. Briefly, cells were washed with PBS, followed by addition of freshly prepared delipidated medium containing lipid precursors. After labelling, the medium was removed and cells were washed twice with PBS. After ultraviolet irradiation, cells were collected and lysed in lysis buffer (50 mM HEPES–NaOH, pH 7.4, 100 mM NaCl, 5 mM EDTA, 1% Triton X-100 (v/v), 0.5% deoxycholate (w/v) and protease inhibitor cocktail). After lysis, samples were subjected to immunoprecipitation. After SDS–PAGE and western blotting, radioactively labelled proteins were detected by digital autoradiography (β -Imager 2000, Biospace).

FRET assay. FRET was used to probe the interaction of TMDs with pentaenoyl-lipids directly. FRET experiments were conducted on a Jasco 6500 unit spectrofluorometer (Jasco). Proteoliposomes (protein/lipid, 1:5,000) were diluted in a quartz cuvette in buffer (10 mM HEPES/KOH pH 7.4) to a final concentration of 0.1 mM. The proteoliposomes were incubated at 25 °C for 5 min under continuous stirring. The extent of FRET between TMD and pentaenoyl-lipids was determined by recording emission spectra from 310 to 540 nm. Emission spectra were collected, exciting at 280 nm the Trp present in the TMD. Slit widths of 5 nm were used for both excitation and emission.

Full Methods and any associated references are available as Supplementary information.

Received 12 January; accepted 30 November 2011.

Published online 9 January 2012.

1. Coskun, U. & Simons, K. Cell membranes: the lipid perspective. *Structure* **19**, 1543–1548 (2011).

2. Popoff, V., Adolf, F., Brugger, B. & Wieland, F. COPI budding within the Golgi stack. *Cold Spring Harb. Perspect. Biol.* doi:10.1101/cshperspect.a005231 (15 August 2011).
3. Béthune, J. *et al.* Coatamer, the coat protein of COPI transport vesicles, discriminates endoplasmic reticulum residents from p24 proteins. *Mol. Cell. Biol.* **26**, 8011–8021 (2006).
4. Reinhard, C. *et al.* Receptor-induced polymerization of coatamer. *Proc. Natl Acad. Sci. USA* **96**, 1224–1228 (1999).
5. Brügger, B. *et al.* Evidence for segregation of sphingomyelin and cholesterol during formation of COPI-coated vesicles. *J. Cell Biol.* **151**, 507–518 (2000).
6. Beck, R., Ravet, M., Wieland, F. T. & Cassel, D. The COPI system: molecular mechanisms and function. *FEBS Lett.* **583**, 2701–2709 (2009); corrigendum **583**, 3541 (2009).
7. Haberkant, P. *et al.* Protein-sphingolipid interactions within cellular membranes. *J. Lipid Res.* **49**, 251–262 (2008).
8. Thiele, C., Hannah, M. J., Fahrenholz, F. & Huttner, W. B. Cholesterol binds to synaptophysin and is required for biogenesis of synaptic vesicles. *Nature Cell Biol.* **2**, 42–49 (2000).
9. Kuerschner, L. *et al.* Polyene-lipids: a new tool to image lipids. *Nature Methods* **2**, 39–45 (2005).
10. Russ, W. P. & Engelman, D. M. The GxxxG motif: a framework for transmembrane helix-helix association. *J. Mol. Biol.* **296**, 911–919 (2000).
11. Senes, A., Gerstein, M. & Engelman, D. M. Statistical analysis of amino acid patterns in transmembrane helices: the GxxxG motif occurs frequently and in association with β -branched residues at neighboring positions. *J. Mol. Biol.* **296**, 921–936 (2000).
12. Jones, D. T., Taylor, W. R. & Thornton, J. M. A mutation data matrix for transmembrane proteins. *FEBS Lett.* **339**, 269–275 (1994).
13. Contreras, F. X., Basanez, G., Alonso, A., Herrmann, A. & Goni, F. M. Asymmetric addition of ceramides but not dihydroceramides promotes transbilayer (flip-flop) lipid motion in membranes. *Biophys. J.* **88**, 348–359 (2005).
14. Bakrac, B. *et al.* A toxin-based probe reveals cytoplasmic exposure of Golgi sphingomyelin. *J. Biol. Chem.* **285**, 22186–22195 (2010).
15. Li, X. M., Smaby, J. M., Momsen, M. M., Brockman, H. L. & Brown, R. E. Sphingomyelin interfacial behavior: the impact of changing acyl chain composition. *Biophys. J.* **78**, 1921–1931 (2000).
16. Niemelä, P., Hyvönen, M. T. & Vattulainen, I. Structure and dynamics of sphingomyelin bilayer: insight gained through systematic comparison to phosphatidylcholine. *Biophys. J.* **87**, 2976–2989 (2004).
17. Niemelä, P. S., Hyvönen, M. T. & Vattulainen, I. Influence of chain length and unsaturation on sphingomyelin bilayers. *Biophys. J.* **90**, 851–863 (2006).
18. Presley, J. F. *et al.* ER-to-Golgi transport visualized in living cells. *Nature* **389**, 81–85 (1997).
19. Scales, S. J., Pepperkok, R. & Kreis, T. E. Visualization of ER-to-Golgi transport in living cells reveals a sequential mode of action for COPII and COPI. *Cell* **90**, 1137–1148 (1997).
20. Keller, P., Toomre, D., Diaz, E., White, J. & Simons, K. Multicolour imaging of post-Golgi sorting and trafficking in live cells. *Nature Cell Biol.* **3**, 140–149 (2001).
21. Simpson, J. C. *et al.* An RNAi screening platform to identify secretion machinery in mammalian cells. *J. Biotechnol.* **129**, 352–365 (2007).
22. Jackson, M. E. *et al.* The KDEL retrieval system is exploited by *Pseudomonas* exotoxin A, but not by Shiga-like toxin-1, during retrograde transport from the Golgi complex to the endoplasmic reticulum. *J. Cell Sci.* **112**, 467–475 (1999).

Supplementary Information is linked to the online version of the paper at www.nature.com/nature.

Acknowledgements The authors would like to thank T. Sachsenheimer for technical assistance, A. Brodde for help with lipid synthesis, D. Cassel for comments on the manuscript, and the members of the Wieland laboratory for discussion. This work was supported by a grant of the German research foundation (DFG, TRR83) to B.B. and F.W. and by ERC grants to E.L. (209825) and G.v.H. (AdG232648); F.-X.C. was supported by a FEBS fellowship and A.M.E. by the Peter and Traudl Engelhorn foundation.

Author Contributions F.-X.C., A.M.E. and P.H. designed and performed the experiments. P.B. performed the bioinformatics analyses under the supervision of A.E., G.v.H. and A.M.E.; E.L. designed, performed and interpreted molecular dynamics simulation experiments. B.G. performed *in vivo* crosslinking experiments. C.Th. provided reagents and helped to establish photolabelling and FRET experiments. C.Ti. and R.P. provided reagents and tools and supported A.M.E. concerning VSV-G experiments. F.W. and B.B. designed the experiments and wrote the manuscript.

Author Information Reprints and permissions information is available at www.nature.com/reprints. The authors declare no competing financial interests. Readers are welcome to comment on the online version of this article at www.nature.com/nature. Correspondence and requests for materials should be addressed to F.W. (felix.wieland@bzh.uni-heidelberg.de) and B.B. (britta.bruegger@bzh.uni-heidelberg.de).

Structure of the carboxy-terminal region of a KCNH channel

Tinatina I. Brelidze¹, Anne E. Carlson¹, Banumathi Sankaran² & William N. Zagotta¹

The KCNH family of ion channels, comprising *ether-à-go-go* (EAG), EAG-related gene (ERG), and EAG-like (ELK) K⁺-channel subfamilies, is crucial for repolarization of the cardiac action potential¹, regulation of neuronal excitability² and proliferation of tumour cells³. The carboxy-terminal region of KCNH channels contains a cyclic-nucleotide-binding homology domain (CNBHD) and C-linker that couples the CNBHD to the pore⁴. The C-linker/CNBHD is essential for proper function and trafficking of ion channels in the KCNH family^{5–9}. However, despite the importance of the C-linker/CNBHD for the function of KCNH channels, the structural basis of ion-channel regulation by the C-linker/CNBHD is unknown. Here we report the crystal structure of the C-linker/CNBHD of zebrafish ELK channels at 2.2-Å resolution. Although the overall structure of the C-linker/CNBHD of ELK channels is similar to the cyclic-nucleotide-binding domain (CNBD) structure of the related hyperpolarization-activated cyclic-nucleotide-modulated (HCN) channels¹⁰, there are marked differences. Unlike the CNBD of HCN, the CNBHD of ELK displays a negatively charged electrostatic profile that explains the lack of binding and regulation of KCNH channels by cyclic nucleotides^{4,11}. Instead of cyclic nucleotide, the binding pocket is occupied by a short β -strand. Mutations of the β -strand shift the voltage dependence of activation to more depolarized voltages, implicating the β -strand as an intrinsic ligand for the CNBHD of ELK channels. In both ELK and HCN channels the C-linker is the site of virtually all of the intersubunit interactions in the C-terminal region. However, in the zebrafish ELK structure there is a reorientation in the C-linker so that the subunits form dimers instead of tetramers, as observed in HCN channels. These results provide a structural framework for understanding the regulation of ion channels in the KCNH family by the C-linker/CNBHD and may guide the design of specific drugs.

KCNH channels are voltage-gated K⁺ channels that regulate the electrical excitability of heart and nerve cells. Similar to other K⁺-selective channels, KCNH channels are composed of four subunits surrounding a centrally located pore. Each subunit contains a voltage-sensor domain (transmembrane segments S1–S4), and a pore domain (transmembrane segments S5–S6 and an intervening pore-forming loop)⁴ (Fig. 1a). KCNH channels have a Per-Arnt-Sim (PAS) domain in the amino-terminal region and a C-linker and CNBHD in the C-terminal region^{4,12} (Fig. 1a). Many of the unique gating properties of KCNH channels arise from these intracellular domains^{5–7,13,14}. Whereas the structure of the N-terminal region has been solved for ERG channels^{12,15–17}, there is no structural information on the C-linker/CNBHD for any of the KCNH channels.

KCNH channels are part of a large family of cyclic-nucleotide-regulated channels that includes the HCN and cyclic-nucleotide-gated (CNG) channels (Supplementary Fig. 1a). Unlike HCN and CNG channels¹⁸, KCNH channels are not regulated by direct binding of cyclic nucleotides^{4,11}. Instead, it has been suggested that the CNBHD of KCNH channels may be an orphan receptor for an as yet unidentified

channel regulator¹⁹. Indeed, it has been recently shown that mouse EAG1 channels are regulated by the direct binding of flavonoids to the C-linker/CNBHD¹⁹. In addition, the C-linker/CNBHD has been shown to interact with the N-terminal PAS domain and regulate gating^{6–8}. Mutations in both of these regions in human ERG1 channels cause long-QT syndrome (LQTS), a heart arrhythmia that can cause cardiac death²⁰. Therefore the C-linker/CNBHD is an important regulatory domain in KCNH channels.

To understand the role of the C-linker/CNBHD in KCNH channel function, we sought to determine the X-ray structure of the C-linker/CNBHD of an ion channel in the KCNH family. Using a screen based on fluorescence-detection size-exclusion chromatography (FSEC)²¹,

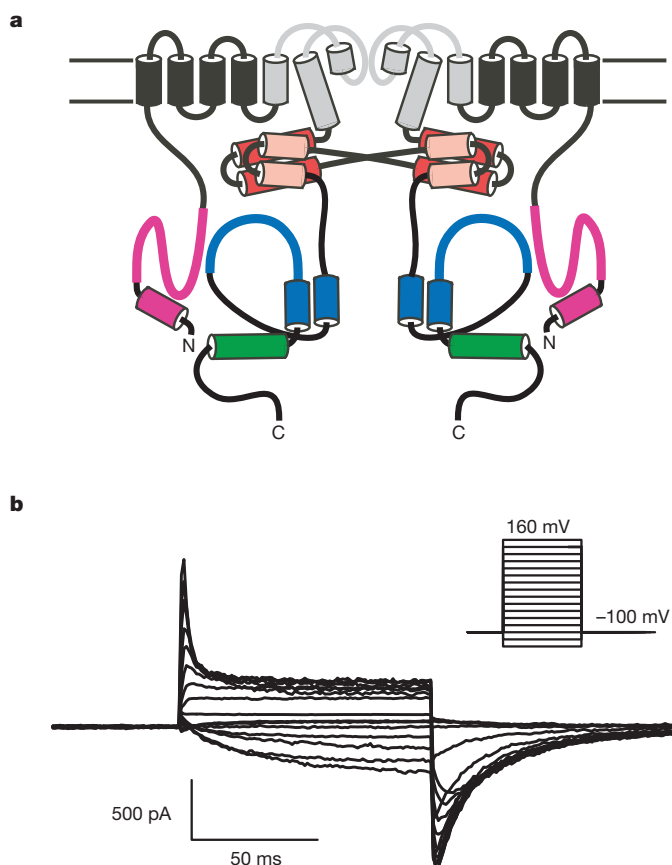


Figure 1 | Topology and electrophysiological properties of zebrafish ELK channels. **a**, Cartoon of two of the four subunits of ELK channels. The pore-forming loop and S5–S6 transmembrane domains are grey. The N-terminal α -helix and PAS domain are magenta. The ‘elbow’ and ‘shoulder’ regions of the C-linker are represented by the red and pink cylinders, respectively. The α -C-helix, represented by a cylinder, is green and the rest of the CNBHD is blue. **b**, Currents from zebrafish ELK channels recorded in the inside-out patch configuration.

¹Department of Physiology and Biophysics, University of Washington School of Medicine, Box 357290, Seattle, Washington 98195-7290, USA. ²Berkeley Center for Structural Biology, Lawrence Berkeley National Laboratory, 1 Cyclotron Road, BLDG 6R2100, Berkeley, California 94720, USA.

we identified the C-linker/CNBHD of *Danio rerio* (zebrafish) ELK as a potential candidate for crystallization. Zebrafish ELK shares substantial sequence similarity with mammalian ELK channels (Supplementary Fig. 1c).

Expression of zebrafish ELK channels in *Xenopus laevis* oocytes gave rise to robust voltage-activated K^+ currents with electrophysiological characteristics similar to the ones reported previously for mammalian ELK channels^{22–25} (Fig. 1b). Zebrafish ELK channels were activated by depolarizing voltage steps and showed inactivation at voltages $>+40$ mV (Fig. 1b). The half-maximal activation voltage ($V_{1/2}$) was -45.3 ± 3.2 mV ($n = 18$) with a slope of e-fold per 13.8 ± 0.6 mV ($n = 18$) (Supplementary Fig. 1b). In comparison, human ELK2 channels activate with $V_{1/2}$ of -22.8 ± 0.5 mV and a slope of 18.1 ± 0.4 mV, and inactivate at voltages $>+20$ mV (ref. 22). As previously observed for mouse EAG and human ERG channels^{4,11}, application of cAMP had no

effect on the currents through zebrafish ELK channels (Supplementary Fig. 1b).

The C-linker/CNBHD of zebrafish ELK channels crystallized in two space groups, C222₁ and P12₁1, and diffracted X-rays to 2.2- and 2.3-Å resolution, respectively (Supplementary Table 1). The structure of the zebrafish ELK C-linker/CNBHD was solved by the single-wavelength anomalous dispersion (SAD) phasing method using selenomethionine derivative crystals.

The crystal structure revealed that the C-linker of zebrafish ELK channels consists of six α -helices ($\alpha A'$ – $\alpha F'$) with $\alpha A'$ and $\alpha B'$ helices forming an antiparallel helix–turn–helix motif. The CNBHD consists of eight β -strands forming an antiparallel β -roll, three α -helices (αA – αC), and a short β -strand ($\beta 9$) after the αC -helix (Fig. 2a). The general architecture of the CNBHD of ELK is similar to the fold of CNBDs in other proteins²⁶.

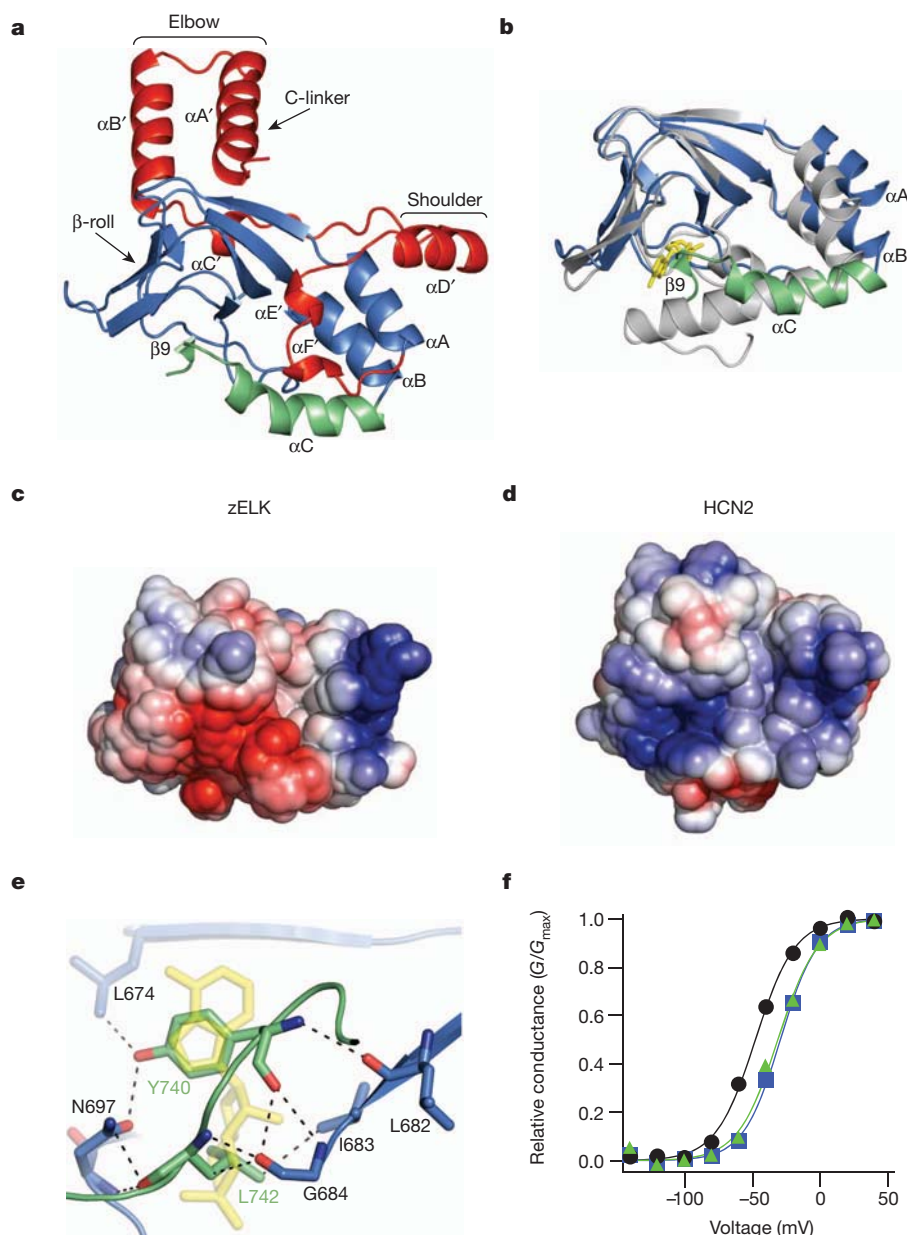


Figure 2 | Structure of the C-linker/CNBHD. **a**, Ribbon representation of a monomer of the C-linker/CNBHD of zebrafish ELK (zELK) channels. **b**, Alignment of the CNBHD of zebrafish ELK (the αC -helix is green and the rest is blue) and mouse HCN2 (grey) channels¹⁰. cAMP in the HCN2 structure is yellow. **c**, **d**, Electrostatic potential surface of the CNBHD of zebrafish ELK (**c**) and HCN2 channels (**d**), viewed in the same orientation as in **b**. **e**, Residues

in the β -roll cavity interacting with residues Y740 and L742 of the intrinsic ligand. Dashed lines show both polar and non-polar interactions. cAMP from the HCN2 structure is shown in yellow. **f**, Representative conductance–voltage relationships for wild-type (black), Y740A mutant (blue) and $\Delta 740$ –742 mutant (green) zebrafish ELK channels.

Although the overall folds of the CNBHDs of ELK and HCN2 channels are similar, superposition of the two structures reveals remarkable differences (Fig. 2b and Supplementary Fig. 2a). The root mean squared deviation (r.m.s.d.) for the α -carbons of the two structures (residues 626–740 of zebrafish ELK and residues 523–635 of mouse HCN2; ref. 10) is 4.7 Å with the largest differences observed for the three α -helices in the CNBHD. The α A- and α B-helices of ELK are moved away from the cavity formed by the β -roll that serves as the cyclic-nucleotide-binding pocket in other CNBD-containing proteins. The α A-helix is moved by about 4.5 Å and the α B-helix is moved by about 3.4 Å relative to their positions in the cAMP-bound form of HCN2. The position of the α A-helix of ELK is similar to the position of the α A-helix in cAMP-bound MlotiK channels²⁷ and the position of the α B-helix is similar to the unliganded MlotiK channels^{27–29} (Supplementary Fig. 3). The differences in the α C-helix are even more marked. The α C-helix of ELK is shorter and bent, and is followed by a short β -strand, β 9 (Fig. 2b). These differences all reside in the α -helices of the CNBD that undergo ligand-dependent conformational changes in HCN and CNG channels.

Out of the ten residues that directly interact with cAMP in HCN2 channels, only three (V667, L677 and G684) are conserved in zebrafish ELK channels (Supplementary Fig. 4). Moreover, most of the residues in the phosphate-binding cassette of HCN2, including R591, are not conserved, and the α P-helix is missing in zebrafish ELK. The electrostatic profiles of the CNBHD of ELK and HCN2 channels reveal that the putative ligand-binding pocket formed by the β -roll cavity is negatively charged for ELK but positively charged for HCN2 channels (Fig. 2c, d). The negatively charged electrostatic profile would not be favourable for binding of a negatively charged cyclic nucleotide. Consistent with this, crystallization of zebrafish ELK in the presence of 5 mM cAMP did not reveal any new electron density corresponding to cAMP (Supplementary Table 1 and data not shown). These differences in the CNBD structures probably account, at least in part, for the lack of cyclic nucleotide regulation of KCNH channels^{4,11}.

The zebrafish ELK CNBHD structure displays another unique feature: the β 9-strand after the α C-helix forms direct interactions with the β -roll cavity in ELK channels (Fig. 2e and Supplementary Figs 2b and 5). Interestingly, the phenyl ring of Y740 on the β 9-strand is positioned in an analogous place to the purine ring of cAMP in HCN2 channels and L742 is positioned in an analogous place to the cyclic phosphate of cAMP¹⁰. Virtually all ion channels in the KCNH family have either tyrosine or phenylalanine at the position corresponding to Y740 in zebrafish ELK and a leucine at position corresponding to L742 (Supplementary Fig. 1c). These observations raise an intriguing possibility that the β 9-strand might act as an intrinsic ligand, a portion of the protein that occupies the ligand-binding site whose displacement regulates the channel.

To explore a possible regulatory role of the β 9-strand, we examined the effect of mutations in the β 9-strand on the function of intact zebrafish ELK channels. Zebrafish ELK channels with either a point mutation Y740A or deletion of the β 9-strand (Δ 740–742) exhibited robust voltage-activated currents that inactivated at voltages $> +40$ mV, similar to wild-type ELK channels (Supplementary Fig. 6a). However, for both mutations, the $V_{1/2}$ values for activation were significantly larger ($P < 0.01$, Student's *t*-test) than the $V_{1/2}$ of wild-type channels (wild type: -45.3 ± 3.2 mV, $n = 18$; Y740A: -29.8 ± 4.4 mV, $n = 19$; Δ 740–742: -28.3 ± 4.4 mV, $n = 11$) (Fig. 2f and Supplementary Fig. 6b). This 15 mV shift in the voltage dependence of activation in the mutants is similar in magnitude to the effect of cAMP on HCN channels, lending further support to the possibility that the β 9-strand may function as an intrinsic ligand for ELK channels. Interestingly, mutations in the region corresponding to the β 9-strand of human ERG channels are associated with LQTS^{20,30}. Additional experiments will need to be done to further test the intrinsic ligand hypothesis.

Similar to HCN channels, the C-linker of zebrafish ELK channels is the primary region of intersubunit interactions in the crystal structure

with a buried solvent accessible surface area of about 2,520 Å² for each subunit (Fig. 3a). The intersubunit interface can be likened to an 'elbow on the shoulder', where the 'elbow' formed by the α A'- and α B'-helices of one subunit is resting on the 'shoulder' formed by the α D'-helix and the α C'- α D' loop of the neighbouring subunit (Figs 2a, 3a, d and Supplementary Fig. 7). The structure of the elbow-on-the-shoulder interface between neighbouring subunits is very similar between ELK and HCN2 channels (Fig. 3d), except that the region before the α D'-helix is not α -helical in ELK.

Unexpectedly, however, the elbow-on-the-shoulder interface in zebrafish ELK occurs with a two-fold related subunit (rotated by 180°), instead of a four-fold related subunit (rotated by 90°) like in HCN channels (Fig. 3a, b). This difference results from a $\sim 55^\circ$ rotation in the region after the α B'-helix in ELK relative to HCN2 channels (Fig. 3c). The implication of this marked rotation of the 'elbow' is a dimeric assembly of the C-linker/CNBHDs in the zebrafish ELK structure (Fig. 3a), as opposed to the tetrameric assembly of the C-linker/CNBHDs in HCN channels¹⁰ (Fig. 3b). The intersubunit interface and the dimeric assembly are preserved in both sets of molecules in the asymmetric unit and for both crystal forms of zebrafish ELK (Supplementary Fig. 8), suggesting that they are independent of crystal contacts. FSEC experiments also revealed that the GFP-tagged C-linker/CNBHD of zebrafish ELK channels dimerizes at sufficiently

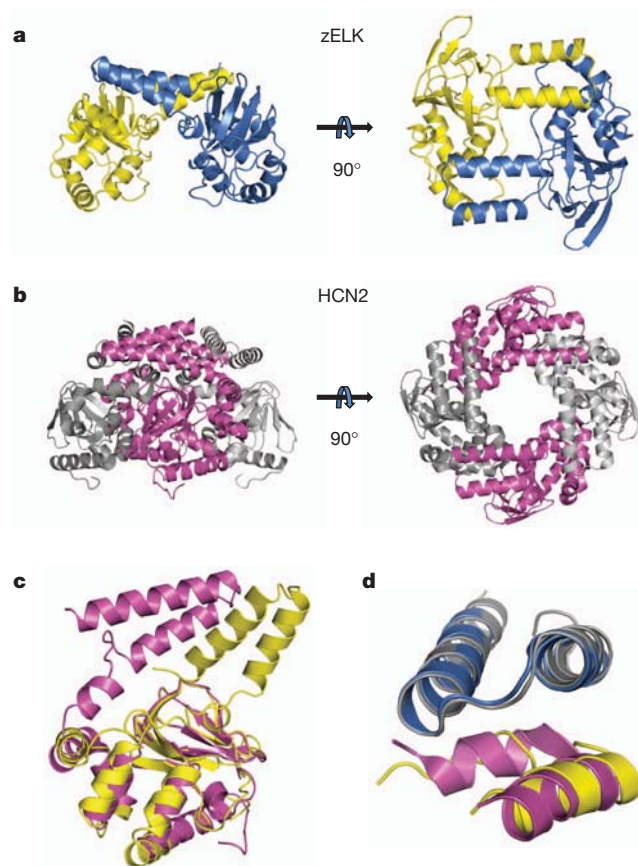


Figure 3 | Structural comparison of the C-linker regions and quaternary arrangement of the C-linker/CNBHDs of zebrafish ELK and HCN2 channels. **a**, A dimer formed by the C-linker/CNBHD of zebrafish ELK (zELK) channels viewed perpendicular (left) and parallel (right) to the two-fold axis. **b**, A tetramer formed by the C-linker/CNBHD of HCN2 channels viewed perpendicular (left) and parallel (right) to the four-fold axis. **c**, Superposition of the ribbon representations of the C-linker/CNBHD monomers of zebrafish ELK (yellow) and mouse HCN2 channels (magenta) using the alignment of the α -carbons of the CNBDs of these structures. **d**, Superposition of the elbow-on-the-shoulder interface of zebrafish ELK (blue, elbow; yellow, shoulder) and mouse HCN2 channels (grey, elbow; magenta, shoulder).

high concentrations in solution (Supplementary Fig. 9). Additional experiments would be required to determine if the quaternary state of the C-linker/CNBHD in intact channels has a two-fold or four-fold symmetry (Supplementary Discussion and Supplementary Fig. 10).

Here we present the first crystal structure, to our knowledge, of the C-linker/CNBHD of a KCNH channel. The structure reveals a putative ligand-binding pocket that differs markedly from the cyclic-nucleotide-binding pocket of HCN channels and does not appear to bind cyclic nucleotides. Instead of a ligand, the putative ligand-binding pocket of zebrafish ELK channels is occupied by a novel β 9-strand after the α C-helix. Mutations of the β 9-strand shifted the voltage dependence of activation, suggesting that the β 9-strand is a regulatory element for ELK channels that acts as an intrinsic ligand. The crystal structure also displays an unexpected conformation of the C-linker that leads to dimerization of the C-linker/CNBHDs of zebrafish ELK channels. These findings provide a structural framework to understand the regulation of KCNH channels by the C-linker/CNBHD.

METHODS SUMMARY

Protein purification. The C-linker/CNBHD of zebrafish ELK (amino acids Q543–L750) was subcloned into a modified pMalc2T vector (New England Biolabs) containing an N-terminal MBP affinity tag followed by a thrombin cleavage site. The protein was expressed in BL21 (DE3) *Escherichia coli* cells as previously described¹¹, purified on an amylose affinity column and then on an ion-exchange column after an overnight cleavage with thrombin at 4 °C. The purified protein was concentrated to 20–30 mg ml⁻¹ for crystallization. Selenomethionine derivatives were generated as previously described¹⁰.

Crystallography. Crystals were grown at 20 °C using the sitting-drop vapour diffusion method. 150-nl drops of the concentrated protein and reservoir solutions were mixed 1:1 by a Mosquito (TTP LABTECH). The final protein solution contained: ~250 mM KCl, 1 mM TCEP, 30 mM HEPES, 100 mM citric acid, pH 3.5. The reservoir solution contained: 6% w/v 1,5-diaminopentane dihydrochloride, 180 mM ammonium acetate, 22.5% (w/v) PEG 3350, 90 mM Tris; pH 8.5 for crystal T141; 1.8 M non-detergent sulphobetaine (NDSB)-211, 180 mM ammonium acetate, 22.5% (w/v) PEG 3350, 90 mM Tris, pH 8.5 for crystal T42; 6% (w/v) D-(+)-galactose, 180 mM ammonium sulphate, 22.5% (w/v) PEG 3350, 90 mM HEPES, pH 7.5 for crystal T26; and 5 mM cAMP, 180 mM ammonium acetate, 22.5% (w/v) PEG 3350, 90 mM Tris, pH 8.5 for crystal T84.

The crystallographic data are summarized in Supplementary Table 1 and details of the structure determination are described in Methods.

Electrophysiology. The full-length zebrafish ELK channel (GenInfo Identifier (GI) 159570347) with a C-terminal Flag epitope was generated by Bio Basic Inc. and subcloned into the pGEMHE oocyte expression vector. Expression of the wild-type and mutant zebrafish ELK channels in *Xenopus* oocytes and current recordings were done as previously described¹¹. Both pipette and bath solutions contained 130 mM KCl, 10 mM HEPES, 0.2 mM EDTA, pH 7.2. 1 mM cAMP was added to the bath solution as indicated.

Full Methods and any associated references are available in the online version of the paper at www.nature.com/nature.

Received 29 May; accepted 23 November 2011.

Published online 9 January 2012.

- Sanguinetti, M. C. & Tristani-Firouzi, M. hERG potassium channels and cardiac arrhythmia. *Nature* **440**, 463–469 (2006).
- Zhang, X. *et al.* Deletion of the potassium channel Kv12.2 causes hippocampal hyperexcitability and epilepsy. *Nature Neurosci.* **13**, 1056–1058 (2010).
- Camacho, J. *Ether-à-go-go* potassium channels and cancer. *Cancer Lett.* **233**, 1–9 (2006).
- Ganetzky, B., Robertson, G. A., Wilson, G. F., Trudeau, M. C. & Titus, S. A. The Eag family of K⁺ channels in *Drosophila* and mammals. *Ann. NY Acad. Sci.* **868**, 356–369 (1999).
- Al-Owais, M., Bracey, K. & Wray, D. Role of intracellular domains in the function of the hERG potassium channel. *Eur. Biophys. J.* **38**, 569–576 (2009).
- Stevens, L., Ju, M. & Wray, D. Roles of surface residues of intracellular domains of hERG potassium channels. *Eur. Biophys. J.* **38**, 523–532 (2009).
- Gustina, A. S. & Trudeau, M. C. hERG potassium channel gating is mediated by N- and C-terminal region interactions. *J. Gen. Physiol.* **137**, 315–325 (2011).
- Muskett, F. W. *et al.* Mechanistic insight into human *ether-à-go-go*-related gene (hERG) K⁺ channel deactivation gating from the solution structure of the EAG domain. *J. Biol. Chem.* **286**, 6184–6191 (2011).

- Zhou, Z., Gong, Q., Epstein, M. L. & January, C. T. HERG channel dysfunction in human long QT syndrome. Intracellular transport and functional defects. *J. Biol. Chem.* **273**, 21061–21066 (1998).
- Zagotta, W. N. *et al.* Structural basis for modulation and agonist specificity of HCN pacemaker channels. *Nature* **425**, 200–205 (2003).
- Brelidze, T. I., Carlson, A. E. & Zagotta, W. N. Absence of direct cyclic nucleotide modulation of mEAG1 and hERG1 channels revealed with fluorescence and electrophysiological methods. *J. Biol. Chem.* **284**, 27989–27997 (2009).
- Morais Cabral, J. H. *et al.* Crystal structure and functional analysis of the HERG potassium channel N terminus: a eukaryotic PAS domain. *Cell* **95**, 649–655 (1998).
- Schonherr, R. & Heinemann, S. H. Molecular determinants for activation and inactivation of HERG, a human inward rectifier potassium channel. *J. Physiol. (Lond.)* **493**, 635–642 (1996).
- Wang, J., Trudeau, M. C., Zappia, A. M. & Robertson, G. A. Regulation of deactivation by an amino terminal domain in human *ether-à-go-go*-related gene potassium channels. *J. Gen. Physiol.* **112**, 637–647 (1998).
- Muskett, F. W. *et al.* Mechanistic insight into hERG K⁺ channel deactivation gating from the solution structure of the EAG domain. *J. Biol. Chem.* **286**, 6184–6191 (2011).
- Li, Q. *et al.* NMR solution structure of the N-terminal domain of hERG and its interaction with the S4–S5 linker. *Biochem. Biophys. Res. Commun.* **403**, 126–132 (2010).
- Ng, C. A. *et al.* The N-terminal tail of hERG contains an amphipathic α -helix that regulates channel deactivation. *PLoS ONE* **6**, e16191 (2011).
- Craven, K. B. & Zagotta, W. N. CNG and HCN channels: two peas, one pod. *Annu. Rev. Physiol.* **68**, 375–401 (2006).
- Brelidze, T. I., Carlson, A. E., Davies, D. R., Stewart, L. J. & Zagotta, W. N. Identifying regulators for EAG1 channels with a novel electrophysiology and tryptophan fluorescence based screen. *PLoS ONE* **5**, e12523 (2010).
- Splawski, I. *et al.* Spectrum of mutations in long-QT syndrome genes. *KVL QT1*, *HERG*, *SCN5A*, *KCNK1*, and *KCNK2*. *Circulation* **102**, 1178–1185 (2000).
- Kawate, T. & Gouaux, E. Fluorescence-detection size-exclusion chromatography for precrystallization screening of integral membrane proteins. *Structure* **14**, 673–681 (2006).
- Becchetti, A. *et al.* The functional properties of the human *ether-à-go-go*-like (hELK2) K⁺ channel. *Eur. J. Neurosci.* **16**, 415–428 (2002).
- Engelard, B., Neu, A., Ludwig, J., Roeper, J. & Pongs, O. Cloning and functional expression of rat *ether-à-go-go*-like K⁺ channel genes. *J. Physiol. (Lond.)* **513**, 647–654 (1998).
- Trudeau, M. C., Titus, S. A., Branchaw, J. L., Ganetzky, B. & Robertson, G. A. Functional analysis of a mouse brain Elk-type K⁺ channel. *J. Neurosci.* **19**, 2906–2918 (1999).
- Zou, A. *et al.* Distribution and functional properties of human KCNH8 (Elk1) potassium channels. *Am. J. Physiol. Cell Physiol.* **285**, C1356–C1366 (2003).
- Rehmann, H., Wittinghofer, A. & Bos, J. L. Capturing cyclic nucleotides in action: snapshots from crystallographic studies. *Nature Rev. Mol. Cell Biol.* **8**, 63–73 (2007).
- Altieri, S. L. *et al.* Structural and energetic analysis of activation by a cyclic nucleotide binding domain. *J. Mol. Biol.* **381**, 655–669 (2008).
- Clayton, G. M., Silverman, W. R., Heginbotham, L. & Morais-Cabral, J. H. Structural basis of ligand activation in a cyclic nucleotide regulated potassium channel. *Cell* **119**, 615–627 (2004).
- Schunke, S., Stoldt, M., Lecher, J., Kaupp, U. B. & Willbold, D. Structural insights into conformational changes of a cyclic nucleotide-binding domain in solution from *Mesorhizobium loti* K1 channel. *Proc. Natl Acad. Sci. USA* **108**, 6121–6126 (2011).
- Napolitano, C. *et al.* Genetic testing in the long QT syndrome: development and validation of an efficient approach to genotyping in clinical practice. *J. Am. Med. Assoc.* **294**, 2975–2980 (2005).

Supplementary Information is linked to the online version of the paper at www.nature.com/nature.

Acknowledgements We thank M. Munari, S. Camp, S. Cunningham and G. Sheridan for excellent technical assistance. We thank the beamline staff at the Advanced Light Source (ALS) and especially P. Zwart for help with data analysis. We also thank the members of the Zagotta laboratory for helpful discussions. This work was supported by the Howard Hughes Medical Institute, National Institutes of Health (NIH) grant R01 EY010329 (W.N.Z.) and NIH grant F32 HL095241 (A.E.C.). The Berkeley Center for Structural Biology is supported in part by the NIH, National Institute of General Medical Sciences and the Howard Hughes Medical Institute. The ALS is supported by the Director, Office of Science, Office of Basic Energy Sciences, of the US Department of Energy under contract no. DE-AC02-05CH11231.

Author Contributions T.I.B. and W.N.Z. conceived the experiments. T.I.B. performed the crystallographic experiments, and B.S. helped with the crystallographic data analysis. A.E.C. and W.N.Z. performed the electrophysiology experiments and data analysis. T.I.B. and W.N.Z. wrote the manuscript.

Author Information Atomic coordinates and structure factors for the reported crystal structures have been deposited with the Protein Data Bank under accession codes 3UKN, 3UKT and 3UKV (see Supplementary Table 1 for identifications). Reprints and permissions information is available at www.nature.com/reprints. The authors declare no competing financial interests. Readers are welcome to comment on the online version of this article at www.nature.com/nature. Correspondence and requests for materials should be addressed to W.N.Z. (zagotta@u.washington.edu).

METHODS

FSEC. The C-linker/CNBHD of zebrafish ELK channels (amino acids Q543–L750) was covalently fused to a C-terminal GFP in the pCGFP-BC bacterial expression vector provided by T. Kawate and E. Gouaux²¹. The construct was transformed into BL21 (DE3) cells. 5 ml cultures of the cells were grown at 37 °C, induced with IPTG and harvested by centrifugation. The cell pellets were resuspended in a lysis buffer (500 mM KCl, 1 mM TCEP, 30 mM HEPES, 1 mM PMSF and 2.5 mg ml^{−1} DNase; pH 8.0) and sonicated. Insoluble protein was separated by centrifugation and the supernatant was analysed on a Superdex 200 10/300 GL column (GE Healthcare).

Scale-up protein purification. The C-linker/CNBHD of zebrafish ELK (amino acids Q543–L750) was subcloned into a modified pMALc2T vector (New England Biolabs) containing an N-terminal MBP affinity tag followed by a thrombin cleavage site. The protein was expressed in BL21 (DE3) *Escherichia coli* cells as previously described¹¹. The cells were harvested by centrifugation, resuspended in a lysis buffer (500 mM KCl, 1 mM TCEP, 30 mM HEPES, 1 mM PMSF and 2.5 mg ml^{−1} DNase; pH 8.0) and lysed in an Emulsiflex-C5 (Avestin). Insoluble protein was separated by centrifugation. The C-linker/CNBHD of zebrafish ELK was purified on an amylose affinity column and was then loaded on a HiTrap SP FF ion-exchange column following an overnight cleavage with thrombin at 4 °C. The protein was eluted with a linear KCl gradient and 100 mM citric acid (pH 3.5) was added to the final protein solution to increase the solubility of the protein at high concentrations. The protein was concentrated to 20–30 mg ml^{−1} for crystallization. Selenomethionine derivatives were generated as previously described^{10,31}.

Crystallization. Crystals were grown at 20 °C using the sitting-drop vapour diffusion method. 150-nl drops of the concentrated protein and reservoir solution were mixed 1:1 by a Mosquito (TTP LABTECH). The final protein solution contained: ~250 mM KCl, 1 mM TCEP, 30 mM HEPES, 100 mM citric acid, pH 3.5. The reservoir solution contained: 6% w/v 1,5-diaminopentane dihydrochloride, 180 mM ammonium acetate, 22.5% (w/v) PEG 3350, 90 mM Tris; pH 8.5 for crystal T141; 1.8 M non-detergent sulphobetaine (NDSB)-211, 180 mM ammonium acetate, 22.5% (w/v) PEG 3350, 90 mM Tris, pH 8.5 for crystal T42; 6% (w/v) D-(+)-galactose, 180 mM ammonium sulphate, 22.5% (w/v) PEG 3350, 90 mM HEPES, pH 7.5 for crystal T26; and 5 mM cAMP, 180 mM ammonium acetate, 22.5% (w/v) PEG 3350, 90 mM Tris, pH 8.5 for crystal T84. The crystals were cryoprotected in reservoir solution supplemented with 25% glycerol before being flash frozen in liquid nitrogen.

Data collection and structure determination. Diffraction data sets were collected at the Advanced Light Source (beamline 8.2.1) at Lawrence Berkeley National Laboratory in Berkeley, California. Data were analysed with Mosfilm³² and HKL2000³³ software. Molecular replacement using the structure of the C-linker/CNBHD of HCN2 channels as a search model failed to find a solution. Therefore, the structure of the zebrafish ELK C-linker/CNBHD was solved by the SAD phasing of selenomethionine derivative crystal T141 using PHENIX³⁴ followed by phase extension to 2.25 Å resolution using a native data set. Structures for the rest of the data sets were solved by molecular replacement using this structure as a search model followed by numerous cycles of refinement in PHENIX and manual model building in Coot³⁵. The molecular replacement was carried out using Phaser in PHENIX³⁴. The asymmetric unit contained three molecules in the C222₁ space group and four in the P12₁1 space group. The structures of different ELK molecules in the asymmetric unit and molecules in the two different space groups were very similar, with r.m.s.d. values for the α -carbons calculated for the entire sequence of the resolved C-linker/CNBHD ranging from 0.4–0.7 Å (Supplementary Fig. 8). The crystallographic data and refinement statistics are summarized in Supplementary Table 1. Electron density was visible for all but

several terminal residues in molecules A and B of the native structure in the C222₁ space group. Molecules A and B of the native C222₁ structure were used for analysis in this paper. Analysis with Molprobity³⁶ of the final models indicated no Ramachandran outliers for T42 and T26 structures, and 0.59 (%) for T84. Figures were made using PyMOL³⁷. The topology of the C-linker/CNBHD of zebrafish ELK was defined by PROCHECK (<http://www.ebi.ac.uk/pdbsum/>). The phylogenetic tree in Supplementary Fig. 1a was computed with Cobalt³⁸ (<http://www.ncbi.nlm.nih.gov/tools/cobalt/>). The GI numbers for the amino acid sequences aligned in Supplementary Fig. 1c were: zebrafish ELK, 159570347; human ELK1, 27886667; human ELK2, 26006814; human ERG1, 103488986; mouse EAG1, 487740; bovine CNGA1, 231739; mouse HCN2, 148699724. The electrostatic potential surface calculations were carried out using the APBS³⁹ plugin for PyMOL and the PARSE force field, and coloured from red (−3 kT/e) to blue (+3 kT/e) where k is Boltzmann's constant, T is absolute temperature, and e is the charge on an electron.

Electrophysiology. The full-length zebrafish ELK channel (GI: 159570347) with a C-terminal Flag epitope was generated by Bio Basic Inc. and subcloned into the pGEMHE oocyte expression vector. The cRNA was transcribed using the T7 mMessage mMachine Ultra kit (Ambion). Expression of the wild-type and mutant (Y740A and Δ 740–742) zebrafish ELK channels in *Xenopus* oocytes and current recordings from inside-out patches allowing 10 min for run up following excision were done as described before¹¹. Both pipette and bath solutions contained 130 mM KCl, 10 mM HEPES, 0.2 mM EDTA, pH 7.2. 1 mM cAMP was added to the bath solution as indicated. Zebrafish ELK currents were elicited by applying a series of 100-ms voltage pulses (ranging from −140 to +160 mV in 20 mV increments) from a pre-pulse potential of −140 mV, followed by a 150 ms tail pulse to −100 mV. Currents were leak-subtracted with P/4 protocol. To obtain conductance versus voltage curves, peak tail current amplitudes at −100 mV were normalized to the largest peak conductance amplitude, which followed a step to +40 mV. These normalized data were then plotted against the test voltage, and were fit with a Boltzmann equation:

$$\frac{G}{G_{\max}} = \frac{1}{1 + e^{\left(\frac{V - V_{1/2}}{s}\right)}}$$

where V represents the test voltage, $V_{1/2}$ is the midpoint activation voltage, and s is the slope of the relation.

- Guerrero, S. A., Hecht, H. J., Hofmann, B., Biebl, H. & Singh, M. Production of selenomethionine-labelled proteins using simplified culture conditions and generally applicable host/vector systems. *Appl. Microbiol. Biotechnol.* **56**, 718–723 (2001).
- Collaborative Computation Project 4. The CCP4 suite: programs for protein crystallography. *Acta Crystallogr. D* **50**, 760–763 (1994).
- Otwinowski, Z. & Minor, W. Processing X-ray diffraction data collected in oscillation mode. *Methods Enzymol.* **276**, 307–326 (1997).
- Adams, P. D. et al. PHENIX: a comprehensive Python-based system for macromolecular structure solution. *Acta Crystallogr. D* **66**, 213–221 (2010).
- Emsley, P. & Cowtan, K. Coot: model-building tools for molecular graphics. *Acta Crystallogr. D* **60**, 2126–2132 (2004).
- Chen, V. B. et al. MolProbity: all-atom structure validation for macromolecular crystallography. *Acta Crystallogr. D* **66**, 12–21 (2010).
- DeLano, W. L. The PyMOL molecular graphics system. <http://www.pymol.org> (DeLano Scientific, 2002).
- Huson, D. H. et al. Dendroscope: an interactive viewer for large phylogenetic trees. *BMC Bioinformatics* **8**, 460 (2007).
- Baker, N. A., Sept, D., Joseph, S., Holst, M. J. & McCammon, J. A. Electrostatics of nanosystems: application to microtubules and the ribosome. *Proc. Natl Acad. Sci. USA* **98**, 10037–10041 (2001).

CORRECTIONS & AMENDMENTS

CORRIGENDUM

doi:10.1038/nature10789

Selective killing of cancer cells by a small molecule targeting the stress response to ROS

Lakshmi Raj, Takao Ide, Aditi U. Gurkar, Michael Foley, Monica Schenone, Xiaoyu Li, Nicola J. Tolliday, Todd R. Golub, Steven A. Carr, Alykhan F. Shamji, Andrew M. Stern, Anna Mandinova, Stuart L. Schreiber & Sam W. Lee

Nature **475**, 231–234 (2011)

In this Letter we made errors in the description of the way we performed tumour measurements in the spontaneous (Fig. 2b and d) and the xenograft (Supplementary Fig. 9) mouse models. The legend of Fig. 2 incorrectly states that the graph of plotted tumour measurements represents tumour diameters from “grossly dissected tumours”. Similarly, the Supplementary Fig. 9c legend incorrectly states that “After 3 weeks, tumour masses were excised and measured” and the legend of Supplementary Fig. 9d incorrectly states that: “After 3 weeks treatment, tumour sizes were measured”. Instead, for the experiments in both Fig. 2 and Supplementary Fig. 9 we measured diameters of tumours in live mice at different time points (as indicated on the *x* axis of the graphs) during the course of the treatment. The tumours were measured between the skin surface layers using a caliper.

Additionally, the legend of Supplementary Fig. 9b and c incorrectly refers to “tumour mass(es)” instead of “tumour size(s)”. In the MMTV-PyVT spontaneous tumour model (Fig. 2b and d) and in the xenograft bladder, breast and lung models (Supplementary Fig. 9b, c and d) we measured the length and the width of the tumour. The length was measured along the imaginary longitude of the corpse of the mouse

and the width was measured in the direction of its latitude. In the melanoma xenograft model (Supplementary Fig. 9e) we measured only the width owing to the irregular longitudinal shape of the tumours. For consistency, the graphs in Fig. 2 and Supplementary Fig. 9 represent only the width measurements.

Furthermore, we defined the error bars in Fig. 2 incorrectly: the values in bar graphs in Fig. 2b and d are mean \pm standard deviation ($n = 12$). We also realize that these error bars were misleadingly small when compared to calculated tumour volumes (in cubic centimetres) using the following formula: length \times width² \times $\pi/6$. Tumour volume measurements of control and treated single tumours in the MMTV-PyVT mouse model are shown below (Fig. 1 of this Corrigendum). Although we did observe much higher variability in tumour volumes than in tumour width, the magnitude of the difference between control and treated animals remains the same. In addition, we made errors in indicating the exact number of animals used for each experiment in Supplementary Fig. 9. The correct numbers are 12 animals per group for Supplementary Fig. 9b and seven animals per group for Supplementary Fig. 9c, d and e. Values in Supplementary Fig. 9 are averages (\pm standard deviation; $n = 12$ for Supplementary Fig. 9b, $n = 7$ for Supplementary Fig. 9c, d and e).

We have also been unable to verify without doubt that the image in Supplementary Fig. 9b shows four different mice within the treated and untreated groups and therefore wish to replace this figure (see Fig. 2 of this Corrigendum).

We apologize for any confusion these errors may have caused. The corrections described here do not alter the overall conclusions of this Letter, and all other data still stand.

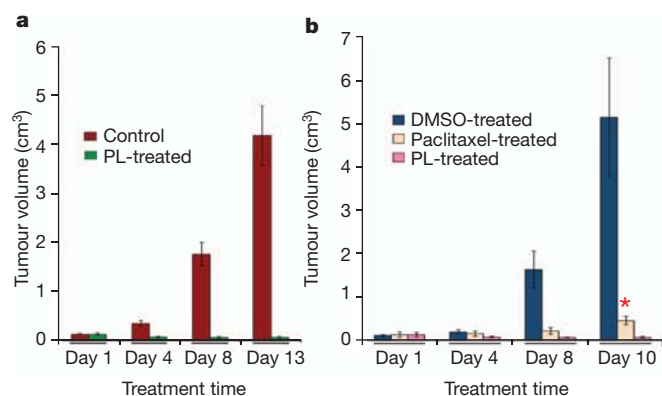


Figure 1 | Additional data (volume measurements) for Fig. 2b and d of the original paper. Tumour volume measurement in MMTV-PyVT mice. **a**, Tumour volume of single tumours from control (dimethyl sulphoxide, DMSO) or piperlongumine (PL)-treated mice were calculated on the basis of the length and width of the lesions after applying the following formula: length \times width² \times $\pi/6$. **b**, Similarly, tumour volumes were calculated from DMSO-, paclitaxel- or PL-treated mice. Values in bar graphs are mean \pm standard deviation ($n = 12$). *Shorter treatment period due to high toxicity of paclitaxel in animals.

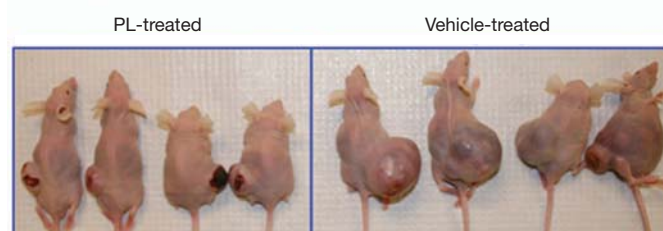


Figure 2 | This is the corrected Supplementary Fig. 9b. Therapeutic activity of PL in xenograft tumour mice bearing EJ bladder cancer cells. Control (vehicle)- and PL-treated mice were killed after six weeks of treatment. Treatment was 1.5 mg kg⁻¹ of PL by intraperitoneal injection daily.

CAREERS

TURNING POINT Antarctic researcher finds success after break from science **p.537**

CAREERS BLOG The latest discussions and news about research jobs go.nature.com/ielkkf

NATUREJOBS For the latest career listings and advice www.naturejobs.com



E. FREEMAN

Alongside landmarks such as the Forbidden City in Beijing, prospective postdocs will find opportunities in environmental science, palaeontology and other areas.

CHINA

The gates are open

There is a wealth of fellowships and postdoctoral openings in China for foreign researchers who aren't afraid of culture shock.

BY JANE QIU

Jacob Wickham knew just a few words of Chinese and still struggled to use chopsticks when he first set foot in Qingtongxia, a remote village in western China. In 2008, Wickham, then a PhD student studying insect biology at the State University of New York in Syracuse, had a fellowship from the East Asia and Pacific Summer Institutes (EAPSI), part of the US National Science Foundation (NSF). He was in China to study the Asian longhorn beetles plaguing tens of thousands of hectares of poplar trees that had been planted to slow desert encroachment. The experience gave Wickham the chance to network and identify research topics relevant to both China and the United States.

His work in the field and his brush with

Chinese culture made such an impression on Wickham that he decided to pursue postdoctoral research in the country. Two years after his EAPSI fellowship, he returned to China on a three-year postdoctoral grant from the NSF's International Research Fellowship Program, studying insect species — in particular the Japanese pine sawyer beetle — that are pests in China and could become invasive if accidentally introduced to the United States. He now works at the Institute of Chemistry in Beijing, part of the Chinese Academy of Sciences (CAS).

OPPORTUNITIES ABOUND

Wickham is one of a growing number of scientists seeking to jump-start their careers in China, attracted by the country's new research infrastructure, expanding scientific

community and thirst for talent. There were 127 applicants for the CAS Fellowship for Young International Scientists in 2011 — an increase of 41% since 2009. About 67% of applications are successful.

China has unique ecological problems that make it attractive to environmental scientists, plenty of fossils to draw palaeontologists, and high investment in clean technology, which encourages climate-change research. Postdoctoral research in the country, especially in these areas, could help young scientists to forge collaborations, make contacts and get training in specialized techniques. Foreign researchers will have to cope with language challenges and culture shock, but the experience can be enriching both personally and professionally.

For several years, the Chinese government ►



Jacob Wickham enjoyed his PhD research in China so much that he returned for his postdoc.

► has been attempting to end the country's brain drain, luring home-grown scientists back from overseas and encouraging young talent to stay put. More recently, it has also sought to draw foreign researchers to its shores. The best funding mechanism is usually a fellowship (see table), because salaries at Chinese institutes are often lower than those in Western countries, and Chinese granting mechanisms can't easily be applied to foreign scientists.

CAS and the National Natural Science Foundation of China (NSFC) both offer Fellowships for Young International Scientists to freshly graduated PhD holders and more experienced postdoctoral researchers of all nationalities. Applicants must contact a principal investigator in a Chinese lab, explain their project and request that the investigator submit an application on their behalf. CAS also runs a joint fellowship scheme with the Third World Academy of Science (TWAS), to support postdocs from other developing countries.

Foreign agencies run programmes, too. Each year, EAPSI provides more than 30 US PhD students with first-hand research experience in mainland China (it also sends researchers to Japan, South Korea, Taiwan, Singapore, Australia and New Zealand). Students spend a week learning about Chinese language and culture in Beijing, before a two-month stint doing research at institutes of their choice. They can also visit other universities and institutes across the country. Options for researchers from outside the United States include the Science and Technology Fellowship Programme in China (STF China), run by the European Union (EU), or initiatives from national funding councils.

Many foreign postdocs say that working in China is far from easy. In daily life, the language barrier is the biggest challenge. "Simple tasks, such as opening a bank account and

going out to do some shopping, are not that simple any more," says Andy Tsun, a British immunologist who has been working at the CAS Shanghai Pasteur Institute for two years.

The EU's STF China fellows receive six months of language and culture training in Beijing at the start of their placements, with short trips to other parts of China. "It's a great innovation for this kind of programme," says Sébastien Chanfreau, a French chemical engineer who spent two years at Nankai University in Tianjin. Chinese placements are "certainly a daunting experience for people who don't speak Chinese and know little about the culture and the way of doing things there", he says.

However, language is not necessarily a problem in the lab or field. Many Chinese researchers speak English well, so foreigners can usually communicate with their colleagues. Meetings of teams that include international researchers are often conducted in English. Of course, more complex communications could be tricky — foreign postdocs acting as supervisors should make sure that instructions are fully understood, to prevent time or work being lost.

RED TAPE

What really baffles most foreign researchers in China is how science is done and administrated. "It definitely takes some time to understand how another culture conducts science in aspects ranging from grant administration to working in the lab and field, and organizing conferences," says Daniel Joswiak, a US glaciologist who has been working at the CAS Institute of Tibetan Plateau Research in Beijing since 2008. "You have to be very proactive."

Postdocs often need to take the initiative when collaborating or learning about a colleague's work. And researchers may need to be forceful to get permits and approvals to work in politically sensitive areas such as Tibet and Xinjiang. To study pest problems, Wickham had to navigate first the State Forestry Administration and then the provincial

forestry bureau. Regulations can be vague and difficult to decipher, and the officials in charge may not be in a rush to process the request. It is essential to monitor each step of the process. "The hierarchical structure can be challenging," says Wickham.

Foreign scientists may find it difficult to plan field projects ahead of time. In many countries, researchers are used to knowing months in advance exactly when they are going into the field, where and for how long. But often in China, "everything is done at the last minute in terms of planning field sites and working with the local government", says Wickham.

"It definitely takes some time to understand how another culture conducts science."

In the lab, however, forward planning is essential: reagents often need to be shipped from overseas, which might take more than a month. This can be frustrating for Western scientists who are used to next-day deliveries. "You have to plan ahead," says Tsun. "If you have a change in project direction, it will take a while to get things going."

There are also restrictive rules for importing and exporting cell lines and transgenic animals, which can also slow things down and complicate international collaborations. "You need to be able to share reagents in science. It's also a way of validating results," says molecular biologist Jannie Danielsen, who has been working at the CAS Beijing Institute of Genomics since early 2011, on a fellowship from the Danish Council for Independent Research.

The Chinese work ethic often makes an impression on foreign researchers. "It's humbling to see people working so hard," says Tsun. He says that half the Pasteur Institute is sometimes still in the lab after 7 or 8 p.m. — something that Tsun rarely saw during his PhD research at the University of Oxford, UK.

But hard work doesn't always translate into

FELLOWSHIPS FOR FOREIGNERS

Agencies in China and abroad offer funding for young scientists hoping to explore the country.

Programme	Target	Duration	Website	Notes
CAS Fellowships for Young International Scientists	Postdocs	1 year	go.nature.com/ectbcu	Renewable; open to all foreign postdocs
NSFC Fellowships for Young International Scientists	Postdocs	6 months to 1 year	go.nature.com/suqyxx	Renewable; open to all foreign postdocs
TWAS-CAS Fellowship Program	Postdocs	6 months to 1 year	go.nature.com/u7kuau	For postdocs from developing countries
EU Science and Technology Fellowship in China	Postdocs	2 years	go.nature.com/julvmc	For EU citizens
NSF International Research Fellowship Program	Postdocs	3 years	go.nature.com/ms7y8	For US citizens or permanent residents
NSF EAPSI	Graduate students	2 months	go.nature.com/gff32a	For US citizens or permanent residents
Next Step Connections	All levels	1 to 6 months	go.nature.com/qnrcrb	Commercial programme offering professional internships in Asia to students and young professionals of all nationalities

creativity. Many of the students “haven’t been trained so much in using their knowledge to generate new ideas and find new solutions”, says Danielsen. “They work extremely hard and very long hours, but I am not sure whether they are able to step back a bit and reflect on the results.” Wickham says that the science is often highly managed by professors, and researchers are not encouraged to take risks or learn from their mistakes.

A DIFFERENT WORLD

Foreigners may find that some practices are anathema to their usual customs. Most academic institutions in China offer financial rewards for getting papers published in journals with high impact factors — often thousands of dollars for the first and corresponding authors (see *Nature* 441, 792; 2006). Such policies threaten to make competition unhealthy and discourage people from working together and exchanging ideas, says Sarah Rothenberg, an environmental scientist who has just joined the University of South Carolina in Columbia after three years at the CAS Institute of Geochemistry in Guiyang. “Science has become a totally different game there,” she says.

Despite the differences, all the researchers contacted for this article say that their Chinese colleagues went out of their way to make them feel welcome and help them to sort out logistical issues such as housing. The country’s ample research funding also helps. “There are problems with money everywhere but China,” says Chanfreau. “I was often told, ‘Money is not a problem, just get what you need.’”

Some foreign postdocs have taken the opportunity to experience Chinese culture outside their research. Chanfreau, for instance, helped to initiate an EU–China science-communication project in Beijing, akin to the international Café Scientifique, in which researchers and the public meet to debate topical issues such as green chemistry, breast cancer and genetic engineering. “The sense of being able to contribute to the public understanding of science in China is extremely rewarding,” says Chanfreau.

The postdocs who find success will be those who are open to a new environment and eager to explore different approaches to science. “A sense of humour and the willingness to be flexible are crucial,” says Corwin Sullivan, a palaeontologist who went to China to pursue a postdoc at the CAS Institute of Vertebrate Paleontology and Paleoanthropology in Beijing in 2005 and is now an associate professor there. “The expats who find China most difficult are those who have a rigid sense of how things should work and refuse to adapt.” ■

Jane Qiu is a freelance writer based in Beijing.

TURNING POINT

Rob McKay

Rob McKay, a glacial sedimentologist at the Victoria University of Wellington in New Zealand, won the 2011 Prime Minister’s MacDiarmid Emerging Scientist prize in December for research on Antarctica’s climate and environmental history.

Why did you leave science after completing a master’s degree in geology?

I did my master’s with Peter Barrett at Victoria University. I went on my first trip to Antarctica with him, and I really enjoyed being in the field. But after I finished in 2000, I had hefty student loans and decided to make some money and see the world. I ended up in the United Kingdom, using the critical-thinking skills honed during my graduate research to edit research reports at an investment company.

What lured you back to do a PhD?

I had kept in touch with Peter, intending to write my master’s results into a paper. But in 2005, he invited me to do PhD research with the Antarctic Geological Drilling project (ANDRILL), a multinational collaboration to investigate past climate change. I had concerns about doing a PhD at the same university that I earned my earlier degrees from. But the geology department had expanded to run the Antarctic Research Centre and had a greater focus on international collaboration. I decided that pursuing a PhD there would be a good career move.

Describe your role in the ANDRILL research.

I was meant to focus on sedimentary petrology, working out the origin of sediments in 1-metre cores from the Antarctic ice shelf. But ANDRILL found evidence of past cycles of ice-sheet expansion and retraction coming out of this one-of-a-kind 1.3-kilometre drill hole. We found 60 cycles of an alternating pattern. Documenting and interpreting these cycles became one of the more important parts of the project, and I worked on that. Our team’s findings confirmed that the ice sheet was highly variable, which had been the subject of speculation.

What did you learn from that experience?

You have to grasp the opportunities presented to you, even if they are high-risk, high-reward. Still, I realized that I should have a back-up plan. Luckily, the 1.3-kilometre drill hole was that plan, and it proved to be quite fruitful.

How have international collaborations helped your career?

I’ve spent 2–3 months at a time on expeditions with people from the United States,



Europe and Japan. These trips are bonding experiences, which I think facilitates continued collaborations — invitations to labs all over the world. Big interdisciplinary projects bring together hugely diverse groups of people. My work on ANDRILL led to a paper in the *Geological Society of America Bulletin* (R. McKay *et al.* *Geol. Soc. Am. Bull.* 21, 1537–1561; 2009), which received a lot of attention from the palaeoclimate community because it was one of the most detailed records yet published of Antarctic climate history and fluctuations in the ice sheet. That led to an invitation to take part in the Integrated Ocean Drilling Program, an international marine-research initiative. I’m taking my palaeoclimate work from the ice sheet to the ocean, trying to determine how ocean chemistry dynamics affect climate.

How will the Emerging Science prize affect your career?

It certainly will help with my imminent job search. It’s prestigious and helps to bring attention to climate research. I hope to use some of the NZ\$200,000 (US\$160,000) prize money to get another PhD student involved in my next project, which is likely to involve sea-level histories around New Zealand, and to fund collaborative research with an overseas lab.

To what do you attribute your success?

There is an element of luck. I was fortunate to work on this amazing drill hole that had features that had never been seen before. I’m also really interested in the research, and have learned to overcome intimidation to put my ideas out there. ■

INTERVIEW BY VIRGINIA GEWIN

ROCK 'N' ROLL ALIENS

The looks and the lifestyle.

BY RALPH GRECO JR

I had just seconds to leap across the stage and catch Dr Malacuplus before he made off with the orb. The Latex Kids were blistering through their latest seven-minute epic guitar assault, and Sinthia Slide, the band's lead singer and my third cousin once removed, was adopting her usual stage pose, channelling one-quarter Janis Joplin, one-quarter Rip Taylor, another part classic Medusa and one-quarter that tiger who had had enough with Siegfried and Roy. As she scared/delighted/aroused the crowd, I realized that my only chance was to use her in a way that would've had her snapping her whip at me if I hadn't been the band's security, confidant and benefactor. As Sinthia set her hips, spread her thighs (as best she could in what she wore) and unfurled her red latex dress down to her knees, she created for me a tighter-than-tight trampoline. I leapt from my perch atop the wall of Marshall stacks, bounced off the front of Sinthia's dress and catapulted over the bands' collective heads straight on to the back of that bald, smelly doctor.

Of course, most of the audience at the Steam Works, an outpost of 7th Avenue and nowheresville New Jersey, thought my aerobatics were part of the show. The LKs truly deliver for their fans. That a six-foot guy with a crew cut, jack-boots and split rivet jeans could come tumbling down from some amps, bounce off the petite lead singer as she held her dress out, shoot across the stage and land on the arch-nemesis of our entire lifestyle community — the doctor liked to steal much more than just off-world glowing orbs of power — prompted a five-minute round of applause and not one raised eyebrow. All of which went far in bolstering my good feelings for the people who, like me, are into latex, leather and lace.

"You said he was bound to show before the end of the season," Sinthia said as the band and I congregated backstage, sipping a round of cold ones.

"I hoped putting the orb out there in full view would pull him out."

"Amazing half-gainer off my pelvis, cousin," she added.

The other three band members — drummer Trudy Sticks, her bassist brother Randee (no last name), and the truly gargantuan, gaunt and to all intents and purposes mute (he truly let his instrument speak for him most of the time) lead guitarist Larry Candy Cane — and I gazed at the lead singer as she made her way across the room in her six-inch-heel patent-leather

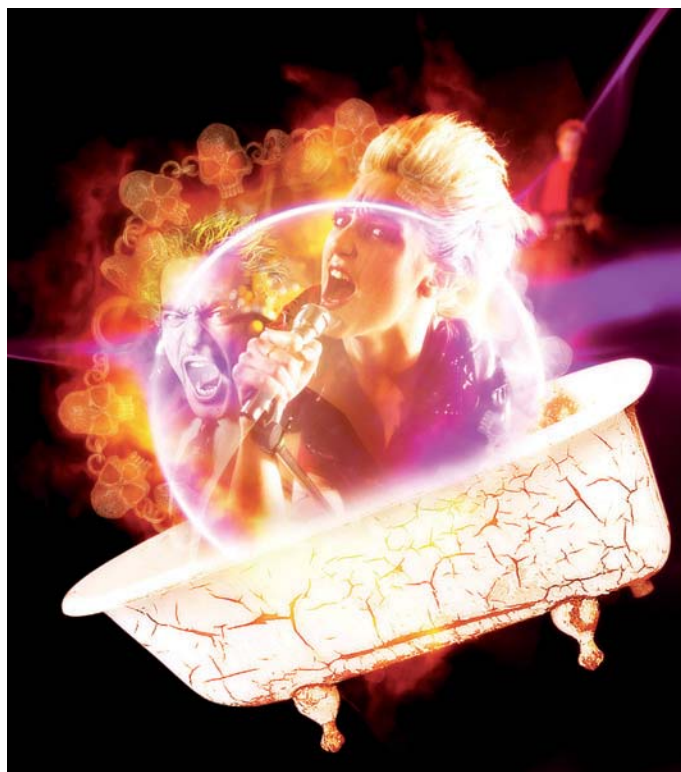
red leather vest and jodhpurs on), I knew I could relax a bit. I had dispatched the evil doctor, secreted him in the back of my van after a quick knockout punch, and I once more had the orb safely tucked under my long trench. The members of LK were never as comfortable staring at the thing as they were Sinthia's butt — seeing as the orb was not of this world.

I was picked as the orb's keeper because the aliens who made it saw I ran with a community. Our goth-that-was-fetish-that-was-rock-and-roll crowd was not easily unnerved and was one they wanted to infiltrate before they made their presence known further to us humans. The charge for the powers the orb gave me — a mere human — was a fee I was collecting as I bent to grab the band's sweaty and slightly worn stage clothes. Our alien friends wanted as many outfits made of weird Earth materials as possible — my part-time job when not with LK was unloading shipments at The Gap — and I shipped what I gathered, as I would the evil doctor, off Earth via the wonderful transportation device I had hidden in my loft bathtub. I never asked for what purpose the scaly little creatures with the red eyes used the band's old sweaty latex, bent bruised buckles and leather, but as I had been promised that the orb would envelop us all in a rather splendidferous, fortunate glow — as it truly seemed to have, as far as this band was concerned

— LK's ever-increasing wardrobe allowance helped us all along nicely.

I left the dressing room and pulled my trench tight round my bare chest, content in the knowledge that I had once again rid the Universe of another bad character — and was collecting some smelly latex and leather for a race more enlightened than our own. ■

Ralph Greco Jr is an internationally published author of short stories, plays, essays, 800 sex 'scripts', children's songs and SEO copy. Ralph is also an ASCAP licensed songwriter/performer and Internet radio DJ. Living in the wilds of suburban New Jersey, USA, Ralph attempts, yet fails, to keep his ever-expanding ego in check.



JACEY

boots. Being together two years, sharing dressing rooms and toilets as we had, and seeing one another in every which way during our rise to the toppermost-poppermost in this wacky modern music biz, Sinthia's body was still a wonder to any of us who spied it bare. But to me what was even more amazing, and a testament to what I really was all about, was that I stared at her boots more than her butt.

The band had a third set yet to deliver, and as the unbuckling, drying off and re-lubing process for their next round of rock fetish-wear began (though The Cane, as we called him, kept his

➔ **NATURE.COM**
Follow Futures on
Facebook at:
go.nature.com/mtoodm

Adenylylation control by intra- or intermolecular active-site obstruction in Fic proteins

Philipp Engel^{1†*}, Arnaud Goepfert^{1,2*}, Frédéric V. Stanger^{1,2}, Alexander Harms¹, Alexander Schmidt³, Tilman Schirmer² & Christoph Dehio¹

Fic proteins that are defined by the ubiquitous FIC (filamentation induced by cyclic AMP) domain are known to catalyse adenylylation (also called AMPylation); that is, the transfer of AMP onto a target protein. In mammalian cells, adenylylation of small GTPases through Fic proteins injected by pathogenic bacteria can cause collapse of the actin cytoskeleton and cell death^{1,2}. It is unknown how this potentially deleterious adenylylation activity is regulated in the widespread Fic proteins that are found in all domains of life and that are thought to have critical roles in intrinsic signalling processes. Here we show that FIC-domain-mediated adenylylation is controlled by a conserved mechanism of ATP-binding-site obstruction that involves an inhibitory α -helix (α_{inh}) with a conserved (S/T)XXE(G/N) motif, and that in this mechanism the invariable glutamate competes with ATP γ -phosphate binding. Consistent with this, FIC-domain-mediated growth arrest of bacteria by the VbhT toxin of *Bartonella schoenbuchensis* is intermolecularly repressed by the VbhA antitoxin through tight binding of its α_{inh} to the FIC domain of VbhT, as shown by structure and function analysis. Furthermore, structural comparisons with other bacterial Fic proteins, such as Fic of *Neisseria meningitidis* and of *Shewanella oneidensis*, show that α_{inh} frequently constitutes an amino-terminal or carboxy-terminal extension to the FIC domain, respectively, partially obstructing the ATP binding site in an intramolecular manner. After mutation of the inhibitory motif in various Fic proteins, including the human homologue FICD (also known as HYPE), adenylylation activity is considerably boosted, consistent with the anticipated relief of inhibition. Structural homology modelling of all annotated Fic proteins indicates that inhibition by α_{inh} is universal and conserved through evolution, as the inhibitory motif is present in ~90% of all putatively adenylylation-active FIC domains, including examples from all domains of life and from viruses. Future studies should reveal how intrinsic or extrinsic factors modulate adenylylation activity by weakening the interaction of α_{inh} with the FIC active site.

In two Fic proteins, IbpA and VopS, that are translocated by pathogenic bacteria into host cells, the ubiquitous FIC domain has been shown to catalyse adenylylation^{1–4}. The crystal structure of the effector domain IbpA(FIC2) in complex with its adenylylated host target Cdc42 has been reported⁵ and a catalytic mechanism has been proposed^{5,6}. IbpA- or VopS-mediated adenylylation of Rho-family GTPases abolishes downstream signalling in human cells and, thus, causes actin cytoskeleton collapse and cell death^{1,2}. By contrast, overexpression of a human Fic protein with similar target specificity, HYPE, had only a marginal effect¹. This suggests that the potentially deleterious adenylylation activity is tightly regulated in HYPE and probably in most of the almost 3,000 Fic proteins that are proposed to have important roles in intrinsic signalling processes in bacteria, archaea and eukaryotes.

VbhT is a bacterial Fic protein of the mammalian pathogen *B. schoenbuchensis*^{7,8}. It is composed of an N-terminal FIC domain

and a C-terminal BID domain (Fig. 1a). The BID domain facilitates protein translocation into mammalian or bacterial target cells through a type IV secretion system or conjugation machinery⁹, respectively, but the target cell and functional role of VbhT are unknown. VbhT arrests growth when expressed in *Escherichia coli* (Fig. 1c and Supplementary Fig. 1a). Growth arrest is repressed by mutation of histidine to alanine (VbhT(H136A)) in the conserved FIC motif HXFX(D/E)GNRXXR. In other Fic proteins, this signature motif has been shown to be essential for target protein adenylylation activity^{1,2,10}, therefore suggesting that toxicity is related to adenylylation of endogenous proteins. Indeed, wild-type VbhT, but not VbhT(H136A), catalysed *in vitro* adenylylation of a putative *E. coli* target protein of approximately 80 kilodaltons (kDa) (Fig. 1d). Furthermore, *E. coli* cells showed filamentation after expression of wild-type VbhT, but not of VbhT(H136A) (Supplementary Fig. 2). A similar phenotype has been described for what is thought to be a hyperactive mutant of the *E. coli* Fic protein¹¹. Co-expression of VbhT with VbhA, encoded by the small open reading frame *vbhA*

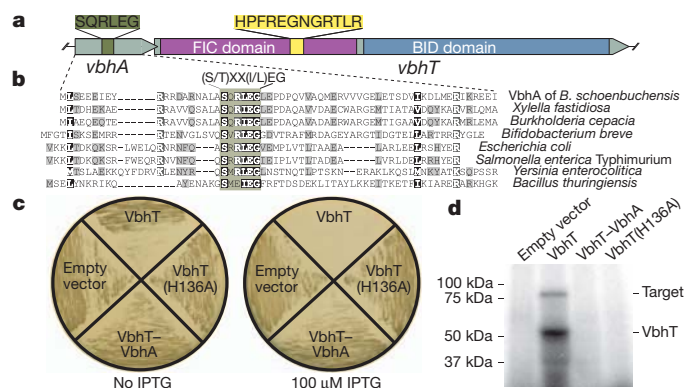


Figure 1 | The small protein VbhA represses the toxic effect (growth arrest) that is mediated by the adenylylation activity of VbhT in *E. coli*. **a**, Genetic organization of the type-IV-secretion-system-associated locus of *B. schoenbuchensis*, which is composed of the overlapping *vbhA* and *vbhT* genes. The FIC and BID domains that are encoded by *vbhT* are shown in different colours. Protein translations of the regions encoding the conserved motif of VbhA and the FIC motif of VbhT are depicted. **b**, Protein alignment of VbhA and a subset of the 158 homologues that are encoded upstream of *fic* loci in different bacteria (see also Supplementary Fig. 4). The most conserved region shows a (S/T)XX(I/L)EG consensus. Sequence accessions and strain designations are given in Supplementary Fig. 4. **c**, Growth of *E. coli* on lysogeny broth (LB) plates after IPTG-induced expression of different VbhT and VbhA constructs. Expression of VbhT shows a toxic effect, whereas bacterial growth is not affected when VbhT(H136A) is expressed or when VbhT and VbhA are co-expressed (VbhT–VbhA). All *E. coli* strains revealed normal growth without induction. Growth curve experiments in LB gave analogous results (Supplementary Fig. 1). **d**, Adenylylation assay with crude cell lysates of *E. coli* ectopically expressing the same constructs as in panel c.

¹Focal Area Infection Biology, Biozentrum, University of Basel, CH-4056 Basel, Switzerland. ²Core Program Structural Biology and Biophysics, Biozentrum, University of Basel, CH-4056 Basel, Switzerland.

³Proteomics Core Facility, Biozentrum, University of Basel, CH-4056 Basel, Switzerland. [†]Present address: Department of Ecology and Evolutionary Biology, Yale University, New Haven, CT 06520-8106, USA.

*These authors contributed equally to this work.

immediately upstream of *vbhT* (Fig. 1a), completely repressed VbhT toxicity, as shown by wild-type-like bacterial growth, normal cell morphology, and inhibition of VbhT-dependent adenylation (Fig. 1 and Supplementary Figs 1a and 2). We also observed VbhT-mediated toxicity and its repression by VbhA in *B. schoenbuchensis*, the natural carrier of this toxin and antitoxin, and in the related species *Bartonella henselae* (Supplementary Fig. 3).

The inhibitory action of VbhA on the VbhT toxin, and the genetic organization of the respective genes in an operon are reminiscent of toxin–antitoxin modules that are found in many bacterial genomes, often associated with mobile genetic elements¹². A comprehensive analysis of the upstream region of FIC-domain-encoding genes (PFAM pf02661) identified 158 bacterial *vbhA* homologues that probably function as antitoxins. Although the sequences are rather diverse, a central (S/T)XX(I/L)EG motif is conspicuous (Fig. 1b and Supplementary Fig. 4). The high-resolution (1.5 Å) crystal structure of VbhA in complex with the FIC domain of VbhT (VbhT(FIC)) (Supplementary Table 1) shows that VbhA is folded into three anti-parallel helices that tightly embrace VbhT(FIC) (Fig. 2a) with the N-terminal helix (α_{inh}), adopting a location that is analogous but distinct to that of the antitoxin Phd in its complex with Doc¹³ (Supplementary Fig. 5). Doc is a Fic protein with a degenerate, probably adenylation-incompetent FIC motif⁴ that may have adopted another toxic activity (Supplementary Information, section 1). The VbhA antitoxin motif locates to the C-terminal part of α_{inh} and is positioned close to the putative ATP-binding site¹⁰ at the N-cap of the helix that follows the active loop of VbhT(FIC). This suggests that the antitoxin competes with ATP binding. VbhA residues Ser 20 and Glu 24 of the inhibitory motif form a hydrogen bond and a salt bridge, respectively, with the conserved Arg147 of VbhT following the active loop.

Intriguingly, structural comparison with other bacterial Fic proteins of known fold (Fic proteins from *S. oneidensis* (SoFic)^{14,15} and from *N. meningitidis* (NmFic)¹⁴ (Fig. 2b, c), and from *Bacteroides thetaiotaomicron* (BtFic)¹⁴ and from *Helicobacter pylori* (HpFic)¹⁴ (Supplementary Fig. 6)) reveals that a structural equivalent of α_{inh} can be part of the FIC domain fold itself. Moreover, these proteins also show the SXXXE(G/N) inhibitory motifs that are, with respect to the FIC active site, arranged exactly as in the VbhA–VbhT(FIC) complex. Along the polypeptide chain, however, these α_{inh} occur at two distinct locations either in the N-terminal part (SoFic and BtFic) or at the C terminus (NmFic and HpFic). Thus, Fic proteins containing α_{inh} can be grouped into three classes (Fig. 2d) depending on whether α_{inh} is provided by an interacting antitoxin (class I) or whether it is part of the FIC fold as an N-terminal helix (class II) or a C-terminal helix (class III).

To investigate the distribution of class II and class III Fic proteins, we predicted the structures of all PFAM FIC domain entries by homology modelling (Supplementary Information, section 1). Including the class I proteins that are identified above, two-thirds of all Fic proteins were classified (Fig. 2e and Supplementary Table 2), with a strong dominance of class II, the class to which human HYPE belongs (Supplementary Tables 3 and 4). The proportion of classified Fic proteins increases to 90% when considering only adenylation-competent Fic proteins that are defined by compliance with the HXFX(D/E)GNRXXR motif (Supplementary Text). This suggests co-evolution of catalytic and inhibitory function. The inhibition motifs that are derived from Psi-Blast (class I) and structural predictions (classes II and III) are shown in Fig. 2f with the overall consensus being (S/T)XXXE(G/N). The strict conservation of the glutamate is striking and indicates that the observed ionic interaction with the second arginine of the conserved FIC motif (Figs 2a–c) is crucial for inhibition. Phylogenetic distribution of class I

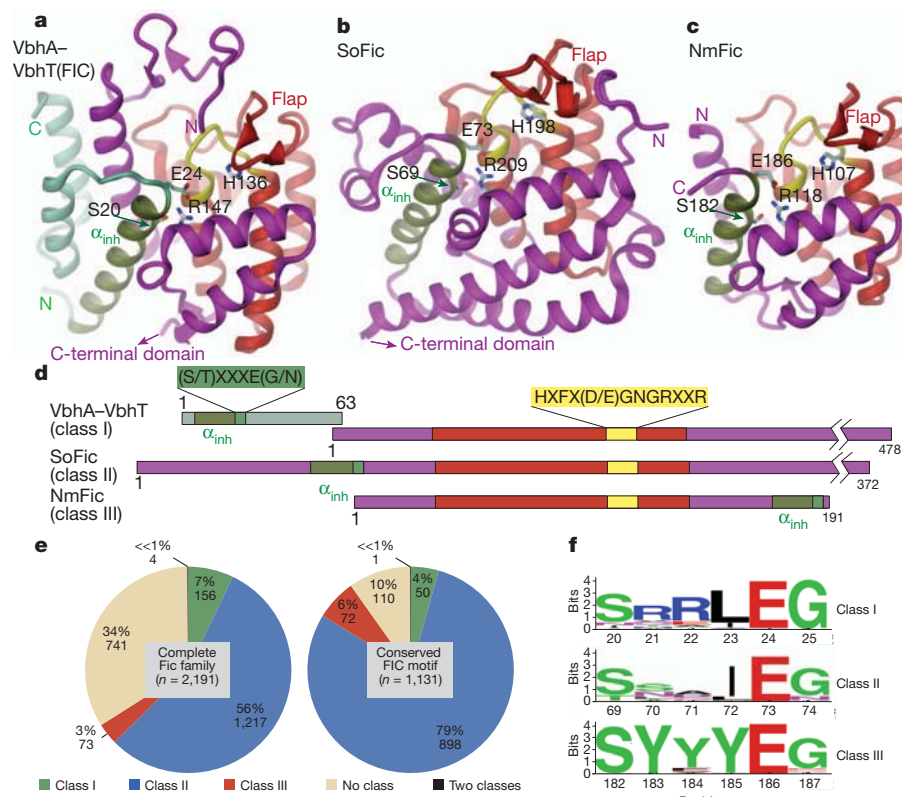


Figure 2 | Structures and classification of Fic proteins according to the position of the inhibitory motif along the polypeptide chain. Structures are shown in cartoon (FIC core as defined by PFAM, red; active site loop with histidine, yellow; inhibitory helix (α_{inh}) with SXXXE(G/N) motif, green) with important residues in full. **a**, Complex of VbhT(FIC) with antitoxin VbhA (green). **b**, SoFic (from *S. oneidensis*, PDB code 3EQX) with C-terminal domain omitted. **c**, NmFic (from *N. meningitidis*, PDB code 2G03). **d**, Linear

organization of motifs in the proteins presented in panels a–c. **e**, Distribution of the three Fic protein classes for the entire family in the PFAM database (left) and the subset of Fic proteins with the conserved FIC motif HXFX(D/E)GNRXXR that is likely to convey adenylation activity (right; see also Supplementary Information, section 1). **f**, Sequence profiles for the inhibition site of the three Fic protein classes.

and class III Fic proteins indicates that each is of monophyletic origin (Supplementary Fig. 7). Fic proteins with a degenerate FIC motif are dispersed over the tree, with the exception of the large cluster of Doc-like toxins. This suggests that there is recurrent degeneration of the conserved FIC motif with concomitant loss of adenylation activity. Consistent with this, deterioration of the FIC motif seems to correlate with the absence of a recognizable inhibitory motif (Supplementary Fig. 7). Fic proteins with a degenerate FIC motif may display catalytic activities different from adenylation, such as phosphocholination, as reported for the *Legionella pneumophila* effector AnkX¹⁶.

Owing to our discovery of the prevalence of the inhibitory motif in Fic proteins, we carried out a detailed analysis of its functional and structural role. For this, NmFic (class III, Fig. 2c) was chosen, as it is the smallest active Fic family protein with known crystallization condition (Supplementary Table 1). As reported before⁶, NmFic exhibits *in vitro* auto-adenylation activity (Fig. 3d). The acceptor site was traced to Y183 of α_{inh} by mass spectrometry (Supplementary Information, section 1, and Supplementary Fig. 8). On the basis of the location of Y183 relative to the active site, auto-adenylation is probably catalysed intermolecularly after partial unfolding or detachment of α_{inh} . Addition of *E. coli* lysate to NmFic did not reveal additional bands on the autoradiograph, and this indicated that there are no NmFic targets in *E. coli* or that the activity of NmFic is inhibited. The latter was shown to be correct as mutation of the inhibitory motif (S182A/E186A, NmFic(SE/AA)) resulted in transfer of radioactivity onto an ~80-kDa *E. coli* protein and enhanced auto-adenylation with an additional acceptor site (Y188; Fig. 3d and Supplementary Fig. 9). Deletion of the entire α_{inh} helix (NmFic($\Delta 8$)) led to similar target protein adenylation, proving that the activity resides in the FIC domain core. However, only weak auto-adenylation was apparent owing to the lack of the acceptor tyrosines in this deletion mutant (Fig. 3d and Supplementary Fig. 8c).

To investigate the inhibitory mechanism, crystals of NmFic proteins were soaked with the non-hydrolysable ATP analogue adenylyl

imidodiphosphate (AMPPNP) (Supplementary Table 1). The NmFic-AMPPNP structure revealed nucleotide binding but with the γ -phosphate disordered (Fig. 3a). Notably, the orientation of the α -phosphate seems to be non-productive, as the position that is in line with the scissile P α -O3 α bond is occluded by H107 and N113 (Supplementary Fig. 10a and Supplementary Movie). To reveal the situation in an inhibition-relieved mutant, the structure of NmFic(SE/AA) was determined to 3.0 Å (Supplementary Fig. 11). Electron density was lacking for α_{inh} , indicating disorder, whereas the nucleotide conformation was well defined. In the NmFic($\Delta 8$)-AMPPNP structure, the same nucleotide conformation was observed (Fig. 3b) and, owing to its high resolution (1.7 Å), the structural basis for the observed relief of inhibition in these mutants became evident. Whereas the adenosine moiety adopts the same position as in the wild-type, the γ -phosphate of the nucleotide is bound to R118, occupying the same position as the carboxylate of the inhibitory E186 in the wild type. As a consequence, the α -phosphate is found to be re-oriented, and the new orientation permits in line attack of a target side chain onto the α -phosphorus to accomplish AMP transfer (Fig. 3c, Supplementary Fig. 10 and Supplementary Movie).

The exact role of the inhibitory glutamate was investigated further by mutagenesis of Fic proteins from the three regulatory classes. In wild-type NmFic, C α and C β of the glutamate are close to the position that is attained by the γ -phosphate position in NmFic($\Delta 8$) (Fig. 3c). Still, an E to G single point mutant may provide sufficient space and main-chain flexibility to allow γ -phosphate binding. Indeed, similar to NmFic($\Delta 8$) and NmFic(SE/AA), the mutant NmFic(E186G) resulted in growth inhibition of *E. coli* (Supplementary Fig. 1b). Likewise, co-expression of VbhT(FIC) and VbhA(E24G), as representatives for class I, caused *E. coli* growth defects (Supplementary Fig. 1a). We also included SoFic, a bacterial class II protein, in this analysis. Consistent with the effects of E to G single point mutants in NmFic and VbhA, mutant SoFic(E73G) revealed a negative effect on *E. coli* growth

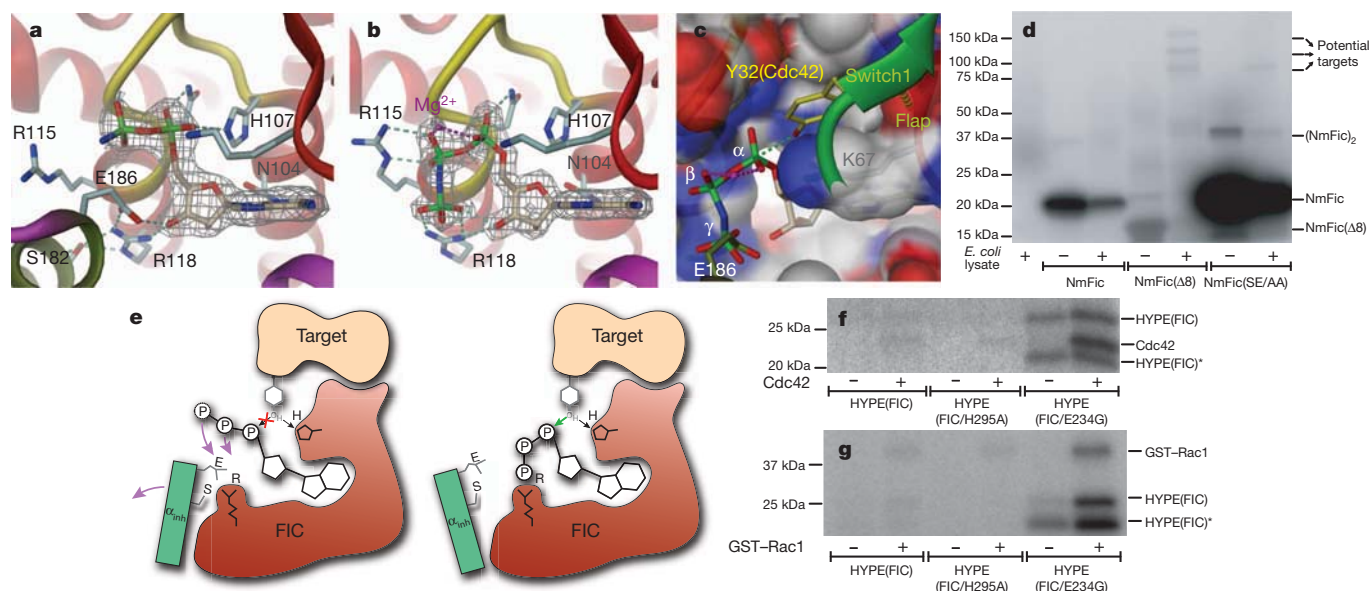


Figure 3 | Structure and function of wild-type and mutant NmFic reveals a general inhibition mechanism corroborated by HYPE protein analysis.

a, Active site of NmFic with bound ATP analogue AMPPNP. The γ -phosphate seems to be disordered and has not been modelled. **b**, Active site of NmFic($\Delta 8$) with bound AMPPNP and Mg^{2+} . The γ -phosphate occupies the position taken by E186 of the SXXXEG motif in the wild-type (as shown in **a**). Also shown are 2F σ - F σ maps that are contoured at 1.2 σ and cover the ligands. **c**, Surface representation of the active site of NmFic($\Delta 8$) with modifiable Y32 (yellow) of the Cdc42 switch1 loop (green) in a position that is obtained from a superposition of the active site loops of NmFic over the IbpA(FIC2)-Cdc42 complex⁵. **d**, Autoradiography of an SDS gel after incubation of wild-type and mutant NmFic with [α -³²P]ATP in the presence or absence of *E. coli* lysate. The

mutants, but not the wild-type, catalyse AMP transfer onto *E. coli* target proteins. **e**, Scheme of a general inhibition mechanism for Fic proteins. The α_{inh} helix (green) with the (S/T)XXE(G/N) motif prevents productive ATP binding. It is only after dissociation of the helix that the ATP γ -phosphate attains the position close to a conserved arginine (indicated by “R”) of the FIC motif. This is accompanied by reorientation of the α -phosphate to allow in-line attack of the target hydroxyl side chain after proton transfer to the active histidine as proposed before⁵. **f**, **g**, Autoradiography after incubation of HYPE(FIC) with α -³²P-ATP in the presence or absence of Cdc42 (**f**) or GST-tagged Rac1 (GST-Rac1) (**g**). HYPE(FIC/E234G) shows enhanced auto-adenylation and target adenylation. HYPE(FIC)* denotes a degradation product of HYPE(FIC).

(Supplementary Fig. 1c) and strongly enhanced auto-adenylation (Supplementary Fig. 12). A similar marked effect on auto-adenylation was observed after mutation of the corresponding residue in human HYPE (HYPE(FIC/E234G)), another class II protein (Fig. 3f, g). It is known that HYPE catalyses Cdc42 and Rac1 adenylation^{1,4}. The rather low adenylation activity of wild-type HYPE on these substrates is markedly enhanced in the HYPE(FIC/E234G) mutant (Fig. 3f, g), demonstrating that the relief of inhibition by α_{inh} enhances not only auto-adenylation but also AMP transfer onto bona fide protein targets.

From this study a general mechanism for the inhibition of the FIC-domain-mediated adenylation has emerged that invokes a glutamate finger from α_{inh} to inter- or intramolecularly block part of the ATP binding site (Fig. 3e). Dissociation of the toxin-antitoxin complex (class I) or intramolecular loosening of the contact between α_{inh} and the FIC domain active site (classes II and III) allows ordered binding of the entire ATP moiety with the α -phosphate in an orientation that is productive for accepting an incoming target hydroxyl side chain.

Class I proteins might exert functions similar to the classical bacterial toxin-antitoxin modules¹², whereas class II and III Fic proteins seem to regulate intrinsic cellular functions that are related to physiological adaptation and cell homeostasis. Conservation of class II Fic proteins in all three kingdoms of life (Supplementary Table 2) emphasizes the important role of the regulatory mechanisms described here. How the adenylation activity is activated by weakening the interaction of α_{inh} with the FIC active site in class II and class III Fic proteins is one of many important questions for future research. We also anticipate our study to be a starting point for rational approaches to modulate the adenylation activities of Fic proteins—approaches that should aid in elucidating the diverse biological functions of these widespread signalling proteins.

METHODS SUMMARY

Toxicity experiments were performed with *E. coli* strain MG1655, which encodes an IPTG (isopropyl- β -D-thiogalactoside)-inducible T7 polymerase (strain AB472). Protein expression was controlled by the addition of either 100 μ M IPTG (induction) or 1% glucose (repression). A PSI-BLAST search for homologues with VbhA of *B. schoenbuchensis* was conducted to identify Fic proteins belonging to class I. Class II and class III proteins were classified by structure predictions using the program HHpred¹⁷. We analysed all 2,189 proteins of the FIC PFAM family (pf02661, release 24). Adenylation assays were carried out using bacterial crude cell lysates for VbhT constructs or purified proteins for NmFic, SoFic and HYPE constructs. For structure determination, VbhA and VbhT(FIC) were co-expressed in the BL21(DE3) strain of *E. coli*, and NmFic, SoFic(Δ 8) and NmFic(SE/AA) in the BL21-AI strain of *E. coli*. VbhA-VbhT(FIC) and NmFic were purified by affinity chromatography followed by size exclusion chromatography. An additional anion exchange chromatography step was performed for NmFic(Δ 8) and NmFic(SE/AA). Diffraction data were collected at beamline X06SA of the Swiss Light Source. For NmFic(Δ 8) and NmFic(SE/AA), we obtained phases by molecular replacement using the NmFic structure (PDB code 2G03) as a search model. The VbhA-VbhT(FIC) complex was solved by molecular replacement using a fragment of BepA (PDB code 2JK8).

Full Methods and any associated references are available in the online version of the paper at www.nature.com/nature.

Received 4 July; accepted 24 November 2011.

Published online 22 January 2012.

1. Worby, C. A. *et al.* The fic domain: regulation of cell signaling by adenylation. *Mol. Cell* **34**, 93–103 (2009).

2. Yarbrough, M. L. *et al.* AMPylation of Rho GTPases by *Vibrio* VopS disrupts effector binding and downstream signaling. *Science* **323**, 269–272 (2009).
3. Roy, C. R. & Mukherjee, S. Bacterial FIC proteins AMP up infection. *Sci. Signal.* **2**, pe14 (2009).
4. Mattoo, S. *et al.* Comparative analysis of *Histophilus somni* immunoglobulin-binding protein A (IbpA) with other Fic domain-containing enzymes reveals differences in substrate and nucleotide specificities. *J. Biol. Chem.* **286**, 32834–32842 (2011).
5. Luong, P. *et al.* Kinetic and structural insights into the mechanism of AMPylation by VopS Fic domain. *J. Biol. Chem.* **285**, 20155–20163 (2010).
6. Xiao, J., Worby, C. A., Mattoo, S., Sankaran, B. & Dixon, J. E. Structural basis of Fic-mediated adenylation. *Nature Struct. Mol. Biol.* **17**, 1004–1010 (2010).
7. Dehio, C. *et al.* *Bartonella schoenbuchii* sp. nov., isolated from the blood of wild roe deer. *Int. J. Syst. Evol. Microbiol.* **51**, 1557–1565 (2001).
8. Engel, P. *et al.* Parallel evolution of a type IV secretion system in radiating lineages of the host-restricted bacterial pathogen *Bartonella*. *PLoS Genet.* **7**, e1001296 (2011).
9. Schulein, R. *et al.* A bipartite signal mediates the transfer of type IV secretion substrates of *Bartonella henselae* into human cells. *Proc. Natl Acad. Sci. USA* **102**, 856–861 (2005).
10. Palanivelu, D. V. *et al.* Fic domain-catalyzed adenylation: insight provided by the structural analysis of the type IV secretion system effector BepA. *Protein Sci.* **20**, 492–499 (2011).
11. Utsumi, R., Nakamoto, Y., Kawamukai, M., Himeno, M. & Komano, T. Involvement of cyclic AMP and its receptor protein in filamentation of an *Escherichia coli* fic mutant. *J. Bacteriol.* **151**, 807–812 (1982).
12. Engelberg-Kulka, H., Amitai, S., Kolodkin-Gal, I. & Hazan, R. Bacterial programmed cell death and multicellular behavior in bacteria. *PLoS Genet.* **2**, e135 (2006).
13. Garcia-Pino, A. *et al.* Doc of prophage P1 is inhibited by its antitoxin partner Phd through fold complementation. *J. Biol. Chem.* **283**, 30821–30827 (2008).
14. Kinch, L. N., Yarbrough, M. L., Orth, K. & Grishin, N. V. Fido, a novel AMPylation domain common to Fic, Doc, and AvrB. *PLoS ONE* **4**, e5818 (2009).
15. Das, D. *et al.* Crystal structure of the Fic (Filamentation induced by cAMP) family protein SO4266 (gjl24375750) from *Shewanella oneidensis* MR-1 at 1.6 Å resolution. *Proteins* **75**, 264–271 (2009).
16. Mukherjee, S. *et al.* Modulation of Rab GTPase function by a protein phosphocholine transferase. *Nature* **477**, 103–106 (2011).
17. Söding, J., Biegert, A. & Lupas, A. N. The HHpred interactive server for protein homology detection and structure prediction. *Nucleic Acids Res.* **33**, W244–W248 (2005).

Supplementary Information is linked to the online version of the paper at www.nature.com/nature.

Acknowledgements We thank T. Glatter for mass spectrometry analysis of samples at the Core Proteomics facility. We thank the staff of beamline X06SA of the Swiss Light Source for assistance with data acquisition. We are grateful to G. Pluschke for providing the genomic DNA of *Neisseria meningitidis*, the ASU Biodesign Institute for providing the plasmid enclosing the *Shewanella oneidensis* Fic protein and S. Mattoo and J. Dixon for providing the pET-GSTX plasmids enclosing HYPE and HYPE(H295A). We also thank D. Bumann and A. Boehm for providing plasmid pC10E and *E. coli* strain AB472, respectively. This work was supported by grants 3100-061777 and 3100-138414 from the Swiss National Science Foundation (to C.D. and T.S., respectively), and grant 51RT O_126008 (InfecX) in the frame of the SystemsX.ch Swiss Initiative for Systems Biology (to C.D.).

Author Contributions P.E., F.V.S. and A.H. cloned recombinant plasmids. P.E. discovered and physiologically characterized VbhT-VbhA as a toxin-antitoxin module and carried out the bioinformatic analysis. A.G. expressed, purified and crystallized VbhA-VbhT(FIC), NmFic(SE/AA) and NmFic(Δ 8), and determined their structures. F.V.S. expressed, purified and crystallized NmFic with AMPPNP and determined the structure. A.G. and A.H. performed the adenylation assays. A.H. carried out the growth curve experiments. A.S. conducted the mass spectrometry analysis. All authors contributed to experimental design and data analysis. The manuscript was written by P.E., A.G., T.S. and C.D.

Author Information The atomic coordinates of VbhA-VbhT(FIC) and the complexes of NmFic, NmFic(SE/AA) and NmFic(Δ 8) with AMPPNP have been deposited in the Protein Data Bank under accession codes 3SHG, 3S6A, 3SN9 and 3SE5, respectively. Reprints and permissions information is available at www.nature.com/reprints. The authors declare no competing financial interests. Readers are welcome to comment on the online version of this article at www.nature.com/nature. Correspondence and requests for materials should be addressed to C.D. (Christoph.Dehio@unibas.ch) or T.S. (Tilman.Schirmer@unibas.ch).

METHODS

Identification of VbhA homologues. VbhA of *B. schoenbuchensis* was queried against a database composed of translated open reading frames (>10 amino acids) identified in the 500-bp upstream region of all *fic* loci (PFAM release 24, 2,189 proteins). Nine rounds of Psi-Blast were performed and hits with an *E*-value <1 manually validated.

***E. coli* toxicity tests and cell filamentation.** *E. coli* AB472, a derivative of MG1655, was transformed with VbhT-expressing plasmids and always handled in LB containing 1% glucose. A single colony was picked, resuspended in 20 µl of LB and plated on LB plates containing 100 µM IPTG (induction) or 1% glucose (repression). Plates were incubated overnight at 37 °C. Growth curves were acquired by measuring optical density of liquid cultures in LB containing 100 µM IPTG that had been inoculated from overnight cultures of single colonies and were grown at 30 °C with continuous shaking. Cell filamentation was visualized by co-transformation of plasmid pC10E that constitutively expresses GFP and examined using fluorescence microscopy.

Conjugation experiments for VbhT toxicity tests in *Bartonella*. Plasmids were introduced into *Bartonella* strains by conjugation from *E. coli* using three-parental mating. *Bartonella* strains were grown for 36–48 h at 35 °C with 5% CO₂ on Columbia base agar plates supplemented with 5% defibrinated sheep blood and 100 µg ml⁻¹ streptomycin. *E. coli* β2150 that harbours helper plasmid pRK2013, and *E. coli* β2150 that contains the VbhT-expressing plasmid were grown overnight at 37 °C in LB supplemented with 50 µg ml⁻¹ kanamycin or 30 µg ml⁻¹ chloramphenicol, respectively, and both media were also supplemented with diamminopimelic acid (DAP) and 1% glucose. After 16 h of incubation, *E. coli* strains were diluted 1:50 in fresh LB medium and grown to a optical density (OD) at 595 nm (OD_{595nm}) of 0.4–0.8. Subsequently, each *E. coli* strain was diluted to OD_{595nm} of 0.25, washed once and resuspended in supplemented M199 medium (containing 10% FCS and 1% glucose). *Bartonella* strains were collected in 1 ml and resuspended in 60 µl of M199 (OD_{595nm} = 1). Each *Bartonella* suspension was mixed with 20 µl of *E. coli* β2150 that harbours pRK2013 and 20 µl of *E. coli* β2150 that harbours the VbhT-expressing plasmid. The conjugation mix was distributed on a conjugation filter on a columbia blood agar (CBA) plate supplemented with 150 µl DAP and 150 µl 1% glucose. After 6 h of incubation under *Bartonella* growth conditions as described before, the bacteria were washed off the filter with 1 ml supplemented M199. Dilutions of bacterial suspensions were plated on lysogeny broth agar (LA) supplemented with DAP, 1% glucose and 30 µg ml⁻¹ chloramphenicol for selecting donors, on CBA supplemented with 1.2 µg ml⁻¹ chloramphenicol for selecting transconjugants, and on CBA supplemented with 100 µg ml⁻¹ streptomycin for selecting recipients. Agar plates were incubated under *Bartonella* growth conditions and colony-forming units were counted after 1 day for donors and after 7 days for recipients and transconjugants.

In vitro adenylation assay. Adenylation activity of VbhT was assessed in an assay using lysates of ectopically expressing *E. coli*. Bacterial pellets were resuspended in reaction buffer (50 mM Tris-HCl pH 8.0, 150 mM NaCl, 0.1 mM EGTA, 15 mM MgCl₂, 140 µg ml⁻¹ RNase A and protease inhibitor cocktail (Roche)) and lysed by sonication. After clearing lysates by centrifugation, supernatants were used for experimentation or stored at -20 °C.

Adenylation reactions were prepared by supplementing 15 µl supernatant from expression cultures with 10 µCi [α -³²P]ATP (Hartmann Analytic) and 25 µl blank *E. coli* supernatant. Adenylation activity of NmFic and SoFic constructs was assessed by incubating 60 µg purified protein with 10 µCi [α -³²P]ATP (Hartmann Analytic) and 25 µl blank *E. coli* supernatant. Reactions were incubated for 1 h at 30 °C, resolved by SDS-PAGE, and adenylation was probed by autoradiography. For HYPE(FIC) assays, 15 ng of pure protein was incubated with 1.6 µg of purified GTPases.

Protein expression and purification. pFVS0011 vector (encoding VbhA and VbhT(FIC)) was transformed into *E. coli* BL21 (DE3). *E. coli* cultures were grown at 37 °C in LB medium supplemented with 50 µg ml⁻¹ of kanamycin to an OD_{595nm} of 0.6 before induction with 0.3 mM IPTG for 16 h at 23 °C. Vectors pFVS0015 (carrying the *NmFic* gene), pFVS0016 (encoding NmFic(Δ8)), pFVS0037 (encoding NmFic(SE/AA)) were transformed into BL21-AI cells. Cells were incubated overnight in 750 ml LB medium that was supplemented with 50 µg ml⁻¹ kanamycin and 1% glucose at 23 °C at 200 r.p.m. until OD_{595nm} of 2 was reached. Bacterial pellets were resuspended in terrific broth medium containing 50 µg ml⁻¹ kanamycin to obtain an OD_{595nm} of approximately 1. Protein expression was induced at 23 °C with 0.1% arabinose and 0.5 mM IPTG for 23 h at 200 r.p.m. Plasmids harbouring HYPE(FIC) and SoFic constructs were transformed in *E. coli* Rosetta (DE3) cells and BL21-AI cells, respectively. The proteins were expressed as described for NmFic.

Cells containing overexpressed VbhA-VbhT(FIC) and NmFic were resuspended in lysis buffer containing 20 mM Tris (pH 7.5), 250 mM NaCl and 25 mM imidazole and disrupted using French press. Cell debris was pelleted by

ultracentrifugation and the supernatant was applied to a His-Trap column (GE Healthcare). The stable complex was eluted with a gradient of elution buffer containing 20 mM Tris (pH 7.5), 250 mM NaCl and 500 mM imidazole. The protein was then concentrated and injected on a Superdex 75 16/60 gel filtration column (GE Healthcare) equilibrated with 10 mM Tris (pH 7.5) and 100 mM NaCl. The pure proteins were concentrated to 6 mg ml⁻¹ for VbhA-VbhT(FIC) and 53 mg ml⁻¹ for NmFic.

The same purification protocol was used for NmFic(Δ8) and NmFic (SE/AA), but with an additional intermediate purification step. After affinity purification, the proteins were adjusted to 20 mM Tris (pH 8.5), 25 mM NaCl, applied to a Resource-Q anion exchange column (Amersham Biosciences) and eluted with a linear gradient of NaCl. Peak fractions were concentrated and further purified by gel filtration chromatography. Purified proteins in 10 mM Tris (pH 7.8), 100 mM NaCl were concentrated to 30 mg ml⁻¹ for NmFic(Δ8) and 51 mg ml⁻¹ for NmFic(SE/AA). SoFic and SoFic(E73G) were purified as described previously¹⁵. HYPE(FIC), HYPE(FIC/H295A) and HYPE(FIC/E234G) were purified in the same way as NmFic. GST-tagged Cdc42 and Rac1 were expressed and purified as described previously^{18,19}.

Crystallization. All crystals were obtained at 20 °C (except for NmFic crystals, which were obtained at 4 °C) using the hanging-drop vapour diffusion method after mixing 1 µl protein solution with 1 µl reservoir solution. VbhA-VbhT(FIC) and NmFic(SE/AA) crystallized in 23% (w/v) PEG 3350 and 0.2 M di-ammonium tartrate, and were cryoprotected with 25% (w/v) PEG 3350, 0.2 M di-ammonium tartrate and 10% glycerol. NmFic crystallized in 5% 2-propanol, 0.1 M MES pH 6.0 and 0.1 M Ca-acetate, and was transferred into 8% 2-propanol, 0.1 M MES pH 6.0, 0.1 M Mg-acetate and 15% glycerol, then into 30% glycerol for cryoprotection. NmFic(Δ8) crystallized with 44% (v/v) PEG 600, 0.1 M Na-citrate pH 5.6. No cryoprotection was needed for data collection. In each case, the substrate analogue complex was produced by crystal soaking for 2 h with 10 mM AMPPNP, 10 mM MgCl₂.

Structure determination. Statistics of data collection and refinement are given in Supplementary Table 1. Diffraction data were collected at beamline X06SA (PXIII) of the Swiss Light Source (λ = 1.0 Å) at 100 K on a MAR CCD detector, processed using MOSFLM²⁰, and scaled with SCALA²¹. The structures were determined by molecular replacement (PHASER²²) using a BepA fragment (PDB code 2JK8¹⁰, residues 30–194) or the uncomplexed NmFic structure (PDB code 2G03, unpublished, Midwest Center for Structural Genomics) as models for structure solution of VbhA-VbhT(FIC) and the different NmFic proteins, respectively. A structure solution of wild-type and mutant NmFic in complex with AMPPNP was straightforward, whereas a weak solution (RFZ = 5.1, TFZ = 3.6) with poor phasing power was obtained for VbhA-VbhT(FIC). The partial model lacking VbhA was refined by rigid-body refinement using REFMAC5 (ref. 23) with three bodies to an *R*_{free} of 52%. Model extension using the module AutoBuild of the PHENIX package²⁴ yielded an almost complete model (*R*/*R*_{free} = 30.8%/35.2%). The remainder of the molecule was traced manually with COOT²⁵ and then by full refinement using PHENIX²⁴. The Ramachandran plot showed that more than 99% of the residues are in favoured regions of the four structures. The figures were generated with Dino (<http://www.dino3d.org>).

Prediction of inhibition motif in Fic proteins. All Fic proteins (PFAM release 24, 2,189 proteins) were subjected to a profile-to-profile comparison with sequences from the PDB using HHpred¹⁷. HHpred builds an alignment of homologues for each query sequence by using iterations of PSI-BLAST searches against the non-redundant database. Secondary structures are then predicted on the PSI-BLAST alignment using PSIPRED²⁶. On the basis of this data, a profile Hidden Markov Model (HMM) is generated. Each query profile is compared with the pre-computed HMMs of the proteins in the PDB to identify structural homologues. In terms of query profiles, the PDB profiles include secondary structure information derived from their three-dimensional structure. We analysed the pairwise profile alignments of each Fic protein with the eight different Fic family members deposited in the PDB. A Fic protein was predicted to belong to class II or class III if the templates' inhibitory motifs were aligned to a corresponding query sequence in the profile alignments (see Supplementary Information, section 1).

Phylogenetic analysis of Fic proteins. Phylogenetic trees of the Fic family were inferred with FastTree 2 (ref. 27) and RAXML 7.0.4 (ref. 28). Trees were built on the amino acid alignment provided by the PFAM database. Unaligned overhanging ends were trimmed off and identical sequences were reduced to one representative. We used local support values based on the Shimodaira-Hasegawa test to estimate the reliability of the tree inferred with FastTree2. The RAXML tree was inferred using the PROTMIXWAGF model and 25 rate categories.

Liquid chromatography-mass spectrometry analysis. 2.5 µM of purified NmFic, NmFic(Δ8) or NmFic(SE/AA) were incubated in reaction buffer (10 mM Tris, pH 8, 100 mM NaCl) in the presence or absence of 50 µM ATP and 50 µM MgCl₂ for 1 h. Proteins were reduced in 5 mM TCEP, alkylated in

10 mM iodoacetamid and digested with sequencing grade trypsin (Promega). The generated peptides were purified with C18 Microspin columns (Harvard Apparatus) and analysed using liquid chromatography–mass spectrometry (LC–MS) or MS on an easy nano-LC system coupled to an LTQ–Orbitrap–Velos mass spectrometer (both from Thermo-Fisher Scientific), as recently described²⁹ using a linear gradient from 95% solvent A (0.15% formic acid, 2% acetonitrile) and 5% solvent B (98% acetonitrile, 0.15% formic acid) to 35% solvent B over 40 min. The data acquisition mode was set to obtain one high-resolution MS scan in the Fourier Transform (FT) part of the mass spectrometer at a resolution of 60,000 (full width at half maximum) and MS–MS scans in the linear ion trap of the 20 most intense ions. The resulting MS2 scans were searched against a *N. meningitidis* protein database containing the target protein sequence, including NmFic and NmFic(SE/AA) sequences, that was obtained from EBI (<http://www.ebi.ac.uk>) using the SEQUEST search algorithm provided in the Proteome Discoverer software package (Thermo-Fisher Scientific). *In silico* trypsin digestion was performed after lysine and arginine (unless followed by proline), with a tolerance of two missed cleavages in fully tryptic peptides. Database search parameters were set to allow phosphoadenosine modification (+329.05252 Da) of threonine and tyrosine residues as variable modification and carboxyamidomethylation (+57.021464 Da) of cysteine residues as fixed modification. The fragment mass tolerance was set to 0.8 Da and the precursor mass tolerance to 15 p.p.m.

Strain construction. For toxicity experiments, the *vbbT* wild-type gene (FN645515) from *B. schoenbuchensis* R1 was cloned into pRSF-Duet1 (pPE0017, His₆-tagged *vbbT*). *VbbT*(H136A) (pPE0034) was constructed by introducing a two-base-pair point mutation in the FIC motif of *vbbT* of pPE0017, as described elsewhere³⁰. Plasmid co-expressing *VbbT* and *VbhA* (*VbbT/VbhA*) was constructed by cloning *vbhA* (FN645515) amplified from *B. schoenbuchensis* R1 into pRSF-Duet1 (pPE0020, HA-tagged *vbhA*). *vbbT* was then cloned into pPE0020, resulting in pPE0021. To construct *VbbT*-expressing plasmids for *Bartonella*, *vbbT* from *B. schoenbuchensis* R1 was cloned into vector pMMB206 (ref. 31) (pVbbT, HA-tagged *vbbT*). pVbbT(H136A) was constructed from pVbbT as described before.

The in-frame deletion of the complete *vbhA/vbbT* operon in *B. schoenbuchensis* (*Bsch ΔvbbA/vbbT*) was generated as described previously by a two-step gene replacement procedure⁹. The mutagenesis vector pPE3005 was constructed by ligating a cassette with the flanking regions of the in-frame deletion into pTR1000⁹.

For protein purification, the full-length *vbhA* gene and part of the *vbbT* gene encoding the FIC domain (*vbbT*(FIC)), amino acid residues 1–198, His₆-tagged) were amplified from plasmid pPE0021 and cloned into the pRSF-Duet1 vector (pFVS0011). *VbhA*(E24G)/*VbbT*(FIC) expression plasmid (pFVS0065) was generated by introducing a two-base-pair mutation in pFVS0011. The *NmFic* gene was amplified with an N-terminal His₆-tag from *N. meningitidis* from coding region of amino acid residues 11–191 and from coding region of amino acid residues 11–167 to generate plasmids expressing NmFic (pFVS0015) and NmFic(Δ8) (pFVS0016), respectively. The S182A/E186A double mutant construct (NmFic(SE/AA)) was generated by introducing two subsequent point mutations in pFVS0015. The E186G mutant construct (NmFic(E186G)) was

generated by the same approach. The *SoFic* gene was amplified from plasmid (ASU biodesign institute, Clone ID SoCD00104192) and cloned with an N-terminal His₆-tag into pRSF-Duet1 (pFVS0040). The *SoFic*(E73G) plasmid (pFVS0058) was generated by introducing a two-base-pair point mutation in pFVS0040. GST–HYPE(E234G) (pFVS0064) was generated by introducing point mutations in the plasmid containing GST–HYPE. From these plasmids, shorter constructs (HYPE(FIC), HYPE(FIC/E234G) and HYPE(FIC/H295A)) only carrying the FIC domain of HYPE (from amino acids 187 to 437) were generated. For the expression of human Cdc42 and Rac1, the *Cdc42*–Q61L and *Rac1*–Q61L coding sequences were amplified from plasmid pRK5myc L61 Cdc42³² and pRK5FLAG L61 Rac1 (ref. 32) and cloned into pGex6p1 with an N-terminal GST-tag, resulting in pAH088 and pAH060, respectively. The wild-type variants of Cdc42 and Rac1 were generated from the mutant constructs through polymerase chain reaction (PCR)-based site-directed mutagenesis³⁰ (resulting in pAH059 and pAH071). All primers and the resulting vectors are summarized in Supplementary Tables 5 and 6.

18. Self, A. J. & Hall, A. Purification of recombinant Rho/Rac/G25K from *Escherichia coli*. *Methods Enzymol.* **256**, 3–10 (1995).
19. Smith, S. J. & Rittinger, K. Preparation of GTPases for structural and biophysical analysis. *Methods Mol. Biol.* **189**, 13–24 (2002).
20. Leslie, A. G. The integration of macromolecular diffraction data. *Acta Crystallogr. D* **62**, 48–57 (2006).
21. Collaborative Computational Project, Number 4. The CCP4 suite: programs for protein crystallography. *Acta Crystallogr. D* **50**, 760–763 (1994).
22. McCoy, A. J. *et al.* Phaser crystallographic software. *J. Appl. Crystallogr.* **40**, 658–674 (2007).
23. Murshudov, G. N., Vagin, A. A. & Dodson, E. J. Refinement of macromolecular structures by the maximum-likelihood method. *Acta Crystallogr. D* **53**, 240–255 (1997).
24. Adams, P. D. *et al.* PHENIX: a comprehensive Python-based system for macromolecular structure solution. *Acta Crystallogr. D* **66**, 213–221 (2010).
25. Emsley, P. & Cowtan, K. Coot: model-building tools for molecular graphics. *Acta Crystallogr. D* **60**, 2126–2132 (2004).
26. Jones, D. T. Protein secondary structure prediction based on position-specific scoring matrices. *J. Mol. Biol.* **292**, 195–202 (1999).
27. Price, M. N., Dehal, P. S. & Arkin, A. P. FastTree 2—approximately maximum-likelihood trees for large alignments. *PLoS ONE* **5**, e9490 (2010).
28. Stamatakis, A. RAxML-VI-HPC: maximum likelihood-based phylogenetic analyses with thousands of taxa and mixed models. *Bioinformatics* **22**, 2688–2690 (2006).
29. Schmidt, A. *et al.* Absolute quantification of microbial proteomes at different states by directed mass spectrometry. *Mol. Syst. Biol.* **7**, 510 (2011).
30. Zheng, L., Baumann, U. & Reymond, J. L. An efficient one-step site-directed and site-saturation mutagenesis protocol. *Nucleic Acids Res.* **32**, e115 (2004).
31. Dehio, C. & Meyer, M. Maintenance of broad-host-range incompatibility group P and group Q plasmids and transposition of Tn5 in *Bartonella henselae* following conjugal plasmid transfer from *Escherichia coli*. *J. Bacteriol.* **179**, 538–540 (1997).
32. Rhomberg, T. A., Truttmann, M. C., Guye, P., Ellner, Y. & Dehio, C. A translocated protein of *Bartonella henselae* interferes with endocytic uptake of individual bacteria and triggers uptake of large bacterial aggregates via the invasome. *Cell. Microbiol.* **11**, 927–945 (2009).

Cysteinyl leukotriene type I receptor desensitization sustains Ca^{2+} -dependent gene expression

Siaw-Wei Ng¹, Daniel Bakowski¹, Charmaine Nelson¹, Ravi Mehta¹, Robert Almeyda², Grant Bates² & Anant B. Parekh¹

Receptor desensitization is a universal mechanism to turn off a biological response; in this process, the ability of a physiological trigger to activate a cell is lost despite the continued presence of the stimulus. Receptor desensitization of G-protein-coupled receptors involves uncoupling of the receptor from its G-protein or second-messenger pathway followed by receptor internalization¹. G-protein-coupled cysteinyl leukotriene type I (CysLT1) receptors regulate immune-cell function and CysLT1 receptors are an established therapeutic target for allergies, including asthma². Desensitization of CysLT1 receptors arises predominantly from protein-kinase-C-dependent phosphorylation of three serine residues in the receptor carboxy terminus³. Physiological concentrations of the receptor agonist leukotriene C_4 (LTC_4) evoke repetitive cytoplasmic Ca^{2+} oscillations, reflecting regenerative Ca^{2+} release from stores, which is sustained by Ca^{2+} entry through store-operated calcium-release-activated calcium (CRAC) channels⁴. CRAC channels are tightly linked to expression of the transcription factor *c-fos*⁵, a regulator of numerous genes important to cell growth and development⁶. Here we show that abolishing leukotriene receptor desensitization suppresses agonist-driven gene expression in a rat cell line. Mechanistically, stimulation of non-desensitizing receptors evoked prolonged inositol-trisphosphate-mediated Ca^{2+} release, which led to accelerated Ca^{2+} -dependent slow inactivation of CRAC channels and a subsequent loss of excitation–transcription coupling. Hence, rather than serving to turn off a biological response, reversible desensitization of a Ca^{2+} mobilizing receptor acts as an ‘on’ switch, sustaining long-term signalling in the immune system.

The paradox of receptor desensitization is how long-term responses can be evoked if the receptor is inactivated. This is a particularly acute problem in immune cells, in which cell differentiation and clonal selection develop over hours in the continued presence of external cues.

Stimulation of rat basophilic leukaemia (RBL-1) cells with LTC_4 , acting exclusively on CysLT1 receptors^{7,8} (Supplementary Fig. 1), led to cytoplasmic Ca^{2+} signals (Fig. 1a) followed by robust expression of *c-fos* at both messenger RNA (Fig. 1b, c)⁴ and protein levels (Fig. 1d, e). Maximal activation of CRAC channels with thapsigargin led to a similar increase in *c-fos* expression (Fig. 1b–e). Both LTC_4 and thapsigargin induce *c-fos* expression through the build-up of Ca^{2+} microdomains near open store-operated CRAC channels^{4,5}. Thapsigargin led to a larger, more sustained Ca^{2+} signal than LTC_4 (Fig. 1a)^{4,5} and the rate of Ca^{2+} entry through CRAC channels was approximately twofold more for thapsigargin than LTC_4 (Fig. 1f), consistent with patch-clamp recordings⁷. The similar increase in Ca^{2+} -dependent *c-fos* expression to LTC_4 and thapsigargin was therefore surprising, given the significant difference in CRAC channel activation.

We considered various explanations for why CysLT1 receptor activation and thapsigargin evoked similar *c-fos* levels despite marked differences in the extent of CRAC channel activation. These included: (1) CysLT1 receptors tapped into a different signalling mechanism linking CRAC channel microdomains to *c-fos* expression; (2) local Ca^{2+} entry through CRAC channels was larger after receptor activation

because LTC_4 hyperpolarized the membrane potential; and (3) cytoplasmic Ca^{2+} and protein kinase C (PKC) interacted synergistically to drive gene expression in response to CysLT1 receptor activation. Evidence against these possibilities is presented in Supplementary Figs 2–4. Instead, gene expression showed high sensitivity to Ca^{2+} entry, enabling CysLT1 receptor activation to couple effectively to *c-fos* transcription (Supplementary Fig. 5), as well as rapidly and high gain. Combined, this ensures efficient gene expression to bursts of CRAC channel activity after physiological levels of receptor stimulation.

Experiments described in Fig. 1g and h revealed an important role for PKC in receptor-dependent gene expression. The structurally distinct PKC blockers G06983 and calphostin C abolished *c-fos* expression (Fig. 1g, h). PKC block had a marked effect on the Ca^{2+} signal evoked by agonist. Whereas cytoplasmic Ca^{2+} oscillations were routinely observed with LTC_4 (Fig. 1i), the response was converted into a large, single, slowly decaying Ca^{2+} spike after PKC inhibition (Fig. 1i, j). Acute stimulation with PMA in the absence of LTC_4 failed to induce significant *c-fos* expression (data not shown)⁹, demonstrating that PKC activity per se was not sufficient to induce *c-fos* expression in these cells. The PKC inhibitors had no effect on thapsigargin-evoked *c-fos* expression (Fig. 1k) or cytoplasmic Ca^{2+} signals (Fig. 1l). Thapsigargin (2 μM) activates CRAC channels maximally (Supplementary Fig. 5) and, by blocking SERCA pumps (which can be located near CRAC channels¹⁰), reduces the decay of Ca^{2+} gradients radiating from the plasma membrane. It is possible that other non-receptor-dependent stimuli, which raise local Ca^{2+} levels less effectively than 2 μM thapsigargin, might activate *c-fos* in a manner dependent on basal PKC activity, but this activity would be unusual in that it is not stimulated acutely by PMA in the presence of sub-maximal CRAC channel activation (Supplementary Fig. 4).

In RBL cells, exposure to the phorbol ester PMA for several hours downregulates several PKC isozymes¹¹. Using this protocol, we found that *c-fos* expression was substantially reduced in response to CysLT1 receptor stimulation (Fig. 1m), whereas no significant reduction was seen when thapsigargin was used instead (Fig. 1m) or when inactive 4 α -phorbol replaced PMA (data not shown). Similar to PKC blockers, the Ca^{2+} signal to LTC_4 was prolonged after PKC downregulation (Fig. 1n). This prolonged Ca^{2+} signal did not reflect a change in Ca^{2+} clearance mechanisms (Supplementary Fig. 6); instead, it is characteristic of loss of receptor desensitization, particularly for CysLT1 receptors, in which desensitization is mediated predominantly by PKC³ and prevention of desensitization leads to broader Ca^{2+} signals¹². Inhibition of CysLT1 receptor desensitization is predicted to lead to greater inositol trisphosphate (InsP_3) production and hence more extensive Ca^{2+} store emptying. Several findings are consistent with this. First, Ca^{2+} release to LTC_4 lasted approximately five times longer when PKC was blocked than in control cells (Fig. 2a, expanded in inset). Second, the amount of Ca^{2+} remaining within the stores, measured as the ionomycin-sensitive Ca^{2+} response¹³, was substantially less after activation of CysLT1 receptors in the presence of PKC block than in control cells (Fig. 2a). Third, InsP_3 production, measured using the green fluorescent protein–pleckstrin homology

¹Department of Physiology, Anatomy and Genetics, University of Oxford, Parks Road, Oxford OX1 3PT, UK. ²Department of Ear-Nose-Throat Surgery, John Radcliffe Hospital, Oxford OX3 9DH, UK.

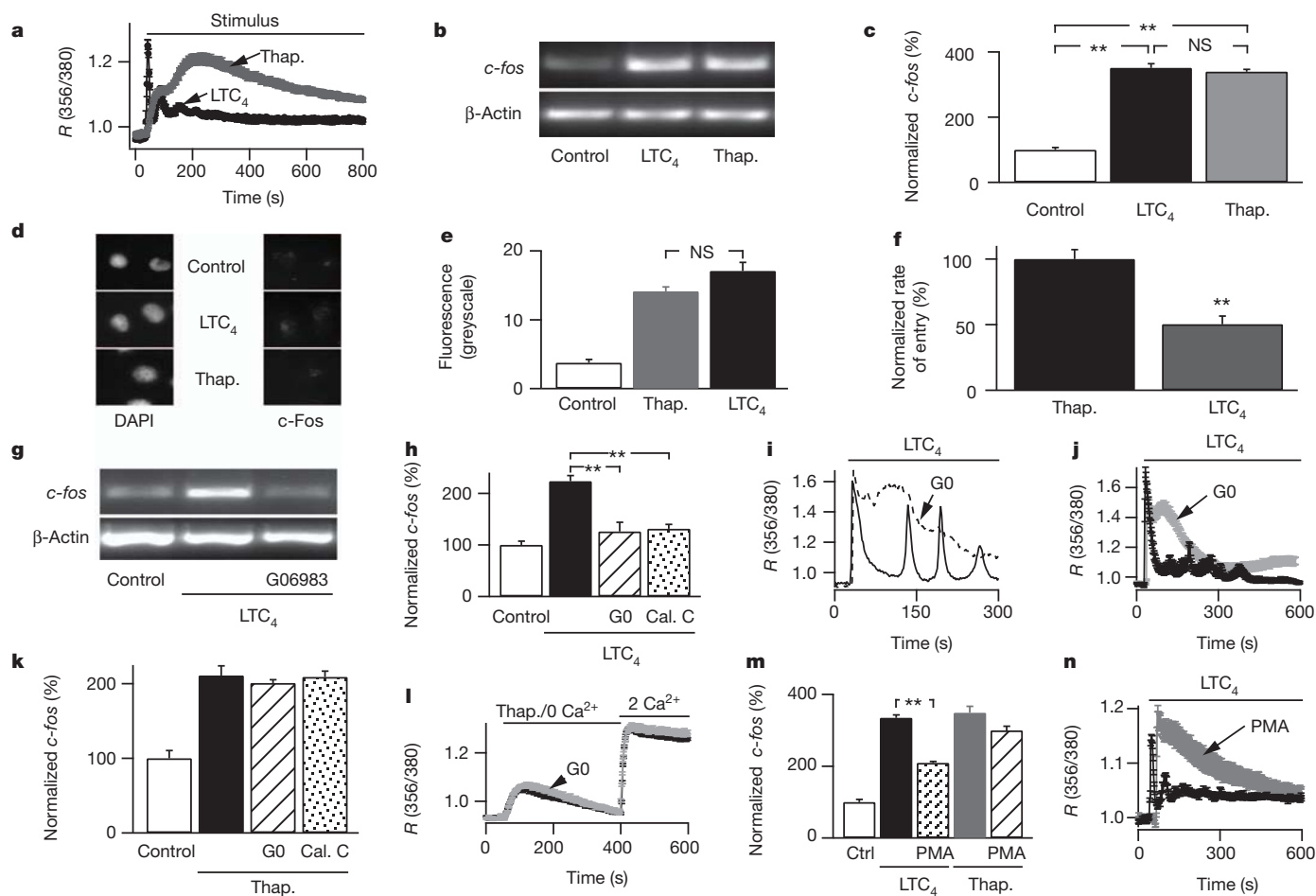


Figure 1 | CysLT1-receptor-dependent *c-fos* expression requires PKC. **a**, Averaged Ca^{2+} signals to LTC_4 and thapsigargin (Thap.) are compared (>50 cells per graph). $R(356/380)$, ratio of fluorescence measured at 356 and 380 nm. **b**, *c-fos* expression is compared between control (non-stimulated), 160 nM LTC_4 - and 2 μ M thapsigargin-stimulated cells. Stimulus was present for 8 min. **c**, Histograms show averaged responses from three independent experiments. LTC_4 and thapsigargin groups were different from control ($P < 0.001$), but not from one another ($P > 0.3$; analysis of variance (ANOVA)). **d**, Cells stained with antibody against *c-Fos* protein. DAPI, 4',6-diamidino-2-phenylindole. **e**, Aggregate data are compared ($n > 20$ per bar). Thapsigargin and LTC_4 groups were different from control ($P < 0.001$) but not from one another ($P = 0.11$). **f**, Ca^{2+} entry rate was measured after readmission of Ca^{2+} to cells stimulated with LTC_4 or thapsigargin in Ca^{2+} -free solution ($*P < 0.01$). **g**, G06983 (1 μ M; 10 min pre-treatment) suppresses LTC_4 -induced *c-fos* expression. **h**, Histogram comparing the effects of PKC blockers. LTC_4 control group (LTC_4 in the absence of PKC block) was different from the other groups

($P < 0.01$). There were no significant differences between the other groups. G0, G06983. Cal. C, calphostin C. **i**, Single-cell Ca^{2+} signals to LTC_4 are compared for the conditions shown. **j**, Averaged data are compared (>45 cells for each condition). **k**, Histogram showing *c-fos* expression to thapsigargin in the presence of PKC blockers. All thapsigargin-treated groups were significantly different from control ($P < 0.001$) but were not significantly different from one another. **l**, Ca^{2+} signals to thapsigargin are unaffected by PKC block. 0 Ca^{2+} , Ca^{2+} -free external solution; 2 Ca^{2+} , external solution containing 2 mM Ca^{2+} . **m**, Downregulation of PKC (PMA; 500 nM, 24 h) reduces LTC_4 - but not thapsigargin-induced *c-fos* expression (data from four independent experiments). All stimulated groups were significantly different from control ($P < 0.01$). For LTC_4 the PMA group was different from the LTC_4 control ($P < 0.01$). For thapsigargin, the PMA groups were not different from the thapsigargin control ($P = 0.07$). Ctrl, control. **n**, PKC downregulation alters the LTC_4 -evoked Ca^{2+} signal. Error bars show data \pm s.e.m. NS, not significant.

(GFP-PH) construct¹⁴, increased to a greater extent when PKC was inhibited (Fig. 2b).

Cytoplasmic Ca^{2+} inhibits CRAC channels through mechanisms of fast and slow inactivation¹⁵. The prolonged Ca^{2+} release evoked by LTC_4 in the presence of non-desensitizing receptors could therefore inactivate CRAC channels to suppress agonist-evoked gene expression. In support of this, accumulation of the slow Ca^{2+} chelator EGTA in the cytoplasm rescued gene expression to CysLT1 receptor activation in the presence of PKC block (Fig. 2c, d). Ca^{2+} -dependent fast inactivation of CRAC channels is unlikely to contribute here because (1) it is unaffected by the slow chelator EGTA^{16,17}, which reversed the inhibitory effects of PKC block (Fig. 2c, d), and (2) the rate and extent of fast inactivation were unaltered by CysLT1 receptor activation in the presence of PKC downregulation (Fig. 3a). Instead, Ca^{2+} -dependent slow inactivation is likely to be the dominant mechanism because (1) it too is suppressed by cytoplasmic EGTA^{18,19}, (2) the

Ca^{2+} dependence of slow inactivation has a dissociation constant (K_d) of $\sim 0.5 \mu$ M and full block occurs at $\sim 1 \mu$ M (Fig. 3b), which is similar to the peak Ca^{2+} rise evoked by LTC_4 in the presence of PKC inhibitors or following downregulation of PKC ($0.87 \pm 0.1 \mu$ M), and (3) Ca^{2+} -dependent slow inactivation develops with a time course similar to the duration of the prolonged Ca^{2+} rise caused by LTC_4 following loss of PKC activity^{18,19}.

If prolonged Ca^{2+} release to non-desensitizing CysLT1 receptors leads to slow inactivation of CRAC channels, then development of a calcium-release-activated calcium current (I_{CRAC}) to a subsequent stimulus should be impaired. Pre-activation of CysLT1 receptors reduced I_{CRAC} evoked by thapsigargin but only in the presence of PKC block (Fig. 3c). No such inhibitory effect was seen when cells were dialysed with a strongly buffered Ca^{2+} -containing pipette solution, which prevents the development of slow inactivation (Fig. 3d). Increasing the time between the termination of Ca^{2+} release and

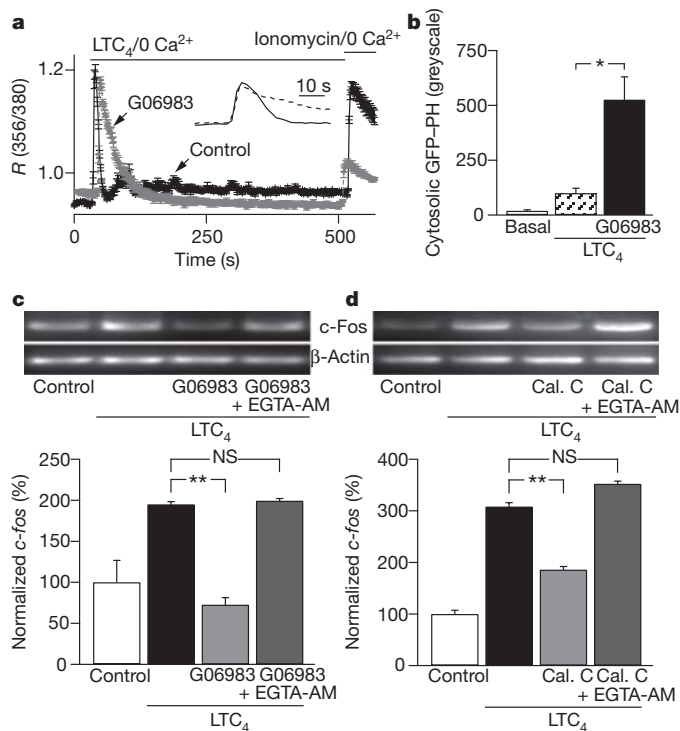


Figure 2 | Gene expression to non-desensitizing CysLT1 receptors is rescued by preventing a cytoplasmic Ca^{2+} rise. **a**, Stimulation with LTC_4 in the presence of G06983 evokes a more sustained Ca^{2+} release response, and this leads to more extensive store depletion (measured through the extent of Ca^{2+} release evoked by $5 \mu\text{M}$ ionomycin). Both LTC_4 and ionomycin were applied in Ca^{2+} -free external solution. Inset compares the kinetics of Ca^{2+} release. **b**, Cytosolic GFP-PH levels, a measure of InsP_3 levels, rise when CysLT1 receptors are stimulated in the presence of G06983. **c**, Top, loading cells with the Ca^{2+} chelator EGTA prevents loss of gene expression to agonist when PKC is blocked. Bottom, aggregate data from five independent gels are summarized. **d**, As in **c**, but calphostin C was used to block PKC instead. Bottom, aggregate data from three independent gels are summarized. Error bars show data \pm s.e.m. NS, not significant.

subsequent store-operated Ca^{2+} entry should enable some recovery from Ca^{2+} -dependent slow inactivation and this should partially rescue gene expression. When Ca^{2+} influx was evoked a few minutes after Ca^{2+} release, significant, albeit incomplete, rescue of Ca^{2+} entry (Fig. 3e) and *c-fos* transcription (Fig. 3f) occurred in cells stimulated with LTC_4 in the presence of PKC inhibition. Hence, allowing CRAC channels time to recover from Ca^{2+} -dependent inactivation results in partial rescue of agonist-driven gene expression.

Our attempts to express the PKC-insensitive CysLT1 receptor, in which S313, S315 and S316 had been mutated to alanines, were thwarted by the difficulty of expressing these receptors³, although in a few cells we observed that Ca^{2+} oscillations to LTC_4 were less frequent (3.1 ± 0.5 versus 5.4 ± 0.4 , 4 and 6 cells, respectively) and the initial spike was a little broader (~ 1.25 -fold) than mock-transfected cells.

To place our findings in a physiological context, we turned to the human nasal polyp, which is rich in mast cells²⁰. The polyp and associated nasal mucosa are largely self-contained, providing an excellent 'quasi *in vivo* human system'. Mast cells from polyps, acutely isolated from patients undergoing surgery, respond to LTC_4 and express functional CRAC channels^{7,8}. Stimulation with LTC_4 activated *c-Fos* protein expression in mast cells isolated from polyps (Fig. 3g) and this was reduced by pre-treatment with either calphostin C or G06983 (Fig. 3h). PKC inhibitors had no inhibitory effect when thapsigargin was used instead.

Western blots revealed the presence of Ca^{2+} -dependent PKC- α , - β and - ζ isozymes^{11,21} but only faint expression of PKC- δ and - ϵ (Fig. 4a).

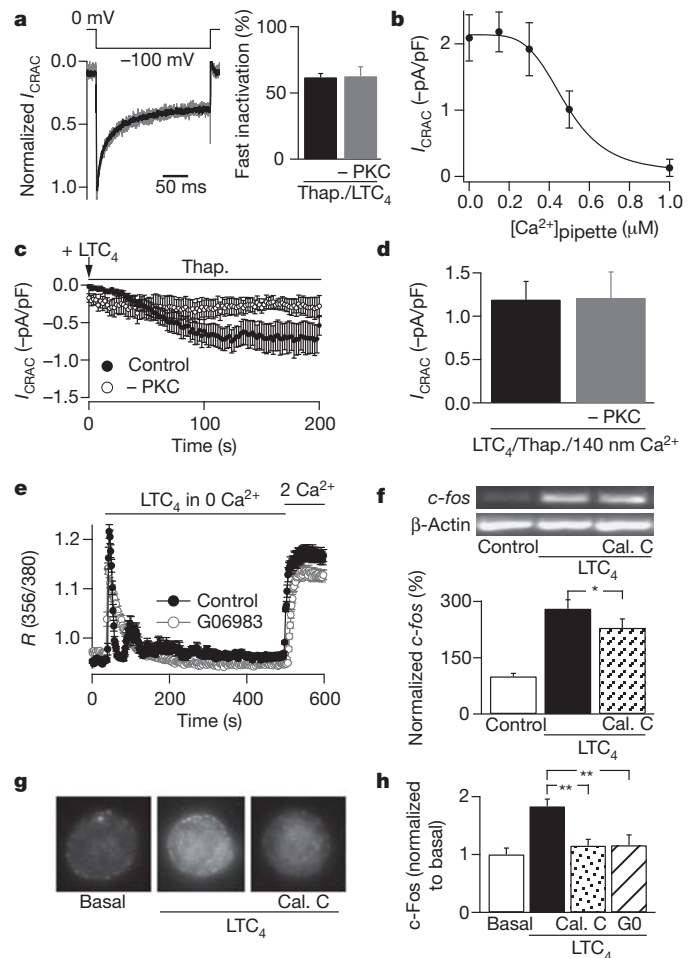


Figure 3 | Ca^{2+} -dependent slow inactivation underlies suppression of *c-Fos* expression to non-desensitizing CysLT1 receptors. **a**, Ca^{2+} -dependent fast inactivation is unaffected by non-desensitizing receptors (labelled -PKC). Cells were stimulated with LTC_4 (160 nM) before breaking in with a pipette solution containing thapsigargin and buffered Ca^{2+} (140 nM) and fast inactivation was measured within 60 s of break-in. **b**, Dependence of Ca^{2+} -dependent slow inactivation on patch pipette Ca^{2+} concentration. pA, picoamperes; pF, piconfarads. $[\text{Ca}^{2+}]_{\text{pipette}}$, concentration of Ca^{2+} in pipette. **c**, Stimulation of non-desensitizing receptors with LTC_4 before break-in significantly reduced the size of I_{CRAC} that developed in response to dialysis with thapsigargin in weak buffer (0.2 mM EGTA). **d**, As in **c**, but cells were dialysed with a pipette solution containing strong Ca^{2+} buffer (10 mM EGTA, 140 nM free Ca^{2+}). **e**, Store-operated Ca^{2+} entry recovers partially by increasing the time interval between Ca^{2+} release and subsequent Ca^{2+} entry. **f**, *c-fos* expression to non-desensitizing receptor stimulation is rescued partially when Ca^{2+} entry occurs several minutes after Ca^{2+} release has reached completion. **g**, *c-Fos* expression in human nasal mast cells after CysLT1 receptor activation is suppressed by PKC inhibition. **h**, Aggregate data are compared (12–17 cells per bar; three patients each). Error bars show data \pm s.e.m. NS, not significant.

Overnight PMA exposure significantly reduced PKC- α and - β expression, but not PKC- ζ (Fig. 4a, b). Their weak expression made PKC- δ and - ϵ difficult to quantify. Confocal microscope studies confirmed robust expression of PKC- α , - β and - ζ (Fig. 4c), with barely detectable levels of PKC- δ and - ϵ (data not shown). Overnight PMA exposure significantly reduced PKC- α and - β but not - ζ at the cellular level (Fig. 4d). Knockdown of PKC- α using a targeted short interfering RNA (siRNA) approach (Fig. 4e) resulted in a broadening of the first Ca^{2+} oscillation evoked by LTC_4 , indicative of less receptor desensitization, and fewer Ca^{2+} oscillations in each cell (Supplementary Fig. 7). Knockdown of PKC- β had a much weaker effect on the Ca^{2+} oscillations (Supplementary Fig. 7). Knockdown of PKC- α or PKC- α plus - β simultaneously, but not PKC- β alone, reduced LTC_4 -driven

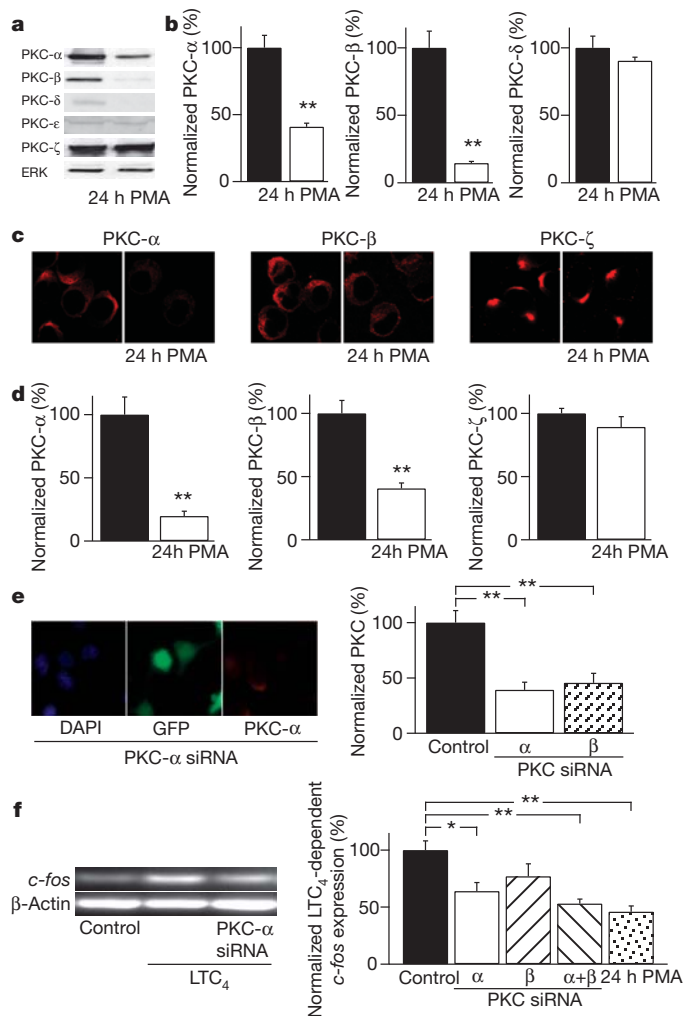


Figure 4 | PKC- α regulates CysLT1 receptor-driven *c-fos* transcription.

a, Expression of PKC- α , - β and - ζ (western blot) is shown in control cells and cells exposed to PMA for 24 h. **b**, Quantification of data from three independent experiments, as in **a**. **c**, Confocal microscope images of PKC expression for the conditions shown. Cells were fixed before analysis. Original magnification, $\times 100$. **d**, Quantification of images from experiments, as in **c**. **e**, siRNA against PKC- α or - β significantly reduces corresponding protein expression. Left, DAPI staining of nuclei; middle, GFP expression (indicating transfection); and right, PKC- α expression after siRNA-mediated knockdown. Right, aggregate data from four experiments are depicted. Both siRNA groups were different from control ($P < 0.005$). Error bars show data \pm s.e.m. NS, not significant. **f**, Knockdown of PKC- α , - β and PKC- α plus - β on LTC₄-dependent *c-fos* expression. Data are compared with mock-transfected cells. For comparison, 24 h exposure to PMA is included. All treated groups were significantly different from the LTC₄ control (black bar) group except siRNA PKC- β knockdown ($P > 0.1$). PKC- α plus - β and 24 h PMA groups had $P < 0.01$; PKC- α group had $P < 0.05$. Error bars show data \pm s.e.m. NS, not significant.

c-fos expression to an extent similar to that seen after overnight PMA treatment (Fig. 4f). Stimulation of non-G-protein-coupled FC ϵ RI antigenic receptors in RBL-2H3 cells activates *c-fos* expression primarily through PKC- δ and - ϵ ²². Although it is possible that these PKC isoforms also contribute to gene expression under our conditions, our results nevertheless suggest a major role for PKC- α in G-protein-coupled-receptor desensitization, and thus coupling to the nucleus.

Collectively, our findings reveal a counterintuitive function for desensitization of a phospholipase-C-coupled receptor. Rather than terminating a response, homologous receptor desensitization is essential for maintaining excitation–transcription coupling. Desensitization of CysLT1 receptors is mediated principally by PKC-dependent phosphorylation³. Prevention of receptor desensitization through either

acute block or degradation of PKC or after knockdown of PKC- α all led to loss of Ca²⁺-dependent gene expression, despite potentiation of Ca²⁺ release to agonist. Mechanistically, the prolonged Ca²⁺ release phase accelerated Ca²⁺-dependent slow inactivation of CRAC channels, resulting in loss of Ca²⁺ entry. Because Ca²⁺ microdomains near open CRAC channels drive *c-fos* expression, the decline in CRAC channel activity abolishes excitation–transcription coupling. The interval between Ca²⁺ oscillations after CysLT1 receptor activation is ~ 25 s (ref. 4). Because InsP₃ has a short half-life in the cytoplasm (~ 1 s)²³, receptor desensitization will presumably lower InsP₃ levels during the interspike interval. Store refilling will occur quickly and CRAC channel activity will be transient after CysLT1 receptor stimulation. The short duration of Ca²⁺ release and thus Ca²⁺ entry, determined by receptor desensitization, will ensure Ca²⁺-dependent slow inactivation does not develop, as this inhibitory mechanism requires a sustained Ca²⁺ rise for several seconds. It is therefore the kinetics of receptor desensitization and recovery from desensitization within a highly Ca²⁺ sensitive and high-gain system that ensures bursts of store-operated Ca²⁺ entry occur that are sufficient for the activation of *c-fos* expression, without the build-up of the Ca²⁺-dependent slow inactivation pathway that would abolish the response.

METHODS SUMMARY

Cultured RBL-1 cells and acutely isolated human nasal polyps were prepared as described previously⁷. Transfection with siRNA constructs was achieved using the AMAXA system. Patch-clamp recordings and cytoplasmic Ca²⁺ measurements followed standard methods⁷. RT-PCR, western blotting and confocal microscopy were carried out as described previously⁵. Error bars are s.e.m.

Full Methods and any associated references are available in the online version of the paper at www.nature.com/nature.

Received 8 April; accepted 23 November 2011.

Published online 9 January 2012.

- Pierce, K. L., Premont, R. T. & Lefkowitz, R. J. Seven-transmembrane receptors. *Nature Rev. Mol. Cell Biol.* **3**, 639–650 (2002).
- Funk, C. D. Leukotriene modifiers as potential therapeutics for cardiovascular disease. *Nature Rev. Drug Discov.* **4**, 664–672 (2005).
- Naik, S. *et al.* Regulation of cysteinyl leukotriene type 1 receptor internalization and signaling. *J. Biol. Chem.* **280**, 8722–8732 (2005).
- Di Capite, J., Ng, S.-W. & Parekh, A. B. Decoding of cytoplasmic Ca²⁺ oscillations through the spatial signature drives gene expression. *Curr. Biol.* **19**, 853–858 (2009).
- Ng, S.-W., Nelson, C. & Parekh, A. B. Coupling of Ca²⁺ microdomains to spatially and temporally distinct cellular responses by the tyrosine kinase Syk. *J. Biol. Chem.* **284**, 24767–24772 (2009).
- Foletta, V. C., Segal, D. H. & Cohen, D. R. Transcriptional regulation in the immune system: all roads lead to AP-1. *J. Leukoc. Biol.* **63**, 139–152 (1998).
- Di Capite, J. L., Shirley, A., Nelson, C., Bates, G. & Parekh, A. B. Intercellular calcium wave propagation involving positive feedback between CRAC channels and cysteinyl leukotrienes. *FASEB J.* **23**, 894–905 (2009).
- Di Capite, J., Nelson, C., Bates, G. & Parekh, A. B. Targeting CRAC channels and leukotriene receptors provides a novel combination strategy for treating nasal polyposis. *J. Allergy Clin. Immunol.* **124**, 1014–1021 (2009).
- Stephan, V., Seibt, A., Koerholz, D. & Wahn, V. Expression of mRNA for the proto-oncogene *c-fos* in rat basophilic leukemia cells. *Cell. Signal.* **9**, 65–70 (1997).
- Jousset, H., Frieden, M. & Demaurex, N. STIM1 knockdown reveals that store-operated Ca²⁺ channels located close to sarco/endoplasmic Ca²⁺ ATPases (SERCA) pumps silently refill the endoplasmic reticulum. *J. Biol. Chem.* **282**, 11456–11464 (2007).
- Ozawa, K. *et al.* Ca²⁺-dependent and Ca²⁺-independent isozymes of protein kinase C mediate exocytosis in antigen-stimulated rat basophilic RBL-2H3 cells. Reconstitution of secretory responses with Ca²⁺ and purified isozymes in washed permeabilized cells. *J. Biol. Chem.* **268**, 1749–1756 (1993).
- Deshpande, D. A. *et al.* PKC-dependent regulation of the receptor locus dominates functional consequences of cysteinyl leukotriene type 1 receptor activation. *FASEB J.* **21**, 2335–2342 (2007).
- Bird, G. S. & Putney, J. W. J. Capacitative calcium entry supports calcium oscillations in human embryonic kidney cells. *J. Physiol.* **562**, 697–706 (2005).
- Stauffer, T. P., Ahn, S. & Meyer, T. Receptor-induced transient reduction in plasma membrane PtdIns(4,5)P₂ concentration monitored in living cells. *Curr. Biol.* **8**, 343–346 (1998).
- Parekh, A. B. & Putney, J. W. J. Store-operated calcium channels. *Physiol. Rev.* **85**, 757–810 (2005).
- Zweifach, A. & Lewis, R. S. Rapid inactivation of depletion-activated calcium current (ICRAC) due to local calcium feedback. *J. Gen. Physiol.* **105**, 209–226 (1995).

17. Fierro, L. & Parekh, A. B. Fast calcium-dependent inactivation of calcium release-activated calcium current (CRAC) in RBL-1 cells. *J. Membr. Biol.* **168**, 9–17 (1999).
18. Zweifach, A. & Lewis, R. S. Slow calcium-dependent inactivation of depletion-activated calcium current. *J. Biol. Chem.* **270**, 14445–14451 (1995).
19. Parekh, A. B. Slow feedback inhibition of calcium release-activated calcium current by calcium entry. *J. Biol. Chem.* **273**, 14925–14932 (1998).
20. Takasaka, T., Kaku, Y. & Hozawa, K. Mast cell degranulation in nasal polyps. *Acta Otolaryngol. Suppl.* **430**, 39–48 (1986).
21. Ozawa, K., Yamada, K., Kazanietz, M. G., Blumberg, P. M. & Beaven, M. A. Different isozymes of protein kinase C mediate feedback inhibition of phospholipase C and stimulatory signals for exocytosis in RBL-2H3 cells. *J. Biol. Chem.* **268**, 2280–2283 (1993).
22. Razin, E., Szallasi, Z., Kazanietz, M. G., Blumberg, P. M. & Rivera, J. Protein kinases C- β and C- ϵ link the mast cell high-affinity receptor for IgE to the expression of c-fos and c-jun. *Proc. Natl Acad. Sci. USA* **91**, 7722–7726 (1994).
23. Kasai, H. & Petersen, O. H. Spatial dynamics of second messengers: IP₃ and cAMP as long-range and associative messengers. *Trends Neurosci.* **17**, 95–101 (1994).

Supplementary Information is linked to the online version of the paper at www.nature.com/nature.

Acknowledgements This work was supported by Medical Research Council grant support to A.B.P. S.-W. N. held a BBSRC-Glaxo-Smith-Kline studentship. We thank G. Miesenboeck and J. Putney for comments on the manuscript.

Author Contributions S.-W.N. performed and analysed Ca²⁺ measurements, RT-PCR, western blots and siRNA knockdown. D.B. performed and analysed patch-clamp recordings. C.N. carried out immunocytochemistry. R.M. helped with Ca²⁺ measurements. R.A. and G.B. supplied human nasal polyps. A.B.P. carried out some patch-clamp experiments, discussed the results, supervised the project and wrote the paper.

Author Information Reprints and permissions information is available at www.nature.com/reprints. The authors declare no competing financial interests. Readers are welcome to comment on the online version of this article at www.nature.com/nature. Correspondence and requests for materials should be addressed to A.B.P. (anant.parekh@dpag.ox.ac.uk).

METHODS

Cell culture and transfection. RBL-1 cells were bought from ATCC and were cultured (37 °C, 5% CO₂) in Dulbecco's modified Eagle medium with 10% fetal bovine serum, 2 mM L-glutamine and penicillin-streptomycin, as previously described²⁴. Cells were transfected with siRNA against Syk (purchased from Invitrogen; 5'-3' sense, CCCUCUGGCAGCUAGUGGAACAUA; antisense, UAAUGUCCACUAGCUGCCAGAGGG) using the Amaxa nucleofection system²⁵. siRNA against PKC isozymes were purchased from Invitrogen; PKC- α sense, GCGACACCUGCGACAUGAAUGUUA; antisense, UGAACAUAUCAU GUCGCAGGUGUCGC; PKC- β sense, GGCUAUAGACCAACACCCAGGC AA; antisense, UUGCCUGGGUGUUUGGUCAUUAGCC. Cells were used 36–48 h after plating.

Human tissue. Human polyps were removed from patients with full ethical consent and with approval from the National Research Ethics Service (REC number 07/H0607/104). Polyps were treated as described⁷ and used within 6 h of surgical removal.

ICRAC recordings. Patch-clamp experiments were conducted in the tight-seal whole-cell configuration at room temperature (20–24 °C) as previously described^{7,24}. Sylgard-coated, fire-polished pipettes had resistances of 4.2–5.5 M Ω when filled with standard internal solution that contained (in mM): Cs⁺ glutamate 145, NaCl 8, MgCl₂ 1, Mg-ATP 2, EGTA 10, CaCl₂ 4.6 mM (free Ca²⁺ ~140 nM), HEPES 10, pH 7.2 with CsOH. In some experiments, weak Ca²⁺ buffer was used instead (0.2 mM EGTA and no added CaCl₂). A correction of +10 mV was applied for the subsequent liquid junction potential that arose from this glutamate-based internal solution. The composition of the extracellular solution was (in mM): NaCl 145, KCl 2.8, CaCl₂ 10, MgCl₂ 2, CsCl 10, D-glucose 10, HEPES 10, pH 7.4 with NaOH.

I_{CRAC} was measured by applying voltage ramps (–100 to +100 mV in 50 ms) at 0.5 Hz from a holding potential of 0 mV. For fast inactivation, step pulses (250 ms duration) were applied from 0 mV to –100 mV every 2 s. Currents were filtered using an 8-pole Bessel filter at 2.5 kHz and digitized at 100 μ s. Currents were normalized by dividing the amplitudes (measured from the voltage ramps at –80 mV) by the cell capacitance. Capacitative currents were compensated before each ramp by using the automatic compensation of the EPC-9/2 (HEKA Elektronik) patch-clamp amplifier. For I_{CRAC} , leak currents were subtracted by averaging 2–3 ramp currents obtained just before I_{CRAC} had started to develop, and then subtracting this from all subsequent currents.

Ca²⁺ imaging. Ca²⁺ imaging experiments were carried out at room temperature (21–24 °C) using the IMAGO CCD camera-based system from TILL Photonics, as described previously²⁵. Cells were alternately excited at 356 and 380 nm (20 ms exposures) and images were acquired every 2 s. Images were analysed offline using IGOR Pro for Windows. Cells were loaded with Fura 2-AM (2 μ M) for 40 min at room temperature in the dark and then washed three times in standard external solution of composition (in mM) NaCl 145, KCl 2.8, CaCl₂ 2, MgCl₂ 2, D-glucose 10, HEPES 10, pH 7.4 with NaOH. Cells were left for 15 min to allow further de-esterification. Ca²⁺-free solution had the following composition (in mM) NaCl 145, KCl 2.8, MgCl₂ 2, D-glucose 10, HEPES 10, EGTA 0.1, pH 7.4 with NaOH).

EGTA-AM loading. Cells were loaded with EGTA by incubation for 45 min with EGTA-AM as described⁵.

Confocal microscopy. Cells were fixed in 4% paraformaldehyde in phosphate buffer for 30 min at room temperature. All the washes used 0.01% PBS (137 mM NaCl, 2.7 mM KCl, 8 mM Na₂HPO₄, 1 mM KH₂PO₄). The cells were blocked with 2% BSA and 10% goat serum for 1 h. Anti-c-Fos, -PKC- δ , -PKC- ϵ and -PKC- ζ were used in carrier (0.2% BSA, 1% goat serum) and left overnight at 4 °C and were purchased from Cell Signalling. Anti-PKC- α and - β were used in carrier (0.2% BSA, 1% goat serum) and left overnight at 4 °C and were purchased from Santa Cruz. The secondary anti-rabbit IgG was a HandL chain-specific (goat) fluorescein conjugate (Alexa Fluor 568, excitation at 578 nm, emission at 603 nm wavelength) from Invitrogen. This was used in PBS for 2 h at room temperature. The cells were mounted in Vectashield mounting medium. Images were obtained using a Leica confocal microscope, as described⁷.

Western blotting. Total cell lysates (50 μ g) were separated by SDS-PAGE on a 10% gel and electrophoretically transferred to nitrocellulose membrane, as described⁷. Membranes were blocked with 5% non-fat dry milk in TBS plus 0.1% Tween 20 (TBST) buffer for 1 h at room temperature. Membranes were washed with TBST three times and then incubated with primary antibody overnight at 4 °C. Anti-PKC- δ , - ϵ and - ζ antibodies were obtained from New England Biolabs and used at 1:2,500 dilution. Anti-PKC- α , - β and total ERK2 antibodies were purchased from Santa Cruz Biotechnology. PKC- α and - β antibodies were used at 1:2,500 dilution and total ERK antibody was used at a dilution of 1:5,000. The membranes were then washed with TBST again and incubated with a 1:2,500 dilution of goat anti-rabbit secondary antibody IgG from Santa Cruz Biotechnology for 1 h at room temperature. After washing with TBST, the bands were developed for visualization using ECL-plus western blotting detection system (GE Healthcare). Gels were quantified using the UN-SCAN-IT software package (Silk Scientific). Total ERK2 is widely used as a control for gel loading. The antibody does not discriminate between phosphorylated (and hence active) and non-phosphorylated ERK2 and therefore detects the total amount of this protein, regardless of whether the kinase has been activated. The extent of PKC was therefore normalized to the total amount of ERK2 present in each lysate, to correct for any differences in amount of cells used for each experiment.

RT-PCR. Total RNA was extracted from RBL cells by using an RNeasy Mini Kit (Qiagen), as described^{4,5}. RNA was quantified spectrophotometrically by absorbance at 260 nm. Total RNA (1 μ g) was reverse-transcribed using the iScriptTM cDNA Synthesis Kit (Bio-Rad), according to the manufacturer's instructions. Following cDNA synthesis, PCR amplification was then performed using BIO-X-ACTTM Short DNA Polymerase (Bioline) with primers specific for the detection of *c-fos* were synthesized by Invitrogen. The PCR products were electrophoresed through an agarose gel and visualized by ethidium bromide staining.

Statistics. Results are presented as means \pm s.e.m. Statistical significance was assessed using Student's *t*-test for comparison between two groups or ANOVA followed by a post-hoc Newman Keuls multiple comparison test for the difference between groups and results were considered significant at **P* < 0.05, ***P* < 0.01.

24. Glitsch, M. D., Bakowski, D. & Parekh, A. B. Activation of the store-operated Ca²⁺ current ICRAC is compromised by inhibitors of the lipoxygenase family of enzymes. *J. Physiol. (Lond.)* **539**, 93–106 (2002).
25. Ng, S.-W., Di Capite, J. L., Singaravelu, K. & Parekh, A. B. Sustained activation of the tyrosine kinase Syk by antigen in mast cells requires local Ca²⁺ influx through Ca²⁺ release-activated Ca²⁺ channels. *J. Biol. Chem.* **283**, 31348–31355 (2008).

Structures of cytochrome P450 17A1 with prostate cancer drugs abiraterone and TOK-001

Natasha M. DeVore¹ & Emily E. Scott¹

Cytochrome P450 17A1 (also known as CYP17A1 and cytochrome P450c17) catalyses the biosynthesis of androgens in humans¹. As prostate cancer cells proliferate in response to androgen steroids^{2,3}, CYP17A1 inhibition is a new strategy to prevent androgen synthesis and treat lethal metastatic castration-resistant prostate cancer⁴, but drug development has been hampered by lack of information regarding the structure of CYP17A1. Here we report X-ray crystal structures of CYP17A1, which were obtained in the presence of either abiraterone, a first-in-class steroidal inhibitor recently approved by the US Food and Drug Administration for late-stage prostate cancer⁵, or TOK-001, an inhibitor that is currently undergoing clinical trials^{4,6}. Both of these inhibitors bind the haem iron, forming a 60° angle above the haem plane and packing against the central I helix with the 3β-OH interacting with asparagine 202 in the F helix. Notably, this binding mode differs substantially from those that are predicted by homology models and from steroids in other cytochrome P450 enzymes with known structures, and some features of this binding mode are more similar to steroid receptors. Whereas the overall structure of CYP17A1 provides a rationale for understanding many mutations that are found in patients with steroidogenic diseases, the active site reveals multiple steric and hydrogen bonding features that will facilitate a better understanding of the enzyme's dual hydroxylase and lyase catalytic capabilities and assist in rational drug design. Specifically, structure-based design is expected to aid development of inhibitors that bind only CYP17A1 and solely inhibit its androgen-generating lyase activity to improve treatment of prostate and other hormone-responsive cancers.

CYP17A1 is a membrane-bound dual-function monooxygenase with a critical role in the synthesis of many human steroid hormones¹. The 17α-hydroxylase activity of CYP17A1 is required for the generation of glucocorticoids such as cortisol, but both the hydroxylase and 17,20-lyase activities of CYP17A1 are required for the production of androgenic and oestrogenic sex steroids (Supplementary Fig. 1). CYP17A1 is an important target for the treatment of breast and prostate cancers that proliferate in response to oestrogens and androgens^{2,3}. In the absence of structural information, CYP17A1 inhibitors have been

designed that are thought to bind the cytochrome P450 haem iron⁴, but it has been difficult to rationalize or predict other structural features that are critical for effective and selective CYP17A1 inhibition. In addition, structural information is important for understanding 17-hydroxylase deficiencies and may also improve our understanding of polycystic ovary disease⁷. We determined the structures of human CYP17A1 when bound to two clinically relevant CYP17A1 inhibitors (Supplementary Fig. 2). Abiraterone is the active form of a prodrug that was recently approved by the US Food and Drug Administration for metastatic prostate cancer^{5,8} and is under investigation for breast cancer⁹. TOK-001 is currently undergoing clinical trials for prostate cancer⁴.

A truncated, His-tagged version of the human CYP17A1 protein was generated from a synthetic complementary DNA that was engineered to remove the single amino-terminal transmembrane helix, and this CYP17A1 was expressed in *Escherichia coli*. The resulting CYP17A1 was membrane bound and so it was solubilized with detergent before purification. This CYP17A1 binds abiraterone (17-(3-pyridyl)androsta-5,16-dien-3β-ol) (Fig. 1a) and TOK-001 (17-(1H-Benzimidazol-1-yl)androsta-5,16-dien-3β-ol) with decreases in absorbance at 402 nm and increases in absorbance at 424 nm, consistent with nitrogen binding to the haem iron (type II interaction) with dissociation constant (K_d) values of <100 nM (Fig. 1a, inset). Similar titrations with the substrates progesterone (Fig. 1b) and pregnenolone revealed decreases in absorbance at 419 nm and increases in absorbance at 385 nm, which is indicative of the ligand displacing water from the haem (type I interaction). CYP17A1 binds pregnenolone (K_d <100 nM) more tightly than progesterone (K_d 229 ± 14 nM; Fig. 1b, inset). We found that full-length enzyme¹⁰ had a similar k_{cat} and three-fold higher Michaelis constant (k_{cat} 1.31 ± 0.03 min⁻¹, K_m 11.4 ± 0.7 μM) compared to the truncated form (k_{cat} 1.31 ± 0.03 min⁻¹, K_m 3.7 ± 0.3 μM). The half-maximum inhibitory concentration (IC₅₀) values for abiraterone (201 ± 1 nM) were lower than for TOK-001 (503 ± 1 nM) (Fig. 1c). Thus, truncated human CYP17A1 is a functional enzyme in terms of ligand binding, catalytic function and inhibition.

Both structures with abiraterone (2.6 Å) and TOK-001 (2.4 Å) demonstrate the characteristic cytochrome P450 fold (Fig. 2a) and have four very similar protein copies in each asymmetric unit

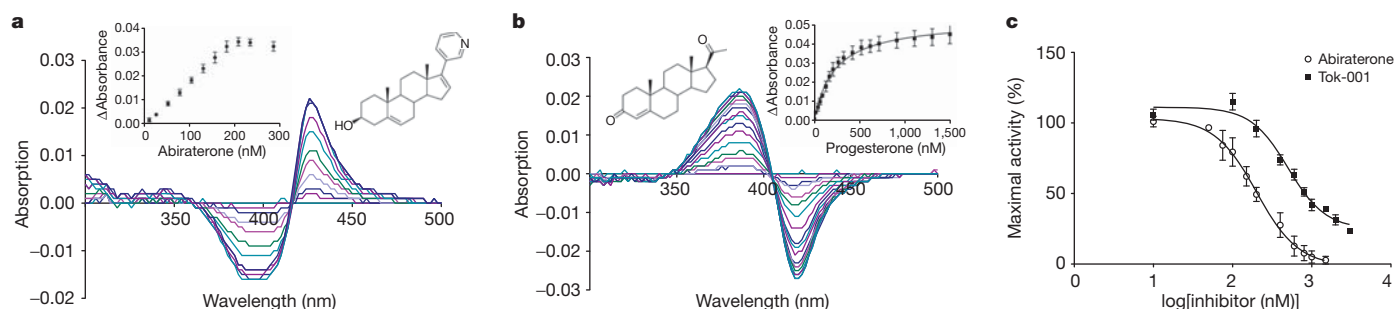


Figure 1 | Function of CYP17A1 and inhibition by clinical compounds. **a**, CYP17A1 titration with abiraterone (10–274 nM) yields progressive shifts in the ultraviolet–visible difference spectrum that indicate nitrogen binding to

haem iron. **b**, Similar titration with progesterone (10–1535 nM) indicates water displacement from the haem iron. **c**, IC₅₀ of abiraterone (circles) and TOK-001 (squares) for progesterone 17α-hydroxylation.

¹Department of Medicinal Chemistry, 1251 Wescoe Hall Drive, University of Kansas, Lawrence, Kansas 66045, USA.

(Supplementary Table 1). Consistent with spectral binding data, abiraterone and TOK-001 bind with the nitrogen of the C17 pyridine or benzimidazole, respectively, forming a coordinate covalent bond with the haem iron (Fig. 2b, d). The steroidal cores of these inhibitors rise at an angle of 60° above the haem plane, directed between the F and G helices (Fig. 2b, d), and essentially overlap with each other (Fig. 2f). The unsubstituted α -face packs flat against the I helix where G301, A302 and adjacent residues form a highly complementary hydrophobic planar surface (Fig. 2b). The 3β -OH groups of abiraterone (Fig. 2b) and TOK-001 (Fig. 2d) hydrogen bond with N202 in the F helix (~ 2.6 Å and ~ 2.4 Å, respectively).

Although inhibitors occupy the majority of the enclosed active site, the void extends beyond these ligands in several directions. First, the active site wall nearest the inhibitor β -face is not as complementary to the steroid core as to the α -face. The C18 and C19 methyl groups project towards a crevice between the B' helix, the $\beta 4$ loop and the loop following the F helix (Fig. 2b). Only three side chains of the cavity wall come within 4 Å of C18 or C19. The cavity wall facing the β -face of abiraterone or TOK-001 is primarily lined with hydrophobic atoms of A105, S106, A113, F114, I206, L209, V236 and V482 (Fig. 2c), but there are two notable exceptions. R239 and D298 extend from the G and I helices, respectively, to orient their basic and acidic termini towards C6. These two polar side chains flank a substantial extension of the active site void adjacent to C6. Second, in the abiraterone structure there is unfilled space in the active site cavity adjacent to the pyridine

ring bordered by V366, A367, I371 and V483 (Fig. 2c), and this volume is occupied by benzimidazole in the TOK-001 structure (Fig. 2e). Last, the most substantial active site cavity extension is from the 3β -OH of the inhibitors over the top of helix I and along the underside of helices F and G. This cavity is mostly lined by hydrophobic residues (I198, L243 and F300), but its 'roof' is bordered by several polar F and G helix residues (Y201, N202 and R239; Fig. 2c) that interact with, or are located near, water molecules in this region. The overall cavity containing TOK-001 is similar to that observed when abiraterone is bound, except that the available void volume over helix I is slightly smaller (Fig. 2e).

The single direct hydrogen bond between inhibitors and the protein is part of a larger hydrogen bonding network. In the abiraterone complex this network involves N202, E305, several conserved water molecules, R239, the backbone carbonyl of G297 and, in some molecules, Y201 (Fig. 3). Although Y201 is not within hydrogen bonding distance to these waters for molecules A and B, the side chain rotates slightly towards abiraterone in molecules C and D to interact with one or both of the water molecules. TOK-001 has a very similar hydrogen bonding network (Supplementary Fig. 3). These interactions are strongly reminiscent of the interactions that are conserved in the androgen, oestrogen, glucocorticoid, mineralocorticoid and progesterone receptors¹¹ (Fig. 4a, b). In each receptor, the 3β -OH or 3-keto group of steroids binds within a deep receptor pocket and forms hydrogen bonds with a glutamine or glutamate, an arginine and often a conserved water

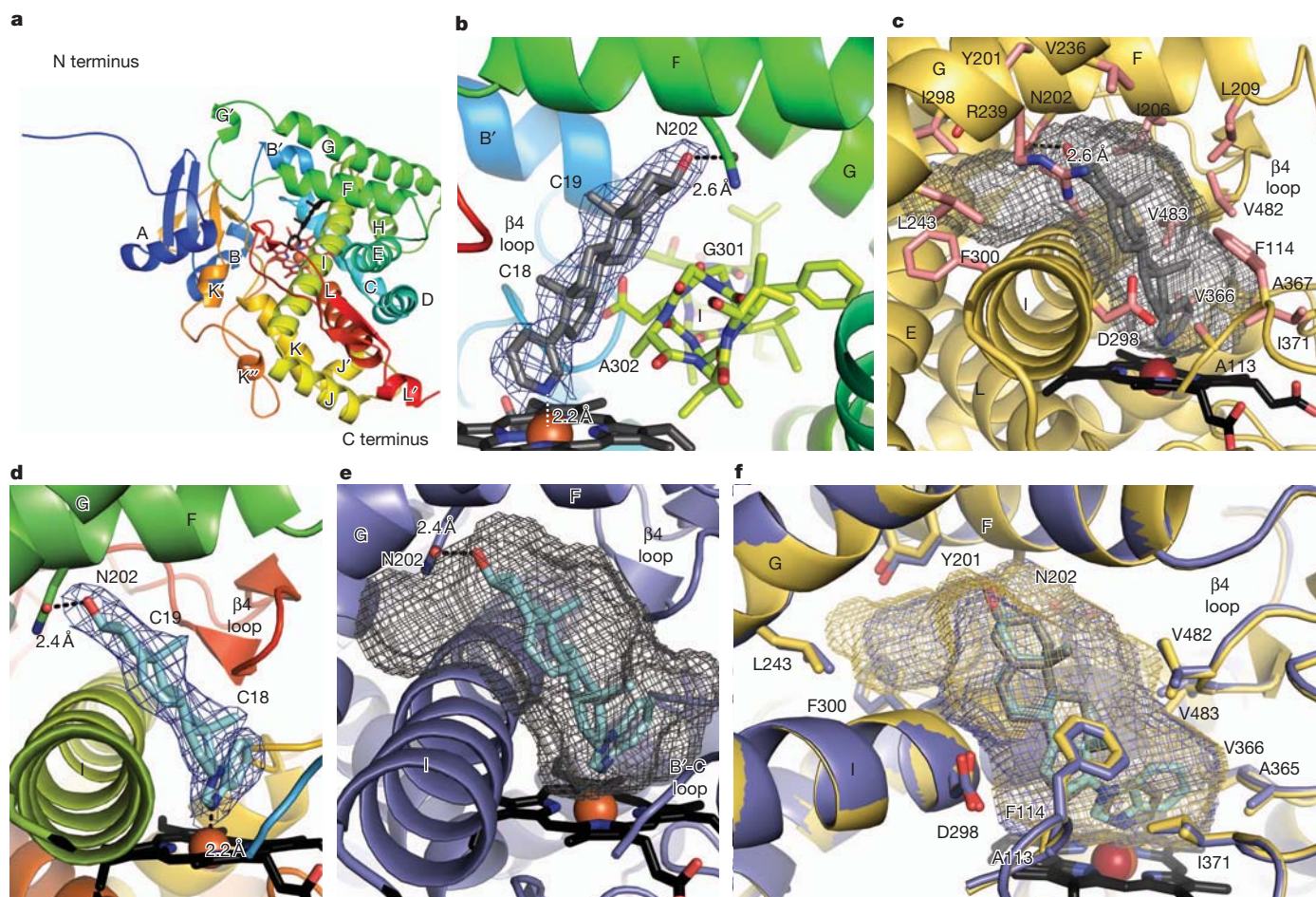


Figure 2 | CYP17A1 ligand binding. In the stick and sphere representations, non-carbon atoms are indicated in blue (N), red (O), black (haem), grey (abiraterone), cyan (TOK-001) and by a dark red sphere (Fe). **a**, A coloured representation of the CYP17A1-abiraterone structure, from the N terminus (blue) to the C terminus (red). **b**, Abiraterone binds ($2|F_o| - |F_c|$ density at 1σ ; blue mesh) at an angle of approximately 60° from haem against helix I (yellow).

c, Abiraterone cavity (grey mesh), rotated approximately 180° in relation to **b**. **d**, TOK-001 binding ($2|F_o| - |F_c|$ density at 1σ ; blue mesh). **e**, TOK-001 cavity (grey mesh). **f**, Abiraterone structure (yellow) superimposed on TOK-001 structure (purple) with respective voids (mesh). The B' helix has been removed from panels c-f so that it is possible to view the ligands.

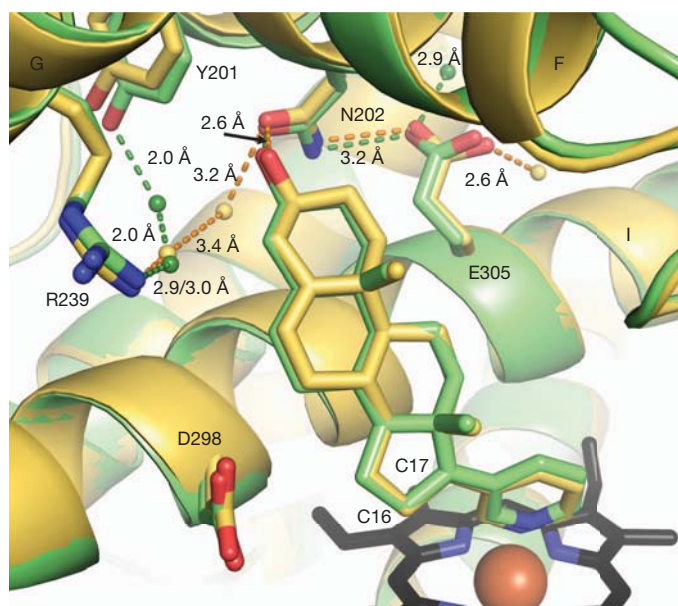


Figure 3 | Hydrogen bond network with abiraterone. CYP17A1 has a hydrogen bonding network at the top of the active site that interacts with abiraterone. Molecules A and B (yellow), and C and D (green) have slightly different networks, with the main difference being the involvement of Y201. Water molecules are indicated by small spheres. Hydrogen bonds are represented by dashed lines and the distances between them are indicated.

molecule. These interactions are critical for ligand recognition by hormone receptors¹² and may also contribute to CYP17A1 selectivity for pregnenolone, progesterone and their 17 α -hydroxy derivatives. Notably, TOK-001 is both a CYP17A1 inhibitor and androgen receptor

antagonist¹³, and the similarity of these binding modes is probably the reason for this dual mechanism of action.

Orientations of the native CYP17A1 substrates are of substantial value in understanding the function of this enzyme. Pregnenolone and progesterone were docked into the CYP17A1–abiraterone structure modelled as the Fe(IV)=O (compound I) catalytic state. Progesterone maintained the N202 hydrogen bond. The distances from C17 and C16 to the catalytic oxygen were 3.7 Å and 3.9 Å, respectively, distances that are consistent with the experimentally observed major 17 α -OH and minor 16 α -OH progesterone metabolites. The pregnenolone 3 β -OH hydrogen was also bonded to N202 and the C17 atom was 3.6 Å from the Compound I oxygen (Supplementary Fig. 4). However, the active site topology may be altered in the presence of substrates and this is an important area for further investigation.

CYP17A1 can be compared to three other P450 enzymes that are involved in steroidogenesis or cholesterol metabolism with reported steroid complex structures: CYP19A1 (aromatase)¹⁴, CYP11A1 (cholesterol side-chain cleavage enzyme)¹⁵ and CYP46A1, a cholesterol 24-hydroxylase¹⁶. Although all four enzymes maintain the canonical cytochrome P450 fold, CYP19A1, CYP11A1 and CYP46A1 orient steroids in the opposite direction from CYP17A1 so that the steroid ligands are positioned over the K–L loop directed towards the β 1 sheet (as shown for CYP11A1 in Fig. 4c) instead of oriented towards helices F and G.

More than 50 CYP17A1 mutations have been identified, and most of these were identified in patients with 17-hydroxylase deficiencies. The biochemical effects of many clinical mutations can be rationalized by examining the CYP17A1 structure (Supplementary Fig. 5 and Supplementary Table 2). Mutations R96W, R125Q, H373D/N and R440H/C all alter residues that directly interact with the haem propionates and probably disrupt haem binding, resulting in the complete loss of activity that was observed^{17–22}. Mutations E305G, R347H/C, R358Q and R449A eliminate only the lyase activity of CYP17A1^{23–25}. E305 forms a hydrogen bond to N202 in the active site, indicating a role in substrate positioning, whereas the other residues are on the proximal face of the protein (Supplementary Fig. 5), and this is consistent with their proposed role in cytochrome *b*₅ binding^{23,26}, which promotes lyase activity. Finally, reduction of the minor 16 α -hydroxyprogesterone metabolite is reported for the artificial mutation A105L²⁷, consistent with its location in the active site facing the β -face where the additional bulk may reduce the steroid movement within the active site.

Abiraterone and TOK-001 have several features that make them effective inhibitors of CYP17A1: first, a heterocyclic nitrogen that coordinates to the haem iron; second, a planar α -face to pack against the I helix; and third, hydrogen bonding interactions of 3 β -OH with conserved polar residues in a hydrogen binding network. These structures provide a model for the binding of substrates and other inhibitors that is very different from binding orientations that have previously been proposed by homology modelling and docking studies and from structures that have been demonstrated in other steroid-metabolizing cytochrome P450 enzymes. Perhaps most importantly, the cavity that is observed is not bilobed as predicted by many modelling studies^{28,29}. CYP17A1 interactions with these inhibitors are instead more reminiscent of steroid binding to steroid receptors, and this may be the origin of the TOK-001 dual mechanism of action. Thus, these structures contribute to a better understanding of the function and inhibition of CYP17A1 in a way that should substantially benefit the apprehension of enzyme dysfunction in clinical disease and enable structure-based drug design of CYP17A1 inhibitors for treating hormone-responsive cancers, particularly prostate cancer.

METHODS SUMMARY

A synthetic cDNA for human CYP17A1 was modified to delete residues 2–19, substitute the hydrophilic sequence Arg 20–Arg 21–Cys 22–Pro 23 with Ala 20–Lys 21–Lys 22–Thr 23 and add a carboxy-terminal four-histidine tag (Supplementary Fig. 6) before cloning into the pCWo⁺ plasmid and overexpression in *Escherichia*

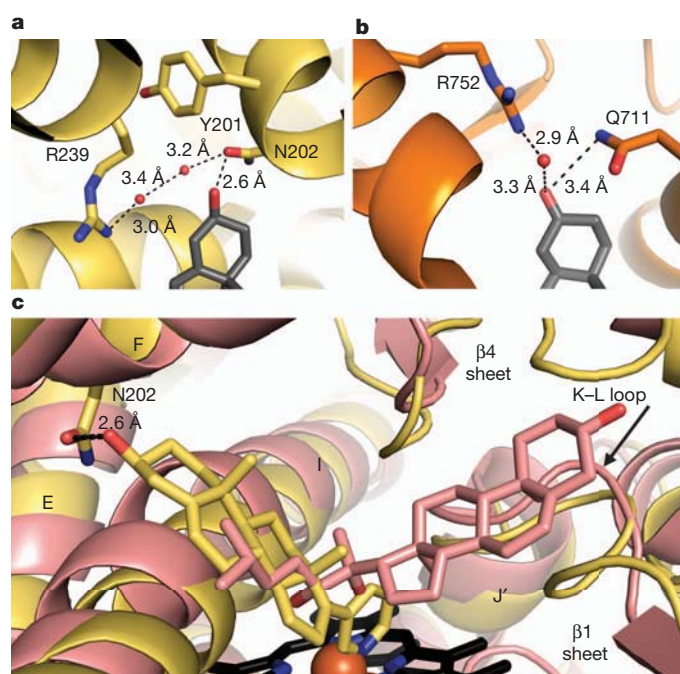


Figure 4 | CYP17A1 compared to the androgen receptor and CYP11A1. **a**, The hydrogen bonding network near the abiraterone 3 β -OH involves N202, R239 and conserved waters. **b**, The androgen receptor (PDB 3L3X) has a similar hydrogen bond network with R752, Q711 and several waters that interact with the dihydrotestosterone ketone. **c**, The structure of CYP17A1 with abiraterone (yellow) superimposed on the structure of CYP11A1 with 20,22-dihydroxycholesterol (PDB 3NA0, pink). This shows that there are markedly different steroid orientations between the two structures.

coli JM109 cells. Protein was purified by nickel affinity, cation exchange and size exclusion chromatography. Abiraterone was synthesized (see Methods). Binding affinities were determined using an ultraviolet–visible spectral shift assay. Progesterone 17 α -hydroxylation was evaluated using HPLC separation and ultraviolet detection. For crystallography, inhibitors were included throughout purification. Crystals were grown from CYP17A1 (30 mg ml⁻¹) complexed with inhibitor using hanging-drop vapour diffusion to equilibrate against 30% PEG 3350, 0.175 M Tris, pH 8.5, 0.30 M ammonium sulphate and 3% glycerol. Diffraction data were collected and phased by molecular replacement. Iterative model building and refinement generated the final model. Substrates were docked using Surflex-Dock.

Full Methods and any associated references are available in the online version of the paper at www.nature.com/nature.

Received 12 May; accepted 30 November 2011.

Published online 22 January 2012.

- Miller, W. L. & Auchus, R. J. The molecular biology, biochemistry, and physiology of human steroidogenesis and its disorders. *Endocr. Rev.* **32**, 81–151 (2011).
- Attard, G., Reid, A. H., Olmos, D. & de Bono, J. S. Antitumor activity with CYP17 blockade indicates that castration-resistant prostate cancer frequently remains hormone driven. *Cancer Res.* **69**, 4937–4940 (2009).
- Yap, T. A., Carden, C. P., Attard, G. & de Bono, J. S. Targeting CYP17: Established and novel approaches in prostate cancer. *Curr. Opin. Pharmacol.* **8**, 449–457 (2008).
- Vasaitis, T. S., Bruno, R. D. & Njar, V. C. CYP17 inhibitors for prostate cancer therapy. *J. Steroid Biochem. Mol. Biol.* **125**, 23–31 (2011).
- de Bono, J. S. et al. Abiraterone and increased survival in metastatic prostate cancer. *N. Engl. J. Med.* **364**, 1995–2005 (2011).
- Molina, A. & Belidegrun, A. Novel therapeutic strategies for castration resistant prostate cancer: inhibition of persistent androgen production and androgen receptor mediated signaling. *J. Urol.* **185**, 787–794 (2011).
- Auchus, R. J., Geller, D. H., Lee, T. C. & Miller, W. L. The regulation of human P450c17 activity: relationship to premature adrenarche, insulin resistance and the polycystic ovary syndrome. *Trends Endocrinol. Metab.* **9**, 47–50 (1998).
- Attard, G. et al. Phase I clinical trial of a selective inhibitor of CYP17, abiraterone acetate, confirms that castration-resistant prostate cancer commonly remains hormone driven. *J. Clin. Oncol.* **26**, 4563–4571 (2008).
- Brodie, A., Njar, V., Macedo, L. F., Vasitis, T. S. & Sabnis, G. The Coffey Lecture: steroidogenic enzyme inhibitors and hormone dependent cancer. *Urol. Oncol.* **27**, 53–63 (2009).
- Imai, T. et al. Expression and purification of functional human 17 α -hydroxylase/17,20-lyase (P450c17) in *Escherichia coli*. Use of this system for study of a novel form of combined 17 α -hydroxylase/17,20-lyase deficiency. *J. Biol. Chem.* **268**, 19681–19689 (1993).
- Huang, P., Chandra, V. & Rastinejad, F. Structural overview of the nuclear receptor superfamily: insights into physiology and therapeutics. *Annu. Rev. Physiol.* **72**, 247–272 (2010).
- Pereira de Jesus-Tran, K. et al. Comparison of crystal structures of human androgen receptor ligand-binding domain complexed with various agonists reveals molecular determinants responsible for binding affinity. *Protein Sci.* **15**, 987–999 (2006).
- Vasaitis, T. et al. Androgen receptor inactivation contributes to antitumor efficacy of 17 α -hydroxylase/17,20-lyase inhibitor 3 β -hydroxy-17-(1H-benzimidazole-1-yl)androsta-5,16-diene in prostate cancer. *Mol. Cancer Ther.* **7**, 2348–2357 (2008).
- Ghosh, D., Griswold, J., Erman, M. & Pangborn, W. Structural basis for androgen specificity and oestrogen synthesis in human aromatase. *Nature* **457**, 219–223 (2009).
- Mast, N. et al. Structural basis for three-step sequential catalysis by the cholesterol side chain cleavage enzyme CYP11A1. *J. Biol. Chem.* **286**, 5607–5613 (2011).
- Mast, N. et al. Crystal structures of substrate-bound and substrate-free cytochrome P450 46A1, the principal cholesterol hydroxylase in the brain. *Proc. Natl Acad. Sci. USA* **105**, 9546–9551 (2008).
- Dhir, V. et al. Steroid 17 α -hydroxylase deficiency: Functional characterization of four mutations (A174E, V178D, R440C, L465P) in the CYP17A1 gene. *J. Clin. Endocrinol. Metab.* **94**, 3058–3064 (2009).
- Rosa, S. et al. Clinical, genetic and functional characteristics of three novel CYP17A1 mutations causing combined 17 α -hydroxylase/17,20-lyase deficiency. *Horm. Res. Paediatr.* **73**, 198–204 (2010).
- Katsumata, N., Ogawa, E., Fujiwara, I. & Fujikura, K. Novel CYP17A1 mutation in a Japanese patient with combined 17 α -hydroxylase/17,20-lyase deficiency. *Metabolism* **59**, 275–278 (2010).
- Ergun-Longmire, B. et al. Two novel mutations found in a patient with 17 α -hydroxylase enzyme deficiency. *J. Clin. Endocrinol. Metab.* **91**, 4179–4182 (2006).
- Sahakitrungruang, T., Tee, M. K., Speiser, P. W. & Miller, W. L. Novel P450c17 mutation H373D causing combined 17 α -hydroxylase/17,20-lyase deficiency. *J. Clin. Endocrinol. Metab.* **94**, 3089–3092 (2009).
- Biason-Lauber, A. et al. 17 α -hydroxylase/17,20-lyase deficiency as a model to study enzymatic activity regulation: role of phosphorylation. *J. Clin. Endocrinol. Metab.* **85**, 1226–1231 (2000).
- Lee-Robichaud, P. et al. The cationic charges on Arg347, Arg358 and Arg449 of human cytochrome P450c17 (CYP17) are essential for the enzyme's cytochrome b₅-dependent acyl-carbon cleavage activities. *J. Steroid Biochem. Mol. Biol.* **92**, 119–130 (2004).
- Gupta, M. K., Geller, D. H. & Auchus, R. J. Pitfalls in characterizing P450c17 mutations associated with isolated 17,20-lyase deficiency. *J. Clin. Endocrinol. Metab.* **86**, 4416–4423 (2001).
- Tiosano, D. et al. Metabolic evidence for impaired 17 α -hydroxylase activity in a kindred bearing the E305G mutation for isolate 17,20-lyase activity. *Eur. J. Endocrinol.* **158**, 385–392 (2008).
- Auchus, R. J., Lee, T. C. & Miller, W. L. Cytochrome b₅ augments the 17,20-lyase activity of human P450c17 without direct electron transfer. *J. Biol. Chem.* **273**, 3158–3165 (1998).
- Swart, A. C., Storbeck, K. H. & Swart, P. A single amino acid residue, Ala 105, confers 16 α -hydroxylase activity to human cytochrome P450 17 α -hydroxylase/17,20-lyase. *J. Steroid Biochem. Mol. Biol.* **119**, 112–120 (2010).
- Haider, S. M., Patel, J. S., Poojari, C. S. & Neidle, S. Molecular modeling on inhibitor complexes and active-site dynamics of cytochrome P450 C17, a target for prostate cancer therapy. *J. Mol. Biol.* **400**, 1078–1098 (2010).
- Jagusich, C. et al. Synthesis, biological evaluation and molecular modelling studies of methyleneimidazole substituted biaryls as inhibitors of human 17 α -hydroxylase/17,20-lyase (CYP17). Part I: heterocyclic modifications of the core structure. *Bioorg. Med. Chem.* **16**, 1992–2010 (2008).

Supplementary Information is linked to the online version of the paper at www.nature.com/nature.

Acknowledgements X-ray data were collected at the Stanford Synchrotron Radiation Lightsource (SSRL). The SSRL Structural Molecular Biology Program is supported by the US Department of Energy Office of Biological and Environmental Research and by the US National Institutes of Health (NIH), National Center for Research Resources, Biomedical Technology Program and the National Institute of General Medical Sciences. We thank C.-J. Liu and the University of Kansas (KU) Center of Biomedical Research Excellence (COBRE) Center for Cancer Experimental Therapeutics for synthesizing abiraterone (NIH RR030926), M. R. Waterman for the full-length CYP17A1 construct, J. Wang for assistance with the Fe(IV)=O construct used in docking and A. Skinner and J. Aubé for manuscript suggestions. This research was funded by the NIH through the KU COBRE Center for Protein Structure and Function (NIH RR17708) and GM076343.

Author Contributions N.M.D. engineered, expressed, characterized, purified and crystallized CYP17A1 under the direction of E.E.S. N.M.D. and E.E.S. jointly performed X-ray diffraction experiments, solved and refined the structures, and wrote the manuscript. N.M.D. performed the docking studies of CYP17A1.

Author Information Atomic coordinates and structure factors for the reported crystal structures have been deposited with the Protein Data Bank under the accession codes 3RUK for CYP17A1 with abiraterone and 3SWZ for CYP17A1 with TOK-001. Reprints and permissions information is available at www.nature.com/reprints. The authors declare no competing financial interests. Readers are welcome to comment on the online version of this article at www.nature.com/nature. Correspondence and requests for materials should be addressed to E.E.S. (eescott@ku.edu).

METHODS

Synthesis and characterization of abiraterone. A stirred solution of 17-iodoandrosta-5,16-dien-3 β -ol (600 mg, 1.5 mmol) in tetrahydrofuran (20 ml) in a 100-ml round-bottomed flask was purged with argon. Bis(triphenylphosphine) palladium (II) chloride catalyst (11 mg, 0.016 mmol) and then diethyl(3-pyridyl) borane (265 mg, 1.8 mmol) were added. To the resultant orange solution, an aqueous solution of sodium carbonate (2 M, 5 ml) was added. The flask was fitted with a reflux condenser and the apparatus was purged again with argon. The mixture was then heated under reflux (at $\sim 80^\circ\text{C}$) and stirred for 4 days then allowed to cool. The mixture was poured into water and extracted with hot toluene (3×30 ml). The toluene extracts were dried (using Na_2CO_3) and concentrated. Column chromatography was performed with Et_2O and toluene (with a ratio of 1:2) as the eluent to give abiraterone (350 mg, 66%) as a white crystalline solid: melting point $228\text{--}230^\circ\text{C}$; IR O-H stretching frequency ν_{max} 3307 cm^{-1} ; ^1H NMR peak shifts in ppm (δ) 1.07 (s, 3, H-19), 1.09 (s, 3, H-18), 3.54 (m, 1, H-3 α), 5.41 (dm, 1, J = 5.2 Hz, H-6), 6.01 (m, 1, H-16), 7.24 (dd, 1, pyridyl H-5), 7.66 (dd, 1, pyridyl H-4), 8.47 (dd, 1, pyridyl H-6), 8.63 (d, 1, pyridyl H-2); ^{13}C NMR δ 151.69, 147.92, 147.84, 141.19, 133.68, 132.98, 129.24, 123.03, 121.32, 71.65, 57.56, 50.36, 47.34, 42.32, 37.19, 36.71, 35.26, 31.81, 31.64, 30.45, 20.88, 19.35, 16.59. The high resolution mass spectrum calculated the mass to charge ratio (m/z) $\text{C}_{24}\text{H}_{32}\text{NO}$ $[\text{M}+\text{H}]^+$ to be 350.2484. The experimental value was 350.2491. Abiraterone was 99% pure by liquid chromatography mass spectrometry.

CYP17A1 design, expression and purification. The human CYP17A1 cDNA was synthesized with codon optimization for *E. coli* expression (Blue Heron Biotechnology). A truncated and His-tagged construct was generated by truncation of the N-terminal transmembrane helix ($\Delta 2\text{--}19$), substitution of Arg 20-Arg 21-Cys 22-Pro 23 with Ala 20-Lys 21-Lys 22-Thr 23, and addition of a C-terminal four-residue histidine tag (Supplementary Fig. 6). N-terminal modifications were designed to increase solubility. This altered cDNA was inserted into the pCWori⁺ expression vector and expressed in *E. coli* JM109 cells.

Cells were grown, collected and disrupted, as described previously^{10,30}. After centrifugation (5,000g), CYP17A1 was solubilized with either 4.8 mM Cymal-5 (for crystallography; Affymetrix) or 2% Emulgen 913 (for assays; Desert Biologicals) and then underwent ultracentrifugation (80,000g) for 60 min. The lysate was loaded onto a nickel nitrilotriacetic acid agarose (Qiagen) column and purified, as reported elsewhere³⁰. Eluted CYP17A1 fractions were pooled, diluted fivefold with buffer A (50 mM Tris, pH 7.4, 20% glycerol, 100 mM glycine and 1 mM EDTA) and loaded on a HiTrap CM fast flow column (GE Healthcare). Protein was eluted in buffer A with 0.5 M NaCl, concentrated to ~ 1 ml, and loaded on a Superdex 200 16/60 size exclusion column (GE Healthcare). For crystallography, 10 μM abiraterone or TOK-001 (Shanghai Haoyuan Chemexpress) was added to all buffers.

Protein crystallization, data collection and structure determination. CYP17A1 crystals were grown using hanging-drop vapour diffusion equilibration. CYP17A1 (30 mg ml^{-1}) in buffer A supplemented with 10 μM abiraterone or TOK-001, 2.4 mM Cymal-5 and 0.5 M NaCl was equilibrated against 30% PEG 3350, 0.175 M Tris, pH 8.5, 0.30 M ammonium sulphate and 3% glycerol at 20°C . Crystals were cryoprotected in 7:1 mother liquor:ethylene glycol and flash cooled in liquid nitrogen. Native data sets were collected at 0.98 Å, 100 K at the Stanford Synchrotron Radiation Laboratory beamline 9-2. Data were processed using Mosflm³¹ and Scala³². The abiraterone complex was solved by molecular replacement using BALBES³³ with a final search model based on CYP2R1 (PDB 3CZH), and the TOK-001 structure was solved using Phaser³² with the abiraterone structure as a search model. Model building and refinement were accomplished iteratively using COOT³⁴ and Refmac³⁵ in CCP4³². Structure validation was performed using WHATCHECK³⁶ and PROCHECK³⁷. Ramachandran plot analysis reveals per cent favourable/additional allowed/generously allowed/disallowed residues are 86.3/13.2/0.5/0.0 (abiraterone structure) and 86.2/13.3/0.5/0.0 (TOK-001 structure). X-ray statistics are provided (Supplementary Table 1). Probe-occupied voids were

calculated using VOIDOO³⁸ (probe radius = 1.4 Å; grid mesh = 0.4 Å). All figures were prepared using MacPyMOL³⁹.

Docking. The CYP17A1 active site was defined as described for other cytochromes P450 (ref. 40) with the addition of an oxygen molecule directly coordinated to the haem to mimic compound I of the cytochrome P450 catalytic cycle. Substrate coordinates were prepared and energy was minimized with SYBYL (Tripos International). Charges were assigned using the Gasteiger and Marsili method. Surflex-Dock⁴¹ (Tripos International) was used to dock ligands as previously described³⁸. The active site was a 10 Å sphere around the haem and pregnenolone. Movement of pregnenolone within the active site was not substantial, with the distances from C17 to O=Fe(IV) as 4.5 Å, from C16 to O=Fe(IV) as 4.5 Å, and from C21 to O=Fe(IV) as 3.0 Å for the lowest energy pose.

Enzyme activity and IC_{50} determinations. Progesterone 17 α -hydroxylation was evaluated using a modified HPLC method with ultraviolet detection⁴². CYP17A1 (50 pmol) and rat NADPH-cytochrome P450 reductase⁴³ were mixed with a ratio of 1:4, incubated on ice (20 min) and added to buffer (50 mM Tris, pH 7.4 and 5 mM MgCl_2) containing progesterone (0–50 μM) to a total volume of 500 μl . Phosphatidylcholine (25 μg) was included for side-by-side kinetic comparisons with the full-length enzyme¹⁰. For IC_{50} determinations, inhibitor concentrations were 0–1.5 μM for abiraterone and 0–3.0 μM for TOK-001. After warming (37°C , 3 min), reactions were initiated by the addition of NADPH (20 μl 25 mM), incubated for 10 min (37°C), quenched with 20% trichloroacetic acid (300 μl) and placed on ice. The 17 α -hydroxyprogesterone metabolite was identified by ultraviolet detection at 248 nm after HPLC separation and co-eluted with authentic standards. The HPLC mobile phase was 40% acetonitrile, 60% water with 1% acetic acid and run at 1 ml min^{-1} (Luna (Phenomenex), 5 μm , C18, 50×4.6 mm).

Ligand binding assays. Ligand binding assays were based on spectral differences that were detected after ligand titration and were performed as described³⁸, except that the CYP17A1 concentration was 0.1 μM , the path length was 5 cm and the tight binding equation was used.

Functional data were analysed using Prism (GraphPad Software) and presented as mean \pm standard error.

- Pechurskaya, T. A., Lukashevich, O. P., Gilep, A. A. & Usanov, S. A. Engineering, expression, and purification of “soluble” human cytochrome P45017 α and its functional characterization. *Biochemistry* **73**, 806–811 (2008).
- Leslie, A. G. W. MOSFLM 6.0 (Cambridge, 1998).
- Collaborative Computational Project, Number 4. The CCP4 suite: programs for protein crystallography. *Acta Crystallogr. D* **50**, 760–763 (1994).
- Long, F., Vagin, A. A., Young, P. & Murshudov, G. N. BALBES: a molecular replacement pipeline. *Acta Crystallogr. D* **64**, 125–132 (2008).
- Emsley, P. & Cowtan, K. Coot: model-building tools for molecular graphics. *Acta Crystallogr. D* **60**, 2126–2132 (2004).
- Murshudov, G. N., Vagin, A. A. & Dodson, E. J. Refinement of macromolecular structures by the maximum-likelihood method. *Acta Crystallogr. D* **53**, 240–255 (1997).
- Hoof, R. W., Vriend, G., Sander, C. & Abola, E. E. Errors in protein structures. *Nature* **381**, 272 (1996).
- Laskowski, R. A., MacArthur, M. W., Moss, D. S. & Thornton, J. M. PROCHECK: a program to check the stereochemical quality of protein structures. *J. Appl. Crystallogr.* **26**, 283–291 (1993).
- DeVore, N. M. *et al.* Key residues controlling binding of diverse ligands to human cytochrome P450 2A enzymes. *Drug Metab. Dispos.* **37**, 1319–1327 (2009).
- DeLano, W. L. The PyMol Molecular Graphics System (DeLano Scientific, 2002).
- Kleywegt, G. J. & Jones, T. A. Detection, delineation, measurement and display of cavities in macromolecular structures. *Acta Crystallogr. D* **50**, 178–185 (1994).
- Jain, A. N. Surflex: fully automatic flexible molecular docking using a molecular similarity-based search engine. *J. Med. Chem.* **46**, 499–511 (2003).
- Hutschenreuter, T. U., Ehmer, P. B. & Hartmann, R. W. Synthesis of hydroxy derivatives of highly potent non-steroidal CYP 17 inhibitors as potential metabolites and evaluation of their activity by a non cellular assay using recombinant human enzyme. *J. Enzyme Inhib. Med. Chem.* **19**, 17–32 (2004).
- Shen, A. L., Porter, T. D., Wilson, T. E. & Kasper, C. B. Structural analysis of the FMN binding domain of NADPH-cytochrome P-450 oxidoreductase by site-directed mutagenesis. *J. Biol. Chem.* **264**, 7584–7589 (1989).

Creation and diagnosis of a solid-density plasma with an X-ray free-electron laser

S. M. Vinko¹, O. Ciricosta¹, B. I. Cho², K. Engelhorn², H.-K. Chung³, C. R. D. Brown⁴, T. Burian⁵, J. Chalupský⁵, R. W. Falcone^{2,6}, C. Graves⁷, V. Hájková⁵, A. Higginbotham¹, L. Juha⁵, J. Krzywinski⁷, H. J. Lee⁷, M. Messerschmidt⁷, C. D. Murphy¹, Y. Ping⁸, A. Scherz⁷, W. Schlotter⁷, S. Toleikis⁹, J. J. Turner⁷, L. Vysin⁵, T. Wang⁷, B. Wu⁷, U. Zastrau¹⁰, D. Zhu⁷, R. W. Lee⁷, P. A. Heimann², B. Nagler⁷ & J. S. Wark¹

Matter with a high energy density ($>10^5$ joules per cm^3) is prevalent throughout the Universe, being present in all types of stars¹ and towards the centre of the giant planets^{2,3}; it is also relevant for inertial confinement fusion⁴. Its thermodynamic and transport properties are challenging to measure, requiring the creation of sufficiently long-lived samples at homogeneous temperatures and densities^{5,6}. With the advent of the Linac Coherent Light Source (LCLS) X-ray laser⁷, high-intensity radiation ($>10^{17}$ watts per cm^2 , previously the domain of optical lasers) can be produced at X-ray wavelengths. The interaction of single atoms with such intense X-rays has recently been investigated⁸. An understanding of the contrasting case of intense X-ray interaction with dense systems is important from a fundamental viewpoint and for applications. Here we report the experimental creation of a solid-density plasma at temperatures in excess of 10^6 kelvin on inertial-confinement time-scales using an X-ray free-electron laser. We discuss the pertinent physics of the intense X-ray-matter interactions, and illustrate the importance of electron-ion collisions. Detailed simulations of the interaction process conducted with a radiative-collisional code show good qualitative agreement with the experimental results. We obtain insights into the evolution of the charge state distribution of the system, the electron density and temperature, and the time-scales of collisional processes. Our results should inform future high-intensity X-ray experiments involving dense samples, such as X-ray diffractive imaging of biological systems, material science investigations, and the study of matter in extreme conditions.

The experiment was performed at the LCLS soft X-ray materials science instrument (SXR), where a 1.0- μm -thick aluminium (Al) foil was irradiated with 80-fs X-ray pulses at photon energies in the range 1,560–1,830 eV (at and above the Al K edge). The LCLS pulse contained $\sim 10^{12}$ photons with an energy bandwidth of $\sim 0.4\%$. The X-ray pulse was focused by means of bendable Kirkpatrick-Baez mirrors, and the focal spot was characterized *ex situ* by analysing imprints in lead tungstate (ref. 9), indicating a spot size of $9.1 \pm 0.8 \mu\text{m}^2$, that is, a peak intensity of $1.1 \times 10^{17} \text{ W cm}^{-2}$. Aluminium was studied because it is a prototypical free-electron metal, presenting all the intricacies of a high-electron-density system, yet possessing a relatively simple atomic structure. Our main target diagnostic is X-ray emission spectroscopy, sensitive to recombination from the L to the K shell, that is, to Al K α emission, in the spectral range 1,460–1,680 eV.

The absorption process in the Al foil is dominated by K-shell photoabsorption, ejecting a core electron into the continuum, because the cross-section for L-shell and valence-band photoionization is over a factor 10 smaller. After photoionization, the filling of the K-shell hole proceeds mainly by KLL Auger decay, producing an ion with two holes in the L shell. Radiative emission accounts for the remaining 3.8% of

the total recombination from the L shell¹⁰. In Fig. 1 we plot the spectrally resolved X-ray emission over a range of excitation photon energies between 1,560 and 1,830 eV. The spectra show the main K α peak around 1,487 eV, followed by a series of peaks corresponding to emission from higher charge states due to a growing number of L-shell holes.

The observation of K α emission from highly charged ions in a dense system is not of itself novel, being routinely observed when charged-particle beams (such as ions or optical-laser-generated energetic electrons) interact with solid targets^{11–17}. However, our results differ from these experiments in two important ways. First, in our experiment the K-shell holes are created exclusively by intense, quasi-monochromatic X-ray photons rather than by collisions with broadband energetic particles. The main absorption process (creating K-shell holes) will therefore only take place in a particular ion if the photon energy lies above that ion's K edge, or, given that the X-rays are so intense, if a K electron is resonantly pumped to a vacant L-shell state. It follows that the X-ray free-electron laser (FEL) acts not only as a pump—exciting electrons and heating the system—but also as a selective probe, in that

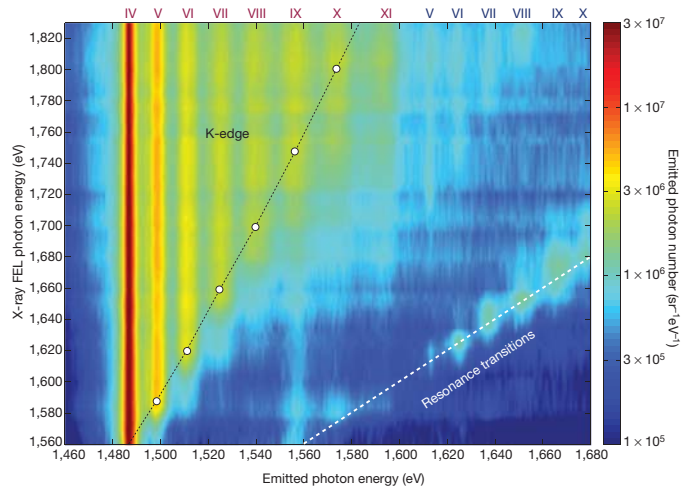


Figure 1 | Spectrally resolved K α emission as a function of the X-ray FEL excitation photon energy. The colour coding (bar on right) refers to the emission intensity on a logarithmic scale. Roman numerals (top) indicate the charge state of the emission peak: red, for states with a single K-shell hole; blue, for states with a double K-shell hole. Peaks around the resonance line (dashed white line, indicating where the FEL photon energy equals the emitted photon energy) correspond to emission from resonantly-pumped K–L transitions. Open circles, K edges for the various charge states calculated in the SCFLY code, which includes the ionization potential depression in the dense plasma according to a modified version of the Stewart-Pyatt model^{21,22}.

¹Department of Physics, Clarendon Laboratory, University of Oxford, Parks Road, Oxford OX1 3PU, UK. ²Lawrence Berkeley National Laboratory, 1 Cyclotron Road, California 94720, USA. ³Atomic and Molecular Data Unit, Nuclear Data Section, IAEA, PO Box 100, A-1400, Vienna, Austria. ⁴Plasma Physics Department, AWE Aldermaston, Reading RG7 4PR, UK. ⁵Institute of Physics ASCR, Na Slovance 2, 18221 Prague 8, Czech Republic. ⁶Department of Physics, University of California, Berkeley, California 94720, USA. ⁷SLAC National Accelerator Laboratory, 2575 Sand Hill Road, Menlo Park, California 94025, USA. ⁸Lawrence Livermore National Laboratory, 7000 East Avenue, Livermore, California 94550, USA. ⁹Deutsches-Elektronensynchrotron DESY, Notkestrasse 85, 22603 Hamburg, Germany. ¹⁰IQO, Friedrich-Schiller-Universität Jena, Max-Wien-Platz 1, 07743 Jena, Germany.

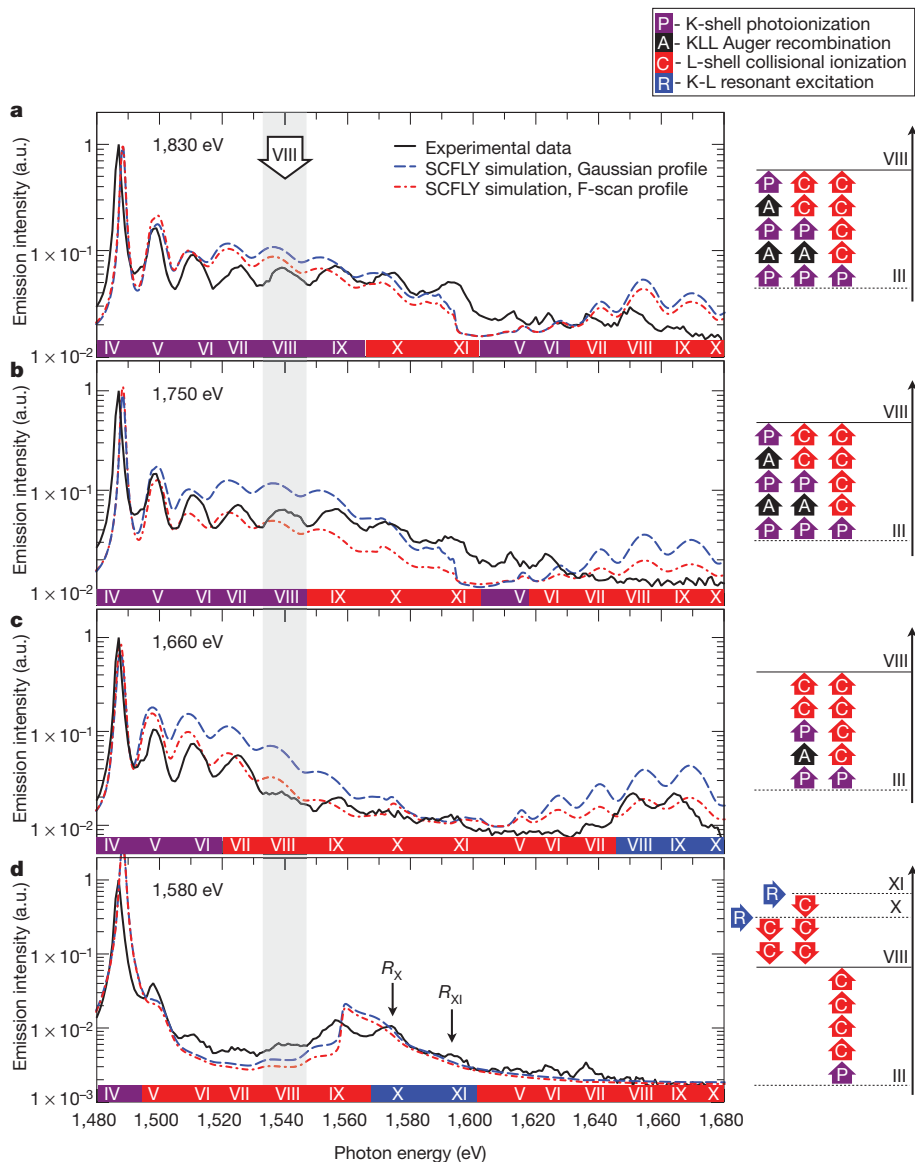


Figure 2 | Experimental and theoretical spectra, and charge-state emission pathways. Left, calculated emission spectra (dashed lines) according to the SCFLY code for four X-ray energies (a, 1,830 eV; b, 1,750 eV; c, 1,660 eV; d, 1,580 eV), compared with the experimental results presented in Fig. 1 (solid lines). The two simulation curves correspond to different X-ray intensity distributions on target: a Gaussian profile and the measured F-scan profile. Also shown (right) are the various pathways leading to emission from an ion with five L-shell holes in the final state (VIII), observed as the fifth emission peak: these pathways depend strongly on the wavelength of the X-ray excitation. R_X and R_{XI} correspond to emission from resonant transitions between K- and L-shell states in an ion containing seven or eight L-shell holes, respectively (states X and XI). Colour bars below each plot on left indicate the dominant mechanism contributing to the emission intensity for the various charge states (Roman numerals). a.u., arbitrary units.

the K-shell holes and subsequent $K\alpha$ emission only occur from a select range of ion charge states, depending on the FEL photon energy. As shown in Fig. 1, the range of ions from which we see K-shell emission is indeed strongly dependent on the energy of the incident photon: at photon energies just above the neutral K edge only a limited number of ionization stages is observed, whereas at the highest photon energy of 1,830 eV we observe all possible ionization stages corresponding to the filling of a single K-shell hole. In addition, at specific photon pump energies, we observe emission from resonantly pumped single- and double-hole K-shell states, marked as resonance transitions in Fig. 1. We label all emission peaks according to their K- and L-shell charge state (the three M-shell electrons are free-electron-like in ground-state Al): that is, the main $K\alpha$ peak corresponds to charge state IV and the higher energy peaks correspond to states in the range V–XI. The second important difference to note is that in our experiment the population of L-shell states, and the charge state distribution (CSD), is seen to be determined predominantly by electron–ion collisional processes within the heated dense system, rather than directly by the X-ray pulse. Therefore, provided the photon energy is sufficiently high to satisfy the probe condition described above for all charge states, the $K\alpha$ emission spectrum contains information on the CSD of the hot system, on the electron temperature and on electron–ion collision rates (best observed in the case of resonances where not one but several emission peaks are observed at a single pump energy).

This pivotal role of collisions in determining the observed spectra and the CSD is evinced by two main features in the data. The first is the relatively uniform intensity of the $K\alpha$ emission as a function of charge state. For isolated atoms, successive sequential photoionization of the K-shell occurs, with the dominant ionization pathway being a P-A-P-A... process (where P indicates photoionization, and A Auger decay)⁸. As each P-A sequence results in two electrons being ejected from the L shell, the populations of ions with an even number of ejected electrons dominate over those with an odd number ejected. In contrast, for the solid-density system, the dynamics are distinctly different, and we observe no odd–even asymmetry in the $K\alpha$ emission. This is due to the high electron–ion collision rates, which compete with both the P and A processes. Our simulations (below) show that the collisional and Auger rates are comparable at the peak of the pulse at the highest intensities. The second piece of evidence for the important role of collisions is the observation of emission corresponding to resonantly pumped single and double-core-hole states in ion stages for which direct photo-ionization of a K-shell electron is energetically forbidden. As the number of electrons in the L shell decreases, the reduced screening results in tighter binding of the K electrons, increasing the K-edge energy as a function of ion stage (see Fig. 1). Thus, for a particular photon energy, the ejection of a K electron is only possible up to a certain ion stage, explaining the observed fundamental trend where $K\alpha$ emission is seen from higher charge states as the photon energy is

increased. Nevertheless, this principle can be violated, as the density is so high that additional collisional ionization occurs, promoting further L electrons to the continuum (in addition to those ionized by Auger recombination). Such collisional ionization takes place for ions with two K electrons present and, importantly, is also sufficiently rapid that it can produce further L-shell vacancies in ions already containing a K-shell hole (that is, after photoabsorption, yet before Auger or radiative decay). In the former case, ions with K-edge energies higher than the incident photon energy can be created, but further photo-excitation of K-shell electrons to the continuum for these ions is no longer possible, as the K edge exceeds the photon energy. In the latter case, two interesting effects arise.

First, some $K\alpha$ emission is still seen from ion stages which have K-edge energies higher than the photon energy, via a process whereby photo-excitation of the K shell occurs at a lower ion stage, collisions ionize further L-shell electrons in the presence of the K-shell hole, then radiative decay occurs producing $K\alpha$ emission. This effect can be seen in Fig. 1 by comparing the spectrum for a given LCLS photon energy with the calculated energy of the K edge for a particular ion stage. Although accurate independent measurements of the K-edge positions in these hot-dense conditions are not available (we note that our results provide some information in this regard, albeit blurred by strong collisional effects), forcing us to rely on computational modelling, we note that in order to explain the spectra in terms of a K-edge shift alone in the absence of collisional ionization, the calculated shifts would need to be incorrect by several hundred electron volts for the highest charge states. Such a large discrepancy is implausible, but more importantly, would also lead to severely inconsistent simulation results for the emission spectrum. We further note that this observation also cannot be explained by multi-photon ionization, which scales with the square of wavelength, and is negligible even at these intensities in the X-ray regime.

Second, resonant photo-pumping of K-shell electrons to the L shell (rather than to the continuum) is energetically permitted for ions with both a single and a double K-shell hole in the final state. Radiative decay of these states produces the resonance emission highlighted in Fig. 1. Such emission appears prominently for states with two holes in the K-shell (marked as V–X for X-ray excitation in the range 1,600–1,680 eV), as well as from highly ionized states with a single K-shell hole (emission from peaks X and XI at excitation energies around 1,580 eV). In particular, we note that several peaks are observed on resonance rather than just one, indicating that the collisional rates are similar to, or larger than, Auger recombination rates.

To further interpret our results, we have performed time-dependent population kinetics calculations, using the SCFLY code¹⁸. These

simulations provide atomic level populations, CSDs, emission spectra, total absorbed energies and electron temperatures. The calculations are based on a rate-equation model that includes sequential single-photon absorption, spontaneous and stimulated emission, collisional excitation, ionization and their inverses, as well as the effects of opacity via an escape-factor formalism. We plot the calculated spectra for four X-ray excitation energies compared with our experimental measurements in Fig. 2. The interaction processes leading to the observed emission from a specific charge state (VIII) are shown alongside for the four X-ray photon energies, illustrating the different pathways resulting from a combination of direct K-shell photoionization, electron collisional ionization and resonant K–L transitions. We note that the emission intensity from the various charge states is not trivially related to the population of those charge states.

The simulated spectra successfully reproduce the experimental trends in a qualitative manner, however, quantitative differences can still be observed for several charge state emission intensities. This is in part due to uncertainties in the experimental intensity distribution on target, which is challenging to accurately account for (illustrated by the two simulation curves in Fig. 2, corresponding to different spatial profiles), in part to the simplifications made necessary for an efficient atomic-kinetics code, but mostly to uncertainties regarding fundamental physical parameters in warm and hot dense systems, such as the rates for inner-shell transitions, collisional ionization, Auger recombination in highly ionized hollow atoms, and the ionization potential depression. This last point regarding physical parameters is particularly acute in the case of emission from double-core-hole states, where the agreement between experiment and simulation is poorest. Nonetheless, given the qualitative agreement with the spectra and the straightforward energy absorption mechanism, the combined effect of these uncertainties on the basic thermodynamic quantities is not expected to be significant. The calculated electron temperature, free-electron density and CSD are shown in Fig. 3. Temperatures in excess of 100 eV are found, which do not depend strongly on the excitation wavelength. Further, higher X-ray photon energies invariably yield higher temperatures by the end of the pulse, despite having an initially lower absorption cross-section. This can be explained by thermal collisions governing the CSD: as the temperature rises, low charge states are depleted and higher-energy X-rays, which couple more efficiently to higher charge state transitions, deposit more energy in the system. To quantitatively evaluate this collisional effect, we illustrate in Fig. 4 the photoionization, Auger recombination and collisional ionization rates as a function of time for transitions populating and de-populating the single-core-hole charge state VII. We observe that by the peak of the pulse, at temperatures above 100 eV, electron–ion collisional

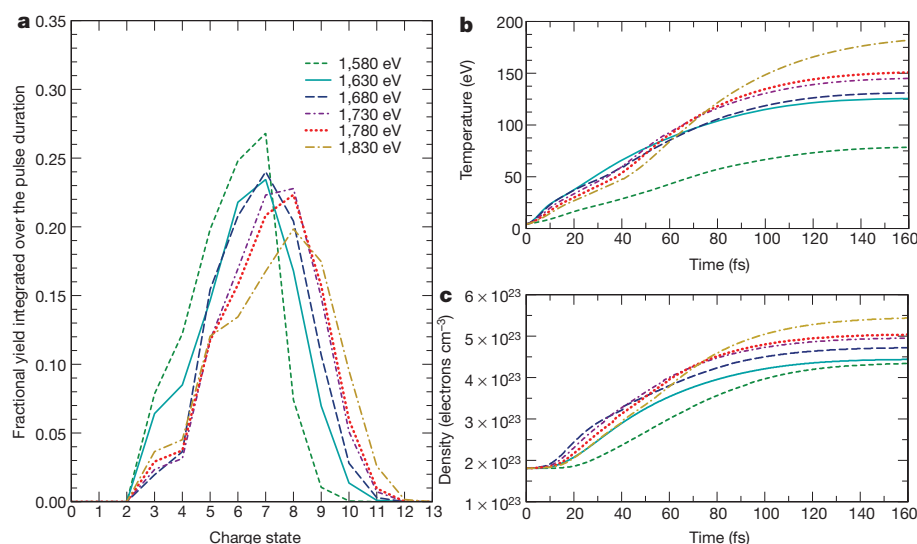


Figure 3 | Temperature, density and charge state distribution at peak intensity. **a**, Calculated charge state distribution, integrated over the duration of a temporally Gaussian pulse. The calculations correspond to the centre of the X-ray spot, at the highest spatial intensities. **b**, **c**, The temperature (**b**) and density (**c**) of the electronic system over a range of excitation energies. The peak of the X-ray pulse is centred at 80 fs, with a FWHM of 80 fs.

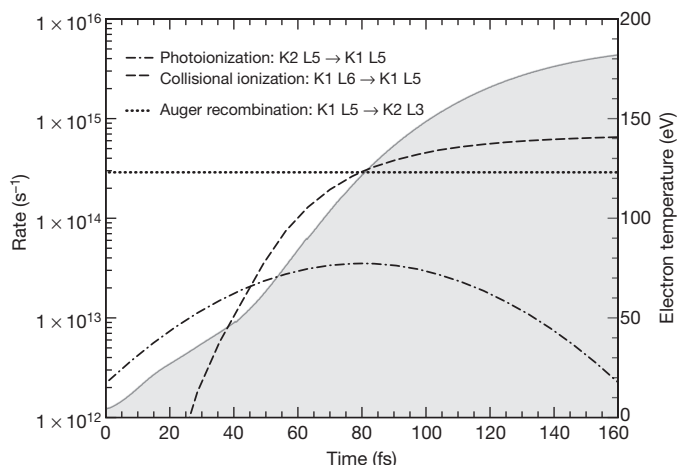


Figure 4 | Rates for atomic and collisional processes. Comparison between K-shell photoionization, collisional ionization and Auger recombination rates (broken curves, left-hand vertical axis) involved in populating and depopulating charge state VII at an X-ray photon energy of 1,830 eV. This state is one of the most populated for conditions leading to a peak temperature of ~ 100 eV. The calculation is conducted with a Gaussian beam (80 fs FWHM) centred at 80 fs. The electron temperature is given by the solid curve with grey shading under (right-hand vertical axis). By the peak of the pulse at 80 fs, the collisional ionization rate exceeds all others, dominating the population dynamics.

processes dominate the evolution of the CSD, and the dynamics of the system is determined by its temperature rather than by the intense X-ray excitation field. This result is fully consistent with our experimental results shown in Fig. 1.

Finally, in the context of creating well-defined states of matter in extreme conditions, we note that the duration of the pulse, heating of the electrons, photoionization and Auger decay are all rapid processes compared with atomic motion and hydrodynamic expansion of the target. For example, an aluminium ion at 150 eV travels only 5 nm in 100 fs, and thus a crude estimate of the hydrodynamic expansion time would be 20 ps for a 1 μm target. Given that electron-ion relaxation times are expected to be less than 10 ps (ref. 19), these results bode well for the creation of uniform-density hot and warm dense matter.

METHODS SUMMARY

A schematic illustration of the experimental set-up is given in Supplementary Fig. 1. The spectroscopy was conducted by means of a flat ammonium dihydrogen phosphate crystal (ADP) in the $\langle 101 \rangle$ orientation with a spectral resolution of 0.9–1.3 eV across the photon energy range of interest. All spectroscopic data were collected in single-shot acquisition mode, with a fresh region of the target exposed for every shot. Figure 1 was obtained by binning a total of around 550 single-shot spectra according to the measured X-ray photon energy in 5-eV bins.

Simulations of the experimental emission were conducted using an adapted version of the collisional-radiative code SCFLY¹⁸, which is based on the widely available FLYCHK simulation suite²⁰. SCFLY solves the rate equations for non-LTE (local thermal equilibrium) plasmas using a super-configuration description of the atomic structure of the system and provides a spectral module, which uses the computed level populations to calculate the X-ray emission spectra. Several important improvements have been included to make SCFLY applicable to X-ray FEL-driven systems: an increased number of super-configurations, the inclusion of hollow atoms and a self-consistent, absorption-driven temperature calculation. Each calculation provides an emission spectrum for a single X-ray intensity. To account for the experimental intensity distribution on target, 26 simulations covering the full range of probed intensities were computed for each X-ray excitation energy. The final spectra are obtained by averaging these over the three-dimensional interaction region, weighted according to the intensity distribution profile measured by the imprints technique in lead tungstate (PbWO_4). This intensity distribution, named the F-scan profile, which is obtained following the method described in ref. 9, is compared to the Gaussian intensity distribution consistent with the measured spot size (full-width at half-maximum, FWHM) in Fig. 2.

Full Methods and any associated references are available in the online version of the paper at www.nature.com/nature.

Received 27 August; accepted 29 November 2011.

Published online 25 January 2012.

1. Taylor, R. J. *The Stars: Their Structure and Evolution* 2nd edn (Cambridge Univ. Press, 1994).
2. Chabrier, G. Plasma physics and planetary astrophysics. *Plasma Phys. Contr. Fusion* **51**, 124014 (2009).
3. Helled, R., Anderson, J. D., Podolak, M. & Schubert, G. Interior models of Uranus and Neptune. *Astrophys. J.* **726**, 15 (2011).
4. Lindl, J. Development of the indirect-drive approach to inertial confinement fusion and the target physics basis for ignition and gain. *Phys. Plasmas* **2**, 3933–4024 (1995).
5. Remington, B. A., Drake, R. P. & Ryutov, D. D. Experimental astrophysics with high power lasers and Z pinches. *Rev. Mod. Phys.* **78**, 755–807 (2006).
6. Nagler, B. et al. Turning solid aluminium transparent by intense soft X-ray photoionization. *Nature Phys.* **5**, 693–696 (2009).
7. Linac Coherent Light Source. <https://lcls.slac.stanford.edu> (2011).
8. Young, L. et al. Femtosecond electronic response of atoms to ultra-intense X-rays. *Nature* **466**, 56–61 (2010).
9. Chalupský, J. et al. Spot size characterization of focused non-Gaussian X-ray laser beams. *Opt. Express* **18**, 27836–27845 (2010).
10. Bambynek, W. et al. X-Ray fluorescence yields, Auger, and Coster-Kronig transition probabilities. *Rev. Mod. Phys.* **44**, 716–813 (1972).
11. Saemann, A. et al. Isochoric heating of solid aluminum by ultrashort laser pulses focused on a tapered target. *Phys. Rev. Lett.* **82**, 4843–4846 (1999).
12. Rossall, A. K. et al. X-ray back-lighter characterization for iron opacity measurements using laser-produced aluminium K-alpha emission. *J. Phys. At. Mol. Opt. Phys.* **43**, 155403 (2010).
13. Bailey, J. et al. Observation of K α X-ray satellites from a target heated by an intense ion beam. *Laser Part. Beams* **8**, 555–562 (1990).
14. Burnett, N. H., Enright, G. D., Avery, A., Loen, A. & Kieffer, J. C. Time-resolved K α spectra in high-intensity laser-target interaction. *Phys. Rev. A* **29**, 2294–2297 (1984).
15. Back, C. A. et al. Study of K α absorption structures in a subcritical-density laser-produced plasma. *Phys. Rev. A* **46**, 3405–3412 (1992).
16. Rousse, A. et al. Efficient K α x-ray source from femtosecond laser-produced plasmas. *Phys. Rev. E* **50**, 2200–2207 (1994).
17. Gauthier, J.-C. et al. Theoretical and experimental studies of laser-produced plasmas driven by high-intensity femtosecond laser pulses. *Phys. Plasmas* **4**, 1811–1817 (1997).
18. Chung, H.-K., Chen, M. H. & Lee, R. W. Extension of atomic configuration sets of the non-LTE model in the application to the K α diagnostics of hot dense matter. *High Energy Density Phys.* **3**, 57–64 (2007).
19. Siwick, B. J., Dwyer, J. R., Jordan, R. E. & Miller, R. J. D. An atomic-level view of melting using femtosecond electron diffraction. *Science* **302**, 1382–1385 (2003).
20. Chung, H.-K., Chen, M. H., Morgan, W. L., Ralchenko, Y. & Lee, R. W. FLYCHK: Generalized population kinetics and spectral model for rapid spectroscopic analysis for all elements. *High Energy Density Phys.* **1**, 3–12 (2005).
21. Stewart, J. C. & Pyatt, K. D. Jr. Lowering of ionization potentials in plasmas. *Astrophys. J.* **144**, 1203–1211 (1966).
22. Chung, H.-K., Lee, R. W., Chen, M. H. & Ralchenko, Y. *The How To for FLYCHK* (NIST, 2008).

Supplementary Information is linked to the online version of the paper at www.nature.com/nature.

Acknowledgements Portions of this research were carried out on the SXR instrument at the LCLS, a division of SLAC National Accelerator Laboratory and an Office of Science user facility operated by Stanford University for the US Department of Energy. The SXR instrument and the Resonant Coherent Imaging (RCI) endstation are funded by a consortium whose membership includes the LCLS, Stanford University through the Stanford Institute for Materials Energy Sciences (SIMES), Lawrence Berkeley National Laboratory (LBNL), University of Hamburg through the BMBF priority programme FSP 301, and the Center for Free Electron Laser Science (CFEL). S.M.V., O.C. and J.S.W. thank the UK EPSRC for funding (EP/F020449/1 and EP/H035877/1). B.I.C., K.E., R.W.F. and P.A.H. acknowledge US DOE Basic Energy Science contract DE-AC03-76SF00098 and SSAA programme contract DE-FG52-06NA26212. T.B., J.C., L.J. and L.V. appreciate funding by grants LC510, LC528, LA08024, ME10046, P108/11/1312, P205/11/0571, IAAX00100903 and KAN300100702. U.Z. thanks the German Ministry for Education and Research (BMBF) for funding under FSP 301. C.D.M. was supported by UK EPSRC (EP/G007187/1). We also thank G. Gregori (Oxford University) for discussions.

Author Contributions S.M.V., B.I.C., K.E., C.R.D.B., A.H., H.J.L., C.D.M., Y.P., S.T., U.Z., P.A.H., B.N. and J.S.W. performed the experiment and acquired the data. B.I.C., K.E., R.W.F. and P.A.H. analysed the data. S.M.V., O.C., H.-K.C., R.W.L. and J.S.W. performed the theoretical work. S.M.V., R.W.L. and J.S.W. wrote the paper. M.M., W.S. and J.J.T. operated the SXR beamline and the LCLS diagnostics. C.G., A.S., T.W., B.W. and D.Z. operated the RCI endstation. T.B., J.C., V.H., L.J., J.K. and L.V. performed the spot-size characterisation and analysis. All authors contributed to the work presented here and to the final paper.

Author Information Reprints and permissions information is available at www.nature.com/reprints. The authors declare no competing financial interests. Readers are welcome to comment on the online version of this article at www.nature.com/nature. Correspondence and requests for materials should be addressed to S.M.V. (sam.vinko@physics.ox.ac.uk).

METHODS

Experimental set-up. During the experiment, the total pulse energy was recorded on a shot-to-shot basis using a gas detector in the LCLS front-end enclosure. We measured an average pulse energy of 0.8–1.4 mJ, depending on the photon wavelength. Approximately 30–34% of this energy is delivered to the target owing to the transmission of the beamline optics between the gas detector and the Resonant Coherent Imaging (RCI) experimental chamber²³. During the course of the experiment, we scanned a photon energy range of 1,580–1,830 eV. The photon energy values are derived from the electron beam energies provided by the LCLS online diagnostics, the values of which were calibrated at the Al K edge both before and after the data acquisition. This method provides an accuracy of better than 5 eV in the absolute calibration, and is approximately constant over the entire range of energies investigated.

Data analysis. The noise filtering for the data analysis was conducted by analysing the number of counts per CCD (charge-coupled device) pixel: photons of 1,600 eV are seen to produce approximately 150 counts above the thermal noise level on the CCD detector, which is sufficient to isolate the signal and reduce the noise considerably. Any change in beam position on the sample will alter the crystal diffraction angle slightly, causing a shift in where wavelengths are mapped on to the detector. We have accounted for this positioning jitter effect by cross-correlating each single shot with the average spectrum and adjusting the positions of the $K\alpha$ satellite peaks accordingly to overlap. The wavelength axis of the final spectrum is then calibrated by fitting the positions of the main $K\alpha$ peak and its satellites to previously published values¹³. This eliminates the need to use geometric considerations to map the detector pixels to wavelength and is considerably more accurate. We did not measure the temporal profile of the LCLS beam or the pulse length. Instead, the LCLS electron bunch length was measured (80 fs FWHM) and assumed to be a good indication of the X-ray pulse duration. However, this value should only be considered as an upper bound on the pulse duration, with recent experiments reporting results consistent with 2–3 times shorter pulses^{8,24}.

Modelling. Simulations of the experimental emission were conducted using the SCFLY code^{18,20} adapted to simulate FEL-driven systems. It has recently been reported that these modifications enable SCFLY to successfully simulate X-ray–matter interactions in the non-collisional regime limit²⁵. For the work presented here, which extends this study to the highly collisional regime, a complete set of super-configurations for all ionic species of aluminium up to the $n = 3$ shell are considered in the code. We have further verified that the spectrum exhibits a negligible dependence on the temporal structure of the X-ray pulse, provided the total fluence is constant, by comparing calculated spectra obtained by using a Gaussian temporal profile with a simulated self-amplified spontaneous emission FEL pulse of equal duration and fluence, following ref. 26.

The energies used in the simulations are calculated according to the relativistic configuration average model following a Dirac–Hartree–Slater method²⁷. The agreement in peak position that can be observed between simulation and experiment, within ~ 3 eV (0.2%) for the highest charge states, was deemed sufficient within the context of our investigation. It can however be improved on by using a fine structure model for the energy levels, albeit at a significant additional computational cost.

23. Sorokin, A. A., Jastrow, U., Juranić, P., Kapitzki, S. & Tiedtke, K. *Report on Pulse Energy Monitoring at the SXR Beamline Using Gas-Monitor Detectors* (Technical report, SLAC, 2010).
24. Düsterer, S. *et al.* Femtosecond x-ray pulse length characterization at the Linac Coherent Light Source free-electron laser. *New J. Phys.* **13**, 093024 (2011).
25. Cericosta, O., Chung, H.-K., Lee, R. W. & Wark, J. S. Simulations of neon irradiated by intense X-ray laser radiation. *High Energy Density Phys.* **7**, 111–116 (2011).
26. Bonifacio, R., De Salvo, L., Pierini, P., Piovella, N. & Pellegrini, C. Spectrum, temporal structure, and fluctuations in a high-gain free-electron laser starting from noise. *Phys. Rev. Lett.* **73**, 70–73 (1994).
27. Chen, M. H., Crasemann, B. & Mark, H. Relativistic K-shell Auger rates, level widths, and fluorescence yields. *Phys. Rev. A* **21**, 436–441 (1980).

Gated regulation of CRAC channel ion selectivity by STIM1

Beth A. McNally¹, Agila Somasundaram¹, Megumi Yamashita¹ & Murali Prakriya¹

Two defining functional features of ion channels are ion selectivity and channel gating. Ion selectivity is generally considered an immutable property of the open channel structure, whereas gating involves transitions between open and closed channel states, typically without changes in ion selectivity¹. In store-operated Ca^{2+} release-activated Ca^{2+} (CRAC) channels, the molecular mechanism of channel gating by the CRAC channel activator, stromal interaction molecule 1 (STIM1), remains unknown. CRAC channels are distinguished by a very high Ca^{2+} selectivity and are instrumental in generating sustained intracellular calcium concentration elevations that are necessary for gene expression and effector function in many eukaryotic cells². Here we probe the central features of the STIM1 gating mechanism in the human CRAC channel protein, ORAI1, and identify V102, a residue located in the extracellular region of the pore, as a candidate for the channel gate. Mutations at V102 produce constitutively active CRAC channels that are open even in the absence of STIM1. Unexpectedly, although STIM1-free V102 mutant channels are not Ca^{2+} -selective, their Ca^{2+} selectivity is dose-dependently boosted by interactions with STIM1. Similar enhancement of Ca^{2+} selectivity is also seen in wild-type ORAI1 channels by increasing the number of STIM1 activation domains that are directly tethered to ORAI1 channels, or by increasing the relative expression of full-length STIM1. Thus, exquisite Ca^{2+} selectivity is not an intrinsic property of CRAC channels but rather a tuneable feature that is bestowed on otherwise non-selective ORAI1 channels by STIM1. Our results demonstrate that STIM1-mediated gating of CRAC channels occurs through an unusual mechanism in which permeation and gating are closely coupled.

Functional CRAC channels are tetramers of ORAI1 subunits^{3–5}, with the pore flanked by residues of the first transmembrane domain (TM1) of each subunit^{6,7} (Fig. 1a). To localize the gate region that governs STIM1-dependent activation, we mutated individual pore-lining residues to Cys and analysed state-dependent differences in the sensitivity of mutant channels to methanethiosulphonate (MTS) Cys-reactive reagents^{6,8}. Because the unusually narrow CRAC channel pore^{9,10} prevents entry of the relatively large MTS reagents⁶, we performed these studies in the E106D ORAI1 mutant, which has a wider pore yet maintains store-dependent activation¹⁰. With this as a background, several TM1 pore-lining residues, including V102C and G98C, became accessible to the small MTS reagent, MTSEA, with G98C showing particularly strong sensitivity to this reagent (Fig. 1 and Supplementary Fig. 1). Inhibition of G98C by MTSEA could be protected by La^{3+} (Fig. 1b, d), which blocks CRAC channels by binding to residues in the outer vestibule⁶, and this is consistent with modification of G98C occurring from within the pore.

To determine differences in MTSEA accessibility between closed and open channels, we quantified the relief of MTSEA blockade that was elicited by the reducing agent bis(2-mercaptoethyl)sulphone (BMS)⁶. Resting cells were exposed to MTSEA for 100–120 s and subsequently, CRAC current (I_{CRAC}) was activated by passive store depletion (Fig. 1c). These experiments indicated that modification of

G98C was profoundly state-dependent, with no modification occurring in closed channels (Fig. 1c, e). By contrast, D110C, a pore-lining residue located in the outer vestibule, was modified to similar extents in both closed and open states (Fig. 1e). The most straightforward explanation for this result is that the closed channel conformation prevents access of MTSEA to G98C, suggesting that the gate is located externally to G98 but below D110. As the key pore-lining TM1 residues in this region are E106 and V102, the gated access of G98C implicates these residues as potential candidates for the gate. E106 controls Ca^{2+} selectivity^{11–13} and is not thought to regulate store-operated gating¹⁰, leaving V102 as the most promising residue for further study.

Previous reports suggest that V102 is located very close to the central symmetry axis of the channel^{6,7}, that is, in a narrow constriction of the pore. If V102 is a component of the gating mechanism, mutations at this locus would be predicted to destabilize channel gating. Consistent with this possibility, a Cys mutation of V102 eliminated store-dependent gating. Cells expressing V102C ORAI1 and STIM1 displayed a large standing I_{CRAC} after whole-cell break-in (Fig. 2a). Moreover, resting cells exhibited constitutive Ca^{2+} entry and activation of the Ca^{2+} -dependent nuclear factor of activated T cell (NFAT) transcription factor (Supplementary Fig. 2), indicating that V102C ORAI1 channels are constitutively active.

Several lines of evidence indicated that the constitutive activation of V102C ORAI1 is STIM1-independent. Large La^{3+} -sensitive standing currents were seen in cells expressing V102C ORAI1 alone (Fig. 2b). Furthermore, Ca^{2+} imaging and NFAT activation experiments revealed constitutive Ca^{2+} entry in these cells (Fig. 2c and Supplementary Fig. 2c). Recent evidence indicates that STIM1 drives the redistribution of ORAI1 into discrete puncta after endoplasmic reticulum (ER) store depletion². However, when expressed alone, V102C ORAI1 remained diffusely distributed in the plasma membrane (Fig. 2d). Moreover, I_{CRAC} in these cells did not show Ca^{2+} -dependent fast inactivation (CDI) (Supplementary Fig. 3). Because puncta formation and CDI require STIM1 (ref. 14–16), these results indicate that when over-expressed alone, the mutant channels are functionally free of STIM1. Consistent with this interpretation, knockdown of endogenous STIM1 in HEK293 cells did not affect the constitutive V102C current (Supplementary Table 1). However, when V102C ORAI1 was co-expressed with STIM1, puncta formation, interaction with STIM1, and CDI were indistinguishable from the behaviour of wild-type ORAI1 (Fig. 2d and Supplementary Figs 3 and 4). Additional analyses indicated that introducing the mutations E106A or R91W, which abrogate store-operated ORAI1 activity^{11,12,17}, strongly diminished V102C ORAI1 currents (Supplementary Fig. 5a), indicating that these residues are essential for both store-operated and constitutive activation modes of ORAI1. Mutation of the equivalent residue in Orai3 (V77C) also resulted in a STIM1-independent activation phenotype similar to that seen in V102C ORAI1 (Supplementary Fig. 6). Together, these results indicate that the V102C mutation destabilizes the channel gate, resulting in STIM1-independent constitutive ORAI1 activation.

Many ion channels including nicotinic acetylcholine receptors and the mechanosensitive channel MscL are reported to use hydrophobic

¹Department of Molecular Pharmacology and Biological Chemistry, Northwestern University School of Medicine, 303 E Chicago Avenue, Ward 8-296, Chicago, Illinois 60611, USA.

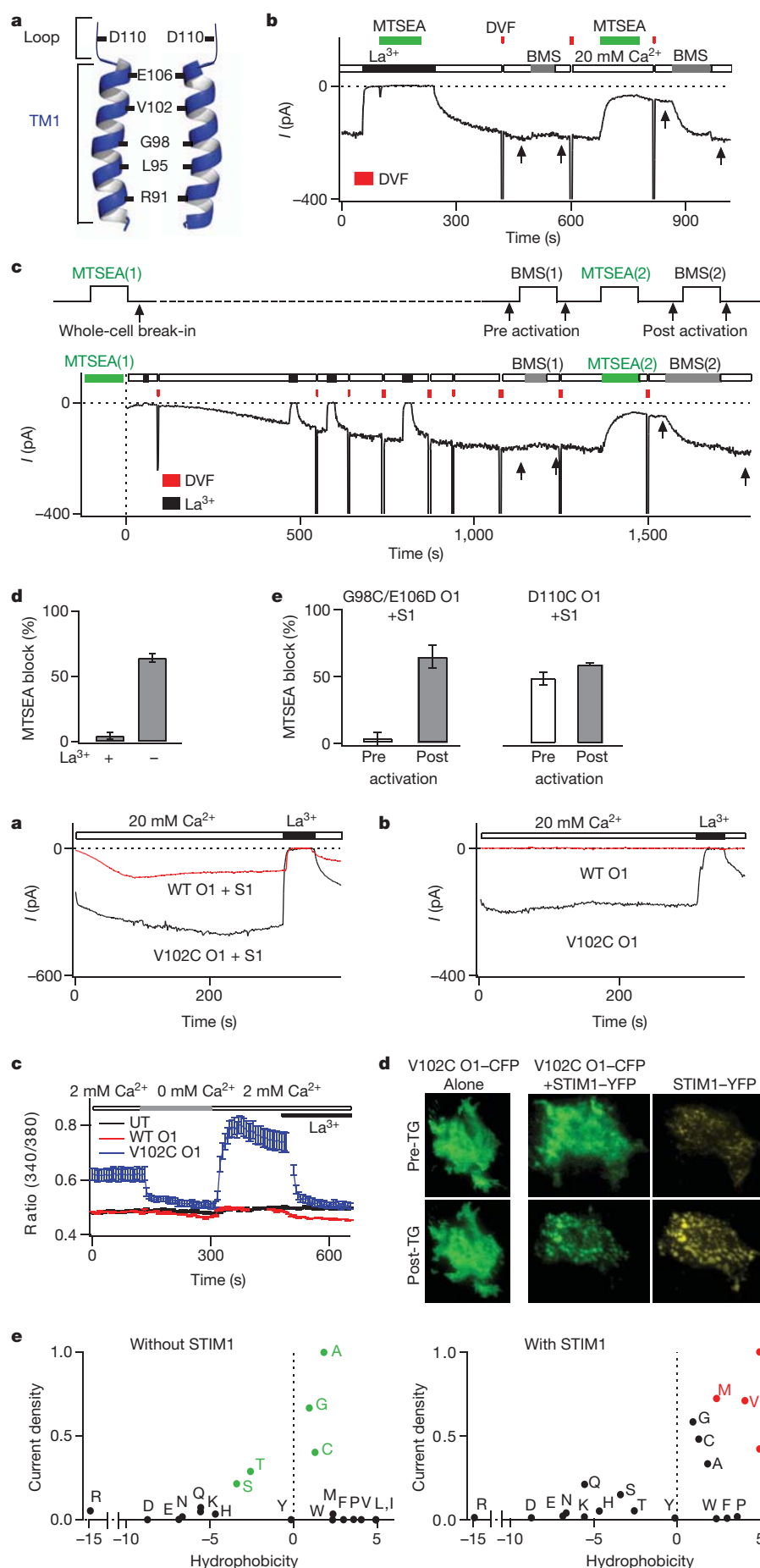


Figure 1 | State-dependent accessibility of pore-lining residues localizes the activation gate to the extracellular TM1 region.

a, Schematic representation of the key pore-lining residues in ORAI1 (refs 6, 7). **b**, MTSEA modification of G98C is protected by La^{3+} . A HEK293 cell co-expressing G98C/E106D ORAI1 (O1) and STIM1 was exposed to two applications of MTSEA (100 μM), the first in the presence of La^{3+} (100 μM) and the second after washout of La^{3+} . Periodic applications of a divalent free (DVF, red rectangles) solution facilitated washout of La^{3+} . MTSEA inhibition was quantified by the relief of block induced by BMS (5 mM) (arrows). **c**, State-dependent modification of G98C. MTSEA (200 μM) was applied for 120 s to resting cells and then washed off. After whole-cell break-in, I_{CRAC} was activated by passive store depletion by dialysing in BAPTA. BMS was applied to examine relief from MTSEA blockade (arrows). A second application of MTSEA and BMS provides a measure of blockade in open channels. A DVF solution was periodically applied to monitor Na^{+} - I_{CRAC} . **d**, Summary of MTSEA blockade of open G98C/E106D ORAI1 in the presence and absence of La^{3+} . **e**, Summary of blockade of G98C/E106D and D110C ORAI1 by MTSEA in closed and open channels. Values are mean \pm s.e.m.

Figure 2 | Mutations at V102 cause STIM1-independent ORAI1 activation.

a, Time course of the development of I_{CRAC} in cells expressing wild-type (WT) or V102C ORAI1 and STIM1 after whole-cell break-in. Intracellular Ca^{2+} stores were depleted by dialysing cells with 8 mM BAPTA. **b**, V102C ORAI1 currents are constitutively active in the absence of STIM1 co-expression. **c**, Intracellular calcium concentration [Ca^{2+}]_i measurements in HEK293 cells expressing the indicated ORAI1 constructs in the absence of STIM1. UT, untransfected. **d**, Localization of V102C ORAI1–cyan fluorescent protein (CFP) before, and after, ER Ca^{2+} store depletion in the absence (left) or presence (right) of STIM1–yellow fluorescent protein (YFP). **e**, Mutational analysis of V102. Normalized current densities of V102 substitutions plotted against the solvation energies of the substituted amino acids³⁰ in the presence or absence of STIM1 co-expression. Currents were normalized to the mutant that yielded the maximal current density for each condition (Ala for STIM1-free cells and Ile in STIM1-co-expressing cells). Green, mutants that yield large constitutively active currents in the absence of STIM1; red, mutants that are not constitutively active but that require STIM1 for activation. TG, thapsigargin.

residues (Leu, Val and Ile) as gates to inhibit the flux of ions^{18–20}. To explore the possibility that V102 comprises a hydrophobic gate in ORAI1, we investigated the side-chain dependence at this position for constitutive activation. We observed constitutive activity with several mildly hydrophobic and polar substitutions, including Cys, Gly, Ala, Ser and Thr (Fig. 2e). Conversely, substitutions to the highly hydrophobic amino acids Leu, Ile and Met resulted in only STIM1-dependent activation, as seen in wild-type ORAI1. Large hydrophobic residues such as Trp, Tyr and Phe attenuated both the constitutive and STIM1-induced currents, probably because of pore occlusion, as expected for a position that is nestled in a narrow region of the pore^{6,7} (Supplementary Fig. 5b). Substitutions to extremely polar residues such as Glu, Asp, Lys and Arg resulted in non-functional channels with or without STIM1, probably owing to secondary effects of these mutations on the nearby selectivity filter at E106. Despite these deviations, however, the overall pattern is consistent with the hypothesis that V102 comprises a hydrophobic gate, with less hydrophobic substitutions producing a leaky gate.

CRAC channels are extraordinarily Ca^{2+} selective and poorly permeable to the large monovalent cation Cs^+ . However, the ion selectivity of STIM1-free V102C ORAI1 channels differed from wild-type ORAI1 channels in both respects. STIM1-free V102C ORAI1 channels showed significantly lower Ca^{2+} permeability ($P < 0.0001$), as demonstrated by the left-shifted reversal potentials of mutant Ca^{2+} currents (Fig. 3a). Consistent with this interpretation, replacement of extracellular Na^+ with NMDG⁺, an impermeant ion, revealed significant Na^+ conduction in these channels ($P < 0.0001$) (Fig. 3b). Direct estimates of

fractional Ca^{2+} currents using fluo-4 indicated that V102C ORAI1 conducts only 36% of the Ca^{2+} carried by wild-type ORAI1 in 20 mM Ca^{2+} (Supplementary Fig. 7a). In addition, unlike wild-type channels, STIM1-free V102C channels were highly permeable to the large monovalent cation Cs^+ (Fig. 3a–c and Supplementary Table 1).

Unexpectedly, co-expressing exogenous STIM1 together with V102C ORAI1 enhanced the Ca^{2+} permeability and lowered the Cs^+ permeability of V102C ORAI1, effectively correcting its aberrant ion selectivity (Fig. 3a–c). STIM1 also modified permeation of V102C ORAI1 for Ba^{2+} and Sr^{2+} (Supplementary Fig. 7b). Modification of ion selectivity by STIM1 was not unique to V102C ORAI1 but occurred in all constitutively active V102X mutants (Supplementary Table 1). These changes in ion selectivity required direct STIM1–ORAI1 interactions, as modification of V102C ORAI1 ion selectivity was nullified in the V102C/L276D ORAI1 double mutant (Fig. 3d), in which STIM1–ORAI1 binding was impaired (Supplementary Fig. 4b, c)²¹. STIM1-free and STIM1-bound V102C channels also displayed very different minimal pore widths (Fig. 3e), directly demonstrating that STIM1 alters the pore structure of V102C channels. Further analyses, using concatenated ORAI1 dimers (see Supplementary Methods) indicated that the subunit stoichiometry of STIM1-free and STIM1-bound mutant channels are identical, arguing that their distinct permeation properties are due to different pore structures of fully assembled, tetrameric channels rather than different subunit stoichiometries (Supplementary Fig. 8). Collectively, these results indicate that STIM1 binding modifies the structural features of the mutant channel

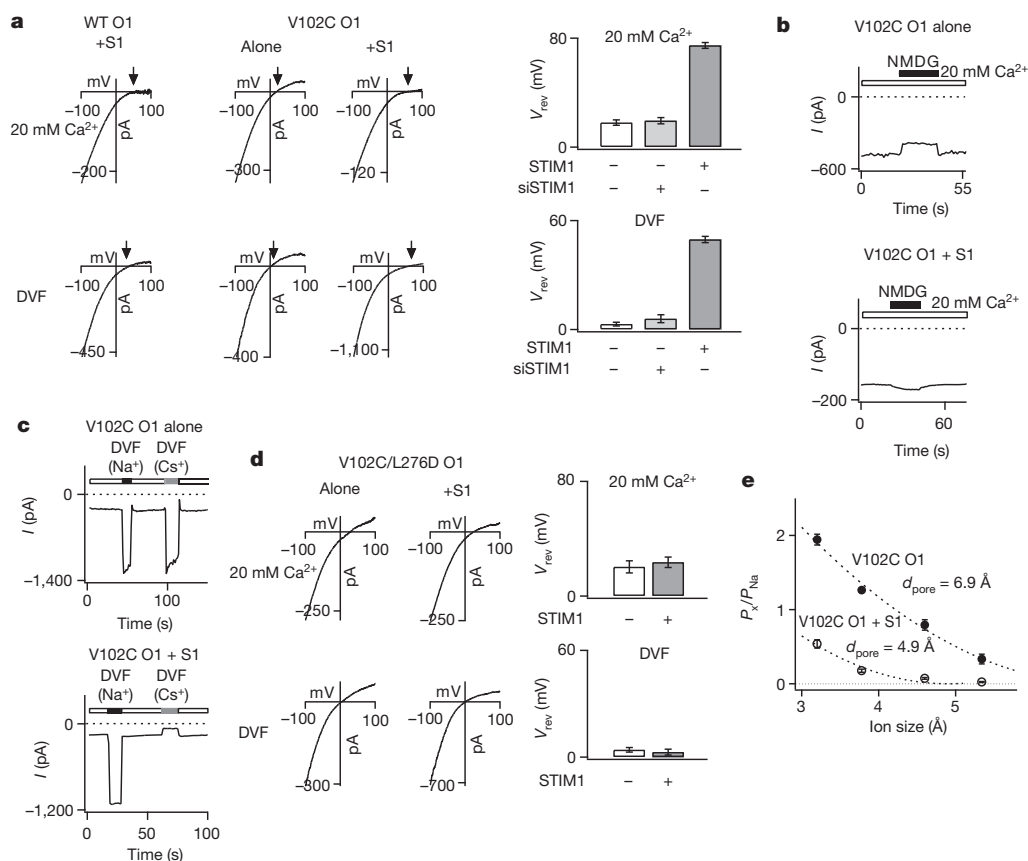


Figure 3 | STIM1 regulates ion selectivity of constitutively active V102C ORAI1 channels. **a**, Current–voltage (I – V) relationships of V102C ORAI1 currents in 20 mM Ca^{2+} and DVF Ringer’s solutions. Arrows emphasize the reversal potential (V_{rev}) in each case. The bar graphs summarize the V_{rev} in the presence or absence of STIM1. Values are mean \pm s.e.m. siSTIM1, short interfering RNA targeting STIM1. **b**, Effects of substituting extracellular Na^+ with NMDG⁺ on V102C ORAI1 currents in the absence or presence of STIM1. **c**, Effects of replacing the standard extracellular Ringer’s solution with Na^+ - or Cs^+ -based DVF solutions. In the absence of STIM1, large Cs^+ currents are seen

in V102C ORAI1 channels. By contrast, no Cs^+ conduction is observed in the presence of STIM1. **d**, I – V relationship of currents in the V102C/L276D ORAI1 double mutant in the presence or absence of STIM1. The bar graphs summarize the V_{rev} values of this mutant in the presence or absence of STIM1. Values are mean \pm s.e.m. **e**, Relative permeabilities of V102C ORAI1 channels to different organic monovalent cations plotted against the size of each cation (test ion P_x and Na^+ P_{Na}). Dotted lines are fits to the hydrodynamic relationship. Values of d_{pore} (the apparent width of the pore) estimated from the fits are 4.9 Å for V102C ORAI1 + STIM1 channels and 6.9 Å for V102C ORAI1 channels.

pore, bestowing permeation properties that are associated with CRAC channels.

The normalization of ion selectivity of mutant channels by STIM1 suggests that their altered ion selectivity in the absence of STIM1 is not merely a byproduct of the mutations, but that it is indicative of a native intermediate activation state that is not readily seen in wild-type channels owing to a closed gate. Recent studies indicate that ORAI1 channels are activated in a nonlinear and cooperative manner by STIM1, with maximal channel activation requiring binding of eight STIM1 molecules per channel^{15,22,23}. We reasoned that if modification of ion selectivity is coupled to the stoichiometry of STIM1 binding, then partial activation of wild-type ORAI1 by a sub-saturating concentration of STIM1 may lead to incomplete normalization of ion selectivity, revealing an intermediate activation state. To test this hypothesis, we used constructs in which wild-type ORAI1 was tethered to either one or two functional STIM1 (S or SS) domains (resulting in four or eight S domains per channel, respectively), as recently described²³. We found that wild-type ORAI1 channels tethered to one S domain per subunit produced currents that were smaller and displayed diminished CDI compared to ORAI1-SS channels (Supplementary Fig. 9a), as expected from the known requirement of STIM1 for CRAC channel activation and inactivation^{15,22,23}. Importantly, reversal potential measurements and ion substitution experiments indicated that unlike ORAI1-SS channels, ORAI1-S channels exhibited diminished Ca^{2+} and enhanced Cs^+ selectivity (Fig. 4a,b). Similar alterations in ion selectivity were also seen when wild-type ORAI1 was expressed with limiting concentrations of full-length STIM1 (Supplementary Fig. 9b). These results support the hypothesis that the V102C mutations stabilize an intermediate channel activation state. To gauge the dose dependence of ion selectivity modulation by STIM1, we examined reversal potentials of V102C and wild-type channels tagged to zero, one or two S domains (Fig. 4c, d). Despite the different starting functional states of wild-type (closed) and V102C (open) channels, STIM1 caused similar,

dose-dependent alterations in ion selectivity in both cases, while concomitantly enhancing activation of wild-type channels (Fig. 4d). Thus, ORAI1 channel activation and changes in ion selectivity probably result from the same underlying energetic changes that are driven by STIM1 binding.

Collectively, our results show that mutations at V102 cause constitutive activation of ORAI1 channels through a mechanism that probably involves destabilization of the channel gate at V102. This disposition of the STIM1 activation gate, in the extracellular region of the pore close to the selectivity filter (E106), is markedly different from the familiar structural designs in K^+ channels and by extension, voltage-gated Ca^{2+} (Ca_v) channels, which are constructed with the gate located at the cytoplasmic end of the pore²⁴. We exploited the constitutive channel activity that resulted from mutations in the putative gate to identify an unusual ion channel gating mode in which STIM1 regulates ion selectivity and the pore architecture of CRAC channels. Activation by STIM1 bestows several key distinctive characteristics that are associated with CRAC channels including high Ca^{2+} selectivity, low Cs^+ permeability and a narrow pore to otherwise non-selective ORAI1 channels. Although the underlying mechanism remains to be established, the close proximity of the putative STIM1 activation gate (V102) to the selectivity filter (E106) probably contributes to the tight coupling of permeation and gating during channel activation. The altered ion selectivity of ORAI1 channels when STIM1 is limiting is reminiscent of the ion selectivity of ORAI1 and ORAI3 channels directly activated by the compound 2-APB, which exhibit lower Ca^{2+} selectivity and higher Cs^+ selectivity than STIM1-activated ORAI channels^{25–28}. These findings indicate that the exquisite Ca^{2+} selectivity of CRAC channels is not an intrinsic and immutable property of ORAI1 but is instead uniquely manifested only in response to STIM1 gating. Given the emerging evidence that indicates that ORAI1 can be activated in a STIM1-independent manner by other cellular activators²⁹, these results raise the possibility that activation of

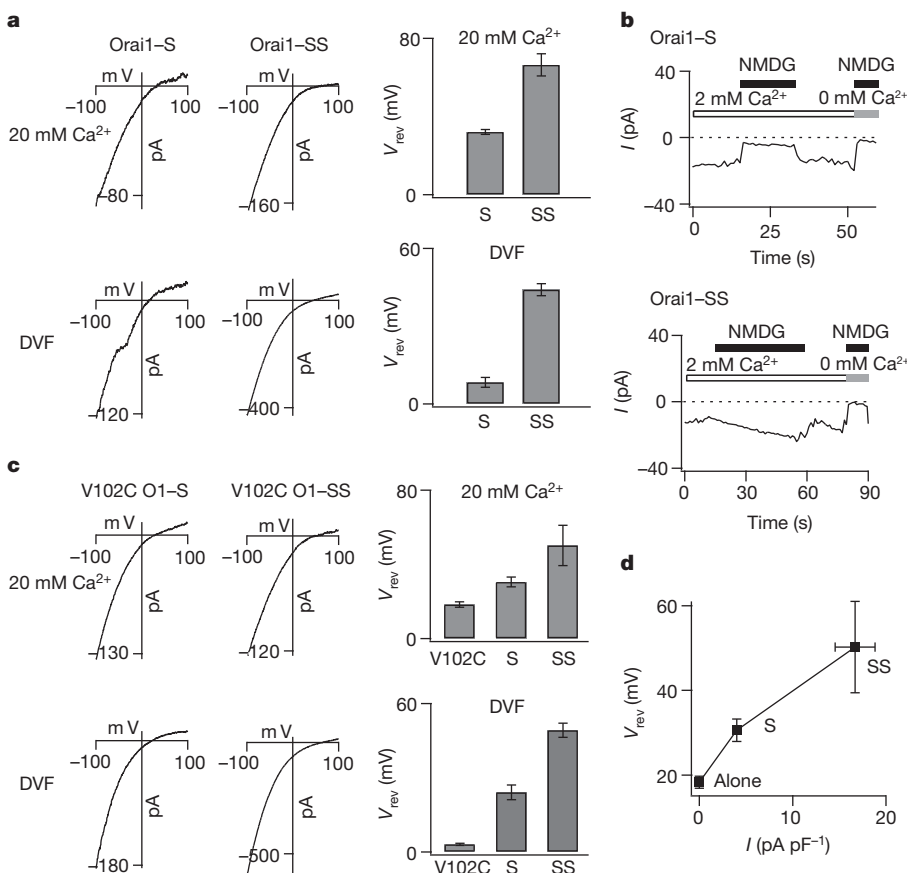


Figure 4 | STIM1 dose-dependently modulates the ion selectivity of ORAI1 channels. **a**, The addition of S domains to wild-type ORAI1 produces a rightward shift in the V_{rev} of I_{CRAC} . I - V relationships of wild-type ORAI1 channels that are tagged to either one or two S domains in the 20 mM Ca^{2+} and DVF Ringer's solutions. The bar graphs summarize the V_{rev} in each solution. Values are mean \pm s.e.m. The top and bottom traces for each condition are from the same cell. **b**, Effects of substituting extracellular Na^+ with an impermeant ion, NMDG $^+$. Removal of Na^+ diminishes the inward current in ORAI1-S channels, but not ORAI1-SS channels. **c**, I - V relationships and reversal potentials of V102C, V102C-S and V102C-SS channels. Values are mean \pm s.e.m. Increasing the number of S domains to the V102C monomer causes a progressive rightward shift in the V_{rev} of I_{CRAC} . **d**, A plot of V102C ORAI1 V_{rev} (in the 20 mM Ca^{2+} Ringer's solution) against current density of wild-type ORAI1 channels tagged to zero, one or two S domains.

highly Ca^{2+} selective or non-selective Orai1 currents may be a general mechanism for cells to tune Ca^{2+} and Na^{+} entry through Orai1 channels depending on the nature of the upstream activation signal.

METHODS SUMMARY

I_{CRAC} was recorded in the standard whole-cell patch-clamp configuration in HEK293 cells transfected with the indicated Orai1 mutants, which were cloned into a bicistronic expression vector that co-expressed GFP. For recording I_{CRAC} , the membrane potential was hyperpolarized from +30 mV (holding) to −100 mV (100 ms) and then ramped from −100 mV to +100 mV (100 ms). MTS reagents were added to a 20 mM Ringer's or divalent-free Ringer's solution at the indicated concentrations. Second-order rate constants of MTSEA blockade were determined at a constant holding potential of −80 mV, as previously described⁶.

Full Methods and any associated references are available in the online version of the paper at www.nature.com/nature.

Received 9 June; accepted 2 December 2011.

Published online 25 January 2012.

- Olcese, R. And yet it moves: conformational states of the Ca^{2+} channel pore. *J. Gen. Physiol.* **129**, 457–459 (2007).
- Hogan, P. G., Lewis, R. S. & Rao, A. Molecular basis of calcium signaling in lymphocytes: STIM and Orai. *Annu. Rev. Immunol.* **28**, 491–533 (2010).
- Mignen, O., Thompson, J. L. & Shuttleworth, T. J. Orai1 subunit stoichiometry of the mammalian CRAC channel pore. *J. Physiol.* **586**, 419–425 (2008).
- Penna, A. *et al.* The CRAC channel consists of a tetramer formed by Stim-induced dimerization of Orai dimers. *Nature* **456**, 116–120 (2008).
- Madl, J. *et al.* Resting-state Orai1 diffuses as homotetramer in the plasma membrane of live mammalian cells. *J. Biol. Chem.* **285**, 41135–41142 (2010).
- McNally, B. A., Yamashita, M., Engh, A. & Prakriya, M. Structural determinants of ion permeation in CRAC channels. *Proc. Natl Acad. Sci. USA* **106**, 22516–22521 (2009).
- Zhou, Y., Ramachandran, S., Oh-Hora, M., Rao, A. & Hogan, P. G. Pore architecture of the Orai1 store-operated calcium channel. *Proc. Natl Acad. Sci. USA* **107**, 4896–4901 (2010).
- Karlin, A. & Akabas, M. H. Substituted-cysteine accessibility method. *Methods Enzymol.* **293**, 123–145 (1998).
- Prakriya, M. & Lewis, R. S. Regulation of CRAC channel activity by recruitment of silent channels to a high open-probability gating mode. *J. Gen. Physiol.* **128**, 373–386 (2006).
- Yamashita, M., Navarro-Borely, L., McNally, B. A. & Prakriya, M. Orai1 mutations alter ion permeation and Ca^{2+} -dependent inactivation of CRAC channels: evidence for coupling of permeation and gating. *J. Gen. Physiol.* **130**, 525–540 (2007).
- Prakriya, M. *et al.* Orai1 is an essential pore subunit of the CRAC channel. *Nature* **443**, 230–233 (2006).
- Yeromin, A. V. *et al.* Molecular identification of the CRAC channel by altered ion selectivity in a mutant of Orai. *Nature* **443**, 226–229 (2006).
- Vig, M. *et al.* CRACM1 multimers form the ion-selective pore of the CRAC channel. *Curr. Biol.* **16**, 2073–2079 (2006).
- Mullins, F. M., Park, C. Y., Dolmetsch, R. E. & Lewis, R. S. STIM1 and calmodulin interact with Orai1 to induce Ca^{2+} -dependent inactivation of CRAC channels. *Proc. Natl Acad. Sci. USA* **106**, 15495–15500 (2009).
- Scrimgeour, N., Litjens, T., Ma, L., Barritt, G. J. & Rychkov, G. Y. Properties of Orai1 mediated store-operated current depend on the expression levels of STIM1 and Orai1 proteins. *J. Physiol.* **587**, 2903–2913 (2009).
- Derler, I. *et al.* A Ca^{2+} release-activated Ca^{2+} (CRAC) modulatory domain (CMD) within STIM1 mediates fast Ca^{2+} -dependent inactivation of Orai1 channels. *J. Biol. Chem.* **284**, 24933–24938 (2009).
- Feske, S. *et al.* A mutation in Orai1 causes immune deficiency by abrogating CRAC channel function. *Nature* **441**, 179–185 (2006).
- Doyle, D. A. Structural changes during ion channel gating. *Trends Neurosci.* **27**, 298–302 (2004).
- Miyazawa, A., Fujiyoshi, Y. & Unwin, N. Structure and gating mechanism of the acetylcholine receptor pore. *Nature* **423**, 949–955 (2003).
- Chang, G., Spencer, R. H., Lee, A. T., Barclay, M. T. & Rees, D. C. Structure of the MscL homolog from *Mycobacterium tuberculosis*: a gated mechanosensitive ion channel. *Science* **282**, 2220–2226 (1998).
- Navarro-Borely, L. *et al.* STIM1-Orai1 interactions and Orai1 conformational changes revealed by live-cell FRET microscopy. *J. Physiol.* **586**, 5383–5401 (2008).
- Hoover, P. J. & Lewis, R. S. Stoichiometric requirements for trapping and gating of Ca^{2+} release-activated Ca^{2+} (CRAC) channels by stromal interaction molecule 1 (STIM1). *Proc. Natl Acad. Sci. USA* **108**, 13299–13304 (2011).
- Li, Z. *et al.* Graded activation of CRAC channel by binding of different numbers of STIM1 to Orai1 subunits. *Cell Res.* **21**, 305–315 (2011).
- Yellen, G. The voltage-gated potassium channels and their relatives. *Nature* **419**, 35–42 (2002).
- Peinelt, C., Lis, A., Beck, A., Fleig, A. & Penner, R. 2-Aminoethoxydiphenyl borate directly facilitates and indirectly inhibits STIM1-dependent gating of CRAC channels. *J. Physiol.* **586**, 3061–3073 (2008).
- Zhang, S. L. *et al.* Store-dependent and -independent modes regulating Ca^{2+} release-activated Ca^{2+} channel activity of human Orai1 and Orai3. *J. Biol. Chem.* **283**, 17662–17671 (2008).
- Schindl, R. *et al.* 2-aminoethoxydiphenyl borate alters selectivity of Orai3 channels by increasing their pore size. *J. Biol. Chem.* **283**, 20261–20267 (2008).
- Yamashita, M., Somasundaram, A. & Prakriya, M. Competitive modulation of CRAC channel gating by STIM1 and 2-aminoethoxydiphenyl borate (2-APB). *J. Biol. Chem.* **286**, 9429–9442 (2011).
- Feng, M. *et al.* Store-independent activation of Orai1 by SPCA2 in mammary tumors. *Cell* **143**, 84–98 (2010).
- Radzicka, A., Pedersen, L. & Wolfenden, R. Influences of solvent water on protein folding: free energies of solvation of cis and trans peptides are nearly identical. *Biochemistry* **27**, 4538–4541 (1988).

Supplementary Information is linked to the online version of the paper at www.nature.com/nature.

Acknowledgements We thank C. Lingle, R. Lewis, K. Swartz, J. Sack, A. Gross, L. Tirado-Lee and T. Hornell for discussions and comments on the manuscript. This work was supported by NIH grant NS057499 to M.P. An American Heart Association predoctoral fellowship supported A.S.

Author Contributions B.A.M. generated, expressed and functionally characterized the Orai1 mutants by patch-clamp electrophysiology with help from M.Y. The Ca^{2+} imaging, FRET imaging, TIRF microscopy and western blot analysis of Orai1 mutants were performed by A.S. B.A.M., A.S. and M.P. contributed to the writing and editing of the paper.

Author Information Reprints and permissions information is available at www.nature.com/reprints. The authors declare no competing financial interests. Readers are welcome to comment on the online version of this article at www.nature.com/nature. Correspondence and requests for materials should be addressed to M.P. (m-prakriya@northwestern.edu).

METHODS

Cells. HEK293 cells were maintained in suspension in a medium containing CD293 supplemented with 4 mM GlutaMAX (Invitrogen) at 37 °C, 5% CO₂. For imaging and electrophysiology, cells were plated and adhered to poly-L-lysine-coated coverslips at the time of passage, and grown in a medium containing 44% DMEM (Mediatech), 44% Ham's F12 (Mediatech), 10% fetal calf serum (HyClone), 2 mM glutamine, 50 U ml⁻¹ penicillin and 50 µg ml⁻¹ streptomycin.

Plasmids and transfections. Cys mutations that were used for characterization using electrophysiology were engineered into the previously described C-terminal Myc-tagged ORAI1 construct (MO7O ORAI1) in the bicistronic expression vector pMSCV-CITE-eGFP-PGK-Puro¹¹. For generating the tandem dimers, the basic 'building blocks' (monomeric ORAI1 (MO7O) and the Bluescript SK⁺ vector with ORAI1 attached to a linker) were obtained from T. Shuttleworth and constructed as previously described³. The orientation and number of subunits in the final constructs were confirmed by restriction enzyme analysis and western blot analysis. The ORAI1-S-eGFP and ORAI1-SS-eGFP constructs were kind gifts of T. Xu. The ORAI1-CFP, STIM1-YFP, and CFP-ORAI3 plasmids have been previously described^{21,28}. Site-directed mutagenesis to generate ORAI1 mutations was performed using the QuikChange Site-Directed Mutagenesis Kit (Stratagene) according to manufacturer's instructions and the results were confirmed by DNA sequencing. For electrophysiology, the indicated ORAI1 constructs were transfected into HEK293 cells either alone or together with a construct expressing unlabelled STIM1 (pCMV6-XL5, Origene Technologies). Cells were transfected with the indicated STIM1 and/or ORAI1 complementary DNA (ratio of 10:1 by mass for electrophysiology) using TransPass D2 (NEB Labs) and studied 24 h later. Cells that were transfected with siSTIM1 (Ambion) were studied 72 h following transfection.

Electrophysiology. Currents were recorded in the standard whole-cell configuration at room temperature on an Axopatch 200B amplifier (Molecular Devices) interfaced to an ITC-18 input-output board (Instrutech). Routines developed by R. S. Lewis and M. Prakriya on the Igor Pro software (Wavemetrics) were used for stimulation, data acquisition and data analysis. Data are corrected for the liquid junction potential of the pipette solution relative to Ringer's in the bath (−10 mV). The holding potential was +30 mV. The standard voltage stimulus consisted of a 100-ms step hyperpolarization to −100 mV followed by a 100-ms ramp depolarization from −100 to +100 mV, applied at 1-s intervals. Unless noted otherwise, the peak currents during the −100 mV pulse were measured for data analysis. For examining Ca²⁺-dependent fast inactivation, the voltage protocol consisted of a 300-ms step decrease to −100 mV, applied at 2-s intervals. Unless otherwise indicated, *I*_{CRAC} was activated by passive depletion of intracellular Ca²⁺ stores by internal dialysis of 8 mM BAPTA through the pipette solution. To prevent complications arising from the changing membrane potential in the standard step-ramp voltage protocol, rate constants of blockade by MTS reagents were determined at a constant potential of −80 mV by acquiring 200-ms sweeps of current at 4 Hz. All currents were acquired at 5 kHz and low-pass filtered with a 1-kHz Bessel filter built into the amplifier. All data were corrected for liquid junction potential of the pipette solution and for leak currents collected in 50–150 µM LaCl₃.

MTS reagent protocol. The protocol for analysis of state-dependent modification of ORAI1 bearing Cys mutants is described in Fig. 1c. For the D110C mutant, this protocol was slightly modified to adjust for the formation of spontaneous disulphide bonds in this mutant⁶. The protocol included an additional application of the

reducing agent BMS 90–120 s before the first MTSEA application to remove pre-existing disulphide bonds, as described previously⁶.

Solutions. The standard extracellular Ringer's solution contained 130 mM NaCl, 4.5 mM KCl, 20 mM CaCl₂, 10 mM tetraethylammonium chloride (TEA-Cl), 10 mM D-glucose, and 5 mM Na-HEPES (pH 7.4). The DVF Ringer's solution contained 150 mM NaCl, 10 mM HEDTA, 1 mM EDTA, 10 mM TEA-Cl and 5 mM HEPES (pH 7.4). The 110-mM Ca²⁺ solution contained 110 mM CaCl₂, 10 mM D-Glucose and 5 mM HEPES (pH 7.4). The standard internal (pipette) solution contained 135 mM Cs-aspartate, 8 mM MgCl₂, 8 mM BAPTA and 10 mM Cs HEPES (pH 7.2). In experiments examining CDI, BAPTA was replaced with EGTA to accentuate CDI. In these experiments, the internal solution contained 125 mM Cs-aspartate, 10 mM EGTA, 3 mM MgCl₂, 8 mM NaCl and 10 Cs HEPES (pH 7.2). Stock solutions of MTS reagents (Toronto Research Chemicals) were prepared as previously described⁶.

Data analysis. Reversal potentials were measured from the average of several leak-subtracted sweeps (4–6 sweeps) in each cell. Measurements were taken from 6–15 cells per mutant per condition. In cases in which the *I*–*V* curve asymptotically approached the *x* axis at very positive membrane potentials with no clear reversal (for example, in wild-type ORAI1-expressing cells), the reversal potential was assigned as +80 mV. The MTSEA reaction rate constant was estimated from single exponential fits to the current decline after MTSEA application. The apparent second-order modification rate constant *k*_{on} was calculated from the relationship:

$$k_{\text{on}} = \frac{1}{\tau[\text{MTS}]}$$

where [MTS] is the concentration of the MTS reagent.

Relative permeabilities were calculated from changes in the reversal potential using the Goldman–Hodgkin–Katz voltage equation:

$$\frac{P_x}{P_{\text{Na}}} = \frac{[\text{Na}]_o}{[\text{X}]_o} e^{\Delta E_{\text{rev}} F/RT}$$

where *R*, *T* and *F* have their usual meanings, *P*_X and *P*_{Na} are the permeabilities of the test ion and Na⁺, respectively, [X] and [Na] are the ionic concentrations, and Δ*E*_{rev} is the shift in reversal potential when the test cation is exchanged for Na⁺. To estimate the minimal width of ORAI1 channels, the relative channel permeabilities for a series of organic monovalent cations of increasing size were examined as described before¹⁰. The cations used were ammonium (3.2 Å), methylammonium (3.78 Å), dimethylammonium (4.6 Å) and trimethylammonium (5.34 Å). These experiments were carried out in buffered Ca²⁺-free solutions to avoid the potent blocking effects of Ca²⁺ ions on monovalent *I*_{CRAC}. The data were fitted to the hydrodynamic relationship¹⁰:

$$\frac{P_X}{P_{\text{Na}}} = k \left(1 - \frac{d_{\text{ion}}}{d_{\text{pore}}} \right)^2$$

where *d*_{ion} is the diameter of the tested ion and *d*_{pore} is the apparent width of the pore.

All data were corrected for leak currents collected in 20 mM Ca²⁺ + 50–150 µM La³⁺. All curve fitting was done by least-squares methods using built-in functions in Igor Pro 5.0.

Structure of the human M2 muscarinic acetylcholine receptor bound to an antagonist

Kazuko Haga^{1*}, Andrew C. Kruse^{2*}, Hidetsugu Asada^{3,4*}, Takami Yurugi-Kobayashi^{3,4}, Mitsunori Shiroishi^{4,5}, Cheng Zhang², William I. Weis^{2,6}, Tetsuji Okada¹, Brian K. Kobilka², Tatsuya Haga¹ & Takuya Kobayashi^{3,4,7}

The parasympathetic branch of the autonomic nervous system regulates the activity of multiple organ systems. Muscarinic receptors are G-protein-coupled receptors that mediate the response to acetylcholine released from parasympathetic nerves^{1–5}. Their role in the unconscious regulation of organ and central nervous system function makes them potential therapeutic targets for a broad spectrum of diseases. The M2 muscarinic acetylcholine receptor (M2 receptor) is essential for the physiological control of cardiovascular function through activation of G-protein-coupled inwardly rectifying potassium channels, and is of particular interest because of its extensive pharmacological characterization with both orthosteric and allosteric ligands. Here we report the structure of the antagonist-bound human M2 receptor, the first human acetylcholine receptor to be characterized structurally, to our knowledge. The antagonist 3-quinuclidinyl-benzilate binds in the middle of a long aqueous channel extending approximately two-thirds through the membrane. The orthosteric binding pocket is formed by amino acids that are identical in all five muscarinic receptor subtypes, and shares structural homology with other functionally unrelated acetylcholine binding proteins from different species. A layer of tyrosine residues forms an aromatic cap restricting dissociation of the bound ligand. A binding site for allosteric ligands has been mapped to residues at the entrance to the binding pocket near this aromatic cap. The structure of the M2 receptor provides insights into the challenges of developing subtype-selective ligands for muscarinic receptors and their propensity for allosteric regulation.

Muscarinic receptors constitute a family with five subtypes, M1–M5 (ref. 1). M1, M3 and M5 subtypes couple with the G_q family of G proteins, and M2 and M4 subtypes with the G_i/G_o family of G proteins. Previous work showing that the muscarinic action by a series of choline esters and other substances in various tissues could be differentiated from their nicotinic action² led to muscarinic acetylcholine receptors being defined as a functional concept. Muscarinic receptors are now known to be G-protein-coupled receptors (GPCRs)³ and the nicotinic receptor a ligand-gated ion channel. Muscarinic receptors were initially defined biochemically as proteins that specifically bound 3-quinuclidinyl-benzilate (QNB) and N-methylscopolamine (NMS). They were among the first GPCRs to be purified from cerebral membranes⁴, and to be functionally reconstituted with purified G protein in lipid vesicles³. The M1 receptor⁵ together with the β_2 adrenergic receptor⁶ were the first neurotransmitter-activated GPCRs to be cloned, revealing the seven transmembrane (TM) segment topology initially observed for rhodopsin⁷, and subsequently found to be common to all members of the GPCR family.

As a consequence of their roles in both the central and parasympathetic nervous systems, muscarinic receptors are targets for the treatment of a spectrum of disorders including Alzheimer's disease,

schizophrenia and Parkinson's disease, and chronic obstructive pulmonary disease⁸. However, developing highly subtype-selective orthosteric drugs for muscarinic receptors has been challenging and thus far largely unsuccessful. Recent drug discovery efforts have therefore shifted to the development of small molecule allosteric modulators. Muscarinic receptors have long been a model system for studying allosteric regulation of GPCR signalling because of their exceptional propensity to bind allosteric ligands⁹. To understand better the structural basis for challenges in developing orthosteric drugs and the susceptibility for allosteric regulation, we obtained a crystal structure of the M2 receptor.

In our initial efforts to obtain the structure of the M2 receptor we expressed and purified M2 receptor lacking most of the third intracellular loop (IL3) and the native glycosylation sites. The central part of IL3 of the M2 receptor can be removed without impairing its ability to bind to agonists or activate G proteins¹⁰, and IL3 was shown to have a flexible structure¹¹. Using this modified M2 receptor bound to the high-affinity inverse agonist *R*-(–)-3-QNB, we performed crystallization by hanging-drop vapour diffusion and obtained crystals that diffracted to around 9 Å, but were not able to improve the quality of these crystals. We subsequently replaced IL3 of the M2 receptor with T4 lysozyme (T4L) as initially described for the β_2 adrenergic receptor¹² (Supplementary Fig. 1a). This method has been used to obtain crystal structures of four other GPCRs: the adenosine A_{2A} receptor¹³, the CXCR4 receptor¹⁴, the dopamine receptor D3 (ref. 15) and most recently the histamine H₁ receptor¹⁶. The binding properties of M2-T4L with muscarinic ligands were essentially the same as for the wild-type M2 receptor (Supplementary Fig. 1b, c), indicating that the overall TM architecture of M2-T4L was minimally affected by introduction of T4L. The M2-T4L receptor was subsequently crystallized in lipidic cubic phase. A 3.0 Å structure was solved by molecular replacement from a data set obtained by merging diffraction data from 23 crystals.

As is typical for proteins crystallized by the lipidic cubic phase method, the lattice for the M2 receptor shows alternating aqueous and lipidic layers with M2 receptor molecules embedded in the latter while T4L is confined to aqueous regions (Supplementary Fig. 2). Within the membrane plane, receptor molecules are packed closely against one another, alternating orientations within the bilayer. There are abundant hydrophobic contacts between receptor molecules within the membrane, whereas polar interactions primarily involve contacts between T4L molecules as well as receptor–T4L interactions.

The overall structure of the M2 receptor (Fig. 1a) is similar to that of rhodopsin and other recently crystallized inactive GPCR structures (compared in Supplementary Fig. 3). The cytoplasmic surface of the M2 receptor is in an inactive conformation, but as with most other GPCR structures, there is no interaction involving Arg 121^{3.50} (superscripts indicate Ballesteros–Weinstein numbers) in the conserved

¹Department of Life Science, Faculty of Science, Gakushuin University, Meiji 1-5-1, Tokyo 171-8588, Japan. ²Department of Molecular and Cellular Physiology, Stanford University School of Medicine, 279 Campus Drive, Stanford, California 94305, USA. ³Department of Medical Chemistry and Cell Biology, Kyoto University Faculty of Medicine, Konoe-cho, Yoshida, Sakyo-Ku, Kyoto 606-8501, Japan. ⁴Human Receptor Crystallography Project, ERATO, Japan Science and Technology Agency, Konoe-cho, Yoshida, Sakyo-Ku, Kyoto 606-8501, Japan. ⁵Graduate School of Pharmaceutical Sciences, Kyushu University, 3-1-1 Maidashi, Higashi-ku, Fukuoka 812-8582, Japan. ⁶Department of Structural Biology, Stanford University School of Medicine, 299 Campus Drive, Stanford, California 94305, USA. ⁷Japan Science and Technology Agency, Core Research for Evolutional Science and Technology (CREST), Kyoto University Faculty of Medicine, Kyoto 606-8501, Japan.

*These authors contributed equally to this work.

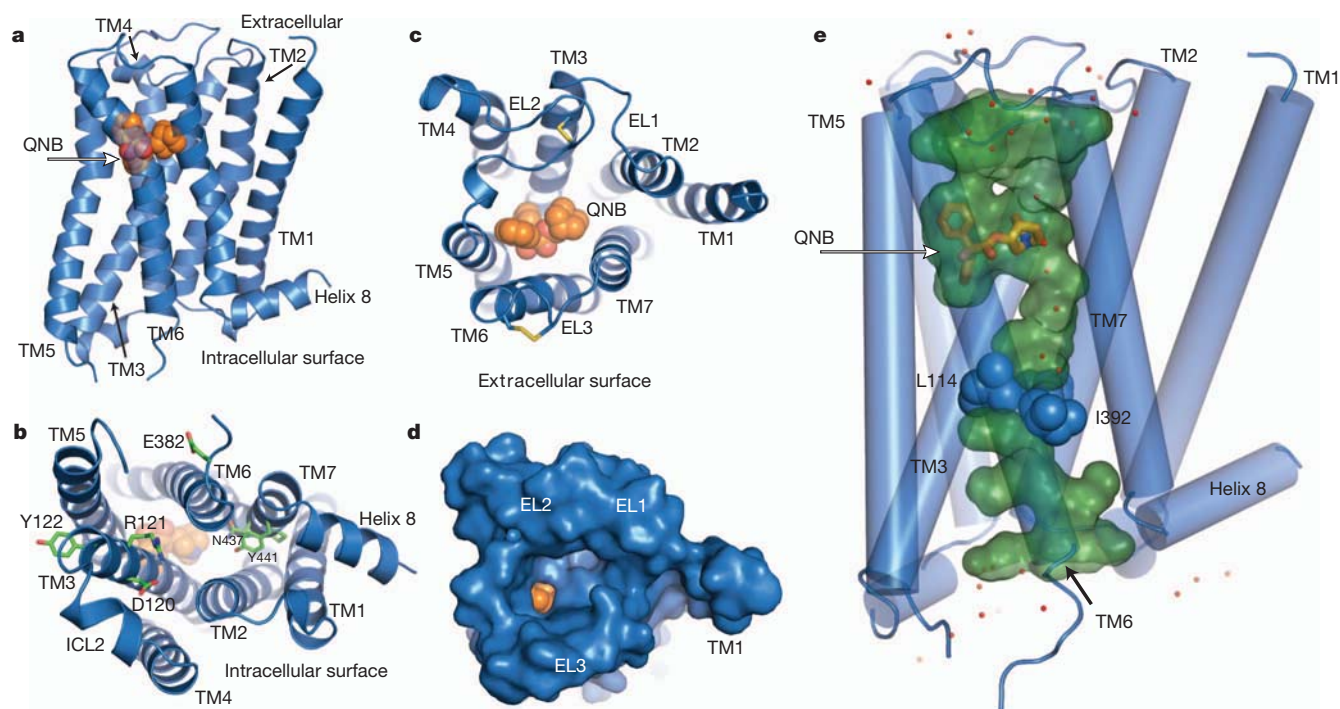


Figure 1 | The M2 receptor with bound QNB. **a–e**, The M2 receptor is shown as a blue ribbon and QNB as orange spheres. **a**, M2 receptor in profile. **b**, Cytoplasmic surface showing conserved DRY residues in TM3. **c**, Extracellular view into QNB binding pocket. **d**, Extracellular view with solvent-accessible-surface rendering shows a funnel-shaped vestibule and a

nearly buried QNB binding pocket. **e**, Aqueous channel (green) extending from the extracellular surface into the transmembrane core is interrupted by a layer of three hydrophobic residues (blue spheres). Well-ordered water molecules are shown as red dots.

E/DRY sequence in TM3 and Glu 382^{6,30} in TM6 (Fig. 1b). Instead, the Arg 121^{3,50} side chain forms a salt bridge only with Asp 120^{3,49}. In rhodopsin, the homologous residues form part of a charge–charge interaction that stabilizes the cytoplasmic ends of TM3 and TM6 in an inactive state¹⁷. The second intracellular loop shows a helical conformation similar to that first seen for the turkey β_1 adrenergic receptor¹⁸.

GPCR crystal structures show the greatest differences in the extracellular surface (Supplementary Fig. 3). The M2 receptor has a relatively simple and open extracellular surface (Fig. 1c, d) with the longer extracellular loop (ECL)2 stabilized by a conserved disulphide with Cys 96^{3,25} at the N terminus of TM3 and Cys 176 in the middle of ECL2. In addition, the second disulphide bond was detected between C413 and C416 in the ECL3. The extracellular surface of the M2 receptor most resembles that of the dopamine D3 receptor (Supplementary Fig. 3).

Crystal structures of GPCRs reveal a network of hydrogen bonding interactions that extend from the binding pocket to the cytoplasmic surface. However, a distinctive feature of the M2 receptor is that this network is part of a long, continuous aqueous channel extending from the extracellular surface to a depth of approximately 33 Å when measured from ECL2 (Fig. 1e). This channel contains the ligand binding pocket, but extends beyond the ligand and is separated from the cytoplasmic surface by a hydrophobic layer formed by three amino acids: Leu 65^{2,46} in TM2, Leu 114^{4,43} in TM4 and Ile 392^{6,40} in TM6. Each of these is absolutely conserved among all five muscarinic subtypes. The dimensions of the channel below the QNB binding site are large enough to accommodate a long, extended orthosteric ligand. Supplementary Fig. 4 compares the aqueous channels of other GPCRs.

The ligand QNB binds within a deeply buried pocket defined by the side chains of TM3, 4, 5, 6 and 7 (Fig. 2a–c and Supplementary Fig. 5 and Supplementary Table 3). An aromatic cage encloses the amine and forms a lid over the ligand, separating the orthosteric site from the extracellular vestibule. Asp 103^{3,32} and Asn 404^{6,52} serve to orient the ligand in the largely hydrophobic binding cavity, with Asn 404^{6,52} forming paired hydrogen bonds with the hydroxyl and carbonyl groups

in QNB while Asp 103^{3,32} engages in a charge–charge interaction with the amine moiety of the ligand (Fig. 2). The TM amino acids that form the QNB binding pocket are identical in all five muscarinic receptor subtypes (Supplementary Table 1), consistent with results of QNB binding experiments on M1–M4 receptors, and with site-directed mutagenesis experiments on M1 (ref. 19), M2 (ref. 20) and M3 (ref. 21) receptors. Only Phe 181, which extends downward from ECL2 and interacts with one of the two phenyl rings on QNB (Fig. 2), differs from all other muscarinic receptor subtypes, which have leucine in the homologous position. The importance of Asp^{3,32} for both agonist and antagonist binding has been demonstrated in mutagenesis and covalent-labelling experiments and modelling studies^{19–22}. In contrast, mutation of Asn 404^{6,52} to Ala on M1 (ref. 23) and M3 (ref. 24) receptors was shown to greatly affect binding of QNB but have little effect on binding of or activation by acetylcholine. It is possible that Asn 404^{6,52} is hydrogen bonded with the ester group of QNB but not that of acetylcholine.

The M2 and other muscarinic receptors represent one of four families of acetylcholine binding proteins to be structurally characterized thus far. Figure 3a shows the orthosteric binding site of the M2 receptor with acetylcholine docked with the *gauche* form of the O–C2–C1–N dihedral angle, which places the choline group in the aromatic cage interacting with Asp 103^{3,32}, while the carbonyl oxygen is tentatively bound to Asn 404^{6,52} (Fig. 3a). The natural agonist acetylcholine is much smaller than the bulky antagonist QNB. As described in the agonist-bound structure of the β_2 adrenergic receptor, the contraction of the ligand binding pocket is expected as a result of an inward shift of TM5 (ref. 25). This result is consistent with the previous mutation studies showing that Thr 187^{5,39} and Thr 190^{5,42} in TM5 (Fig. 2) alter binding of most agonists but not of antagonists²⁰. Bulky compounds capable of blocking activation-related contraction of the pocket would be very efficient in locking the M2 receptor in an inactive conformation, as is exemplified here by the antagonist QNB. It has been proposed that the conformational change of the M2 receptor upon activation might be

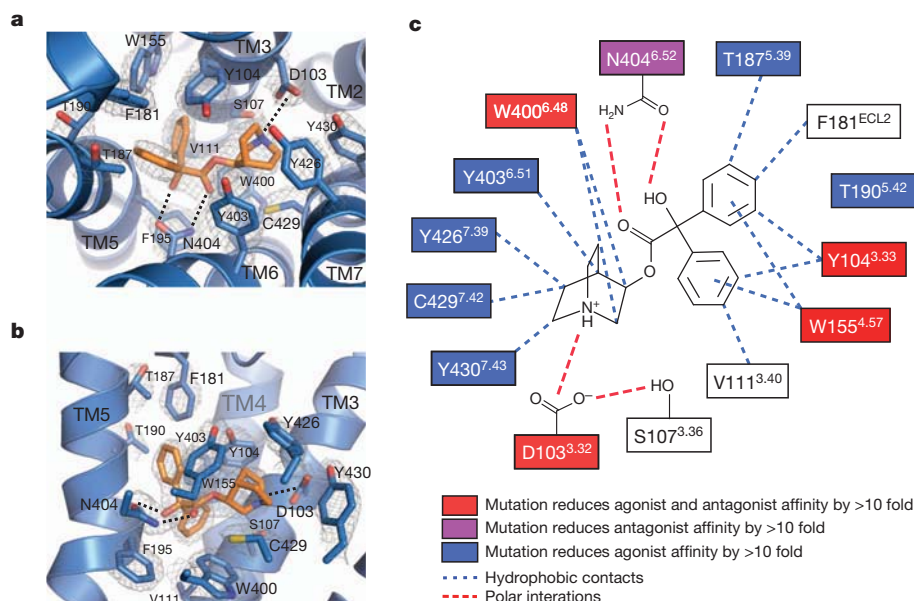


Figure 2 | Binding interactions between the M2 receptor and QNB.

a, b, Two views of the QNB binding pocket. Amino acids within 4 Å of the ligand are shown as light blue sticks, with QNB in orange. Nitrogen and oxygen atoms are coloured dark blue and red, respectively. Polar interactions are indicated by dashed lines. A $2F_o - F_c$ map is shown in wire at 1.5σ contour. **c,** A schematic representation of QNB binding interactions is shown. Mutations of

amino acids in the red boxes have been shown to reduce both antagonist and agonist binding by more than tenfold. Mutations of the amino acid in the purple boxes reduce antagonist binding affinity by more than tenfold. Mutations of amino acids in the blue boxes reduce agonist binding by more than tenfold. Blue dotted lines indicate potential hydrophobic interactions and red lines indicate potential polar interactions.

accompanied by a conformational change of acetylcholine from the *gauche* to the *trans* form of the O–C2–C1–N dihedral angle²⁶. It remains to be determined in which pose acetylcholine binds to the M2 receptor or to the M2-receptor–G-protein complex, and whether acetylcholine hydrogen bonds with Asn 404^{6,52} or other residues.

In a striking example of convergent evolution, the orthosteric site of the M2 receptor exhibits many features noted previously as common

structural elements in unrelated acetylcholine binding proteins²⁷. Like the M2 receptor, a nicotinic acetylcholine receptor homologue bound to acetylcholine (Fig. 3b) shows an aromatic cage comprised of three tyrosines and a tryptophan, although it notably lacks a counterion to the choline group²⁸, whereas in the M2 receptor this role is filled by Asp 103^{3,32}. A bacterial acetylcholine binding protein, ChoX, from *Sinorhizobium meliloti* (Fig. 3c) also possesses an aromatic cage, and

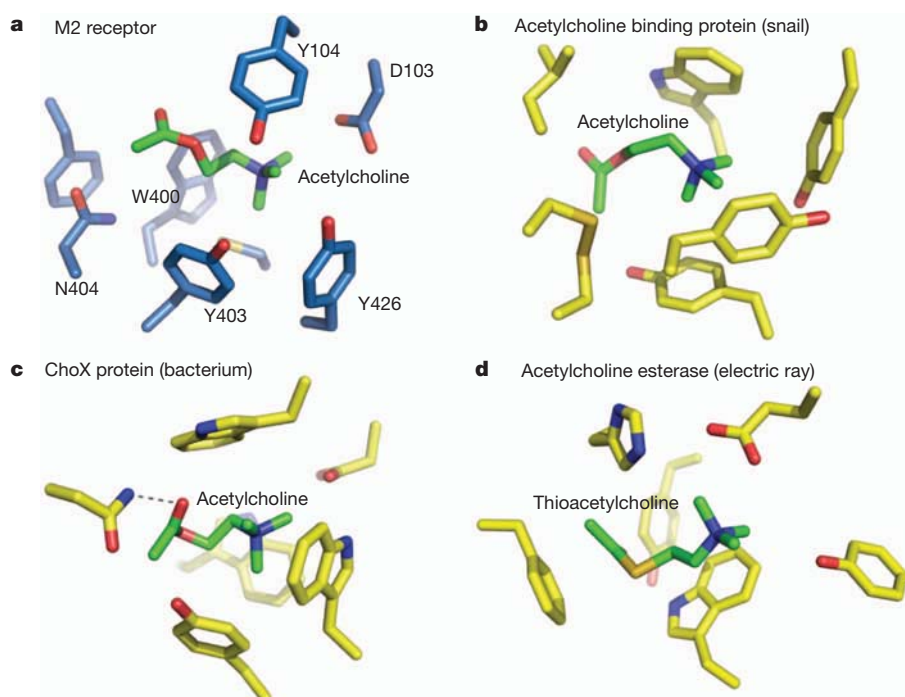


Figure 3 | Convergent evolution of acetylcholine binding sites.

a, Acetylcholine is modelled into the crystal structure of the M2 receptor. **b,** Acetylcholine binding pocket in the crystal structure of the acetylcholine binding protein from the snail *Aplysia californica* (PDB accession 2XZ5).

c, Acetylcholine binding pocket in the acetylcholine binding protein ChoX from the Gram negative bacterium *Sinorhizobium meliloti* (PDB accession 2RIN). **d,** Binding site for thio-acetylcholine in the enzyme acetylcholine esterase from the electric ray *Torpedo californica* (PDB accession 2C4H).

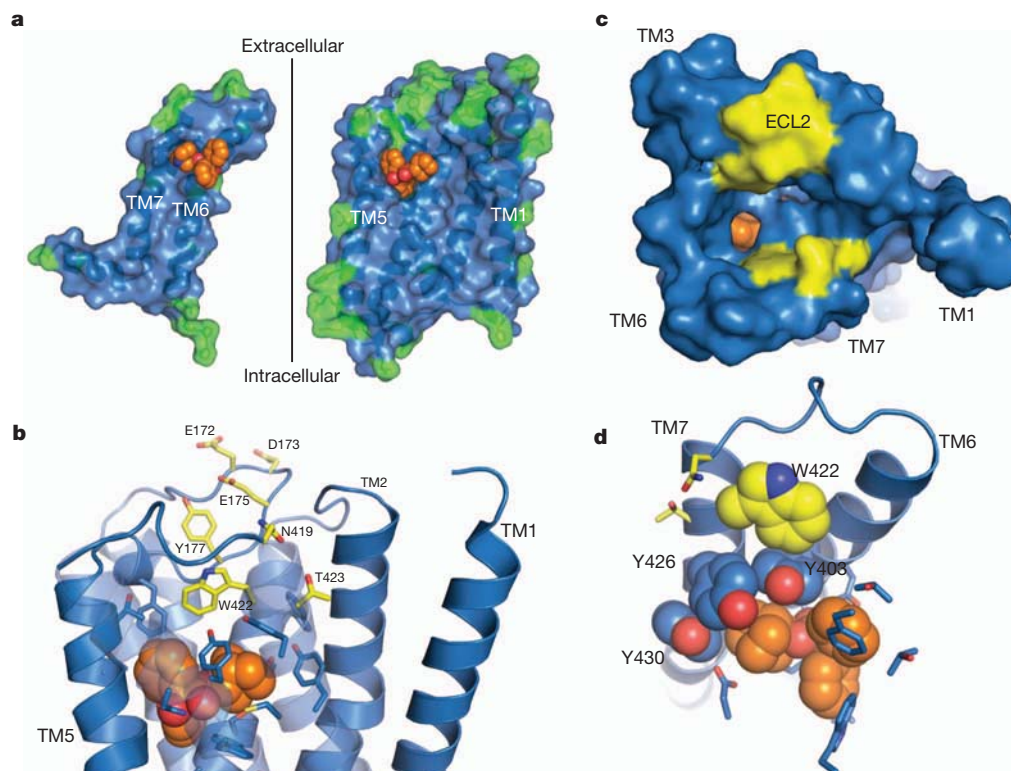


Figure 4 | Allosteric binding in the M2 receptor. **a**, Differences between the M2 and M4 receptors are shown as green residues mapped onto the inner surface of the M2 receptor (blue), with QNB in orange spheres. The sequence conservation within the orthosteric site is apparent, while residues outside show more variability. **b–d**, Mutations that alter allosteric binding are shown with yellow carbons, and amino acids involved in QNB binding are shown with blue

carbons as sticks or spheres. **b**, **c**, Different views of possible allosteric binding sites in the M2 receptor. The surface view in **c** shows the positions of possible allosteric binding sites (yellow) lining the path to the QNB binding pocket. **d**, Trp 422 (yellow spheres), implicated in binding of allosteric ligands, forms an edge-to-face aromatic interaction with Tyr 403, part of the aromatic cage (blue spheres) of the orthosteric site.

like the M2 receptor has an aspartate in close proximity to the amine engaging in a charge–charge interaction²⁹. Also like the M2 receptor, ChoX has an asparagine hydrogen bonding to the ligand carbonyl. Like these proteins, the enzyme acetylcholine esterase (Fig. 3d) uses an aromatic cage and a carboxylate to bind the choline group, while the (thio)acetyl group interacts with a phenylalanine, probably through π – π interactions³⁰. Taken together, these structures suggest that an aromatic cage and buried carboxylate are likely to be critical elements for acetylcholine recognition and binding in general.

There is a growing interest in the development of allosteric ligands for GPCR targets. This is motivated by the ability to develop more subtype-selective drugs targeted at less conserved regions of the receptor. Moreover, allosteric ligands modulate the effects of natural hormones and neurotransmitters, and may therefore regulate receptor activity in a more physiological manner. As noted above, the orthosteric binding pocket is highly conserved among all muscarinic receptor subtypes. Allosteric regulation of GPCRs was first observed for the M2 receptor and this receptor has been one of the most extensively characterized allosteric model systems⁹. Figure 4a shows the inner surface of the M2 receptor, highlighting residues that are not conserved with its closest relative, the M4 receptor. It can be seen that the orthosteric binding pocket and transmembrane core are highly conserved. The greatest diversity is observed in the extracellular loops and the extracellular end of TM segments that form the entrance to the orthosteric binding pocket. These amino acids represent structural diversity that could be exploited for the development of more subtype-selective ligands⁹. Of interest, site-directed mutagenesis and chimaeric receptor studies have implicated several of these amino acids in the binding of several well-characterized allosteric modulators⁹. As shown in Fig. 4b–d, these residues are located in ECL2 and the amino-terminus of TM7 at the entrance to the binding pocket. Trp 422^{7,35}, a residue implicated in the

binding of several allosteric modulators, appears to form an edge-to-face π – π interaction with Tyr 403^{6,51}, part of the aromatic cage surrounding the charged amine of the orthosteric ligand (Fig. 4d). Binding of allosteric ligands to this site would be expected to influence the association and disassociation rates of orthosteric ligands.

The structure of the M2 receptor provides insights into both orthosteric and allosteric regulation of muscarinic receptors. The development of more selective drugs for muscarinic receptors will probably require exploitation of the more diverse allosteric surface, either as exclusively allosteric ligands or as ligands that occupy both orthosteric and allosteric sites.

METHODS SUMMARY

Untagged human M2 muscarinic acetylcholine receptor was expressed in Sf9 cells with the IL3 replaced with T4 lysozyme, then extracted with digitonin and sodium cholate and purified by ligand affinity chromatography, then exchanged into decyl maltoside buffer. Purified receptor was crystallized by the lipidic cubic phase technique following addition of a stabilizing neopentyl glycol detergent. Data collection was performed at Advanced Photon Source beamlines 23ID-B and 23ID-D, and the structure solved by molecular replacement. Refinement statistics are given in Supplementary Table 2.

Full Methods and any associated references are available in the online version of the paper at www.nature.com/nature.

Received 10 August; accepted 1 December 2011.

Published online 25 January 2012.

1. Hulme, E. C., Birdsall, N. J. & Buckley, N. J. Muscarinic receptor subtypes. *Annu. Rev. Pharmacol. Toxicol.* **30**, 633–673 (1990).
2. Dale, H. H. The action of certain esters and ethers of choline, and their relation to muscarine. *J. Pharmacol. Exp. Ther.* **6**, 147–190 (1914).
3. Haga, K. *et al.* Functional reconstitution of purified muscarinic receptors and inhibitory guanine nucleotide regulatory protein. *Nature* **316**, 731–733 (1985).

4. Haga, K. & Haga, T. Purification of the muscarinic acetylcholine receptor from porcine brain. *J. Biol. Chem.* **260**, 7927–7935 (1985).
5. Kubo, T. *et al.* Cloning, sequencing and expression of complementary DNA encoding the muscarinic acetylcholine receptor. *Nature* **323**, 411–416 (1986).
6. Dixon, R. A. *et al.* Cloning of the gene and cDNA for mammalian β -adrenergic receptor and homology with rhodopsin. *Nature* **321**, 75–79 (1986).
7. Ovchinnikov, Y. A. Rhodopsin and bacteriorhodopsin: structure–function relationships. *FEBS Lett.* **148**, 179–191 (1982).
8. Wess, J., Eglén, R. M. & Gautam, D. Muscarinic acetylcholine receptors: mutant mice provide new insights for drug development. *Nature Rev. Drug Discov.* **6**, 721–733 (2007).
9. Gregory, K. J., Sexton, P. M. & Christopoulos, A. Allosteric modulation of muscarinic acetylcholine receptors. *Curr. Neuropharmacol.* **5**, 157–167 (2007).
10. Kameyama, K., Haga, K., Haga, T., Moro, O. & Sadée, W. Activation of a GTP-binding protein and a GTP-binding-protein-coupled receptor kinase (β -adrenergic-receptor kinase-1) by a muscarinic receptor M2 mutant lacking phosphorylation sites. *Eur. J. Biochem. FEBS* **226**, 267–276 (1994).
11. Ichiyama, S. *et al.* The structure of the third intracellular loop of the muscarinic acetylcholine receptor M₂ subtype. *FEBS Lett.* **580**, 23–26 (2006).
12. Rosenbaum, D. M. *et al.* GPCR engineering yields high-resolution structural insights into β_2 -adrenergic receptor function. *Science* **318**, 1266–1273 (2007).
13. Jaakola, V. P. *et al.* The 2.6 Å crystal structure of a human A_{2A} adenosine receptor bound to an antagonist. *Science* **322**, 1211–1217 (2008).
14. Wu, B. *et al.* Structures of the CXCR4 chemokine GPCR with small-molecule and cyclic peptide antagonists. *Science* **330**, 1066–1071 (2010).
15. Chien, E. Y. *et al.* Structure of the human dopamine D3 receptor in complex with a D2/D3 selective antagonist. *Science* **330**, 1091–1095 (2010).
16. Shimamura, T. *et al.* Structure of the human histamine H₁ receptor complex with doxepin. *Nature* **475**, 65–70 (2011).
17. Palczewski, K. *et al.* Crystal structure of rhodopsin: A G protein-coupled receptor. *Science* **289**, 739–745 (2000).
18. Warne, T. *et al.* Structure of a β_1 -adrenergic G-protein-coupled receptor. *Nature* **454**, 486–491 (2008).
19. Hulme, E. C., Lu, Z. L. & Bee, M. S. Scanning mutagenesis studies of the M₁ muscarinic acetylcholine receptor. *Receptors Channels* **9**, 215–228 (2003).
20. Heitz, F. *et al.* Site-directed mutagenesis of the putative human muscarinic M₂ receptor binding site. *Eur. J. Pharmacol.* **380**, 183–195 (1999).
21. Wess, J. Mutational analysis of muscarinic acetylcholine receptors: structural basis of ligand/receptor/G protein interactions. *Life Sci.* **53**, 1447–1463 (1993).
22. Goodwin, J. A., Hulme, E. C., Langmead, C. J. & Tehan, B. G. Roof and floor of the muscarinic binding pocket: variations in the binding modes of orthosteric ligands. *Mol. Pharmacol.* **72**, 1484–1496 (2007).
23. Ward, S. D., Curtis, C. A. & Hulme, E. C. Alanine-scanning mutagenesis of transmembrane domain 6 of the M₁ muscarinic acetylcholine receptor suggests that Tyr381 plays key roles in receptor function. *Mol. Pharmacol.* **56**, 1031–1041 (1999).
24. Bluml, K., Mutschler, E. & Wess, J. Functional role in ligand binding and receptor activation of an asparagine residue present in the sixth transmembrane domain of all muscarinic acetylcholine receptors. *J. Biol. Chem.* **269**, 18870–18876 (1994).
25. Rasmussen, S. G. *et al.* Structure of a nanobody-stabilized active state of the β_2 adrenoceptor. *Nature* **469**, 175–180 (2011).
26. Furukawa, H. *et al.* Conformation of ligands bound to the muscarinic acetylcholine receptor. *Mol. Pharmacol.* **62**, 778–787 (2002).
27. Zacharias, N. & Dougherty, D. A. Cation- π interactions in ligand recognition and catalysis. *Trends Pharmacol. Sci.* **23**, 281–287 (2002).
28. Brams, M. *et al.* Crystal structures of a cysteine-modified mutant in loop D of acetylcholine-binding protein. *J. Biol. Chem.* **286**, 4420–4428 (2011).
29. Oswald, C. *et al.* Crystal structures of the choline/acetylcholine substrate-binding protein ChoX from *Sinorhizobium meliloti* in the liganded and unliganded-closed states. *J. Biol. Chem.* **283**, 32848–32859 (2008).
30. Colletier, J. P. *et al.* Structural insights into substrate traffic and inhibition in acetylcholinesterase. *EMBO J.* **25**, 2746–2756 (2006).

Supplementary Information is linked to the online version of the paper at www.nature.com/nature.

Acknowledgements We thank S. Iwata at Kyoto University for supporting the production of M2 receptor, and we acknowledge support from the Japan Society for the Promotion of Science (Research for Future Program) (T.H.), from the Japan Science and Technology Corporation (CREST) (T.H.), from the Ministry of Education, Culture, Sports, Science and Technology of Japan (Grants-in-Aid for Scientific Research on Priority Area 15083201 (T.H.), from the Japan Science and Technology Corporation (ERATO) (T.K.), from Toray Science Foundation (T.K.), from Takeda Science Foundation (T.K.), from Ichiro Kanehara Foundation (T.K.), from The Sumitomo Foundation (T.K.), from the National Institutes of Health Grants NS028471 and GM083118 (B.K.K.), from the Mathers Foundation (B.K.K. and W.I.W.), and from the National Science Foundation (A.C.K.). We thank T. S. Kobilka for organizing the GPCR Workshop 2010 that brought together the research groups, and for facilitating this collaboration.

Author Contributions K.H. purified M2 and M2-T4L receptors, characterized their ligand binding activity, and performed attempts to crystallize them with hanging drop and other methods for more than ten years. A.C.K. crystallized the M2-T4L receptors in lipidic cubic phase, collected and processed diffraction data, solved and refined the structure, and assisted with manuscript preparation. H.A. set up the expression system and expressed M2-T4L in large amounts using the insect cell/baculovirus expression system. T.Y.-K. expressed M2 and M2-T4L receptors using a yeast expression system, and purified and crystallized M2 and M2-T4L receptors for five years. M.S. constructed several mutants of M2-T4L and evaluated their stabilities. C.Z. assisted with data collection and processing. W.I.W. oversaw data processing and refinement. T.O. gave advice to K.H. and T.H. on crystallization of the M2 receptor and interpretation of its structure. B.K.K. oversaw lipidic cubic phase crystallization, assisted with data collection, and wrote the manuscript together with T.H. and T.K. T.H., together with K.H., has engaged in biochemical studies of muscarinic receptors for more than thirty years, prepared M2 and M2-T4L receptors, and wrote part of the manuscript. T.K. has been collaborating with T.H. for five years, designed the receptor production strategy with T.H., and wrote part of the manuscript.

Author Information Coordinates and structure factors for M2-T4L are deposited in the Protein Data Bank under accession code 3UON. Reprints and permissions information is available at www.nature.com/reprints. The authors declare no competing financial interests. Readers are welcome to comment on the online version of this article at www.nature.com/nature. Correspondence and requests for materials should be addressed to B.K.K. (kobilka@stanford.edu), T.H. (tatsuya.haga@gakushuin.ac.jp) or T.K. (t-coba@mfour.med.kyoto-u.ac.jp).

METHODS

Construction of M2-T4L expression vectors for Sf9 cells. The coding sequence of the human M2-T4L receptor fusion protein was designed to have N-linked glycosylation sites (Asn 2, Asn 3, Asn 6 and Asn 9) mutated to aspartic acid and cysteine-less T4L (C54T, C97A) residues 2–161 inserted into the IL3, replacing M2 residues 218–376. This construct was synthesized (TAKARA Bio), and cloned into the pFastbac1 Sf9 expression vector (Invitrogen) as illustrated in Supplementary Fig. 1a. A TAA stop codon was placed after the R466 codon, terminating translation. The synthesized M2-T4L receptor described above was confirmed by sequencing.

Expression and membrane preparation. Recombinant baculovirus was made from pFastbac1-M2-T4L using the Bac-to-Bac system (Invitrogen)³¹. The M2-T4L protein was expressed in baculovirus-infected Sf9 insect cells as described previously³². Sf9 insect cells were prepared at a density of 1.0×10^6 cells ml^{-1} and suspended in 5 litres of the IPL-41/SF900 II complex media or ESF921 insect media. Media containing Sf9 insect cells were transferred into the CELLBAG 22 L/O (GE Healthcare) and cultured for 4 days with the following culture conditions: 20 r.p.m., 8.5° rocking angle, 30% O_2 , 0.25 l min^{-1} of air flow rate and 27°C . After 4 days, 200 to 300 ml of the M2-T4L baculovirus stock (approximate multiplicity of infection (m.o.i.), 2) and 700 to 800 ml of IPL-41/SF900 II complex media were transferred into the CELLBAG (final culture volume, 6 litres) and infected for 2 days under the following infection conditions: 22 r.p.m., 8.5° rocking angle, 50% O_2 , air flow rate, 0.25 l min^{-1} and 27°C . Two days later, a fraction of the cells was harvested for the binding assay and the remaining cells were centrifuged at 6,000g for 10 min and harvested. The cell pellet was washed with 250 ml of PBS without calcium chloride and magnesium chloride (PBS(–)) and resuspended with 100 ml of PBS(–) containing a protease inhibitor cocktail tablet (Roche). Final concentration of protease inhibitors was $2.5 \mu\text{g ml}^{-1}$ pepstatin, $2 \mu\text{g ml}^{-1}$ PMSF, $20 \mu\text{g ml}^{-1}$ leupeptin and 0.5 mM benzamidine. Cells were quick frozen in liquid nitrogen and stored at -80°C .

The membrane was prepared from the M2-T4L-expressing Sf9 insect cells as described previously³¹. For the preparation of membranes from insect cells, Sf9 insect cells were centrifuged at 1,500g for 10 min at 4°C . The pellet was washed with PBS(–), then resuspended in 100 ml of hypotonic buffer containing 10 mM HEPES at pH 7.5, 20 mM KCl, 10 mM MgCl_2 and protease inhibitor cocktail, followed by Dounce homogenization to resuspend the membranes. Insect cell membranes were centrifuged at 100,000g for 30 min and the pellets were resuspended in 10 mM HEPES at pH 7.5, 10 mM MgCl_2 , 20 mM KCl, 40% glycerol, and snap-frozen in liquid nitrogen and then stored at -80°C until use. Membrane proteins were quantified using the bicinchoninic acid (BCA) method (Pierce) using a BSA standard.

Purification of M2-T4L-QNB. M2-T4L was expressed in Sf9 cells, solubilized with digitonin/Na-cholate solution, and purified by using an affinity column with aminobenzotropine (ABT) as a ligand³³, as described below. The whole procedure was carried out at 4°C . Sf9 membrane preparations with 2.1 kg of wet weight and approximately $1.5 \mu\text{mol}$ of [^3H]QNB binding sites were solubilized with 1% digitonin, 0.35% Na-cholate, 10 mM K-phosphate buffer (pH 7.0) (KPB), 50 mM NaCl, 1 mM EDTA, a cocktail of protease inhibitors (41). The supernatant was applied to two ABT columns run in parallel (500 ml each), followed by washing with 0.1% digitonin, 0.1% Na-cholate, 20 mM KPB, 150 mM NaCl (21×2) at a rate of approximately 90 ml h^{-1} . M2-T4L was eluted from the ABT columns with 0.5 mM atropine, 0.1% digitonin, 0.1% Na-cholate, 20 mM KPB, 150 mM NaCl in 2 l elution volume for each column, and was bound to a column of hydroxyapatite (30 ml), which was washed at a rate of $30\text{--}50 \text{ ml h}^{-1}$ with a series of solutions as follows: (1) 0.1% digitonin, 0.1% Na-cholate, 20 mM KPB (100 ml); (2) $5 \mu\text{M}$ QNB, 0.1% digitonin, 0.1% Na-cholate, 20 mM KPB (600 ml); (3) 0.35% Na-cholate, 20 mM KPB (600 ml); (4) 0.2% decylmaltoside, 20 mM KPB (500 ml); (5) 0.2% decylmaltoside, 150 mM KPB (100 ml); (6) 0.2% decylmaltoside, 500 mM KPB (60 ml). M2-T4L-QNB was finally eluted with 0.2% decylmaltoside, 1 M KPB (50 ml). The eluate was concentrated to approximately 1 ml (approximately 30 mg protein per ml) with Amicon Ultra (MILLIPORE), followed by dialysis against 0.2% decylmaltoside, 20 mM Tris-HCl buffer (pH 7.5) and storage in -80°C . The yield was estimated to be approximately 50% on the assumption that the recovered protein is pure M2-T4L. Protein concentration was determined using BCA Protein Assay (PIERCE). Because we purified M2-T4L as a complex with QNB we could not estimate the [^3H]QNB binding activity because the dissociation rate of QNB is too slow. However, in preliminary experiments using [^3H]QNB or dissociable atropine as eluants, we confirmed that the receptor is purified to near homogeneity. The purity of M2-T4L was confirmed by SDS-PAGE and gel permeation chromatography (Supplementary Fig. 6). All the QNB used in purification and crystallization was the high-affinity enantiomer, R(–)-3-QNB.

Measurement of ligand binding activity. Ligand binding activity of wild-type M2 and M2-T4L receptors was determined as described previously³⁴. Briefly, the receptors solubilized from Sf9 membranes were incubated with 0.1–4 nM [^3H]QNB with or without $1 \mu\text{M}$ atropine, or with 2 nM [^3H]QNB with various concentrations of carbamylcholine or atropine in 0.1% digitonin, 20 mM KPB for 60 min at 30°C (total volume 0.2 ml). The amount of [^3H]QNB bound to receptors was assayed by using a small column of Sephadex G50 fine (2 ml). The density of [^3H]QNB binding sites in the particulate fraction of M2-T4L was 17 pmol per mg of protein on average and ranged from 5.3–35 pmol per mg of total protein.

Crystallization. QNB-bound M2-T4L was concentrated to 20 mg ml^{-1} in decyl maltoside buffer in a volume of approximately 100 μl . A 10% stock solution of lauryl maltose neopentyl glycol detergent (MNG, Anatrace) with 100 mM NaCl and 20 mM HEPES pH 7.5 was then added to the protein to a final concentration of 1% (w/v) of MNG detergent. The sample was incubated for 1 h on ice, then diluted to 1 ml in 0.1% MNG buffer and reconstituted to 50 mg ml^{-1} before reconstitution. The final volume of protein sample at this concentration was typically 20–30 μl . Protein was reconstituted in cubic phase by mixing with a 1.5-fold weight excess of a 10:1 monoolein:cholesterol mix by the twin-syringe method³⁵. Briefly, the protein and lipid were mixed by passage through coupled syringes 100 times either by hand or using a Gryphon LCP robot (Art Robbins Instruments). The reconstituted protein was dispensed using a modified ratchet device (Hamilton) or using the Gryphon LCP robot in 40 nl drops to either 24-well or 96-well glass sandwich plates and overlaid with 0.8 μl precipitant solution. A single crystallization lead was initially identified using an in-house screen and then optimized. Crystals for data collection were grown in 25–35% PEG 300, 100 mM ammonium phosphate, 2% 2-methyl-2,4-pentanediol, 100 mM HEPES pH 7.0–7.8. Crystals reached full size and were harvested after 3–4 days at 20°C . Typical crystals are shown in Supplementary Fig. 7.

Data collection and processing. Diffraction data were measured at the Advanced Photon Source beamlines 23 ID-B and 23 ID-D. Several hundred crystals were screened, and a final data set was compiled using diffraction wedges of typically 5 degrees from the 23 most strongly diffracting crystals. Data reduction was performed using HKL2000³⁶. Diffraction quality was very heterogeneous, with some crystals diffracting to 2.3 Å whereas others failed to diffract past 3.5 Å. Among the best crystals, most diffracted to 3.0–2.5 Å. Severe radiation damage and anisotropic diffraction resulted in low completeness in higher resolution shells. We report this structure to an overall resolution of 3.0 Å. Despite the low completeness in high resolution bins, inclusion of these reflections significantly improved map quality. Highest shell $\langle I \rangle / \langle \sigma I \rangle$ is relatively low, in large part due to anisotropy of the diffraction. The final resolution cut-off was chosen on the basis of completeness and $\langle I \rangle / \langle \sigma I \rangle$ in the spherical highest shell, but analysis of average $F/\sigma F$ values along reciprocal space axes suggests resolution limits (based on average $F/\sigma F > 3$) of 3.5, 2.9 and 2.7 Å along a^* , b^* and c^* , respectively. The real space c -axis is normal to the plane of the lipid membrane in the crystal.

Structure solution and refinement. The structure was solved by molecular replacement using Phaser^{37,38} with the structure of the inactive β_2 adrenergic receptor and T4L used as search models (PDB accession 2RH1). The initial molecular replacement model was further fitted by rigid body refinement followed by simulated annealing and restrained refinement in Phenix³⁹. Iterative manual rebuilding and refinement steps were performed with Coot and phenix.refine, respectively. Figures were prepared with PyMOL, and Ramachandran statistics were calculated with MolProbity.

- Asada, H. *et al.* Evaluation of the *Pichia pastoris* expression system for the production of GPCRs for structural analysis. *Microb. Cell Fact.* **10**, 24 (2011).
- Weber, W., Weber, E., Geisse, S. & Memmert, K. Optimisation of protein expression and establishment of the Wave Bioreactor for Baculovirus/insect cell culture. *Cytotechnology* **38**, 77–85 (2002).
- Haga, K. & Haga, T. Affinity chromatography of the muscarinic acetylcholine receptor. *J. Biol. Chem.* **258**, 13575–13579 (1983).
- Haga, T., Haga, K. & Hulme, E. C. in *Receptor Biochemistry: A Practical Approach* (ed. Hulme, E. C.) 51–78 (Oxford Univ. Press, 1990).
- Caffrey, M. & Cherezov, V. Crystallizing membrane proteins using lipidic mesophases. *Nature Protocols* **4**, 706–731 (2009).
- Otwinowski, Z. & Minor, W. Processing of x-ray diffraction data collected in oscillation mode. *Methods Enzymol.* **276**, 307–326 (1997).
- McCoy, A. J. Solving structures of protein complexes by molecular replacement with Phaser. *Acta Crystallogr. D* **63**, 32–41 (2007).
- McCoy, A. J. *et al.* Phaser crystallographic software. *J. Appl. Cryst.* **40**, 658–674 (2007).
- Afonine, P. V., Grosse-Kunstleve, R. W. & Adams, P. D. A robust bulk-solvent correction and anisotropic scaling procedure. *Acta Crystallogr. D* **61**, 850–855 (2005).

Maternal and paternal genomes contribute equally to the transcriptome of early plant embryos

Michael D. Nodine^{1,2} & David P. Bartel^{1,2}

In animals, maternal gene products deposited into eggs regulate embryonic development before activation of the zygotic genome¹. In plants, an analogous period of prolonged maternal control over embryogenesis is thought to occur based on some gene-expression studies^{2–6}. However, other gene-expression studies and genetic analyses show that some transcripts must derive from the early zygotic genome^{7–14}, implying that the prevailing model does not fully explain the nature of zygotic genome activation in plants. To determine the maternal, paternal and zygotic contributions to the early embryonic transcriptome, we sequenced the transcripts of hybrid embryos from crosses between two polymorphic inbred lines of *Arabidopsis thaliana* and used single-nucleotide polymorphisms diagnostic of each parental line to quantify parental contributions. Although some transcripts seemed to be either inherited from primarily one parent or transcribed from imprinted loci, the vast majority of transcripts were produced in near-equal amounts from both maternal and paternal alleles, even during the initial stages of embryogenesis. Results of reporter experiments and analyses of transcripts from genes that are not expressed in sperm and egg indicate early and widespread zygotic transcription. Thus, in contrast to early animal embryogenesis, early plant embryogenesis is mostly under zygotic control.

The prevailing model for the maternal-to-zygotic transition in plants proposes that most early embryonic messenger RNAs are maternally derived transcripts, resulting either from maternal inheritance or from higher transcriptional activity of maternally derived genes until the globular stages (in which the embryo proper has between ~32 to >100 cells)^{2,6,15}. Because fundamental patterning events, including apical-basal and radial axis formation^{16,17}, occur during the preglobular stages, this model implies that key cell-specification decisions are mostly under maternal control. However, this model is difficult to reconcile with other studies that report equivalent maternal and paternal expression of interrogated genes in preglobular stages^{8,9,11} and zygotic-recessive behaviour of mutants with preglobular developmental phenotypes^{12–14}.

To determine the origins of embryonic transcripts globally, we crossed polymorphic Col-0 and Cvi-0 *Arabidopsis thaliana* accessions and performed RNA-seq on poly(A)⁺ RNA isolated from hybrid embryos with either one-to-two, eight, or ~32 cells in the embryo proper (hereafter referred to as 1-cell/2-cell, 8-cell and ~32-cell embryos). To control for inherent expression differences between Col-0 and Cvi-0 loci, the same procedure was performed using embryos derived from reciprocal crosses. Illumina sequencing of the six samples yielded 73,955,956 reads that both perfectly and uniquely matched the transcribed regions of 23,874 genes (Supplementary Table 1). Overall, transcript levels from the same stage but different reciprocal crosses were highly correlated ($r \geq 0.96$; Supplementary Fig. 1). This reproducibility and sequencing depth indicated that our results would be informative for inferring the maternal, paternal and zygotic contributions to the early embryonic transcriptome.

The prevailing model for the maternal-to-zygotic transition predicted that at the early embryonic stages transcripts would derive primarily

from maternal alleles, and then at the globular stage they would derive more evenly from both alleles because at this stage the zygotic genome would be active. In contrast to this expectation, we found equal amounts of paternally and maternally derived reads at all three stages, including the 1-cell/2-cell and 8-cell embryos (Fig. 1a). When examining transcripts with at least five reads overlapping single-nucleotide polymorphisms (SNPs) in each cross, most were expressed equally from the maternal and paternal alleles, even at the earliest stage (Fig. 1b and Supplementary Data 1; note that in the Col-0 × Cvi-0

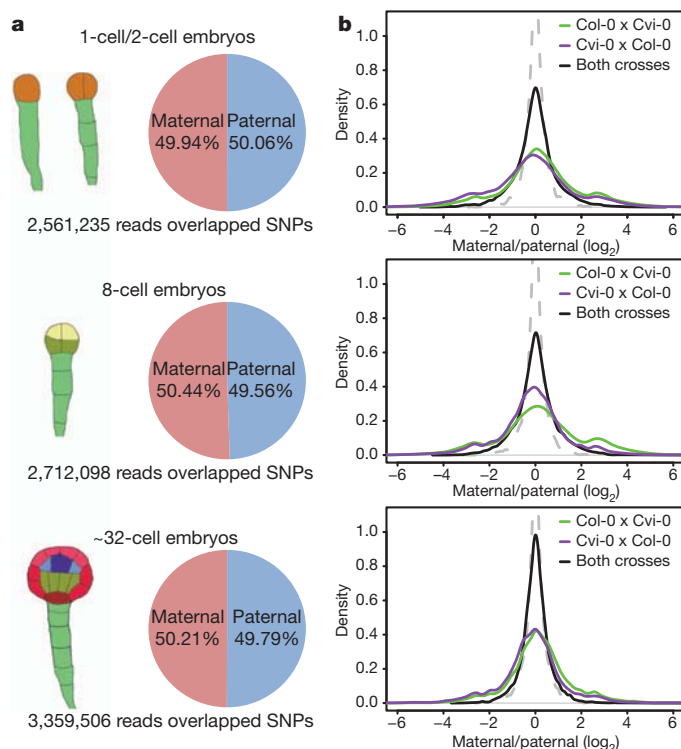


Figure 1 | Maternal and paternal genomes contribute equally to the early embryonic transcriptome. **a**, Proportion of RNA-seq reads overlapping maternal and paternal SNPs within transcribed regions of annotated genes. Drawings illustrate stages of isolated embryos, coloured to represent the diversity of cell lineages in each stage. Pie charts show proportions of reads overlapping maternal and paternal SNPs. **b**, Distributions of maternal-to-paternal ratios (\log_2) in 1-cell/2-cell (top), 8-cell (middle) and ~32-cell (bottom) embryos. Maternal-to-paternal ratios were calculated for transcripts that had ≥ 5 SNP-overlapping reads from the Col-0 × Cvi-0 cross (green; $n > 7,388$ for each stage) or the Cvi-0 × Col-0 cross (purple; $n > 8,071$ for each stage), and transcripts that had ≥ 5 SNP-overlapping reads from both reciprocal crosses (black; $n > 6,892$ for each stage). Binomial modelling determined the distributions expected for transcripts examined in both reciprocal crosses if there had been no parent-of-origin effects and no noise apart from stochastic counting variability (grey dashed lines).

¹Whitehead Institute for Biomedical Research, 9 Cambridge Center, Cambridge, Massachusetts 02142, USA. ²Howard Hughes Medical Institute and Department of Biology, Massachusetts Institute of Technology, Cambridge, Massachusetts 02139, USA.

cross, the maternal parent is Col-0, as the convention is to write the maternal parent first). In each cross, small but discernable subpopulations of transcripts were derived predominantly from either maternal or paternal alleles. However, in the respective reciprocal cross those same transcripts tended to derive from the opposite parent, which showed that rather than arising from parent-of-origin effects, these subpopulations arose mostly from genotypic effects, that is, from preferential expression from either the Col-0 or Cvi-0 alleles. Thus, when considering results of both crosses together, no overall maternal (or paternal) bias was observed, and at each stage the distribution of maternal-to-paternal ratios resembled that predicted for equal contribution from both alleles, with most of the variability explained by stochastic counting statistics, as modelled by the binomial distribution (Fig. 1b). The remainder of the variability was attributed to both additional noise (both experimental and biological) and a small subset of transcripts with parent-of-origin effects, for which the number that were maternally enriched approximately equalled the number that were paternally enriched.

Because most transcripts were derived from the maternal and paternal genomes in near-equal amounts, we hypothesized that either equal amounts of each transcript were inherited upon fertilization or the zygotic genome was activated much earlier than previously proposed. Supporting the latter possibility, the fold-change distributions centred at 0.0 (\log_2), showing no hint of the maternal bias that would be expected if the egg, with its larger cytoplasm, contributed more RNA than the sperm (Fig. 1b). In addition, 543 transcripts had at least four-fold higher reads per million (genome- and cDNA-matching reads) values at the 8-cell stage than at the 1-cell/2-cell stages, which suggested active transcription of the corresponding genes between the 1-cell/2-cell and 8-cell stages (as the alternative model of differential mRNA stability would require a large decrease in total mRNA between these two stages; Supplementary Data 1). Furthermore, 1,138 transcripts that were previously called undetectable in both egg and sperm microarray data sets^{18,19} were among the top 50% most abundant transcripts in our 1-cell/2-cell data sets (Supplementary Data 1). These results, taken together with the observation that transcripts for RNA polymerase II subunits were among the most abundant in the early embryo (Supplementary Table 2), suggested that during the initial stages of embryogenesis many transcripts are transcribed from both maternal and paternal alleles, and that this transcription, combined with turnover of inherited transcripts, quickly overwrites most parent-of-origin biases present when the egg and sperm first fuse.

To test directly whether maternally and paternally inherited genes are transcribed in very early embryos, we used the LhG4/pOp transactivation system²⁰. In this system, one parent contained a transgene encoding the LhG4 transcription factor under the control of either the *RPS5A* or the *UBI3* promoter (chosen because they generate products that can be found in the early embryo^{9,21}), whereas the other parent harboured a nuclear-localized green fluorescent protein (GFP) reporter transgene under the control of the artificial pOp promoter to which LhG4 binds and transcriptionally activates (*pOp::GFP*). Because one gamete contributed the reporter gene and the other gamete contributed its activator, any reporter expression dependent on the activator could not occur until after the zygotic genome was transcriptionally active. No GFP signal was observed in embryos carrying the *pOp::GFP* reporter gene but no activator, which confirmed the absence of leaky expression in either the gametes or embryo (Fig. 2). GFP signal was detected in zygotes within 4–8 h after fertilization from crosses that brought the reporter together with its activator, regardless of whether the reporter was inherited through the egg or sperm (Fig. 2). The GFP signal in the early zygote was not as strong as that in the endosperm, which might indicate a slight delay in activation of the genome of the very early zygote or might result from more robust transcription in the endosperm. Nonetheless, when considered together our results demonstrate that both maternally and paternally inherited chromosomes are transcriptionally active at least in 1-cell embryos and most likely before.

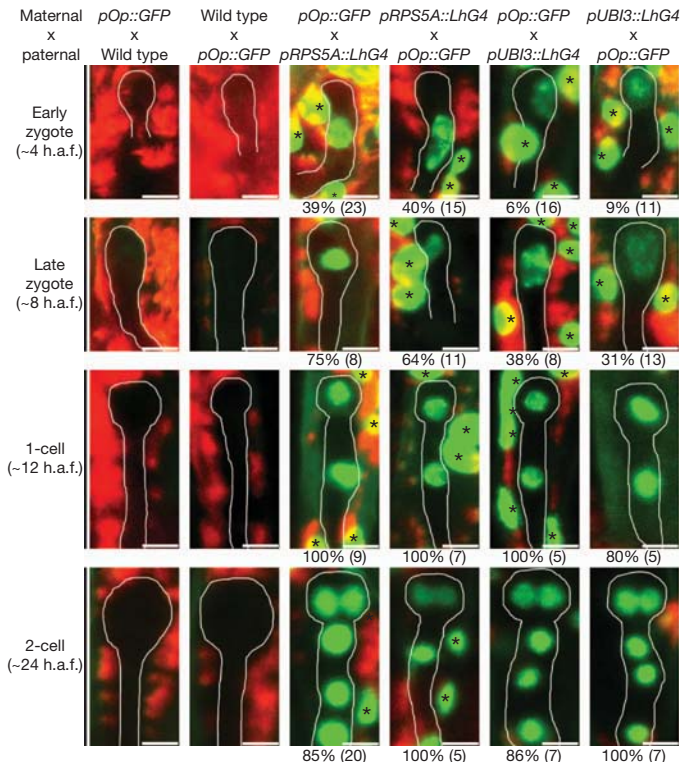


Figure 2 | Maternally and paternally inherited transgenes are transcribed in the initial stages of embryogenesis. Confocal scanning laser microscopy images show early embryos from the indicated crosses, which were between plants with a transgenic reporter (*pOp::GFP*) and either plants without an activator (wild type) or plants with a transgenic activator driven from either the *RPS5A* or the *UBI3* promoter (*pRPS5A::LhG4* or *pUBI3::LhG4*, respectively). Embryonic stages and the approximate number of hours after fertilization (h.a.f.) are shown to the left. GFP signal is indicated by green nuclei; background autofluorescence is shown in red. Embryos are outlined in white for clarity. Asterisks indicate endosperm nuclei. Of the seeds with GFP signal in endosperm (*n* in parentheses), the percentage that also had GFP signal in embryos is indicated below each image. In endosperm, expression from maternal alleles is expected to be twofold higher than that from paternal alleles, but this difference is not observed in these images because the GFP signal in the endosperm was beyond its dynamic range. Scale bars represent 10 μ m.

Having established that most early embryonic transcripts derived equally from the maternal and paternal genomes, we turned our attention to the few that might be preferentially inherited or preferentially expressed from the maternal or paternal alleles. For most early embryonic transcripts the genotype of the allele had a larger effect on transcript levels than did parent of origin (Figs 1b and 3a). Indeed, hundreds of transcripts were preferentially expressed from either the Col-0 or Cvi-0 allele irrespective of their parent of origin (Supplementary Data 2), presumably as direct consequences of either DNA-sequence or epigenetic differences between the Col-0 and Cvi-0 alleles. This prevalence of genotypic/epigenotypic effects over parent-of-origin effects led to significant negative correlations between the maternal-to-paternal ratios at each stage (Fig. 3a, Pearson's $r < -0.43$, $P < 10^{-15}$). Nonetheless, at each stage a small subset of transcripts passed our cutoffs for classification as maternally or paternally enriched, that is, fourfold maternally or paternally enriched in each cross, and not exceeding the false discovery rate (FDR) threshold of 0.05 (Pearson's χ^2 tests, Benjamini and Hochberg FDR). With these cutoffs, 77 and 45 transcripts were designated maternally and paternally enriched, respectively, in at least one stage (Fig. 3a and Supplementary Data 3). For five transcripts, an independent assay involving diagnostic cleavage of an amplified polymorphic sequence was performed, and for all five, the parent-of-origin effects were confirmed (Supplementary Fig. 2).

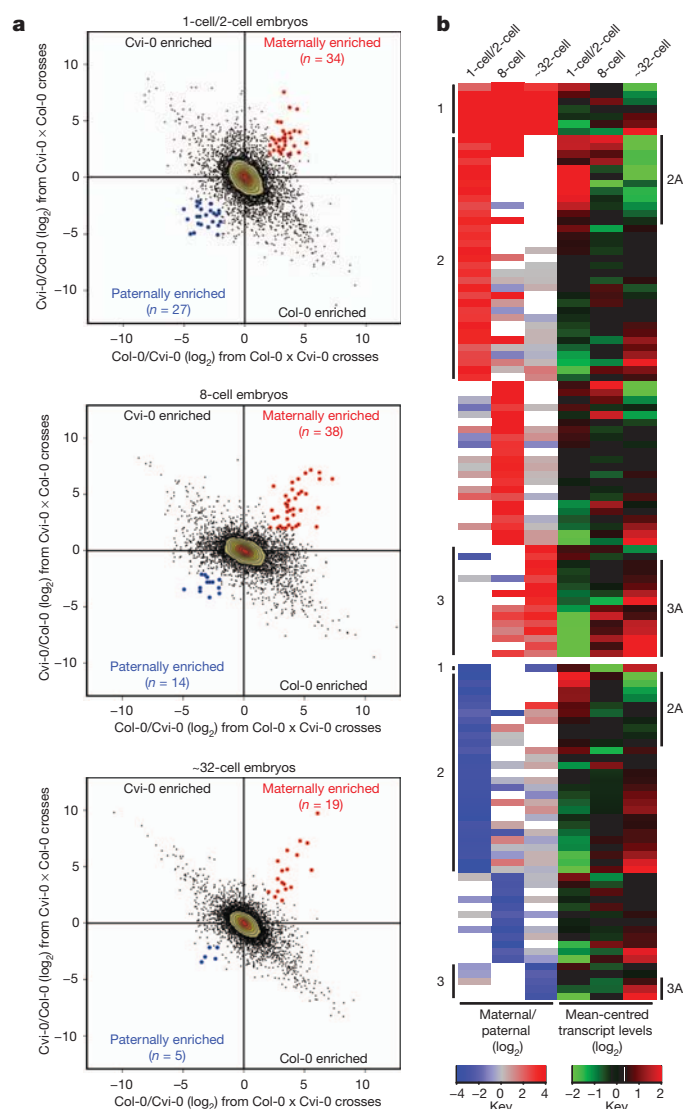


Figure 3 | Dozens of transcripts are preferentially inherited or preferentially expressed. **a**, Maternal-to-paternal ratios for transcripts in 1-cell/2-cell, 8-cell and ~32-cell embryos. Ratios for transcripts that had ≥ 8 SNP-overlapping reads in both the Col-0 \times Cvi-0 and Cvi-0 \times Col-0 crosses are plotted. Points, as well as the numbers, that passed cutoffs for maternally or paternally enriched transcripts (see text) are indicated in red and blue, respectively. **b**, Heat maps of both maternal-to-paternal ratios and changes in transcript levels for transcripts passing cutoffs as maternally (top) or paternally (bottom) enriched in at least one of the three stages. Maternal-to-paternal ratios are colour-coded (key), unless the transcript had < 8 SNP-overlapping reads in one cross, in which case the corresponding heat-map value is not coloured. Changes in the levels of a transcript (reads per million) relative to its mean are colour-coded (key). Numbers to the left indicate candidates for both preferential inheritance and preferential expression (1), preferential inheritance (2) or preferential expression (3). Numbers to the right highlight a subset of the class 2 transcripts, which had relatively high levels in 1-cell/2-cell embryos compared to ~32-cell embryos and thus potentially derived mainly from preferential inheritance (2A), or a subset of class 3 transcripts, which had relatively low levels in 1-cell/2-cell embryos compared to ~32-cell embryos and thus potentially derived mainly from parent-of-origin-specific transcription (3A).

Although the maternal enrichment of some transcripts might be due to their transport from maternal sporophytic tissues, such a mechanism cannot explain paternal enrichment. Some transcripts had strong parent-of-origin effects in 1-cell/2-cell embryos, suggesting that they were preferentially inherited from one parent (Fig. 3b). Confirmation that these biases are indeed due to inheritance would substantially add to the single previously documented example of an

inherited transcript in plants²². Other transcripts had stronger parent-of-origin effects at later stages, suggesting that they were preferentially expressed from either the maternally or the paternally inherited allele (Fig. 3b). This potential parent-of-origin-specific expression implied a form of imprinting in the *Arabidopsis* embryo. Genome-wide approaches similar to ours but looking much later after fertilization greatly expanded the list of genes with parent-of-origin-specific expression in the endosperm but did not identify such genes in embryos^{23,24}. Thus, the imprinting-like phenomenon that we observed in early embryos is short lived, which suggests that it differs from the more persistent imprinting previously characterized in either endosperm or mammals²⁵. For example, it might involve alternative chromatin states inherited from the egg and sperm, which after several cell divisions equilibrate between the two alleles. Such a mechanism would not necessarily require DNA methylation, although we note that in the only previous report of imprinting in plant embryos (at the *MEE1* locus of maize), methylation marks are lost from maternal alleles at the initial stages of embryogenesis, but then re-established to match the paternal alleles at later stages²⁶.

Our results showing that during the initial stages of *Arabidopsis* embryogenesis both the maternal and paternal genomes are active and make essentially equivalent contributions to the embryonic transcriptome are in marked contrast to a recent report that ~88% of the 2-cell/4-cell embryonic transcriptome is derived from the maternal genome². That study, published while our manuscript was in preparation, used SNPs in the transcriptomes of hybrid embryos derived from a cross between the Ler-1 (maternal parent) and Col-0 (paternal parent) accessions to estimate maternal and paternal genomic contributions. Because results from the reciprocal cross were not reported, the previous study could not distinguish parent-of-origin effects from genotypic effects. However, because an analysis unable to account for genotypic effects would be expected to misidentify transcripts as paternally derived as frequently as it misidentifies them as maternally derived, we considered other possibilities for the discrepancy between their results and ours. Our pilot studies had shown that early embryos must be extensively washed to prevent seed-coat RNA contamination, and indeed we found evidence that the embryo RNA samples of ref. 2 contained large amounts of seed-coat mRNA (Supplementary Fig. 3). Because the seed coat is a maternal tissue, this contamination explained why they observed such a large bias in maternal RNAs.

Genes zygotically required for the initial zygotic division have been identified in *Arabidopsis*^{9,12,13}. Moreover, paternal gene expression has been detected for 24 endogenous genes and a transgene in maize zygotes^{8,27}, and *de novo* transcription has been demonstrated recently in tobacco zygotes²⁸. Rather than interpreting these findings as exceptions to the model or as differences between species, our transcriptome-wide analyses and reporter data strongly support the proposal of an alternative model for the maternal-to-zygotic (or, to put it more precisely, the maternal/paternal-to-zygotic) transition in plants. In this model, the zygotic genome is activated within the first few hours after fertilization, and equal transcription of both maternal and paternal alleles generates most of the early embryonic transcriptome at the 1-cell stage or before. Our model implies that although the maternal and paternal gene products are inherited in the zygote upon fertilization and contribute to its development²², the zygotic gene products are the ones that primarily control the initial cell-specification events of embryogenesis.

METHODS SUMMARY

Col-0 and Cvi-0 seed stocks were obtained from the *Arabidopsis* Biological Resource Center. Flowers were emasculated 1 day before crossing, and pools of 20 1-cell/2-cell, 8-cell and ~32-cell embryos were hand-dissected approximately 40, 64 and 78 h after pollination, respectively. RNA isolation, linear amplification of poly(A) RNA and strand-specific RNA-seq were as described²¹, except that embryos were extensively washed before RNA isolation. After removing adaptor sequences, reads were mapped to both the *A. thaliana* genome and transcript models (Col-0 genome reference, TAIR10) with the Bowtie short-read aligner²⁹.

Reads were also mapped to a 'pseudo' Cvi-0 genome and Cvi-0 transcript models, in which SNPs in the Col-0 genome and transcript models were replaced with Cvi-0 variants (ftp://ftp.arabidopsis.org/home/tair/Sequences/Polymorphism_datasets/Ecker_Cvi_snps.txt) generated by the 1001 Genomes Project. Reads that both perfectly and uniquely matched either the genomes or transcript models were retained, and those overlapping transcribed regions of annotated genes were evaluated for overlap with SNPs. Those diagnostic of one genome or the other were tallied after normalizing for differences in sequencing yield between samples. Tallies for multiple SNPs within the same gene were combined before calculating maternal-to-paternal ratios for each transcript.

Full Methods and any associated references are available in the online version of the paper at www.nature.com/nature.

Received 5 September; accepted 1 December 2011.

Published online 22 January 2012.

1. Tadros, W. & Lipshitz, H. D. The maternal-to-zygotic transition: a play in two acts. *Development* **136**, 3033–3042 (2009).
2. Autran, D. *et al.* Maternal epigenetic pathways control parental contributions to *Arabidopsis* early embryogenesis. *Cell* **145**, 707–719 (2011).
3. Vielle-Calzada, J. P., Baskar, R. & Grossniklaus, U. Delayed activation of the paternal genome during seed development. *Nature* **404**, 91–94 (2000).
4. Baroux, C., Blanvillain, R. & Gallois, P. Paternally inherited transgenes are down-regulated but retain low activity during early embryogenesis in *Arabidopsis*. *FEBS Lett.* **509**, 11–16 (2001).
5. Grimanelli, D., Perotti, E., Ramirez, J. & Leblanc, O. Timing of the maternal-to-zygotic transition during early seed development in maize. *Plant Cell* **17**, 1061–1072 (2005).
6. Baroux, C., Autran, D., Gillmor, C. S., Grimanelli, D. & Grossniklaus, U. The maternal to zygotic transition in animals and plants. *Cold Spring Harb. Symp. Quant. Biol.* **73**, 89–100 (2008).
7. Springer, P. S., Holding, D. R., Groover, A., Yordan, C. & Martienssen, R. A. The essential Mcm7 protein PROLIFERA is localized to the nucleus of dividing cells during the G₁ phase and is required maternally for early *Arabidopsis* development. *Development* **127**, 1815–1822 (2000).
8. Meyer, S. & Scholten, S. Equivalent parental contribution to early plant zygotic development. *Curr. Biol.* **17**, 1686–1691 (2007).
9. Weijers, D., Geldner, N., Offringa, R. & Jurgens, G. Seed development: Early paternal gene activity in *Arabidopsis*. *Nature* **414**, 709–710 (2001).
10. Sprunck, S., Baumann, U., Edwards, K., Langridge, P. & Dresselhaus, T. The transcript composition of egg cells changes significantly following fertilization in wheat (*Triticum aestivum* L.). *Plant J.* **41**, 660–672 (2005).
11. Ingouff, M. *et al.* Zygotic resetting of the HISTONE 3 variant repertoire participates in epigenetic reprogramming in *Arabidopsis*. *Curr. Biol.* **20**, 2137–2143 (2010).
12. Xu, J. *et al.* EMBRYONIC FACTOR 1 encodes an AMP deaminase and is essential for the zygote to embryo transition in *Arabidopsis*. *Plant J.* **42**, 743–758 (2005).
13. Ronceret, A. *et al.* The first zygotic division in *Arabidopsis* requires *de novo* transcription of thymidylate kinase. *Plant J.* **53**, 776–789 (2008).
14. Muralla, R., Lloyd, J. & Meinke, D. Molecular foundations of reproductive lethality in *Arabidopsis thaliana*. *PLoS ONE* **6**, e28398 (2011).
15. Pillot, M. *et al.* Embryo and endosperm inherit distinct chromatin and transcriptional states from the female gametes in *Arabidopsis*. *Plant Cell* **22**, 307–320 (2010).
16. Mayer, U., Torres Ruiz, R. A., Berleth, T., Misera, S. & Jurgens, G. Mutations affecting body organization in the *Arabidopsis* embryo. *Nature* **353**, 402–407 (1991).
17. Laux, T., Wurschum, T. & Breuninger, H. Genetic regulation of embryonic pattern formation. *Plant Cell* **16** (Suppl. 1), S190–S202 (2004).
18. Wuest, S. E. *et al.* *Arabidopsis* female gametophyte gene expression map reveals similarities between plant and animal gametes. *Curr. Biol.* **20**, 506–512 (2010).
19. Borges, F. *et al.* Comparative transcriptomics of *Arabidopsis* sperm cells. *Plant Physiol.* **148**, 1168–1181 (2008).
20. Moore, I., Galweiler, L., Grosskopf, D., Schell, J. & Palme, K. A transcription activation system for regulated gene expression in transgenic plants. *Proc. Natl Acad. Sci. USA* **95**, 376–381 (1998).
21. Nodine, M. D. & Bartel, D. P. MicroRNAs prevent precocious gene expression and enable pattern formation during plant embryogenesis. *Genes Dev.* **24**, 2678–2692 (2010).
22. Bayer, M. *et al.* Paternal control of embryonic patterning in *Arabidopsis thaliana*. *Science* **323**, 1485–1488 (2009).
23. Gehring, M., Missirian, V. & Henikoff, S. Genomic analysis of parent-of-origin allelic expression in *Arabidopsis thaliana* seeds. *PLoS ONE* **6**, e23687 (2011).
24. Hsieh, T. F. *et al.* Regulation of imprinted gene expression in *Arabidopsis* endosperm. *Proc. Natl Acad. Sci. USA* **108**, 1755–1762 (2011).
25. Feil, R. & Berger, F. Convergent evolution of genomic imprinting in plants and mammals. *Trends Genet.* **23**, 192–199 (2007).
26. Jahnke, S. & Scholten, S. Epigenetic resetting of a gene imprinted in plant embryos. *Curr. Biol.* **19**, 1677–1681 (2009).
27. Scholten, S., Lorz, H. & Kranz, E. Paternal mRNA and protein synthesis coincides with male chromatin decondensation in maize zygotes. *Plant J.* **32**, 221–231 (2002).
28. Zhao, J. *et al.* Dynamic changes of transcript profiles after fertilization are associated with *de novo* transcription and maternal elimination in tobacco zygote, and mark the onset of the maternal-to-zygotic transition. *Plant J.* **65**, 131–145 (2011).
29. Langmead, B., Trapnell, C., Pop, M. & Salzberg, S. L. Ultrafast and memory-efficient alignment of short DNA sequences to the human genome. *Genome Biol.* **10**, R25 (2009).

Supplementary Information is linked to the online version of the paper at www.nature.com/nature.

Acknowledgements We thank J. Ecker and the 1001 Genomes Project for generating the list of Cvi-0 SNPs; the J. Harada and R. Goldberg laboratories for making the *Arabidopsis* seed development LCM microarray data sets publicly available; I. Moore for the transactivation vectors; J. Long for the *UBI3* promoter fragment; the Whitehead Genome Technology Core for sequencing; and D. Meinke for providing a curated list of preglobular zygotic-recessive mutants before publication. This work used the W. M. Keck Biological Imaging Facility at the Whitehead Institute and was supported by NIH grant GM067031 (D.P.B.) and NIH Postdoctoral Fellowship GM084656 (M.D.N). D.P.B. is an Investigator of the Howard Hughes Medical Institute.

Author Contributions M.D.N. designed and performed the experiments. M.D.N. and D.P.B. interpreted the results and wrote the manuscript.

Author Information Raw and processed RNA-seq data sets have been deposited into NCBI GEO (<http://www.ncbi.nlm.nih.gov/geo/>) under accession number GSE33713. Reprints and permissions information is available at www.nature.com/reprints. The authors declare no competing financial interests. Readers are welcome to comment on the online version of this article at www.nature.com/nature. Correspondence and requests for materials should be addressed to D.P.B. (dbartel@wi.mit.edu).

METHODS

Plant growth and embryo dissections. Col-0 and Cvi-0 seed stocks were obtained from the *Arabidopsis* Biological Resource Center. Plants were grown at 22 °C in a Conviron growth chamber with a 16-h light/8-h dark cycle. Flowers were emasculated 1 day before crossing, and pools of 20 1-cell/2-cell, 8-cell and ~32-cell embryos were hand-dissected approximately 40, 64 and 78 h after pollination, respectively.

Embryo dissections were performed in water on glass slides using a SZH stereo microscope (Olympus) with 128× magnification. Tungsten needles (Fine Science Tools) were used to cut open the seeds and remove the embryos from the rest of the seed material. For each embryo, a heat-pulled borosilicate glass microcapillary pipette (Harvard Apparatus) was used to move it to a depression slide containing 50 µl water. The embryo was then washed two additional times by serial transfer to slides containing 50 µl water, using a new pipette and fresh water for each transfer. Washed embryos were collected in 30 µl of RNAlater (Ambion).

RNA-seq and analyses. RNA isolation, linear amplification of poly(A) RNA and strand-specific RNA-seq were as described²¹, except that embryos were extensively washed before RNA isolation. After removing adaptor sequences, reads were mapped to both the *A. thaliana* genome and transcript models (Col-0 genome reference, TAIR10) with the Bowtie short-read aligner²⁹. Reads were also mapped to a 'pseudo' Cvi-0 genome and Cvi-0 transcript models, in which SNPs in the Col-0 genome and transcript models were replaced with Cvi-0 variants (ftp://ftp.arabidopsis.org/home/tair/Sequences/Polymorphism_datasets/Ecker_Cvi_snps.txt) generated by the 1001 Genomes Project. Reads that both perfectly and uniquely matched either the genomes or transcript models were retained, and those overlapping transcribed regions of annotated genes were evaluated for overlap with SNPs. To normalize for differences in library sizes, the numbers of reads representing each transcript were divided by the total number of reads matching the genome and transcript models. SNP-overlapping reads were assigned to one of the parental genomes and tallied for each transcript, combining tallies for multiple SNPs within the same transcript.

Statistical analyses and graphics. Statistical analyses were performed and associated graphics were generated with the R statistical computing base package³⁰. The SciPy tools for Python were used to calculate χ^2 test statistics and associated probabilities.

Transgenic lines. The pBIN+LhG4-GW vector was generated by digesting both the pBIN+LhG4 vector and the attR1/attR2-containing vector GWRFa:pET42a

with KpnI and ligating together the appropriate digestion fragments. *RPS5A* and *UBI3* promoter fragments were amplified with appropriate primer pairs, cloned into pENTR-D/TOPO (Invitrogen) and then recombined with pBIN+LhG4-GW to generate pRPS5A::LhG4-GW and pUBI3::LhG4-GW, respectively. The pV-TOP-GFP vector was generated by double-digesting pV-TOP(E3) and NLSGFPF1R1::pCR8 with HindIII and PmeI, and ligating together the appropriate digestion fragments to replace the GUS reporter with a nuclear-localized GFP reporter. NLSGFPF1R1::pCR8 was created by amplifying pCGTAG with appropriate primers and cloning into pCR8/GW-TOPO (Invitrogen). pOp::GFP was then generated by digesting pV-TOP-GFP and GWF1R3::pENTR with SalI, and ligating together the appropriate digestion fragments. GWF1R3::pENTR was created by amplifying the attR1/attR2 Gateway cassette from GWRFa:pET42a with a series of overlap extension PCRs to remove internal SalI sites and add SalI sites on the ends of amplicons, which were then cloned into pENTR/D-TOPO (Invitrogen). Oligonucleotides used to generate the above constructs are listed in Supplementary Table 3. All constructs were transformed into Col-0 by *Agrobacterium*-mediated transformation. Because the progeny of T₁ lines gave more robust GFP signal than did progeny of established lines, T₁ lines were used for all reporter crosses. Embryos from crosses using at least 13 *pOp::GFP*, four *pRPS5A::LhG4* and six *pUBI3::LhG4* independent T₁ lines were examined.

Microscopy. For confocal scanning laser microscopy, developing seeds were mounted in 50 mM potassium phosphate buffer, pH 7.2, with 5% glycerol. A 488-nm laser on a Zeiss LSM 510 confocal microscope was used to excite GFP and seed autofluorescence, and images were collected at 505–530 nm and 644–719 nm, respectively.

Analyses of cleaved amplified polymorphic sequences. Transcripts containing a SNP that created or disrupted a restriction site in the corresponding cDNA were selected for analysis. Random hexamers (Invitrogen) were used for reverse transcription with Superscript III (Invitrogen) and primers flanking the SNPs were used for amplification (Supplementary Table 3). The amplified DNA was digested with the appropriate restriction enzyme (New England Biolabs; Supplementary Table 4). Digestion products were resolved on 2% agarose gels stained with ethidium bromide, and bands were quantified with Quantity One 1-D analysis software (Bio-Rad).

30. R Development Core Team. *R: A Language and Environment for Statistical Computing* (R Foundation for Statistical Computing, Austria, 2010).

High-throughput decoding of antitrypanosomal drug efficacy and resistance

Sam Alford¹, Sabine Eckert^{2†}, Nicola Baker¹, Lucy Glover¹, Alejandro Sanchez-Flores², Ka Fai Leung³, Daniel J. Turner^{2†}, Mark C. Field³, Matthew Berriman² & David Horn¹

The concept of disease-specific chemotherapy was developed a century ago. Dyes and arsenical compounds that displayed selectivity against trypanosomes were central to this work^{1,2}, and the drugs that emerged remain in use for treating human African trypanosomiasis (HAT)³. The importance of understanding the mechanisms underlying selective drug action and resistance for the development of improved HAT therapies has been recognized, but these mechanisms have remained largely unknown. Here we use all five current HAT drugs for genome-scale RNA interference target sequencing (RIT-seq) screens in *Trypanosoma brucei*, revealing the transporters, organelles, enzymes and metabolic pathways that function to facilitate antitrypanosomal drug action. RIT-seq profiling identifies both known drug importers^{4,5} and the only known pro-drug activator⁶, and links more than fifty additional genes to drug action. A bloodstream stage-specific invariant surface glycoprotein (ISG75) family mediates suramin uptake, and the AP1 adaptin complex, lysosomal proteases and major lysosomal transmembrane protein, as well as spermidine and *N*-acetylglucosamine biosynthesis, all contribute to suramin action. Further screens link ubiquinone availability to nitro-drug action, plasma membrane P-type H⁺-ATPases to pentamidine action, and trypanothione and several putative kinases to melarsoprol action. We also demonstrate a major role for aquaglyceroporins in pentamidine and melarsoprol cross-resistance. These advances in our understanding of mechanisms of antitrypanosomal drug efficacy and resistance will aid the rational design of new therapies and help to combat drug resistance, and provide unprecedented molecular insight into the mode of action of antitrypanosomal drugs.

African trypanosomes are transmitted by the tsetse insect vector and circulate in the bloodstream and tissue fluids of their mammalian hosts. These protozoan parasites cause HAT, also known as sleeping sickness, and the livestock disease known as Nagana. HAT is typically fatal if there is no chemotherapeutic intervention. The public health situation has improved recently with increased monitoring and chemotherapy averting more than 1.3 million disability-adjusted life years (DALYs) in the year 2000 and the estimated number of cases at less than 70,000 in 2006 (ref. 7). However, therapies have many problems, including severe toxicity and increasing resistance, which is a major concern owing to the absence of a vaccine or therapeutic alternatives³. The current HAT therapies are pentamidine or suramin, which are only suitable for the first stage of the disease before central nervous system involvement, and eflornithine, nifurtimox or melarsoprol for advanced disease³ (Supplementary Table 1). All of these drugs were developed well before the advent of molecular, target-based therapy and, with the exception of eflornithine, they elicit their antitrypanosomal effects by disrupting unknown targets. HAT treatment failure rates were reported to be increasing for suramin, when this drug was still in use in West Africa in the 1950s⁸, and melarsoprol treatment failure is a current and increasing problem⁹.

We used genome-scale tetracycline-inducible RNA interference (RNAi) library screens in *T. brucei* to identify the genes that contribute to drug action. In these screens, replicating cells only persist in an otherwise toxic environment if knockdown confers a selective advantage (Fig. 1a); note that knockdown is not expected to identify drug targets. The RNAi library consists of ~750,000 clones, each transformed with one RNAi construct, and represents >99% of the approximately 7,500 non-redundant *T. brucei* gene set. Because each gene is identified by an average of approximately five different RNAi sequences, true leads can be identified with high confidence and potential off-target false leads can be minimized (see Supplementary Methods). Screens were performed using all current HAT drugs and each yielded a population of cells displaying an inducible drug resistance phenotype after eight or fourteen days of selection (Fig. 1b and Supplementary Fig. 1). Genomic DNA from these cells was subjected to RIT-seq¹⁰ to create profiles of RNAi targets associated with increased resistance and to identify the genes that contribute to drug susceptibility. Genome-wide association maps show read density for 7,435 *T. brucei* genes (Fig. 1c). We defined genes with 'primary signatures' as those associated with two or more independent RIT-seq tags, each with a read density of >99; the screens yielded 55 of these signatures (Fig. 1c; see Supplementary Methods and Supplementary Data 1). Previous work linked the P2 adenosine transporter 1 (AT1) to melarsoprol uptake^{4,11–13}, an amino acid transporter family member (AAT6) to eflornithine uptake^{5,13,14} and a nitroreductase (NTR) to nifurtimox activation^{6,14}. Each of these genes is identified on the appropriate genome-wide association map (Fig. 1c), providing validation for our screens and indicating excellent genome-scale coverage in the RNAi library. Selected read-density signatures that establish new genetic links to drug susceptibility are shown in Fig. 1d.

The known eflornithine transporter is the only primary signature from the eflornithine screen. By contrast, the suramin screen revealed 28 genes associated with primary signatures (Fig. 1c and Supplementary Data 1). Suramin, which has been used for HAT therapy since the 1920s¹⁵, is a colourless sulphated naphthylamine related to trypan red. Because this drug has a strong negative charge, it cannot cross lipid membranes by passive diffusion. Genes that are linked to the action of suramin encode ISG75, the function of which is unknown¹⁶, four lysosomal proteins (the cathepsin L (CatL) and CBP1 peptidases, p67 and Golgi/lysosomal protein 1 (GLP1)), all four subunits of the adaptin complex (AP1), which are involved in endosomal, clathrin-mediated trafficking, and multiple spermidine and *N*-acetylglucosamine biosynthetic enzymes (Supplementary Fig. 2 and Supplementary Data 1).

Eight of these genes were selected for further analysis. We assembled multiple independent inducible RNAi strains for each gene and confirmed that knockdown (Fig. 2a and Supplementary Fig. 3) increased suramin resistance in every case (Fig. 2b and Supplementary Fig. 4). We then determined subcellular localization for the putative major facilitator superfamily transporter (MFST); the tandem of three closely

¹London School of Hygiene and Tropical Medicine, Keppel Street, London, WC1E 7HT, UK. ²The Wellcome Trust Sanger Institute, Hinxton, Cambridge, CB10 1SA, UK. ³Department of Pathology, University of Cambridge, Tennis Court Road, Cambridge, CB2 1QP, UK. [†]Present address: Oxford Nanopore Technologies, 4 Robert Robinson Avenue, Oxford, OX4 4GA, UK.

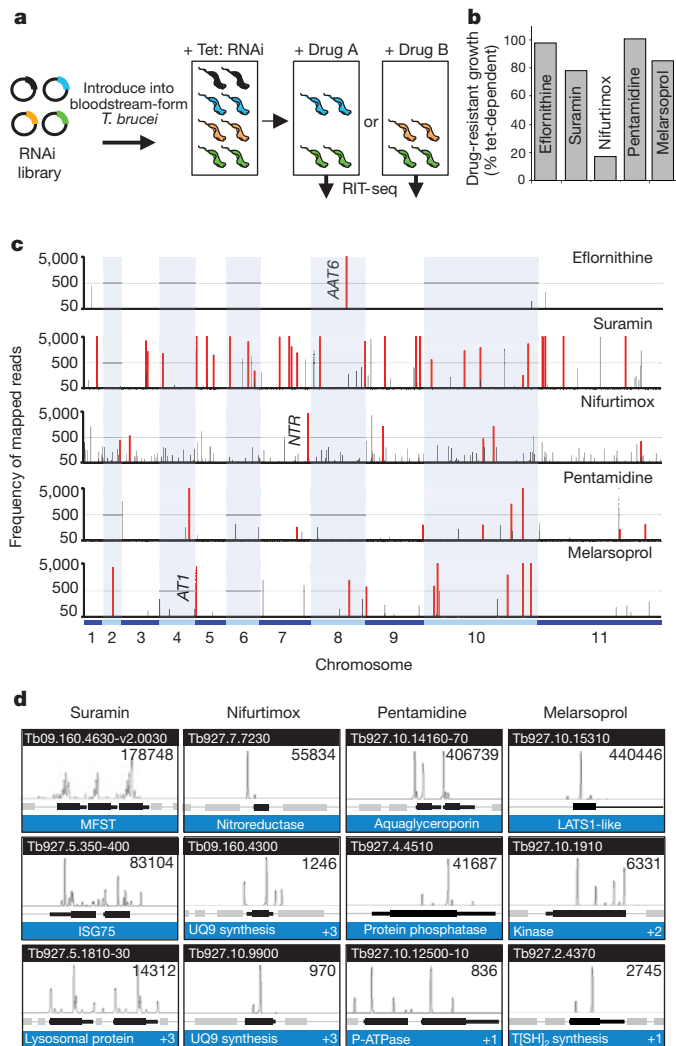


Figure 1 | Identification of drug efficacy determinants in *T. brucei*. **a**, A schematic showing the RNAi library screening approach. The expected outcomes are given for RNAi targets that fail to affect drug resistance (black), increase resistance to drug A (blue), drug B (orange) or both (green). **b**, Each screen yielded a population displaying tetracycline (Tet)-inducible (RNAi-dependent) drug-resistance (see Supplementary Fig. 1). The plot indicates the proportion of the resistance phenotype that is tetracycline inducible. **c**, Genome-wide RIT-seq profiles. Each map represents a non-redundant set of 7,435 protein-coding sequences. Red bars represent 'primary' read-density signatures. Black bars represent all other signatures of >50 reads (see Supplementary Data 1). All three expected 'hits', *AAT6*, *AT1* and *NTR*, are indicated. **d**, Selected signatures. Each peak represents a unique RIT-seq tag. '+', numbers of additional genes identified in each category. See Supplementary Fig. 2 for details and additional signatures.

related *MFST* genes gave the strongest read-density signature in the suramin screen and the greatest half-maximum effective concentration (EC_{50}) increase (> tenfold) following knockdown (Fig. 2b). In contrast to a putative ubiquitin hydrolase (UBH1) identified by the screen, *MFST* and a member of the endomembrane EMP70 family partitioned into the *T. brucei* membrane fraction, as expected (Fig. 2c), and *MFST* localized to the lysosome as did the major lysosomal type I membrane glycoprotein, p67 (ref. 17), which was also identified in the screen (Fig. 2d). Because *ISG75* trafficking is ubiquitin dependent¹⁸, we investigated whether UBH1 influenced *ISG75* expression. UBH1 knockdown reduced *ISG75* but not *ISG65* expression (Fig. 2e), suggesting that de-ubiquitination by UBH1 specifically affects *ISG75* copy number; clearly this mimics the direct effect of RNAi against *ISG75*. A vacuolar protein sorting factor, *Vps5*, which positively controls *ISG75* expression¹⁹, and a second putative ubiquitin hydrolase, were

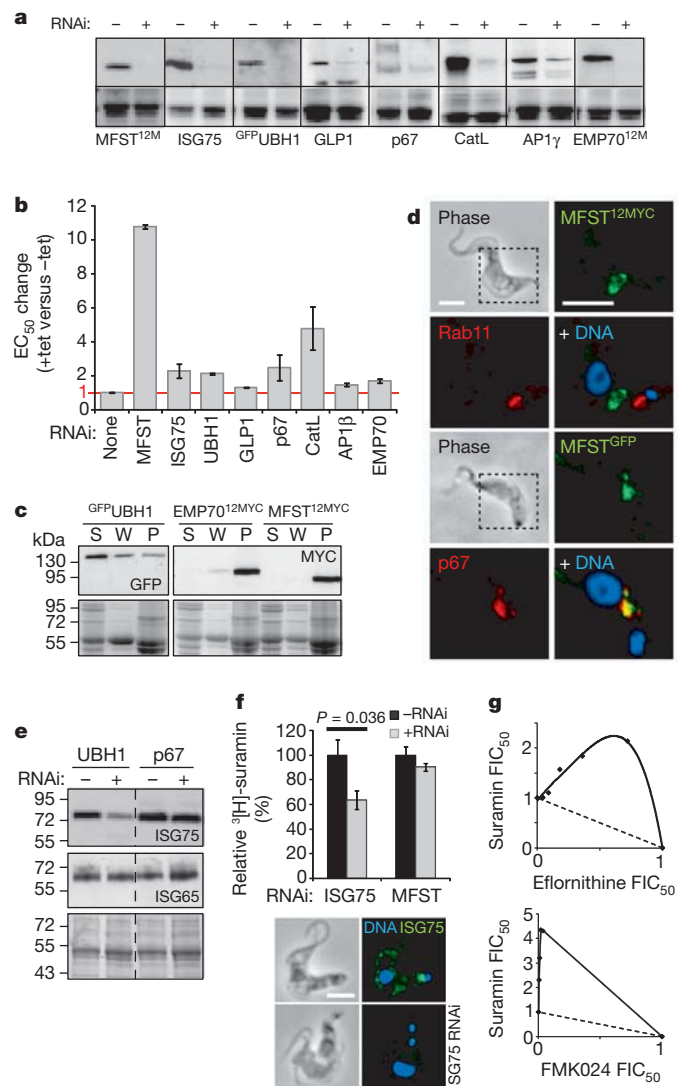


Figure 2 | A network of proteins link *ISG75*, endocytosis and lysosomal functions to suramin action. **a**, Western blots demonstrate knockdown; Coomassie stains serve as loading controls. Tags, green fluorescent protein (GFP) and 12×MYC epitope (12M). See Supplementary Fig. 3 for growth curves. **b**, Endosomal and lysosomal factors and *ISG75* contribute to suramin action. Error bars, s.d. from independent RNAi strains (see Supplementary Fig. 4). **c**, *MFST* and *EMP70* are membrane associated. The western blots show supernatant (S), wash (W) and pellet (P; membrane fraction). **d**, *MFST* co-localizes with lysosomal protein, p67, but not recycling endosomes (Rab11). Dashed boxes, areas magnified in fluorescent images. **e**, Knockdown of UBH1 specifically decreases *ISG75* expression. **f**, *ISG75* mediates suramin binding. Error bars, s.d. from duplicate experiments. *P* value from Student's *t*-test. *ISG75* knockdown is shown. Scale bar, 5 μm. **g**, The CatL–CatB, and ODC inhibitors FMK024 and eflornithine, respectively, antagonize suramin action. Isobolograms showing 50% fractional inhibitory concentrations (FIC₅₀). The solid lines indicate antagonism. The dashed lines indicate expected outcomes for no interaction.

also identified by the screen (see Supplementary Fig. 2 and Supplementary Data 1), suggesting that *ISG75* copy number is highly connected to suramin resistance. To investigate whether *ISG75* contributes to suramin binding, we performed whole-cell binding assays using ³[H]-labelled suramin. Cells that were depleted for *ISG75* displayed significantly and specifically reduced suramin binding (Fig. 2f).

We observed a greater than fourfold increase in EC_{50} after knockdown of the CatL-like protease known as brucipain, another abundant lysosomal protein²⁰, and an orthogonal assay using a dual-specificity CatL–CatB inhibitor revealed inhibitor antagonism (Fig. 2g), indicating that protease activity enhances suramin toxicity. Taken together, the

results demonstrate a central role for lysosomal functions in suramin action. As four enzymes that are involved in spermidine biosynthesis, including ornithine decarboxylase (ODC), were linked to suramin action (Supplementary Data 1), we used eflornithine to specifically inhibit ODC, which again revealed inhibitor antagonism (Fig. 2g; Supplementary Table 1). Thus, ODC activity enhances suramin toxicity, probably through spermidine biosynthesis. Suramin endocytosis²¹ and intralysosomal accumulation²² have previously been demonstrated in *T. brucei* and an acquired suramin resistance phenotype was stable in bloodstream stage *T. brucei* but was not expressed in the insect stage²³. The RIT-seq profile reported here, bloodstream-stage-specific expression of ISG75¹⁶ and strong downregulation of endocytic and lysosomal activities in the insect stage²⁴, are all consistent with stage-specific, intralysosomal accumulation of suramin.

Work with dyes and arsenicals revealed the first examples of resistance to chemotherapy a century ago and, based on cross-resistance, it was deduced that there are shared mechanisms contributing to the action of certain 'parasitotropic' compounds¹. Among current HAT therapies, cross-resistance has been documented only for melarsoprol and pentamidine⁹, but our understanding of the mechanism remains incomplete. Both drugs enter trypanosomes through the P2 AT1 but additional, dual-specificity transporters are predicted⁹. To identify cross-resistance mechanisms, we analysed all pair-wise comparisons among our screens (Fig. 3a). A single robust signature emerged, implicating two closely related aquaglyceroporins (AQPs)²⁵ in melarsoprol and pentamidine cross-resistance. To directly test the role of the AQPs, we generated a strain that was deficient in *aqp2* and *aqp3* (*aqp2/aqp3*-null strain) (Fig. 3b). The EC₅₀ was increased more than 2-fold and 15-fold for melarsoprol and pentamidine, respectively, in *aqp2/aqp3*-null cells compared to wild-type cells (Fig. 3c). Our favoured hypothesis involves regulation of dual-specificity transporters by AQPs.

The nifurtimox, pentamidine and melarsoprol screens yielded eight, nine and nine genes associated with primary signatures, respectively. The major primary signature in the nifurtimox profile identified the mitochondrial, flavin-dependent nitroreductase that activates this class of nitro pro-drugs⁶. We also identified the putative flavokinase that converts riboflavin to FMN, an essential nitroreductase cofactor⁶. Four additional signatures identified genes that encode proteins linked to ubiquinone biosynthesis (Supplementary Fig. 2 and Supplementary Data 1), in support of the hypothesis that nitroreductase, like NADH dehydrogenases, transfers electrons from NADH to ubiquinone to generate ubiquinol⁶. We assembled RNAi strains for one of these factors and demonstrated that knockdown increased the EC₅₀ for nifurtimox by approximately 1.5-fold (Supplementary Fig. 5). Thus, six gene signatures support a dominant role for nitroreductase in nifurtimox activation and suggest that this is dependent upon the availability of the FMN cofactor and the natural substrate.

Pentamidine is an aromatic diamidine, a nucleic acid binding drug that accumulates to millimolar concentrations and collapses trypanosome mitochondrial membrane potential²⁶. Two primary signatures from the pentamidine screen identify genes encoding P-type ATPases (Supplementary Fig. 2 and Supplementary Data 1), and one of these represents the plasma membrane H⁺-ATPases, HA1, HA2 and HA3 (ref. 27). We assembled RNAi strains for these ATPases and demonstrated that knockdown increased the EC₅₀ for pentamidine more than eightfold (Supplementary Fig. 5), suggesting that an HA1–3 dependent proton motive force is required to drive pentamidine uptake. We used a similar approach to demonstrate a greater than twofold increase in the EC₅₀ for pentamidine following knockdown of a putative protein phosphatase (Supplementary Fig. 5).

Melarsoprol acts primarily by forming a stable adduct with trypanothione, known as Mel T²⁸, but whether this adduct reduces or increases toxicity has remained unclear. The melarsoprol screen identified a link to trypanothione synthase and trypanothione reductase (Supplementary Fig. 2 and Supplementary Data 1), suggesting that the Mel T adduct is toxic. Three other primary signatures identified an

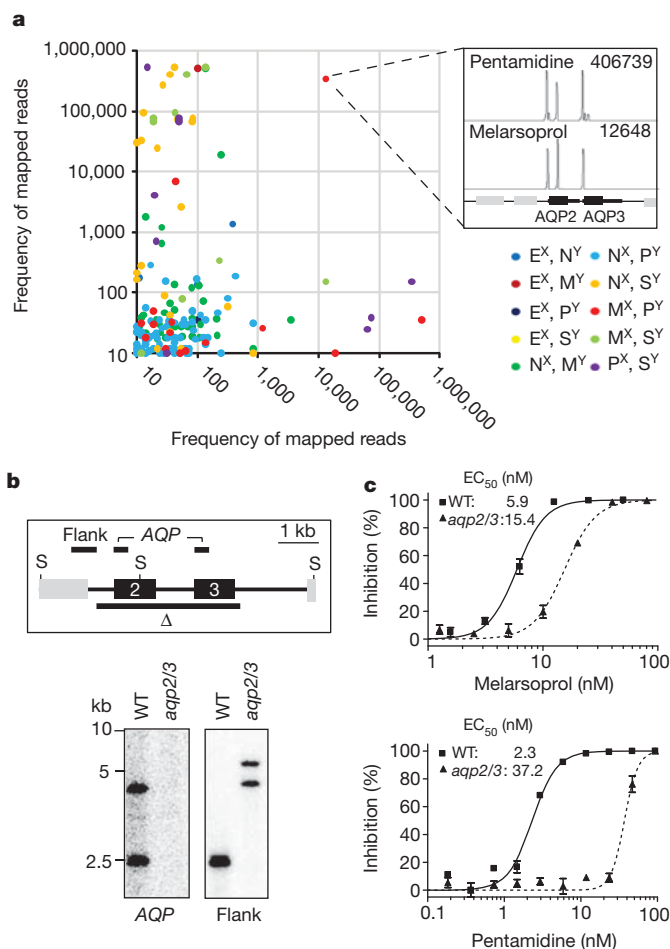


Figure 3 | *aqp2/aqp3*-null cells are melarsoprol, pentamidine cross-resistant. **a**, Analysis of read density for all (74,350) possible pair-wise comparisons of a non-redundant *T. brucei* gene set. E, eflornithine; M, melarsoprol; N, nifurtimox; P, pentamidine; S, suramin; ^X and ^Y, axes representing each data set. The box on the right shows the read-density signatures for this locus (Tb927.10.14160–70). **b**, AQP2 and AQP3 knockout was confirmed by Southern blot analysis. Δ , the region deleted; S, *SacII*; WT, wild type. Bars indicate probes. **c**, EC₅₀ analysis indicates melarsoprol, pentamidine cross-resistance in *aqp2/aqp3*-null cells. Error bars, s.d. from triplicate assays and independent null strains.

over-representation ($P = 2.3 \times 10^{-9}$, χ^2 test) of putative protein kinases (Supplementary Fig. 2 and Supplementary Data 1), and another signature identified a gene encoding a highly phosphorylated protein related to the amino-terminal segment of the large tumour suppressor, LATS1 (see Supplementary Fig. 2a). We used independent strains to confirm that LATS1-like knockdown increased the EC₅₀ for melarsoprol by approximately 1.5-fold (Supplementary Fig. 5). On the basis of these signatures, we suggest a role for a signalling cascade in melarsoprol susceptibility. Our findings are summarized in Fig. 4. In particular, we propose that suramin uptake occurs through ISG75-mediated endocytosis (Fig. 4a). Metabolic pathways that contribute to suramin or nifurtimox action are detailed in Fig. 4b.

All but one of the current HAT drugs was developed in the absence of an understanding of the chemical–biological relationships underlying toxicity or selectivity. Our RIT-seq profiles revealed more than 50 *T. brucei* genes that enhance drug susceptibility, unearthing interactions that are largely inaccessible using other approaches. Notably, the knockdown approach and the sensitivity of RIT-seq allow access to essential proteins, complexes and pathways such as H⁺-ATPase, the adaptin complex and spermidine biosynthesis. Our results also show the utility of drugs as molecular probes for functional networks. In particular, the findings highlight factors that contribute to drug

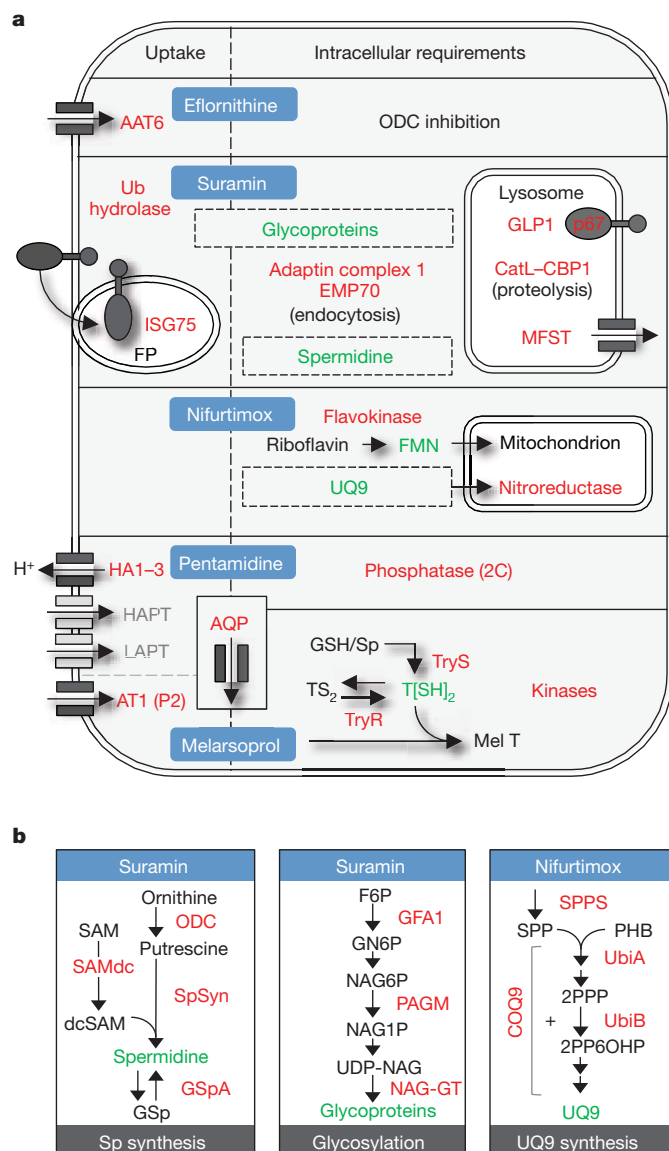


Figure 4 | Determinants of drug efficacy in African trypanosomes.

a, b, Proteins (red) and metabolites (green) that are linked to drug action. **a**, A schematic summarizing the findings from the RIT-seq screens. In the case of suramin, we propose that ISG75 binds the drug at the cell surface. ISG75 trafficking then delivers the complex, through the flagellar pocket (FP), to the endosomal system, leading to accumulation in the lysosome where the drug is liberated by proteases. The MFST may deliver the drug to the cytosol. HAPT, high-affinity pentamidine transporter; LAPT, low-affinity pentamidine transporter; TS₂, oxidised trypanothione; T[SH]₂, reduced trypanothione; UQ9, ubiquinone 9. **b**, Biosynthetic pathways that are linked to drug action. See Supplementary Data 1 for definitions and further details.

accumulation or the generation of toxic metabolites, features that could be exploited to deliver or generate novel toxins. Additionally, absence or loss of function could explain innate or acquired resistance; suramin resistance or melarsoprol and pentamidine cross-resistance may be due to reduced MFST or AQP expression, respectively (for examples, see Supplementary Fig. 6). These advances in our understanding of drug-trypanosome interactions will facilitate rational approaches to the design of more efficacious and durable therapies, and will be useful for monitoring the emergence and spread of resistance.

METHODS SUMMARY

Assembly of the bloodstream-form *T. brucei* RNAi library and RIT-seq were reported previously¹⁰. Briefly, a tetracycline-inducible RNAi plasmid library,

containing randomly sheared genomic fragments (with a mean fragment size of ~600 bp) under the control of head-to-head, tetracycline-inducible phage T7 promoters²⁹, was targeted to a single genomic locus that had been validated for robust expression³⁰. The long double-stranded RNAs (dsRNAs) that were generated in the presence of tetracycline are processed to produce a pool of short interfering RNAs that programme the endogenous RNAi machinery to mediate sequence-specific destruction of the cognate messenger RNA. For this study, the library was grown under inducing conditions with drug selection, and genomic DNA was isolated from surviving populations. For RIT-seq profiling, adaptor-ligated sequencing libraries were prepared from each genomic DNA sample and used to amplify DNA fragments containing RNAi cassette-insert junctions in semi-specific PCR reactions; one primer was specific for the RNAi vector and the other for the Illumina adaptor. Size-selected DNA was sequenced with 76 cycle runs on an Illumina GAI. Sequencing reads containing a nine-base RNAi cassette-insert junction sequence were then mapped to the *T. brucei* reference genome. In cases in which loss of function increases drug tolerance, RNAi-target sequence representation is increased relative to the otherwise susceptible population, revealing 'hot spots'. Thus, RNAi target fragments serve as templates for the production of dsRNA and also provide unique sequence identifiers for each clonal population.

Full Methods and any associated references are available in the online version of the paper at www.nature.com/nature.

Received 23 September; accepted 7 December 2011.

Published online 25 January 2012.

- Ehrlich, P. Address in pathology, on chemotherapy: delivered before the seventeenth international congress of medicine. *BMJ* **2**, 353–359 (1913).
- Williamson, J. in *The African Trypanosomiasis* (ed. Mulligan, H. W.) (Allen and Unwin, 1970).
- Fairlamb, A. H. Chemotherapy of human African trypanosomiasis: current and future prospects. *Trends Parasitol.* **19**, 488–494 (2003).
- Mäser, P., Sutterlin, C., Kralli, A. & Kaminsky, R. A nucleoside transporter from *Trypanosoma brucei* involved in drug resistance. *Science* **285**, 242–244 (1999).
- Vincent, I. M. et al. A molecular mechanism for eflornithine resistance in African trypanosomes. *PLoS Pathog.* **6**, e1001204 (2010).
- Wilkinson, S. R., Taylor, M. C., Horn, D., Kelly, J. M. & Cheeseman, I. A mechanism for cross-resistance to nifurtimox and benznidazole in trypanosomes. *Proc. Natl Acad. Sci. USA* **105**, 5022–5027 (2008).
- Fèvre, E. M., Wissmann, B. V., Welburn, S. C. & Lutumba, P. The burden of human African trypanosomiasis. *PLoS Negl. Trop. Dis.* **2**, e333 (2008).
- Pépin, J. & Milord, F. The treatment of human African trypanosomiasis. *Adv. Parasitol.* **33**, 1–47 (1994).
- de Koning, H. P. Ever-increasing complexities of diamidine and arsenical cross-resistance in African trypanosomes. *Trends Parasitol.* **24**, 345–349 (2008).
- Alsford, S. et al. High-throughput phenotyping using parallel sequencing of RNA interference targets in the African trypanosome. *Genome Res.* **21**, 915–924 (2011).
- Carter, N. S. & Fairlamb, A. H. Arsenical-resistant trypanosomes lack an unusual adenosine transporter. *Nature* **361**, 173–176 (1993).
- Matovu, E. et al. Mechanisms of arsenical and diamidine uptake and resistance in *Trypanosoma brucei*. *Eukaryot. Cell* **2**, 1003–1008 (2003).
- Schumann Burkard, G., Jutzi, P. & Roditi, I. Genome-wide RNAi screens in bloodstream form trypanosomes identify drug transporters. *Mol. Biochem. Parasitol.* **175**, 91–94 (2011).
- Baker, N., Alsford, S. & Horn, D. Genome-wide RNAi screens in African trypanosomes identify the nifurtimox activator NTR and the eflornithine transporter AAT6. *Mol. Biochem. Parasitol.* **176**, 55–57 (2011).
- Steverding, D. The development of drugs for treatment of sleeping sickness: a historical review. *Parasit. Vectors* **3**, 15 (2010).
- Overath, P., Chaudhri, M., Steverding, D. & Ziegelbauer, K. Invariant surface proteins in bloodstream forms of *Trypanosoma brucei*. *Parasitol. Today* **10**, 53–58 (1994).
- Peck, R. F. et al. The LAMP-like protein p67 plays an essential role in the lysosome of African trypanosomes. *Mol. Microbiol.* **68**, 933–946 (2008).
- Leung, K. F., Riley, F. S., Carrington, M. & Field, M. C. Ubiquitylation and developmental regulation of invariant surface protein expression in trypanosomes. *Eukaryot. Cell* **10**, 916–931 (2011).
- Koumandou, V. L. et al. Evolutionary reconstruction of the retromer complex and its function in *Trypanosoma brucei*. *J. Cell Sci.* **124**, 1496–1509 (2011).
- Caffrey, C. R. et al. Active site mapping, biochemical properties and subcellular localization of rhodesain, the major cysteine protease of *Trypanosoma brucei rhodesiense*. *Mol. Biochem. Parasitol.* **118**, 61–73 (2001).
- Fairlamb, A. H. & Bowman, I. B. Uptake of the trypanocidal drug suramin by bloodstream forms of *Trypanosoma brucei* and its effect on respiration and growth rate in vivo. *Mol. Biochem. Parasitol.* **1**, 315–333 (1980).
- Vansterkenburg, E. L. et al. The uptake of the trypanocidal drug suramin in combination with low-density lipoproteins by *Trypanosoma brucei* and its possible mode of action. *Acta Trop.* **54**, 237–250 (1993).

23. Scott, A. G., Tait, A. & Turner, C. M. Characterisation of cloned lines of *Trypanosoma brucei* expressing stable resistance to MelCy and suramin. *Acta Trop.* **60**, 251–262 (1996).
24. Natesan, S. K., Peacock, L., Matthews, K., Gibson, W. & Field, M. C. Activation of endocytosis as an adaptation to the mammalian host by trypanosomes. *Eukaryot. Cell* **6**, 2029–2037 (2007).
25. Uzcategui, N. L. *et al.* Cloning, heterologous expression, and characterization of three aquaglyceroporins from *Trypanosoma brucei*. *J. Biol. Chem.* **279**, 42669–42676 (2004).
26. Lanteri, C. A., Tidwell, R. R. & Meshnick, S. R. The mitochondrion is a site of trypanocidal action of the aromatic diamidine DB75 in bloodstream forms of *Trypanosoma brucei*. *Antimicrob. Agents Chemother.* **52**, 875–882 (2008).
27. Luo, S., Fang, J. & Docampo, R. Molecular characterization of *Trypanosoma brucei* P-type H⁺-ATPases. *J. Biol. Chem.* **281**, 21963–21973 (2006).
28. Fairlamb, A. H., Henderson, G. B. & Cerami, A. Trypanothione is the primary target for arsenical drugs against African trypanosomes. *Proc. Natl Acad. Sci. USA* **86**, 2607–2611 (1989).
29. Morris, J. C., Wang, Z., Drew, M. E. & Englund, P. T. Glycolysis modulates trypanosome glycoprotein expression as revealed by an RNAi library. *EMBO J.* **21**, 4429–4438 (2002).
30. Alsford, S., Kawahara, T., Glover, L. & Horn, D. Tagging a *T. brucei* *RRNA* locus improves stable transfection efficiency and circumvents inducible expression position effects. *Mol. Biochem. Parasitol.* **144**, 142–148 (2005).

Supplementary Information is linked to the online version of the paper at www.nature.com/nature.

Acknowledgements We thank J. Morris, Z. Wang, M. Drew and P. Englund for the RNAi plasmid library, V. Yardley for antitrypanosomal drugs, J. Bangs for anti-p67 and CatL sera, D. Russell for anti-GLP1 sera, A. Varghese for assistance with preliminary Sanger sequencing and J. Kelly, M. Taylor and B. Wren for comments on the draft manuscript. The work was funded by grants from The Wellcome Trust (093010/Z/10/Z at the London School of Hygiene & Tropical Medicine, 085775/Z/08/Z at The Wellcome Trust Sanger Institute and 090007/Z/09/Z at The University of Cambridge). N.B. was supported by a Bloomsbury colleges PhD studentship.

Author Contributions S.A., N.B., L.G. and K.F.L. carried out the *T. brucei* manipulation and analyses, S.E., A.S.-F. and D.J.T. carried out the Illumina sequencing and mapping, D.H. coordinated the study and S.A., M.C.F., M.B. and D.H. wrote the paper.

Author Information Sequence data from this study have been submitted to the European Nucleotide Archive at <http://www.ebi.ac.uk/ena> under accession number ERA071064. Reprints and permissions information is available at www.nature.com/reprints. The authors declare no competing financial interests. Readers are welcome to comment on the online version of this article at www.nature.com/nature. Correspondence and requests for materials should be addressed to D.H. (david.horn@lshtm.ac.uk).

METHODS

***T. brucei* growth and drug selection.** The bloodstream-form *T. brucei* MITat 1.2 clone 221a RNAi library¹⁰ was derived using the randomly sheared genomic fragment (with mean fragment length ~600 bp) RNAi plasmid library²⁹. The *T. brucei* RNAi library and 2T1 cells were maintained as described^{29,30}. For selective screens, the RNAi library, maintained throughout at $>5 \times 10^6$ cells, was induced with tetracycline ($1 \mu\text{g ml}^{-1}$) for 24 h and then grown in medium containing tetracycline, plus each HAT drug at $0.5 \times \text{EC}_{50}$ to $3.5 \times \text{EC}_{50}$ (Supplementary Table 1 and Supplementary Fig. 1). All drug stocks were in dimethylsulphoxide.

RIT-seq. Selected populations from each screen were assessed for tetracycline-dependent drug resistance. The RNAi target fragments provide unique identifiers for each clone in the population. As a quality-control step, PCR amplification, agarose gel fractionation and Sanger sequencing of the eluted products were performed as described¹⁴, and followed with RIT-seq analysis¹⁰. All nine genes that were identified by Sanger sequencing were associated with high-density Illumina read-counts (13,000 to 528,000; see Supplementary Data 1a). Briefly, we ran 76-cycle sequencing on an Illumina GAI; this generates sequence tags derived from the ends of the RNAi target fragments. Only sequences containing a terminal RNAi-vector junction sequence (GCCTCGCGA) were mapped to the *T. brucei* 927 reference genome³¹ using the SSAHA sequence alignment algorithm³². After mapping, for each protein coding sequence (CDS) in each experiment, we obtained a count of reads mapping; all genes associated with >9 reads are detailed in Supplementary Data 1b. We also browsed all read-density plots in Artemis³³ for signatures that fell outside of CDSs to generate the full non-redundant 'hit list' detailed in Supplementary Data 1a.

Read-density signatures. Genome coverage in the current RNAi library represents $>99\%$ of all genes, with 5 RNAi targets per gene on average¹⁰; shorter genes are expected to be represented by fewer RNAi targets. Our screens yielded 5–59 genes (0.07 – 0.8%) with a >99 RIT-seq tag (a tag with a read density of >99 ; the eflornithine screen yielded 5, the suramin screen 59 the nifurtimox screen 54, the pentamidine screen 17 and the melarsoprol screen 19). In each screen, at least one gene was associated with a $>50,000$ RIT-seq tag (Supplementary Data 1a). From this set, we derived 55 genes with 'primary signatures', those associated with two or more >99 RIT-seq tags. If these tags were randomly distributed, we would expect a single primary signature from 300 screens using eflornithine or from two screens using suramin, assigning a high degree of confidence to the vast majority of observed primary signatures (Supplementary Data 1a). The nifurtimox output is unusual compared to the other outputs and may reflect drug-mediated mutagenesis³⁴; for example, inactivating mutations within *NTR* may prolong the survival of clones carrying unrelated RNAi targets. However, even limited tetracycline-regulated drug resistance (Fig. 1b) and a high number of sequence tags in the nifurtimox screening profile (Supplementary Data 1 and Fig. 1c) had little impact on primary signature confidence. Many of the 130 genes that are associated with 'secondary signatures' in Supplementary Data 1a may also reflect mechanisms of drug action, but here we only considered seven of these genes that were linked to a common function with a primary hit (Supplementary Fig. 2). We observe that, on average, 3.5 tags per gene are associated with the 24 primary, single copy genes that are shown in Supplementary Fig. 2. Minimal library propagation could explain a modest reduction in coverage but we suggest that reduced coverage in the current RIT-seq outputs is primarily explained by major fitness defects following knockdown.

Plasmid construction and strain assembly. The *AQP* locus was disrupted by replacement of a 4,772-bp (*AQP2* and *AQP3*) fragment with *NPT* and *BLA* selectable markers (the *T. brucei* genome is diploid). Gene-specific RNAi fragments of 400–600 bp or 200 bp, to facilitate moderate knockdown in the case of the known essential gene p67 (ref. 17), were amplified using PCR primers designed using RNAi³⁵ and cloned into pRPaiSL for the generation of stem-loop, 'hairpin' dsRNA as the trigger for RNAi³⁶. We used a long, 400–600-bp RNAi target fragment for CatL because RNAi previously produced no growth defect³⁷. However, cells retained 35% CatL activity in that study³⁷, probably explaining why we see a major growth defect when expressing a more potent stem-loop

dsRNA (Supplementary Fig. 3). For epitope tagging at native loci, C-terminal fragments, or an N-terminal fragment (UBH1), were amplified and cloned in pNATx^{TAG} and pNAT^{TAG}x (ref. 36), respectively. Constructs were introduced into 2T1 cells as described³⁰. Full oligonucleotide details are available on request.

Strain analysis. Cumulative growth curves were generated from cultures seeded at 10^5 cells ml^{-1} , counted on a haemocytometer and diluted back to 10^5 cells ml^{-1} as necessary. For EC_{50} assays, RNAi strains were pre-induced for 72 h in $1 \mu\text{g ml}^{-1}$ tetracycline, except CatL and AP1 β , which were pre-induced for 24 h at 2.5 and 1 ng ml^{-1} , respectively. Isobolograms were generated using a checkerboard assay as described³⁸; FMK024 (*N*-morpholineurea-phenylalanyl-homophenylalanylfluoromethyl ketone; Sigma) is an irreversible, dual-specificity inhibitor of CatL and CatB. All EC_{50} assays were carried out using alamarBlue as described^{14,39}. Southern blotting was carried out according to standard procedures⁴⁰. Subcellular fractionation by hypotonic lysis was carried out as described⁴¹. All protein samples were stored in the presence of a protease inhibitor cocktail (Roche) and were not boiled. Whole-cell lysates and hypotonic lysis fractions were separated by SDS-PAGE using standard protocols⁴⁰. Immunofluorescence was carried out as previously described¹⁰. We used specific antisera to detect ISG75 (ref. 42), p67 (ref. 43), CatL¹⁷, GLP1 (ref. 44) and AP1 γ (ref. 45), and anti-MYC or anti-GFP antisera were used to detect tagged versions of MFST, UBH1 and EMP70. To assess suramin binding, cells were collected at mid-log phase and resuspended at 10^7 ml^{-1} in 35 nM [^3H]-suramin (Hartmann Analytic; pre-incubated for 16 h in complete HMI11) at 37°C . Cells were washed in ice-cold PBS, resuspended in $100 \mu\text{l}$ Optiphas Supermix scintillant (Perkin Elmer) and [^3H]-suramin incorporation quantified using a 1450 Microbeta scintillation counter (Perkin Elmer).

- Berriman, M. *et al.* The genome of the African trypanosome *Trypanosoma brucei*. *Science* **309**, 416–422 (2005).
- Ning, Z., Cox, A. J. & Mullikin, J. C. SSAHA: a fast search method for large DNA databases. *Genome Res.* **11**, 1725–1729 (2001).
- Carver, T. *et al.* Artemis and ACT: viewing, annotating and comparing sequences stored in a relational database. *Bioinformatics* **24**, 2672–2676 (2008).
- Buschini, A. *et al.* Genotoxicity reevaluation of three commercial nitroheterocyclic drugs: nifurtimox, benznidazole, and metronidazole. *J. Parasitol. Res.* **2009**, 463575 (2009).
- Redmond, S., Vadvivel, J. & Field, M. C. RNAi: an automated web-based tool for the selection of RNAi targets in *Trypanosoma brucei*. *Mol. Biochem. Parasitol.* **128**, 115–118 (2003).
- Alsford, S. & Horn, D. Single-locus targeting constructs for reliable regulated RNAi and transgene expression in *Trypanosoma brucei*. *Mol. Biochem. Parasitol.* **161**, 76–79 (2008).
- Mackey, Z. B., O'Brien, T. C., Greenbaum, D. C., Blank, R. B. & McKerrow, J. H. A cathepsin B-like protease is required for host protein degradation in *Trypanosoma brucei*. *J. Biol. Chem.* **279**, 48426–48433 (2004).
- Singh, P. K., Tack, B. F., McCray, P. B. Jr & Welsh, M. J. Synergistic and additive killing by antimicrobial factors found in human airway surface liquid. *Am. J. Physiol. Lung Cell. Mol. Physiol.* **279**, L799–L805 (2000).
- R  z, B., Iten, M., Grether-B  hler, Y., Kaminsky, R. & Brun, R. The Alamar Blue assay to determine drug sensitivity of African trypanosomes (*T. b. rhodesiense* and *T. b. gambiense*) *in vitro*. *Acta Trop.* **68**, 139–147 (1997).
- Ausubel, F. M., Brent, R., Kingston, R. E., Moore, D. D., Seidman, J. G., Smith, J. A. & Struhl, K. (eds) *Current Protocols in Molecular Biology* (John Wiley and Sons, 1998).
- Leung, K. F., Dacks, J. B. & Field, M. C. Evolution of the multivesicular body ESCRT machinery; retention across the eukaryotic lineage. *Traffic* **9**, 1698–1716 (2008).
- Ziegelbauer, K. & Overath, P. Organization of two invariant surface glycoproteins in the surface coat of *Trypanosoma brucei*. *Infect. Immun.* **61**, 4540–4545 (1993).
- Kelley, R. J., Brickman, M. J. & Balber, A. E. Processing and transport of a lysosomal membrane glycoprotein is developmentally regulated in African trypanosomes. *Mol. Biochem. Parasitol.* **74**, 167–178 (1995).
- Lingnau, A., Zufferey, R., Lingnau, M. & Russell, D. G. Characterization of tGLP-1, a Golgi and lysosome-associated, transmembrane glycoprotein of African trypanosomes. *J. Cell Sci.* **112**, 3061–3070 (1999).
- Allen, C. L., Liao, D., Chung, W. L. & Field, M. C. Dileucine signal-dependent and AP-1-independent targeting of a lysosomal glycoprotein in *Trypanosoma brucei*. *Mol. Biochem. Parasitol.* **156**, 175–190 (2007).

Conditional modulation of spike–timing–dependent plasticity for olfactory learning

Stijn Cassenaer^{1,2} & Gilles Laurent^{1,3}

Mushroom bodies are a well-known site for associative learning in insects. Yet the precise mechanisms that underlie plasticity there and ensure their specificity remain elusive. In locusts, the synapses between the intrinsic mushroom body neurons and their postsynaptic targets obey a Hebbian spike–timing–dependent plasticity (STDP) rule. Although this property homeostatically regulates the timing of mushroom body output, its potential role in associative learning is unknown. Here we show *in vivo* that pre–post pairing causing STDP can, when followed by the local delivery of a reinforcement–mediating neuromodulator, specify the synapses that will undergo an associative change. At these synapses, and there only, the change is a transformation of the STDP rule itself. These results illustrate the multiple actions of STDP, including a role in associative learning, despite potential temporal dissociation between the pairings that specify synaptic modification and the delivery of reinforcement–mediating neuromodulator signals.

Behavioural and genetic experiments in *Drosophila* and honeybees have revealed that the mushroom body, a brain area containing up to hundreds of thousands of neurons called Kenyon cells, is critical for associative learning of odours^{1–11} but not for the expression of innate odour-driven behaviours⁵ (Fig. 1a). Recent electrophysiological experiments in locusts and other insects show that the responses of Kenyon cells to odours are highly selective and, thus, rare^{12–14}. By contrast, antennal lobe neurons, the source of the olfactory input to Kenyon cells, are few and promiscuous¹². Odour codes are thus ‘compact’ in the antennal lobe—that is, the representation of each odour engages many neurons in a small population—but ‘sparse’ in the mushroom bodies (Fig. 1a). Although sparse codes require larger neuron populations, they are beneficial for memory because they can reduce interference between memory traces^{12,15,16}. Kenyon cells project to two regions, called α - and β -lobes, where they synapse onto small populations of ‘extrinsic’ neurons. In locusts, the synapses between Kenyon cells and β -lobe neurons (bLNs) are modifiable by a Hebbian STDP rule^{17–19} (Fig. 1a), but nothing so far implicates STDP in associative learning there; rather, STDP causes the homeostatic regulation of bLN spike timing¹⁷. Recent experimental results in moths¹⁴ show that Kenyon cell responses to odours recorded during behavioural learning generally occur and end well before reward delivery, indicating that STDP alone cannot support associative conditioning^{20,21}. Neuromodulation has been proposed recently as a potential solution^{22,23}. We address this issue with *in vivo* electrophysiology in locusts and discover a complex interplay between STDP, reinforcer signals and odour codes in mushroom bodies.

Dense odour representations in β -lobes

We first examine odour representations in the β -lobes. Using intradendritic recordings, we sampled the responses of 55 bLNs to up to 16 odours (Methods and Fig. 1b). Each bLN responded to nearly every odour, with responses that differed in intensity, patterning, delay and duration across neuron–odour pairs. The probability that a given bLN responded to an odour was 0.97. On average, a bLN fired action potentials in approximately half of the local field potential (LFP) oscillation cycles during the odour presentation (0.502 ± 0.219 , $n = 126$

neuron–odour pairs, 25 LFP cycles per response): on average, half of the population was active in any given cycle. Hence, these representations resemble those in the antennal lobes¹² (and exceed them in promiscuity) rather than the sparse representations by Kenyon cells, to which bLNs are directly connected.

We tested whether the broad tuning of bLNs might be explained by known features of mushroom body circuits. We implemented a simple model (Methods and ref. 17) constrained by Kenyon cell response statistics and timing¹², by the properties of STDP at Kenyon cell synapses¹⁷ and by Kenyon cell/bLN (KC–bLN) connectivity ratios estimated from experiments¹⁷. With such a model, we could reproduce the bLN firing phase observed experimentally¹⁷ (Fig. 2a, left) but not the odour-response intensity or probability (Fig. 2a, right, and Supplementary Fig. 1.1a). Rather, activity across the model bLN (mbLN) population saturated rapidly when STDP was turned on. This behaviour is a known property of rate-based Hebbian learning in model networks and can be counteracted by imposing synaptic weight bounds or renormalization rules²⁴.

Inhibition limits STDP and saturation

In examining our experimental data on bLN responses to odours, we observed that the periodic excitatory input originating from Kenyon cells was often curtailed by phasic inhibitory postsynaptic potentials (Fig. 2b, arrowheads), with onsets at the typical phase of bLN action potentials. We hypothesized that these inhibitory postsynaptic potentials originate from lateral inhibition among bLNs (as put forward in a theoretical exploration²⁵). This was supported by extracellular stimulation of Kenyon cells (Supplementary Fig. 2) and confirmed in paired bLN recordings. Beta-lobe neurons inhibit each other (Fig. 2c) with an estimated connection probability of 28% ($n = 32$ connections, 2 reciprocally connected pairs). Although unknown so far, other interneuron populations may also contribute to bLN inhibition.

In each oscillation cycle, lateral inhibition reduces the likelihood of late bLN spikes; thus, it should limit the ability of STDP to potentiate KC–bLN synapses. This in turn should curb bLN population activity (see also ref. 26). As predicted, implementing lateral inhibition

¹Division of Biology, California Institute of Technology, Pasadena, California 91125, USA. ²Broad Fellows Program in Brain Circuitry, California Institute of Technology, Pasadena, California 91125, USA.

³Max Planck Institute for Brain Research, 60528 Frankfurt am Main, Germany.

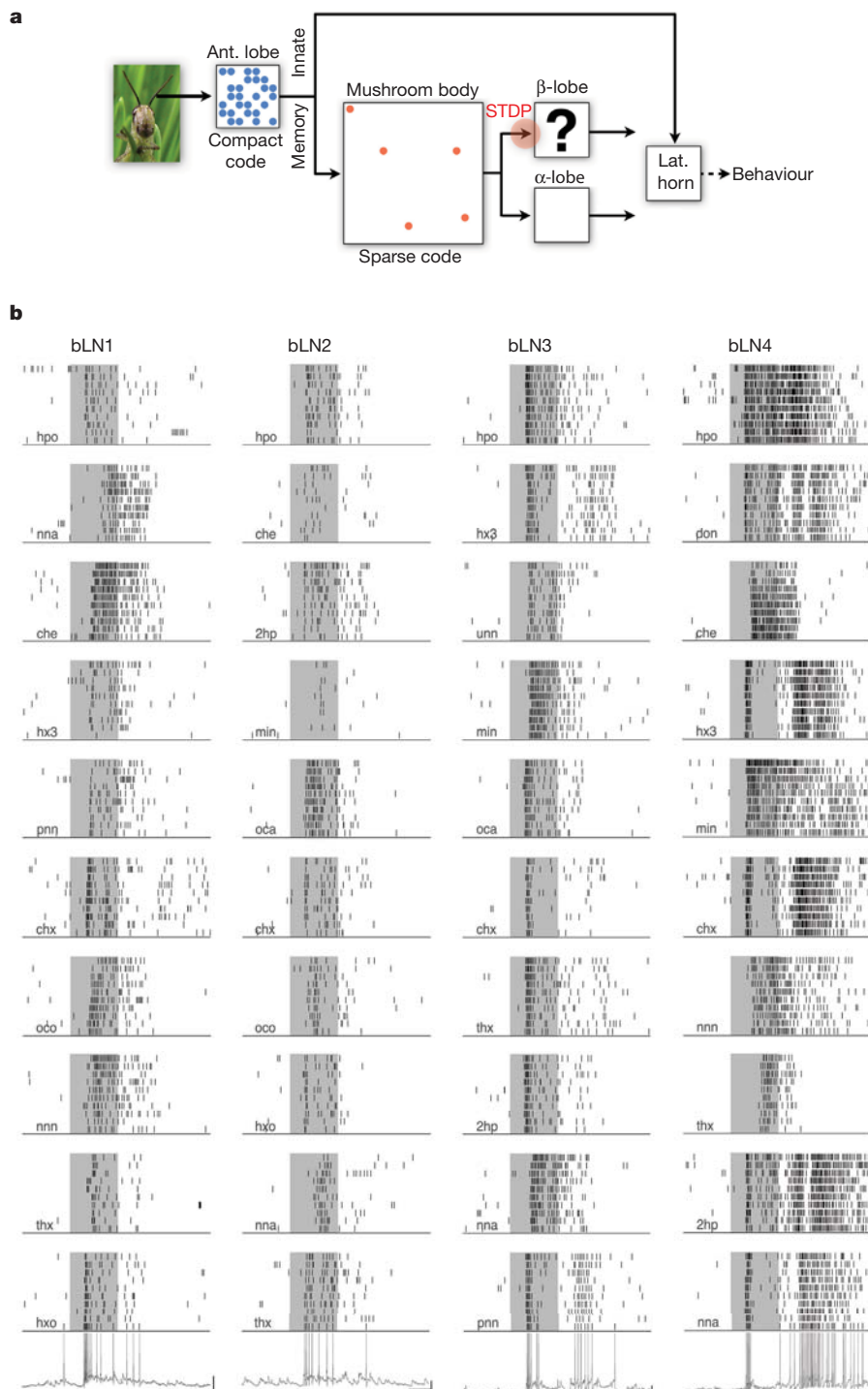


Figure 1 | Beta-lobe neurons are promiscuous. **a**, Olfactory circuit in which bLNs are embedded. Ant., antennal; lat., lateral. **b**, Rasters constructed from *in vivo* intracellular dendritic recordings, illustrating responses of four bLNs (different animals) to ten odours. Shaded region represents odour delivery (1 s). For each bLN, intracellular traces at bottom correspond to the tenth trial with the last odour.

between mbLNs (based on the experimental connectivity estimate and amplitude distribution) reduced population activity to $\sim 50\%$ ($p_{\text{response}} = 0.51 \pm 0.14$ (response probability), $n = 30$ mbLNs; compare with $p_{\text{response}} = 0.49 \pm 0.18$, $n = 30$ bLNs from experiment; Fig. 2d–f). The mBLN spike phase remained centred on π (LFP trough). In addition, the response profiles of those mbLNs were very similar to those recorded experimentally (compare distributions in Fig. 2e, f and moments in Fig. 2g; see also Supplementary Figs 3–5).

Horizontal scale bars, 500 ms; vertical scale bars, 10 mV; spikes are clipped. Odours: 2-heptanone (2hp), cherry (che), *cis*-3-hexen-1-ol (chx), 3,7-dimethyl-2,6-octadiene-nitrile (don), 1-heptanol (hpo), 1-hexen-3-ol (hx3), 1-hexanol (hxo), mint (min), nonanal (nna), 5-nonanone (nnn), octanal (oca), 1-octanol (oco), 3-pentanone (pnn), *trans*-2-hexen-1-ol (thx), 6-undecanone (unn).

We conclude that bLN activity, although very different from the sparse output of Kenyon cells, can be explained by the combined effects of Hebbian STDP at KC–bLN synapses and lateral inhibition between bLNs. The useful consequences are that bLN spikes are tightly phase-locked to the LFP¹⁷ and that instantaneous bLN population activity lies around the midpoint of its dynamic range. This increases the coding capacity of this small population of output neurons and is relevant for plasticity, as explored below.

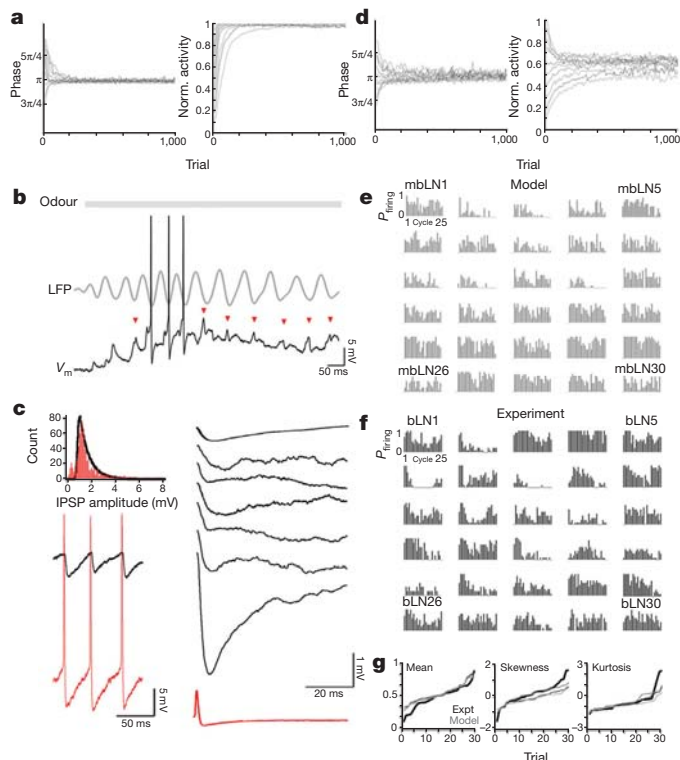


Figure 2 | Saturation of activity caused by STDP can be counteracted by lateral inhibition. **a**, Mean firing phase (left) and normalized population activity (right) in a simulation of a KC–bLN network (30 Izhikevich units⁴⁴, one LFP cycle, 1,000 trials). Each point is a ten-trial average; STDP is turned on in trial 11. Each curve is run with n Kenyon cell inputs per mbLN ($20 < n < 80$, 10% connections in common). STDP regulates bLN firing phase (ref. 17) but inexorably drives bLN population to saturation. **b**, *In vivo* intradendritic recording of bLN membrane potential, V_m , together with LFP during odour presentation. Arrowheads indicate onsets of inhibitory postsynaptic potentials, timed on LFP troughs. **c**, Top left: frequency distribution of inhibitory postsynaptic potential amplitudes, measured at baseline, in 30 bLNs; black curve, fit used for model in **d**. IPSP, inhibitory postsynaptic potential. Bottom left: paired bLN recording revealing direct inhibitory connection. Right: bLN spike-triggered averages from seven distinct bLN pairs. **d**, Simulation of a bLN network as in **a**, except with n Kenyon cell inputs per bLN (here $22 < n < 130$, same drive at simulation onset as in **a**). Lateral inhibition among bLNs is as determined experimentally. Mean phase (left) is minimally affected; network activity (right) settles near midrange. **e**, Simulation of a bLN network as in **d**, extended over 25 LFP cycles, with time-varying Kenyon cell input profiles derived from experiments^{12,17,45}. Post-stimulus time histograms plotted as firing probability versus cycle rank for each of the 30 mbLNs (ten trials), post STDP. **f**, *In vivo* intradendritic responses of 30 bLNs to *trans*-2-hexen-1-ol represented as in **e** (from 16 different animals). **g**, Comparison of experimental (black) and model (grey) bLN response statistics. Same simulation as in **e** (darkest grey) together with two other simulations of the same network with different Kenyon cell input profiles (lighter shades of grey).

Conditional modulation of STDP rule

Mushroom bodies are critical for associative conditioning in insects^{6–11,27}, and second-messenger pathways involved in memorization and retrieval have been described in *Drosophila*^{1,4–7,28,29}. Yet we know little about the synaptic mechanisms underlying conditioning there³⁰, and even less about how specificity is achieved or about the roles that STDP might have in it. Associative learning in insects seems to rely on neuromodulators^{31–35} (for example octopamine (OCT) and dopamine) to mediate unconditioned signals (appetitive and aversive, respectively, for OCT and dopamine). In locusts and other insects, these neuromodulators are delivered nonspecifically by small numbers of octopaminergic³⁶ and dopaminergic³⁷ neurons with projections to the mushroom body lobes (among others), that is, where Kenyon cells contact bLNs.

We assessed the effect of local OCT injection into the β -lobes on plasticity and tuning of those bLNs *in vivo* (Fig. 3). Figure 3d illustrates our experimental schemes, which were designed to probe specificity, that is, the question of how the system determines which synapses should change when the reinforcer is global. During an odour stimulus, two features distinguish odour-evoked Kenyon cell spikes from ‘stray’ spikes produced randomly by non-responding Kenyon cells (most of the Kenyon cells): odour-evoked spikes are synchronized and cause bLNs to spike by their collective action. Hence, odour-evoked release at Kenyon cell synapses occurs within the time window for STDP. We thus tested the effect of OCT injection on synapses that differed only in their temporal features of pre- and postsynaptic activation. In each experiment, we measured the responses of one bLN to Kenyon cell stimulation at a rate of 0.1 s^{-1} at two locations (a pairing location (P) and a control location (C)) and two different times (C 300 ms before P). We found Kenyon cell stimulation sites that converged onto the same recorded bLN in 13 out of 20 experiments.

In ‘test’ trials (Fig. 3d, top), the bLN was depolarized by a brief pulse of current to produce one single action potential 5 s after Kenyon cell stimulation at P, hence well outside the window of $\delta t = t_{\text{post}} - t_{\text{pre}} = \pm 25 \text{ ms}$ required for STDP¹⁷, where t_{post} and t_{pre} are respectively the post- and presynaptic spike times. Pairing consisted of five trials at 0.1 s^{-1} , of either of two kinds. In ‘STDP’ trials, the bLN was fired within $\pm 25 \text{ ms}$ of a Kenyon cell stimulus at P (Fig. 3d, middle). In ‘STDP + OCT’ trials, pairing was as in STDP trials but was followed by one OCT injection (5 pl) 1 s after pairing (Fig. 3d, bottom). Test trials were carried out before STDP trials (Fig. 3a–c, red), after STDP trials (black) and after STDP + OCT trials (blue). All test and pairing trials thus contained the same numbers of pre- and postsynaptic pulses; only their relative timings differed. Examples with three values of δt are shown (Fig. 3a–c). In each, OCT caused a depression. We note that only connections between cells co-activated within the STDP window were depressed (that is, P but not C; see also Supplementary Fig. 6). The depressive action of OCT on synapses undergoing STDP (20 different values of δt ; Fig. 3e, f and Supplementary Fig. 7) was greatest for $\delta t > 0$, converting baseline Hebbian STDP into one where only depression occurred.

To rule out the possibility that the action of OCT resulted not from the pairing *per se*, but from the temporal proximity of OCT delivery to the pairing (P), we reversed the order of C and P ($n = 3$; Supplementary Fig. 8). Again, only the P pathway was affected by OCT (effect of OCT on control (mean \pm s.e.m.): $-0.9 \pm 0.49\%$, $n = 3$ (P then C); $0.2 \pm 2.28\%$, $n = 10$ (C then P); sets statistically equivalent: $P > 0.66$, t -test). Hence, because the control and paired synapses shared the same postsynaptic partner (C and P differed only in the identity of the presynaptic cells and in the timings of the presynaptic spikes relative to those in their common bLN), and because the two sets of presynaptic cells were stimulated within only 300 ms of one another (C then P or P then C), we conclude that the relative timing of pre- and postsynaptic firing is what contributes to making the synapses susceptible to OCT action. We do not know whether pre-post delays longer than $\pm 25 \text{ ms}$ (but shorter than 300 ms) would have equivalent effects. However, almost all odour-evoked Kenyon cell action potentials occur within the range of delays we tested. We conclude that, despite its global release, OCT affects specific synapses—those in which pre- and postsynaptic partners fired within the appropriate delay between one another. This is the case even though OCT was delivered 1 s after the relevant pairing (reproducing a temporal dissociation between conditioned stimulus and unconditioned stimulus¹⁴).

Conditional changes of STDP are specific

The STDP curves in Fig. 3f were obtained *in vivo* with electrical activation of the pre- and postsynaptic cells. We next tested the effect of OCT on the responses of bLNs to odours. We predicted that if OCT depresses KC–bLN synapses that fire within the STDP time window,

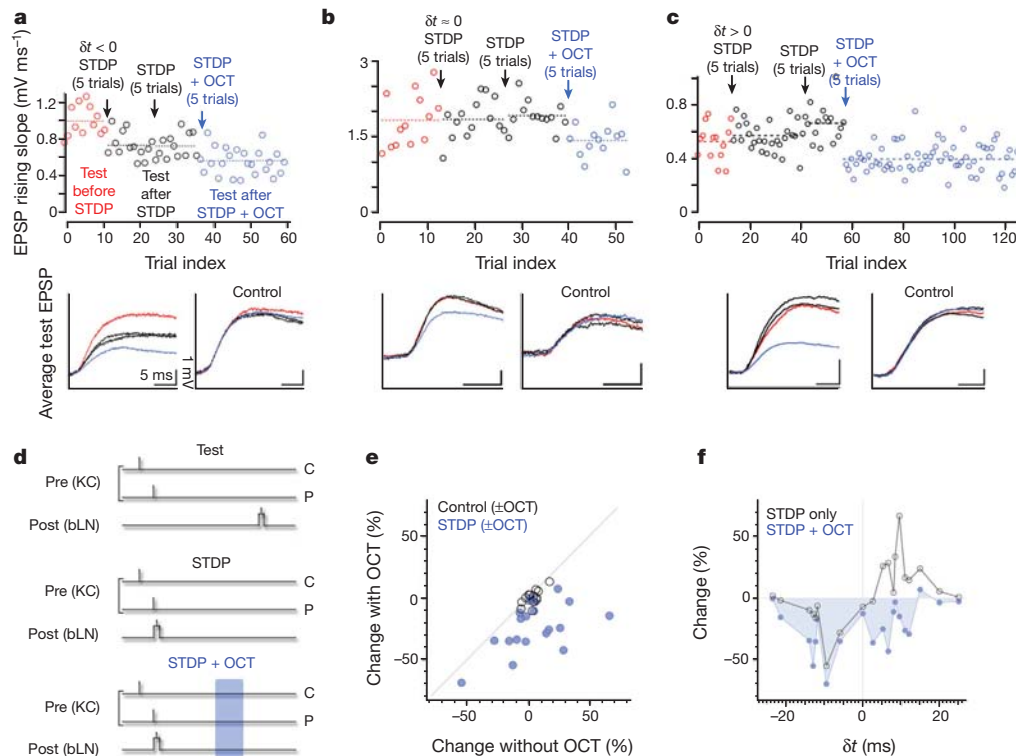


Figure 3 | OCT changes the STDP rule. **a**, Five trials pairing OCT with depressing STDP ($\delta t < 0$) reduced KC–bLN excitatory postsynaptic potential (EPSP) size (blue) more than did two sets of five-trial STDP with negative δt alone (black). EPSPs evoked by interleaved stimulation with the control electrode (embedded among Kenyon cells in a different location) were unaffected (control, bottom right), despite equal exposure to OCT. **b**, Five trials pairing OCT with $\delta t \approx 0$ STDP reduced KC–bLN EPSP size (blue), whereas STDP alone with this δt value had no effect (black). Control EPSPs were unaffected (bottom right). **c**, Five trials pairing OCT with potentiating STDP ($\delta t > 0$) reduced KC–bLN EPSP size after it was potentiated by two bouts of STDP alone with this δt value. Control EPSPs were unaffected (bottom right). **d**, Stimulation protocols. Test trials were used to evaluate the amplitudes of KC–bLN EPSPs before STDP, after STDP and after STDP + OCT, as shown in a–c, and to compute (from multiple experiments) values in e and f. **e**, **f**, control Kenyon cell input; P, paired Kenyon cell input. In test trials, bLNs were depolarized with a 5-ms d.c. pulse (causing a single bLN spike) ~5 s after

extracellular stimulation (0.1-ms pulses) of Kenyon cells in two different locations (C and P, 300 ms apart). In STDP trials, bLNs were depolarized as above, causing a single spike in a narrow window around the time of Kenyon cell stimulation (P). Control Kenyon cell stimulation (C) was offset by 300 ms. STDP + OCT trials were the same as STDP trials, only with the addition of localized OCT injection (50-ms pressure-pulse) in the β -lobe, 1 s after P Kenyon cell stimulation. **e**, Summary data from 20 experiments, plotting for each experiment the effect of STDP + OCT versus STDP alone (blue dots) and plotting control data, with and without OCT, for 13 of 20 experiments (black circles). Changes due to STDP + OCT differ significantly from control + OCT ($P < 0.003$, t -test). Changes due to OCT in control not significantly different from zero ($P > 0.84$, t -test; see also Supplementary Fig. 7). **f**, Comparison between change due to STDP + OCT and change due to STDP alone, each plotted as a function of δt . Changes due to STDP + OCT differ significantly from zero (relative to before STDP: $P < 0.0001$; relative to STDP only: $P < 0.0002$, t -test; see also Supplementary Fig. 7).

it should also reduce bLN output. This was tested first with our model, using an STDP rule modified according to Fig. 3f: responses were reduced in 28 of 30 mBLNs (Fig. 4a, b). We then tested the prediction experimentally with 12 bLNs (18 bLN–odour pairs), each recorded intracellularly from a dendrite. In 16 of 18 instances, OCT caused a reduction of bLN output, averaged over the odour response (Fig. 4c, d). LFP power in the mushroom body calyx was unaffected (Fig. 4f), consistent with unchanged input to the mushroom body.

We also evaluated the specificity of changes in bLN–odour responses. A bLN was presented with three odours in blocks of trials in the order indicated (Fig. 4e, left). OCT was injected 800 ms after odour onset, paired each time with only one of the three odours. As in Fig. 4c, d, the responses of the bLN to the three odours (assembled by odour in three graphs; Fig. 4e, right) were reduced after pairing with OCT (compare blue and red post-stimulus time histograms). The reduction of the response to an odour occurred only after pairing of that particular odour with OCT. For example, responses to cherry and *trans*-2-hexen-1-ol were minimally affected by pairing OCT with 2-heptanone; they became significantly reduced only after the appropriate pairing of either cherry or *trans*-2-hexen-1-ol with OCT. Figure 4f compares summary data for odours paired with OCT ($n = 18$ bLN–odour pairs) to controls ($n = 12$ bLN–odour pairs:

odour responses after pairing of a different odour with OCT ($n = 7$) and odour responses after pairing of electrical Kenyon cell stimulation with OCT ($n = 5$); $n = 18$ LFP recordings simultaneous with intracellular bLN recordings). These results support the observation that OCT specifically depresses contacts between cells co-activated within the STDP window (Fig. 3); they also indicate that KC–bLN pairing and OCT should co-occur within an interval of at most a few tens of seconds.

Discussion

In the absence of OCT, STDP at KC–bLN synapses adaptively regulates the bLN spike phase¹⁷ and bLN population output, helped by the action of lateral inhibition between bLNs (Fig. 2). In the context of reinforcer delivery, STDP gains a new role: it tags—presumably through biochemical changes dependent on pairing—the synapses between connected Kenyon cells and bLNs that have fired an action potential within the STDP pairing window, itself commensurate with the oscillation period in this system³⁸. This renders those synapses susceptible to the action of OCT (which is proposed to mediate positive reinforcement in insect learning^{14,34,39}) and reduces the inhibitory output of the mushroom body mediated by bLNs. Hence, the action of OCT can be specific, even though its release is diffuse and often delayed

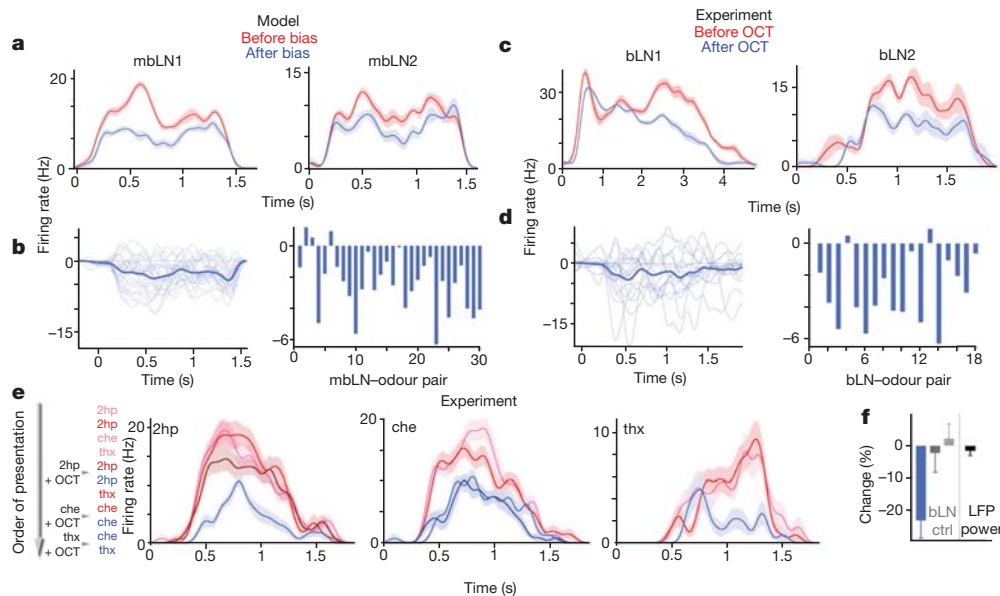


Figure 4 | Odour-specific decrease of mushroom body output by OCT.

a, Simulation of bLN network as in Fig. 2e. Smoothed post-stimulus time histograms (PSTHs) for two mblNs (ten trials; shading, s.e.). Red, responses at equilibrium; blue, responses after ten trials with STDP + OCT curve shown in Fig. 3f. **b**, Left: difference in PSTHs for all 30 mblNs responses before and after five trials of STDP + OCT ('PSTH after pairing' minus 'PSTH before pairing', thin lines). Responses of individual units at particular times can increase or decrease, but average difference (thick line) is less than zero at all times. Right: time-averaged differences for each of the 30 mblNs ('PSTH after pairing' minus 'PSTH before pairing'). In some instances, mblN responses increased (for most units this occurred transiently; for a few mblNs the entire time-averaged response increased). This is due to reduced lateral inhibition (that is, disinhibition) because mblN population activity decreased. **c**, *In vivo* intradendritic recordings of bLN odour responses before and after pairing of the odour with localized OCT injection in the β -lobe (50-ms pressure-pulse, 800 ms after odour onset, either five ($n = 5$) or ten pairing trials ($n = 13$)). PSTHs for two bLNs (ten trials; shading, s.e.): red, responses before odour–OCT pairing; blue, responses after ten trials of odour paired with OCT injection. **d**, Same difference of PSTHs as in **b**, for 18 recorded bLN–odour pairs (12 bLNs). As in the model, responses of individual bLNs can increase or

decrease transiently, but on average there is a net decrease. **e**, OCT-induced changes are odour specific. Three odours are sequentially paired (during five trials) with OCT to assess carry-over of pairing across odours. Order of stimuli is shown at left. Red colours, responses before pairing with OCT; blue colours, responses after pairing. Odours are presented in ten-trial blocks and PSTHs are shown for each block (shading, s.e.). Changes due to nonspecific pairing are minimal by comparison with those due to odour-specific pairing. **f**, Summary data comparing the effect of odour–OCT pairing (blue: $n = 18$ bLN–odour pairs, 12 bLNs) with those of controls (grey: $n = 12$ bLN–odour pairs, 9 bLNs; black (LFP controls): $n = 18$ recordings simultaneous with intracellular bLN recordings). Dark grey ($n = 7$), effect on bLN response to non-paired odour before and after pairing another odour with OCT. Light grey ($n = 5$), effect on bLN response to non-paired odour before and after pairing electrical activation of Kenyon cells with OCT. Black, effect on LFP power (10–30-Hz band, recorded in mushroom body) before and after pairing odour with OCT. Changes due to pairing odour with OCT differ significantly from zero ($P < 0.0006$, t -test) and from those in the three control conditions ($P < 0.002$ – 0.022 , t -test). Changes in control conditions were not significantly different from zero ($P > 0.72$ (dark grey), 0.64 (light grey) and 0.33 (black)).

relative to the conditioned (odour) stimulus. This provides experimental support for related theoretical propositions^{23,40,41}. Our results also solve the temporal dissociation puzzle revealed in experiments¹⁴.

Because the selectivity of synaptic change allowed by STDP relies on the rare co-occurrence of pre- and postsynaptic spikes, it is beneficial that Kenyon cell firing is rare and that odour representations by Kenyon cells are sparse, as observed^{12–14}. We propose that olfactory associative memories are stored, at least in part, as sparse sets of synaptic weights between Kenyon cells and mushroom body output neurons. In the absence of reinforcer, STDP and lateral inhibition between bLNs set the (default) instantaneous output of the β -lobe network near the middle of its dynamic range. This serves at least two purposes. First, it maximizes the number of possible distinct combinations of simultaneously active bLNs. Second, it ensures that the output of the network can be increased or decreased, if an associative reinforcer is to co-occur. It is possible that some of the molecular pathways revealed by *Drosophila* neurogenetics^{6,9,11} have a role in the phenomenon described here. The functional form of STDP has recently been shown to depend on neuromodulatory context in mammalian brain slices^{22,42,43}, suggesting that our results may have broad implications for STDP and learning.

METHODS SUMMARY

All results were obtained *in vivo* from locusts housed in a crowded colony. Odours were delivered by injection of a controlled volume of odorized air within a

constant stream of desiccated air. The results presented here are derived from intradendritic recordings, made using sharp micropipettes, of 76 neurons in 55 locusts. LFPs were recorded with silicon probes (NeuroNexus) in the mushroom body Kenyon cell soma cluster. Octopamine (100 μ M) was injected locally into the mushroom body β -lobe using a picopump (WPI). Electrical stimulation of Kenyon cell somata was done with modified tetrodes (FHC). Stimulation protocols and data analysis were carried out using specialized software (LABVIEW, National Instruments; IGOR, Wavemetrics; and MC_STIMULUS, Multichannel Systems). Simulations of networks of 'Izhikevich units'⁴⁴ were done using MATLAB (Mathworks).

Full Methods and any associated references are available in the online version of the paper at www.nature.com/nature.

Received 16 September; accepted 8 December 2011.

Published online 25 January 2012.

- McGuire, S. E., Le, P. T. & Davis, R. L. The role of *Drosophila* mushroom body signaling in olfactory memory. *Science* **293**, 1330–1333 (2001).
- Tully, J. B. C. T. in *Drosophila: A Practical Approach* (ed. Roberts, D. B.) 265–317 (Oxford Univ. Press, 1998).
- de Belle, J. S. & Heisenberg, M. Associative odor learning in *Drosophila* abolished by chemical ablation of mushroom bodies. *Science* **263**, 692–695 (1994).
- Tully, T. & Quinn, W. G. Classical conditioning and retention in normal and mutant *Drosophila melanogaster*. *J. Comp. Physiol. A* **157**, 263–277 (1985).
- Heisenberg, M., Borst, A., Wagner, S. & Byers, D. *Drosophila* mushroom body mutants are deficient in olfactory learning. *J. Neurogenet.* **2**, 1–30 (1985).
- Quinn, W. G., Harris, W. A. & Benzer, S. Conditioned behavior in *Drosophila melanogaster*. *Proc. Natl Acad. Sci. USA* **71**, 708–712 (1974).

7. Keene, A. C. & Waddell, S. *Drosophila* olfactory memory: single genes to complex neural circuits. *Nature Rev. Neurosci.* **8**, 341–354 (2007).
8. Akalal, D. B. *et al.* Roles for *Drosophila* mushroom body neurons in olfactory learning and memory. *Learn. Mem.* **13**, 659–668 (2006).
9. Davis, R. L. Olfactory memory formation in *Drosophila*: from molecular to systems neuroscience. *Annu. Rev. Neurosci.* **28**, 275–302 (2005).
10. Gerber, B., Tanimoto, H. & Heisenberg, M. An engram found? Evaluating the evidence from fruit flies. *Curr. Opin. Neurobiol.* **14**, 737–744 (2004).
11. Heisenberg, M. Mushroom body memoir: from maps to models. *Nature Rev. Neurosci.* **4**, 266–275 (2003).
12. Perez-Orive, J. *et al.* Oscillations and sparsening of odor representations in the mushroom body. *Science* **297**, 359–365 (2002).
13. Turner, G. C., Bazhenov, M. & Laurent, G. Olfactory representations by *Drosophila* mushroom body neurons. *J. Neurophysiol.* **99**, 734–746 (2008).
14. Ito, I., Ong, R. C.-Y., Raman, B. & Stopfer, M. Sparse odor representation and olfactory learning. *Nature Neurosci.* **11**, 1177–1184 (2008).
15. Kanerva, P. *Sparse Distributed Memory* (MIT Press, 1988).
16. Papadopoulou, M., Cassenaer, S., Nowotny, T. & Laurent, G. Normalization for sparse encoding of odors by a wide-field interneuron. *Science* **332**, 721–725 (2011).
17. Cassenaer, S. & Laurent, G. Hebbian STDP in mushroom bodies facilitates the synchronous flow of olfactory information in locusts. *Nature* **448**, 709–713 (2007).
18. Markram, H., Lübke, J., Frotscher, M. & Sakmann, B. Regulation of synaptic efficacy by coincidence of postsynaptic APs and EPSPs. *Science* **275**, 213–215 (1997).
19. Bi, G. Q. & Poo, M. M. Synaptic modifications in cultured hippocampal neurons: dependence on spike timing, synaptic strength, and postsynaptic cell type. *J. Neurosci.* **18**, 10464–10472 (1998).
20. Abbott, L. F. & Nelson, S. B. Synaptic plasticity: taming the beast. *Nature Neurosci.* **3**, 1178–1183 (2000).
21. Meeks, J. P. & Holy, T. E. Pavlov's moth: olfactory learning and spike-timing-dependent plasticity. *Nature Neurosci.* **11**, 1126–1127 (2008).
22. Pawlak, V. Timing is not everything: neuromodulation opens the STDP gate. *Front. Syn. Neurosci.* **2**, 146 (2010).
23. Izhikevich, E. M. Solving the distal reward problem through linkage of STDP and dopamine signaling. *Cereb. Cortex* **17**, 2443–2452 (2007).
24. Güti, R., Aharonov, R., Rotter, S. & Sompolinsky, H. Learning input correlations through nonlinear temporally asymmetric Hebbian plasticity. *J. Neurosci.* **23**, 3697–3714 (2003).
25. Huerta, R., Nowotny, T., García-Sánchez, M., Abarbanel, H. D. I. & Rabinovich, M. I. Learning classification in the olfactory system of insects. *Neural Comput.* **16**, 1601–1640 (2004).
26. Masquelier, T. & Thorpe, S. J. Unsupervised learning of visual features through spike timing dependent plasticity. *PLoS Comput. Biol.* **3**, e31 (2007).
27. Waddell, S. & Quinn, W. G. Learning how a fruit fly forgets. *Science* **293**, 1271–1272 (2001).
28. Isabel, G., Pascual, A. & Preat, T. Exclusive consolidated memory phases in *Drosophila*. *Science* **304**, 1024–1027 (2004).
29. Gervasi, N., Tchénio, P. & Preat, T. PKA dynamics in a *Drosophila* learning center: coincidence detection by rutabaga adenylyl cyclase and spatial regulation by dunce phosphodiesterase. *Neuron* **65**, 516–529 (2010).
30. Wang, Y., Mamiya, A., Chiang, A. S. & Zhong, Y. Imaging of an early memory trace in the *Drosophila* mushroom body. *J. Neurosci.* **28**, 4368–4376 (2008).
31. Claridge-Chang, A. *et al.* Writing memories with light-addressable reinforcement circuitry. *Cell* **139**, 405–415 (2009).
32. Kim, Y. C., Lee, H. G. & Han, K. A. D1 dopamine receptor dDA1 is required in the mushroom body neurons for aversive and appetitive learning in *Drosophila*. *J. Neurosci.* **27**, 7640–7647 (2007).
33. Riemensperger, T., Voller, T., Stock, P., Buchner, E. & Fiala, A. Punishment prediction by dopaminergic neurons in *Drosophila*. *Curr. Biol.* **15**, 1953–1960 (2005).
34. Schwaerzel, M. *et al.* Dopamine and octopamine differentiate between aversive and appetitive olfactory memories in *Drosophila*. *J. Neurosci.* **23**, 10495–10502 (2003).
35. Mizunami, M. & Matsumoto, Y. Roles of aminergic neurons in formation and recall of associative memory in crickets. *Front. Behav. Neurosci.* **4**, 172 (2010).
36. Brautig, P. Suboesophageal DUM neurons innervate the principal neuropiles of the locust brain. *Phil. Trans. R. Soc. Lond. B* **332**, 221–240 (1991).
37. Wendt, B. & Homberg, U. Immunocytochemistry of dopamine in the brain of the locust *Schistocerca gregaria*. *J. Comp. Neurol.* **321**, 387–403 (1992).
38. Laurent, G. & Naraghi, M. Odorant-induced oscillations in the mushroom bodies of the locust. *J. Neurosci.* **14**, 2993–3004 (1994).
39. Hammer, M. An identified neuron mediates the unconditioned stimulus in associative olfactory learning in honeybees. *Nature* **366**, 59–63 (1993).
40. Güti, R. & Sompolinsky, H. The tempotron: a neuron that learns spike timing-based decisions. *Nature Neurosci.* **9**, 420–428 (2006).
41. Huerta, R. & Nowotny, T. Fast and robust learning by reinforcement signals: explorations in the insect brain. *Neural Comput.* **21**, 2123–2151 (2009).
42. Seol, G. H. *et al.* Neuromodulators control the polarity of spike-timing-dependent synaptic plasticity. *Neuron* **55**, 919–929 (2007).
43. Shen, W., Flajolet, M., Greengard, P. & Surmeier, D. J. Dichotomous dopaminergic control of striatal synaptic plasticity. *Science* **321**, 848–851 (2008).
44. Izhikevich, E. M. Simple model of spiking neurons. *IEEE Trans. Neural Netw.* **14**, 1569–1572 (2003).
45. Mazor, O. & Laurent, G. Transient dynamics versus fixed points in odor representations by locust antennal lobe projection neurons. *Neuron* **48**, 661–673 (2005).

Supplementary Information is linked to the online version of the paper at www.nature.com/nature.

Acknowledgements This work was funded by the Lawrence Hanson Chair at Caltech, the National Institutes on Deafness and other Communication Disorders, Caltech's Broad Fellows Program, the Office of Naval Research (grants N00014-07-1-0741 and N00014-10-1-0735) and the Max Planck Society. We are grateful to L.-P. Mok for help with locust dissections and to E. Schuman, A. Siapas, E. Lubenov, M. Papadopoulou and members of the Laurent lab for comments on the manuscript.

Author Contributions S.C. and G.L. designed the experiments and simulations, discussed the results and wrote the paper. S.C. carried out the experiments and simulations.

Author Information Reprints and permissions information is available at www.nature.com/reprints. The authors declare no competing financial interests. Readers are welcome to comment on the online version of this article at www.nature.com/nature. Correspondence and requests for materials should be addressed to G.L. (gilles.laurent@brain.mpg.de) or S.C. (stijn@caltech.edu).

METHODS

Preparation and stimuli. All results were obtained *in vivo* from locusts (*Schistocerca americana*) housed in an established, crowded colony. Young adults of either sex were immobilized in a holder. Both antennae were secured in place with respect to the olfactory delivery system and remained intact for olfactory stimulation. The brain was exposed, desheathed and superfused with locust saline, as previously described³⁸.

Odour delivery. Odours were diluted 10% v/v in paraffin oil. They were delivered by injection of a controlled volume of odorized air within a constant stream of desiccated air. Total airflow was set to 0.85 l min^{-1} and the odour was further diluted by one-third in air. Teflon tubing was used at and downstream of the mixing point to prevent odour lingering and cross-contamination.

Intradendritic recordings. Sharp electrode recordings from the dendrites of bLNs were made with borosilicate glass micropipettes (d.c. resistance, 150–200 M Ω) filled with 1 M potassium acetate. The cell type from which the data are derived could be recognized by several characteristics: responses to odour, subthreshold baseline activity profile and response to electrical stimulation of Kenyon cells¹⁷. Recordings from bLNs were always made from dendrites in the β -lobe. To assess changes in bLN instantaneous firing rate, bLN spike times were either binned per simultaneously recorded LFP cycle (Fig. 2f) or convolved with a 50-ms Gaussian kernel to generate smoothed PSTHs (Fig. 4c, e; shading, s.e.). EPSP slope was measured as the maximum slope over the 10–90% range of maximum amplitude. The average EPSP waveforms shown at bottom in Fig. 3a–c were computed from the same data as the slope measurements shown at top in Fig. 3a–c. The electrical stimulation rate was 0.1 s^{-1} (with no intertrial gap). The results in this work were obtained from 55 animals; in two instances the same animal was used for two distinct bLNs with OCT injection.

LFP recordings. LFPs were recorded in the mushroom body Kenyon cell soma layer using Michigan probes (<http://www.neuronexustech.com>).

Electrical stimulation. Twisted-wire tetrodes obtained from FHC (no. CE4B75) were modified for monopolar stimulation, with the casing serving as the anode. The tips of the tetrodes were splayed such that the distance between the exposed tips was approximately equal to 60% of the diameter of the mushroom body calyx. The exposed end of the stimulating electrode was embedded among Kenyon cell somata. The tetrodes were electroplated with gold solution to impedances of 200–350 k Ω at 1 kHz. Stimulating currents (5–140 μA , 0.1 ms) were generated using an STG1000 Multichannel System (as in ref. 17).

OCT injection. Patch pipettes were back-filled with a 100 μM OCT hydrochloride, 0.01% Fast Green solution. A pneumatic picopump (WPI) was used to apply one 50-ms, 5-p.s.i. pressure pulse per trial. Each pulse injected $\sim 5 \text{ pl}$ (as measured by previous injection into a drop of oil). The injected solution was localized to the β -lobe, as verified by bounded diffusion of the Fast Green dye.

Simulations. All simulations were carried out with networks of Izhikevich units⁴⁴. Networks consisted of 30 units each with dynamics given by

$$\frac{dv}{dt} = 0.04v^2 + 5v + 140 - u + I$$

$$\frac{du}{dt} = a(bv - u)$$

where $a = 0.02$, $b = 0.2$, $c = -65$, $d = 8$ and if $v \geq 30$ then $v \leftarrow c$ and $u \leftarrow u + d$. Synaptic interactions and external inputs were introduced through the I term, which for the j th unit takes the form

$$I_j = \sum_i w_{\text{bLN}}(i, j) f_{\text{bLN}}(i) + \sum_k w_{\text{KC}}(k, j) f_{\text{KC}}(k)$$

Here w_{bLN} is a matrix of inhibitory weights among network units, f_{bLN} is the vector of spike times generated by the network, w_{KC} is a matrix of excitatory input weights and f_{KC} is the vector of spike times that constitutes the input to the network. At every trial, f_{KC} is drawn from a distribution characterized by three experimental observations: odour-evoked Kenyon cell spiking phase distribution relative to the LFP¹², average odour-evoked Kenyon cell population PSTH⁴⁵ and Kenyon cell baseline activity¹². The matrix w_{bLN} is estimated from experimental recordings and kept fixed during the simulation. The matrix w_{KC} is drawn from a normal distribution at the onset of the simulation, with variable means for different initial conditions; it is updated in every trial according to

$$\Delta w = \begin{cases} \lambda f_{-}(w) K(\Delta t) & \text{if } \Delta t \leq 0 \\ \lambda f_{+}(w) K(\Delta t) & \text{if } \Delta t > 0 \end{cases}$$

The temporal filter, $K(\Delta t)$, is the experimentally derived STDP curve: either the unbiased Hebbian form as in ref. 17 or the depression-biased form that results from pairing with OCT as in Fig. 3f. The learning rate was set by the number of pairings carried out to arrive at the STDP curve in experiments. The weight dependences of the updating functions $f_{+}(w)$ and $f_{-}(w)$ are as follows:

$$f_{+}(w) = (1 - w)^{\mu}$$

$$f_{-}(w) = w^{\mu}$$

As described in ref. 24, the value of μ determines the shape of the equilibrium weight distribution. A value ($\mu = 0.08$) was chosen such that the weight distribution in the simulation at equilibrium matched the experimental EPSP size distribution (Supplementary Information, section 3). As described above, parameters in the model were constrained by experimental estimates, except for a , b , c and d , which characterize the dynamics of individual model units. These parameters took the typical values used for regular spiking neurons⁴⁴.

Mutations in kelch-like 3 and cullin 3 cause hypertension and electrolyte abnormalities

Lynn M. Boyden¹, Murim Choi^{1*}, Keith A. Choate^{2*}, Carol J. Nelson-Williams¹, Anita Farhi¹, Hakan R. Toka³, Irina R. Tikhonova⁴, Robert Bjornson⁴, Shrikant M. Mane⁴, Giacomo Colussi⁵, Marcel Lebel⁶, Richard D. Gordon⁷, Ben A. Semmekrot⁸, Alain Poujol⁹, Matti J. Välimäki¹⁰, Maria E. De Ferrari⁵, Sami A. Sanjad¹¹, Michael Gutkin¹², Fiona E. Karet¹³, Joseph R. Tucci¹⁴, Jim R. Stockigt¹⁵, Kim M. Keppler-Noreuil¹⁶, Craig C. Porter¹⁷, Sudhir K. Anand¹⁸, Margo L. Whiteford¹⁹, Ira D. Davis²⁰, Stephanie B. Dewar²¹, Alberto Bettinelli²², Jeffrey J. Fadrowski²³, Craig W. Belsha²⁴, Tracy E. Hunley²⁵, Raoul D. Nelson²⁶, Howard Trachtman²⁷, Trevor R. P. Cole²⁸, Maury Pinsk²⁹, Detlef Bockenhauer³⁰, Mohan Shenoy³¹, Priya Vaidyanathan³², John W. Foreman³³, Majid Rasoulpour³⁴, Farook Thameem³⁵, Hania Z. Al-Shahrouri³⁵, Jai Radhakrishnan³⁶, Ali G. Gharavi³⁶, Beatrice Goilav³⁷ & Richard P. Lifton¹

Hypertension affects one billion people and is a principal reversible risk factor for cardiovascular disease. Pseudohypoaldosteronism type II (PHAII), a rare Mendelian syndrome featuring hypertension, hyperkalaemia and metabolic acidosis, has revealed previously unrecognized physiology orchestrating the balance between renal salt reabsorption and K^+ and H^+ excretion¹. Here we used exome sequencing to identify mutations in kelch-like 3 (*KLHL3*) or cullin 3 (*CUL3*) in PHAII patients from 41 unrelated families. *KLHL3* mutations are either recessive or dominant, whereas *CUL3* mutations are dominant and predominantly *de novo*. *CUL3* and BTB-domain-containing kelch proteins such as *KLHL3* are components of cullin-RING E3 ligase complexes that ubiquitinate substrates bound to kelch propeller domains^{2–8}. Dominant *KLHL3* mutations are clustered in short segments within the kelch propeller and BTB domains implicated in substrate⁹ and cullin⁵ binding, respectively. Diverse *CUL3* mutations all result in skipping of exon 9, producing an in-frame deletion. Because dominant *KLHL3* and *CUL3* mutations both phenocopy recessive loss-of-function *KLHL3* mutations, they may abrogate ubiquitination of *KLHL3* substrates. Disease features are reversed by thiazide diuretics, which inhibit the Na-Cl cotransporter in the distal nephron of the kidney; *KLHL3* and *CUL3* are expressed in this location, suggesting a mechanistic link between *KLHL3* and *CUL3* mutations, increased Na-Cl reabsorption, and disease pathogenesis. These findings demonstrate the utility of exome sequencing in disease gene identification despite the combined complexities of locus heterogeneity, mixed models of transmission and frequent *de novo* mutation, and establish a fundamental role for *KLHL3* and *CUL3* in blood pressure, K^+ and pH homeostasis.

A small number of genes causing Mendelian forms of hypertension have been identified, establishing the role of increased renal salt reabsorption in its pathogenesis^{10–12}. The study of PHAII has identified a physiological mechanism that orchestrates activities of diverse electrolyte flux pathways, allowing maximal salt reabsorption in response to aldosterone when angiotensin II (AII) is elevated, as in settings of reduced intravascular volume (hypovolaemia), versus maximal potassium secretion in settings of hyperkalaemia, in which aldosterone is elevated without changes in AII¹. The role of WNK kinases in this process was revealed by discovery of their mutation in a small fraction of PHAII kindreds¹¹. Dominant gain-of-function mutations in *WNK4* or *WNK1* lead to constitutively increased salt reabsorption in the distal nephron regardless of volume status, resulting in hypertension, and inhibition of K^+ secretion despite marked hyperkalaemia^{1,11,13–17}.

We studied a cohort of 52 PHAII kindreds, including 126 affected subjects with renal hyperkalaemia and otherwise normal renal function; hypertension and acidosis were present in 71% and 82%, respectively. There was wide variation in disease severity and age of clinical presentation (Supplementary Figs 1 and 2). Mutations in *WNK1* or *WNK4* were present in only seven of these kindreds (13%). Those without *WNK* mutations had only 2.0 ± 1.4 affected members, complicating mapping efforts.

Exome sequencing of eleven unrelated PHAII index cases without *WNK* mutations was performed. Index cases and affected relatives (five trios and one quartet) were also subjected to genome-wide SNP genotyping. Tabulation of high quality novel protein-altering variants revealed 124 genes with three or more variants, 50 with four or more, and 23 with five. Concurrent analysis of linkage among the multiplex families was used to prioritize loci harbouring variants that co-segregated with

¹Department of Genetics and Howard Hughes Medical Institute, Yale University School of Medicine, New Haven, Connecticut 06510, USA. ²Department of Dermatology, Yale University School of Medicine, New Haven, Connecticut 06510, USA. ³Renal Division, Brigham and Women's Hospital, Boston, Massachusetts 02115, USA. ⁴Yale Center for Genome Analysis, Yale University, New Haven, Connecticut 06510, USA. ⁵Nephrology Unit, Niguarda-Ca' Granda Hospital, Milan 20162, Italy. ⁶Department of Medicine, Laval University, Québec G1K 7P4, Canada. ⁷Endocrine Hypertension Research Centre, University of Queensland School of Medicine, Brisbane QLD 4006, Australia. ⁸Department of Pediatrics, Canisius Wilhelmina Hospital, Nijmegen 6500 GS, Netherlands. ⁹Department of Pediatrics, Pays d'Aix Hospital, Aix-en-Provence 13616, France. ¹⁰Division of Endocrinology, Department of Medicine, Helsinki University Central Hospital, Helsinki 00290, Finland. ¹¹Department of Pediatrics and Adolescent Medicine, American University Medical Center, Beirut 1107 2020, Lebanon. ¹²Hypertension Research Center, University of Medicine and Dentistry of New Jersey, Newark, New Jersey 07103, USA. ¹³Department of Medical Genetics, University of Cambridge, Cambridge CB2 1TN, United Kingdom. ¹⁴Division of Endocrinology, Roger Williams Medical Center, Providence, Rhode Island 02908, USA. ¹⁵Department of Endocrinology and Diabetes, Ewen Downie Metabolic Unit, Alfred Hospital, Melbourne VIC 3004, Australia. ¹⁶Division of Medical Genetics, Department of Pediatrics, University of Iowa Children's Hospital, Iowa City, Iowa 52242, USA. ¹⁷Division of Nephrology, Department of Pediatrics, Medical College of Wisconsin, Milwaukee, Wisconsin 53226, USA. ¹⁸Department of Pediatrics, David Geffen School of Medicine at UCLA, Los Angeles, California 90095, USA. ¹⁹Duncan Guthrie Institute of Medical Genetics, Royal Hospital for Sick Children, Glasgow G3 8SJ, United Kingdom. ²⁰Baxter Healthcare Corporation, McGaw Park, Illinois 60085, USA. ²¹Department of Pediatrics, University of Pittsburgh School of Medicine, Pittsburgh, Pennsylvania 15261, USA. ²²Division of Pediatrics, Mandic Hospital, Merate 23807, Italy. ²³Department of Pediatrics, Johns Hopkins School of Medicine, Baltimore, Maryland 21287, USA. ²⁴Division of Nephrology, Department of Pediatrics, Saint Louis University Health Sciences Center, St Louis, Missouri 63110, USA. ²⁵Division of Nephrology, Department of Pediatrics, Vanderbilt University Medical Center, Nashville, Tennessee 37232, USA. ²⁶Division of Nephrology, Department of Pediatrics, University of Utah, Salt Lake City, Utah 84132, USA. ²⁷Division of Nephrology, Cohen Children's Medical Center of New York, New Hyde Park, New York 11040, USA. ²⁸West Midlands Regional Genetics Service, Birmingham Women's Hospital, Birmingham B15 2TG, United Kingdom. ²⁹Division of Nephrology, Department of Pediatrics, University of Alberta, Edmonton T6G 2M7, Canada. ³⁰Renal Unit, University College London Institute of Child Health, London WC1N 1EH, United Kingdom. ³¹Department of Nephrology, Royal Manchester Children's Hospital, Manchester M27 4HA, United Kingdom. ³²Department of Endocrinology, Children's National Medical Center, Washington, District of Columbia 20010, USA. ³³Department of Pediatrics, Duke University Medical Center, Durham, North Carolina 27710, USA. ³⁴Division of Nephrology, Connecticut Children's Medical Center, Hartford, Connecticut 06106, USA. ³⁵Division of Nephrology, Department of Medicine, University of Texas Health Science Center, San Antonio, Texas 78229, USA. ³⁶Department of Medicine, Columbia University College of Physicians and Surgeons, New York, New York 10032, USA. ³⁷Division of Nephrology, Children's Hospital at Montefiore, Bronx, New York 10467, USA.

*These authors contributed equally to this work.

disease; this identified 28 genes with novel protein-altering variants that co-segregated with disease in two or more multiplex families. This revealed *KLHL3* as a strong candidate, with novel *KLHL3* mutations comprising five alleles in three kindreds, all of which co-segregated with the trait. These include one kindred in which affected members are homozygous for a nonsense mutation (W470X), one in which affected members are compound heterozygotes for two missense mutations (F322C and S410L), and one segregating a heterozygous missense mutation (R528H). As a confirmation of significance, Fisher's exact test was used to compare the prevalence of novel protein-altering variants in all genes in PHAII cases versus 699 control exomes. A single gene, *KLHL3*, showed a burden of mutation that surpassed genome-wide significance ($P = 1.1 \times 10^{-8}$; Supplementary Tables 1–3).

KLHL3 was sequenced in all PHAII index cases, identifying novel mutations in 24 (Fig. 1a, b and Supplementary Figs 3 and 4). Nearly all are at positions conserved among orthologues (Supplementary Fig. 5). Sixteen kindreds have heterozygous mutations that co-segregate with the trait under a dominant model (log of odds (lod) score 6.9, < -2 under other models). In contrast, eight index cases inherited mutations in both *KLHL3* alleles. In these kindreds, affected members are confined to siblings of index cases who inherited the same two mutations, whereas unaffected relatives inherited zero or one mutation (lod score 4.3 for a recessive model, < -2 for other models). Recessive transmission has not been previously described for PHAII. Consistent with two modes of transmission, subjects with dominant *KLHL3* mutations had significantly higher serum K^+ levels (6.2 ± 0.6 mM)

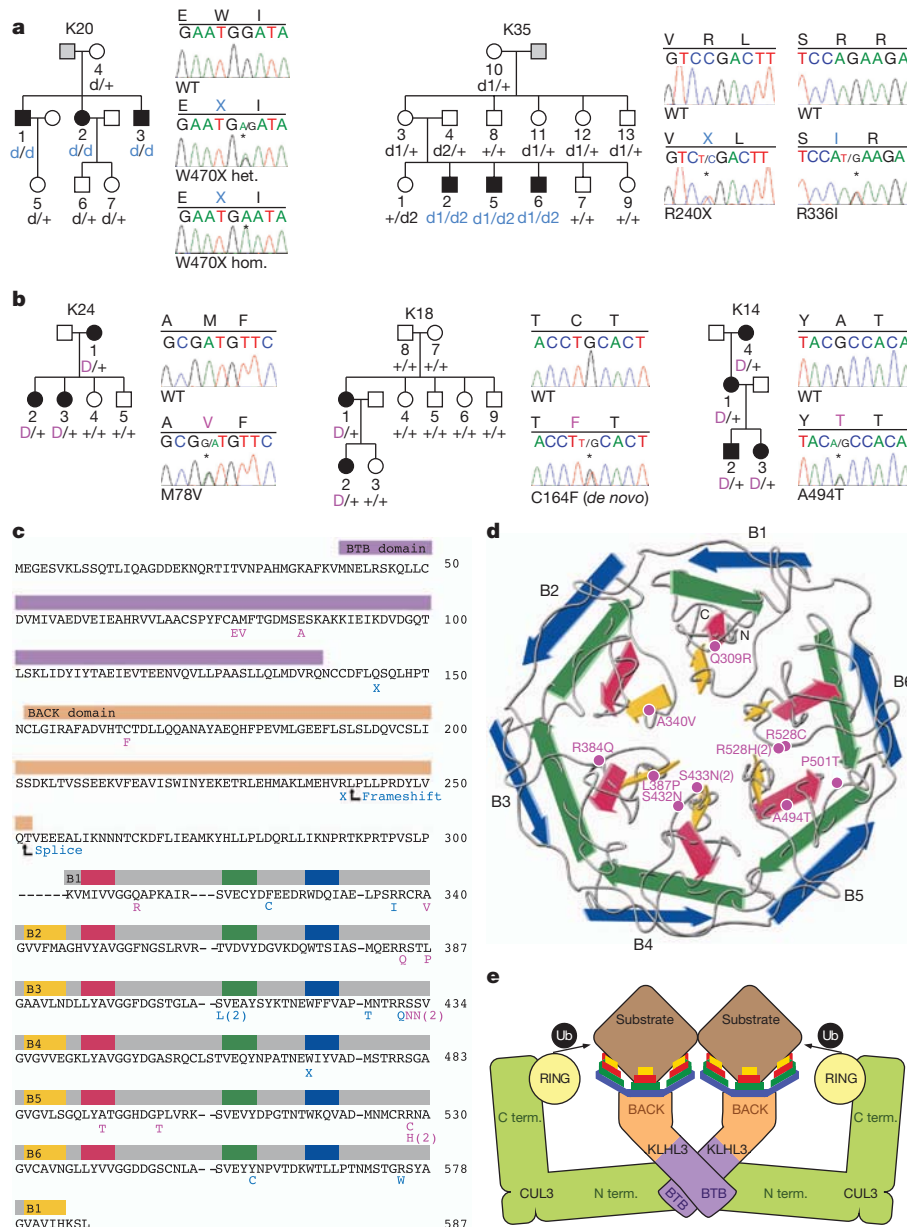


Figure 1 | Recessive and dominant *KLHL3* mutations in PHAII kindreds. **a**, **b**, Representative kindreds demonstrating recessive (**a**) and dominant (**b**) *KLHL3* mutations (all 24 kindreds are shown in Supplementary Figs 3 and 4). Affected, unaffected and phenotype-undetermined subjects are denoted by black, white and grey symbols, respectively. *KLHL3* alleles are denoted by '+' (wild type), 'd' (recessive mutation) and 'D' (dominant mutation). Sequence traces show wild-type (WT) and mutant (*) alleles and encoded amino acids. het., heterozygous; hom., homozygous. **c**, *KLHL3* protein structure. Coloured bars indicate BTB domain (lavender), BACK domain (peach) and kelch

propeller blades (B1–B6, grey) with β -strands 'a–d' in yellow, red, green and blue, respectively. Recessive (light blue) and dominant (pink) mutations are shown; recurrences are indicated by numbers. **d**, Kelch propeller schematic, from the *KLHL2* crystal structure²⁷. β -Strands are coloured as in **c**; dominant mutations are indicated. **e**, CRL schematic, comprising a BTB-containing kelch protein (*KLHL3*), CUL3 and a ubiquitin (Ub)-transfer-mediating RING protein, with substrate bound via the kelch propeller. The complex is shown as a dimer²⁷. C term., C terminus; N term., N terminus.

than heterozygotes for recessive mutations (4.8 ± 0.6 mM) ($P < 10^{-4}$, Student's *t*-test; normal range 3.5–5.0 mM). These findings establish that PHAII can be caused by either recessive or dominant *KLHL3* mutations. Importantly, we infer that mutations in dominant kindreds are probably dominant-negative, because they phenocopy the features of recessive disease.

KLHL3 contains an amino-terminal BTB domain, a BACK domain, and carboxy-terminal kelch-like repeats that form a six-bladed β -propeller structure^{2,4,5} (Fig. 1c–e). There are over 50 BTB-containing kelch (BTB-kelch) genes in humans⁴; their propeller domains bind substrate proteins, promoting substrate ubiquitination via interaction of the BTB domain with CUL3, a component of a cullin–RING E3 ubiquitin ligase (CRL)^{3,5,6}. Ubiquitination serves diverse functions, including targeting proteins for proteasomal degradation as well as non-degradative roles such as modulation of protein activity, interaction and localization^{7,8}.

Whereas recessive *KLHL3* mutations are distributed throughout the encoded protein, dominant *KLHL3* mutations show marked clustering (Fig. 1c). Nine of sixteen dominant mutations alter one of the last four amino acids of the six 'd–a' loops that connect the outermost ('d') β -strand of one kelch propeller blade to the innermost ('a') β -strand of the next blade. Two others are in 'b–c' loops. These dominant PHAII mutations lie near the hub of the propeller (Fig. 1d) at or near sites implicated in substrate binding in paralogues⁹ (Supplementary Fig. 5). Three other dominant mutations cluster within the BTB domain, at or

near sites implicated in cullin binding in paralogues⁵. We infer that dominant mutations in *KLHL3* probably impair binding either to specific substrates or to CUL3.

After accounting for *KLHL3*, *WNK1* and *WNK4* mutations, 21 PHAII kindreds without mutations remained. We considered the presumed functional partner of *KLHL3*, *CUL3* (Fig. 1e), as a potential candidate. Among PHAII exomes, novel heterozygous *CUL3* variants were suggested in two. Sequencing *CUL3* in all index cases identified 17 with novel heterozygous mutations, all in cases without *KLHL3*, *WNK1* or *WNK4* mutations (Fig. 2a and Supplementary Fig. 6). Eight of these mutations were documented to be *de novo*, providing overwhelming evidence that these mutations are disease-causing. *CUL3* mutations all cluster in sites implicated in splicing of exon 9, including the intron 8 splice acceptor ($n = 4$), the intron 9 splice donor ($n = 5$), the putative intron 8 splice branch site ($n = 5$), and a putative splice enhancer in exon 9 ($n = 3$, within a TTGGA(T/A)) splice enhancer consensus sequence¹⁸) (Fig. 2b).

To test the impact of these mutations on splicing, *CUL3* genomic DNA spanning exon 8 to exon 10 containing either wild-type sequence or one of nine PHAII mutations was cloned and expressed in HEK293 cells, and the spliced RNA products were analysed. Whereas the wild-type sequence produces a properly spliced product containing all three exons, each of the mutants produces a predominant product that skips exon 9, joining exon 8 to exon 10 (Fig. 2c, d). This results in an in-frame 57 amino acid deletion (residues 403–459) in the segment linking the

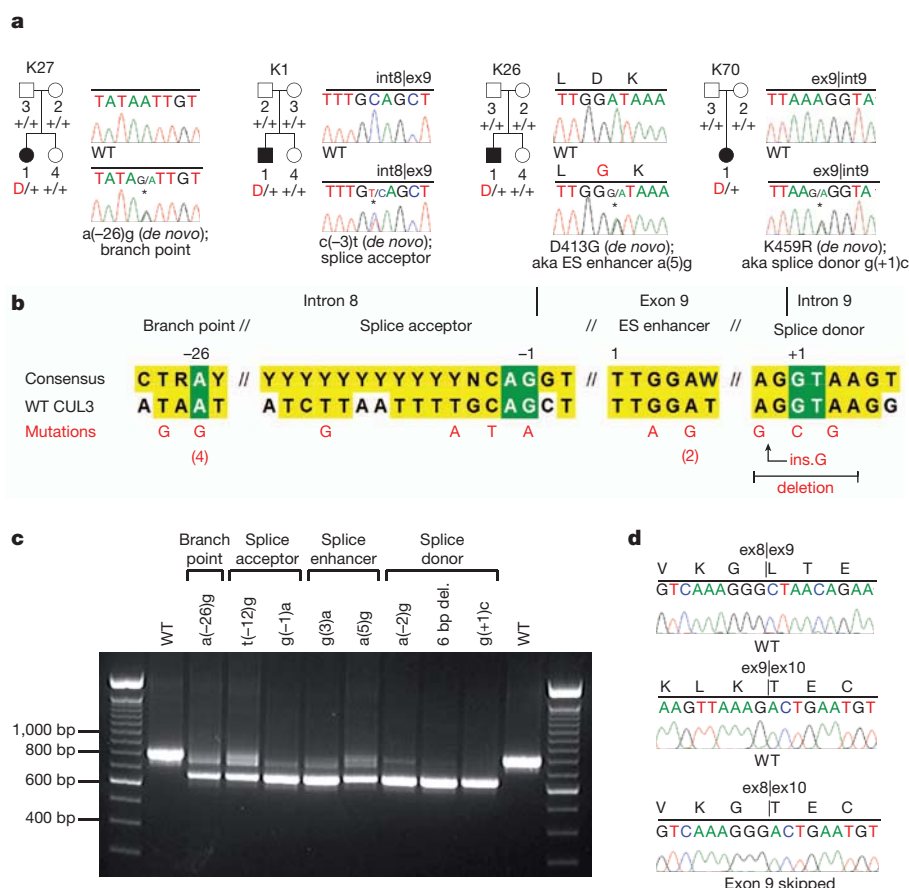


Figure 2 | Dominant *CUL3* mutations in PHAII kindreds cause skipping of exon 9. **a**, Representative kindreds demonstrating *CUL3* mutations, depicted as in Fig. 1 (all 17 kindreds are shown in Supplementary Fig. 6). int8, intron 8; ex9, exon 9; int9, intron 9. Positions are numbered relative to splice sites and the first base of the exonic splice (ES) enhancer. **b**, *CUL3* mutation locations. Consensus splicing sequences^{18,28} and corresponding wild-type *CUL3* sequences are shown; invariant bases (green) and consensus homology (yellow) are indicated. Mutations are shown in red; recurrences are indicated by

numbers. Ins.G, insertion of a G (guanine). **c**, Reverse transcription–polymerase chain reaction (RT–PCR) of spliced RNA. Wild-type *CUL3* constructs produce a single product including exons 8, 9 and 10 (844 bp); all nine mutants tested produce a predominant product that skips exon 9 (673 bp). **d**, Representative RT–PCR sequences. The wild-type construct produces complementary DNA with properly spliced junctions between exons 8–9 (top) and 9–10 (middle), whereas the mutant construct (splice donor g(+1)c) produces cDNA joining exon 8 to exon 10 (bottom).

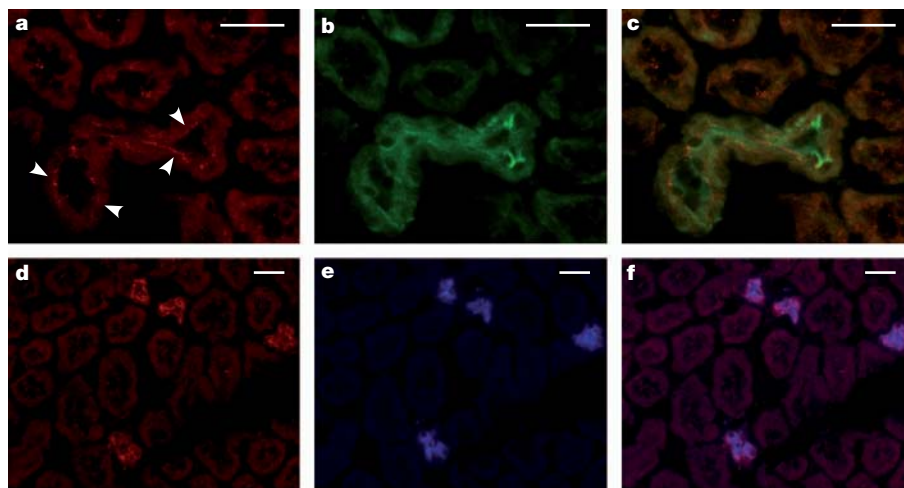


Figure 3 | *KLHL3* expression in the kidney. a–f, Mouse kidney sections stained with antibodies to *KLHL3* (red), *TRPM6* (a marker of the DCT²⁹, green) and *AQP2* (a marker of the collecting duct³⁰, blue). Scale bars, 25 μ m. a–c, Staining for *KLHL3* (a), *TRPM6* (b) and the merged image

(c) demonstrates *KLHL3* expression in the DCT with apical localization (arrowheads). d–f, Staining for *KLHL3* (d), *AQP2* (e) and the merged image (f) demonstrates *KLHL3* expression in the collecting duct.

BTB-binding and RING-binding domains of *CUL3*. The fact that *CUL3* mutations phenocopy recessive *KLHL3* mutations suggests that they abrogate *CUL3* function at *KLHL3* targets.

As with PHAII caused by *WNK1* and *WNK4* mutations¹, virtually all patients with *KLHL3* and *CUL3* mutations have been treated with thiazide diuretics, inhibitors of the Na–Cl cotransporter (NCC), resulting in correction of phenotypic abnormalities. *WNK4* regulates the activities of NCC^{13,14,16}, the epithelial Na⁺ channel ENaC¹⁷, and the K⁺ channel ROMK¹⁵, and is co-expressed with these proteins in the renal distal convoluted tubule (DCT) and collecting duct^{11,19,20}. Staining mouse kidney sections with specific antibodies demonstrated that *KLHL3* is predominantly expressed in the DCT and collecting duct, with apical localization in the DCT (Fig. 3). *CUL3* is ubiquitously expressed and is in all nephron segments, with particularly high expression in the proximal tubule, but also in the DCT and collecting duct (Supplementary Fig. 7). These findings are consistent with both proteins having a role in the regulation of salt and electrolyte homeostasis in the distal nephron.

There are highly significant differences in phenotypic severity among PHAII patients with mutations in different genes (Table 1 and Supplementary Figs 1, 2 and Supplementary Table 4). Subjects with *CUL3* mutations presented at much younger ages than those with mutation in *KLHL3*, *WNK1* or *WNK4*, had significantly more severe hyperkalaemia and metabolic acidosis, and were far more likely to have hypertension before age 18 (others commonly develop hypertension at later ages). The majority of subjects with *CUL3* mutations demonstrated failure to thrive or growth impairment. These observations, in conjunction with the high rate of *CUL3* *de novo* mutation, support impairment of reproductive fitness. Among the other mutant loci, there remain significant differences in disease severity (rank order recessive *KLHL3* > dominant *KLHL3* > *WNK4* > *WNK1*).

KLHL3 and *CUL3* mutations account for 79% of kindreds in our cohort. Gene identification was complicated by the combined effects of locus heterogeneity, two modes of transmission at one locus, and few informative meioses. Many so far unsolved Mendelian traits may have similar complexities. Use of control exomes as comparators for analysis of mutation burden may be broadly applicable to discovery of such loci.

The most parsimonious mechanism of *KLHL3* and *CUL3* mutations is that they abrogate ubiquitination of targets normally bound by *KLHL3*, activity that is required for normal modulation of renal salt, K⁺ and H⁺ handling in response to physiological challenge; this speculation will require biochemical verification. The fact that recessive mutations in *KLHL3* cause PHAII without other diverse effects implies either that *KLHL3* targets are highly restricted to the renal salt and electrolyte pathway, or that loss of *KLHL3* function at other targets can be compensated by other loci. BTB-kelch–*CUL3* CRLs can act as dimers, with two substrate-binding domains capable of engaging the same target molecule⁷. This suggests a potential mechanism to explain dominant-negative effects of *KLHL3* and *CUL3* mutations.

CUL3-based CRLs participate in a wide range of critical cellular processes⁸ via binding diverse BTB-domain-containing proteins^{3,5}. *CUL3* mutations affecting all or many of these activities would undoubtedly produce very broad phenotypes. *CUL3* mutations in PHAII merely phenocopy the effects of loss of *KLHL3*, suggesting that they selectively abrogate function at *KLHL3* targets. The stereotypic consequences of *CUL3* mutations, all deleting 57 amino acids in a region linking the BTB-binding and RING-binding domains, support such a specific effect. Consistent with this possibility, introduction of a flexible linker sequence to this region of *CUL1* leaves substrate protein binding and ubiquitin polymerization intact, but nonetheless abolishes ubiquitination of a normal substrate²¹.

Table 1 | PHAII phenotypes, stratified by genotype.

Mutant gene	No. of kindreds	No. of affecteds	Dx/Ref age*	K ⁺ (mM) (nl 3.5–5.0 mM)†	HCO ₃ [−] (mM) (nl 22–28 mM)†	Hypertension at ≤age 18 (%)†
<i>CUL3</i>	17	21	9 ± 6	7.5 ± 0.9	15.5 ± 2.0	94
<i>KLHL3</i> recessive	8	14	26 ± 14	6.8 ± 0.5	17.6 ± 1.5	14
<i>KLHL3</i> dominant	16	40	24 ± 18	6.2 ± 0.6	17.2 ± 2.5	17
<i>WNK4</i>	5	15	28 ± 18	6.4 ± 0.7	20.8 ± 2.3	10
<i>WNK1</i>	2	23	36 ± 20	5.8 ± 0.8	22.4 ± 4.6	13

Dx/Ref age, age at diagnosis or referral. K⁺, serum potassium; HCO₃[−], serum bicarbonate; nl, normal range. Hypertension at ≤age 18 (%), percentage of affected patients diagnosed with hypertension by age 18. Values for Dx/Ref age, K⁺ and HCO₃[−] are means ± standard deviations. Significance of differences among genotype classes was calculated by ANOVA (Dx/Ref age, K⁺, HCO₃[−]) or Fisher's exact test (hypertension).

*P = 0.0002.

†P < 0.0001.

Thiazide diuretics correct abnormalities in virtually all PHAII subjects; similar correction is seen in a mouse model of PHAII with either thiazides or genetic ablation of NCC¹⁶. These findings suggest that increased NCC activity is likely to be a common pathogenic mechanism. Co-expression of KLHL3 and CUL3 with NCC in the DCT, and evidence that NCC is ubiquitinated²² is consistent with this notion. ROMK and the H⁺ ATPase are respectively required for net renal K⁺ secretion²³ and H⁺ secretion²⁴ and are also likely targets, although their activity is expected to be decreased, rather than increased, in PHAII. Another thiazide-sensitive Na–Cl cotransport pathway in the collecting duct has recently been described, suggesting an additional potential target²⁵. Whether a KLHL3–CUL3 CRL acts directly or indirectly on these targets, whether they alter delivery of NCC and other targets to, or retrieval from, the plasma membrane, and what upstream pathways regulate this activity is unknown. Similarly, whether KLHL3–CUL3 and WNKs operate within the same or different pathways is presently unknown; it is of interest that segments of NRF2 that interact with the kelch propeller domain of KEAP1 are highly acidic^{9,26}, akin to the domain of WNK4 that is mutated in PHAII¹¹.

These findings demonstrate previously unrecognized roles for KLHL3 and CUL3. Understanding the upstream regulators and downstream targets of KLHL3–CUL3 activity will provide further insight into the mechanisms underlying maintenance of blood pressure and electrolyte homeostasis in response to diverse environmental challenges.

METHODS SUMMARY

A cohort of 52 PHAII kindreds comprising 126 affected subjects was ascertained, characterized and recruited for study. Index cases of eleven kindreds were chosen for whole exome capture and sequencing, and novel variants were identified. Genes were prioritized for follow-up and subjected to Sanger sequencing of index cases of each kindred. Segregation of rare variants within kindreds was analysed. KLHL3 and CUL3 were localized in kidney by staining with specific antibodies and immunofluorescence microscopy. Effects of CUL3 mutations on RNA splicing were studied by analysis of spliced products produced in mammalian cells.

Full Methods and any associated references are available in the online version of the paper at www.nature.com/nature.

Received 3 September; accepted 22 December 2011.

Published online 22 January 2012.

- Kahle, K. T., Ring, A. M. & Lifton, R. P. Molecular physiology of the WNK kinases. *Annu. Rev. Physiol.* **70**, 329–355 (2008).
- Lai, F. *et al.* Molecular characterization of KLHL3, a human homologue of the *Drosophila kelch* gene. *Genomics* **66**, 65–75 (2000).
- Furukawa, M., He, Y. J., Borchers, C. & Xiong, Y. Targeting of protein ubiquitination by BTB–Cullin 3–Roc1 ubiquitin ligases. *Nature Cell Biol.* **5**, 1001–1007 (2003).
- Prag, S. & Adams, J. C. Molecular phylogeny of the kelch-repeat superfamily reveals an expansion of BTB/kelch proteins in animals. *BMC Bioinformatics* **4**, 42 (2003).
- Stogios, P. J., Downs, G. S., Jauhal, J. J., Nandra, S. K. & Prive, G. G. Sequence and structural analysis of BTB domain proteins. *Genome Biol.* **6**, R82 (2005).
- Hudson, A. M. & Cooley, L. Phylogenetic, structural and functional relationships between WD- and kelch-repeat proteins. *Subcell. Biochem.* **48**, 6–19 (2008).
- Zimmerman, E. S., Schulman, B. A. & Zheng, N. Structural assembly of cullin-RING ubiquitin ligase complexes. *Curr. Opin. Struct. Biol.* **20**, 714–721 (2010).
- Sarikas, A., Hartmann, T. & Pan, Z. Q. The cullin protein family. *Genome Biol.* **12**, 220 (2011).
- Lo, S. C., Li, X., Henzl, M. T., Beamer, L. J. & Hannink, M. Structure of the Keap1:Nrf2 interface provides mechanistic insight into Nrf2 signaling. *EMBO J.* **25**, 3605–3617 (2006).
- Lifton, R. P., Gharavi, A. G. & Geller, D. S. Molecular mechanisms of human hypertension. *Cell* **104**, 545–556 (2001).

- Wilson, F. H. *et al.* Human hypertension caused by mutations in WNK kinases. *Science* **293**, 1107–1112 (2001).
- Choi, M. *et al.* K⁺ channel mutations in adrenal aldosterone-producing adenomas and hereditary hypertension. *Science* **331**, 768–772 (2011).
- Wilson, F. H. *et al.* Molecular pathogenesis of inherited hypertension with hyperkalemia: the Na–Cl cotransporter is inhibited by wild-type but not mutant WNK4. *Proc. Natl Acad. Sci. USA* **100**, 680–684 (2003).
- Yang, C. L., Angell, J., Mitchell, R. & Ellison, D. H. WNK kinases regulate thiazide-sensitive Na–Cl cotransport. *J. Clin. Invest.* **111**, 1039–1045 (2003).
- Kahle, K. T. *et al.* WNK4 regulates the balance between renal NaCl reabsorption and K⁺ secretion. *Nature Genet.* **35**, 372–376 (2003).
- Lalioti, M. D. *et al.* Wnk4 controls blood pressure and potassium homeostasis via regulation of mass and activity of the distal convoluted tubule. *Nature Genet.* **38**, 1124–1132 (2006).
- Ring, A. M. *et al.* WNK4 regulates activity of the epithelial Na⁺ channel *in vitro* and *in vivo*. *Proc. Natl Acad. Sci. USA* **104**, 4020–4024 (2007).
- Fairbrother, W. G., Yeh, R. F., Sharp, P. A. & Burge, C. B. Predictive identification of exonic splicing enhancers in human genes. *Science* **297**, 1007–1013 (2002).
- Bachmann, S., Bostanjoglo, M., Schmitt, R. & Ellison, D. H. Sodium transport-related proteins in the mammalian distal nephron—distribution, ontogeny and functional aspects. *Anat. Embryol. (Berl.)* **200**, 447–468 (1999).
- Welling, P. A. & Ho, K. A comprehensive guide to the ROMK potassium channel: form and function in health and disease. *Am. J. Physiol. Renal Physiol.* **297**, F849–F863 (2009).
- Zheng, N. *et al.* Structure of the Cul1–Rbx1–Skp1–F box^{Skp2} SCF ubiquitin ligase complex. *Nature* **416**, 703–709 (2002).
- Ko, B. *et al.* RasGRP1 stimulation enhances ubiquitination and endocytosis of the sodium–chloride cotransporter. *Am. J. Physiol. Renal Physiol.* **299**, F300–F309 (2010).
- Simon, D. B. *et al.* Genetic heterogeneity of Bartter's syndrome revealed by mutations in the K⁺ channel, ROMK. *Nature Genet.* **14**, 152–156 (1996).
- Karet, F. E. *et al.* Mutations in the gene encoding B1 subunit of H⁺-ATPase cause renal tubular acidosis with sensorineural deafness. *Nature Genet.* **21**, 84–90 (1999).
- Leviel, F. *et al.* The Na⁺-dependent chloride-bicarbonate exchanger SLC4A8 mediates an electroneutral Na⁺ reabsorption process in the renal cortical collecting ducts of mice. *J. Clin. Invest.* **120**, 1627–1635 (2010).
- Tong, K. I. *et al.* Different electrostatic potentials define ETGE and DLG motifs as hinge and latch in oxidative stress response. *Mol. Cell. Biol.* **27**, 7511–7521 (2007).
- Wang, Y. *et al.* MMDB: annotating protein sequences with Entrez's 3D-structure database. *Nucleic Acids Res.* **35**, D298–D300 (2007).
- Zhang, M. Q. Statistical features of human exons and their flanking regions. *Hum. Mol. Genet.* **7**, 919–932 (1998).
- Voets, T. *et al.* TRPM6 forms the Mg²⁺ influx channel involved in intestinal and renal Mg²⁺ absorption. *J. Biol. Chem.* **279**, 19–25 (2004).
- Fushimi, K. *et al.* Cloning and expression of apical membrane water channel of rat kidney collecting tubule. *Nature* **361**, 549–552 (1993).

Supplementary Information is linked to the online version of the paper at www.nature.com/nature.

Acknowledgements We thank the PHAII subjects, their families, and the health care professionals whose participation made this study possible; S. Umlauf and the staff of the Yale Center for Genome Analysis; J. Santosuosso; H. Tirrell and the staff of Beckman Coulter Genomics; V. Klump, Y. Lu, U. Scholl and J. Zhou for providing reagents; W. Hill for artistic assistance with Fig. 1d; and E. Boyden, S. Boyden, L. Cooley and M. Hochstrasser for helpful discussions. This work was supported in part by the Leducq Transatlantic Network on Hypertension and grants from the National Institutes of Health (P30-DK079310 and UL1-RR024139).

Author Contributions L.M.B., M.C., K.A.C. and R.P.L. designed experiments and analysed data. L.M.B., C.J.N.-W. and I.R.T. performed experiments. A.F., H.R.T., G.C., M.L., R.D.G., B.A.S., A.P., M.J.V., M.E.D.F., S.A.S., M.G., F.E.K., J.R.T., J.R.S., K.M.K.-N., C.C.P., S.K.A., M.L.W., I.D.D., S.B.D., A.B., J.J.F., C.W.B., T.E.H., R.D.N., H.T., T.R.P.C., M.P., D.B., M.S., P.V., J.W.F., M.R., F.T., H.Z.A.-S., J.R., A.G.G. and B.G. recruited PHAII subjects and families. R.B. and S.M.M. directed the information technology and DNA sequencing infrastructure. L.M.B. and R.P.L. wrote the manuscript.

Author Information mRNA and protein sequences are available at NCBI under accession numbers NM_017415.2 and NP_059111.2 (KLHL3), NM_003590.3 and NP_003581.1 (CUL3); mutation data is available at dbSNP under batch accession 1056535. Reprints and permissions information is available at www.nature.com/reprints. The authors declare no competing financial interests. Readers are welcome to comment on the online version of this article at www.nature.com/nature. Correspondence and requests for materials should be addressed to R.P.L. (richard.lifton@yale.edu).

METHODS

Study subjects. Index cases were referred for PHAII. Patients and participating family members provided consent to a study protocol approved by the Yale Human Investigation Committee. Control exomes were 699 unrelated subjects of European ancestry without hypertension, sequenced as part of diverse gene discovery projects. Genomic DNA was isolated from venous blood using standard methods.

Exome capture, sequencing and variant calling. Genomic DNA from eleven PHAII index cases and 699 controls was captured on NimbleGen 2.1M human exome arrays (Roche) and sequenced on the Illumina GenomeAnalyzer as previously described³¹. Reads were mapped to the reference genome (hg18) using Maq³² and genotypes of targeted bases were called with SAMtools³³. Variants found in dbSNP v.130 or 1000 Genomes databases were excluded from further analysis. Remaining variants were considered 'novel' and annotated for impact on the encoded protein, conservation and expression³¹. Aligned reads were viewed with the Integrative Genomics Viewer³⁴. Among PHAII cases, 94.2% of targeted bases were read by eight or more independent reads; sensitivity and specificity of heterozygous calls were estimated at 93.7% and 99.9% by comparison to Illumina SNP genotyping. Among controls, 94.4% of targeted bases were read by eight or more independent reads; sensitivity and specificity of heterozygous calls were estimated at 94.5% and 99.8%. Sanger sequencing of 212 novel variants from controls with a SAMtools quality score of ≥ 100 demonstrated validation in 211 and amplification failure in 1, supporting high specificity of variant calls.

SNP genotyping and linkage analysis. For the 11 PHAII index cases and their affected relatives (five trios and one quartet) genome-wide SNP genotyping was performed using Illumina Human610-Quad BeadChips and GenomeStudio software. Approximately 40K tag SNPs were extracted using Plink³⁵. Analysis of linkage was performed using Merlin³⁶, specifying an autosomal dominant model with no phenocopies. Variants from exome sequencing in regions of the genome that were excluded (lod score < -2) were removed from further analysis, while those that supported linkage were prioritized for further evaluation. In kindreds showing potential recessive transmission of PHAII, SNP genotypes were examined for regions of homozygosity, and linkage was performed specifying an autosomal recessive model.

Sanger sequencing of KLHL3 and CUL3. PCR amplification and Sanger sequencing from genomic DNA was performed using standard methods. Primers were designed with Primer3³⁷. Variants identified by exome sequencing were verified. All exons and flanking intronic sequences of *KLHL3* and *CUL3* were sequenced from all PHAII index cases. Previously unidentified mutations were discovered and verified by independent amplification and sequencing. Co-segregation of mutations with disease was determined by sequencing in all available kindred members. *CUL3* exon 9 and its flanking intronic sequence was sequenced in 150 unaffected unrelated controls, none of whom were found to harbour previously unidentified variants. It is noteworthy that because of lower or absent sequence coverage at or near intron-exon junctions, splice donor and acceptor mutations in *CUL3* were suggested in two of the eleven PHAII exomes (SAMtools quality scores 96 and 75) but three branch site mutations were outside the exome sequence and one splice enhancer mutation was poorly covered (SAMtools quality score 3).

Genome-wide assessment of mutation burden. Genes show substantial variation in the prevalence of novel or rare protein-altering variants for biological reasons, including differences in gene size and variation in the proportion of bases that are under purifying selection, and for technical reasons, including difficulties in accurately mapping short sequence reads among closely related paralogues. These factors can limit the ability to directly identify disease loci by simply counting and ranking genes according to the absolute number of such variants, particularly for diseases with substantial locus or model heterogeneity. This gene-to-gene variation can be accounted for by use of control exome data. The prevalence of rare variation in each gene in case exomes was compared to the corresponding prevalence in a large set of control exomes with a Fisher's exact test. Variants included in the analysis were protein-altering (missense, nonsense and splice site mutations) and high quality (≥ 8 independent reads and SAMtools quality score ≥ 100).

For a gene-wise test of rare variant burden in a genome with $\sim 21,000$ genes, correction for multiple testing suggests a threshold *P* value of $\sim 2.4 \times 10^{-6}$, anticipated to produce a false discovery rate (FDR) of one gene per twenty experiments. The FDR of the Fisher's test was evaluated by Monte Carlo simulation, which confirmed an FDR of < 1 gene per 20 experiments (Supplementary Table 1). The power to identify trait-related loci was estimated as a function of the number of variants detected in cases and the number of case exomes sequenced (Supplementary Table 2), and the test was applied comparing the eleven PHAII and 699 control exomes (Supplementary Table 3).

Orthologue and paralogue comparisons. Protein sequences of orthologues and paralogues were aligned with Clustal W³⁸. Crystal structures were examined with Cn3D³⁹. The locations of KLHL3 propeller mutations were compared to the crystal structure of human KLHL2 (PDB accession 2XN4)²⁷, the closest human paralogue⁴ (85% amino acid identity in the propeller). The location of the peptide encoded by *CUL3* exon 9 was approximated by comparison to the crystal structure of human CUL1 (PDB accessions 1LDJ and 1LDK)^{22,27}.

Splicing assay. A 3,782 bp segment of *CUL3*, extending from 287 bp proximal to exon 8 to 327 bp distal to exon 10, was amplified by PCR (Advantage 2 polymerase, Clontech) from genomic DNA of nine PHAII patients with different *CUL3* mutations and one subject with wild-type *CUL3* sequence. Products were cloned into the pcDNA6.2/GW/D-TOPO mammalian expression vector (Invitrogen), and plasmids were purified (QIAprep, Qiagen) and sequenced. HEK293 cells were transfected independently with each plasmid using Lipofectamine 2000 (Invitrogen) and harvested ~ 24 h post-transfection. RNA was isolated using RNeasy with DNase on-column digestion (Qiagen). The spliced expression products were assessed by reverse transcription with oligo(dT) priming (Superscript III RT, Invitrogen) followed by PCR with vector-specific and *CUL3*-specific primers. Products were fractionated and visualized via agarose gel electrophoresis, and sequenced. Untransfected and water controls were negative.

Immunofluorescence. Fresh frozen mouse kidney sections were fixed with ethanol at 4 °C for 30 min and acetone at -20 °C for 3 min, washed with 1 \times PBS, and permeabilized with 0.1% Triton X-100 (Sigma) at room temperature (22 °C) for 10 min. Sections were blocked with 10% donkey serum and 1% bovine serum albumin at room temperature for 1 h, incubated with primary antibodies at room temperature for 1 h or 4 °C overnight, washed four times with 1 \times PBS, incubated with secondary antibody at room temperature for 1 h, and washed four times with 1 \times PBS, with DAPI nuclear counterstain in the second wash. Slides were mounted with Mowiol (Polysciences) and 1% n-propyl gallate (Sigma) as an anti-fade agent. Primary antibodies included 1:100 rabbit anti-KLHL3, 1:50 rabbit anti-CUL3, 1:800 or 1:1,200 guinea pig anti-TRPM6 (ab66655, ab1871, and ab47017; Abcam) and 1:400 or 1:800 goat anti-AQP2 (sc-9882, Santa Cruz Biotechnology). Secondary antibodies, diluted 1:800, included donkey Cy3 anti-rabbit, Cy2 anti-guinea pig and 649 anti-goat IgG (AffiniPure, Jackson ImmunoResearch). Staining with secondary antibodies only was consistently negative.

- Choi, M. *et al.* Genetic diagnosis by whole exome capture and massively parallel DNA sequencing. *Proc. Natl Acad. Sci. USA* **106**, 19096–19101 (2009).
- Li, H., Ruan, J. & Durbin, R. Mapping short DNA sequencing reads and calling variants using mapping quality scores. *Genome Res.* **18**, 1851–1858 (2008).
- Li, H. *et al.* The Sequence Alignment/Map format and SAMtools. *Bioinformatics* **25**, 2078–2079 (2009).
- Robinson, J. T. *et al.* Integrative genomics viewer. *Nature Biotechnol.* **29**, 24–26 (2011).
- Purcell, S. *et al.* PLINK: a tool set for whole-genome association and population-based linkage analyses. *Am. J. Hum. Genet.* **81**, 559–575 (2007).
- Abecasis, G. R., Cherny, S. S., Cookson, W. O. & Cardon, L. R. Merlin—rapid analysis of dense genetic maps using sparse gene flow trees. *Nature Genet.* **30**, 97–101 (2002).
- Rozen, S. & Skaletsky, H. Primer3 on the WWW for general users and for biologist programmers. *Methods Mol. Biol.* **132**, 365–386 (2000).
- Larkin, M. A. *et al.* Clustal W and Clustal X version 2.0. *Bioinformatics* **23**, 2947–2948 (2007).
- Wang, Y., Geer, L. Y., Chappey, C., Kans, J. A. & Bryant, S. H. Cn3D: sequence and structure views for Entrez. *Trends Biochem. Sci.* **25**, 300–302 (2000).

Probing sporadic and familial Alzheimer's disease using induced pluripotent stem cells

Mason A. Israel^{1,2}, Shauna H. Yuan^{1,3}, Cedric Bardy⁴, Sol M. Reyna^{1,2}, Yangling Mu⁴, Cheryl Herrera¹, Michael P. Hefferan⁵, Sebastiaan Van Gorp⁶, Kristopher L. Nazor⁷, Francesca S. Boscolo⁸, Christian T. Carson⁹, Louise C. Laurent⁸, Martin Marsala^{5,10}, Fred H. Gage⁴, Anne M. Remes¹¹, Edward H. Koo³ & Lawrence S. B. Goldstein^{1,3}

Our understanding of Alzheimer's disease pathogenesis is currently limited by difficulties in obtaining live neurons from patients and the inability to model the sporadic form of the disease. It may be possible to overcome these challenges by reprogramming primary cells from patients into induced pluripotent stem cells (iPSCs). Here we reprogrammed primary fibroblasts from two patients with familial Alzheimer's disease, both caused by a duplication of the amyloid- β precursor protein gene¹ (*APP*; termed *APP^{DP}*), two with sporadic Alzheimer's disease (termed *sAD1*, *sAD2*) and two non-demented control individuals into iPSC lines. Neurons from differentiated cultures were purified with fluorescence-activated cell sorting and characterized. Purified cultures contained more than 90% neurons, clustered with fetal brain messenger RNA samples by microarray criteria, and could form functional synaptic contacts. Virtually all cells exhibited normal electrophysiological activity. Relative to controls, iPSC-derived, purified neurons from the two *APP^{DP}* patients and patient *sAD2* exhibited significantly higher levels of the pathological markers amyloid- β (1–40), phospho-tau(Thr 231) and active glycogen synthase kinase-3 β (aGSK-3 β). Neurons from *APP^{DP}* and *sAD2* patients also accumulated large RAB5-positive early endosomes compared to controls. Treatment of purified neurons with β -secretase inhibitors, but not γ -secretase inhibitors, caused significant reductions in phospho-Tau(Thr 231) and aGSK-3 β levels. These results suggest a direct relationship between APP proteolytic processing, but not amyloid- β , in GSK-3 β activation and tau phosphorylation in human neurons. Additionally, we observed that neurons with the genome of one *sAD* patient exhibited the phenotypes seen in familial Alzheimer's disease samples. More generally, we demonstrate that iPSC technology can be used to observe phenotypes relevant to Alzheimer's disease, even though it can take decades for overt disease to manifest in patients.

Alzheimer's disease is a common neurodegenerative disorder, defined post mortem by the increased presence of amyloid plaques and neurofibrillary tangles in the brain². Amyloid plaques are extracellular deposits consisting primarily of amyloid- β peptides, and neurofibrillary tangles are intraneuronal aggregations of hyperphosphorylated tau, a microtubule-associated protein involved in microtubule stabilization³. The causative relationship between amyloid plaque/amyloid- β and tau pathologies is unclear in humans. Although the vast majority of Alzheimer's disease is apparently sporadic with significant non-Mendelian genetic contributions⁴, analyses of cellular and animal models of rare, dominantly inherited familial forms of Alzheimer's disease have driven most ideas about disease mechanisms. These rare cases have mutations or a duplication of *APP*, which encodes the amyloid- β precursor protein, or mutations in the presenilin genes, which encode proteolytic enzymes that cleave APP into amyloid- β

and other fragments. Mouse models that overexpress familial Alzheimer's disease mutations develop extensive plaque deposition and amyloid-associated pathology, but neurofibrillary tangles and significant neuronal loss are conspicuously absent^{5,6}. Fetal human cortical cultures have also been used to study the APP-tau relationship. For example, cortical cultures treated with 20 μ M amyloid- β have elevated phosphorylated tau (p-tau)⁷. However, it is still unclear whether physiologically relevant levels of amyloid- β directly cause elevated p-tau and which kinases are directly involved in this aberrant phosphorylation. Additionally, experimental approaches using fetal human neurons are hindered by limited availability of samples and unknown genetic backgrounds. The recent developments in iPSCs and induced neurons have allowed investigation of phenotypes of neurological diseases *in vitro*^{8,9,10}. However, not all diseases have been successfully modelled using iPSCs¹¹, and it is unclear whether iPSCs can be used to study sporadic forms of disease.

Here we report the derivation and neuronal differentiation of iPSCs from patients with familial and sporadic Alzheimer's disease, as well as from non-demented, age-matched controls. Using purified human neurons we probe three key questions concerning Alzheimer's disease: (1) can iPSC technology be used to observe phenotypes of patients with Alzheimer's disease, even though it can take decades for overt disease to manifest; (2) is there a causative relationship between APP processing and tau phosphorylation; and (3) can neurons with the genome of a *sAD* patient exhibit phenotypes seen in familial Alzheimer's disease samples? Supplementary Fig. 1 summarizes the experimental approach and findings.

We characterized *APP* metabolism in fibroblasts before reprogramming to iPSCs (Supplementary Fig. 2). *APP* expression and amyloid- β secretion were quantified in early-passage primary fibroblasts from two non-demented control (NDC) individuals, two *sAD* patients and two *APP^{DP}* patients (Table 1). The presence of the genomic duplication was confirmed in fibroblasts. Relative to NDC and *sAD* cells, *APP^{DP}* fibroblasts expressed higher levels of *APP* mRNA and secreted 1.5- to twofold higher amounts of amyloid- β (1–40) peptides into culture media compared to NDC cells. We did not detect significant increases in amyloid- β (1–42/1–40) or amyloid- β (1–38/1–40) in patient samples versus controls.

We generated iPSC lines by transducing fibroblasts with retroviruses encoding *OCT4*, *SOX2*, *KLF4*, *c-MYC* and, in one-third of cultures, *EGFP*. Each of the six individuals was represented by three clonal iPSC lines. All 18 iPSC lines maintained embryonic stem (ES)-cell-like morphology, expressed the pluripotency-associated proteins NANOG and TRA1-81, maintained euploid karyotypes, expressed endogenous locus-derived *SOX2*, repressed retroviral transgenes, and could differentiate into cells of ectodermal, mesodermal and

¹Howard Hughes Medical Institute and Department of Cellular and Molecular Medicine, University of California, San Diego, La Jolla, California 92093, USA. ²Biomedical Sciences Graduate Program, University of California, San Diego, La Jolla, California 92093, USA. ³Department of Neurosciences, University of California, San Diego, La Jolla, California, USA. ⁴The Salk Institute for Biological Studies, La Jolla, California 92037, USA. ⁵Department of Anesthesiology, University of California, San Diego, La Jolla, California 92093, USA. ⁶Department of Anesthesiology, Maastricht University Medical Center, Maastricht 6202 AZ, Netherlands. ⁷Department of Chemical Physiology, The Scripps Research Institute, La Jolla, California 92037, USA. ⁸Department of Reproductive Medicine, University of California, San Diego, La Jolla, California 92093, USA. ⁹BD Biosciences, La Jolla, California 92037, USA. ¹⁰Institute of Neurobiology, Slovak Academy of Sciences, Kosice SK-04001, Slovakia. ¹¹Department of Clinical Medicine, Neurology and Clinical Research Center, University of Oulu, Oulu FIN-90015, Finland.

Table 1 | Summary of patient information

Code	Diagnosis	Gender	Family history	Age at onset	Age at biopsy	MMSE at biopsy	APOE
NDC1	Non-demented control	M	Possible	N/A	86	30	2-3
NDC2	Non-demented control	M	N	N/A	86	30	3-3
sAD1	Sporadic AD	F	N	78	83	4	3-3
sAD2	Sporadic AD	M	N	78	83	18	3-3
APP ^{DP1}	Familial AD, APP duplication	M	Y	46	51	21	3-3
APP ^{DP2}	Familial AD, APP duplication	F	Y	53	60	17	3-3

MMSE, mini mental state examination (perfect score = 30). AD, Alzheimer's disease.

endodermal lineages *in vitro* (Fig. 1a–d, Supplementary Figs 3a–e and 4). All lines tested (one per individual) formed teratomas when injected into nude rats (Supplementary Fig. 5). Supplementary Table 1 provides details of each iPSC line.

Variability in differentiation efficiency exists between pluripotent cell lines. To analyse variability in our iPSC lines, we used a fluorescence-activated cell sorting (FACS)-based method of neuronal differentiation and purification (summarized in Supplementary Fig. 6), based on work described previously¹². Briefly, the 18 iPSC lines were first differentiated into cultures containing neural rosettes (Supplementary Fig. 3f). From these cultures, neural progenitor cells (NPCs) were purified and the efficiency of NPC formation was assessed by CD184⁺CD15⁺CD44[−]CD271[−] immunoreactivity. These FACS-purified NPCs maintained expression

of NPC-associated markers, such as SOX2 and nestin, over multiple passages (Fig. 1c, d). NPCs were differentiated for 3 weeks into heterogeneous cultures containing neurons (Supplementary Fig. 3g, h). *APP* copy number was faithfully maintained in differentiated cultures (Supplementary Fig. 3i). From these cultures, neurons were purified to near homogeneity, and the efficiency of neuron generation was assessed by CD24⁺CD184[−]CD44[−] immunoreactivity. No significant differences between any of the individuals in the efficiency of NPC or neuronal differentiation were detected (Fig. 1k, l).

Although we observed variability in differentiation among lines from each individual, the extent of inter-individual variation was less than observed intra-individual variability. These results suggest that any observed biochemical aberrations in neurons, if present in multiple lines derived from the same patient, are probably caused by features of that patient's genotype. Purified neurons were plated at a density of 2×10^5 cells per well of a 96-well plate and cultured for an additional 5 days. More than 90% of cells in these cultures were neurons, as judged by the presence of β III-tubulin⁺, MAP2⁺ projections (Fig. 1e–h). Genome-wide mRNA expression profiles of five representative purified neuronal cultures were compared to the parental iPSC lines and samples from fetal brain, heart, liver and lung (Supplementary Fig. 7 and Supplementary Table 2). Unsupervised hierarchical clustering analysis revealed that purified neurons most closely resembled fetal brain samples, in part due to a global upregulation of neuronal genes. Interestingly, the largest difference between fetal brain samples and purified neurons was downregulation in purified neurons of the hippo signalling cascade (~ 6.1 fold), which regulates proliferation of cells such as NPCs and glia^{13,14}.

We determined multiple electrophysiological properties of purified neurons to assess passive membrane properties and synaptic connectivity (Fig. 1i, j, Supplementary Table 3 and Supplementary Fig. 8). Notably, virtually all neurons tested generated voltage-dependent action potentials and currents (Fig. 1i), which were blocked by tetrodotoxin (Supplementary Fig. 8). Transient bath application of ionotropic receptor agonists (25 μ M muscimol or 10 μ M AMPA) evoked transient currents, showing that purified neurons expressed functional GABA and AMPA receptors, respectively (Supplementary Table 3). To determine whether neurons were also able to form functional synaptic contacts, we analysed continuous whole-cell voltage clamp recordings. We detected spontaneous inhibitory and/or excitatory synaptic currents in a subset of cells ($\sim 40\%$). Analysis of the kinetics of those events combined with reversible blockade using GABA_A or AMPA receptor antagonists demonstrated that the neurons not only fire action potentials but also made functional synaptic contacts (Supplementary Table 3). The electrophysiological results were supported by analysis of expression of protein markers of glutamatergic and GABAergic neuronal subtypes (VGluT1 and GABA, respectively), which were detected by immunofluorescence, with approximately 15% of cells staining brightly for VGluT1 and 8% for GABA, and most remaining neurons staining dimly for one of the markers (Supplementary Fig. 9a). RNAs indicative of glutamatergic, GABAergic and cholinergic subtypes (that is, *VGLUT1*, *GAD67* and *CHAT*, respectively) were detected by quantitative polymerase chain reaction (qPCR). Importantly, no significant differences in neuronal subtypes were detected between patients and controls (Supplementary Fig. 9b–f).

Elevated or altered secretion of amyloid- β peptides by fibroblasts is a feature common to all familial Alzheimer's disease mutations

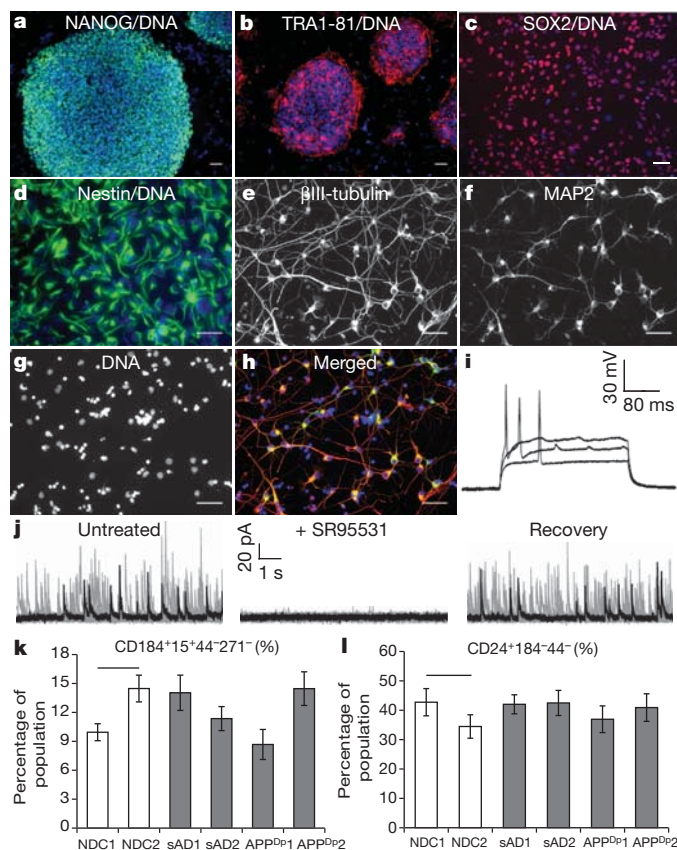


Figure 1 | Generation of iPSC lines and purified neurons from APP^{DP}, sAD and NDC fibroblasts. a, b, iPSC lines express NANOG and TRA1-81. c, d, iPSC-derived, FACS-purified NPCs express SOX2 and nestin. e–h, iPSC-derived, FACS-purified neurons express MAP2 and β III-tubulin. Scale bars in a–h, 50 μ m. i, Representative action potentials in response to somatic current injections. Data from iPSC line APP^{DP2}. j, Spontaneous synaptic activity was detected (voltage clamp recording at the reversal potential of sodium (0 mV)) and reversibly blocked by GABA_A receptor antagonist SR95531 (10 μ M). Each panel represents ~ 4 min continuous recordings separated in 25 sweeps (grey traces) and superimposed for clarity. Black traces represent a single sweep. Data from iPSC line NDC2.1. k, l, No significant difference was seen between NDCs and any patient's cultures in the ability of iPSCs to generate NPCs at day 11 ($P = 0.08$, $n = 9$), or the ability of NPCs to form neurons at 3 weeks ($P = 0.82$, $n = 9$). Error bars indicate s.e.m.

identified so far^{15,16}. It is not known if iPSC-derived neurons from familial Alzheimer's disease patients maintain the elevated amyloid- β production seen in the parental fibroblasts. In sAD fibroblasts and other peripheral cells, APP expression and amyloid- β secretion are not consistently altered¹⁷. To determine if iPSC-derived neurons from APP^{DP} and sAD patients exhibit elevated amyloid- β secretion, amyloid- β levels in neuron-conditioned media were measured and normalized to total protein levels of cell lysates. Purified neurons from patients APP^{DP1} and APP^{DP2}, each represented by three independently derived iPSC lines, secreted significantly higher levels of amyloid- β (1–40) compared to mean NDC levels (Fig. 2a). Neurons from patient sAD2 also had significantly higher amyloid- β (1–40) levels compared to NDC neurons, even though no difference was observed between the fibroblasts of sAD2 and NDC individuals. We found that amyloid- β (1–42) and amyloid- β (1–38) levels in these purified neuronal cultures were often below the detection range of our assay, owing to the relatively small number of neurons purified. By cell type, neurons exhibited a larger difference in amyloid- β levels between APP^{DP} and NDC than fibroblasts, further suggesting that fibroblasts are not fully predictive of neuronal phenotypes (Fig. 2b).

Genetic evidence implicates altered or elevated APP processing and amyloid- β levels as the driving agents behind familial Alzheimer's disease² and, because of identical neuropathology, sporadic Alzheimer's disease. However, tau, although not genetically linked to Alzheimer's disease, forms neurofibrillary tangles, which correlate better with disease severity than plaque numbers¹⁸. The mechanism by which altered APP processing might cause elevated p-tau and neurofibrillary tangle pathology is unclear. Tau phosphorylation at Thr 231, one of several tau phosphoepitopes, regulates microtubule stability¹⁹ and correlates with both neurofibrillary tangle number and degree of cognitive decline^{20,21}. To determine if tau phosphorylation at Thr 231 is elevated in APP^{DP} and sAD neurons, we measured the amount of p-tau(Thr 231) relative to total tau levels in lysates from purified neurons from three iPSC lines from each of the NDC, sAD and APP^{DP} patients. Neurons from both APP^{DP} patients had significantly higher p-tau/total tau ratios than neurons from NDC lines (Fig. 2c). p-Tau/total tau in the two sAD patients mirrored the amyloid- β findings: no difference was observed between sAD1 and NDC neurons whereas sAD2 neurons had significantly increased p-tau/total tau.

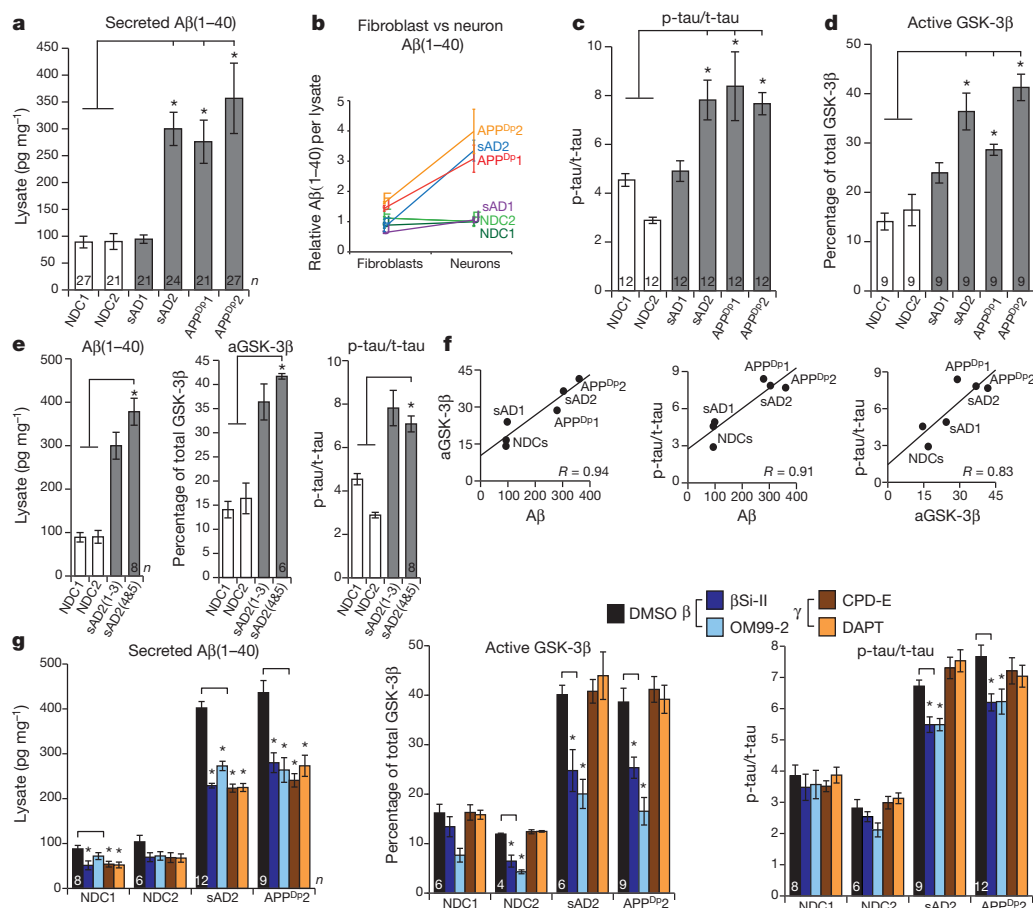


Figure 2 | Increased amyloid- β , p-tau and aGSK-3 β in sAD2 and APP^{DP} neuronal cultures. **a**, Purified neurons from sAD2, APP^{DP1} and APP^{DP2} secrete increased amyloid- β (1–40) (β (1–40)) compared to NDC samples ($P = 0.0012$, 0.0014 and <0.0001 , respectively). **b**, Amyloid- β differences between patients and controls are larger in neurons versus fibroblasts. Data sets are relative to NDC mean. **c**, **d**, Neurons from sAD2, APP^{DP1} and APP^{DP2} have increased aGSK-3 β (percentage non-phospho-Ser 9) and p-tau/total tau (p-tau/t-tau) compared to NDC samples (aGSK-3 β , $P < 0.0001$, 0.0005 and 0.0001 ; p-tau/total tau, $P < 0.0001$, 0.0001 and 0.0002). In **a–d**, n values on graphs indicate the number of biological replicates per patient, contributed equally by three iPSC lines. **e**, sAD2 findings verified in two additional iPSC lines (sAD2.4 and sAD2.5). sAD2(1–3) indicates findings from initial sAD2

iPSC lines. For amyloid- β , aGSK-3 β and p-tau/total tau, sAD2 remained significantly higher than controls ($P < 0.0001$). No significant difference was found between original and secondary sAD2 lines ($P = 0.14$, 0.44 , 0.63). **f**, Strong positive correlations between amyloid- β (1–40), aGSK-3 β and p-tau/total tau in purified neurons. Pearson $R = 0.94$, 0.91 and 0.83 , respectively. **g**, Twenty-four hour treatment with β - and γ -secretase inhibitors reduced secreted amyloid- β (1–40) compared to control treatment. β -Secretase inhibitors partially rescued aGSK-3 β and p-tau/total tau in sAD2 and APP^{DP2} neurons ($P < 0.01$ for aGSK-3 β , $P < 0.03$ for p-tau). γ -Secretase inhibition did not significantly affect aGSK-3 β and p-tau/total tau. In **g**, number of treatment sets is indicated on the graph (n), NDCs are represented by two iPSC lines each and sAD2 and APP^{DP2} are represented by three. Error bars indicate s.e.m.

Tau can be phosphorylated by multiple kinases. The kinase GSK-3 β can phosphorylate tau at Thr 231 *in vitro* and co-localizes with neurofibrillary tangles and pre-tangle phosphorylated tau in sAD post-mortem neurons²². GSK-3 β is thought to be constitutively active but is inactivated when phosphorylated at Ser 9 (ref. 23). To determine if iPSC-derived neurons with elevated p-tau have increased GSK-3 β activity, the proportion of aGSK-3 β in purified neurons was calculated by measuring the amount of GSK-3 β lacking phosphorylation at Ser 9 relative to total GSK-3 β levels. We observed that neurons from patients APP^{DP1}, APP^{DP2} and sAD2 had significantly higher aGSK-3 β than NDC neurons (Fig. 2d). The amyloid- β , GSK-3 β and tau findings of sAD2 were verified by analysing an additional two iPSC lines (sAD2.4 and sAD2.5; characterization in Supplementary Fig. 10), and we observed that levels remained consistently elevated (Fig. 2e). Results are detailed per patient in Supplementary Table 4a, per cell line in Supplementary Fig. 11, and per cell culture in Supplementary Table 5.

Although amyloid- β , p-tau and GSK-3 β clearly have roles in Alzheimer's disease pathogenesis, their relationship is unclear. We observed that iPSC-derived neurons exhibited strong or very strong correlations between amyloid- β (1–40), p-tau/total tau and aGSK-3 β levels (Fig. 2f and Supplementary Table 4b). We reasoned that if APP proteolytic products, such as amyloid- β or carboxy-terminal fragments (CTFs), have a causative role in p-tau and aGSK-3 β elevation, then inhibiting γ - or β -secretase activity could reduce p-tau and aGSK-3 β . We treated purified neurons from NDC1, NDC2, sAD2 and APP^{DP2} (2–3 iPSC lines each) with γ -secretase inhibitors (CPD-E and DAPT) or β -secretase inhibitors (β SI-II and OM99-2) for 24 h and measured amyloid- β , GSK-3 β and p-tau/total tau compared to vehicle-treated samples. All inhibitors reduced amyloid- β (1–40) by similar levels (32–45% in patient samples) (Fig. 2g). Intriguingly, for both sAD2 and APP^{DP2} neurons, we observed that β -secretase inhibitors significantly reduced aGSK-3 β and p-tau/total tau (Fig. 2g, and shown per iPSC line in Supplementary Fig. 12). Neither γ -secretase inhibitor significantly differed from control-treated samples for aGSK-3 β levels and p-tau/total tau.

We extended phenotypic characterization of sAD2 and APP^{DP} by analysing endosomal and synaptic markers in FACS-purified neurons co-cultured with astrocytes for 12 days. Accumulation of large RAB5⁺ early endosomes in neurons has been observed in autopsies from sporadic Alzheimer's disease and some forms of familial Alzheimer's disease^{24,25}. As β -secretase is localized to endosomes and has an acidic pH optimum, it has been proposed that early endosomes potentially mediate the effects of APP processing on downstream pathologies such as increased p-tau, neurofibrillary tangles, synaptic loss and apoptosis²⁶; however, these hypotheses have been difficult to test directly without live, patient-specific neurons. To determine if early endosome phenotypes are present in iPSC-derived neurons from

Alzheimer's disease patients, purified neurons from NDC1, NDC2, sAD2 and APP^{DP2} (two iPSC lines each) co-cultured with astrocytes were harvested and large and very large RAB5⁺ early endosomes (1–2.1 μm^3 and 2.1–7 μm^3) in neuronal soma were counted. Whereas control neurons generally had few RAB5⁺ structures >1 μm^3 , neurons from both sAD2 and APP^{DP2} frequently had RAB5⁺ early endosomes highly similar in volume, morphology and localization to what has been observed in autopsy samples (Fig. 3a–c). When compared, the neurons from both sAD2 and APP^{DP2} had significantly increased numbers of both large and very large early endosomes relative to controls (Fig. 3d). We sought to determine if neuronal cultures from sAD2 and APP^{DP2} also contained reduced levels of the presynaptic marker synapsin I. In Alzheimer's disease autopsies, synaptic loss is one of the strongest pathological correlates with dementia severity, and in regions of the brain affected by Alzheimer's disease, the presynaptic marker synapsin I is decreased in patients versus controls^{27,28}. To analyse synapsin I levels in iPSC-derived neurons co-cultured with astrocytes, we quantified synapsin I⁺ puncta on MAP2⁺ dendrites (Fig. 3e). We found no significant difference between NDCs and either sAD2 or APP^{DP2} in the number of puncta per μm dendrite (Fig. 3f). Extended culture periods may be required to study Alzheimer's disease-associated loss of synaptic proteins.

The results of this study provide strong evidence that iPSC technology can be used in concert with post-mortem samples and animal models to study early pathogenesis and drug response in sporadic and familial Alzheimer's disease. In purified, electrophysiologically active neurons from one sporadic Alzheimer's disease and two APP^{DP} patients, each represented by at least three clonally derived iPSC lines, we observed significantly increased levels of three major biochemical markers of Alzheimer's disease: amyloid- β (1–40), aGSK-3 β and p-tau/total tau. Increased sAD2 amyloid- β levels were not observed in the parental fibroblasts, suggesting a cell-type-specific phenotype. Among the individuals in this study, not only did strong correlations exist between amyloid- β (1–40), p-tau/total tau and aGSK-3 β , but both p-tau/total tau and aGSK-3 β levels were also partially rescued in neurons from sAD2 and APP^{DP} following treatment with β -secretase inhibitors, suggesting that the APP processing pathway has a causative role in tau Thr 231 phosphorylation in human neurons. Because γ -secretase inhibition did not cause a significant effect, products of APP processing other than amyloid- β may have a role in induction of GSK-3 β activity and p-tau. One potential culprit is the β -CTF, the levels of which correlate with axonopathies in mouse models harbouring APP duplications²⁹ and mediate early endosome accumulation in human Down's syndrome fibroblasts³⁰. The observation that neurons from patients sAD2 and APP^{DP2} have early endosome phenotypes raises the question of how aberrant early endosomes relate to other phenotypes of Alzheimer's disease, such as axonopathies, synaptic loss and cell death,

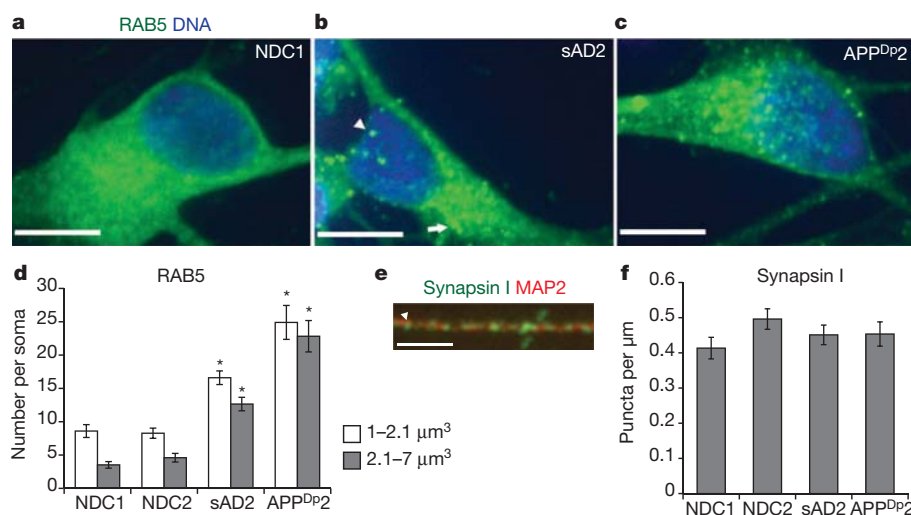


Figure 3 | Analysis of early endosome and synapsin levels in purified neurons co-cultured with astrocytes. **a–c**, Extended focus images of Rab5-stained neuronal soma from NDC1, sAD2 and APP^{DP2}. Arrowhead in **b** marks a 1–2.1 μm^3 early endosome, and the arrow marks a 2.1–7 μm^3 early endosome. Scale bars, 10 μm . **d**, Neurons from sAD2 and APP^{DP2} have significantly increased numbers of large and very large early endosomes compared to NDC neurons ($P < 0.0001$, $n = 40$ neurons from two iPSC lines per individual). **e**, Representative image of synapsin I (green) on a MAP2⁺ dendrite (red). Arrowhead marks a synapsin I⁺ punctum. Scale bar, 3 μm . **f**, No significant difference between patients and controls in the number of synapsin⁺ structures per μm dendrite ($P = 1.00$, $n = 40$ dendrites from two iPSC lines per individual). Neurons were scored blinded to genotype. Error bars indicate s.e.m.

in human neurons. Neurons and synapses rely heavily on endocytic pathways, and thus iPSC technology can now be used to study the role of this dynamic process in live patient-specific neurons. One point of caution is that it is possible that the cultures of purified neurons that we generated and studied may not have been fully mature, as they lacked repetitive action potentials and had limited spontaneous activity. Although some types of mature neurons also have these properties, it is conceivable that the phenotypes we observed might be modified by duration of *in vitro* culture. In this context, while there is debate about when Alzheimer's disease phenotypes initiate, evidence exists that Alzheimer's disease-like pathology can occur in Down's syndrome fetuses as early as 28 weeks of gestation²⁴.

Our finding that the genome of patient sAD2, but not patient sAD1, generates significant Alzheimer's disease phenotypes in purified neurons has important implications. First, this finding suggests that an unknown frequency of sporadic Alzheimer's disease patients will have genomes that generate strong neuronal phenotypes. The frequency of such genomes in the sporadic Alzheimer's disease population cannot be determined from the small sample size we report and will require a larger sample size to ask how frequent such genomes are in the clinical population diagnosed with sporadic Alzheimer's disease. Second, the genome of sAD2 clearly harbours one or more variants that generate Alzheimer's disease phenotypes, which can thus be elucidated by future molecular genetic studies. Third, we speculate that sporadic Alzheimer's disease might be sub-divided depending on whether neurons themselves are altered, as in the case of sAD2, as opposed to other cell types such as astrocytes, which could be altered in other cases, for example, sAD1. Thus, future iPSC studies examining larger numbers of patients and controls have the potential to provide great insight into the mechanisms behind the observed heterogeneity in sporadic Alzheimer's disease pathogenesis, the role of different cell types, patient-specific drug responses, and prospective diagnostics.

METHODS SUMMARY

iPSC generation and differentiation. Primary fibroblast cultures were established from dermal punch biopsies taken from individuals following informed consent and Institutional Review Board approval. To generate iPSCs, fibroblasts were transduced with MMLV vectors containing the complementary DNAs for *OCT4*, *SOX2*, *KLF4*, *c-MYC* and \pm *EGFP*. iPSC-derived NPCs were differentiated for 3 weeks, neurons were purified by FACS, and amyloid- β , p-tau/total tau and aGSK-3 β were measured on purified control and mutant neurons from multiple lines cultured in parallel for an additional 5 days by multi-spot electrochemiluminescence assays (Meso Scale Diagnostics). Early endosomes were analysed by confocal microscopy on purified neurons co-cultured with human astrocytes (Lonza) for 12 days. To ensure reproducible and consistent data, we found that it is important to differentiate and evaluate neurons from full sets of mutant and control iPSC lines together.

Statistics. $P < 0.05$ was considered statistically significant. Individuals were statistically compared to the total NDC pool by Tukey's test. Drug responses were compared to controls by Dunnett's method. N values signify the total number of separate cultures analysed, with each iPSC line contributing equally to the total.

Full Methods and any associated references are available in the online version of the paper at www.nature.com/nature.

Received 29 June 2011; accepted 4 January 2012.

Published online 25 January 2012.

1. Rovelet-Lecrux, A. *et al.* APP locus duplication in a Finnish family with dementia and intracerebral haemorrhage. *J. Neurol. Neurosurg. Psychiatry* **78**, 1158–1159 (2007).
2. Tanzi, R. E. & Bertram, L. Twenty years of the Alzheimer's disease amyloid hypothesis: a genetic perspective. *Cell* **120**, 545–555 (2005).
3. Ballatore, C., Lee, V. M. Y. & Trojanowski, J. Q. Tau-mediated neurodegeneration in Alzheimer's disease and related disorders. *Nature Rev. Neurosci.* **8**, 663–672 (2007).
4. Gatz, M. *et al.* Role of genes and environments for explaining Alzheimer disease. *Arch. Gen. Psychiatry* **63**, 168–174 (2006).
5. Games, D. *et al.* Alzheimer-type neuropathology in transgenic mice overexpressing V717F β -amyloid precursor protein. *Nature* **373**, 523–527 (1995).
6. Roberson, E. D. *et al.* Reducing endogenous tau ameliorates amyloid β -induced deficits in an Alzheimer's disease mouse model. *Science* **316**, 750–754 (2007).
7. Busciglio, J., Lorenzo, A., Yeh, J. & Yankner, B. A. β -Amyloid fibrils induce tau phosphorylation and loss of microtubule binding. *Neuron* **14**, 879–888 (1995).

8. Ebert, A. D. *et al.* Induced pluripotent stem cells from a spinal muscular atrophy patient. *Nature* **457**, 277–280 (2009).
9. Nguyen, H. N. *et al.* LRRK2 mutant iPSC-derived DA neurons demonstrate increased susceptibility to oxidative stress. *Cell Stem Cell* **8**, 267–280 (2011).
10. Qiang, L. *et al.* Directed conversion of Alzheimer's disease patient skin fibroblasts into functional neurons. *Cell* **3**, 359–371 (2011).
11. Urbach, A., Bar-Nur, O., Daley, G. Q. & Benvenisty, N. Differential modeling of fragile X syndrome by human embryonic stem cells and induced pluripotent stem cells. *Cell Stem Cell* **6**, 407–411 (2010).
12. Yuan, S. H. *et al.* Cell-surface marker signatures for the isolation of neural stem cells, glia and neurons derived from human pluripotent stem cells. *PLoS ONE* **6**, e17540 (2011).
13. Cao, X., Pfaff, S. L. & Gage, F. H. YAP regulates neural progenitor cell number via the TEA domain transcription factor. *Genes Dev.* **22**, 3320–3334 (2008).
14. Reddy, B. V. & Irvine, K. D. Regulation of *Drosophila* glial cell proliferation by Merlin-Hippo signaling. *Development* **138**, 5201–5212 (2011).
15. Citron, M. *et al.* Excessive production of amyloid β -protein by peripheral cells of symptomatic and presymptomatic patients carrying the Swedish familial Alzheimer disease mutation. *Proc. Natl Acad. Sci. USA* **91**, 11993–11997 (1994).
16. Scheuner, D. *et al.* Secreted amyloid β -protein similar to that in the senile plaques of Alzheimer's disease is increased *in vivo* by the presenilin 1 and 2 and APP mutations linked to familial Alzheimer's disease. *Nature Med.* **2**, 864–870 (1996).
17. Gasparini, L. *et al.* Peripheral markers in testing pathophysiological hypotheses and diagnosing Alzheimer's disease. *FASEB J.* **12**, 17–34 (1998).
18. Arriagada, P. V., Growdon, J. H., Hedley-Whyte, E. T. & Hyman, B. T. Neurofibrillary tangles but not senile plaques parallel duration and severity of Alzheimer's disease. *Neurology* **42**, 631 (1992).
19. Cho, J.-H. & Johnson, G. V. W. Primed phosphorylation of tau at Thr 231 by glycogen synthase kinase 3 β (GSK3 β) plays a critical role in regulating tau's ability to bind and stabilize microtubules. *J. Neurochem.* **88**, 349–358 (2004).
20. Buerger, K. *et al.* CSF tau protein phosphorylated at threonine 231 correlates with cognitive decline in MCI subjects. *Neurology* **59**, 627–629 (2002).
21. Buerger, K. *et al.* CSF phosphorylated tau protein correlates with neocortical neurofibrillary pathology in Alzheimer's disease. *Brain* **129**, 3035–3041 (2006).
22. Cho, J. & Johnson, G. Glycogen synthase kinase 3 β phosphorylates tau at both primed and unprimed sites. *J. Biol. Chem.* **278**, 187–193 (2003).
23. Dajani, R. *et al.* Crystal structure of glycogen synthase kinase 3 β : structural basis for phosphate-primed substrate specificity and autoinhibition. *Cell* **105**, 721–732 (2001).
24. Cataldo, A. M. *et al.* Endocytic pathway abnormalities precede amyloid β deposition in sporadic Alzheimer's disease and Down syndrome: differential effects of APOE genotype and presenilin mutations. *Am. J. Pathol.* **157**, 277–286 (2000).
25. Cataldo, A. *et al.* Endocytic disturbances distinguish among subtypes of Alzheimer's disease and related disorders. *Ann. Neurol.* **50**, 661–665 (2001).
26. Nixon, R. A. Endosome function and dysfunction in Alzheimer's disease and other neurodegenerative diseases. *Neurobiol. Aging* **26**, 373–382 (2005).
27. Hamos, J. E., DeGennaro, L. J. & Drachman, D. A. Synaptic loss in Alzheimer's disease and other dementias. *Neurology* **39**, 355–361 (1989).
28. Qin, S., Hu, X. Y., Xu, H. & Zhou, J. N. Regional alteration of synapsin I in the hippocampal formation of Alzheimer's disease patients. *Acta Neuropathol.* **107**, 209–215 (2004).
29. Salehi, A. *et al.* Increased *App* expression in a mouse model of Down's syndrome disrupts NGF transport and causes cholinergic neuron degeneration. *Neuron* **51**, 29–42 (2006).
30. Jiang, Y. *et al.* Alzheimer's-related endosome dysfunction in Down syndrome is β -independent but requires APP and is reversed by BACE-1 inhibition. *Proc. Natl Acad. Sci. USA* **107**, 1630–1635 (2010).

Supplementary Information is linked to the online version of the paper at www.nature.com/nature.

Acknowledgements We thank D. Galasko, M. Sundsmo, J. Rivera, J. Fontaine, C. Gigliotti and B. Yu at the University of California, San Diego (UCSD) Alzheimer's Disease Research Center for patient samples and data (grant AGO 5131); S. Dowdy and N. Yoshioka for viral vectors; B. Balderas at BD Biosciences for antibodies; C. Santucci and S. Nguyen for teratoma assay assistance; the UCSD Neuroscience Microscopy Shared Facility (grant P30 NS047101); and Planned Parenthood of the Pacific Southwest for fetal brain specimens. Funding was from California Institute of Regenerative Medicine (CIRM) comprehensive grants (M.M., F.H.G., L.S.B.G.), CIRM predoctoral fellowship (M.A.I.), FP7 Marie Curie IOF (C.B.), Weatherstone Foundation fellowship (K.L.N.), National Institutes of Health K12 HD001259, the Hartwell Foundation (L.C.L., F.S.B.), the Lookout Fund and the McDonnell Foundation (F.H.G.). L.S.B.G. is an investigator with the Howard Hughes Medical Institute.

Author Contributions M.A.I. and L.S.B.G. conceived the project; M.A.I. and L.S.B.G. designed the experiments; M.A.I., S.H.Y., C.B., S.M.R., Y.M., C.H., M.P.H., S.V.G., M.M., K.L.N. and F.S.B. performed the experiments; M.A.I., S.H.Y. and C.T.C. developed differentiation methods; A.M.R. and E.H.K. provided APP^{DP} patient samples and information; F.H.G. supervised C.B. and Y.M.; M.M. supervised M.P.H. and S.V.G.; L.C.L. supervised K.L.N. and F.S.B.; M.A.I. and L.S.B.G. wrote the manuscript; F.H.G., E.H.K. and A.M.R. edited the manuscript.

Author Information Data have been deposited in the Gene Expression Omnibus under accession GSE34879. Reprints and permissions information is available at www.nature.com/reprints. The authors declare no competing financial interests. Readers are welcome to comment on the online version of this article at www.nature.com/nature. Correspondence and requests for materials should be addressed to L.S.B.G. (lgoldstein@ucsd.edu).

METHODS

Patients and fibroblast derivation. NDC and sAD individuals were enrolled in the longitudinal study at the UCSD Alzheimer's Disease Research Center. APP^{DP} individuals were patients at the Department of Clinical Medicine, Neurology, Oulu University Hospital, Oulu, Finland. For all individuals, dermal punch biopsies were taken following informed consent and Institutional Review Board approval. Primary fibroblast cultures were established from biopsies using established methods³¹. Fibroblasts were cultured in DMEM containing 15% FBS, L-glutamine and penicillin/streptomycin.

iPSC generation and expansion. iPSCs were generated as described³², with the following modifications. The cDNAs for *OCT4*, *SOX2*, *KLF4*, *c-MYC* and *EGFP* were cloned into pCX4 vectors³³ and vectors were packaged into VSVG-pseudotyped retroviruses. For each patient, three independent viral transductions were performed. Three wells, each containing $\sim 1 \times 10^5$ fibroblasts, were transduced with retroviruses. On days 2–8, 2 mM valproic acid was added to cultures. Potential iPSC colonies were picked at ~ 3 weeks and transferred to 96-well plates containing irradiated mouse embryonic fibroblasts (MEFs). For passaging, cells were dissociated with TryPLE (Invitrogen). The efficiency of potential iPSC colony formation was roughly 100 colonies per 1×10^5 fibroblasts at 3 weeks. The efficiency of successful establishment of a stable iPSC line from an initial colony was roughly 10%.

Karyotype analysis and pluripotency assays. Karyotype analysis was performed by Cell Line Genetics. iPSCs were assayed for teratoma formation by injections into spinal cords of athymic rats, as previously described³⁴, with the following modifications: cells were dissociated with Accutase (Innovative Cell Technologies) and passed through a 100- μ m mesh filter before injections and each animal received 10 injections of roughly 10,000 cells. For *in vitro* pluripotency assays, iPSC cultures were dissociated with dispase, and embryoid bodies were generated in low-attachment plates in media containing 15% fetal bovine serum (FBS). After 7 days, cultures were plated on Matrigel (BD Biosciences)-coated glass coverslips and cultured for 7 days.

Genotyping and qPCR. To determine APP copy number, genomic DNA was isolated from fibroblasts or differentiated NPCs. qPCR was performed using FastStart Universal SYBR Green Master Mix (Roche) and analysed on an Applied Biosystems 7300 Real Time PCR System using the $\Delta\Delta C_T$ method. APP levels were normalized to mean β -globin/albumin. To compare RNA levels between samples, RNA was purified (PARIS kit, Ambion), DNase treated (Ambion) and reverse transcribed (Superscript II, Invitrogen). For transgene expression, primers detected a sequence common to all transgenes, and expression was normalized to the housekeeping gene *NONO*. PCR to detect endogenous *SOX2* expression was performed using Qiagen HotStarTaq and primers previously described³⁵.

Immunocytochemistry and microscopy. Cells were fixed in 4% paraformaldehyde, permeabilized with buffer containing TritonX-100 and stained with primary and secondary antibodies (see below). Samples, except for early endosome studies, were imaged on a Nikon TE2000-U inverted microscope and acquired using Metamorph software (Molecular Devices). ImageJ software (National Institutes of Health) was used to pseudo-colour images, adjust contrast, and add scale bars. Endosomes and synapses were imaged on a PerkinElmer UltraVIEW VoX microscope with a $\times 60$ objective and a z-step of 0.5 μ m. Quantifications were done blinded to genotype.

Antibodies. The antibodies used for FACS purification of cells were TRA1-81-APC, CD184-APC, CD15-FITC, CD24-PECy7, CD44-PE and CD271-PE (all from BD Biosciences) and were used at a concentration of one test per 1×10^6 cells. The following antibodies were from Millipore: AFP (mouse 1:1,000), APP^{FL} (22C11, ms 1:1,000), SMA (ms 1:50), *SOX2* (rb 1:2,000), synapsin I (rb 1:500); from Sigma: GABA (rb 1:200), MAP2a/b (ms 1:500), tau total (rb 1:500), tau Thr 231 (rb 1:150). Other vendors: APP^{CTF} (Zymed rb 1:500), GAPDH (Ambion ms 1:250), VGLUT1 (Synaptic Systems rb 1:200), NANOG (Santa-Cruz rb 1:200), nestin (Santa-Cruz rb 1:1,000), RAB5A (Santa-Cruz rb 1:50), synuclein (BD ms 1:500), tau PHF1 (Pierce ms 1:500), β III-tubulin (Covance ms 1:2,000), β III-tubulin (Covance rabbit 1:1,000) anti-rabbit Alexa Fluor 488 (Invitrogen 1:200) and anti-mouse Alexa Fluor 568 (Invitrogen 1:200).

Neuronal differentiation and FACS. To ensure reproducible and consistent data, we found that it is important to differentiate and evaluate neurons from full sets of mutant and control iPSC lines together. Differentiation to NPCs and neurons was performed as previously described¹². 3×10^5 FACS-purified TRA1-81⁺ cells were seeded onto 3×10 cm plates that were seeded the previous day with 5×10^5 PA6 cells³⁶. At day 11, cells were dissociated with Accutase and $\sim 5 \times 10^5$ CD184⁺CD15⁺CD44⁺CD271⁺ NPCs were FACS-purified and plated onto poly-ornithine/laminin-coated plates and cultured with bFGF. At passage 7, NPCs were differentiated with BDNF, GDNF and cAMP. After 3 weeks of differentiation, cells were dissociated with Accutase and CD24⁺CD184⁺CD44⁺ cells were purified. FACS was performed with a FACSAria II (BD Biosciences) and

analysed with FloJo (Tree Star). Differentiation methods are also summarized in Supplementary Fig. 6.

Gene expression profiling. Total RNA was extracted from collected sample pellets (Ambion mirVana; Applied Biosystems) according to the manufacturer's protocol. RNA quantity (Qubit RNA BR Assay Kits; Invitrogen) and quality (RNA6000 Nano Kit; Agilent) was determined to be optimal for each sample before further processing. 200 ng RNA per sample was amplified using the Illumina Total Prep RNA Amplification Kit according to manufacturer's protocol and quantified as above. 750 ng biotinylated RNA per sample was hybridized to Illumina HT-12v4 Expression BeadChips, scanned with an Illumina iScan Bead Array Scanner, and quality controlled in GenomeStudio and the lumi bioconductor package. All RNA processing and microarray hybridizations were performed in house according to manufacturer's protocols. In GenomeStudio, probes were filtered for those detected with a *P* value of 0.01 in at least one sample and exported for normalization in R. Raw probe expression values were transformed and normalized using the robust spline normalization (RSN) as implemented in the lumi R/Bioconductor package. Probes were further filtered for those having a minimum value of 150 in at least two samples and a minimum difference between any two samples (maximum value minus minimum value) of at least 150.

Electrophysiology methods. Electrophysiology was performed on purified neurons, 5 days after FACS. For whole-cell patch-clamp recordings, individual coverslips were transferred into a heated recording chamber and continuously perfused (1 ml min⁻¹) with artificial cerebrospinal fluid (ACSF) bubbled with a mixture of CO₂ (5%) and O₂ (95%) and maintained at 25 °C. The ACSF contained 124 mM NaCl, 3 mM KCl, 1.3 mM MgSO₄, 26 mM NaHCO₃, 1.25 mM NaHPO₄, 20 mM glucose and 2 mM CaCl₂ (all chemicals from Sigma). For targeted whole-cell recordings, we used a $\times 40$ water-immersion objective, differential interference contrast filters (all Olympus), a digital camera (Rolera XR -Qimaging), a halogen (Olympus), a digitizer 1440A/ Multiclamp 700B and Clampex 10.3 (Molecular devices). The resistance of the patch electrodes was between 3–5 MOhm. Patch electrodes were filled with two different internal solutions both containing 4 mM NaCl, 10 mM Na-HEPES, 10 mM D-glucose, nucleotides (0.3 mM GTP, 2 mM Mg-ATP, 0.2 mM cAMP) 0.15% biocytin and 0.06% rhodamine. For current-clamp experiments, the internal solution also contained 130 mM K-gluconate, 6 mM KCl and 0.2 mM K-EGTA; in all other experiments, it contained instead: 126 mM Cs-gluconate, 6 mM CsCl and 0.2 mM Cs-EGTA. The pH and osmolarity of the internal solution were close to physiological conditions (pH 7.3, 290–300 mOsm). Data were all corrected for liquid junction potentials (10 mV). Electrode capacitances were compensated on-line in cell-attached mode (~ 7 pF). Recordings were low-pass filtered at 2 kHz, digitized, and sampled at intervals of 50 μ s (20 kHz). To control the quality and the stability of the recordings throughout the experiments, access resistance, capacitance and membrane resistance were continuously monitored on-line and recorded. The access resistance of the cells in our sample was 21 ± 1 MOhm. Electrophysiological statistical analysis was assisted with Clampfit 10.3, Igor Pro 6, Prism 5 and Microsoft Excel. Mean \pm standard error of the mean were reported.

Amyloid- β , p-tau/total tau and aGSK-3 β measurements. FACS-purified neurons were plated at 2×10^5 per well of a 96-well plate. Cells were cultured for an additional 5 days with a full media change on day 3. Amyloid- β was measured with MSD Human (6E10) Abeta3-Plex Kits (Meso Scale Discovery). p-tau/total tau was measured with a MSD Phospho(Thr231)/Total Tau Kit. aGSK-3 β was measured with MSD Phospho/Total GSK-3 β Duplex Kit. Fibroblast and neuronal amyloid- β levels were normalized to total protein levels determined by BCA assay (Thermo Scientific). aGSK-3 β (the per cent of unphosphorylated GSK-3 β at Ser 9) was calculated by manufacturer's recommendations: $(1 - (2 \times \text{phospho signal})/(\text{phospho signal} + \text{total signal})) \times 100$.

Inhibitor treatments. CPD-E (Compound-E) and DAPT were used at a final concentration of 200 nM. β Si-II (β -secretase inhibitor II) and OM99-2 were used at 10 μ M and 750 nM, respectively. 1 μ l of inhibitor or vehicle was added to the existing culture media of parallel cultures on day 4 and cultures were harvested on day 5. All inhibitors were from EMD Chemicals and were dissolved in DMSO.

Endosomal analysis. 1.5×10^5 per FACS-purified neurons were plated per well of a 96-well plate that was seeded the previous day with 5,000 human astrocytes (Lonza). After 12 days of culture, cultures were stained for RAB5 and β III-tubulin and imaged on a PerkinElmer UltraVIEW VoX microscope with a $\times 60$ objective and a z-step of 0.5 μ m. Quantification was performed blinded to genotype with Volocity software (PerkinElmer) on β III-tubulin⁺ cells only.

Statistics. Data were analysed using JMP software (SAS Institute). *P* < 0.05 was considered statistically significant. Individuals were statistically compared to the total NDC pool by ANOVA followed by Tukey's test. *N* values signify the total number of separate cultures analysed, with each iPSC line contributing equally to the total. Drug responses were compared to controls by Dunnett's method. Correlations were determined by calculating Pearson coefficients (*R*).

31. Takashima, A. in *Current Protocols in Cell Biology* Ch. 2 12 (John Wiley & Sons, 2001).
32. Park, I.-H., Lerou, P. H., Zhao, R., Huo, H. & Daley, G. Q. Generation of human-induced pluripotent stem cells. *Nature Protocols* **3**, 1180–1186 (2008).
33. Akagi, T., Sasai, K. & Hanafusa, H. Refractory nature of normal human diploid fibroblasts with respect to oncogene-mediated transformation. *Proc. Natl Acad. Sci. USA* **100**, 13567–13572 (2003).
34. Emre, N. *et al.* The ROCK inhibitor Y-27632 improves recovery of human embryonic stem cells after fluorescence-activated cell sorting with multiple cell surface markers. *PLoS ONE* **5**, e12148 (2010).
35. Takahashi, K. *et al.* Induction of pluripotent stem cells from adult human fibroblasts by defined factors. *Cell* **131**, 861–872 (2007).
36. Kawasaki, H. *et al.* Induction of midbrain dopaminergic neurons from ES cells by stromal cell derived inducing activity. *Neuron* **28**, 31–40 (2000).

PLANT BIOLOGY

Equal-parenting policy

During early embryo development in animals, maternal genes are expressed in preference to those of the zygote — the newly fertilized egg. But in plants it seems that zygote genomes switch on within hours of fertilization.

CHRISTOPHER J. HALE
& STEVEN E. JACOBSEN

Fertilization occurs when two gametes merge to form a zygote. The zygote's genome comprises two sets of chromosomes — one maternal, the other paternal. In animals, the stages of development immediately after fertilization are disproportionately controlled by maternally inherited factors, with the zygotic genome being switched on gradually in waves of activation¹. Whether plants undergo a similar maternal-to-zygotic transition in genomic activity has been a long-standing question. In contrast to previous work², Nodine and Bartel³ show, in a paper published on *Nature's* website today, that a plant zygote's transcriptome — its total complement of protein-coding RNA transcripts — contains relatively equal maternal and paternal contributions. It seems, therefore, that plants and animals have evolved distinct strategies for managing the early steps in the transition from two gametes to an organism with maternal and paternal copies of the genome.

For the plant species *Arabidopsis thaliana*, a wealth of whole-genome sequence data exists for closely related yet genetically distinct lines known as ecotypes⁴. To directly measure the respective contributions of the maternal and paternal genomes to the zygotic transcriptome, Nodine and Bartel crossed two of these ecotypes and sequenced the RNA content of the resulting zygote. Using the genetic differences between the parents, they then matched these RNAs to either the maternal or the paternal genome.

The authors observed a near-equal abundance of RNA sequences derived from each parental genome in the plant embryos as early as the one- to two-cell stage. Only a small number of genes showed biased expression. They also performed reciprocal crosses — switching which ecotype provided the male and female gamete. It emerged that most of these cases of bias were probably due to genetic or epigenetic differences (chemical modifications that alter gene expression without affecting the DNA sequence) between the two ecotypes used, rather than being a result of which ecotype was used as the male or the female parent. These findings imply that the plant zygotic genome

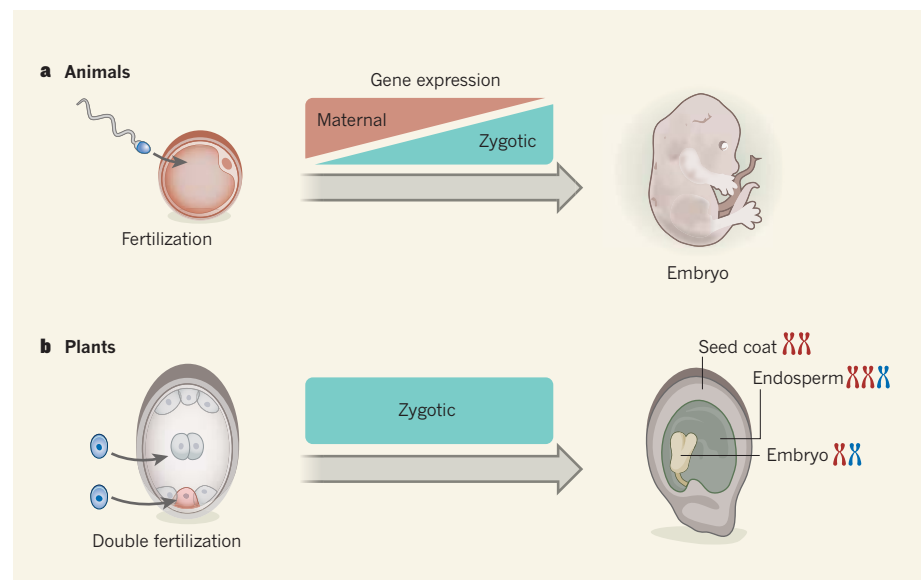


Figure 1 | Maternal-to-zygotic genomic transition in plants and animals. **a**, In animals, a single fertilization event between maternal and paternal gametes forms the zygote (not shown). Initially, the animal embryo is under predominant control of the maternal genome, and the zygotic genome is only gradually activated over the course of embryogenesis. **b**, In plants, a double fertilization process generates the zygote and the endosperm tissue. Both the endosperm and the embryo are encased in maternal tissue that generates the seed coat. Chromosome symbols represent maternal (red) and paternal (blue) genomes. Nodine and Bartel³ show that, in contrast to the case for animals, the plant zygotic genome is activated almost immediately after fertilization.

is essentially switched on only hours after fertilization.

Nodine and Bartel's results are in contrast to other reports^{2,5} suggesting that the maternal-to-zygotic transition in plants is gradual, as is the case for animals. The most comprehensive of these reports², published last year, used a genomics approach similar to that of the current study, and found that more than 80% of the *Arabidopsis* transcriptome in early embryos is derived from the maternal genome.

What might explain such different results between the two studies? Nodine and Bartel³ suggest that the most likely answer is that the embryo samples of the earlier study were contaminated by maternal tissue. This is because, in *Arabidopsis* as in other flowering plants, the embryo is surrounded by a seed coat and other maternally derived tissue (Fig. 1), making the isolation of high-purity embryonic tissue difficult — a problem for the extremely sensitive genome-sequencing

techniques used in both studies. After observing this maternal-contamination effect in pilot studies, Nodine and Bartel³ overcame the problem by extensively washing the isolated embryo cells.

One question arising from Nodine and Bartel's study is why activation of the zygotic genome is so different between plants and animals. Because the two kinds of organisms evolved multicellularity independently⁶, and have very different life histories, it is perhaps not surprising that the maternal-to-zygotic transition also differs between them. In plants, gametes are generated from cells derived from a pool of undifferentiated cells that are also responsible for generating structures such as leaves^{7,8}, rather than from a distinct germ-cell lineage as occurs in animals. In addition, fertilization itself is radically different in flowering plants compared with animals, with each seed being the product of two fertilization events (Fig. 1b). In this process, one fertilization event

forms the endosperm, a tissue that is functionally similar to the mammalian placenta, and which contains two sets of maternal chromosomes and one set of paternal chromosomes. A second fertilization event results in the formation of the embryo. It is noteworthy that, although Nodine and Bartel show that the embryo experiences equal transcriptome contributions from both parental genomes, gene expression in the embryo-nourishing endosperm shows extensive parental influence⁹; these effects are due to uneven nuclear 'dosage' as well as to epigenetic imprinting effects.

Another question is how the early plant embryo coordinates rapid integration of two genomes and the concomitant activation of a resulting zygotic genome. In animals, a suite of mechanisms acts to clear maternal factors, such as proteins and RNAs, from the developing zygote and to activate the zygotic genome^{1,10}. It is unclear whether similar mechanisms operate in plants. Tantalizingly,

epigenetic processes such as DNA methylation and demethylation, as well as regulatory small RNA molecules, have recently been implicated⁹ in the control of both gamete and endosperm development. Future studies of these pathways may reveal mechanisms for the regulation of gene expression in embryonic plants.

Understanding how a functional plant genome so quickly emerges from two progenitor genomes is vital for understanding plant development, and for informing approaches to plant breeding and plant biotechnology. In many crop species, combining two different parental genomes can generate regular and predictable hybrid vigour, known as heterosis. In some species this vigour is obvious very early in development¹¹. Consistent with these observations, Nodine and Bartel's work³ suggests that zygotic-genome dynamics in plants, including, perhaps, some aspects of heterosis, are established almost immediately after fertilization. ■

Christopher J. Hale is in the Department of Molecular, Cell and Developmental Biology, and **Steven E. Jacobsen** is at the Howard Hughes Medical Institute, University of California, Los Angeles, Los Angeles, California 90095, USA.

e-mails: cjhale@ucla.edu; jacobsen@ucla.edu

1. Tadros, W. & Lipshitz, H. D. *Development* **136**, 3033–3042 (2009).
2. Autran, D. *et al. Cell* **145**, 707–719 (2011).
3. Nodine, M. D. & Bartel, D. P. *Nature* <http://dx.doi.org/10.1038/nature10756> (2012).
4. Cao, J. *et al. Nature Genet.* **43**, 956–963 (2011).
5. Vielle-Calzada, J.-P., Baskar, R. & Grossniklaus, U. *Nature* **404**, 91–94 (2000).
6. Grosberg, R. K. & Strathmann, R. R. *Annu. Rev. Ecol. Evol. Syst.* **38**, 621–654 (2007).
7. Sundaresan, V. & Alandete-Saez, M. *Development* **137**, 179–189 (2010).
8. Twell, D. *Sex. Plant Reprod.* **24**, 149–160 (2011).
9. Feng, S., Jacobsen, S. E. & Reik, W. *Science* **330**, 622–627 (2010).
10. Walser, C. B. & Lipshitz, H. D. *Curr. Opin. Genet. Dev.* **21**, 431–443 (2011).
11. Meyer, S., Pospisil, H. & Scholten, S. *Plant Mol. Biol.* **63**, 381–391 (2007).

Crystal structure of the channelrhodopsin light-gated cation channel

Hideaki E. Kato¹, Feng Zhang², Ofer Yizhar², Charu Ramakrishnan², Tomohiro Nishizawa¹, Kunio Hirata³, Jumpei Ito⁴, Yusuke Aita⁴, Tomoya Tsukazaki¹, Shigehiko Hayashi⁵, Peter Hegemann⁶, Andrés D. Maturana⁴, Ryuichiro Ishitani¹, Karl Deisseroth² & Osamu Nureki¹

Channelrhodopsins (ChRs) are light-gated cation channels derived from algae that have shown experimental utility in optogenetics; for example, neurons expressing ChRs can be optically controlled with high temporal precision within systems as complex as freely moving mammals. Although ChRs have been broadly applied to neuroscience research, little is known about the molecular mechanisms by which these unusual and powerful proteins operate. Here we present the crystal structure of a ChR (a C1C2 chimera between ChR1 and ChR2 from *Chlamydomonas reinhardtii*) at 2.3 Å resolution. The structure reveals the essential molecular architecture of ChRs, including the retinal-binding pocket and cation conduction pathway. This integration of structural and electrophysiological analyses provides insight into the molecular basis for the remarkable function of ChRs, and paves the way for the precise and principled design of ChR variants with novel properties.

Organisms ranging from archaeobacteria to human beings capture energy and/or information contained within environmental sources of light by using photoreceptors called rhodopsins, which consist of seven-transmembrane-helix proteins, called opsins, covalently linked to retinal. On the basis of primary sequences, the corresponding opsin genes are classified into two groups: microbial (type I) and animal (type II). Type I opsin genes are found in archaea, eubacteria, fungi and algae, whereas type II opsin genes are expressed in animals, including human beings. The type II proteins indirectly influence transmembrane ion currents by coupling to G-protein-based signal transduction pathways. In contrast, the type I proteins (not normally found in animals) include direct-light-activated regulators of transmembrane ion conductance, such as the light-driven ion pumps called bacteriorhodopsins and halorhodopsins (BRs and HRs)^{1,2} and the light-driven ion channels ChRs³. The light-driven ion pumps have been extensively studied, and structure–function relationships are well known. As opposed to these ion pumps, very little is known about the structure of ChRs or the mechanism by which these seven-transmembrane proteins conduct cations in a light-dependent manner³.

Beginning in 2005, it was found that ChRs could be expressed in mammalian neurons to mediate precise and reliable control of action potential firing in response to light pulses, without the need for exogenous retinal in vertebrate systems^{4–9}. ChRs have now been used to control neuronal activity in a wide range of animals, resulting in insights into fundamental aspects of circuit function as well as dysfunction and treatment in pathological states^{10,11}. However, despite the rapid progress of optogenetics (a technology also encompassing the use of ion pumps, such as HRs), virtually nothing is known about how a seven-transmembrane protein can form a light-switchable channel for cations. Although a rough helical arrangement was visible in the recently published ChR2 electron microscopy structure of two-dimensional crystals at 6 Å resolution, amino acid positioning and insights into channel function remained completely lacking¹². A high-resolution three-dimensional image would be of enormous value, not only to enhance understanding of microbial opsin-based channels,

but also to guide optogenetics in the generation of ChR variants with novel function related to spectrum, selectivity and kinetics. Even with limited structural models, ChR variants have been engineered with faster or extended open-state lifetimes^{13–17}, shifted absorption spectra^{13,17,18}, reduced desensitization^{6,18–20}, and increased expression and photocurrent magnitude^{6,15–17,19}. These advances represent the tip of the iceberg in terms of what could be achieved for all of the above properties, as well as for altered ion selectivity and unitary (single-channel) conductance properties, if detailed structural knowledge could be obtained to facilitate true electrostatic calculations and molecular dynamics simulations.

Here we present the ChR crystal structure at 2.3 Å resolution. This high-resolution information, along with electrophysiological analyses, has revealed the fundamentals of ChR architecture and guides the way to a basic working model for channelrhodopsin function.

Overall ChR structure

ChR2 from *C. reinhardtii* consists of 737 amino acids; the seven transmembrane domains (TMs) and photocurrent functionality are all contained within the amino-terminal ~300 amino acids. To identify the most promising candidates for structural studies, we constructed and explored an extensive range of different ChRs and ChR chimaeras with distinct carboxy-terminal truncations. Using fluorescence-detection size-exclusion chromatography (FSEC)²¹, we found that a novel chimaeric and truncated sequence termed C1C2, primarily consisting of ChR1 (ref. 3) without its C terminus and with the last two TMs swapped for those from ChR2 (related to previous chimaeras^{19,20,22} but with an additional six-amino-acid modification of the C terminus, namely removal of the sequence NKGTKG), was not only expressed well in Sf9 insect cells but also showed good stability and monodispersity as well as similar spectral characteristics to previous chimaeras²² (Supplementary Fig. 1). The crystals obtained from fully dark-adapted C1C2 in the lipidic cubic phase belonged to the C222₁ space group and diffracted X-rays to 2.3 Å resolution. We solved the C1C2 structure by the multiple anomalous dispersion (MAD)

¹Department of Biophysics and Biochemistry, Graduate School of Science, The University of Tokyo, 2-11-16 Yayoi, Bunkyo-ku, Tokyo 113-0032, Japan. ²Department of Bioengineering and Howard Hughes Medical Institute, Stanford University, Stanford, California 94305, USA. ³RIKEN SPring-8 Center, Hyogo 679-5148, Japan. ⁴Bioengineering Department, Nagaoka University of Technology, Niigata 940-2188, Japan. ⁵Department of Chemistry, Graduate School of Science, Kyoto University, Kyoto 606-8502, Japan. ⁶Institute of Biology, Experimental Biophysics, Humboldt-University, Invalidenstrasse 42, D-10115 Berlin, Germany.

method, using mercury-derivatized crystals (Supplementary Fig. 2). As far as we know, this is the first example of the phase determination by MAD for the crystal obtained in the lipidic cubic phase.

The truncated C1C2 chimera (residues 1–342) is composed of an N-terminal extracellular domain (N domain, residues 24–83, marked in Fig. 1a, d), the seven TMs (TM1–TM7; residues 84–317) connected by three cytoplasmic loops (ICL1–ICL3) and three extracellular loops (ECL1–ECL3), and the C-terminal intracellular domain (C domain, residues 318–356) (Fig. 1b, d). In addition to the region spanning the N-terminal residues 1–23, which is processed as a signal peptide (data not shown), residues 24–48, 110–117 and 343–356 are structurally disordered and invisible in the electron density map, whereas the core transmembrane region is clearly resolved (Fig. 1a). Searches of the Protein Data Bank using the Dali server (<http://ekhidna.biocenter.helsinki.fi/dali>) suggested that the N domain, consisting of a short 3_{10} -helix and two β -strands, has a novel fold. Within each C1C2 protomer, 6 lipids and 43 water molecules were observed.

Two C1C2 protomers were found to be tightly associated into a closely apposed dimer, as previously predicted from electron microscopy¹². Interfacial interactions occur in the N domain, ECL1, TM3 and TM4 of each molecule (Fig. 1b, c). Notably, Cys 66 (27), Cys 73 (34) and Cys 75 (36) in the N domain (ChR2 numbering is shown in parentheses here and below for comparison with earlier literature) form three disulphide bonds between protomers. As Cys 73 and Cys 75 are highly conserved in ChRs, this interaction may contribute to stabilizing the N-domain interaction and molecular dimerization (Supplementary Fig. 3).

Structural comparison with BR

We next compared the C1C2 structure with that of BR and bRh (bovine rhodopsin). The primary sequence of ChR is similar to that

of BR as well as other microbial opsins, such as xanthorhodopsin and sensory rhodopsin II (Supplementary Fig. 4). Consistent with this sequence similarity, C1C2 superimposed well on BR (PDB accession 1IW6)²³, but not on bRh (PDB accession 3C9L)²⁴ (Fig. 1d and Supplementary Fig. 5). TM3–6 between C1C2 and BR are very similar, and the position of the protonated Schiff base is conserved (Fig. 1e), whereas there are three distinct features between the two structures. First, C1C2 has additional N-terminal and C-terminal domains. The N domain, as noted above, contributes to dimer formation, and the C domain may be involved in subcellular localization and scaffolding in *Chlamydomonas*; for example, to tether ChR to the algal eyespot²⁵. Second, TM7 of C1C2 protrudes into the intracellular space, projecting ~ 18 Å from the membrane surface, and the intracellular end of TM7 is shifted towards the central axis of the monomer by 2.7 Å, as compared with BR (Fig. 1d). Although the function of this protruding part of TM7 is unclear, His 313, His 317 and Gly 318 may contribute to stabilizing the intracellular C domain via a water-mediated hydrogen-bonding network (Supplementary Fig. 6). Last, and most importantly, the C1C2 extracellular ends of TM1 and TM2 are tilted outward by 3.0 Å and 4.1 Å, respectively, compared to those of BR (Fig. 1e). These tilts enlarge the cavity formed by TM1, 2 and 7 and allow water influx for a cation-translocation pathway, as discussed later.

Retinal-binding pocket, Schiff base and counterion

As in other microbial-type rhodopsins, all-*trans* retinal (ATR) is covalently bound to Lys 296 (257) on TM7 (Lys 216 in BR), forming the Schiff base. As in BR, five aromatic residues (Trp 163, Phe 217, Trp 262, Phe 265 and Phe 269) are located around the polyene chain and the β -ionone ring, forming a hydrophobic pocket for ATR (Fig. 2a, b), whereas Cys 167 (128), Thr 198 (159) and Ser 295 (256) form a less-hydrophobic pocket, and may contribute to colour shift (Fig. 2a, b).

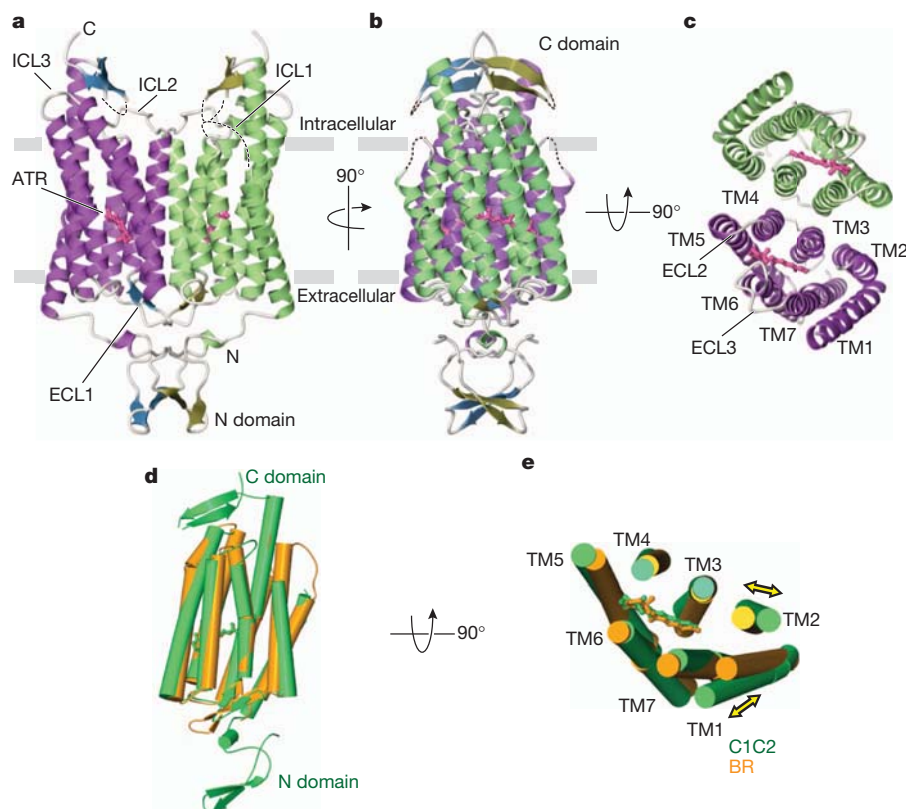


Figure 1 | Structure of C1C2 and comparison with BR. a–c, Crystal structure of the C1C2 dimer, viewed parallel to the membrane from two angles (a, b), and viewed from the extracellular side (c). C1C2 consists of the N domain, the seven transmembrane helices (TM1–TM7) connected by extracellular loops (ECL1–ECL3) and intracellular loops (ICL1–ICL3), and the C domain. Disordered

regions are represented as dotted lines. The ATR is coloured pink. d, e, Side view (d) and extracellular view (e) of the superimposed TMs of C1C2 (green) and BR (orange). The yellow double arrows indicate the shifts of the extracellular parts of TM1 and TM2.

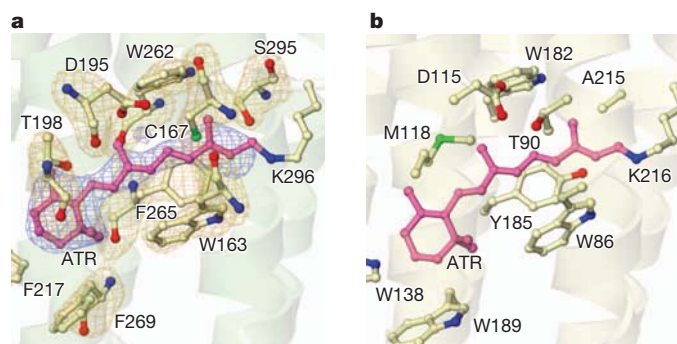


Figure 2 | Structural comparison of the retinal-binding pocket between C1C2 and BR. **a**, Structure of the retinal-binding pocket of C1C2, with an omit map of ATR at 3σ and of the surrounding residues (subtract 39 from the C1C2 residue number to obtain Chr2 numbering) at 3.5σ . **b**, Structure of the retinal-binding pocket of BR.

A previous report suggested that the side chains of Cys 167 (128) and Asp 195 (156) (Thr 90 and Asp 115 in BR) directly hydrogen bond with each other²⁶ (Fig. 2a), and that this interaction may function as the molecular switch to direct transition to the conducting state. However, in the present C1C2 structure, the distances between the thiol group of Cys 167 and the carboxyl oxygen atoms of Asp 195 are 4.4 Å and 4.6 Å, respectively, and the thiol group of Cys 167 is not associated with Asp 195, but with the π -electron system in the retinal molecule (Fig. 2a).

In BR, a water molecule receives a proton from the protonated Schiff base and donates a proton to Asp 85 (ref. 27; Fig. 3b); this arrangement is conserved in C1C2. However, in C1C2 the distances from the protonated Schiff base are 4.4 Å, 3.4 Å and 3.0 Å respectively for the water molecule, Glu 162 (123) (Asp 85 in BR) and Asp 292 (253) (Asp 212 in BR) (Fig. 3a, b). Therefore, in C1C2, Asp 292 or

possibly Glu 162, but not the water located between them, may directly receive a proton from the protonated Schiff base. In BR, Asp 212 retains a low pK_a because it is hydrogen bonded to Tyr 57 and Tyr 185, which do not move during the photocycle (Fig. 3b). On the other hand, in C1C2, Tyr 57 and Tyr 185 are substituted with Phe 133 and Phe 265, and Asp 292 only forms a hydrogen bond with water (Fig. 3a); thus Asp 292 could move relatively freely in the photocycle. Therefore in C1C2, the pK_a of Asp 292 can change, in contrast to the corresponding residue in BR. Moreover, the pK_a values of Glu 162 and Asp 292, calculated using PROPKA²⁸ (Supplementary Table 2), showed that Glu 162 may be protonated and Asp 292 may be deprotonated in our structure. Thus, we suggest that Asp 292, rather than Glu 162, is the primary proton acceptor in C1C2, consistent with the finding that Glu 123 mutants show current amplitudes similar to wild type^{13,17}. To verify further this notion, we expressed the E162A and D292A mutants of C1C2 in HEK293 cells, and recorded photocurrents in response to 465-nm light pulses (Fig. 3c, d and Supplementary Figs 7 and 8), revealing that replacement of Glu 162 by alanine resulted in moderately decreased currents, whereas the substitution of Asp 292 by alanine almost completely abolished photocurrents despite robust membrane expression. Moreover, the onset time constant (τ_{ON}) of the D292A mutant was significantly larger than that of wild type (Supplementary Fig. 9), consistent with the structure showing that Asp 292, rather than Glu 162, may be the major proton acceptor from the protonated Schiff base in ChR.

Electronegative pore framed by four TM helices

We calculated the electrostatic surface potential of C1C2, which revealed an electronegative pore formed by TM1, 2, 3 and 7 (Fig. 4a). In this pathway, a number of negatively charged residues, including Glu 129 (90), Glu 136 (97) and Glu 140 (101), as well as Glu 162 (123) and Asp 292 (253), are aligned along the pore (Fig. 4b). Because most of the negatively charged residues are derived

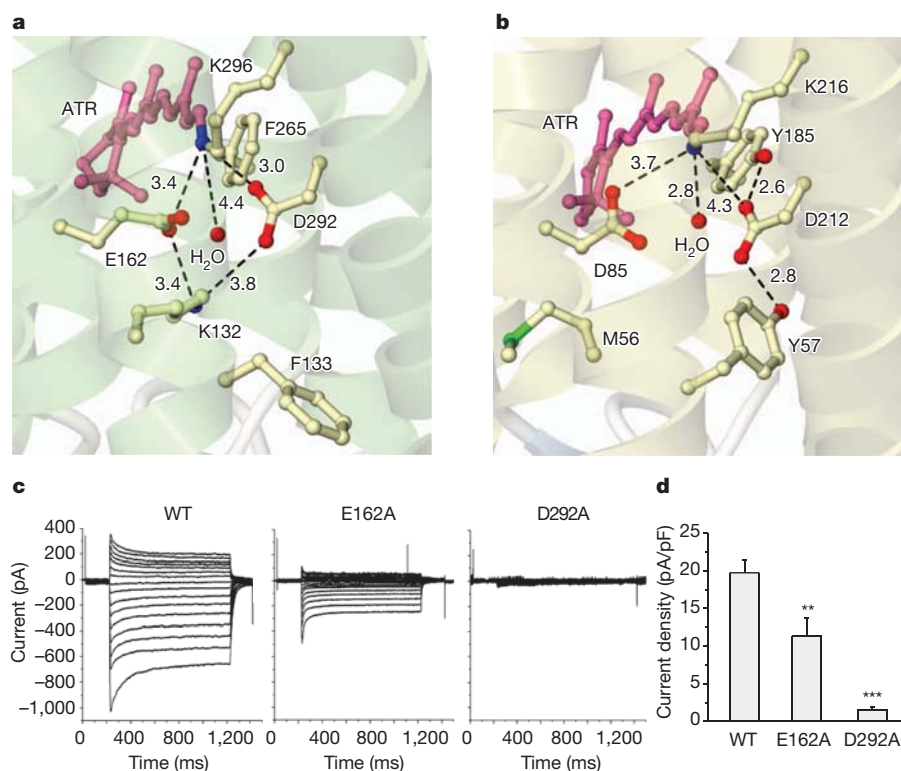


Figure 3 | The protonated Schiff base and its counterions in C1C2 and BR. **a**, **b**, Structures of the environment around the Schiff base in C1C2 (**a**) and BR (**b**). Numbers indicate the distance between two atoms connected by dashed lines. **c**, Effects of the mutation of two possible counterions on the

photocurrent. Photocurrents on C1C2-expressing HEK293 cells were measured at 16 different holding potentials. WT, wild type. **d**, The peak amplitudes of the photocurrents, normalized by the cell's input capacitance. Values are means and s.e.m. of 7–15 experiments. ** $P < 0.01$, *** $P < 0.001$.

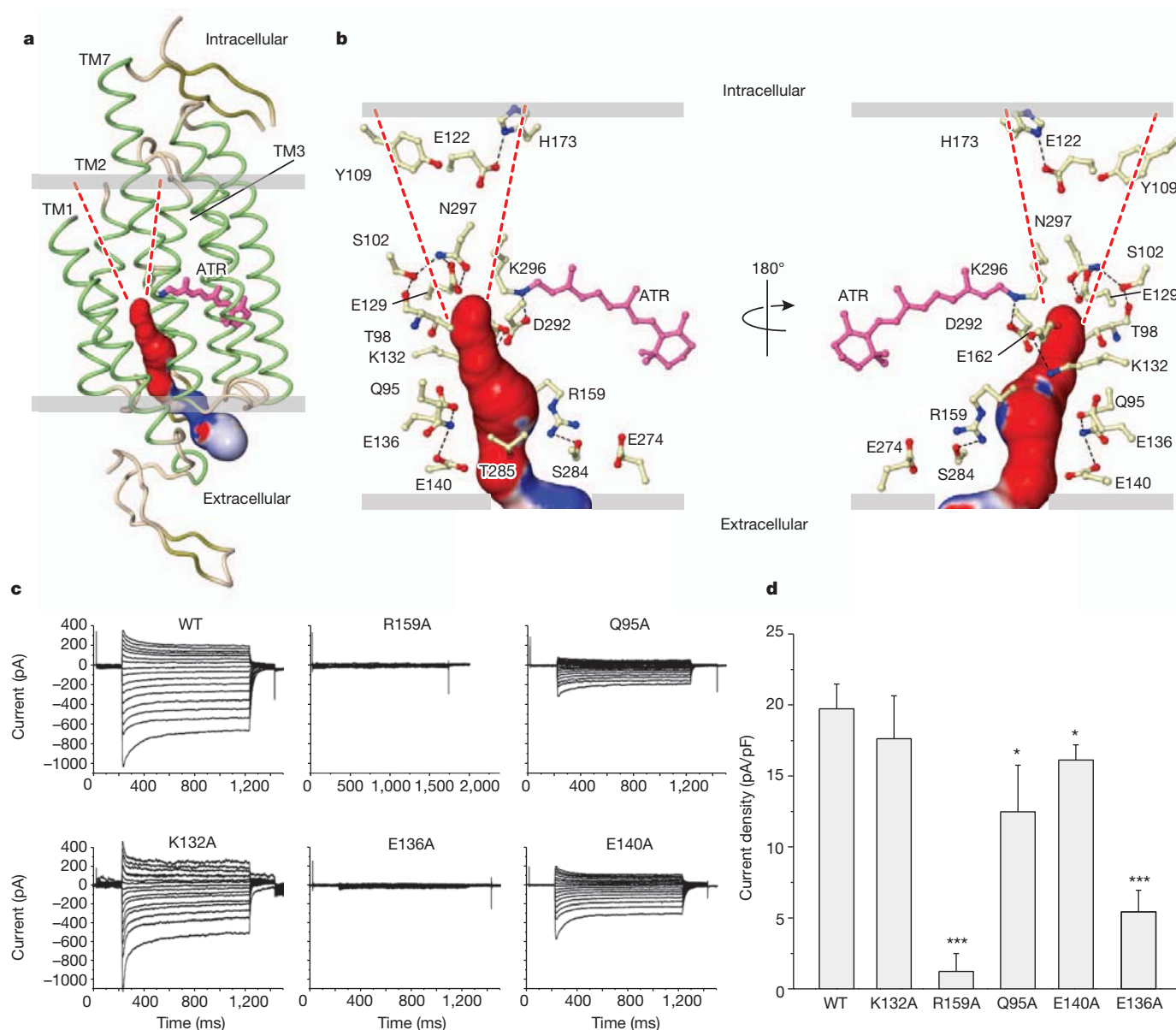


Figure 4 | Cation-conducting pathway formed by TM1, 2, 3 and 7. **a**, Pore-lining surface calculated by the CAVER³⁷ program, coloured by the electrostatic potential. Dashed red lines indicate putative intracellular vestibules. **b**, Close-up views of the surface of the pore, with the 17 polar lining residues (subtract 39 from the C1C2 residue number to obtain Chr2 numbering). Hydrogen bonds

are shown as black dashed lines. **c**, Photocurrents of mutants of the five residues within the pathway, measured under the same conditions as in Fig. 3c. **d**, The peak amplitudes of the photocurrents, as in Fig. 3d. * $P < 0.05$, *** $P < 0.001$. Error bars represent s.e.m.

from TM2, we suggest that the ion conductance and selectivity of C1C2 are mainly defined by TM2.

On the extracellular side of the pore, a vestibule formed by the N domain and ECL1–3 opens up to a diameter of about 8 Å, where Lys 154 (115), Lys 209 (170) and Arg 213 (174) form a slightly electropositive surface around the vestibule (Supplementary Fig. 10). Deeper within the vestibule, Arg 159 (120), Tyr 160 (121), Glu 274 (235) and Ser 284 (245) form a weak electronegative surface and fix the positions of TM3, 6 and 7 by a water-mediated hydrogen-bond network (Supplementary Fig. 11a). As these four residues are highly conserved not only in ChRs but also in BRs (Arg 82, Tyr 83, Glu 194 and Glu 204, respectively), and the corresponding residues in BR reportedly have an important role in proton pumping, we generated the R159A mutant in C1C2. We found that this mutant did not produce a photocurrent despite robust membrane expression (Fig. 4c, d and Supplementary Figs 7 and 8); because the orientation of Arg 159 is quite different from the corresponding Arg residue in

BR, and these residues form the extracellular hydrophilic surface, we suggest that this conserved cluster has an important role in creation of the extracellular vestibule, rather than in proton movement as in BR (Supplementary Fig. 11b).

In the middle of the pore, 12 polar residues (Gln 95 (56), Thr 98 (59), Ser 102 (63), Glu 122 (83), Glu 129 (90), Lys 132 (93), Glu 136 (97), Glu 140 (101), Glu 162 (123), Thr 285 (246), Asp 292 (253) and Asn 297 (258)) form a hydrophilic and strongly electronegative surface (Fig. 4b). To investigate contributions to ChR function, we measured photocurrents, kinetics and selectivity for four mutants (Q95A, K132A, E136A, E140A) (Fig. 4c, d and Supplementary Figs 7–9 and 12). The K132A mutant had faster kinetics and similar current amplitude relative to wild type, whereas the Q95A and E140A mutants exhibited moderately reduced currents, and the E136A mutant showed very little photocurrent, despite robust membrane expression. Three of the four mutants (Q95A, K132A and E136A) altered ion selectivity (Supplementary Fig. 12); therefore, we suggest that this

pore is important for cation conduction and that, as previously suggested²⁹, Glu 136 (97) is essential.

Although this putative cation-conducting pathway is opened towards the extracellular side, the cytoplasmic side of this pathway is occluded owing to two constrictions (Figs 4b and 5). The first constriction is formed by three highly conserved polar residues: Ser 102 (63), Glu 129 (90) and Asn 297 (258) (Figs 4b and 5a). In this constriction site, Ser 102, with a β -OH group that hydrogen bonds to the main-chain carbonyl oxygen of Thr 98, fixes the position of Asn 297 and, in turn, Asn 297 fixes Glu 129 by hydrogen bonds. Glu 129 protrudes into and occludes the pore. To analyse this putative channel gate, we prepared four mutants (S102D, E129A, E129Q and N297D) and measured photocurrents, kinetics and ion selectivity (Supplementary Figs 7–9, 12 and 13). We found that E129A, E129Q and N297D affect ion selectivity and S102D, E129Q and N297D affect channel kinetics (Supplementary Figs 9 and 12). These results, consistent with previous work^{30,31}, indicate the importance of these three residues and suggest that cations pass through this constriction site in the conducting state.

The second constriction is formed by the phenol group of Tyr 109 (70) (Figs 4b and 5b). Given the high *B*-factor of the C-terminal end of TM1 (Supplementary Fig. 14) and a previous Fourier transform infrared spectroscopy (FT-IR) study showing that the α -helices undergo conformational changes during the photocycle³², movement of the TM1 C-terminal end may open the pore exit formed between TM1, 2 and 7. As TM1 does not directly interact with the retinal chromophore, the signal of retinal isomerization is expected to be transmitted to TM1 via movements of TM2, 3 and/or 7. However, we cannot exclude the possibility that movements of TM2, 3 and/or 7 form a cytoplasmic vestibule next to Tyr 109, and further studies will be required to identify the pore exit.

Discussion

This first crystal structure of a light-gated cation channel in the closed/dark state at 2.3 Å resolution provides insight into ChR dimerization, retinal binding and cation conductance. Moreover, owing to the large N domain unique to ChR, it has been difficult to align precisely the ChR sequence with other microbial rhodopsins (notably BR), and the present structure-based alignment (Supplementary Fig. 4) will assist in the design and interpretation of functional analyses, including electrophysiological and spectroscopic studies of ChR at the molecular level.

The structural features around the ATR, Schiff base, and conduction pathway also provide insight into the blueshifted absorption spectrum of ChR ($\lambda_{\text{max}} = 470$ nm), as compared to that of BR ($\lambda_{\text{max}} = 568$ nm). In general, the maximum absorption wavelength of retinal proteins is

determined by the energy difference between ground (S_0) and excited (S_1) states, and this gap is mainly affected by the planarity of the conjugated system of the retinal chromophore, the distance between the protonated Schiff base and its counterion, and the interaction of the chromophore with polar or polarizable residues³³. Although the planarity of the ATR is unchanged between ChR and BR, the counterion of ChR, Asp 292, is located ~ 1 Å closer to the Schiff base than the corresponding Asp residue of BR (Fig. 3a, b), and the negatively charged residues are aligned along the conducting pathway (Fig. 4a, b). These environments are likely to stabilize the S_0 state of ChR, thus enlarging the energy gap between the S_0 and S_1 states and thereby causing the relative absorption spectrum blueshift.

Much about the photocycle remains unknown but is thought to be similar to that of BR^{31,34,35}, in which the essential early event is the dipole change of the protonated Schiff base, which alters the nitrogen pK_a by several orders of magnitude. In the case of ChRs, this may cause the release of the Schiff base proton to Asp 292 (probably not to either Glu 162 or water because Asp 292 is closer than these other two moieties, which also may explain why the D292A mutant is inactive; Fig. 3). The protonation of Asp 292 is likely to repel Lys 132 (93), as with Arg 82 in BR, and this movement may enlarge pore diameter and help cations to pass (Figs 3a and 4b). It is also thought that channel opening may be coupled with reprotonation of the Schiff base. Given the calculated pK_a (Supplementary Table 2) and the distance from the Schiff base nitrogen atom, we suggest two candidates for this proton donor—Glu 122 and Glu 129 (Supplementary Fig. 15)—but further studies, including structural determinations of photocycle intermediate states, will be required to refine our model.

In recent years, many strategies have been applied to create ChR variants with improved properties for optogenetics, ranging from designer ChR variants based on functional and structural similarities between BR and ChR (E123X, H134R, C128X, I131V, D156A, T159C, C1V1)^{6,13–15,17,19,36}, to chimaera construction along with mutagenesis (ChRGR, L132C, ChD, ChEF, C1V1)^{16–19} (Fig. 6a). These approaches have generated a number of ChR variants with useful properties, but the high-resolution crystal structure is a prerequisite for the design of ChR variants with ideal properties. The present crystal structure describes the environment around the retinal-binding pocket (Fig. 6a, b), which will enable optimized design of red- and blueshifted ChR variants. In addition, structure of the cation-conducting pathway may facilitate construction of ChR variants with improved photocurrents, photo-sensitivity, cation selectivity and kinetics. For example, K132A and Q95A show strong photocurrents and K^+ selectivity (Supplementary Figs 9 and 12), which could be useful to suppress neural activity.

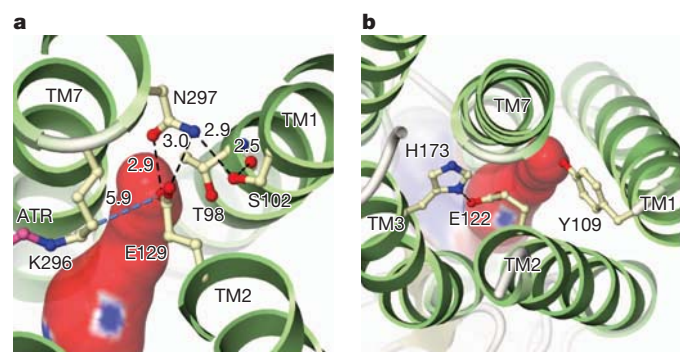


Figure 5 | Two constriction sites on the cytoplasmic side of C1C2 in the closed state. **a**, The first constriction site is formed by Ser 102 (63), Glu 129 (90) and Asn 297 (258). Hydrogen bonds are shown as black dashed lines. The blue dashed line represents a possible proton transfer pathway. **b**, The second constriction, made by Tyr 109. The cavity formed by TM1, 2 and 7 is occluded by Tyr 109, and the cavity formed by TM2, 3 and 7 is occluded by Glu 122 and His 173.

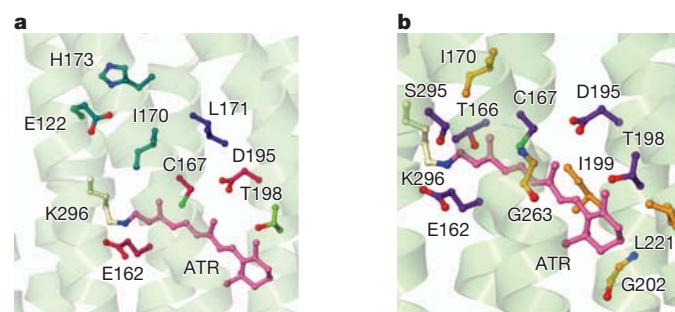


Figure 6 | Distribution of known mutations and possible candidates for future mutations. **a**, Mutations that affect both the absorption spectrum and the kinetics (Cys 167 (128), Glu 162 (123) and Asp 195 (156); deep red), the conductance (Thr 198 (159); light green), the selectivity (Leu 171 (132); dark blue) and the kinetics (Glu 122 (83), Ile 170 (131) and His 173 (134); dark cyan) of ChR2. **b**, Polar (Glu 162 (123), Thr 166 (127), Cys 167 (128), Asp 195 (156), Thr 198 (159) and Ser 295 (256); magenta) and non-polar (Ile 170 (131), Ile 199 (160), Gly 202 (163), Leu 221 (182) and Gly 263 (224); orange) residues surrounding ATR.

To understand the photocycle in more detail, further structural studies, including determination of crystal structures in intermediate states, are clearly needed. However, the present structural information represents a key step in enabling the principled design of ChR variants with new properties, and will accelerate both applications of optogenetics to intact-systems biology, and basic mechanistic understanding of these remarkable photoreceptor proteins.

METHODS SUMMARY

C1C2 was cloned into cleavable enhanced green fluorescent protein (EGFP)-His₆ fusion pFastBac1 vector. The fusion protein was expressed in insect cells, solubilized in 2.5% (w/v) *n*-dodecyl- β -D-maltoside (DDM) and 0.5% (w/v) cholesteryl hemisuccinate, and purified by nickel affinity chromatography. After that, the C-terminal EGFP was cleaved by His-tagged tobacco etch virus (TEV) protease (homemade). Then the sample mixture was passed through Ni-NTA resin again to remove the cleaved His-tagged EGFP and TEV protease. The sample was further purified by size-exclusion chromatography. Crystals were grown in a lipidic cubic phase using monoolein. Diffraction data were measured at beamline X06SA of the Swiss Light Source and at beamline BL32XU of SPring-8. The structure was solved by the MAD method using mercury derivative. Data collection and refinement statistics are presented in Supplementary Table 1. Electrophysiological recordings were conducted using patch-clamp on HEK293 cells expressing the wild-type and mutant C1C2.

Full Methods and any associated references are available in the online version of the paper at www.nature.com/nature.

Received 28 October 2011; accepted 3 January 2012.

Published online 22 January 2012.

- Oesterhelt, D. & Stoekenius, W. Rhodopsin-like protein from the purple membrane of *Halobacterium halobium*. *Nat. New Biol.* **233**, 149–152 (1971).
- Matsuno-Yagi, A. & Mukohata, Y. Two possible roles of bacteriorhodopsin; a comparative study of strains of *Halobacterium halobium* differing in pigmentation. *Biochem. Biophys. Res. Commun.* **78**, 237–243 (1977).
- Nagel, G. *et al.* Channelrhodopsin-1: a light-gated proton channel in green algae. *Science* **296**, 2395–2398 (2002).
- Boyden, E. S., Zhang, F., Bamberg, E., Nagel, G. & Deisseroth, K. Millisecond-timescale, genetically targeted optical control of neural activity. *Nature Neurosci.* **8**, 1263–1268 (2005).
- Li, X. *et al.* Fast noninvasive activation and inhibition of neural and network activity by vertebrate rhodopsin and green algae channelrhodopsin. *Proc. Natl Acad. Sci. USA* **102**, 17816–17821 (2005).
- Nagel, G. *et al.* Light activation of channelrhodopsin-2 in excitable cells of *Caenorhabditis elegans* triggers rapid behavioral responses. *Curr. Biol.* **15**, 2279–2284 (2005).
- Ishizuka, T., Kakuda, M., Araki, R. & Yawo, H. Kinetic evaluation of photosensitivity in genetically engineered neurons expressing green algae light-gated channels. *Neurosci. Res.* **54**, 85–94 (2006).
- Bi, A. *et al.* Ectopic expression of a microbial-type rhodopsin restores visual responses in mice with photoreceptor degeneration. *Neuron* **50**, 23–33 (2006).
- Zhang, F., Wang, L. P., Boyden, E. S. & Deisseroth, K. Channelrhodopsin-2 and optical control of excitable cells. *Nature Methods* **3**, 785–792 (2006).
- Yizhar, O., Fenno, L. E., Davidson, T. J., Mogri, M. & Deisseroth, K. Optogenetics in neural systems. *Neuron* **71**, 9–34 (2011).
- Fenno, L., Yizhar, O. & Deisseroth, K. The development and application of optogenetics. *Annu. Rev. Neurosci.* **34**, 389–412 (2011).
- Muller, M., Bamann, C., Bamberg, E. & Kuhlbrandt, W. Projection structure of channelrhodopsin-2 at 6 Å resolution by electron crystallography. *J. Mol. Biol.* **414**, 86–95 (2011).
- Gunaydin, L. A. *et al.* Ultrafast optogenetic control. *Nature Neurosci.* **13**, 387–392 (2010).
- Berndt, A., Yizhar, O., Gunaydin, L. A., Hegemann, P. & Deisseroth, K. Bi-stable neural state switches. *Nature Neurosci.* **12**, 229–234 (2009).
- Berndt, A. *et al.* High-efficiency channelrhodopsins for fast neuronal stimulation at low light levels. *Proc. Natl Acad. Sci. USA* **108**, 7595–7600 (2011).
- Kleinlogel, S. *et al.* Ultra light-sensitive and fast neuronal activation with the Ca²⁺-permeable channelrhodopsin CatCh. *Nature Neurosci.* **14**, 513–518 (2011).
- Yizhar, O. *et al.* Neocortical excitation/inhibition balance in information processing and social dysfunction. *Nature* **477**, 171–178 (2011).
- Wen, L. *et al.* Opto-current-clamp actuation of cortical neurons using a strategically designed channelrhodopsin. *PLoS ONE* **5**, e12893 (2010).
- Lin, J. Y., Lin, M. Z., Steinbach, P. & Tsien, R. Y. Characterization of engineered channelrhodopsin variants with improved properties and kinetics. *Biophys. J.* **96**, 1803–1814 (2009).

- Wang, H. *et al.* Molecular determinants differentiating photocurrent properties of two channelrhodopsins from *Chlamydomonas*. *J. Biol. Chem.* **284**, 5685–5696 (2009).
- Kawate, T. & Gouaux, E. Fluorescence-detection size-exclusion chromatography for precrystallization screening of integral membrane proteins. *Structure* **14**, 673–681 (2006).
- Tsunoda, S. P. & Hegemann, P. Glu 87 of channelrhodopsin-1 causes pH-dependent color tuning and fast photocurrent inactivation. *Photochem. Photobiol.* **85**, 564–569 (2009).
- Matsui, Y. *et al.* Specific damage induced by X-ray radiation and structural changes in the primary photoreaction of bacteriorhodopsin. *J. Mol. Biol.* **324**, 469–481 (2002).
- Stenkamp, R. E. Alternative models for two crystal structures of bovine rhodopsin. *Acta Crystallogr. D* **64**, 902–904 (2008).
- Mittelmeier, T. M., Boyd, J. S., Lamb, M. R. & Dieckmann, C. L. Asymmetric properties of the *Chlamydomonas reinhardtii* cytoskeleton direct rhodopsin photoreceptor localization. *J. Cell Biol.* **193**, 741–753 (2011).
- Nack, M. *et al.* The DC gate in Channelrhodopsin-2: crucial hydrogen bonding interaction between C128 and D156. *Photochem. Photobiol. Sci.* **9**, 194–198 (2010).
- Lanyi, J. K. Proton transfers in the bacteriorhodopsin photocycle. *Biochim. Biophys. Acta* **1757**, 1012–1018 (2006).
- Bas, D. C., Rogers, D. M. & Jensen, J. H. Very fast prediction and rationalization of pK_a values for protein-ligand complexes. *Proteins* **73**, 765–783 (2008).
- Sugiyama, Y. *et al.* Photocurrent attenuation by a single polar-to-nonpolar point mutation of channelrhodopsin-2. *Photochem. Photobiol. Sci.* **8**, 328–336 (2009).
- Ruffert, K. *et al.* Glutamate residue 90 in the predicted transmembrane domain 2 is crucial for cation flux through channelrhodopsin 2. *Biochem. Biophys. Res. Commun.* **410**, 737–743 (2011).
- Piazza, A. P. *et al.* Bioinformatic and mutational analysis of channelrhodopsin-2 cation conducting pathway. *J. Biol. Chem.* <http://dx.doi.org/10.1074/jbc.M111.326207> (2011).
- Radu, I. *et al.* Conformational changes of channelrhodopsin-2. *J. Am. Chem. Soc.* **131**, 7313–7319 (2009).
- Lasogga, L., Rettig, W., Otto, H., Wallat, I. & Bricks, J. Model systems for the investigation of the opsin shift in bacteriorhodopsin. *J. Phys. Chem. A* **114**, 2179–2188 (2010).
- Ritter, E., Stehfest, K., Berndt, A., Hegemann, P. & Bartl, F. J. Monitoring light-induced structural changes of Channelrhodopsin-2 by UV-visible and Fourier transform infrared spectroscopy. *J. Biol. Chem.* **283**, 35033–35041 (2008).
- Bamann, C., Kirsch, T., Nagel, G. & Bamberg, E. Spectral characteristics of the photocycle of channelrhodopsin-2 and its implication for channel function. *J. Mol. Biol.* **375**, 686–694 (2008).
- Bamann, C., Gueta, R., Kleinlogel, S., Nagel, G. & Bamberg, E. Structural guidance of the photocycle of channelrhodopsin-2 by an interhelical hydrogen bond. *Biochemistry* **49**, 267–278 (2010).
- Petrík, M. *et al.* CAVER: a new tool to explore routes from protein clefts, pockets and cavities. *BMC Bioinformatics* **7**, 316 (2006).

Supplementary Information is linked to the online version of the paper at www.nature.com/nature.

Acknowledgements We thank Y. Tanaka, T. Higuchi, M. Hattori and H. Nishimasu for useful discussions; T. Hino for technical support; and the beamline staff members at BL32XU of SPring-8 (Hyogo, Japan) and at X06SA of the Swiss Light Source (Villigen, Switzerland) for technical help during data collection. This work was supported by the Japan Society for the Promotion of Science (JSPS) through its “Funding Program for World-Leading Innovative R&D on Science and Technology (FIRST program)” to O.N., by a grant for the National Project on Protein Structural and Functional Analyses from the Ministry of Education, Culture, Sports, Science and Technology (MEXT) to O.N., and by a Grant-in-Aid for Scientific Research (S) from MEXT to O.N. F.Z. is supported by the McKnight Foundation. K.D. is supported by the Gatsby Charitable Foundation and the Keck, Snyder, Woo, and Yu Foundations, as well as by the National Institutes of Health, and the Defense Advanced Research Project Agency Reorganization and Plasticity to Accelerate Injury Recovery (DARPA REPAIR) program.

Author Contributions H.E.K. performed the structural determination of C1C2, prepared the mutants, measured the spectral property of C1C2 and wrote the paper. A.D.M. performed the electrophysiological analyses of C1C2. J.I. helped A.D.M. to take pictures of C1C2 and to determine membrane expression. Y.A. helped A.D.M. to perform patch-clamp experiments. T.T., T.N., R.I. and O.N. assisted with the structural determination. K.H. assisted with the data collection of C1C2. O.N., F.Z. and K.D. conceived the study; F.Z., O.Y. and K.D. helped to organize the project; S.H. and P.H. provided input on structural considerations; and C.R. with K.D. constructed the final C1C2 that enabled crystal structure determination. All authors discussed the results and commented on the manuscript. O.N. and K.D. supervised all aspects of the work and wrote/edited the manuscript.

Author Information Data have been deposited at the Protein Data Bank under accession number 3UG9. Reprints and permissions information is available at www.nature.com/reprints. The authors declare no competing financial interests. Readers are welcome to comment on the online version of this article at www.nature.com/nature. Correspondence and requests for materials should be addressed to O.N. (nureki@biochem.s.u-tokyo.ac.jp) or K.D. (deissero@stanford.edu).

METHODS

Expression and purification of C1C2. Chimaeras between ChR1 and ChR2 from *C. reinhardtii* and other algal species were subcloned into the pCGFP-EU vector²¹ for expression in HEK293 cells. The tobacco etch virus (TEV) protease cleavage site, the coding sequence of enhanced GFP (EGFP), and the octa-histidine tag (EGFP-His₈) were introduced at the C terminus of the chimaeric constructs. All constructs were screened by FSEC analysis²¹. The gene encoding the best chimaera (C1C2) was subcloned into the modified pFastBac1 vector for expression in Sf+ insect cells. Baculovirus-infected Sf+ cells were cultured in Sf900II (Invitrogen) at 27 °C for 24 h, and then the temperature was reduced to 20 °C. Cells were harvested 72 h after infection by centrifugation at 6,000g for 10 min. The pellets were disrupted by two passages through a microfluidizer at 15,000 pounds per square inch, and were resuspended in a buffer containing 300 mM NaCl, 50 mM Tris-HCl, pH 8.0, 5% glycerol and 0.1 mM phenylmethylsulfonyl fluoride (PMSF). The cell debris was cleared by centrifugation at 10,000g for 40 min, and the crude membrane fraction was collected by ultracentrifugation (Ti45 rotor, 43,000 r.p.m., 1 h). This fraction was solubilized in a buffer containing 300 mM NaCl, 50 mM Tris-HCl, pH 8.0, 5% glycerol, 20 mM imidazole, 0.1 mM PMSF, 2.5% *n*-dodecyl- β -D-maltoside (DDM) and 0.5% cholesteryl hemisuccinate (CHS). The insoluble material was removed by ultracentrifugation (Ti70 rotor, 45,000 r.p.m., 30 min), and the supernatant was mixed with Ni-NTA resin (QIAGEN). After binding for 1 h, C1C2 was eluted in buffer supplemented with 300 mM imidazole. Following the cleavage of EGFP-His₈ by His-tagged TEV protease (homemade), the sample was reloaded onto the Ni-NTA column to remove the cleaved EGFP-His₈. The flow-through containing C1C2 was collected, concentrated, and further purified by size-exclusion chromatography in 150 mM NaCl, 50 mM Tris-HCl, pH 8.0, 5% glycerol, 0.05% DDM and 0.01% CHS. Peak fractions were pooled and concentrated to $\sim 10 \text{ mg ml}^{-1}$ for crystallization. For the mercury derivative, the concentrated protein was incubated with a sixfold molar excess of methyl mercury chloride at 20 °C for 1 h. The derivative was ultracentrifuged and used for crystallization experiments.

Crystallization. C1C2 was mixed with monoolein (Sigma) in a 2:3 protein to lipid ratio (w/w). Aliquots (100 nl) of the protein-LCP mixture were spotted on a 96-well sandwich plate and overlaid by 1 μl of precipitant solution by the crystallization robot, mosquito LCP (TTP LabTech). Native crystals were obtained in 30–34% (w/v) PEG500DME, 100 mM Na citrate, pH 6.0, 100 mM MgCl₂, 100 mM NaCl and 100 mM (NH₄)₂SO₄, whereas the derivative crystals were grown in 31% (w/v) PEG500DME, 100 mM HEPES-NaOH, pH 7.0, 200 mM Li₂SO₄ and 10 mM ATP. All crystals were incubated for 2–3 weeks in the dark. They were harvested using micromounts (MiTeGen), and were flash-cooled in liquid nitrogen without any additional cryoprotectant.

Structure determination. X-ray diffraction data sets for the native and mercury-derivatized protein crystals were collected on beamline X06SA at SLS and beamline BL32XU at SPring-8, using a 1- μm -wide, 15- μm -high microbeam³⁸. Data were indexed and scaled with the programs XDS³⁹ and SCALA⁴⁰, or with DENZO and SCALEPACK from the HKL2000 program suite (HKL Research). Experimental phases were determined by the MAD method, using the four Hg sites identified with the program SHELX⁴¹. Subsequent refinements of the heavy atom parameters and phase calculations were performed with the program SHARP⁴². The data collection and phasing statistics are shown in Supplementary Table 1. The initial model structure of C1C2 was built with the program Phyre⁴³, using the *Anabaena* sensory rhodopsin structure (PDB accession 1XIO) as the template. The resultant structure was manually modified to fit into the experimental electron density maps, using the program Coot⁴⁴. The structure was

then refined with the program Phenix⁴⁵. Figures were prepared with Cuemol (<http://www.cuemol.org>).

Electrophysiology. HEK293 cells were cultured on poly-lysine-coated, glass-bottom culture dishes (Matsunami), and were transfected with 0.5 μg of a plasmid construct containing the GFP-tagged C1C2 or the GFP-tagged C1C2 mutants. At 24–30 h after transfection, the cells were placed in a bath medium, containing 140 mM NaCl, 1 mM CaCl₂, 2 mM MgCl₂, 10 mM HEPES and 5 mM glucose (pH 7.4 with NaOH), under an inverted microscope (Olympus IX71). Calcium and potassium photocurrents were measured by replacing 140 mM NaCl by 90 mM CaCl₂ or 140 mM KCl accordingly. For proton photocurrents, cell bath was 5 mM NaCl, 135 mM *N*-methyl-D-glucamine, 1 mM CaCl₂, 2 mM MgCl₂, 10 mM HEPES and 5 mM glucose (pH 6.4). A borosilicate patch pipette (Harvard Apparatus), with a resistance of about 5–8 M Ω , was filled with 140 mM KCl, 5 mM EGTA, 2 mM MgCl₂ and 10 mM HEPES (pH 7.2 with KOH). C1C2 currents were recorded in the voltage-clamp mode and in the whole-cell configuration. The cells were held at a membrane potential of -80 mV , and were depolarized by 10 mV voltage steps of 1.8 s up to $+70 \text{ mV}$. The light-dependent currents were activated 200 ms after the depolarization step, with 465 nm light (1.5 mW mm^{-2}) for 1,000 ms, elicited by a high power LED illumination system (LEX2-B, Brainvision) connected to an A/D converter (Digidata 1440, Axon CNS, Molecular Devices), controlled by the pClamp10 software (Axon CNS). The light power was 1.5 mW mm^{-2} . Currents were measured using an Axopatch 200B amplifier (Axon CNS, Molecular Devices), filtered at 2 KHz, and sampled at 5 KHz, using a Digidata 1440A digitizer (Axon CNS) controlled by the pClamp10 software (Axon CNS).

Fluorescence measurements. The cells were transfected with 0.5 μg wild-type C1C2 or C1C2 mutants, using Eugene 6, for 30 h. The cells were then washed with PBS and fixed with 4% paraformaldehyde in PBS for 20 min at room temperature (20 °C), and washed again with PBS before microscopy observation. GFP fluorescence was observed with a laser confocal microscope (FV1000 Olympus). To estimate membrane expression of C1C2 and its mutants, the ratio between the membrane fluorescence and cytosolic were determined.

Ultraviolet/visible spectroscopy. Ultraviolet/visible absorption spectra were recorded with an Ultrospec 3300 pro ultraviolet/visible spectrophotometer (Amersham Biosciences) by use of 1-cm quartz cuvettes. Freshly prepared C1C2 was used for the measurements. pH was adjusted by addition of 100 volumes of buffer solution yielding final concentrations of 50 mM Na citrate, pH 4.0, 50 mM Na acetate, pH 5.0, 50 mM Na cacodylate, pH 6.0, 50 mM HEPES, pH 7.0, 50 mM Tris, pH 8.0 and 9.0, or 50 mM CAPS, pH 10.0, plus 150 mM NaCl, 5% glycerol, 0.05% DDM and 0.01% CHS.

38. Hirata, K. *et al.* New micro-beam beamline at SPring-8, targeting at protein microcrystallography. *AIP Conference Proceedings* **1234**, 893–896 (2010).
39. Kabsch, W. XDS. *Acta Crystallogr. D* **66**, 125–132 (2010).
40. Evans, P. Scaling and assessment of data quality. *Acta Crystallogr. D* **62**, 72–82 (2006).
41. Schneider, T. R. & Sheldrick, G. M. Substructure solution with SHELXD. *Acta Crystallogr. D* **58**, 1772–1779 (2002).
42. de La Fortelle, E. & Bricogne, G. Maximumlikelihood heavy-atom parameter refinement for multiple isomorphous replacement and multiwavelength anomalous diffraction methods. *Methods Enzymol.* **276**, 472–494 (1997).
43. Kelley, L. A. & Sternberg, M. J. Protein structure prediction on the Web: a case study using the Phyre server. *Nature Protocols* **4**, 363–371 (2009).
44. Emsley, P., Lohkamp, B., Scott, W. G. & Cowtan, K. Features and development of Coot. *Acta Crystallogr. D* **66**, 486–501 (2010).
45. Adams, P. D. *et al.* PHENIX: a comprehensive Python-based system for macromolecular structure solution. *Acta Crystallogr. D* **66**, 213–221 (2010).

Flu transmission work is urgent

Yoshihiro Kawaoka explains that research on transmissible avian flu viruses needs to continue if pandemics are to be prevented.

Highly pathogenic avian H5N1 influenza viruses first proved lethal in humans in 1997 in Hong Kong. Since 2003, 578 confirmed infections have resulted in 340 deaths (go.nature.com/epb7ts). Now widespread in parts of south-east Asia and the Middle East, H5N1 viruses have killed or led to the culling of hundreds of millions of birds.

To date, H5N1 viruses have not been transmitted between humans. Some experts have argued that it is impossible. But given the potential consequences of a global outbreak, it is crucial to know whether these viruses can ever become transmissible. Work by my group (accepted by *Nature*) and an independent study (accepted by *Science*) led by Ron Fouchier of the Erasmus Medical Center in Rotterdam, the Netherlands, suggest that H5N1 viruses have the potential to spread between mammals. As the risks of such research and its publication are debated by the community, I argue that we should pursue transmission studies of highly pathogenic avian influenza viruses with urgency.

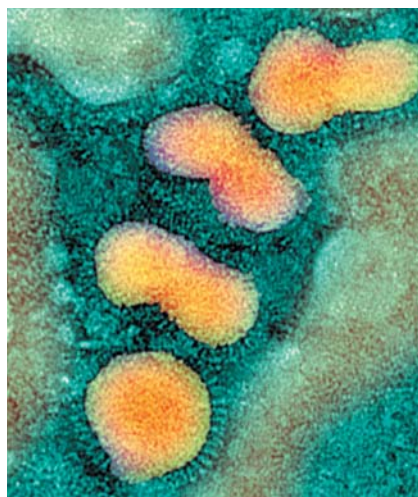
To determine whether H5N1 viruses could be transmitted between humans, my team generated viruses that combined the H5 haemagglutinin (HA) gene with the remaining genes from a pandemic 2009 H1N1 influenza virus. Avian H5N1 and human pandemic 2009 viruses readily exchange genes in experimental settings, and those from a human virus may facilitate replication in mammals. Indeed, we identified a mutant H5 HA/2009 virus that spread between infected and uninfected ferrets (used as models to study the transmission of influenza in mammals) in separate cages via respiratory droplets in the air. Thus viruses possessing an H5 HA protein can transmit between mammals.

Our results also show that not all transmissible H5 HA-possessing viruses are lethal. In ferrets, our mutant H5 HA/2009 virus was no more pathogenic than the pandemic 2009 virus — it did not kill any of the infected animals. And, importantly, current vaccines and antiviral compounds are effective against it.

Fouchier and his team also generated a transmissible H5 HA-possessing virus — meaning that two independent studies have demonstrated the potential for transmissibility of H5 HA-possessing viruses between ferrets. Their mutant H5 HA virus, generated in the genetic background of an H5N1 virus, did kill infected ferrets.

Some people have argued that the risks

of such studies — misuse and accidental release, for example — outweigh the benefits. I counter that H5N1 viruses circulating in nature already pose a threat, because influenza viruses mutate constantly and can cause pandemics with great losses of life. Within the past century, 'Spanish' influenza, which stemmed from a virus of avian origin, killed between 20 million and 50 million people. Because H5N1 mutations that confer transmissibility in mammals may emerge in nature, I believe that it would be irresponsible not to study the underlying mechanisms.



H5N1 avian influenza virus particles.

The new work has implications for pandemic preparedness. There is an urgent need to expand development, production and distribution of vaccines against H5 viruses, and to stockpile antiviral compounds. Both studies identify specific mutations in HA that confer transmissibility in ferrets to H5 HA-possessing viruses. A subset of these mutations has been detected in H5N1 viruses circulating in certain countries. It is therefore imperative that these viruses are monitored closely so that eradication efforts and countermeasures (such as vaccine-strain selection) can be focused on them, should they acquire transmissibility.

Consequently, I believe that the benefits of these studies — the knowledge that H5 HA-possessing viruses pose a risk and the ability to monitor them and develop countermeasures — outweigh the risks. High biosafety and security standards can be met. Our experiments were carried out in a high-containment facility by a small group of highly trained individuals who

operate under strict procedures to prevent the accidental release of viruses.

However, the US National Science Advisory Board for Biosecurity (NSABB) has recommended that details of both studies (including the mutations that confer transmissibility) should be restricted, and released only to select individuals on a 'need-to-know' basis. I acknowledge the advisory role of the NSABB, but I do not concur with its decision.

The primary justification for the NSABB's recommendation is that publication of our data "could enable replication of the experiments by those who would seek to do harm" (go.nature.com/nywkdy). But redacting our papers will not eliminate that possibility — there is already enough information publicly available to allow someone to make a transmissible H5 HA-possessing virus.

The mechanism that the US government proposes for releasing data would also be unwieldy. Thousands of applications to access the research are likely to be filed, and potential background checks would create a huge administrative burden. We cannot afford to lose time if we are to combat emerging pandemic threats. Even if an efficient process can be established, it would be difficult to enforce continued confidentiality in the scientific community.

By contrast, wide data dissemination will attract researchers from other areas to contribute to the field. This is crucial, because new ideas are needed to answer some of the most urgent questions. For example, the specific mutations that we identified suggest that influenza transmission is more complex than anticipated and involves not only the receptor-binding properties of HA, but other biological and physical properties.

The redaction of our manuscript, intended to contain risk, will make it harder for legitimate scientists to get this information while failing to provide a barrier to those who would do harm. To find better solutions to dual-use concerns, the international community should convene to discuss how to minimize risk while supporting scientific discovery. Flu investigators (including me) have agreed to a 60-day moratorium on avian flu transmission research (go.nature.com/ttivj5) because of the current controversy. But our work remains urgent — we cannot give up. ■

Yoshihiro Kawaoka is at the University of Tokyo and the University of Wisconsin-Madison, Madison, Wisconsin 53706, USA. e-mail: kawaokay@svm.vetmed.wisc.edu